XIX International Congress of the Mexican Hydrogen Society

Sociedad Mexicana del Hidrógeno A.C.

Instituto de Investigaciones en Materiales

Proceedings of the XIX International Congress of the Mexican Hydrogen Society

Morelia, Michoacán

01-04 October 2019

In Honor to Dr. Arturo Fernandez Madrigal

ISSN-2448-7120 Año 6 Número 6, 2019

UNAM POSGRADO Ciencia e Ingeniería de Materiales

MICHOACÁN Celebra la vida

Anton Paar

SAIDE

Princeton Applied Research

solartron analytical

Edited by Dr. Karina Suarez Alcantara
KSA thanks to Materials Institute Research- UNAM-DGAPA-PAPPIT IN202719 *Estudio sistemático de alanatos de metales de transición; síntesis y caracterización)*

INFORMACIÓN LEGAL PROCEEDINGS OF THE INTERNATIONAL CONGRESS OF THE MEXICAN HYDROGEN SOCIETY DERECHOS DE AUTOR Y DERECHOS CONEXOS, **Año 6, No. 6, 2019,** es una publicación anual editada por la Sociedad Mexicana del Hidrogeno A. C., Calle Monte Bello No. 108, Col. Colinas del Padre, C.P. 98085, Zacatecas, Zacatecas, México, Teléfono (614) 4394815, Editor responsable: Alejandro López Ortiz., ISSN: 2448-7120, otorgado por el Instituto Nacional del Derecho de Autor. Responsable de la última actualización de este Número, Dr. Alejandro López Ortiz, Cordillera de Guanacaste, 6435, Frac. Cordilleras, C.P. 31124, Chihuahua, Chihuahua, México, teléfono (614) 4394815, correo electrónico lalejan@gmail.com, fecha de última modificación, 8 de Septiembre 2016. Las opiniones expresadas por los autores no necesariamente reflejan la postura del editor de la publicación. Queda prohibida la reproducción total o parcial de, los contenidos e imágenes de la publicación sin previa autorización de la Sociedad Mexicana del Hidrogeno A. C.

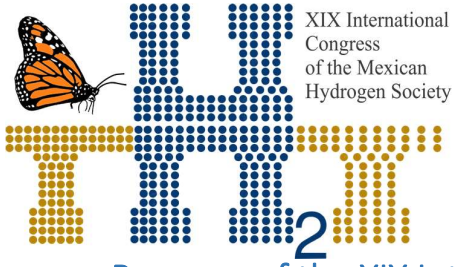

Program of the XIX International Congress of the Mexican Hydrogen Society

Time	Tuesday 01.10.2019			Wednesday 02.10.2019			Thursday 03.10.2019			Friday 04.10.2019		
08:00-08:30	Morelia City Center to UNAM transport											
08:30-09:00	Registration											
09:00-09:20	Pre-Congress course 1, part 1	Pre-Congress course 2, part 1.	Pre-Congress course 3, part 1	Opening (09:00-09:30)			005	011	031	009	017	085
09:20-09:40				Prof. Dr. Arturo Fernandez Madrigal Semblance (09:30-10:00)			008	034	045	023	048	083
09:40-10:00							021	035	071	024	074	077
10:00-10:20				Plenary Conference 1			067	038	096	Plenary Conference 3		
10:20-10:40							076	041	100			
10:40-11:00							084	050	113			
11:00-11:20	Coffee break											
11:20-11:40	Pre-Congress course 1, part 2	Pre-Congress course 2, part 2	Pre-Congress course 3, part 1	002	004	052	Plenary Conference 2			029	106	007
11:40-12:00				033	047	054				062	102	040
12:00-12:20				037	095	058				065	099	042
12:20-12:40				088	107	059	010	078	080	066	098	043
12:40-13:00				079	001	063	112	108	105	076	091	053
13:00-13:20				Sponsor exhibition and photo						Clossening		
13:20-15:00	Lunch											
15:20-15:40				020	006	111	Posters session			UNAM to Morelia City Center transport		
15:40-16:00				022	036	082						
16:00-16:20				051	109	086						
16:20-16:40				055	101	087	HMS Assembly					
16:40-17:00				103	092	070						
17:00-17:30	UNAM to Morelia City Center transport											
18:00-19:00	Welcome cocktail			Cultural activity			Gala Diner					

Topics and place

Plenary conferences	**Aula Magna CSAM**
Pre-Congress course 1	**Aula Magna CSAM**
Pre-Congress course 2	**Aula poniente**
Pre-Congress course 3	**Aula oriente**
Membranes	**Aula poniente**
Fuel cells; components and stacks	**Aula oriente**
Electrolyzers	**Aula poniente**
SOFC	**Aula poniente**
H_2 production	**Aula oriente**
Bioproduction of H_2	**Aula oriente**
DFT	**Aula poniente**
Electrocatalyst	**Aula magna CSAM**
BIO-Microbial fuel cells	**Aula oriente**
Hydrogen storage experimental and theoretical approaches	**Aula poniente**
Renewable energy systems	**Aula poniente**
Nanoestructures materials	**Aula magna CSAM**
Various: 112	**Aula oriente; 078 and 108 Aula magna CSAM**
Poster Session and HMS Assembly	**CIECO**

Plenary conferences

Plenary Conference 1. Hydrogen production through photoelectrolysis: challenges and advances

Dr. Arturo Fernandez Madrigal
IER-UNAM

The International Energy Agency (IEA) proposed an urgent change in the energy sector, due to reduce the generation of greenhouse gases (GHG) and to a lesser extent due to the increase in prices and the decline in oil reserves, emphasizing the expression adopted in 1970, by the General Motors company, "Hydrogen Economy" used to define a new economic model based on hydrogen as a source of energy.

Hydrogen is called an energy vector, that is, it has to be extracted from other raw materials, for this a portion of energy has to be invested, currently more than 90% of the hydrogen produced is through fossil fuels; However, taking into account the proposal for a new energy model based on hydrogen as a fuel, it is vitally important to consider the advantages of renewable sources in favor of the clean production of the vector in question.

There are three different classes that supply the primary energy for hydrogen production: nuclear, fossil fuels and renewable energy. Within renewable energies the sun is the most important; It encompasses three forms of production, biological procedures, thermal decomposition and water electrolysis. This last process is considered the most environmentally friendly, basically consists of breaking down the water molecule into its constituent elements (hydrogen and oxygen). This research focuses on the concept of photoelectrolysis, which is based on this process. The concept of photoelectrolysis was proposed in 1972 by Fujishima and Honda and they demonstrated that a semiconductor with the appropriate properties submerged in an aqueous electrolyte, being illuminated with sunlight can transform the photon's energy into electrochemical energy which It can directly decompose the water molecule. The device where this process is carried out is called a photoelectrochemical cell (PEC).

The PEC is linked to various areas of science: the optical functions required to absorb as much solar radiation as possible and on the other hand the catalytic functions necessary for water separation, resulting in the conversion of solar energy into an energy product. useful hydrogen.

This presentation will address the various configurations developed for the construction of the PECs, as well as the various types of materials used, addressing the current art of these devices.

Plenary Conference 2. Balancing gravimetric and volumetric hydrogen density in MOFs: Computational discovery and experimental demonstration

Dr. Donald Siegel
Mechanical Engineering Department, University of Michigan

Metal organic frameworks (MOFs) are promising materials for the storage of hydrogen fuel due to their high surface areas, tunable properties, and reversible gas adsorption. Although several MOFs are known to exhibit high hydrogen densities on a gravimetric basis, realizing high volumetric capacities remains a challenge. Here, MOFs that achieve high gravimetric and volumetric H_2 densities simultaneously are identified computationally, and demonstrated experimentally. More specifically, the hydrogen capacities of ~100,000 MOFs drawn from databases of known and hypothetical compounds were predicted using empirical correlations and direct atomistic simulations. Based on these predictions, promising MOF candidates were synthesized and evaluated with respect to their usable H_2 capacities. Several MOFs predicted to exhibit high capacities displayed low surface areas upon activation, highlighting the need to understand the factors that control stability. Consistent with the computational predictions, several MOFs were experimentally demonstrated to exhibit an uncommon combination of high usable volumetric and gravimetric capacities. Importantly, the measured capacities exceed those of the benchmark compound MOF-5, the record-holder for combined volumetric/gravimetric performance. These materials-level capacities were subsequently used as input to project system-level performance. Finally, several machine learning algorithms were trained on this computationally-generated database. The relative accuracy of these algorithms was compared, with the most promising algorithm applied to predict H_2 capacities in an additional 400,000 MOFs. Our study illustrates the value of computational screening in pinpointing materials that optimize overall storage performance.

Plenary Conference 3. Biohydrogen production: A strategy for wastewater management

Dr. René Cardeña Dávila
Instituto de Ingeniería, Unidad Académica Juriquilla

In Mexico, wastewater is a problem due to low treatment coverage. Biological processes are the most important and necessary stage for water treatment, they have such a wide versatility that value-added products can be obtained from it. The biohydrogen is produced by biological means by the action of microorganisms by degrading the organic matter present in the water. A substrate with high carbohydrate content will provide better hydrogen productions, for example, agro-industrial or food industry wastewater. Among the most important biological processes of hydrogen production are dark fermentation, photo-fermentation, and bioelectrochemical processes. During dark fermentation, complex molecules are transformed into simple monomers that are easier to assimilate by microorganisms for hydrogen production. However, the dark fermentation only removes between 30 and 40% of the substrate initial, the organic matter that remains in the liquid phase is transformed into more oxidized compounds, mainly volatile fatty acids. These volatile fatty acids serve as a raw material in the photofermentation process or microbial electrolysis cells, obtaining better overall hydrogen yields and better treatment for wastewater.

Pre-congress courses

Pre-congress course 1: X-ray Photoelectron Spectroscopy (XPS): Fundamentals and applications.

Fis. Lazaro Huerta Arcos
Institute of Materials Research, UNAM.
lazaro@iim.unam.mx

XPS consists in measuring the kinetic energy of ionized electrons from the internal orbits of atoms. It is used to obtain quantitative information on chemical states and study the valence band of the first atomic layers of solid materials (1-100 Å) with high precision.

In this workshop, some theoretical and experimental aspects of the techniques will be discussed: X-ray Photoelectron Spectroscopy (XPS / ESCA), angular resolution (ARXPS), Ultraviolet Ray (UPS), Ionic Erosion Depth Profiles using XPS.

Strategies are presented to obtain more information on the technique and the appropriate parameters for measurements and adjustments in spectral deconvolution are detailed.

The main application in research is an analysis of oxidation states in various disciplines and fields such as thin films, nanomaterials, carbon, metals, polymers and surface functionalization, organic materials, tribology, diffusion processes, catalysis, semiconductor, and superconducting materials, among others.

Pre-Congress course 2. Scientific research publication from basic to applied science: papers and patents.

Dr. Ismeli Alfonso Lopez
Morelia Unit Institute of Materials Research, UNAM.

Scientific research has been generally classified in basic and applied, being in both cases necessary the publication of the obtained results. Similitudes and differences exist between their more important kinds of divulgation, being these papers and patents, respectively. For the case of papers no regulations exist about where publish, and generally English is the preferred language; meanwhile for the case of patents in each country exists only one submitting place, and it is mandatary its publication in the official language of that country. It is important to remark that the 80 % of the whole scientific-technical information on the world is published in patents, being then indispensable not only the search in papers data bases, but also of patents. In this course we will address the issue of similarities and differences between papers and patens, including writing and submitting techniques; and tools for scientific-technical information search. Exercises about writing of papers and patents will be also performed, including recommendations for a better presentation of figures.

Pre-Congress course 3. Powder X-ray diffraction, from the begging to the software.

Dra. Karina Suarez

Morelia Unit Institute of Materials Research, UNAM.

X-ray diffraction is a powefull tool for the characterization of new materials. In this quick course, the fundamentals of X-ray diffraction are revisited. Main concepts such as the crystal size, crystallographic data, miscrostrains, etc. are revised. Then, a small experimental session to improve the sample preparation and data collection is performed. The most common erros and a way to avoining they are presented. Finally, the most important software and crystallographic databases for data processing are presented. The Rietveld method is also revisited.

Tabla de contenido

Posters list

Code	Title	Authors
003	Improving the Performance of $CuBi_2O_4$ photocathodes for photoelectrochemical production of hydrogen by Heat-treatment in an inert atmosphere.	S. Cruz Orellana, P. Acevedo Peña, E. Córdoba Tuta
012	Symmetry studies of $La_{0.7}Sr_{0.3}Cr_{0.4}Mn_{0.6}O_{3-\delta}$ perovskite for oxide solid fuel cells	José Juan Alvarado Flores, María Liliana Ávalos Rodríguez, José Guadalupe Rutiaga Quiñones, Jaime Espino Valencia, Jorge Víctor Alcaraz Vera.
014	Adsorption And Activation Of CO_2 On The $Ni_{13-X}cu_x$ (X=0-13) Clusters Supported On Defective Graphene: Insights From First-Principles	H. Cruz-Martínez, F. Montejo-Alvaro, M.G. Salinas-Juárez, J.A. Martínez-Espinosa, M.M. Tellez-Cruz, E.P. Sanchez-Rodriguez, D. I. Medina
015	Synthesis Of Pd Nanoparticles Supported On Mno_x (Mn_3O_4 and α–Mno_2) For The Ethylene Glycol Electro-Oxidation Reaction.	A. López-Coronel, D. Hernández-Zavala, L. Álvarez-Contreras, S. Rivas, M. Guerra-Balcázar, N. Arjona
016	Analysis for an in-situ hydrogen continuous production system by aluminum corrosion in aqueous acid solution using sodium molibdate as a promotor	Erick Arellano Domínguez, Ana Lidia Martinez Salazar, Jonathan De Jesús Malpica Maldonado
018	Improving performance of ZnO dye sensitized solar cell by incorporation of graphene oxide by high energy milling	X. Atanacio-Sánchez, W. J. Pech-Rodríguez, Eddie N. Armendáriz-Mireles, P. C. Meléndez-González, E. Rocha-Rangel
019	The need for a proyect official mexican standard in the management of H_2	María Liliana Ávalos Rodrígue, José Juan Alvarado Flores, Jorge Víctor Alcaraz Vera
025	Influence of doping with neodymium on Pt-Pd bimetallic catalysts supported on γ-alumina for the production of hydrogen by catalytic decomposition of methane.	M. Caballero-Díaz, G. Del Ángel Montes, V. Tostado-Ramirez, M. Barrios Cruz
026	Production of hydrogen using $Pd/\gamma{\cdot}Al_2O_3$ catalysts and the influence of neodymium on the catalytic activity and stability of the catalysts.	M. Caballero-Díaz, G. Del Ángel Montes, E. Castillo Bravo
028	Zinc ferrites for methyl radicals formation: a study of water adsorption influence	Lorenzo Antonio Cruz Santiago, Ana Lidia Martínez Salazar, Benjamín Portales Martínez, Ana Adela Lemus Santana, Edilso Francisco Reguera Ruíz
030	Metal-decorated GeC monolayer for hydrogen storage	Francisco De Santiago, Héctor Muñóz, Álvaro Miranda, Miguel Cruz-Irisson

032	Development of Zn-air batteries using highly-oriented Zn electrodeposited on three-dimensional carbon electrodes	A. L. Díaz-Patiño, E. Ortiz-Ortega, G. Trejo, L. Álvarez-Contreras, M. Guerra-Balcázar, J. Ledesma-García, L. G. Arriaga, N. Arjona
044	Study of N-doped and functionalized carbon nanomaterials as metal-free electrocatalysts towards the oxygen reduction reaction for alkaline fuel cell applications.	E. Garza-Durán, J.G. Alanís- Gutiérrez, G. Vargas-Gutiérrez, B. Escobar-Morales, J. Escorcia-García, I.L. Alonso-Lemus, F.J. Rodríguez-Varela
049	Maximize the generation of hydrogen from the determination of the optimum angle of inclination for solar collectors.	Herrera-Romero J.V., Escobar-Trujillo B.A., Escalante Soberanis M.A., San Pedro L., Flota-Bañuelos M.
056	Study of open combustion of oxy-hydrogen gas and flame propagation at low operating pressures for a flame arrester design.	S. Maldonado-Teodocio, J. M. Sandoval-Pineda, G. J. Gutierréz-Paredes, U. Maza-Nájera
057	Synthesis and Characterization of Ni-Mo_2C nanoparticle core/shell for potential application as a catalyst to bio-fuels production.	Jonathan Jesús Malpica Maldonado, José Aarón Melo Banda, Ana Lidia Martínez Salazar
060	Study of a catalytic bed reactor for the production of hydrogen from bioethanol	Iván Rafael Martínez, J. L. Contreras, José Salmones, Beatriz Zeifert, Tamara Vázquez
061	Modeling a tubular reactor to obtain hydrogen from the dry reforming of etanol.	Iván Ramosa, J.L.Contreras, A. Hernandez, Israel Pala, Beatriz Zeifert Arturo Pallares, Jennipher Perez
064	Biohydrogen production using different consortia of microorganisms.	G. Moreno, G. Buitrón, E. Trably, E. Latrille, A. Marone, G. Santa-Catalina, I. Moreno-Andrade
068	Effect of hydrogen to remove nox of emissions from diesel engines using a Pt-Ag/Al_2O_3-WO_x catalyst	Naomi N. González, Marcos Pinto, J.L.Contreras, Beatriz Zeifert, Gustavo A. Fuentes, Tamara Vázquez and Ricardo López M.
072	TGA study of hydrided magnesium alloys.	M. Osorio-García, R. Y. Hernández Jiménez, C. Casas Quesada, J. M. Cabrera, A. Tejeda Ochoa, J. M. Herrera-Ramírez, Y. Todaka, N. Kametani, M. M. Tellez-Cruz, K. Suárez-Alcántara, J. L. Carrillo-Bucio, N. Torres, J. G. Cabañas Moreno.
075	Photocatalytic activity of TiO_2-CoO as mixed oxide for improved H_2 production	A.Pérez-Larios, R. Gomez, R. Zanella.
078	Metal-free electrocatalysts from Ascophyllum nodosum for alkaline oxygen reduction reaction	Perez-Salcedo, K.Y.; Shi, X.; Kannan, A. M.; Vayssieres, L.; Escobar, B.

081	A pregnancy test powered by a paper-based microfluidic fuel cell using the urine sample as fuel.	C. Romero-Camacho, J. Gamboa, S. Ríos-Ugalde, J. M. Olivares-Ramírez, D. Ortega-Díaz, A. Dector, D. M. Amaya-Cruz, D. Dector.
087	INFLUENCE OF WO3-Zro2-C AS ACTIVE SUPPORT FOR PLATINUM NANOPARTICLES: ENHANCEMENT OF ACTIVITY CATALYTIC OF NO3- And NO2- REDUCTION	C. R. Santiago-Ramírez[1,2], J. Soto-Hernánez[1], L.P.A. Guerrero-Ortega[1], E.Y. Cervantes-Aspeitia[1,2], A. Manzo-Robledo[1], M.L. Hernandez-Pichardo[2,*]
090	Simultaneous characterization of polyelectrolytic membranes by cyclic voltammetry and *in-situ* ftir technique.	A. A. Siller-Ceniceros, L. Francisco-Vieira, D. Morales-Acosta, R. Benavides, E. Cuara-Díaz And L. Da Silva.
093	Design of an electric supply system from an alternator to an oxyhydrogen reactor for a diesel engine.	A. Wintergerst-Felipe, R De G. González-Huerta, E. A. Merchán-Cruz, J. M. Sandoval-Pineda
094	Bifunctional Pt-based electrocatalysts supported on biocarbon functionalized with organometallic ruthenium complex toward the oxygen reduction reaction (ORR) and the oxygen evolution reaction (OER).	M. P. Solórzano Alderete, M. Peralta Contreras, P.C. Meléndez González, J.C. Martínez Loyola, F.J. Rodriguez-Varela, I.L. Alonso-Lemus
097	Study of the electrochemical performance and stability of nitrogen-doped ordered mesoporous carbon hollow spheres	Tamayo-Ordoñez M.C., Tamayo-Ordoñez Y.J., Ayíl-Gutierrez B., Ruiz-Marin A., Tamayo-Ordoñez F.A., Moreno-Davila I.M.M., Ríos-Gonzalez L.J., Acosta-Cruz E.Y., Sosa-Santillán G.J
104	Zeolites from geothermal nanosilica and its evaluation in the dehydration of bioethanol.	J.A. Trejo García, A. Medina Ramírez, B. Ruiz Camacho, J.I. Minchaca Mojica, C.M. López Badillo
110	An overview of LMNO high voltage lithium-ion batteries implementation in a hybrid solar-hydrogen system. Study case "Vivienda Sustentable IPN®"	Jorge Olmedo-González, Guadalupe Ramos-Sánchez, Rosa de Guadalupe González-Huerta
115	Temperature dependence for hydrogen storage in metal hydrides $Mg_{1-x}M_x$ (M=Al, Zn, Ni, x=0.10, 0.12,…, 0.20)	O. Ramírez- Rodriguez, G. Ramírez-Dámaso

PART 1. Abstracts book

001. INFLUENCE OF ER CONTENT ON THE ELECTRICAL PROPERTIES OF CeO_2 SOLID ELECTROLYTES OBTAINED BY MECHANOCHEMISTRY

D.E. Puente-Martínez[1], J.A. Díaz-Guillén[1], S.M. Montemayor[2], J.C. Díaz-Guillén[3], K.P. Padmasree[4], O. Burciaga-Díaz[1] and A.F.Fuentes[4].

[1]Tecnológico Nacional de México, Instituto Tecnológico de Saltillo, 25280-Saltillo, Coahuila, México. dpuente@itsaltillo.edu.mx
[2]CIQA, Blvd. Enrique Reyna Hermosillo 140, 25294-Saltillo, Coahuila, México
[3]COMIMSA-Conacyt, Calle Ciencia y Tecnología 790, Saltillo 400, 25290 Saltillo, Coahuila, México
[4]CINVESTAV Unidad Saltillo, Av. Industria Metalúrgica 1062, Parque Industrial 25900-Ramos Arizpe, Coahuila, México

Different researchers are looking to develop materials with high ionic conductivities at low temperatures (500°C) on views to be applied as solid electrolytes in Solid Oxide Fuel Cells (SOFCs). In this case, doped ceria systems, with general formula EryCe1-yO2-δ (y = 0.05 - 0.15) were synthesized by high energy mechanical milling (20 h) by using a planetary mill. Synthesized powders were then fired (800 - 1500 °C) and analyzed by XRD (Figure 1a). Morphology and chemical composition of these materials were analyzed by SEM (Figure 1b) in uniaxially pressed and sintered pellets (1500°C). Electrical properties of these materials were analyzed by impedance spectroscopy as a function of temperature and frequency. Diffraction patterns of milled powders indicate the formation of solid solutions after 20 hours of milling, and also reveal a notorious positive effect of temperature on the crystallinity of these phases. Analysis of electrical properties corroborates the viability of these ceramics to be used in Intermediate temperature SOFC.

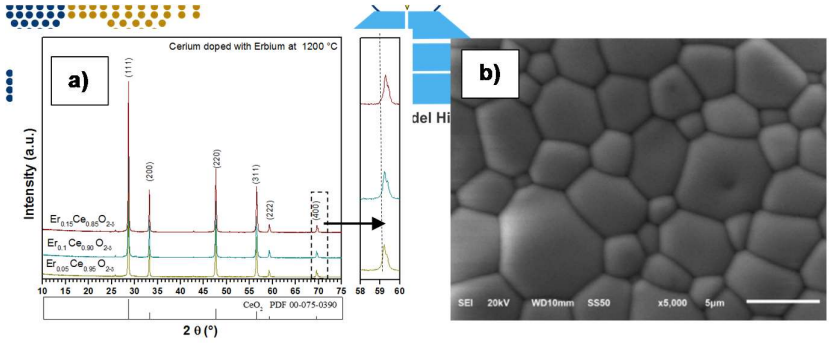

Figure 1. XRD patterns of Er-doped ceria after firing at 1200 °C (a). Morphology of pressed and sintered samples (1500°C) obtained by SEM (b).

Reference: [1] L. Li, B. Zhu, J. Zhang, International Journal of Hydrogen Energy, (2018), 43, 12909-12916.

Acknowledgements: This work was financially supported by CONACYT.

002. EFFECT OF WATER LEVEL ON THE MECHANICAL PROPERTIES OF POLYELECTROLYTIC MEMBRANES USED IN FUEL CELLS.

R. Benavides*, V. Berlanga, F. González, L. Francisco, D. Morales-Acosta, L. da Silva

Centro de Investigación en Química Aplicada, Bvld. Enrique Reyna No. 140, Col. San José de los Cerritos, 25294. Saltillo, Coahuila, México, E-mail: roberto.benavides@ciqa.edu.mx

Polymeric membranes, depending on their molecular structure, have their own mechanical properties, which in turn will impact on their possibility to be used as an ion conductor in a fuel cell. Water management is an important characteristic for their performance, since usually is through water that ions can have the possibility to permeate the membrane. It is also well-known that sulfonated materials are intrinsically hygroscopic and that adsorbed water impact on the mechanical properties, to a certain extent, due to its ability to plasticize the polymer structure. Membranes of two Nafion grades (117 and 212) and copolymer St-BuA sulfonated membranes with three levels of sulfonation (50, 100 and 150 % of theoretical aromatic rings) were hydrated to different levels (0, 25, 50, 75 and 100% gravimetrically measured for each membrane specific water uptake) to evaluate mechanical property. The complex modulus (E*) was calculated from isothermal flexure deformations obtained from a Termomechanical Analysis (TMA) instrument, with variation on force for deformation. Results indicate stable water uptake for both Nafion membranes, but variable water uptake for sulfonated St-BuA copolymers, increasing along sulfonation level. Differences on mechanical behavior were found between the two grades of Nafion and an expected trend of mechanical property for the St-BuA membranes along water level.

Acknowledgements
The authors acknowledge CONACyT for the economical support through the research project FC3004

003. IMPROVING THE PERFORMANCE OF $CuBi_2O_4$ PHOTOCATHODES FOR PHOTOELECTROCHEMICAL PRODUCTION OF HYDROGEN BY HEAT-TREATMENT IN AN INERT ATMOSPHERE

S. Cruz Orellana[1], P. Acevedo Peña[2], E. Córdoba Tuta[1]

[1]Escuela de Ingeniería Metalúrgica y ciencia de los materiales, Facultad de Ingeniería Fisicoquímica, Universidad Industrial de Santander, Bucaramanga, Colombia, Nathaliacruz1211@gmail.com
[2]CONACyt-Instituto Politécnico Nacional, CICATA Legaria, Calzada Legaría No. 694, Col Irrigación, Ciudad de México, CDMX, C.P. 11500, Mexico

The use of hydrogen as fuel has remarkable interest due to its outstanding calorific value (120 MJ / kg) and the absence of polluting gases in its combustion process, which avoid emission of greenhouse gases. Photoelectrochemistry is a methods with great potential for hydrogen production, since solar energy is expected to provide the energy necessary to perform the water splitting process. $CuBi_2O_4$ is a p-type semiconductor, and it has been investigated as photocathode in this field because: it absorbs energy in the range of visible light (800 nm), it has a band-gap of 1.8 eV and, in addition, it has an on-set potential of 1, 0 V vs RHE. In this study, $CuBi_2O_4$ films supported on FTO were formed by spin coating technique in the range of 2000-4000 RPM with a subsequent thermal treatment in two different atmospheres. Controlling the atmosphere during the thermal treatment led to an improvement in the photoelectrochemical performance for hydrogen evolution reaction, in comparison with the film thermal treated in ambient atmosphere.

004. IMPEDANCE MEASUREMENT ON A PEM FUEL CELL RUNNING ON A LOAD USING O2 AND AIR ALTERNATIVELY AT THE CATHODE.

C. M. Bautista-Rodríguez (*) and P. Ozil †.

Laboratoire d'Electrochimie et de Physico-Chimie des Matériaux et des Interfaces (LEPMI) UMR 5631 CNRS-INPG-UJF, ENSEEG, BP 75, 38402 Saint Martin d'Hères, France.

(*) Actual address of corresponding author : Centro de Innovación Aplicada en Tecnologías Competitivas (CIATEC). Omega 201, Industrial Delta, CP 37545, León Guanajuato México. cbautista@ciatec.mx

In this work, an experimental study of the impedance response of H_2/O_2 and H_2/Air PEMFC was carried out with a single cell. An impedance measurement method designed by LEPMI, was proposed allowing a separate measurement for the anode and cathode impedances of a fuel cell running on a constant load. The results are analysed taking into account a different points at long of the performance curve for the PEMFC. The effect due to the reaction kinetics, mass transport limitations and ohmic losses are shown by the impedance spectres measurements at different potential values at long of *E* - *i* curve generated by PEMFC. The main conclusion is that, the impedance response for the anode cannot be neglected in comparison of the cathode impedance spectre measured when pure oxygen feeds the cathode compartment. Furthermore, a contribution is observed on the impedance spectre by water production at medium and high potential. On the other way, if oxygen source is air, the impedance diagrams show that oxygen diffusion phenomena present in the cathode becomes a limiting step.

Keywords: PEMFC, Impedance, water generation, Nafion, Electrodes.

005. SLUDGE-DERVIED BIOCARBON AS ANODE CATALYST FOR BIOENERGY PRODUCTION FROM PHARMACEUTICAL WASTEWATER IN AN MFC.

S. García-Mayagoitia[1], F. Fernández-Luqueño[1], D. Morales-Acosta[2], F. López-Valdez[3], I.L. Alonso-Lemus[4], B. Escobar-Morales[5], L. De la Torre-Saenz[6], F.J. Rodríguez-Varela[1*]

[1]Sustentabilidad de los Recursos Naturales y Energía, Cinvestav Unidad Saltillo, Av. Industria Metalúrgica No. 1062, Parque Industrial Ramos Arizpe, Coahuila, C.P. 25900, México.
[2] Instituto Politécnico Nacional CIBA, Tepetitla De Lardiazabal C.P. 90700, Tlaxcala, México.
[3] Centro de Investigación en Química Aplicada, Blvd. Enrique Reyna Hermosillo 140. Saltillo, Coahuila, 25294, México.
[4] CONACYT, Sustentabilidad de los Recursos Naturales y Energía, CINVESTAV-IPN Unidad Saltillo
[5] CONACYT, Centro de Investigación Científica de Yucatán (CICY), Calle 43 No. 130, Col. Chuburná de Hidalgo, Mérida, Yucatán, C.P. 99200, México.
[6] Centro de Investigación en Materiales Avanzados S. C. Miguel Cervantes 120, Chihuahua, Chih. C.P. 31136, México
javier.varela@cinvestav.edu.mx

Over the last few years, there has been an increasing interest on the development of Microbial Fuel Cells (MFC). MFC are bioelectrochemical devices in which, the kinetics of the electron transfer is enhanced by using an anode catalyst where a biofilm of the microorganism grows, forming a bioanode. In order to reduce the costs of MFC, low-cost anode catalysts should be developed. The catalyst must also have a high biocompatibility with the microorganism.
In this work, a biosolid (BS) from wastewater sewage sludge from the food industry has been pirolyzed, activated with KOH and functionalized with different concentrations of methanol (0.15, 0.5 and 1.0 M) to obtain a non-noble metal biocarbon catalyst (BCC). The XRD pattern of BCC indicates that the material is amorphous in nature, with a broad (002) peak attributed to a graphitic phase in its structure. Also, some reflections attributed to crystalline phases have been observed. Chemical composition analysis by EDS of BCC shows the presence of C,O, Na, Mg, Al, Si, P, S, Cl, K, Ca, Ti and Fe in the biocarbon, which explains the crystalline reflections. BS shows a composition with 72.0, 18.96, and 0.22 (wt. %) C, O and K respectively. Meanwhile, BCC has a reduction in C content, with an increase in O and K (29.23, 23.54 17.29 wt. %, respectively), attributed to the KOH activation. Nonetheless, BCC shows biocompatibility with *Bacilus subtilis* (*B. subtilis*, used as electroactive bacteria) as observed from SEM and FESEM analysis.
Bioanodes composed of BCC + *B. subtilis* biofilm have been characterized in a half cell with pharmaceutical wastewater (PWW, pH= 6.1) as electrolyte. The cyclic voltammograms (CVs) show their biocatalytic activity, generating high current densities (j) from the oxidation of organic matter in PWW. The biocatalytic activity of the bioanodes is higher than that of an anode without *B. subtilis*, i.e., containing only BCC. These results indicate that sludge-derived biocarbons are promising anode catalysts for MFC applications, due to their catalytic activity, electrochemical stability and biocompatibility with electroactive bacteria.

Acknowledgements
The authors wish to thank CONACYT for financial support through grants 241526, 250632, 253986 and 287225.

006. EFFECT OF LANTHANIDE DOPING ON THE ELECTRICAL PROPERTIES OF YPSZ SOLID ELECTROLYTES ON VIEWS TO THEIR USE IN SOFC

K.A. González-García[1*], J.A. Díaz-Guillén[1], S.M. Montemayor[2], J.C. Díaz-Guillén[3], A.F.Fuentes[4]

[1] Tecnológico Nacional de México, Instituto Tecnológico de Saltillo, 25280-Saltillo, Coahuila, México, kagonzalez86@gmail.com
[2] CIQA, Blvd. Enrique Reyna Hermosillo 140, 25294-Saltillo, Coahuila, México
[3] COMIMSA-Conacyt, Calle Ciencia y Tecnología 790, 25290 Saltillo, Coahuila, México
[4] CINVESTAV Unidad Saltillo, Av. Industria Metalúrgica 1062, Parque Industrial 25900-Ramos Arizpe, Coahuila, México

In this research, samples of YPSZ are doped with different lanthanides and their electrical properties analyzed on views to be used as solid electrolytes in SOFC. These solid solutions of general formula $Zr_{x-1}Y_{0.04}$ $Ln_xO_{2-\delta}$ (Ln = Sm, Nd and Gd, x = 0.05 - 0.2) were obtained by mechanical milling, starting from high purity oxides of the involved elements. The synthesis consisted in 20 hours of milling in a planetary mill using zirconia container and balls, followed by a firing at 1500°C. The samples before and after sintering were characterized by XRD. The figure 1a shows the XRD patterns for samples with different gadolinium percentages after the heat treatment. Milled powders were also uniaxially pressed and sintered at 1500°C. Morphology and chemical composition were analyzed by FE-SEM. Electrical properties were studied by impedance spectroscopy. Conductivity versus frequency and temperature of a representative sample is showed in figure 1b. The results revealed that these materials show electrical properties similar to some well-known ionic conductors [1], and can be considered to be used in SOFC.

Keywords: SOFC, YPSZ, mechanical milling, electrical properties, solid electrolytes.

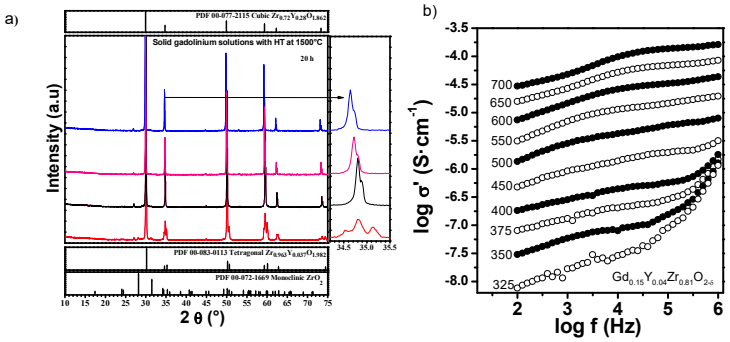

Figure 1a. XRD pattern of the gadolinium samples after heat treatment at 1500°C (a).

Figure 1b. Conductivity versus frequency graph for a selected composition $Gd_{0.15}Y_{0.04}Zr_{0.81}O_{1.905}$ (b).

References

[1] Salazar- Zertuche M. et al., "Ionic Conductivity of $Ln_4Zr_3O_{12}$ solid electrolytes syntesized by mechanochemistry", International Journal of Hydrogen Energy, **(2018)**, Vol.44, 1-8 pp.

Acknowledgements This work was financially supported by CONACYT CB- 166 995, and CV-860984.

007. SYSTEMATICS EFFECTS PRODUCED BY AN AIR COMPRESSOR INTRODUCTION DOWNSTREAM OF AN ELECTROLYZER.

C.Y. Montalvo-Fernandez[1], J.M. Sandoval–Pineda[1], R. G. Rodríguez-Cañizo[1], R. de G. González-Huerta[2].

[1]Instituto Politécnico Nacional, Escuela Superior de Ingeniería Mecánica y Eléctrica, Sección de Estudios de Posgrado e Investigación, Unidad Azcapotzalco, Av. de las Granjas 682, Col. Santa Catarina, CP 02250, CDMX.
[2]Instituto Politécnico Nacional, Escuela Superior de Ingeniería Química e Industrias Extractivas, Laboratorio de Electroquímica y Corrosión. UPALM, CP 07738, Ciudad de México.

E-mail: ingmontalvo_ipn@hotmail.com, Tel: +525520048912

Oxyhydrogen production and application involve many difficulties as transportation and storage which carry on high technological issues due to sophisticated and costly equipment used. Those factors have brought with them the necessity to produce Oxyhydrogen "*in situ*" to leave aside storage elements. Thus, the gas needs to be immediately produced and consumed. Despite, this kind of applications have substantial bounds, as low generation pressure to be used in industrial applications where high pressure is prevailing.
In this paper it is involved the experimentation and evaluation of systematics effects in generation of Oxyhydrogen "*in situ*" when pression is applied to the system. A Factorial Design (2^k) is applied to analyze the response in order to find the best mix of factors to obtain a high flame temperature and an increasing pressure. Four design alternatives are proposed (Drag Compression and three kind of direct compression with flow variation), which are analyzed through MiniTAB® Software. According to obtained results, where it is possible to determine the existing relationship in Electrolyte Temperature, OHH-Air mixture and OHH flow rate, modifications were improved to the system and experimentation was again executed to find new system's upgrades. Also, a high outlet pressure of mixture and flame was reached up 16 PSI and calorific power could be relatively maintained.
Many of upgrades found, are the need to use airtight containers, getting control of system temperature and pipe substitution. Materials is also an important criterion to avoid problems with electrolyzer, because of that, the present job was also relevant in terms of used materials.

Key words: air compressor, Downstream, Oxyhydrogen "in situ", Factorial Design, system's upgrades.

008. COMPARATIVE STUDY IN THE ELECTROCHEMICAL CHARACTERIZACTION OF A MICROBIAL FUEL CELL

Luis Alberto Meza Cova[1], Areli del Carmen Ortega Martínez[*1], Diana Laura Orozco Delgado[1], Sathish Kumar Kamaraj[2], Oswaldo Guzmán López[1], María del Carmen Cuevas Díaz[1]

[1]Facultad de Ciencias Químicas, Universidad Veracruzana, Avenida Universidad Km 7.5 colonia Santa Isabel I, Coatzacoalcos, Veracruz, 96535, México. areortega@uv.mx
[2]Instituto Tecnológico de Aguascalientes. Av. Adolfo López Mateos 1801Oriente Bona Gens, 20256, Aguascalientes, Aguascalientes, México.

Keywords. Caracterization, iron-reducing bacterial, microbial fuel cell

Microbial fuel cell (MFC) technology has attracted increasing attention in the last decade due to growing concern about the global energy crisis. In particular, the use of microorganisms in MFC to convert organic and inorganic materials into electricity. Research has been conducted to understand bacterial metabolism in electrodes, to examine different substrates, to select optimal electrode / catalyst materials and to optimize reactor configurations. One of the key issues in MFC studies is to investigate biological and / or abiotic factors that limit energy production, understand and overcome them. These limiting factors can be represented by the internal resistance (R_{int}) of a MFC [1]. There are currently techniques to determine the R_{int} and electrochemical parameters such as the electrochemical impedance spectroscopy (EIS) technique, which is a powerful tool used in MFC to evaluate the R_{int} of electrodes, membrane and electrolyte [2]. Another technique used to characterize MFC is the polarization curve obtained by variable external resistances and linear sweep voltammetry (LSV), which can provide important information about its total internal resistance and its maximum power point. Therefore, the main purpose was to evaluate the R_{int} of the MFC with polarization curve by variable external resistances and EIS, as well as the evaluation of electrochemical parameters to determine its maximum power by means of polarization curve by variable external resistors and LSV [3].
In the present project, an air cathode MFC with a capacity of 150 mL was used and it was fed with two microbial consortia, iron-reducing bacteria (IRB) and sulfate-reducing bacteria (SRB). Accurate results were obtained in the evaluation of internal resistance using the EIS technique, for the IRB consortium the total internal resistance was 15 KΩ and 5 KΩ for the SRB consortium. On the other hand, the linear sweep voltammetry technique showed superior results in all parameters compared to the polarization curve technique by variable external resistors.

References

[1] He, Z., y Mansfeld, F. (2009). Exploring the use of electrochemical impedance spectroscopy (EIS) in microbial fuel cell studies. *Energy Environ. Sci.,* 215-219.
[2] Huerta, G. V., Casillas, D. C., y Feria, O. S. (2011). Aplicación de la espectroscopia de impedancia electroquímica en la caracterización de celdas de combustible tipo PEM utilizando PdCo como catalizador catódico. *Centro de Investigación y de Estudios Avanzados del Instituto Politécnico Nacional*(II), 224-238.
[3] Watson, V. J., y Logan, B. E. (2011). Analysis of polarization methods for elimination of power overshoot in microbial fuel cells. *Electrochem. Commun., 13*, 54-56.

009. EFFECT OF CO_2 AND STEAM IN THE GASIFICATION KINETICS OF PALM KERNEL SHELL FOR H_2 PRODUCTION USING TGA

J. Acevedo[1], F. Posso[2], E. Arenas[3]

[1]Grupo de Investigación Eureka UDES, Universidad de Santander, Cúcuta, Col., jua.acevedo@mail.udes.edu.co
[2]Grupo de Investigación Nuevas Tecnologías, Universidad de Santander, Bucaramanga, Col.
[3]Grupo de Investigación Energía y Termodinámica, Universidad Pontificia Bolivariana, Medellín, Col.

In this work the effect of CO_2 and steam as gasifying agents in the gasification of the palm kernel shell (PKS) in a thermogravimetric analyzer (TGA) was studied, in order to determine the kinetic parameters for the design, construction and operation of the gasifiers, as well as for process scale-up for biomass co-gasification for production of syngas, especially hydrogen [1]. A physicochemical characterization of PKS was carried out by proximate and ultimate analyses, obtaining a high calorific value (19.53 MJ/Kg) compared with other agroindustrial biomasses [2], thus demonstrating the energy potential of PKS. The low moisture content (7.43%) makes the drying process less intense and, therefore, the gasification more efficient. On the other hand, thermal decomposition studies of PKS were performed in a TGA (STA PT1600, Linseis). They were carried out in two areas: (i) pyrolysis, with two heating rates (15 and 30 °C/min) and a nitrogen flow of 50 ml/min; and (ii) isothermal gasification, using three temperatures (750, 850 and 950 °C) and two gasifying agents (CO_2 and steam), operating time (60 min). The kinetic parameters of the gasification stage were determined: activation energy (E), pre-exponential factor (A) and reaction order (n), using three models to interpret the experimental results: linear model (LM) [3], grain model (GM) [4] and volumetric model (VM) [5]. In Table 1, the results indicate that ML and MG have the best fit with the experimental results of gasification of PKS with steam and CO_2, respectively. In addition, it is evident that gasification with CO_2 has a greater reactivity, since the energy barrier to reach to initiate heterogeneous reactions is lower, similar to that reported in [1], all this contributes to the study of H_2 production from palm kernel shell in Colombia.

Table 1. Kinetic parameters PKS gasification

Parameter	Steam			CO_2		
	LM	GM	VM	LM	GM	VM
E (KJ/mol)	125.79	103.22	62.49	114.41	99.87	91.27
A (s^{-1})	26.23	8.26	1.58	9.20	6.30	95.51
n	0	0.33	0.99	0	0.33	0.99
R^2	0.966	0.934	0.661	0.951	0.965	0.205

References

[1] Lahijani P., et al., Bioresour. Technol., **2013**, 138, 124–130.
[2] Marrugo G., et al., Energy Fuels, **2016,** 30, 8386–98.
[3] Suresh K., et al., Int. J. Environ. Res., **2013**, 7 (1), 97-104.
[4] Szekely J. and Evans J., Chem Eng Sci., **1970**, 25, 1091–107.
[5] Zuo H., et al., Int J Miner Metall Mater, **2015**, 22, 363-70.

Acknowledgements
To Universidad de Santander and Universidad Pontificia Bolivariana for the financial and logistical support for the development of the research project.

010. NOVEL *PERIPLANETA AMERICANA* DERIVED-BIOCARBON ELECTROCATALYSTS WITH EXCEPTIONALLY HIGH CATALYTIC ACTIVITY FOR THE OXYGEN REDUCTION REACTION IN ALKALINE MEDIA

J.-G. Alanís-Gutiérrez[1], J.-G. Bocarando-Chacon[1], B. Escobar-Morales[2], S. Garcia-Mayagoitia[3], F.-J. Rodríguez-Varela[3], I.-L. Alonso-Lemus[4]*

1Universidad Tecnológica de Querétaro (UTEQ), Avenida Pie de la Cuesta # 2501, C.P. 76148 Querétaro, Qro., México.
2Centro de Investigación Científica de Yucatán (CICY), Calle 43 No. 130, Col. Chubumá de Hidalgo, Mérida, Yucatán, C.P. 31136, México.
3Sustentabilidad de los Recursos Naturales y Energía, CINVESTAV, Unidad Saltillo, Av. Industrial Metalurgia No.1062, Parque Industrial, Ramos Arizpe, Coahuila, C.P. 25900, México.
4CONACYT, Grupo de Sustentabilidad de los Recursos Naturales y Energía, CINVESTAV Saltillo, Av. Industrial Metalurgia No.1062, Parque Industrial, Ramos Arizpe, Coahuila, C.P. 25900, México.
**ivonne.alonso@cinvestav.mx*

Fuel cells (FCs) converts chemical energy into electrical energy directly through the oxidation of a fuel and the reduction of oxygen with high efficiencies and low/zero emissions [1]. However, the main drawback to its large-scale commercialization is the use of platinum as catalyst. In order to reduce the FCs costs, Pt-free electrocatalysts has been development with high catalytic activity for the Oxygen Reduction Reaction (ORR), which take place in the FCs cathode.

In this work, a novel Pt-free electrocatalysts has been development using *Periplaneta Americana* (cockroach species very common in Mexico) as raw material for the biocarbon synthesis. In addition, the biocarbon has been activated using potassium hydroxide and treated with an iron salt by thermal process. The most active electrocatalysts is the Fe-N-doped *Periplaneta Americana* derived-biocarbon labelled as Fe-N-PAB, which have high catalytic activity for the ORR with an onset potential (E0) of 0.95 V vs. RHE and a current density j = -4.93 mA cm^{-2} at 0.2 V vs- RHE. Moreover, this electrocatalysts has a low hydrogen peroxide generation ($\%H_2O_2 \approx 8.4$) and the electron number transferred (n), is of 3.83. Furthermore, the electrochemical performance of this novel CucaAFe electrocatlsyst is comparable with a commercial 20% Pt-electrocatalysts (E_0= 1.00 V vs. RHE, j= -4.36 $mAcm^{-2}$, $\%H_2O_2$ = 1.95 and n= 3.96).

These results indicate that this novel electrocatalyst is a promising alternative for the use in FCs cathodes. In addition, this has advantages as its availability because it is obtained from an abundant biomass source.

References

[1] Universidad de Castilla-La Mancha (UCLM). Pilas de combustible. Ciencia e Inovacion España, Cerámicos y Vidrios Bloque IV: [Fecha de consulta Abril 2019]. Obtenido de: http://ocw.uc3m.es/ciencia-e-oin/ceramicas-y-vidrios/bloque-iv/pilas_de_combustible-1.pdf

011. TRIMETALLIC NANOCATALYSTS WITH INCREASED ACTIVITY AND DURABILITY FOR THE ORR OF Pt_2NiCo/C

H. M. Alfaro-López[1, 2], H. Cruz-Martínez[1], H. Rojas-Chávez[3], M. A. Padilla-Islas[1], M. M. Tellez-Cruz[1], O. Solorza-Feria[1]

[1]Departamento de Química, Cinvestav, Av. Instituto Politécnico Nacional 2508, San Pedro Zacatenco, Gustavo A. Madero, Ciudad de México, C.P. 07360, Mexico
[2]Escuela Superior de Ingeniería Mecánica y Eléctrica – Departamento de Ingeniería Eléctrica - Edif. 2, Instituto Politécnico Nacional, U.P.A.L.M., Col. Lindavista. C.P. 07738, Ciudad de México.
[3]Tecnológico Nacional de México, Instituto Tecnológico de Tláhuac II, Camino Real 625, Col. Jardines del Llano, San Juan Ixtayopan. Tláhuac, CDMX, C.P. 13508, Mexico.

The synthesis, physical characterization, and electrochemical evaluation of the carbon dispersed Pt_2NiCo nanocatalyst are analyzed toward the oxygen reduction reaction (ORR) in an acid electrolyte. Here, a novel ternary electrocatalyst synthesized by a chemical route using a mixture of benzyl ether, oleylamine, and oleic acid as dissolvent, as well as tungsten hexacarbonyl as reducing agent, is reported. The physical properties of the Pt_2NiCo/C nanocatalyst were investigated using XRD, EDXS-SEM, and TEM, while the catalytic properties of the Pt_2NiCo/C and commercial Pt/C nanocatalysts were determined through CV, CO-stripping, and RDE electrochemical techniques. XRD and EDXS-SEM corroborated the presence of the three metals in the nanoparticles; while through TEM, the Pt_2NiCo nanoparticles of ~ 10 nm were observed. The measured specific activity for the synthesized nanocatalyst is ~ 6.4 times higher than Pt/C, while its calculated mass activity is ~ 2.2 times higher than Pt/C. The specific and mass activity of the synthesized material is maintained after the accelerated stability test, whereas for Pt/C, these catalytic properties decrease

012. SYMMETRY STUDIES OF $La_{0.7}Sr_{0.3}Cr_{0.4}Mn_{0.6}O_{3-\delta}$ PEROVSKITE FOR OXIDE SOLID FUEL CELLS

José Juan Alvarado Flores[1], María Liliana Ávalos Rodríguez[2], José Guadalupe Rutiaga Quiñones[1], Jaime Espino Valencia[3] and Jorge Víctor Alcaraz Vera[4]

[1]Facultad de Ingeniería en Tecnología de la Madera, Universidad Michoacana de San Nicolás de Hidalgo. Santiago Tapia 403, CP 58000, Morelia, Michoacán, México, doctor.ambientalista@gmail.com
[2]Centro de Investigación en Geografía Ambiental, Universidad Nacional Autónoma de México. Antigua Carretera a Pátzcuaro No. 8701, C.P. 58190, Morelia, Michoacán, México
[3]Facultad de Ingeniería Química, Universidad Michoacana de San Nicolás de Hidalgo. Francisco J. Mújica S/N, Col. Felicitas del Rio, C.P. 58000, Morelia, Michoacán, México
[4]Instituto de Investigaciones Económicas y Empresariales, Universidad Michoacana de San Nicolás de Hidalgo. Francisco J. Mújica S/N, Col. Felicitas del Rio, C.P. 58000, Morelia, Michoacán, México.

This work is focused on nanocrystalline solid oxide fuel cell synthesis and characterization (SOFC) anodes of $La_{0.7}Sr_{0.3}Cr_{0.4}Mn_{0.6}O_{3-\delta}$ (perovskite-type) with Nickel, Copper and Copper-nickel compounds. All nanocomposites impregnated have been synthesized by ethylene glycol modified sol–gel method to get a porous cermet electrode. The phase transitions and crystal structure of $La_{0.7}Sr_{0.3}Cr_{0.4}Mn_{0.6}O_{3-\delta}$ composites were studied by time resolved x-ray diffraction, Rietveld, and high-resolution transmission electron microscopy. Electrical and structural characterization by four-point probe method for conductivity. Composite powders were compressed into 10-mm diameter discs with 25–75 wt% Ni, XCu (x = 25-45%) and $XCu_{0.75}Ni_{0.25}$ (x = 25-75%). Symmetry-breaking by phase transition from high temperature has been identified and confirmed. it has been detected a cationic inter-diffusion between Cu and Ni interphase crystals during this reduction process. Only some perovskite compositions are viable for use as anodes in intermediate temperature solid oxide fuel cells (SOFC-IT).

014. ADSORPTION AND ACTIVATION OF CO_2 ON THE $Ni_{13-X}Cu_X$ (X=0-13) CLUSTERS SUPPORTED ON DEFECTIVE GRAPHENE: INSIGHTS FROM FIRST-PRINCIPLES

H. Cruz-Martínez[1], F. Montejo-Alvaro[2], M.G. Salinas-Juárez[3], J.A. Martínez-Espinosa[1], M.M. Tellez-Cruz[4], E.P. Sanchez-Rodriguez[1], D. I. Medina[1]

[1]Tecnologico de Monterrey, Escuela de Ingeniería y Ciencias, E-mail: hcruzm@tec.mx
[2]Cinvestav, Programa de Doctorado en Nanociencias y Nanotecnología
[3]UNAM, Facultad de Estudios Superiores Zaragoza
[4]Cinvestav, Departamento de Química

Different materials have been used as nanocatalysts for the CO_2 conversion to value-added chemical products. Among which the 3*d* transition metals nanoparticles have demonstrated a good catalytic activity for the conversion of CO_2. In recent years, the bimetallic nanoparticles have demonstrated superior catalytic activities than monometallic nanoparticles. In this sense, in this work, the stability of the $Ni_{13-x}Cu_x$ (x=1-13) clusters supported on defective graphene were investigated. In addition, the adsorption and activation of CO_2 on the unsupported $Ni_{13-x}Cu_x$ (x=0-13) clusters and on the $Ni_{13-x}Cu_x$ (x=0-13) clusters supported on defective graphene were elucidated. All initial structures were optimized by density functional theory (DFT) using the Orca package. The revised Perdew–Burke–Ernzerhof functional and split valence polarization basis set were used for all calculations. The stability of the $Ni_{13-x}Cu_x$ (x=0-13) clusters supported on defective graphene was significantly improved. The DFT calculations also revealed that the bimetallic clusters supported on defective graphene activate the CO_2 molecule. Nowadays, we are investigating the CO_2 hydrogenation to methane on the $Ni_{13-x}Cu_x$ (x=0-13) clusters supported on defective graphene.

Keywords: Nanocatalysts; DFT; Defective graphene; CO_2 adsorption

Acknowledgements
H. Cruz-Martínez acknowledges CONACYT for the postdoctoral. The authors acknowledge the computational resource provided by the ABACUS-I supercomputer from CINVESTAV.

015. SYNTHESIS OF PD NANOPARTICLES SUPPORTED ON MnO_X (Mn_3O_4 AND α–MnO_2) FOR THE ETHYLENE GLYCOL ELECTRO-OXIDATION REACTION

A. López-Coronel,[1] D. Hernández-Zavala,[1, 2] L. Álvarez-Contreras,[3] S. Rivas,[4] M. Guerra-Balcázar,[4] N. Arjona[1*].

[1] Centro de Investigación y Desarrollo Tecnológico en Electroquímica S. C., México, wvelazquez@cideteq.mx
[2] Universidad Politécnica de Guanajuato, México.
[3] Centro de Investigación en Materiales Avanzados S. C., México
[4] Facultad de Ingeniería, Universidad Autónoma de Querétaro, México

Ethylene glycol is widely used in the industrial sector. This low-cost polyalcohol can be used as fuel in the area of energy conversion (fuel cells). There are several challenges to solve for the succesful use of ethylene glycol as fuel, one of them involves the use of non-carbonaceous supports to provide a longer useful life. In this work, the use of manganese oxides as supports for the electro-oxidation reaction of ethylenen glycol is explored. These oxides were synthesized by the polyol method using hydrogen peroxide (H_2O_2) and ammonium persulfate (APS) as oxidizing agents. According with X-ray diffraction, the nature of the oxidizing agents has influence in the structural modification of manganese oxide. The use of APS allowed the formation of α–MnO_2 phase, while the use of H_2O_2 resulted in the formation of Mn_3O_4. Scanning and transmission electron microscopies (SEM and TEM) indicated that these materials presented fiber and spherical-like shapes, respectively. The length of the wires was of several micrometers; however, the diameters ranged in nanometric scale (8-20nm). Mn_3O_4 had particle sizes of 20±4 nm. On the other hand, TEM analysis of palladium nanoparticles supported on these oxides displayed sizes ranging between 4-7nm. It is worth mentioning that these Pd nanparticles were synthesized directly in the manganise oxide supports through the polyol method. In terms of electrocatalytic evaluation, Pd/α–MnO_2 showed higher activity than the Pd/Mn_3O_4 electrocatalyst. This was determined by varying the concentration of ethylene glycol (0.1-2M), the supporting electrolyte (0.1- 1M KOH) and the operation temperature (20-50°C). In addition, electrochemical impedance spectroscopy experiments indicated that the increase in activity was related to the improvement of electronic properties, where the Pd/α–MnO_2 electrocatalyst presented a lower charge transfer resistance.

Keywords: ethylene glycol, fuel cells, electrocatalyst, manganese oxides, supports, nanomaterials.

Acknowledgements
The authors express their gratitude to CONACYT for the financial support granted for the development of this research through the project CONACyT SENER-Energy Sustainability-INNOVATE UK Grant no. 269546. In addition, authors acknowledge the SEM/TEM facilities provided by CIMAV-nanotech.

016. ANALYSIS FOR AN IN-SITU HYDROGEN CONTINUOUS PRODUCTION SYSTEM BY ALUMINUM CORROSION IN AQUEOUS ACID SOLUTION USING SODIUM MOLIBDATE AS A PROMOTOR

Erick Arellano Domínguez[1], Ana Lidia Martinez Salazar[1], Jonathan Jesús Malpica Maldonado[1]

[1]Tecnológico Nacional de México, Instituto Tecnológico de Ciudad Madero, Centro de Investigación en Petroquímica, Prol. Bahía del Aldair, Av. de las Bahías, S/N Parque Pequeño y Medio Industrial, C.P. 89600, Altamira, Tamps, México, erick.ad.14@gmail.com

This study reports hydrogen production by corrosion of aluminum alloy in hydrochloric acid (HCl) [1] 1.39M using sodium molibdate (Na_2MoO_4) [2,3] as promotor of the reaction. This production could have the capability of be used into a 100W proton exchange membrane (PEM) fuell cell [4,5] as an entrance gas. The hydrogen production process is based on the electrochemical reaction of aluminum in pressence of HCl solution [1]. A gas chromatography study reports a low moisture content on production gas that is a specific requirement of the proton exchange membrane fuel cell utilized. The initial reaction temperature was 75°C [3,6] and the results obtained through this process were favorable for demand requested by a 100W PEM fuel cell stack that was 1.3 L/min of H_2 99% pure. X-ray diffraction (XRD) have been used to prove that the promoter is reactivated by the end of the reaction. Through the reaction the stoichiometryconvertion measurement have been used and it reports a final convertion of 63% at the end of the production measured.

References

(1) El-Meligi, A. A. Hydrogen Production by Aluminum Corrosion in Hydrochloric Acid and Using Inhibitors to Control Hydrogen Evolution. *Int. J. Hydrogen Energy* **2011**, *36* (17), 10600–10607.
(2) Kwolek, P., Kaminski, A., Dychton, K., Drajewicz, M. & Sieniawski, J. The corrosion rate of aluminium in the orthophosphoric acid solutions in the presence of sodium molybdate. Corros. Sci. **2016,** 106, 208–216.
(3) Li, X.; Deng, S.; Fu, H. Sodium Molybdate as a Corrosion Inhibitor for Aluminium in H 3 PO 4 Solution. Corros. Sci. **2011**, 53 (9), 2748–2753.
(4) Kim, T.; Kwon, S. Design and Development of a Fuel Cell-Powered Small Unmanned Aircraft. Int. J. Hydrogen Energy **2012**, 37 (1), 615–622.
(5) Kim, J.; Kim, T. Compact PEM Fuel Cell System Combined with All-in-One Hydrogen Generator Using Chemical Hydride as a Hydrogen Source. Appl. Energy **2015**, 160, 945–953.
(6) Razavi-Tousi, S. S.; Szpunar, J. A. Mechanism of Corrosion of Activated Aluminum Particles by Hot Water. Electrochim. Acta **2014**, 127, 95–105.

Acknowledgements

We gratefully aknowledge the financial support of this work to Conacyt for the No. 903177 scholarship through Centro de Investigacion en Petroquimica, Instituto tecnológico de Ciudad Madero.

017. ELECTROCATALYSIS OF SHAPE-CONTROLLED AND SEMISPHERICAL NANOPARTICLES SYNTHESIZED DIRECTLY ON ZrO_2 CERAMIC SUPPORT WITHOUT ANY CARBON CO-SUPPORT

N. Arjona[1]*, O. Ambriz-Peláez[1], L. Álvarez-Contreras[2], M. Guerra-Balcázar[3], S. Rivas[3]

[1] Centro de Investigación y Desarrollo Tecnológico en Electroquímica S. C., México.
[2] Centro de Investigación en Materiales Avanzados S. C., México
[3] Facultad de Ingeniería, Universidad Autónoma de Querétaro, México
*corresponding author: wvelazquez@cideteq.mx

Keywords: methanol oxidation, zirconia, Pd nanocubes, ethylene glycol oxidation.

Recent advances on the development of new materials for energy conversion have been directed i) to the designing of shape-controlled nanoparticles with a predominant domain of a facet and high shape-stability, and ii) to development of semispherical nanoparticles with enhanced activity due to improvement of electronic or structural characteristics. The succesful use of these materials in the energy conversion area for long-term applications depends on the use of highly corrosion-resistant supports. In this manner, ceramics are ideal to be use as supports; however, most of literature concerning ceramics deals with the use of carbon allotropes as co-supports. In this work, Pt nanoparticles and Pd nanocubes were synthesized directly on ZrO_2 without the assistance of any carbon support, and the activity was tested for the methanol and ethylene glycol electro-oxidation reactions, respectively. The synthesized Pt/ZrO_2 material displayed main particles sizes of 6 nm, while Pd nanocubes supported on ZrO_2 presented average particles sizes close to 10 nm. The activity evaluation demonstrated that Pt/ZrO_2 had a similar performance than a commercial Pt/C [1]; however, Pd/ZrO_2 displayed better activity in terms of current density than a commercial Pd/C catalyst associated with the abundance of {100} facets.

Acknowledgements
The authors express their gratitude to CONACYT for the financial support granted for the development of this research through the project CONACyT SENER-Energy Sustainability-INNOVATE UK Grant no. 269546. In addition, authors acknowledge the SEM/TEM facilities provided by CIMAV-nanotech.

References
[1] A. Aguilar-Vallejo, L. Álvarez-Contreras, M. Guerra-Balcázar, J. Ledesma-García, L. G. Arriaga, N. Arjona, S. Rivas, ChemElectroChem 6 (2019) 2107-2118.

018. IMPROVING PERFORMANCE OF ZnO DYE SENSITIZED SOLAR CELL BY INCORPORATION OF GRAPHENE OXIDE BY HIGH ENERGY MILLING

X. Atanacio-Sánchez[1], W.J. Pech-Rodríguez[1], Eddie N. Armendáriz-Mireles[1], P.C. Meléndez-González[2], E. Rocha-Rangel[1]*

[1]Universidad Politécnica de Victoria, Av. Nuevas Tecnologías 5902, Parque Científico y Tecnológico de Tamaulipas, Ciudad Victoria, Tamaulipas, C.P. 87138.

[2]Programa de Nanociencias y Nanotecnología, Cinvestav Unidad Saltillo, Av. Industria Metalúrgica 1062, Parque Industrial Ramos Arizpe. Ramos Arizpe, Coahuila, C.P 25900, México.
*E-mail: erochar@upv.edu.mx

At today great interest has been paid to hydrogen production by water electrolysis due to their simplicity and low cost. Dye sensitized solar cell are promising devices as renewable electrical power source to achieve water electrolysis because they possess high theoretical efficiency compared with Si based solar cells.
In this research, ZnO photocatalyst was modified with graphene oxide (GO) by means of high energy milling. The anode of the dye sensitized solar cell (DSSC) was fabricated by electrophoretic deposition of the photocatalyst onto flexible electrodes. The obtained materials were characterized by FTIR, XRD and SEM-EDS. The efficiency of the ZnO-GO was estimated from the VI curve, measured under simulated sunlight. The obtained results demonstrate that ZnO-GO have higher efficiency compared with the ZnO. The latter can be explained by the better dispersion of ZnO that enhance the dye adsorption onto the fabricated anode.

Acknowledgements

We thank CONACYT for master scholarships provided to X. Atanacio through grant 725432.

019. THE NEED FOR A PROYECT OFFICIAL MEXICAN STANDARD IN THE MANAGEMENT OF H_2

María Liliana Ávalos Rodríguez[1], José Juan Alvarado Flores[2], Jorge Víctor Alcaraz Vera[3]

[1] Centro de Investigación en Geografía Ambiental, Universidad Nacional Autónoma de México. Antigua Carretera a Pátzcuaro No. 8701, C.P. 58190, Morelia, Michoacán, México. Mail: lic.ambientalista@gmail.com
[2] Facultad de Ingeniería en Tecnología de la Madera, Universidad Michoacana de San Nicolás de Hidalgo. Santiago Tapia 403, CP 58000, Morelia, Michoacán, México.
[3]Instituto de Investigaciones Económicas y Empresariales, Universidad Michoacana de San Nicolás de Hidalgo. Francisco J. Mújica S/N, Col. Felicitas del Rio, C.P. 58000, Morelia, Michoacán, México.

Currently there is a global interest in the management of H_2 as an effective energy alternative that dissociates the dependence on fossil fuels, however, several studies have observed that resistance to H_2 prevails, especially in developing countries, the dangers and risks that its management represents. Despite this, there are a large number of publications that promote the sustainable management of H_2 and point out the advantages of its use in anthropogenic systems, which several countries with recognized technological advances, such as Germany, Spain, Canada, the United States and China, Japan, South Korea, among others, have not hesitated to promote the management of H_2 and incorporate the activities that arise from it, in a legal framework. It has been observed that, in Mexico, there is no legislation with respect to H2, which promotes sustainable management, because energy dependence on fossil fuels still prevails. In the same way, it has been observed that there are no Official Mexican Standards that establish rules and specifications on H_2 management. In this context, this study aims to analyze the need to build, promote, publish and disseminate a Draft Official Mexican Standard (NOM) on H_2 management, based on the existing legal needs and absences. The main findings show that there is a legal feasibility in the promulgation of a NOM on H_2 management, which should consider, among other things: minimum safety requirements in the design, construction, operation and maintenance of H_2 storage terminals; as well as, the rules for obtaining and distributing the H_2.

020. MOF 253-Pt A VIABLE OPTION FOR HYDROGEN PRODUCTION VIA PHOTOCATALYSIS

V. Ávila Vázquez[1] *, J. N. Pérez Viramontes[2] I.L. Escalante-García[2], V. H. Collins Martínez[3] , S.M. DurónTorres[2].

[1]Unidad Profesional Interdisciplinaria de Ingeniería Campus Zacatecas- Instituto Politécnico Nacional. Calle Circuito del Gato 202, Ciudad Administrativa, 98160 Zacatecas, Zac
[2]Universidad Autónoma de Zacatecas, Área de Ciencias Químicas, Carretera Zacatecas-Guadalajara km 6, Ejido "La Escondida", Edificio 6, C.P. 98160, Zacatecas, Zac.
[3]S.C. Depto. de Ingeniería y Química de Materiales, Centro de Investigación en Materiales Avanzados, Miguel de Cervantes 120, Complejo Industrial Chihuahua, 31190 Chihuahua, Mexico
** Corresponding author: vav_taba@hotmail.com*

Metal–Organic Frameworks (MOFs) have attracted increasing attention for the creation of solid-state platforms for catalysis applications, the MOFs are solid materials formed by metal ions (or clusters) coordinated to multidentate organic molecules [1]. The use of sunlight for the direct conversion of water into fuel is envisioned as essential process for sustainable production of hydrogen [2]. This work presents the results the physicochemical characterization of MOF 253 using Pt as metal ion for Hydrogen production from water. The material was synthesized by microwave methods, the specific surface of the particles ranged from 105.8 m^2/g. Their composition was studied by means of X-ray diffraction. The widths of band gaps were examined using UV-VIS spectroscopy. The Eg values of MOF 253-Pt were 3.27 eV. The photocatalytic activity of the samples prepared was tested on hydrogen production 128 µmol in 8 h with catalytic load of 10 mg compared with produced one by TiO_2 of 223 µmol de H_2 with catalytic load of 50 mg. MOF 253-Pt represents a viable option for the production of H_2 via photocatalysis.

References

[1] Sonja Pullen, Sascha Ott , Photochemical Hydrogen Production with Metal–Organic FrameworksTop Catal (**2016**) 59:1712–1721.
[2] Olivier Rosseler, Muthukonda V. Shankar 1, Maithaa Karkmaz-Le Du, Loïc Schmidlin, Nicolas Keller *, Valérie Keller, Solar light photocatalytic hydrogen production from water over Pt and Au/TiO2(anatase/rutile) photocatalysts: Influence of noble metal and porogen promotion, Journal of Catalysis 269 (**2010**) 179–190

021. CONVERSION OF CRUDE GLYCEROL TO PYOCYANIN FROM *Pseudomonas aeruginosa* NEJ01R FOR USE IN BIOELECTROCHEMICAL SYSTEMS

Bacame-Valenzuela F. J[1,2], Sandoval-González A[1,2], Cruz-Hernández M. G[1], Valdez-Paz J[1], Reyes-Vidal Y[1,2].

[1]Centro de Investigación y Desarrollo Tecnológico en Electroquímica, Parque Tecnológico Querétaro s/n Sanfandila, Pedro Escobedo, Querétaro, México. C.P. 76703, [2]CONACYT-Centro de Investigación y Desarrollo Tecnológico en Electroquímica, Parque Tecnológico Querétaro s/n Sanfandila, Pedro Escobedo, Querétaro, México. C.P. 76703. mreyes@cideteq.mx

Different options to the demand for obtain renewable feedstocks and green energy sources are biofuels, being the most widely used biodiesel and recently bioelectricity [1]. However, in the production process, crude glycerol is generated as a principal by-product, which contains 50-60% of crude glycerol, 12-16% of alkalis, 15-18% of methyl esters, 8-12% of methanol and 2-3% of water. Others elements present in this waste are Ca, Mg, P or S [2]. Crude glycerol can be used as a carbon source. It has been reported that some bacteria, as *Citrobacter, Klebsiella, Clostridium, Lactobacillus*, metabolize this substrate [3]. *Pseudomonas aeruginosa* species are able to use complex substrates as a carbon source. This microorganism is characterized for being a producer of phenazine-derived compounds, mainly pyocyanin, a molecule known for its diverse biological activity and its ability as mediator for transfer extracelullar electrons. Therefore, the objective of this work was to use crude glycerol for the pyocyanin synthesis by *P. aeruginosa* NEJ01R and use in bioelectrochemical systems. It demonstrates that *P. aeruginosa* NEJ01R at a concentration of 1%, pH 10, 30 °C and 76 rpm, produces 1 µg/mL of pyocyanin. Using the above-mentioned conditions in a double chamber microbial fuel cell, the production of a current density of 29 µA/cm^2 and power density of 15 µW/cm^2 were achieved. The capacity of *P. aeruginosa* NEJ01R to use a by-product as a carbon source in the production of a redox metabolite, useful for transfer electrons to produce bioelectricity was demonstrated.

References

[1] Franca R., Souza P., Lima E., Costa A. An extended techno-economic analysis of the utilization of glycerol as an alternative feedstock for methanol production. Clean Techn. Environ. Policy. (**2017**) 19:1855–1865.
[2] Maru B., López F., Kengen S., Constantí M., Medina F. Dark fermentative hydrogen and ethanol production from biodiesel waste glycerol using a co-culture of *Escherichia coli* and *Enterobacter* sp. Fuel. (**2016**) 186: 375–384.
[3] Krasnan V., Plza M., Marr A., Markosová K., Rosenberg M., Rebros M. Intensified crude glycerol conversion to butanol by immobilized *Clostridium pasteurianum*. Biochem. Eng. J. (**2018**) 134:114–119.

Acknowledgements

This work was supported by SEP-CONACYT-Ciencia Básica. Project No. 258159. CB-2015-01. Authors thanks to FORDECYT, Consorcio del Agua, Project 297116.

022. HYDROGEN PRODUCTION BY WATER PHOTOCATALYSIS

J. D. Becerra-Ruiz[1], J. C. Jáuregui-Correa[1], I. Rangel-Vazquez[2], G. Del Angel-Montes[2]

1Faculty Engineering, Autonomous University of Querétaro Cerro de las Campanas S/N. Z.C. 76010. Querétaro, Qro. México E-mail: jbecerra29@alumnos.uaq.mx
2 Autonomous Metropolitan University - Iztapalapa Unit, Chemical Dept., Av. San Rafael Atlixco 186. Z.C. 09340. Ciudad de México. México.

The importance that it has taken now to look for new sources of energy that are economical, abundant, friendly with environment and renewable. One of these sources is Hydrogen (H_2) because when it is burned water vapor is produced. One of most viable sources of renewable H_2 is water and can be obtained by electrochemistry, biochemistry and photocatalysis. Photocatalysis of water can be one of best options to obtain H_2, since it is possible to use spectrum of sunlight with help of a photocatalyst. One of these photocatalysts is TiO_2. However, this material needs to be modified since recombination rate of pairs e- / h+ is almost immediate. TiO_2 can be modified by dopage or addition with other oxides, one of these oxides is Graphene Oxide (GO).

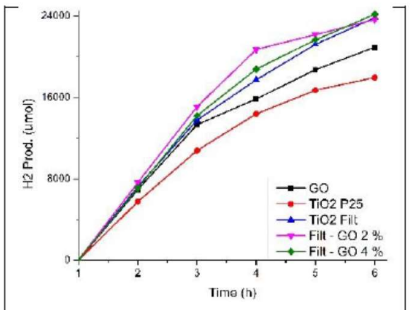

Fig. 1. H2 production for 6 hrs.

Some works of H_2 production using TiO_2 with Graphene who had following results. Zhang *et al.* (2010), Cheng *et al.* (2011) and Xiang *et al.* (2011), produced 86 µmol/h, 668 µmol/h and 736 µmol/h of H_2 [1-3]. It should be mentioned that GO is a type of Graphene but with functional groups. In this work we will study TiO_2 compound (synthesized in laboratory) impregnated with GO in different proportions (0.5, 2 and 4% in weight); compared to TiO_2 (Degussa P25). For production of H_2 (Fig.1), the reaction was carried out using 50 mg of photocatalyst TiO_2-GO in 1:1 solution of water and methanol in Nitrogen atmosphere for 6 hrs and irradiated with UV light. This reaction was followed every hour with Shimadzu GC 2014 gas chromatograph. A maximum of 24,153 µmol was obtained at sixth hour with Filt-GO 4% photocatalyst, which was 1.3 times better than P25.

References

[1] X. Zhang, H. Li, X. Cui, Y. Lin, J. Mater. Chem. 20 **(2010)** 2801.
[2] P. Cheng, Z. Yang, H. Wang, W. Cheng, M. Chen, W. Shangguan, G. Ding, Int. J. Hydrogen Energy. 37 **(2011)** 2224–2230.
[3] Q. Xiang, M. Jaroniec, Nanoscale, **(2011)** 3670–3678.

Acknowledgements

Thanks for the CONACyT-SENER 631485 maintenance grant and the CONACyT-SENER National Mobility Grant.To UAM - Iztapalapa for facilities for carrying out this project. We also acknowledge to CONACYT for support SEP-CONACYT project CB-2013-01-220191.

023. BIOHYDROGEN PRODUCTION USING ACIDIC CHEESE WHEY IN AN EGSB REACTOR

Germán Buitrón, Manuel A. Cuautle-Marín

Laboratory for Research on Advanced Processes for Water Treatment, Instituto de Ingeniería, Unidad Académica Juriquilla, Universidad Nacional Autónoma de México, Blvd. Juriquilla 3001, Querétaro 76230, Mexico, E-mail: GBuitronM@ii.unam.mx

Cheese whey (CW) is a potential substrate for biohydrogen production because its high carbohydrate content as well as the high biodegradability [1]. It contains lactose (45-50 g/L), soluble proteins (6-8 g/L), lipids (4-5 g/L) and mineral salts (8-10% of dried extract). The CW as a by-product from the manufacture of hard, semi-hard or soft cheese, is known as sweet whey and has a pH of 5.9 to 6.6 while the manufacture of mineral–acid precipitated casein, yields acidic whey, with a pH of 4.3 to 4.6 [2]. Supplemental alkalinity and pH control is required so as to avoid acidification during dark fermentation. The aim of this paper is to evaluate the performance of biohydrogen production by supplying either sodium hydroxide or sodium bicarbonate for pH maintenance in an EGSB reactor operated under different organic loading rates (OLR) variying from 7 to 42 g-total carbohydrates/L-d and using an acidic CW effluent. An EGSB reactor was operated under mesophilic condition (35°C). Methanogenic granular sludge was used as inoculum. Hydrodynamic stress was used for inoculum acclimation by applying an upflow velocity of 5m/h for entire experiment and acidic conditions [3]. Acidic cheese whey (CW) wastewater obtained from a cheese factory at the State of Queretaro, Mexico was employed. The results indicate that the highest biohydrogen productivity (4.34 LH_2/L-d) was obtained when NaOH was used and an OLR of 32 g-total carbohydrates/L-d was applied. However, the addition of bicarbonate in the feeding influent produces large amounts of carbon dioxide. It was observed that the neutralization agent decreased the granule diameter. This research evidenced the importance of the type of alkali employed for the pH control. The dissociation of bicarbonate generates carbon dioxide diluting the hydrogen concentration and decreasing the productivity. The application of high hydrodynamic stress in acidic condition makes a robust reactor to avoid methane generation, reduction of granule diameter and improving mass transfer at the same time.

References

[1] Carvalho, F., Prazeres, A. R., Rivas, J. **(2013).** Cheese whey wastewater: Characterization and treatment.Sci. Total Environ. 445–446, 385–396.
[2] Venetsaneas, et al. **(2009)**. Using cheese whey for hydrogen and methane generation in a two-stage continuous process with alternative pH controlling approaches. Bioresour. Technol. 100, 3713–3717.
[3] Hernández-Mendoza, C. E., Buitrón, G. **(2014)** Suppression of methanogenic activity in anaerobic granular biomass for hydrogen production: Anaerobic granules for hydrogen production. J. Chem. Technol. Biotechnol. 89, 143–149.

Acknowledgements

Technical assistance of Gloria Moreno and Jaime Pérez is acknowledged. Financial founds of CONACYT-SENER project (247006) are acknowledged.

024. BIOHYDROGEN PRODUCTION FROM AGAVE BAGASSE HYDROLYSATES

Germán Buitrón, Sharon Cobos-Valdez and Karla Muñoz-Páez

Laboratory for Research on Advanced Processes for Water Treatment, Instituto de Ingeniería, Unidad Académica Juriquilla, Universidad Nacional Autónoma de México, Blvd. Juriquilla 3001, Querétaro 76230, Mexico, E-mail: GBuitronM@ii.unam.mx

Acid hydrolysis of lignocellulosic material such as agave bagasse (generated during Tequila production) produces fermentable sugars and inhibitors (furfural and hydroxymethylfurfural), which could be a limiting factor to produce biohydrogen by dark fermentation. The treatments for the elimination of these by-products include activated carbon. The objective of this study was to evaluate the production of biohydrogen using detoxified hydrolysates at two temperatures (50 and 25 °C) and at three initial concentrations. The acid hydrolysate of agave bagasse contained 12.3 g/L soluble carbohydrates, 97.3 mg/L of hydroxymethylfurfural and 229.2 mg / L of furfural. The detoxification process was performed using the modified methodology presented by Lee et al. [1] at 50 °C and 25 °C. The production of H_2 in batch was followed using duplicates. Three concentrations levels of hydrolysate (without detoxification and detoxification) of 35, 50 and 75% were evaluated. Xylose (5 g/L) was used as the control. Anaerobic granular sludge heat treated was used as inoculum. Detoxification positively affected the biohydrogen production. With the concentration of hydrolysate at 75%, the treatment at 25 °C generated 1.6 times more hydrogen than the amount obtained with the hydrolysate without treatment. However, no significant effect was observed on the maximum production of H_2. A higher quantity of acetate was produced using the hydrolysates without detoxification (SD).However, that was not associated with the maximum production of H_2. This could be due to the fact that some of the inhibitors present in the hydrolysate without detoxification generated a change in the metabolic routes towards the production of acetate. That is the case of H_2 by homoacetogenesis [2]. Once the concentration of this inhibitor decreased with the detoxification treatments the generation of acetate was reduced. The maximal production of hydrogen was observed with the detoxified hydrolysates at 25 ºC and the highest concentration tested.

References

[1] Lee, J. M., Venditti, R. A., Jameel, H., Kenealy, W. R. **(2011)**. Biomass Bioenergy, 35, 626–63.
[2] Saady, N. M. C. **(2013)**. Int. J. Hydrogen Energy, 38, 13172–13191.

Acknowledgements

Technical assistance of Gloria Moreno and Jaime Pérez is acknowledged. Financial founds of CONACYT-SENER project (247006) are acknowledged.

025. INFLUENCE OF DOPING WITH NEODYMIUM ON Pt-Pd BIMETALLIC CATALYSTS SUPPORTED ON Γ-ALUMINA FOR THE PRODUCTION OF HYDROGEN BY CATALYTIC DECOMPOSITION OF METHANE

M. Caballero-Díaz[1, 2*], G. Del Ángel Montes[1], V. Tostado-Ramirez[1], M. Barrios Cruz[1]

[1] Carrera de Ingeniería Química, UNAM, Facultad de Estudios Superiores Zaragoza, Batalla del 5 de Mayo, Colonia Ejército de Oriente, Iztapalapa, C.P. 09230 México, Ciudad de México.
[2]Universidad Autónoma Metropolitana-Unidad Iztapalapa, Departamento de Química, Área de Catálisis, Av. San Rafael Atlixco No. 186, C.P. 09340, A.P 55-534. México D. F. México.
** Corresponding author: 55-20032433 and e-mail: marcabdi@yahoo.com.mx*

The application of methane thermal decomposition (TDM) to produce H_2 and solid carbon has been proposed as a potential technology for the period of transition to the H_2 economy [1]. The decarbonisation of fossil fuels, and especially the treatment of natural gas by the thermal decomposition of methane (TDM), has been proposed as a potential technology in the transition to the H_2 economy [2]. In the present work the effect of the addition of neodymium to the Pt-Pd catalyst was studied inorder to obtain a greater selectivity to hydrogen.
Three Pd-Pt catalysts supported on γ-Al_2O_3 and γ-Al_2O_3-Nd_2O_3 at 1 and 10% by weight were synthesized, by wet impregnation of the supports with (H_2PtCl_6 6 H_2O and $PdCl_2$) (Strem Chemicals, 99.99%) aqueous solution. The solids were left in stirring for 3 h, and then, the water is evaporated using a vacuum evaporator bath at 60 °C and vacuum of 72 millibars. The solids were dried in an oven at 120 ° C for 12 hours, then calcined at 500 ° C with air flow at 60 ml / min for 5 hours and finally the catalysts were reduced in a H_2 flow at 60 ml/min and 500 ° C for 5 hours. Supports, and catalysts were characterized using different characterization methods such as X-ray diffraction, N_2 adsorption-desorption, X-Ray photoelectron spectrometry, Temperature Programmed Reduction, infrared of CO and Pyridine, High Resolution Transmission Electron Microscopy and Temperature Programmed Oxidation analysis. The decomposition reaction of the methane was carried out in a temperature range of 400 to 750 ° C with a previous activation with nitrogen (30 ml/min at 200 ° C) and the flow of the reagent (methane) was 2 ml/min. To achieve this, an electric furnace was used with a tubular quartz reactor with a porous plate inside to contain the catalyst (50 mg). For the analysis of the reaction products a gas chromatograph Shimadzu GC-2014 was used.
The results that were obtained were the following: 1) The bimetallic Pt-Pd/A and of Pt-Pd/ANd1% showed higher conversion than the PtPd/ANd10% catalyst. 2) Whereas, the highest hydrogen production was obtained on PtPd/A catalyst. 3) The presence of Nd inhibits the selectivity towards hydrogen as the Nd increases (1 and 10 wt%). It is assumed that neodymium could interact stronger with the Pt-Pd bimetallic particles causing a high deposit of the coque on the metal sites, poisoning the active sites.

References

[1] T.M. Ivancic, et al.Discovery of a new Al species in hydrogen reactions of NaAlH4 J Phys Chem Lett, (2010), 1 (15) pp. 2412-2416.
[2] G Thomas. Overview of storage development DOE hydrogen program. Annu Rev; 2000.

Acknowledgements

We acknowledge to CONACYT for the support provided to the project SEP-CONACYT CB2013-01-220191 and Marina Caballero Diaz thanks to the CONACYT for the grant awarded No 387137/255851.

026. PRODUCTION OF HYDROGEN USING Pd/γ·Al_2O_3 CATALYSTS AND THE INFLUENCE OF NEODYMIUM ON THE CATALYTIC ACTIVITY AND STABILITY OF THE CATALYSTS

M. Caballero-Díaz[1, 2]*; G. Del Ángel Montes[2]; E. Castillo Bravo[1]

[1] Carrera de Ingeniería Química, UNAM, Facultad de Estudios Superiores Zaragoza, Batalla del 5 de Mayo, Colonia Ejército de Oriente, Iztapalapa, C.P. 09230 México, Ciudad de México.
[2]Universidad Autónoma Metropolitana-Unidad Iztapalapa, Departamento de Química, Área de Catálisis, Av. San Rafael Atlixco No. 186, C.P. 09340, A.P 55-534. México D. F. México.
** Corresponding author: 55-20032433 and e-mail: marcabdi@yahoo.com.mx*

Increasing environmental concerns has prompted the search for clean fuels to avoid emissions of greenhouse-gas (GHG) like COx, NOx, and SOx. Hydrogen has recently emerged as a clean energy, which is carbon free to replace the fossil fuels, resulting in the great demand of hydrogen production [1–3]. The energy produced by the combustion of hydrogen is 4 and 2.40 times more than the that of coal and natural gas combustion, respectively [4,5]. The more used method for H_2 production is the steam reforming of methane [6]. To obtain hydrogen from methane decomposition reaction, γ-Al_2O_3 and γ-Al_2O_3 doped supports with 1 and 10 wt% of neodymium were synthesized. Once the supports were prepared, the Pd/γ-Al_2O_3 and Pd/γ-Al_2O_3-Nd catalysts were obtained by wet impregnation method (1 wt% of palladium). Such materials were characterized using different techniques such as X-ray diffraction, N_2 adsorption-desorption, Transmission Electron Microscopy, X-Ray photoelectron spectrometry, Temperature Programmed Reduction, Infrared of Pyridine adsorption and CO and Temperature Programmed Oxidation analysis. The methane conversion was carried out at temperatures of 400, 500, 600, 700 and 750 °C to hydrogen production. For the analysis of the reaction products a gas chromatograph Shimadzu GC-2014 was used. Experiments were conducted using a quartz tubular reactor, electric oven, a type K thermocouple and a mass of 0.05 g of catalyst was employed.

The increase in area in the AND1% support with respect to the γ-alumina can be attributed to the fact that the neodymium does not block the pores and deposited on external surface of γ-alumina and for ANd10 support, neodymium is not fully dispersed and only partially blocks the pores of the γ-alumina. While the incorporation of neodymium (1 and 10 wt%) decreased the volume and the pore diameter with respect to the γ-alumina alone, this behavior would be due to deposition of Nd_2O_3 at the alumina pores mouth. After adding the Pd as active metal (1 wt. % nominal), the BET surface area, pore diameter and the pore volume decreased, which can be due to the pore blocking of the support after metal addition and the destruction of the mesoporous structure.

References

[1] Nasir Uddin M, Wan Daud WMA, Abbas HF. Energy Convers Manag (2015);90:218–29.
[2] Anjaneyulu C, Naresh G, Kumar VV, Tardio J, Rao TV, Venugopal A. ACS Sustain Chem Eng (2015);3:1298–305.
[3] Bayat N, Rezaei M, Meshkani F. Int J Hydrogen Energy (2016);41:5494–503.

Acknowledgements

We acknowledge to CONACYT for the support provided to the project SEP-CONACYT CB 2013-01-220191 and Marina Caballero Diaz thanks to the CONACYT for the grant awarded No 387137/255851.

028. ZINC FERRITES FOR METHYL RADICALS FORMATION: A STUDY OF WATER ADSORPTION INFLUENCE

Lorenzo Antonio Cruz Santiago[1*], Ana Lidia Martínez Salazar[1], Benjamín Portales Martínez[2], Ana Adela Lemus Santana[2], Edilso Francisco Reguera Ruíz[2]

[1] Ciencias de la Ingeniería, Instituto Tecnológico de Ciudad Madero, Tamaulipas, México.
[2] Laboratorio Nacional de Conversión y Almacenamiento de Energía, Centro de Investigación en Ciencia Aplicada y Tecnología Avanzada - Unidad Legaría, IPN, CDMX, México.
**lacrus8@gmail.com*

The oxidative coupling of methane is a reaction that involves formation of methyl radicals via hydrogen abstraction from the methane by active surface oxygen available in some catalysts, such as iron oxides. In this work, we synthesized $Fe(III)_{tet}[Zn_xFe(II)_{1-x}Fe(III)]_{oct}O_4^{2-}$ x=0.00,0.25,0.50,0.75,1 systems through coprecipitation route. The $Zn(NO_3)_2$, $Fe(NH_4)_2(SO_4)_2$ and $FeCl_3$ precursors were mixed with constant stirring at 50°C until homogenization was achieved. In next step, a solution of NaOH was added dropwise to mixture. Then, temperature was increased to 65°C and mixture was kept under constant stirring for 2 hours. Washings were carried out in triplicate before drying step, which was carried out at 30°C for 24 hours. Ferrites were characterized by infrared spectroscopy, X-ray diffraction, and thermogravimetric analysis. Infrared spectroscopy confirmed the ferrites presence, with bands in 300–650 cm^{-1} range that belong to Fe-O bond in Fe_3O_4. X-ray diffraction report of the synthesized samples matches well with COD 96-900-5839 (magnetite) and 96-230-0616 (zinc ferrite) cards. By thermogravimetry along with differential scanning calorimetry, we analize physisorption and chemisorption phenomena of the water molecule on zinc ferrites up to 500°C. Study of water adsorption in ferritic systems clarifies the possibility that these can be used in methyl radicals formation using Fenton's process.

Keywords: Zinc ferrite, coprecipitation, methane, water adsorption.

Acknowledgements

We thank Instituto Politécnico Nacional for providing necessary resources to carry out the research.

029. HYDROGEN PRODUCTION FROM CORNCOB USING A SIMULTANEOUS SACCHARIFICATION AND FERMENTATION PROCESS CONFIGURATION

Luis E. De la Cruz-Andrade[1], Lizeth A. Paredes-Peña[1], Héctor G. Sifuentes-Sánchez[1], José G. Moreno-Cedillos[1], Angélica L. Ortiz-Cruz [1], Mónica Muñoz[1], Ileana M.M. Moreno-Dávila[1], José A. Rodríguez- de la Garza[1], Miguel A. Medina-Morales[1], Thelma K. Morales-Martínez[1], Leopoldo J. Rios-González[1*]

[1]Departament of Biotechnology, School of Chemistry, Autonomous University of Coahuila, Mexico.
**leopoldo.rios@uadec.edu.mx*

Hydrogen, wich can be produced by biotechnological means, is considered a major energy source for the future. Considering that it is important to use agroindustrial wastes for bioenergy production, corncob may be considered as an important feedstock for hydrogen production [1]. The main goal of this work was to evaluate the process configuration of simultaneous saccharification and fermentation (SSF). In a vacuum bioreactor 9.08 g of corncob with 50 mL of culture media flushed with N_2. For enzymatic hydrolysis, 0.26 mL of CellicCTec3 was also added for the SSF configuration and 5 mL of *Clostridium acetobutylicum* inoculum for fermentation. The bioprocess was carried out at 35 °C, 200 rpm, sampling for 168 hours. Hydrogen production was measured in a gas chromatographer. According to the obtained results, an accumulation of 89 mL L^{-1} of hydrogen was reached at 168 hours. It is evident that the process configuration is achieving its purpose. For hydrogen to be produced, sugars must be present for its metabolization by *C. acetobutylicum*, which were released by the enzymes. This result paves the way for biomass degradation and hydrogen production by SSF.

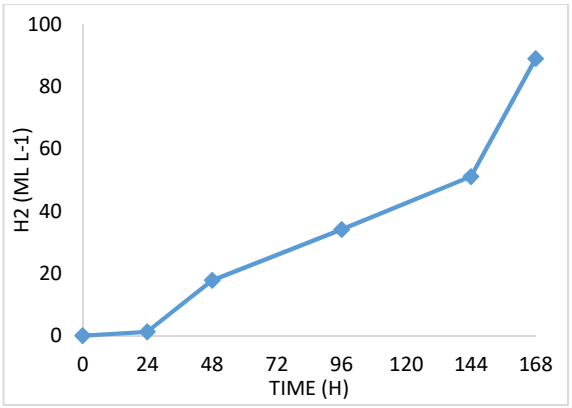

References
[1] X.M. Guo, E. Trably, E. Latrille, H. Carrere, J.P. Steyer Hydrogen production from agricultural waste by dark fermentation: a review. International Journal of Hydrogen Energy, (**2010**), pp. 10660-10067

Acknowledgements
The authors are grateful to the Autonomous University of Coahuila for the financial support provided through the CGEPI.

030. METAL-DECORATED GeC MONOLAYER FOR HYDROGEN STORAGE

Francisco de Santiago, Héctor Muñóz, Álvaro Miranda, José E. González and Miguel Cruz-Irisson

Instituto Politécnico Nacional, ESIME-Culhuacán, Av. Santa Ana 1000, CP 04440, Ciudad de México, México, fdesantiagov0900@alumno.ipn.mx

Because of their large surface and low density, bidimensional (2D) nanostructures are optimal for hydrogen storage. It has been proposed that a germanium carbide 2D monolayer may be more flexible than graphene, retaining some of its interesting properties [1,2]. In this work, we carry out a Density-Functional-Theory systematic study on the possible use of a GeC monolayer as hydrogen store. In order to physisorb the H_2 molecules, we propose alkali and transition metal (TM) atoms. The calculations suggest that transition metal atoms tend to be more strongly adsorbed than alkali metal atoms, which are in the threshold of chemisorption. The K-decorated case has the largest H_2 capacity for alkali metals, which agrees with results for germanene [3]. Cu-decorated GeC monolayers can adsorb the most H_2 molecules among the TM cases, however, their gravimetric capacity decreases because TM atoms are heavier than alkali atoms. These results may help in the development of optimal hydrogen storage systems for use in fuel cells for mobile applications.

References

[1] H. Şahin, S.C., M. Topsakal, E. Bekaroglu, E. Akturk, R. T. Senger, and S. Ciraci. Phys. Rev. B, **2009**, 80, 155453
[2] X.-S. Che, Z.-T. Liu, Y.-P. Li and T.-T. Tan. J. Alloys Compd, **2013**, 577, 15-18.
[3] K. I. M. Rojas, A. R. C. Villagracia, J. L. Moreno, M. David, N. B. Arboleda. Int. J. Hydrogen Energy, **2018**, 43(9), 4393-4400.

Acknowledgements

This work was partially supported by multidisciplinary projects IPN-SIP 2018-1937 and individual project IPN-SIP-2019-5830. Computations were performed at the supercomputer Miztli of DGTICUNAM (Project LANCAD-UNAM-DGTIC-180) and at supercomputer Abacus-I of CINVESTAV-EDOMEX. F.S. and H.M. would like to thank BEIFI-IPN and CONACYT for their financial support.

031. SILIGENE WITH ALKALI AND ALKALINE EARTH METAL ADATOMS FOR HYDROGEN STORAGE

Francisco de Santiago, Álvaro Miranda, Miguel Cruz-Irisson

Instituto Politécnico Nacional, ESIME-Culhuacán, Av. Santa Ana 1000, CP 04440, Ciudad de México, México, fdesantiagov0900@alumno.ipn.mx

Because of their large exposed surface, atomically thin layers like graphene and silicene have been proposed as ideal hydrogen storage materials for mobile applications. However, functionalization is needed to make these monolayers able to adsorb hydrogen molecules. The tendency of adatoms to aggregate over graphene, hindering H_2 adsorption, has spawned a search of alternative monolayers to avoid this problem. In this work, we propose the functionalization of siligene (a SiGe monolayer) with alkaline and alkali-earth metals for the adsorption of molecular hydrogen. We use Density Functional Theory to analyze the functionalization of the monolayer with the metal atoms, and then the physisorption of H_2 by the adatoms. The calculations show that aggregation of alkaline metal adatoms is improbable, contrary to akaline-earth metal adatoms. The adatoms tend to chemisorb on the hollow spaces at the center of the hexagons of the honeycomb lattice. Potassium is the most favorable adatom, as it can physisorb up to six H_2 molecules with an acceptable strength. The results show that siligene may be an acceptable alternative for mobile hydrogen storage to other monolayers that suffer from the problem of clusterization.

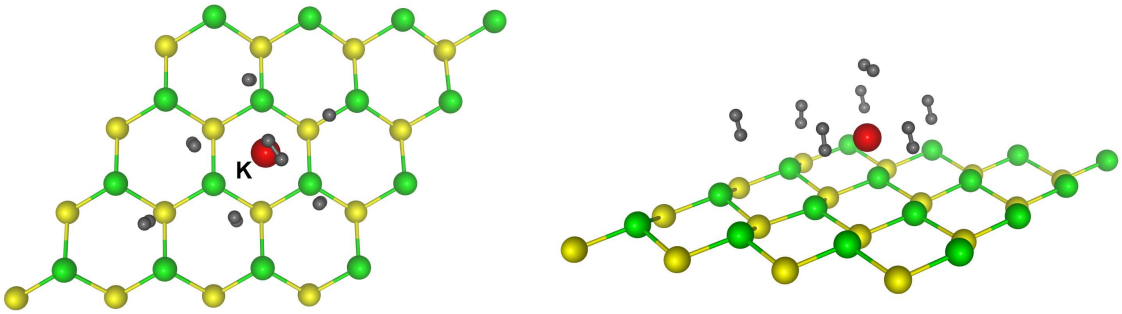

Fig. 1 Superior and lateral view of the siligene supercell decorated by K showing the maximum number of molecules it can physisorb.

Acknowledgements

This work was partially supported by multidisciplinary projects IPN-SIP 2018-1937 and individual project IPN-SIP-2019-5830. Computations were performed at the supercomputer Miztli of DGTICUNAM (Project LANCAD-UNAM-DGTIC-180) and at supercomputer Abacus-I of CINVESTAV-EDOMEX. F.S. would like to thank BEIFI-IPN and CONACYT for their financial support.

032. DEVELOPMENT OF Zn-AIR BATTERIES USING HIGHLY-ORIENTED Zn ELECTRODEPOSITED ON THREE-DIMENSIONAL CARBON ELECTRODES

A. L. Díaz-Patiño[1], E. Ortiz-Ortega[1], G. Trejo[1], L. Álvarez-Contreras[2], M. Guerra-Balcázar[3], J. Ledesma-García[3], L. G. Arriaga[1] and N. Arjona[1]*

[1]Centro de Investigación y Desarrollo Tecnológico en Electroquímica S. C., Parque Tecnológico Querétaro, Sanfandila, Pedro Escobedo, C.P. 76703, Querétaro, México.
[2]Centro de Investigación en Materiales Avanzados S. C., Complejo Industrial Chihuahua, Chihuahua, C. P. 31136, México.
[3]Facultad de Ingeniería, División de Investigación y Posgrado, Universidad Autónoma de Querétaro, Querétaro, C. P. 76010, México.
** Corresponding author: wvelazquez@cideteq.mx; noe.arjona@yahoo.com.mx*
Tel: +52 (442) 211 60 00 ext. 7874.

The metal-air batteries are an alternative to supply the energy demand of different technologies [1], however, this battery has certain issues to solve such as the formation of Zn dendrites in the charging process; passivation in the discharge process and low ionic conductivity by the electrolyte, these conflicts can be solved by using Zn with high crystallographic ordering and using polyacrylic acid partially crisscrossed with Potassium (PAAK) as gelled polymer electrolyte (GPE) [2]. In the present work, the effect of the PAAK composition was evaluated on the physicochemical properties and the performance of a Zn-Air battery. The GPE electrolytes were synthesized at 3, 6, 8 and 10 wt.% and were characterized by Raman microscopy, FTIR, viscosity and ionic conductivity, the anodic electrode was synthesized by electrochemistry test and characterized by SEM, Raman microscopy, XRD, and XPS. The performance of the battery was obtained by means of polarization curves, which revealed that the GPE at a concentration of 3 wt.% obtained the highest power of the battery (16.3 mW) which is even higher than with an aqueous electrolyte (KOH 6M), while the GPE at 10 wt.% possesses a dynamic viscosity of 27660 cP that favors limits for mass transport. The proper viscosity of the electrolyte compared to an aqueous solution 6 M KOH (<5 cP) does not compromise the performance of the metal-air battery and was attributed to the ability of the gel to retain KOH molecules in its polymer network.

References

Nano Energy, **2019**, 56, 454-462.
Funct. Mater. Lett, **2016**, 9, 1630001-1-1630001-11

Acknowledgements

The authors express their gratitude to CONACYT for the financial support granted for the development of this research. CONACyT SENER-Energy Sustainability- INNOVATE UK Grant no. 269546. Acknowledgments to the laboratories of other institutions that contribute with CIMAV NANOTECH, LABMyN.

033. CHITOSAN-POLYPYRROLE MEMBRANE AS AN ALTERNATIVE FOR PEM TYPE FUEL CELLS.

Alejandra Díaz Rivera[1], Celso Hernández Tenorio[1], Claudia Alicia Cortes Escobedo[2], Miguel Villanueva Castañeda[1], Hilda Moreno Saavedra[1], Arturo Tepale Cortes[1].

[1]División de Estudios de Posgrado e Investigación, Tecnológico Nacional de México/Instituto Tecnológico de Toluca, Av. Tecnológico s/n, Col. Agrícola Bellavista, CP 52149 Metepec, EdMx, México
[2]Centro de Investigación e Innovación Tecnológica, Instituto Politécnico Nacional, Azcapotzalco, Ciudad de México 02250, México

The present work focuses on study the chitosan doped with pyrrole (Py) by a glow plasma discharge in aqueous solution, through its chemical structure, morphology, proton conductivity and thermogravimetry for applications in fuel cells. Chitosan is a biodegradable polymer that contains a large number of -NH2 and -OH groups bonded to glucose units, resulting in a hydrophilic material that offers better adsorption and selectivity than Nafion [1]. The synthesis of the membrane was carried out by evaporation and the doping by plasma in times of 20, 40 and 60 minutes with concentrations of 0.1 M and 0.2 M, with average thickness of 480 nm. The morphological characterization showed that chitosan membranes have a smoother surface compared to those treated with pyrrole, which have a higher roughness that improves hydrophilicity and proton conductivity [2]. Infrared spectroscopy analysis showed the presence of polypyrrole functional groups producing interactions between amines, hydroxyl groups and C-N bonds; resulting in water resistant and mechanically stable membranes. The thermogravimetric analysis showed a degradation in a range of 40 to 70% at a temperature of 200 to 400 °C, confirming the thermal stability of the membranes and the proton conductivity significantly increased with the doping time in a range of 10^{-4} and 10^{-3} S/cm.

References

[1] Kumar Divya, Dipak Frog, Subbiah Alwarappan, Meenakshi Sundaram Sri Abirami Saraswathi, Alagumalai Nagendrana. Investigating the usefulness of chitosan based proton exchange membranes tailored with exfoliated molybdenum disulfide nanosheets for clean energy applications. Carbohydr. Polym. 208 (2019), pp. 504-512. Doi: 10.1016 / j.carbpol.2018.12.092.
[2] Saad Ahmed, Yangben Cai, Muhammad Ali, Santosh Khanal, Shiai Xu. Preparation and performance of nanoparticle-reinforced chitosan proton-exchange membranes for fuel-cell applications. J. Appl. Polym. Sci. 136 (2018), pp 1-7. Doi: 10.1002 / app.46904.

Acknowledgments

This research work was supported by Instituto Tecnológico de Toluca, Center for Research and Technological Innovation (CIITEC), National Polytechnic Institute (IPN), National Council of Science and Technology (CONACYT).

034. SYNTHESIS OF Ni BASED ELECTROCATALYSTS BY USING INTERMITTENT MICROWAVE HEATING REDUCTION PROCESS FOR ETHANOL OXIDATION REACTION.

L.R. Vidales-Gallardo[1], Eddie N. Armendáriz-Mireles[1], E. Rocha-Rangel[1], W.J. Pech-Rodríguez[1]*

[1]Universidad Politécnica de Victoria, Av. Nuevas Tecnologías 5902, Parque Científico y Tecnológico de Tamaulipas, Ciudad Victoria, Tamaulipas, C.P. 87138.
**E-mail: wpechr@upv.edu.mx*

This work is focused on the design and development of Ni based electrocatalysts by using intermittent microwave heating polyol reduction process.
The electrocatalysts were synthesized under different sequences of irradiation time and Ni concentration in order to investigate the effects on the ethanol oxidation reaction.
The obtained electrocatalyst was physical and chemical characterized by X-ray diffraction, Scanning electron microscopy with energy dispersive X-ray spectroscopy and Fourier-Transform Infrared Spectroscopy. Meanwhile, their electrochemical activity for ethanol oxidation was studied by cyclic voltammetry, chronoamperometry and electrochemical impedance spectroscopy. The results indicated that the synthesized parameters play a key role into the electrochemical activity of the materials. Therefore, it is demonstrated that intermittent microwave irradiation is a promising method to synthetize in a short time and in large scale Ni based electrocatalyst.

Acknowledgements
We thank CONACYT for the master scholarship provide to LR. Vidales-Gallardo. Also, we are gratefully for the help we received from the doctors of the Polytechnic University of Victoria since the road so far has not been simple but thanks to their contributions, support and my effort this research has been carried out.

035. EFFECT OF THE PARTICLE ARCHITECTURE ON THE PALLADIUM CHARGE IN ELECTROCATALYSTS FOR PEM-FC

Eduardo Y. Cervantes-Aspeitia[1], C. R. Santiago-Ramírez[1], Martha L. Hernández-Pichardo[1], R.G. González-Huerta[2] and Paz del Ángel[3].

*[1]ESIQIE-Instituto Politécnico Nacional, Laboratorio de nanomateriales sustentables, Av. IPN s/n, Ciudad de México, 07738. *mhernandezp@ipn.mx*
[2]ESIQIE-Instituto Politécnico Nacional, Laboratorio de electroquímica y corrosión, Av. IPN s/n, Ciudad de México, 07738.
[3]Caracterización de Materiales Sintéticos y Naturales, Instituto Mexicano del Petróleo, Eje Central L. Cárdenas 152, Ciudad de México, 07730.

In this work, Au@Pd core-shell nanoparticles (NPs) supported on vulcan carbon were synthesized by the seed growth method in order to decrease the palladium charge, compared to the commercial Pd/C catalyst. The effect of the bimetallization shows an enhanced activity toward the oxygen reduction reaction (ORR) evaluated in acid medium, as well as the change of the architecture allows a synergic effect between Au and Pd, this allow decreasing the palladium charge percent, from 10% to 5%. Carbon supported palladium nanoparticles is commonly used as a cathode electrocatalyst in fuel cells, but the cost of Pd and the limited world supply are significant barriers to achieve the comercialization of fuel cells [1]. Recent studies show that the bimetallization and the change in the architecture of the NPs allow the development of electrocatalysts with a low content of Pd [2]. The formation of Au@Pd core-shell NPs with an average size of 40 nm is showed at Fig 1A, the dispersion of nanoparticles is showed Fig 1B. By Scanning Electron Microscopy, it was obtained a semi-quantificaction of palladium charge percent, being 5%. Fig 1C shows the linear sweep voltammetry (LSV), in which the circuit potential values are 0.93 V vs NHE for both samples. The Au@Pd/C catalyst shows a higher current density, with a difference of 0.15 mV with respect Pd/C. This effect is related to the rugosity that the Pd has on the Au, which generates a greater number of active sites and therefore greater activity towards the oxygen reduction reaction.

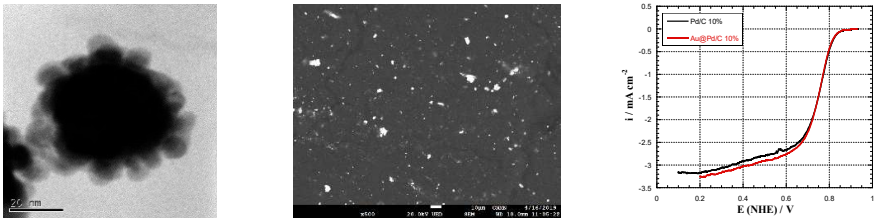

Fig 1. A) Au@Pd core-shell Nps of 40 nm. B) SEM micrograph and C) Linear scanning voltammetry at 5 mVs^{-1} and 1600 rpm in $HClO_4$.

References
[1] Energy Environ. Sci. (2009); 2, 915-931.
[2] Nat Chem (2011); 3, 478–83.

Acknowledgements
SIP project 20195668 and EYCA thanks the financial support from CONACyT within Ph.D fellowship.

036. EFFECT OF STERIC BULK ON ANCHORING GROUP INTERACTIONS IN ORGANIC DYE-SENSITIZED SOLAR CELLS

Luciano da Silva[1]*, Harold Freeman[2]

1Centro de Investigacion en Quımica Aplicada, Blvd. Enrique Reyna H. 140, Saltillo, Coahuila, 25294, Mexico. E-mail: luciano.dasilva@ciqa.edu.mx
2Department of Textile Engineering, Fiber and Polymer Science Program, North Carolina State University. E-mail: hfreeman@ncsu.edu

Dye-sensitized solar cell (DSSC) is a semiconductor photovoltaic device that directly converts solar radiation into electric current. A typical DSSC consists of a mesoporous photo anode with dye-sensitized titanium dioxide (TiO_2) film, an electrolyte containing iodide/triiodide (I/I_3) redox couple, and a counter electrode with platinum (Pt) catalyst. Upon the absorption of light energy, a photo-excited electron is injected from the excited state of the dye (Dye*) into the conduction band of the TiO_2. However, the immobilization of the adsorbing dye molecules onto the surface of semiconducting metal oxide nanoparticles, which collectively act as the working electrode of a DSSC, is crucial for initiating an electrical current via the injection of electrons. Herein we report structure-property relationships for dyes containing a 5-(4-nitrophenyl)tetrazole unit as an anchor group for DSSCs. These dyes have two different anchoring groups (nitro and tetrazole) and different conjugated systems attached through an azo bond. The different conjugated systems are 1-naphthol in **SD-1**, 6-benzoylamine-1-naphthol-3-sulfonic acid in **SD-2** and, N,N-diethylaniline in **SD-3**. This dyes were synthesized and used as the co-adsorbent with HD-2 dye to prepare the photoanode for a dye-sensitized solar cell (DSSC), and its photovoltaic performance evaluated. [1] The short-circuit current and the open-circuit voltage of the DSSC are increased for SD-3 with the co-adsorption and reduced for SD-2 and SD-1, comparing to deoxycholic acid (DCA) as coadsorbent. The energy conversion efficiency of the DSSC is 8,38 % to HD-2 - DCA, 6.09% to HD-2 – SD-1; 6,64% to HD-2 – SD-2 and 7.81% to HD-2 – SD-3, on the TiO_2 photoanode. The results obtained in this work suggest that the steric effects restrict the anchoring ability of the tetrazol groups, by hindering the approach of the TiO_2 surface and by restricting the coplanarity of the system.

References

1- Cheema, H. Islam, A., Han, L. El-Shafei, A. Influence of Number of Benzodioxan-Stilbazole-based Ancillary Ligands on Dye Packing, Photovoltage and Photocurrent in DyeSensitized Solar Cells, Appl. Mater. Interfaces **2014**, 6, 11617−11624.

ACKNOWLEDGMENTS: The authors gratefully acknowledges financial support by a scholarship from Conselho Nacional de Desenvolvimento Científico e Tecnológico (CNPq). The authors wish to thank Dr. Hammad Cheema for providing the sample of HD-2 used in this investigation.

037. EFFECT OF SULFONATION DEGREE ON POLY(ETHER-ETHER-KETONE) FOR FUEL CELL MEMBRANE APPLICATIONS

P.C. Flores-Escareño, D. Morales-Acosta*, R. Benavides Cantú*

Centro de Investigación en Química Aplicada, Bvld. Enrique Reyna No. 140, Col. San José de los Cerritos, 25290. Saltillo, Coahuila, México
** Tel: +52844-4389830 E-mail: diana.morales@ciqa.edu.mx; roberto.benavides@ciqa.edu.mx*

Proton exchange membrane fuel cells (PEMFC) are known to be environment friendly devices to convert chemical energy of a fuel (e.g. hydrogen, methanol) directly into electrical energywith high efficiency, particularly for portable and transport application systems. Polymer electrolyte membrane (PEM) is one of the main component of a PEMFC, with capable to promote proton diffusion from the anode to the cathode. The current focus of research for PEM is, the development of novel sulfonated aromatic hydrocarbon polymers as alternatives to conventional perfluorinated polymers. In this work, a series of sulfonated poly(ether-etherketone) (SPEEK) was prepared by aromatic electrophilic substitution with concentrated sulfuric acid as sulfonating agent, where the variation of reaction time (1-5 h) and temperature (70-90°C) were considerate. The membranes were cast from SPEEK solution in DMAc, which was chosen as the appropriate solvent after solubility tests. The effects of sulfonation time and reaction temperature on the ability to form a membrane and thermal properties were evaluated. The effective formation of PEEK-SO_3H of SPEEK was confirmed by FTIR (with the presence O=S=O, S=O, S-O bands of sulfonic acid group) and thermogravimetric analyses (TGA) were carried out to evaluate the thermal stability of SPEEK, as well as to obtain the degree of sulfonation. Water Uptake (WU), Ion-Exchange Capacity (IEC), Proton Conductivity and sulfonation degree (DS) were also evaluated. IEC values in the ranged between of 1.2-2.27 meq/g are directly related with DS, which is several times higher than that of Nafion ®117 (0.91 meq/g). WU values varied from 11-84%, but most of the membranes also exhibited higher WU over the corresponding Nafion (WU=13%). DS values calculated from the IEC results are in agreement with those determinate from TGA traces. The above results indicate that SPEEK with a DS between 38-80% are promising materials to be used as membranes in PEMFC applications.

Keywords: Proton exchange membranes, membranes, poly(ether-ether-ketone), SPEEK, fuel cells.

Acknowledgements
This work has been supported by the Mexican Council of Science and Technology (CONACyT) through grant 259010. PCFE thanks CONACyT for the support through the PhD scholarship.

038. SYNTHESIS OF MoS_2-Pt ON N-CNT BY ONE-POT STEP FOR HYDROGEN REACTIONS IN H_2-BR_2 FLOW BATTERY

Juan Daniel Frías-Hernández[1], Alejandra de la Rosa-Gómez[1], Ma. Luisa García-Betancourt[2], Sergio M. Durón-Torres[1], Ismailia L. Escalante-García*[1]

*[1]Maestría en Ciencia y Tecnología Química, Unidad Académica de Ciencias Químicas, Universidad Autónoma de Zacatecas, Zacatecas,Zac., México. *ileg@uaz.edu.mx*
[2]Centro de Investigaciones Químicas, Universidad Autónoma de Morelos, Cuernavaca, Mor., México.

Energy storage systems, such as redox flow batteries (RFBs), are an attractive option for an efficient use of solar and wind energy which their application has been limited by their variability and intermittent nature. A RFB stores electrical energy as chemical energy by means of redox reactions of active species in a electrolyte and, the other way around, when a process demands electrical energy. Among the RFB chemistries, the H_2-Br_2 RFB system (E_{cell}=1.09V) is considered for energy storage with a high capacity and power density due to the fast kinetics and great reversibility of the H_2 and Br_2 reactions [1]. However, the diffusion of bromide species from the positive electrode through the membrane towards the negative electrode causes the deactivation of the Pt/C electrocatalyst which is needed for the H_2 reactions. Research efforts have been focused on synthesizing new stable materials that help to prevent the Pt deactivation with high activity to H_2 reaction in the presence of bromine species. MoS_2 has been studied towards the hydrogen evolution reaction and it may be a possibility for the H_2-B_2 RFB system. In this work, MoS_2 and MoS_2-Pt were synthesized on nitrogen-doped carbon nanotubes (N-CNT) by a one-pot step surfactant assisted method. $MoCl_5$ and Na_2MoO_4 were used as molybdenum sources [2]. Scanning electron microscopy (SEM) was performed to study the morphology, particle distribution and size. The activity of the nanocomposites in acidic media with HBr was studied by cyclic voltammetry and linear sweep voltammetry. SEM micrographs showed that MoS_2 or MoS_2-Pt were deposited uniformly at the surface of the N-CNT as spherical-particles with 20 nm diameter approximately. Element mapping by SEM confirmed the formation of MoS_2 active materials. A decrease in the overpotential and increment in current density for hydrogen evolution reaction was observed when using one-pot synthesis compared to mechanical blends. MoS_2- Pt @ N-MWCNT exhibited high stability in the presence of HBr as compared with Pt/C electrodes. Overall, it was observed that a homogeneous particle distribution and high activities depends on the Mo source being $MoCl_5$ a better option than Na_2MoO_4 for an efficient way to prepare alternative Pt/C electrodes for H_2-Br_2 RFB.

References

[1]Cho KT, Tucker MC, Weber AZ. A Review of Hydrogen/Halogen Flow Cells. Energy Technol. junio de 2016;4(6):655-78.
[2] Mourdikoudis S, Liz-Marzán LM. Oleylamine in Nanoparticle Synthesis. Chem Mater. 14 de mayo de 2013;25(9):1465-76.

Acknowledgements The authors acknowledge to the Electrochemical Laboratory at the Universidad Autónoma de Zacatecas for all the facilities to carry out this investigation.

040. 3D ORDERED POROUS SPINEL ($ZnCo_2O_4$) AS ELECTROCATALYST FOR OXYGEN EVOLUTION.

José Béjar,[1] L. Álvarez-Contreras,[2] J. Ledesma-García,[3] N. Arjona and L. G. Arriaga[1*]

[1] Centro de Investigación y Desarrollo Tecnológico en Electroquímica S. C., Querétaro, C. P. 76703, México.
[2] Centro de Investigación en Materiales Avanzados S. C., Complejo Industrial Chihuahua, Chihuahua, C. P. 31136, México
[3] Facultad de Ingeniería, División de Investigación y Posgrado, Universidad Autónoma de Querétaro, Querétaro, C. P. 76010, México.
larriaga@cideteq.mx

Oxygen evolution reaction (OER) remain as the limiting reaction in electrolyzers for their successful used as principal hydrogen source due to its slow kinetic and the use of noble metals such as Ru and Ir as electrocatalysts for this reaction. This is the reason why attention has focused on finding another type of catalyst that allows decreasing the use of noble metals through using non-metallic materials and non-noble metals. The kinetic limiting steps for OER can be decreased using mixtures of metal transition oxides as alternative electrocatalysts; several oxides have been reported in literature presenting good catalytic activity and great stability, these qualities make them a sustainable solution to traditional OER catalysts, besides, increasing the specific area brings about a greater catalytic activity, within the morphologies that promote an increase of this, are the 3-DOM structures, which have attracted attention due to their uniform distribution of pores as well as a greater specific area. In this work we describe the use of a 3-DOM structure made up of a $ZnCo_2O_4$ composition. The electrocatalytic activity was studied by rotating disc electrode (RDE), the kinetic parameters were obtained from Tafel plots. X-ray diffraction (XRD) indicated that 3-DOM material has a spinel structure. The pore size was determinate by BET, morphology was studied by scanning electron microscopy (SEM) and transmission electron microscopy (TEM). These materials showed onsent potentials of 1.48 V and a surface area of 39.77 m^2/g.

041. Pt AND Pt-Sn AS ELECTROCATALYSTS FOR METHANOL OXIDATION REACTION

P.J. Pérez-Díaz[1,*], B. Ruiz-Camacho[1], A. Medina-Ramírez[1]

[1]*Department of Chemical Engineering, University of Guanajuato, DCNE, Col. Noria Alta s/n, C.P. 36050, Guanajuato, Gto., Mexico, e-mail: pperezdiaz01@gmail.com*

Fuel cells are devices capable of generating electric power in a direct and clean way, capable of substituting the conventional batteries even the engines [1,2]. It has been demonstrated that the proton exchange membrane fuel cells (PEMFCs) are the most promising devices, one of them are the direct methanol fuel cells (DMFC) that use methanol as fuel [3]. The methanol is a good option as fuel due to it is found naturally in the liquid form, this makes the methanol easy to manage and store [4]. In other hand, zeolites as the second catalyst can accelerate the alcohols oxidation. The zeolites are compounds of crystalline aluminosilicate of Si, Al y O with a tetrahedral structure; this property will allow enhancing the Pt dispersion and nucleation [5,6]. Moreover, a problem in the fuel cells is the intermediary formation (CO) due to the “Pt poisoning” [7], to attend this issue a bimetallic catalyst of Pt-Sn was proposed with the aim to decrees the intermediary formation and increases the MOR until CO_2. In this work three different electrocatalyst for DMFC were evaluated. For the preparation of the electrocatalysts, a zeolite-carbon with a ratio 3:1 was synthesized as substrate of Pt and Pt:Sn in a ratio 1:1. Additionally Pt supported on carbon Vulcan was synthesized, with the objective of test the effect of the support in the electrocatalytic activity for (MOR) in acidic medium. It was demonstrated that the presence of zeolite in the composite Pt/zeolite-C increase the current density in the MOR in comparison with the conventional Pt/CV catalyst. XRD results showed the crystalline structure of the materials synthesized. The tin presence favors the methanol direct oxidation generating less intermediary, also this addition diminishes the final cost of the cell. Even though the decrease of the platinum in the electrocatalyst reduced the generated conductivity, the Pt/zeolite-C catalyst presented the major stability in the chronoamperometry test.

References

[1] Antolini, E. Catalysts for direct ethanol fuel cells. Journal of Power Sources (2007) 170:1–12
[2] L. Carrette, K.A. Fiedrich, U, Fuel Cells 1 (2001) 5-39
[3] R. Sousa, D. Marques, G. Tremiliosi-filho, E. Rafael, C. Coutanceau, E. Sibert, K. Boniface, J. Power Sources 180 (2008) 283–293.
[4] L. Jiang, G. Sun, Direct Ethanol Fuel Cells (2009) 390–401.
[5] Y. Wang, J.W. Ren, K. Deng, L.L. Gui, Y.Q. Tang, Chem. Mater. 12 (2000) 1622–1627.
[6] D.S. Coombs, Can. Mineral 35 (1997) 1571–1606.
[7] Hoyos, B., Sánchez, C., & González, J. (2007). Celdas de combustible de etanol Pt - based anode catalysts for Direct Ethanol Fuel Cells, (2007) 74:195–202.

Acknowledgements

This work was financially supported by University of Guanajuato through the DAIP . We also thank Lourdes Palma Tirado (Neurobiology Institute-UNAM) for TEM characterization.

042. EFFECT OF THE TiO_2 CONTENT OVER THE ELECTROCATALYTIC BEHAVIOR OF Pt/C-TiO_2 CATALYSTS ON THE OXYGEN REDUCTION REACTION

Reyes-Tapia N.K.[1], García-de la Cruz Ariane[1], Cervantes-Aspeitia E.Y.[1,2], González-Huerta Rosa de Guadalupe[2], Hernández-Pichardo M.L.[1,*],

[1]Laboratorio de Nanomateriales Sustentables, ESIQIE-Instituto Politécnico Nacional. Av. IPN s/n, Ciudad de México 07738.
[2]Laboratorio de Electroquímica y Corrosión, ESIQIE-Instituto Politécnico Nacional. Av. IPN s/n, Ciudad de México 07738.

Platinum catalysts are excellent materials for electrochemical reactions; however, these solids have some disadvantages such as their high price and poor stability against carbon corrosion, which leads to the detachment of metal nanoparticles and a loss of the electrocatalytic activity [1-3]. Thus, in this work, Pt/C-TiO_2 catalysts were prepared with different contents of TiO_2 in order to increase the stability and the catalytic activity of these samples by increasing the interaction between the metallic particles and the support. The samples were characterized by DRX, HRTEM, and XPS. The catalysts were evaluated on the hydrogen evolution reaction (HER) and we found that by using this synthesis method the highest catalytic performance was found by using low TiO_2 contents (3-5 % wt.).

References

[1] J. Ma, A. Habrioux, N. Alonso-Vante, “Enhanced HER and ORR behavior on photodeposited Pt nanoparticles onto oxide–carbon composite”, J Solid State Electrochem, 17 (2013) 1913–1921.
[2] B. Ruiz Camacho, M. A. Valenzuela, R. G. Huerta, N. Alonso-Vante, “Preparation and Characterization of Pt/C and Pt/TiO_2 Electrocatalysts by Liquid Phase Photodeposition”, Topics in Catalysis 54 (2011) 512-518.
[3] T. H. Huynh, H.Q. Pham, A. Van Nguyen, L. G. Bach, V. T. Thanh Ho, “Advanced Nanoelectrocatalyst of Pt Nanoparticles Supported on Robust $Ti_{0.7}Ir_{0.3}O_2$ as a Promising Catalyst for Fuel Cells”, Ind. Eng. Chem. Res. 58 (2019) 675−684.

Acknowledgments

This study was supported by the Instituto Politecnico Nacional through the project SIP-20195668.

043. HYDROGEN PRODUCTION FROM ELECTROLYSIS OF SEAWATER USING PHOTOVOLTAIC CELLS

Rafael Garcia Gutierrez[1], Monica Sauceda Esparza[2], Rafael Cabanillas Lopez[2], Ricardo Rodriguez Carbajal[3], Ricardo Rangel Segura[4]

[1]Departamento de Investigación en Física, Universidad de Sonora, Hermosillo, Sonora, 83000, México, rgarcia@cifus.uson.mx
[2]Departamento e Ingeniería Química, Universidad de Sonora, Hermosillo, Sonora, 83000, México
[3]Departamento de Ingeniería Química, Universidad de Guanajuato, Guanajuato, Gto., 36000, México
[4]Departamento de Ingeniería Química, UMSNH, Morelia, Mich., 58030, México

In the electrolysis of seawater as a source of hydrogen, two options exist for the performance of the electrolysis process. The first option is the total desalination of the sea water and then add alkalis for the process of electrolysis to produce hydrogen in the cathode and oxygen in the anode. The disadvantages of this approach are the high cost of desalination and the water treatment to make it alkaline. The main advantage is the ability to use developed technology for the direct electrolysis of fresh water. The second option is to design an electrolyze system capable of utilizing sea water for direct electrolysis at a low power density and electrolyze only a small portion of the water in contact with the electrodes. The advantage of this method is the lower capital required for the system and natural elimination of the waste brine which is only slightly enriched with salts. Also using this technic is possible to produce important amounts of chlorine as a sub-product and also magnesium as hydroxide that have many uses in the chemical industry.
In this research we produced hydrogen via electrolysis from simply natural resources, seawater and solar energy. In order to carry out this experiment we used water from Bahia of Kino Sonora, a place no too far from the University of Sonora, only 100 kilometers away, and a 100-W solar panel that generate CD electricity using directly sunlight that is an abundant resource in the coasts of Sonora. In this work we have been able to produce about 2 liters of hydrogen per hour and nearly 1.2 liters of chlorine per hour with a normal direct radiation of 900 W/m^2. This technique could be the solution to the fuels problematic of the ethnicities that inhabit the shores of Sonora and other states of México.

Acknowledgements
The authors gratefully acknowledge the Universidad de Sonora, to the CEMIE-SOL and to the Red Solar.

044 STUDY OF N-DOPED AND FUNCTIONALIZED CARBON NANOMATERIALS AS METAL-FREE ELECTROCATALYSTS TOWARDS THE OXYGEN REDUCTION REACTION FOR ALKALINE FUEL CELL APPLICATIONS

E. Garza-Durán[1], J.G. Alanís- Gutiérrez[2], G. Vargas-Gutiérrez[1], B. Escobar-Morales[3], J. Escorcia-García[4], I.L. Alonso-Lemus[5], F.J. Rodríguez-Varela[1*]

[1] Sustentabilidad de los Recursos Naturales y Energía, Cinvestav Unidad Saltillo, Av. Industria Metalúrgica No. 1062, Parque Industrial Ramos Arizpe, Ramos Arizpe, Coahuila, C.P. 25900, México.
[2] Universidad Tecnológica de Querétaro, Av. Pie de la Cuesta No. 2501, Nacional, Santiago de Querétaro, Querétaro, C.P. 76148, México.
[3] CONACYT, Centro de Investigación Científica de Yucatán (CICY), Unidad de Energía Renovable, Calle 43 No. 130 Col. Chuburná de Hidalgo, Mérida, Yucatán, C.P. 97200, México.
[4] CONACYT-CINVESTAV del IPN, Unidad Saltillo, Av. Industria Metalúrgica 1062, Parque Industrial, Ramos Arizpe 25900, Coahuila, México.
[5] CONACYT, Sustentabilidad de los Recursos Naturales y Energía, Cinvestav Unidad Saltillo.
[*] javier.varela@cinvestav.edu.mx 52 +844 438-9600 (Ext. 8526)

Carbon-based nanomaterials are a promissing alternative to replace the Pt-based electrocatalysts for the oxygen reduction reaction (ORR), due to their electrochemical properties and low cost. In this study, three N-doped and functionalized carbon-based electrocatalysts have been developed: graphene (N-Gf), carbon nanofibers (N-CNFf) and a 3D hybrid composite (N-GCNFf), all of them sinthetized by low cost, green and scalable methods. N-Gf has been synthesized by one-step ball milling process using graphite as carbon source and melamine as both exfoliating agent and nitrogen source. Self-doped N-CNFf have been obtained by the electrospinning technique, using as precursor a mixture of polymethyl methacrylate/polyacrylonitrile (PMMA/PAN). The N-GCNFf electrocatalyst has been obtained by mixing N-G and N-CNF (1:1 wt. ratio) by sonication in a dimethylformamide:H_2O (10:1 volume ratio) solution. All the materials was submitted to a mild acid functionalization treatment.

The physicochemical characterization included X-ray diffraction (XRD), Raman spectroscopy, field emission scanning electron microscopy (FESEM) and energy-dispersive X-ray spectroscopy (EDS).The catalytic activity for the ORR has been evaluated by the Rotating Ring-Disk Electrode (RRDE) technique in 0.5 M KOH electrolyte. The linear sweep voltametry (LSV) polarization curves show that N-Gf, N-CNFf and N-GCNFf have an onset potential of the ORR (E_{onset}) of 0.90, 0.84 and 0.89 V and a current density (j) of -3.5, -2.2 and -2.19 mA cm-2 at 0.2 V vs. RHE), respectively. Moreover, the electron transfer number (n) is 3.7, 3.2 and 3.5, while the percentage of H_2O_2 is 15, 39 and 24% at N-Gf, N-CNFf and N-GCNFf, respectively. Therefore, these results suggest that the N-Gf is the electrocatalyst with the best electrochemical performance for the ORR, followed by N-GCNFf and N-CNFf.

Acknowledgements
The authors wish to thank CONACYT for financial support through grants 241526, 250632 and 253986.

045. REDUCTION AND OXIDATION KINETICS OF $NiWO_4$ AS AN OXYGEN CARRIER FOR HYDROGEN STORAGE BY CHEMICAL LOOPING PROCESS.

P.E. González-Vargas; J.M. Salinas-Gutiérrez; M.J. Meléndez-Zaragoza; V. Collins-Martínez; A. López-Ortiz *

Centro de Investigación en Materiales Avanzados, S.C., Miguel de Cervantes 120, Complejo Industrial Chihuahua
Chihuahua, Chih. México. C.P. 31136
** Tel: +52 6144394815; e-mail: alejandro.lopez@cimav.edu.mx*

ABSTRACT

Chemical looping process (CL) have been used for various purposes, one is the hydrogen storage using metal oxides (MeO) as the only source of oxygen (oxygen carriers) to produce water ($MeO + H_2 = Me + H_2O$) and regenerating the metal oxide with a steam oxidizing atmosphere for the hydrogen release ($Me + H_2O = MeO + H_2$). It was previously proved the potential capacity of $NiWO_4$ as an oxygen carrier to be used on CL process, to confirm these a kinetic study was performed on the involved redox reactions and their kinetic parameters are presented. In order to evaluate the nickel tungstate ($NiWO_4$) oxidation and reduction kinetics, this was thermogravimetrically tested (TGA) in three redox cycles in a temperature range of 730 to 870°C and reductive atmosphere from ca. 2 to 5 v% of H_2/Ar, while oxidation employed concentrations from ca. 0.8 to 2.2 v% H_2O/Ar. For the kinetic study, the data corresponded to the second cycle reduction or oxidation period for each experimental condition. Results indicate a global first order reaction for the reduction of the material (n = 1), while an order reaction of n = 0.8 for the oxidation reaction. Activation energies of 85.1 kJ/mol and 63.1 kJ/mol for the reduction and oxidation reactions were found, respectively. A process simulation employed the obtained kinetics parameters to evaluate the theoretical potential application of $NiWO_4$.

Keywords: $NiWO_4$; kinetics; chemical hydrogen storage; chemical looping.

047. HEAT SOURCES IN A PEMFC STACK: A NUMERICAL STUDY BASED ON CFD TECHNIQUES

Christian Hernández[1], Juan M. Sierra[1], S. J. Figueroa-Ramírez[1], H. J. Mandujano Ramírez[1], L. C. Ordóñez[2]

[1]Universidad Autónoma del Carmen, 070145@mail.unacar.mx, jsierra@pampano.unacar.mx
[2]Centro de Investigación Científica de Yucatán, lcol@cicy.mx

The indiscriminate use of fossil fuels to satisfy our energy requirements has caused society to seek the renewable energy sources (solar, wind, geothermal, biomass and hydroelectric) and clean technologies; however, among the different clean technologies that exist we can find the PEM fuel cells (PEM, is the acronym for Proton Exchange Membrane), which have attracted the attention of many scientists and engineers due to their high efficiency, modularity and zero emissions. The PEMFC uses hydrogen as fuel and oxygen as oxidant (some devices use “air”) and as a final process the cell produces deionized water that is displaced outside the cell with the rest of the oxidant that did not react within the fuel cell. As in a thermal machine, the main energy losses from the conversion of the fuel to electricity are dissipated as heat through an auxiliary system. In fuel cells, the energy is released in form of electricity and heat by a ratio of 50%-50% [1].
In this paper a Computational Fluid Dynamics (CFD) study in a PEM fuel cell is presented. The purpose of this study is focused on heat transfer produced in a fuel cell aerostack (10 cells). It is known that there are basically 3 sources of heat generation in a PEMFC, which are called as entropic heat of reactions, heat from the ohmic resistance (joule effect) and heat from the condensation of water vapor (latent heat). The understanding of these sources of heat generation provide useful information to solve the problems of hot zones in the PEMFC which result in the degradation of the membrane and the catalyst, the dehydration or overhydration of the membrane, among others.

References

S. Shahsavari, A. Desouza, M. Bahrami, and E. Kjeang, “Thermal Analysis of Air-Cooled PEM Fuel Cells”, **2012**, Elsevier, International Journal of Hydrogen Energy 37, [18261-18271].

Acknowledgements

The authors gratefully acknowledge to UNACAR for the granted support to perform the numerical simulations in their computing equipment and the use of Ansys ® software license. In addition, the author gratefully acknowledges CONACyT for the master’s scolarship and the financial support from the project 254667 “Consolidación del Laboratorio de Energía Renovable del Sureste (LENERSE)”.

048. PHOTOELECTROCATALYTIC OXIDATION OF PHENOL AND BISPHENOL A ON ZnO AND RuO_2 MATERIALS

Anaïs Hernández Hernández[1, 2], Aurora A. Flores Caballero[1], Román Cabrera Sierra[1], Luis A. Estudillo Wong[2], Arturo Manzo-Robledo[1]*

[1] Departamento de Ingeniería Química SEPI, Escuela Superior de Ingeniería Química e Industrias Extractivas (ESIQIE)-IPN. Ciudad de México, 07738, México, amanzor@ipn.mx
[2] Departamento de Sociedad y Política Ambiental, CIIEMAD, Instituto Politécnico Nacional, calle 30 de Junio de 1520, CDMX, 07340 México

The environmental pollution has increasing due to the fast-growing population. For example, industrial waste has an important impact as these effluents could contain organic compounds such as phenol and bisphenol A (BPA) [1]. In this work the photoelectrochemical interaction of these molecules were evaluated at the interface of ZnO and RuO_2 in neutral conditions [2]. In a first approach, RAMAN spectroscopy showed that the vibration modes corresponds to each structure in study. On the other hand, these materials were deposited by spin coating on ITO conductive glass, using as a substrate and working electrode. The photoelectrochemical properties were evaluated in a three electrode cell using graphite rod and Ag/AgCl as counter (CE) and reference electrode (RE) respectively in 0.5 M K_2SO_4. Cyclic voltammetry (CV) from -0.25 to 0.8 V/(Ag/ AgCl), Mott-Schottky (MS) analysis and electrochemical impedance spectroscopy (EIS) under dark and UV at 365 nm conditions were carried out. The photoelectrochemical oxidation of phenol and BPA were compared at dark and UV illumination-conditions. The results indicate an oxidation-degradation processes that is more marked in presence of ZnO, due to a more efficient formation of holes in the valence band (VB) and producing hydrogen at the cathode of the cell. Also, the EIS results put in clear that the charge transfer process during polarization is linked with the oxidation of the probe molecules.

References

[1] V.Silva-Castro J.C. Durán-Álvarez J.Mateos-Santiago A.A.Flores-Caballero L.Lartundo-Rojas A. Manzo-Robledo, “Photo-electrochemical and interfacial-process analysis of WO_3 nanostructures supported on TiO_2: An approach to BPA oxidation” Materials Science in Semiconductor Processing Volume 72, December **2017**, Pages 115-121.
[2] V. Vaiano M. Matarangolo J.J. Murcia H. Rojas J.A. Navío M.C. Hidalgo, “Enhanced photocatalytic removal of phenol from aqueous solutions using ZnO modified with Ag” Applied Catalysis B: Environmental Volume 225, 5 June **2018**, Pages 197-206

Acknowledgements

ESIQIE-SIP-IPN-20195212. CONACyT (project DEMS 160333, 247208).

049. MAXIMIZE THE GENERATION OF HYDROGEN FROM THE DETERMINATION OF THE OPTIMUM ANGLE OF INCLINATION FOR SOLAR COLLECTORS

Herrera-Romero J.V.[a,b], Escobar-Trujillo B.A.[a], Escalante Soberanis M.A.[b],San Pedro L.[b] , Flota-Bañuelos M. [b]

[a] Facultad de Ingeniería, Universidad Veracruzana, Campus Coatzacoalcos, Av. Universidad km 7.5, Col. Santa Isabel, C.P. 96535, Coatzacoalcos, Veracruz, México.
[b] Facultad de Ingeniería, Universidad Autónoma de Yucatán, Av. Industrias no contaminantes por periférico norte, col. Cordemex. Apdo. Postal 150, Mérida, Yucatán, México
vidherrera@uv.mx, bescobedo@uv.mx, mauricio.escalante@correo.uady.mx, liliana.cedillo@correo.uady.mx, manuel.flota@correo.uady.mx

The design and development of solar energy systems require knowledge of the variation and optimal utilization of solar radiation on a surface during a period. The amount of solar radiation received on a surface is affected by its orientation and its angle of inclination [1,2]. Therefore, the angle of inclination is one of the important parameters to capture the maximum incident solar radiation on a surface, and it is essential to maximize the energy production of the system [3-5]. In this study, the optimum angle of inclination of solar collectors for solar energy systems is determined by obtaining a simple formula for the calculation. The values of the total solar radiation on the surface of the collector are found in a specific location of study. Based on the results, the energy delivery was calculated for a case study in which a pre-heating process is carried out to yield high temperature electrolysis in combination with solar thermal energy.

Keywords: Alternating energies, orientation of solar collectors, maximization of solar radiation, orientation of solar collectors.

References

Duffie, J. A., & Beckman, W. A. (**2013**). *Solar engineering of thermal processes*. John Wiley & Sons.
Handoyo, E. A., & Ichsani, D. (**2013**). The optimal tilt angle of a solar collector. *Energy Procedia*, *32*, 166-175.
Despotovic, M., & Nedic, V. (**2015**). Comparison of optimum tilt angles of solar collectors determined at yearly, seasonal and monthly levels. *Energy Convers. and Manage.*, *97*, 121-131.
Stanciu, C., & Stanciu, D. (**2014**). Optimum tilt angle for flat plate collectors all over the World–A declination dependence formula and comparisons of three solar radiation models. *Energy Convers. and Manage.*, *81*, 133-143.
Patkó, I., Szeder, A., & Patkó, C. (**2013**). Evaluation the impact tilt angle on the sun collectors. *Energy Procedia*, *32*, 222-231.

050. SYNTHESIS AND CHARACTERIZATION OF AuPt AND PdPt BIMETALLIC NANOPARTICLES FOR ALCOHOLS OXIDATION

América Libertad Higareda Alvear[1], Ramiro Pérez Campos[2], Gerardo Antonio Rosas Trejo[3], Rodrigo Esparza[1]

[1] Centro de Física Aplicada y Tecnología Avanzada UNAM, México. alhigareda90@gmail.com
[2] Instituto de Ciencias Físicas, UNAM, México.
[3] Universidad Michoacana de San Nicolás de Hidalgo, México.

Bimetallic nanoparticles (BNPs) present better and even unique properties than monometallic nanoparticles and the bulk material. In recent years, there has been great interest in the search of experimental methods able to have control in the size, morphology, structure and composition of BNPs, due to the dependence of their characteristics with their catalytic properties [1]. This work shows the synthesis of AuPt and PdPt BNPs with different composition Pt:M (M= Au, Pd), which were synthesized by chemical reduction in organic medium. BNPs showed controlled characteristics, which were verified by different characterization techniques such as scanning electron microscopy (SEM), transmission electron microscopy (TEM), X-ray dispersive energy spectroscopy (EDS), X-ray diffraction (DRX), X-ray photoelectron spectroscopy (XPS) and spectroscopy of UV-Vis (UV-Vis) to know their size, size distribution, composition, structure and information crystallographic. Homogeneous BNPs (Figure 1) allowed the preparation of electrocatalysts to analyze the relation composition/catalytic activity for alcohols oxidation by cyclic voltammetry and their possible used in a Proton Exchange Membrane Fuel Cells (PEMFC).

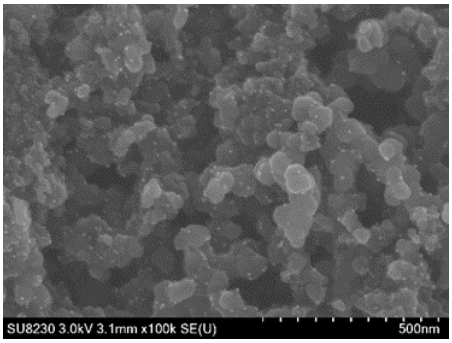

Figure 1. SEM image showed AuPt BNPs supported on Vulcan carbon with 20%wt of active phase, good dispersion and don´t have agglomerations.

References

[1] Bimetallic Nanocrystals: Syntheses, Properties, and Applications
Kyle D. Gilroy, Aleksey Ruditskiy, Hsin-Chieh Peng, Dong Qin, and Younan Xia
Chemical Reviews 2016 116 (18), 10414-10472
DOI: 10.1021/acs.chemrev.6b00211

Acknowledgements
This research was funded by UNAM-PAPIIT with grant IN113317. Centro de Física Aplicada y tecnología Avanzada (CFATA), Laboratorio Nacional de Caracterización de Materiales (LaNCaM) del CFATA-UNAM, Laboratorio Avanzado de Nanoscopía Electrónica (LANE) del Cinvestav, Zacatenco.

051. SONOCHEMICAL SYNTHESIS AND EVALUATION OF $MnMoO_4$ FOR PRODUCE HYDROGEN BY WATER SPLITTING

M. G. Joaquín-Morales[1], S. M. Montemayor[2], V. Collins-Martínez[3], A. López Ortiz[3], M. J. Meléndez Zaragoza[3], J. M. Salinas Gutiérrez[3], W. J. Pech-Rodríguez[4], A. F. Fuentes[1*]

[1]CINVESTAV, Unidad Saltillo, C.P. 25900, Ramos Arizpe, Coah. México, [2]Centro de Investigación en Química Aplicada, Blvd. Enrique Reyna No. 140, Col. San José de los Cerritos, 25294 Saltillo, Coah. México, [3]Centro de Investigación en Materiales Avanzados S. C., Miguel de Cervantes 120, C. P. 31136, Chihuahua, Chih. México, [4]Universidad Politécnica de Victoria, departamento de Ingeniería Mecatrónica. Av. Nuevas Tecnologías 5902, Parque Científico y Tecnológico de Tamaulipas, C. P. 87138 Ciudad Victoria, Tamps. Mexico.
**E-mail: antonio.fernandez@cinvestav.edu.mx*

In the present research, we report the preparation of manganese molybdate ($MnMoO_4$) nanorods by a facile sonochemical method and its photocatalytical activity for Hydrogen production via water splitting was investigated. Analysis of the materials was carried out using thermogravimetric analysis (TGA), Brunauer-Emmett-Teller technique (BET), X-ray diffraction (XRD), scanning electron microscope (SEM) and UV-Vis spectroscopy in order to obtain the crystalline structure, morphological, textural and optical properties of $MnMoO_4$ photocatalyst. Meanwhile, the photocatalytic performance of the synthetized materials were evaluated for H_2 production from desionized water with a solution of methanol, as a sacrificial agent, under simulated sunlight irradiation for eight hours.

Acknowledgements
We thank CONACYT for the PhD scholarship provide to Ma. Guadalupe Joaquín Morales. Also, we are gratefully to Cinvestav Saltillo and Special thanks to National Nanotechnology Laboratory at the Advance Materials Research Center, S. C. (CIMAV).

052. Ni CATALYSTS SUPPORTED ON CARBON, POLYPYRROLE, C-POLYPYRROLE, AND THEIR PERFORMANCE FOR ETHANOL ELECTROOXIDATION REACTION

C. Juárez-Reyes, C. Mena-Duran, B. Escobar, L. C. Ordóñez*

A Unidad de Energía Renovable, Centro de Investigación Científica de Yucatá.Parque Científico Tecnológico de Yucatán. Carretera Sierra Papacal – Chuburná Puerto, km 5. Sierra Papacal, Yucatán, México. C.P: 97302. E-mail: lcol@cicy.mx

In this work, we synthesize nickel catalysts supported on carbon Vulcan and carbon Vulcan-polypyrrole composite materials. The employed synthesis method was the chemical reduction in a microemulsion system. The electrocatalytic activity of the catalysts towards EOR in alkaline medium was determined by cyclic voltammetry (CV) and electrochemical impedance spectroscopy (EIS). The physicochemical characterization of catalysts was carried out using X-ray diffraction (XRD), X-ray photoelectron spectroscopy (XPS), scanning electron microscopy (SEM) and transmission electron microscopy (TEM). Results indicate that Ni spheres had a high electrocatalytic activity and excellent stability for the electro-oxidation of ethanol under alkaline conditions. This activity correlates the low transfer load resistance obtained during the analysis by EIS and the size and shape of the Ni structures observed by SEM. The catalysts activity was improved with the addition of polypyrrole (PPy) to the support. Ni/PPy was the most active to oxidize ethanol under alkaline conditions.

References

[1] Xu, C., Hu, Y., Rong, J., Jiang, S. P., & Liu, Y. (2007). Ni hollow spheres as catalysts for methanol and ethanol electrooxidation. *Electrochemistry Communications*, *9*(8), 2009–2012. https://doi.org/10.1016/J.ELECOM.2007.05.028

Acknowledgments

The authors are grateful for the financing of the SENER-CONACYT-Energy Sustainability Project-254666. Our thanks to Q.I. Tanit Toledano Thompson for the support provided in the MEB and EDS analyzes. The XRD and XPS measurements were made in the LANNBIO Cinvestav Mérida laboratory, under the support of the FOMIX-Yucatán 2008-108160 projects, and CONACYT LAB-2009-01 (No. 123913).

053. THERMAL AND HYDRODYNAMIC DESIGN OF A PHASES SEPARATOR FOR AN ALKALINE ELECTROLYSIS SYSTEM.

Valeria Juárez Casildo[1], Rosa de Guadalupe González Huerta[1*], Rogelio Sotelo Boyás[2]

[1]*Instituto Politécnico Nacional ESIQIE, Laboratorio de Electroquímica, UPALM, CP 07738, Ciudad de México, mail *rosgonzalez_h@yahoo.com.mx*
[2]*Instituto Politécnico Nacional ESIQIE,* Modelado y optimización de procesos de refinación del petróleo y combustibles limpios, *UPALM, CP 07738, Ciudad de México.*

Very promises perspectives exist for the use of hydrogen as a fuel, it is known that hydrogen production with renewables is suitable and environmentally friendly. Today, alkaline water electrolysis has become in a mature technology due to de many studies made in whole world in order to improve efficiency and performance. In an alkaline water electrolysis system (AWES), the core of the process is the coupling between the electrolyser and a phases separator (PS). The latter is usually a jacketed tank where the electrochemical reactor effluent formed by a biphasic mixture is separated. In addition, the proper work of a PS is absolutely important because on this depend the correct electrolyte management and the thermal control of the system in order to achieve a isothermal regime. The main parameters that characterize a PS are the separation factor, liquid retention time and the L / D ratio.

In this paper it is presented a thermal and hydrodynamic design of a phases separator, those was made by solving the equations of an energy and momentum balances, taking into account the physical properties of the fluids at operating conditions (1 atm and 60°C). The biphasic mixture consists on hydrogen, oxygen and an aqueous solution of NaOH at 3.75 M. The design parameters were the characteristics of an alkaline electrolyser (AE) at maximum capacity, in these conditions the gas produce (mixture of H_2 and O_2) and the recycle electrolyte flow 1 SLPM and 1.3 LPM respectively. Also, it was found that the power losses in the AE are 178.6 W. And de apropiate L/D ratio for the system is 3.

References

[1] Horcasitas M., Sandoval J., Grunstein B., Terán L., González R., Design and Manufacture of ICE Test Module to Reduce Gasoline Consumption Using Oxyhydrogen Gas from an Alkaline Electrolyzer, Energy & Fuel (2016), vol. 30, pp. 6640
[2] Haug, P. et al. Process modeling of an alkaline water electrolysis. Journal of Hydrogen energy (2017), vol. 42, pp.15689-15707

Acknowledgements

Thanks to the financial support granted: IPN multidisciplinary project SIP-2024 (2019-2021) and CONACYT project CEMIE-Ocean-249795: Transversal Line I-LT1.

054. CATALYTIC ACTIVITY EVALUATION OF $La_{0.5}Sr_{0.5}CoO_3$ PEROVSKITE FOR METHYL ORANGE DYE DEGRADATION UNDER DARK

L.E. Verduzco[1], A.I. Martinez[1], R. Almanza Salgado[2], S.A. Lozano-Morales[3], M. Avendaño[4], K.P. Padmasree[1]

[1]Cinvestav Unidad Saltillo, Parque Industrial Saltillo-Ramos Arizpe, Ramos Arizpe, Coahuila, 25900, México
[2]Instituto de Ingeniería, Universidad Nacional Autónoma de México, Circuito Ext. S/N, Cd. Universitaria, C. P. 04510, CDMX, México
[3]CONACYT-Centro de Investigación en Química Aplicada, Blvd. Enrique Reyna No. 140, Saltillo, 25294, Coahuila, México
[4]Instituto de Ciencias Aplicadas y Tecnología, Universidad Nacional Autónoma de México, Circuito Ext. S/N, Cd. Universitaria, C. P. 04510, CDMX, México
E-mail: padmasree@cinvestav.edu.mx

Abstract

The pollution in water bodies caused by the discharge of organic dyes from textile industries has been a major concern as these organic dyes negatively affect our environment. In this study, perovskite oxide $La_{0.5}Sr_{0.5}CoO_3$ was synthesized by the Pechini method and evaluate its catalytic activity for the degradation of methyl orange dye pollutant under dark condition. The prepared sample was characterized by X-ray diffraction, scanning electron microscopy, thermal analysis, specific surface area BET, X-ray photoelectron spectroscopy and UV-vis diffuse reflecance spectroscopy. The catalytic activity under different catalyst concentration and pH values was evaluated under dark condition. The kinteic study shows the degration rate was 90% in 20 min under dark and reusabilty study shows the sample is reusable for further degradation. The result shows the $La_{0.5}Sr_{0.5}CoO_3$ catalyst is an efficient alterative material for the degrdation of pollutant dyes in waste water treatmet plants.

References

[1] M. Sun, Y. Jiang, F. Li, M. Xia, B. Xue, D. Liu, Dye degradation activity and stability of perovskite type $LaCoO_{3-x}$ (x= 0-0.75), Mater. Trans. **(2010)** 51, 2208-2214.
[2] H. Chen, J. Motuzas, W. Martens, J. C. Costa, Ceramic metal oxides with Ni^{2+} active phase for the fast degradation of Orange II dye under dark ambiance, Ceram. Int. **(2018)** 44, 6634–6640

Acknowledgements

The authors thanks to CONACYT Mexico for the financial support (CB-84267) and to Secretaria de Ciencia Tecnología e Innovación CDMX, grant number SECITI-048/2016.

055. SYNTHETIC CO_2 CAPTURE MATERIALS FOR HYDROGEN PRODUCTION: A REVIEW

A. López Ortiz[1], M.J. Meléndez Zaragoza[1], S.J. Ramírez González[1,2], V. Collins-Martínez[1]

[1] Departamento de Ingeniería y Química de Materiales, Centro de Investigación en Materiales Avanzados, S.C., Miguel de Cervantes 120, Chihuahua, Chih., 31136, México
[2] Facultad de Ciencias Químicas, Universidad Autónoma de Chihuahua, Circuito Universitario S/N, Campus Uach II, 31125 Chihuahua, Chih.

Hydrogen production from renewable energy sources is a research field that has been proposed as a strategy to reduce CO_2 emissions generated during its production from fossil sources. H_2 production combined with CO_2 capture, through solid absorbents route has represented an opportunity to minimize the need of energy requirements and promote separation of its gaseous products. One of the advantages of using these absorbents is the additional reduction of greenhouse gases emissions and at the same time obtaining H_2 as an energy vector.

Nowadays CO_2 capture materials have presented certain problems such as material degradation as absorption-regeneration cycles increase, therefore these solids are usually synthesized under special conditions and even doped with a compound to improve its capture and regeneration rate Other problems of these materials include their small capture capacity and poor thermal stability. Therefore, an essential part of these H_2 production processes that use simultaneous CO_2 capture lies in the absorbent material, which is desired to have ideal characteristics as:

High capture capacity ($g_{CO2}/g_{material}$), moderate capture temperatures (T<700°C), be generable (can be used in several absorption-regeneration cycles), be able to interact with others materials (i. e. Catalyst) without interfering with the process and to show an adequate capture and regeneration rate.

Accordingly, the objective of this work is to present a review of the latest research progress (last five years) that have reported in the literature related with these absorbent synthetic materials and/or to possess CO_2 capture potential characteristics towards H_2 production. This information pursues to expose a panoramic view of the investigation opportunities in the area and to focus future studies to obtain optimal materials both in its function and preparation.

056. STUDY OF OPEN COMBUSTION OF OXY-HYDROGEN GAS AND FLAME PROPAGATION AT LOW OPERATING PRESSURES FOR A FLAME ARRESTER DESIGN

S. Maldonado-Teodocio[1], J. M. Sandoval-Pineda[1], G. J. Gutierréz-Paredes[1], U. Maza-Nájera[1]

[1]Instituto Politécnico Nacional, ESIME-Azc., SEPI, Av. de las Granjas 682, Col. Santa Catarina, CP 02250, CDMX, 5576279288, su33mt@gmail.com

Hydrogen as fuel or fuel enricher is been using nowadays in engines applications. There are a few studies that approach hydrogen as fuel for burners, but few that talk about a small burners and opened combustion using mixed gases. The main problem resides over hydrogen properties. Chemical reactions of hydrogen combustion often require a small amount of activation energy to get started, but then the energy re-leased by the reaction feeds further reaction in a domino effect. Hydrogen has the highest energy-to-weight ratio of any fuel since hydrogen is the lightest element and has no heavy carbon atoms. For that reason, hydrogen is flammable over a very wide range of concentrations in air (4 – 75%) and it is explosive over a wide range of concentrations (15 – 59%) at standard atmospheric temperature. Under certain conditions, the flame can burn back through the burner exit ports and ignite the potentially explosive gas–air mixture in the piping system. Of course, burner system designers have the expertise to design suitable burners that prevent flashback by flow-control measures. The uses of safety devices like a flame arrestor protect the system against deflagration and detonation caused by flashback from a combustion process.[1]

The present study covers the properties combustion of oxy-hydrogen gas, that is produced by alkaline water electrolysis. Properties of the flame like flame propagation and quenching; laminar flame quenching; deflagration quenching, Maximum Experimental Safe Gap.[2] As well the materials that are using for flame arrestors designs and normative about safety use of hydrogen. This study will be the base of a flame arrester design, that will be directly burning the gas produced by the reactor (electrolyzer) using a small burner; that could quench an oxy-hydrogen flame when stop the supply of fuel.

References

[1] Nabhani, N. Investigation on the application of using hydrogen fuel for furnaces. **2012**, *32*, 89–96.

[2] Wang, L.; Ma, H.; Shen, Z.; Chen, D. Flame Quenching by Crimped Ribbon Flame Arrestor : A Brief Review. *Process Saf. Prog.* **2018**, *00* (00), 1–15. https://doi.org/10.1002/prs.11975.

Acknowledgements

This work is supported by The National Council on Science and Technology (CONACYT) and The National Polytechnic Institute of Mexico (IPN).

057. SYNTHESIS AND CHARACTERIZATION OF Ni-Mo_2C NANOPARTICLE CORE/SHELL FOR POTENTIAL APPLICATION AS A CATALYST TO BIO-FUELS PRODUCTION.

Jonathan Jesús Malpica Maldonado [1], José Aarón Melo Banda [1], Ana Lidia Martínez Salazar [1]

[1] Tecnológico Nacional de México – Instituto Tecnológico de Ciudad Madero - Centro de Investigación en Petroquímica, Prol. Bahía del Aldair, Av. De las Bahías. Parque industrial Tecnia, Altamira, Tamaulipas, México, 89608.jjmm15.inq@gmail.com.

Some studies have compared the catalytic properties between Mo_2C and noble metals, and they have come to the conclusion that these compounds have similar properties [1,2]. This behavior is attributed mainly to the electronic structure and crystalline structure of carbides [3]. Therefore, the use of the noble metals for biofuels production could be replaced by the use of carbides of the transition metals. In recent years several researches have focused its attention on the transformation of microparticles into nanoparticles, which has seen an important change in the physical and chemical properties of the matter. The particles of the transition metals in nanoscale have a high percentage of atoms uncoordinated with the surface, which causes them to be excellent catalysts to different chemical processes. To give a new approach in the improving of catalyst yields, catalysts are synthesized in nanometric scale with a core/shell architecture. This type of nanostructure consists of internal nanoparticles (core) encapsulated by porous materials (shell) [4].

In this research, Mo_2C nanoparticles were synthesized by carburization of Ammonium heptamolybdate tetrahydrate and nickel nitrate hexahydrate as precursor salt and sucrose as carbon source. Before to the carburization is necessary of treated previous into autoclave at 200 °C of the aqueous solution of the precursor salts. The conditions of carburization were at 1073 K, under an atmosphere reducing of H_2. The load of nickel was varied from 0 to 25 wt% [5,6]. All samples were characterized by Scanning Transmission Electron Microscopy (STEM), UV–vis Spectrometry, Dynamic Light Scattering (DLS) and X-Ray Diffraction (XRD) to determine size, optical properties of the nanoparticles and morphology.

References

(1) Liu, P.; Rodriguez, A. Catalytic Properties of Mo Carbide, Nitride and Phosphide a Theoretical Study. *Catal. Letters* **2003**, *91* (3–4), 247.

(2) Kitchin, J. R.; Nørskov, J. K.; Barteau, M. A.; Chen, J. G. Trends in the Chemical Properties of Early Transition Metal Carbide Surfaces : A Density Functional Study. *Catal. Today* **2005**, *105* (1), 66–73. https://doi.org/10.1016/j.cattod.2005.04.008.

(3) Ma, Y.; Guan, G.; Hao, X.; Cao, J.; Abudula, A. Molybdenum Carbide as Alternative Catalyst for Hydrogen Production – A Review. *Renew. Sustain. Energy Rev.* **2016**, *75* (November), 1101–1129. https://doi.org/10.1016/j.rser.2016.11.092.

(4) Chaudhuri, R. G.; Paria, S. Core / Shell Nanoparticles : Classes , Properties , Synthesis Mechanisms , Characterization , and Applications. *Chem. Rev.* **2011**, *112* (4), 2373–2433.

(5) Malpica-Maldonado, J. J.; Melo-Banda, J. A.; Martínez-Salazar, A. L.; Garcia-Hernández, M.; Díaz Z, N. P.; Meraz M, M. A. Synthesis and Characterization of Ni-Mo_2C Particles Supported over Hydroxyapatite for Potential Application as a Catalyst for Hydrogen Production. *Int. J. Hydrogen Energy* **2018**, 1–9. https://doi.org/10.1016/j.ijhydene.2018.08.152.

(6) Ouzzine, M. Spherical Carbons : Synthesis , Characterization and Activation Processes.*Carbon N. Y.* **2013**, *68*, 296–307

058. SYNTHESIS AND CHARACTERIZATION OF $IrRuO_x/TiO_2$ AS ELECTROCATALYST FOR THE OXYGEN EVOLUTION REACTION

Abissaid Martínez Séptimo[1,2], Miguel Ángel Valenzuela Zapata[2], Rosa de Guadalupe González Huerta[2*], Ricardo Zenteno López[2]

[1]Instituto Politécnico Nacional ESIQIE, Lab.Catálisis y Materiales, Zacatenco, 07738, CDMX
[2]Instituto Politécnico Nacional ESIQIE, Laboratorio de Electroquímica, UPALM, C.P. 07738, CDMX, mail: rosgonzalez_h@yahoo.com.mx

Currently, hydrogen has been proposed as a viable energy vector. The most efficient and cleanest method for the production of high purity hydrogen is electrolysis by proton exchange membrane (PEM) electrolysers. However, this production methodology involves high costs due to the use of highly expensive materials such as Ir and Pt for the catalytic layers [1,2]. In this research work, $IrRuO_x$ supported in TiO_2 was obtained by impregnation. The electrocatalyst obtained contains a total nominal amount of 40 Ru % w and 10 Ir % w. This electrocatalyst was chemically and structurally characterized by X-ray fluorescence (XRF), X-ray diffraction (XRD), electron scanning microscopy (SEM) and energy dispersive spectroscopy (EDS). In order to quantify the activity and electrocatalytic stability, were made cyclic voltammetry from 0 to 1 V vs NHE as well as linear voltammetry from 1 to 1.68 V vs NHE in 0.5 M H_2SO_4.

The electrocatalyst had the same electrochemical stability than a 1:3 IrO_2-RuO_2 commercial mechanical mixture (CMM) and showed higher mass activity (89 mA/mg_{metal}) than CMM (60 mA/mg_{metal}). These results are due to a high dispersion of the active phase of Ir-Ru on the support of TiO_2, it was corroborated by the chemical and structural analyses. Membrane-electrodes assembly (MEA) was manufactured. The synthetized electrocatalyst was anodic coating of the test electrolyzer where the oxygen evolution reaction is carried out. Deionized water (≥18 MΩcm) was used. The performance curve was obtained using a controlled current from 0.025 to 0.5 A cm^{-2}. MEA performance whit $IrRuOx/TiO_2$ electrocatalyst anode was lower (5 V @ 0.5 A cm^{-2}) than MEA performance with CMM of IrO_2-RuO_2 (3 V @ 0.5 A cm^{-2}). This lower performance is attributed to the electrical resistance of the material, because of TiO_2 is a semiconductor that generates resistance to the electrons transfer and probably pores of TiO_2 particles do not contain IrO_2-RuO_2.

References

[1] Carmo, M., Fritz, D., Merge, J., Stolen D., 2013, A comprehensive review on PEM water electrolysis, Int. J. Hydrogen Energy, 2013, 38, 4901-4934.
[2] Nicolas Alonso-Vante, Carlos Augusto, Campos Roldán, Rosa de Guadalupe González Huerta, Guadalupe Ramos Sánchez and Arturo Manzo Robledo, Fundamentals of Electrocatalyst Materials and Interfacial Characterization Editorial John Wiley & Sons, Inc, Printed in the USA, 2019, pp 280.

Acknowledgements (10 pt)
The authors would like to thank IPN multidisciplinary project 2024 (2019-2021) and CONACYT CEMIE Oceano-249795, transversal line I-LT1.

059. VULCAN XC-72 FUNCTIONALIZED WITH Cu ORGANOMETALLIC COMPOUND: ENHANCEMENT IN CATALYTIC ACTIVITY OF SUPPORTED Pd NANOCATALYST FOR THE ETHANOL OXIDATION REACTION IN ALKALINE MEDIA

P.C. Meléndez-González[1], M.E. Sánchez-Castro[1,2], J.R. Torres-Lubián[3], B. Escobar-Morales[4], I.L. Alonso-Lemus[5], F.J. Rodríguez-Varela[1,2]*

[1] Programa de Nanociencias y Nanotecnología, Cinvestav Unidad Saltillo, Av. Industria Metalúrgica 1062, Parque Industrial Ramos Arizpe. Ramos Arizpe, Coahuila, C.P 25900, México.
[2] Programa de Sustentabilidad de los Recursos Naturales y Energía, Cinvestav Unidad Saltillo.
[3] Centro de Investigación en Química Aplicada, Blvd. Enrique Reyna No. 140, Saltillo, Coahuila, C.P. 25294, México.
[4] CONACyT-CICY. Calle 43 No. 130 Col. Chuburná de Hidalgo, Mérida, Yucatán. C.P. 97200, México.
[5] CONACYT, Sustentabilidad de los Recursos Naturales y Energía, Cinvestav Unidad Saltillo.
**E-mail: javier.varela@cinvestav.edu.mx*

In this work, Vulcan XC-72 support is functionalized with a home-prepared Cu organometallic compound (labeled $C_{Cu\text{-}mes}$). The effect of the functionalization on the catalytic activity of the 20 wt. % Pd/$C_{Cu\text{-}mes}$ nanocatalyst for the Ethanol Oxidation Reaction (EOR) in 0.5 mol L^{-1} KOH is evaluated by comparing it with that of a typical Pd/C anode. Both nanocatalysts have been synthesized by the polyol method. The chemical composition of the Pd/$C_{Cu\text{-}mes}$ nanocatalysts determined by EDS is close to the nominally expected, with 19 % Pd (wt. %). Additionally, 9 % Cu has been obtained (wt. %), due to the functionalization of the support. XPS analysis of Pd/$C_{Cu\text{-}mes}$ indicates mainly the presence of Cu^0 and Cu^{+2} in the Cu2p region. At the Pd3d region, the species are Pd^0 and Pd^{+2}. In the case of Pd/C, the Pd^0, Pd^{+2} and Pd^{+4} species have been identified. The electrochemical characterization shows that the on-set potential ($E_{on\text{-}set}$) of the EOR at Pd/$C_{Cu\text{-}mes}$ is 0.27 V/RHE, while that on Pd/C is 0.36 V/RHE. Moreover, the mass catalytic activity shows an almost two-fold increase when using the Pd/$C_{Cu\text{-}mes}$ nanocatlayst (1234.42 mA mg_{Pd}^{-1}) compared to Pd/C (663.86 mA mg_{Pd}^{-1}). Meanwhile, CO-stripping measurements show that Pd/C oxidizes CO with $E_{on\text{-}set}$= 0.46 V/RHE and an oxidation potential (E_{ox})= 0.82 V/RHE, while Pd/$C_{Cu\text{-}mes}$ promotes the reaction with $E_{on\text{-}set}$= 0.28 V/RHE and E_{ox}= 0.79 V/RHE. The results suggest that the enhanced catalytic activity of Pd/$C_{Cu\text{-}mes}$ for the EOR is promoted by Pd-Cu metal surface interactions due to the functionalization of Vulcan. Thus, $C_{Cu\text{-}mes}$ is a candidate support for Pd-based nanocatalysts for Alkaline Direct Ethanol Fuel Cells (A-DEFCs) applications.

Acknowledgements
The authors wish to thank CONACYT for financial support through grants 241526, 250632 and 253986.

060. STUDY OF A CATALYTIC BED REACTOR FOR THE PRODUCTION OF HYDROGEN FROM BIOETHANOL

Iván Rafael Martínez[1], J.L.Contreras*[1], José Salmones[2], Beatriz Zeifert[2], Tamara Vázquez[1]

[1] Departamento de Energía, Universidad Autónoma Metropolitana Azcapotzalco, A. Sn. Pablo 180, Col. Reynosa, Ciudad de México, Código Postal 02200, México
[2]ESIQIE, Instituto Politécnico Nacional. UPALM. Zacatenco, Ciudad de México, México.
**jlcl@correo.azc.uam.mx*

In this work, a catalyst has been developed for the ethanol steam reforming reaction (ESR) based on a bimetallic Ni-Co-Hydrotalcite-WOx catalyst that has shown high selectivity to H_2. As a tool for the design of the reactor a two-dimensional mathematical model has been proposed, based on the conservation equations of matter and energy, with the objective of obtaining the conversion and temperature profiles in an integral reactor delimiting the problem by initial and contour conditions. The resolution of the system of parabolic partial differential equations was discretized by a variant of the implicit methodology, called the Crank-Nicholson method. Subsequently, an encoding was implemented in the Wolfram Mathematica® software for mathematical resolution. A series of models have been obtained from the literature that allows obtaining the numerical values of the transport properties required in the simulation. To validate the proposed model, the experiment was carried out in a tubular reactor, packed with catalytic material (PBTR). Composition analyzes were performed through the length of the reactor. The reaction of ESR is endothermic, presenting high energy demand. Therefore the heating was carried out externally using an electric furnace, isolated to eliminate the loss of heat with the outside.

References

[1] Iván Rafael Martínez Cervantes , Tesis de Maestria en Ingenieria de Procesos, Estudio de un reactor de lecho catalítico para la producción de hidrógeno a partir de bioetanol, Universidad Autónoma Metropolitana, Azcapotzalco, 2018.

061. MODELING A TUBULAR REACTOR TO OBTAIN HYDROGEN FROM THE DRY REFORMING OF ETANOL

Iván Ramosa[1], J.L.Contreras*[1], A. Hernandez[1], Israel Pala[2], Beatriz Zeifert [2] Arturo Pallares[1], Jennipher Perez[1]

[1] Departamento de Energía, Universidad Autónoma Metropolitana Azcapotzalco, A. Sn. Pablo 180, Col. Reynosa, Ciudad de México, Código Postal 02200, México
2ESIQIE, Instituto Politécnico Nacional. UPALM. Zacatenco, Ciudad de México, México.
**jlcl@correo.azc.uam.mx*

The reaction of dry ethanol reforming (Dry reforming of ethanol) has been studied, with the purpose of obtaining H_2 mainly from ethanol and CO_2. This was achieved using a Hydrotalcite catalyst with 10% Ni-4.5% Co, obtained by the coprecipitation method. Differential reactor tests were carried out to obtain the reaction rates without resistance to mass and heat transport, and thus obtain a kinetics of the power law type by means of the Gauss-Newton method to obtain the kinetic constant and the order of the reaction. Subsequently, the effectiveness factors are obtained, with a temperature sweep from 550 to 750 ° C, due to the endothermic reaction that is favored at high temperatures. The mass and energy balances for the packed bed reactor have also been modeled, by discretizing the partial differential equations in finite difference form, bidirectionally [1]. Once the equations are discretized, they are solved algebraically to obtain the temperature and conversion profiles along the bed. This was achieved through the use of MATLAB ® software. A maximum conversion of 95% Ethanol and 85% for CO_2 was obtained. As well as a selectivity to H_2 of 92%.

References

[1] Iván Ramos, Tesis de Maestria en Ingenieria de Procesos, Modelado de un Reactor Tubular para obtener Hidrogeno a partir de la Reformación seca de Etanol, Universidad Autónoma Metropolitana, Azcapotzalco, 2018.

062. CO-DIGESTION OF CRUDE GLYCEROL FOR HYDROGEN PRODUCTION USING *CLOSTRIDIUM ACETOBUTYLICUM* ATCC 824

Thelma K. Morales-Martínez[1], Héctor G. Sifuentes-Sánchez[1], Luis E. De la Cruz-Andrade[1], Lizeth A. Paredes-Peña[1], José G. Moreno-Cedillos[1], Angélica L. Ortiz-Cruz [1], Mónica Muñoz[1], Ileana M.M. Moreno-Dávila[1], José A. Rodríguez- de la Garza[1], Miguel A. Medina-Morales[1], Leopoldo J. Rios-González[1*]

[1]Department of Biotechnology, School of Chemistry, Autonomous University of Coahuila, Mexico,
**Corresponding author: Leopoldo J. Rios-González. Email: leopoldo.rios@uadec.edu.mx*
(phone no.) +52-844-4155752

During biodiesel synthesys, glycerol is produced as a byproduct in a ratio 1:10 (glycerol:biodiesel). To make biofuel production economically feasible, it is of major importance to take into consideration a multi-product approach (biofuels, high added value byproducts, biomaterials, among others) under a biorefinery concept. *Clostridium* strains possess the wider and more versatile systems known in regard to substrate uptake. *Clostridium acetobutylicum* has the capability to produce H_2, lactate, acetate, butyrate and ABE (acetone, butanol and ethanol) using glycerol as a solo carbon and energy source. Hydrogen is a ecofriendly renewable fuel due to that its combustion only generates water and renders 3 times more energy than conventional fossil fuels [1]. The aim of the present work was to assess the co-digestion of raw glycerol as strategy to improve the fermentation process using a pure strain of *C. acetobutylicum*. Residual glycerol was provided by a biodiesel production plant. Fermentations were carried out in 120 mL batch reactors, using as inoculum a *C. acetobutylicum* ATCC 824 strain. Assays were carried out under three different conditions: R1) glucose at 60 g/L; R2) glycerol at 60 g/L and R3) Co-digestion with glycerol at 50 g/L and glucose at 10 g/L. All experiments were supplemented with nutrients. The pH was set at 6.7, anaerobic conditions were establish purging the reactors with nitrogen, incubation temperature was 37°C for 96 h. Glucose and glycerol consumption were determined by HPLC and hydrogen production was quantified by gas chromatography (GC FID). Results obtained showed a higher H_2 production in the case of the co-digestion (130 mL) in which glucose concentration was low (R3), a greater amount of raw glycerol consumption (50 to 6.9 g/L) and a higher butanol production was observed. Ongoing research is focusing on process optimization in regard of hydrogen production.

Table 1. Hydrogen and butanol production under different conditions using *C. acetobutylicum* ATCC 824

Reactor	Glucose (g/L)		Glycerol (g/L)		Butanol (g/L) 96 h	H_2 (mL) 96 h
	Initial	Final (96 h)	Initial	Final (96 h)		
R1	60.0	36.5	-	-	1.67	110
R2	-	-	60.0	57.3	1.12	70
R3	10.0	2.2	50.0	6.9	3.35	130

References [1] Moreno-Dávila, I.M.M., Ríos-González, L.J., Rodríguez-de la Garza, J.A., Morales-Martínez, T.K., Garza-García, Y., 2019. Biohydrogen production from paper industry wastes by SSF: A study of the influence of temperature/enzyme loading. Int. J. Hydrogen Energy 4, 0–5.
Acknowledgements The authors are grateful to the CGEPI of Autonomous University of Coahuila for the financial support

063. PLATINUM CHALCOGENIDE (Pt-WS_2) AS ELECTROCATALYST FOR OXYGEN REDUCTION REACTION FOR THE PEMFC

Moreno-Grijalva Grecia Isis[1], Oropeza-Guzmán Mercedes Teresita[1], Alonso-Núñez Gabriel[2], Gochi-Ponce Yadira[1],

[1] Tecnológico Nacional de México/Instituto Tecnológico de Tijuana, Mesa de Otay 22500, México
[2] Universidad Nacional Autónoma de México, Centro de Nanociencias y Nanotecnología, Ensenada, Baja California C. P. 22860, México
grecia.moreno17@tectijuana.edu.mx

Pt-based chalcogenides are strictly studied due to their high and comparable Oxygen Reduction Reaction (ORR) activity in Polymeric Exchange Membrane Fuel Cells (PEMFC). $Pt_xW_yS_z/C$ [1], has been previously synthesized and reported. It presents higher electrochemical activity, tolerance and stability than the commercial electrocatalyst (Pt/C). In comparison with a platinum chalcogenide (Pt_xS_y/C) reported by the same research group [2], thus, the presence of tungstene provides higher catalytic activity while the sulphur contributes with long term stability and tolerance to platinum surface poisoning [3]. Meanwhile, this work accomplish the decreasing of noble metal loading, whereas the chalcogenide concentration increases. Furthermore, carbon nanotubes as electrocatalytic support, stand out for their higher mechanical resistance, electrochemical activity and surface area, more than carbon commonly used [4, 5]. Carbon nanotubes are synthesized by spray pyrolisis [6], purified and functionalized by ultrasonic bath and later on, Pt_xS_y/C nanoparticles are supported into a sustrate by electrophoretic deposition to create a highly dispersed surface and to improve the performance of the electrocatalyst. Electrochemical and physical characterization are carried out to study the ORR activity and also the electrocatalytic morfology and structure.

References

[1] Gochi-Ponce, Y.; Barbosa, R.; L.G. Arriaga, Alonso-Núñez, G.; Alonso-Vante, N. *ECS Trans.,* **2006**, 3, 189-197.
[2] Gochi-Ponce, Y.; Alonso-Núñez, G.; Alonso-Vante, N. *Electrochem. Commun.,* **2006**, 8, 1487-1491.
[3] Feng, Y.; Gago, A.; Timperman, L.; Alonso-Vante, N. *Electrochim. Acta,* **2011,** 56, 1009-1022.
[4] Huang, W.; Ahlfield, J.M.; Zhang, X.; Kohl, P.A. *J. Electrochem. Soc.,* **2017**, 4, 217-223.
[5] Mu, Y.; Liang, H.; Hu, J.; Jiang, L.; Wan, L. *J. Phys. Chem,* **2005,** 109, 22212-22216.
[6] Aguilar-Elguezabal, A.; Antunez, W.; Alonso, G.; Paraguay Delgado, F.; Espinosa, F.; Miki-Yoshida, M. *Diamond Relat. Mater.,* **2006,** 15, 1329-1335.

064. BIOHYDROGEN PRODUCTION USING DIFFERENT CONSORTIA OF MICROORGANISMS

G. Moreno[1], G. Buitrón[1], E. Trably[2], E. Latrille[2], A. Marone[2], G. Santa-Catalina[2], I. Moreno-Andrade[1]

[1]Unidad Academica Juriquilla, Instituto de Ingeniería, Universidad Nacional Autónoma de México, Blvd. Juriquilla 3001, 76230 Querétaro, Mexico. E-mail imorenoa@ii.unam.mx
[2]2LBE, Univ Montpellier, INRA, Narbonne, France.

Origin of the inoculum is one of the most important parameters to consider in the dark fermentation for hydrogen production, since this lead the microbial communities present in the process. The objective of this work was to evaluate the effect of the origin of the inoculum on the production of H_2 in a batch test using three different substrates. Six inoculums (aerobic and anaerobic) were tested for H_2 production with an emphasis on the sub-products obtained (volatile fatty acids [VFA], lactate, ethanol, formate, succinic and propanediol). Hydrogen production was adjusted to the Gompertz model according to [1]. Results of the adjusted kinetics are in table 1. The use of xylose resulted in the highest percentage of H_2 independently of the inoculum source (table 1). The highest H_{max} (195 mL) and % of hydrogen in gas (38.4%) were obtained with the anaerobic inoculum Tb08, while the highest R_{max} (12.5 mL/h) was obtained with an aerobic inoculum Tb05 using xylose as substrate. For the case of glycerol, propanediol was obtained in concentrations from 1463 to 2038 mg/L. Butyrate was the main VFA (from 262 to 1308 mg/L) produced independently of the inoculum except glycerol, where the maximal production was acetate (Tb04= 621±37 mg/L) or propionic (Tb04=871±249 mg/L). The microbial community analysis demonstrated differences in the microbial composition due to the origin of the inoculum. A correlation between the fermentative microorganisms with the H_2 production and sub-products was observed.

Table 1. Hydrogen production from different inoculum and substrates

Type	Inoculum origin	Substrate	Hmax (mL)	Rmax (mL/h)	Lamda (h)	H_2 content (%)	CH_4 content (%)
Anaerobic	Tb03	Glucose	101±26	5.5±0.5	7.7±1.5	26.5±8.3	0.25±0.26
		Xilose	154±18	8.7±1.7	18.8±4.6	26±8	0.18±0.13
		Glycerol	39±2	3.2±0.3	24±0	13.3±0.7	0.28±0.03
	Tb07	Glucose	119±36	3.1±0.7	20.7±0.6	24.1±0.6	0.68±0.08
		Xilose	174±52	4.4±0.8	23.3±3.8	32.1±2.5	0.52±0.37
		Glycerol	33±6	1.4±0.5	35.7±6.0	8.2±1.3	1.21±1.15
	Tb08	Glucose	89±1	1.9±0.3	30±2	23.3±0.1	0.12±0.02
		Xilose	195±18	5.9±0.1	20±3.6	38.4±1.8	0.11±0.01
		Glycerol	63.5±30	1.8±0.9	42±0.7	17.0±7.3	0.32±0.24
Aerobic	Tb04	Glucose	72±3	2.7±0.5	31±1	19.2±0.4	0.07±0.01
		Xilose	143±15	5.6±0.7	21±2	32±0.6	0.13±0.0
		Glycerol	48±3	3.5±0.2	38±0.6	14.8±1.0	N.D
	Tb05	Glucose	116±4	6.4±0.2	17±0	30.2±0.6	0.12±0.02
		Xilose	189±34	12.5±3.5	22±2.7	29±8	0.13±0.12
		Glycerol	44±3	2.9±0.2	21.7±1.5	13.6±0.7	0.19±0.05
	Tb06	Glucose	58±2.5	2.3±0.2	11±0.6	15±0.7	0.06±0.01
		Xilose	130±30	5±1.0	21±1.2	31±4	0.0±0.0
		Glycerol	52±20	2.9±0.9	21±1.0	15.9±5.5	N.D

References

[1] Ramos C, Buitrón G, Moreno I, Chamy R **(2012)**. *Int. J. Hydrogen Energy*. 37, 13288-13295.

Acknowledgements. Financial support “Fondo de Sustentabilidad Energética SENER-CONACYT (Mexico)”(project 247006 Gaseous Biofuels Cluster) is gratefully acknowledged. Angel A. Hernández and Jaime Perez are acknowledged for their technical assistance. This research was also financially supported by the EU program BITA (FP7-PEOPLE-2011-IRSES. Number 295170) about ‘Bioprocess and Control Engineering for Wastewater Treatment’.

065. BIOHYDROGEN PRODUCTION FROM CODIGESTION OF WASTE ACTIVATED SLUDGE AND FOOD WASTE

I. Moreno-Andrade, M. J. Berrocal-Bravo, I. Valdez-Vazquez

[1]Laboratory for Research on Advanced Processes for Water Treatment, Unidad Academica Juriquilla, Instituto de Ingeniería, Universidad Nacional Autónoma de México, Blvd. Juriquilla 3001, 76230 Querétaro, Mexico. E-mail imorenoa@ii.unam.mx

The codigestion of different organic waste has been proposed to increase the hydrogen (H_2) production rate in dark fermentation processes. One of the substrates with a high potential of hydrogen production is food waste [1]. On another hand, the waste activated sludge (WAS) generated in wastewater treatment plants also can be used for the H_2 production, but due to its low carbohydrate content, the H_2 yields are not high. However, the addition of WAS to the food waste has been shown that can improve the biogas production rate, compared to that obtained with the substrates independently [2]. Also, to increase the global energy production from this waste, the use of subproducts of hydrogen production (e.g., volatile fatty acid (VFA), lactic acid, ethanol, etc.) can be used subsequently in a methanogenic step for biogas (methane and CO_2) production. The objective of this work was to evaluate the productivity of hydrogen in a dark fermentation process and methane in methanogenic process by a codigestion of food waste and WAS in a discontinuous process. The results showed that there is a mixing ratio (90-10% food waste-WAS) that favors the production of H_2 (Table 1) above the other mixtures, in addition it can be observed that the addition of sludge facilitates the fermentation to the extent that the latency phase of the process decreases when compared to the case of 100% food waste, which turns into higher rates of hydrogen production. Carbohydrate removal was higher than 88% independently of the mixture evaluated. For the operation of the two-phase process, the highest concentration of H_2 in the biogas (37%) was obtained with an HRT of 16 h, while the highest removal of carbohydrates, volatile solids and COD were obtained with an HRT of 24h, producing the highest production of VFA. During CH_4 production, the biogas composition generated was 69% CH_4 - 29% CO_2, with productivities of 809 mL $CH_4/L_{reactor}/d$.

Table 1. Accumulated H_2 production at various mixing ratios.

Mixture	λ (h)	R_{max} mL H_2/ gVS/h	H_{max} mL H_2/ g-VS	Carbohydrates removal (%)
100% FW	17	2.5	53	93±0.5
90%FW-10%WAS	10	2.6	65	95±1.2
80%FW-20%WAS	6.5	1.7	45	91±2.0
70%FW-30%WAS	5.5	2.0	53	88±4.0
60%FW-40%WAS	5.0	1.8	41	95±3.7
50%FW-50%WAS	4.8	1.7	35	89±1.5
30%FW-70%WAS	3.0	0.4	6	90±3.5
100%WAS	6.5	0.1	1	92±2.3

References

[1] Ramos C, Buitrón G, Moreno I, Chamy R (2012). *Int. J. Hydrogen Energy*. 37, 13288-13295.
[2] Kim DH, Kim SH, Kim HW, Kim MS (2011). *Bioresour. Technol.* 102(18), 8501–8506.

Acknowledgements. Financial support by “Fondo de Sustentabilidad Energética SENER-CONACYT (Mexico)”(project 247006 Gaseous Biofuels Cluster), is gratefully acknowledged. Gloria Moreno and Jaime Perez are acknowledged for their technical assistance.

066. CO-DIGESTION OF DIARY WASTEWATER AND GASOLINE HYDROCARBONS (HUACHICOL) FOR HYDROGEN PRODUCTION IN AN UASB REACTOR USING ANAEROBIC MIXED CULTURES.

Moreno-Dávila I.M.M.[1*], Tamayo-Ordoñez M.C.[1], Estrada-Ortega A.A. [1] , Reyes Ruiz I.D.[1], Morales-Martínez T.K.[1], De la Garza-Rodríguez J.A[1], Gutiérrez-Rodríguez B.[1], Fuentes-Avilés J.G. [2] , Ríos- González L.J. [1]

[r] Department of Biotechnology. Faculty of Chemistry, Autonomous University of Coahuila
Email: imayelamorenod@hotmail.com, mayela.morenodavila@uadec.edu.mx
[2]Department of Instrumental Analysis. Faculty of Chemistry, Autonomous University of Coahuila

Nowadays fossil fuels are in decline and due to poor handling in the delivery of some of these hydrocarbons, especially gasoline in Mexico, it has revealed a phenomenon that had been carried out for decades and with current governmental actions, the practice of stealing the fuel called "huachicol" was discovered.The practices to obtain the huachicol are carried out by criminals who are dedicated to steal gasoline by drilling the pipelines that drive it, causing environmental damage and contamination to soil and water.[1]
In this research, the bioremediation of diary wastewater contaminated with gasoline (huachicol) at a pollution ratio of 5, 10 and 15% was studied by using an anaerobic microbial consortium in an UASB reactor at room temperature. Effects were studied at different hydraulic retention times (0.5,1,6 h). Determination of the effectiveness of the COD reduction was made (approximately 85%) and in the same way, determinations were made to observe the behavior of the some components of the gasoline by means of the thermogravimetric analysis (TGA)[2]. Due to the acid-base and thermal pretreatments of the microbial consortium [3], the production of hydrogen is favored and the hydrogen-consuming and methane-producing bacteries are completely inhibited.

References

[1] Procuraduría General de la República home page. https://datos.gob.mx/busca/dataset/robo-de-hidrocarburos (accessed May.**2018**).
.[2] Janajreh, I., Alshehi, A., and Elagroudy, S. Anaerobic co-digestion of petroleum hydrocarbon waste and wastewater treatment sludge. *International Journal of Hydrogen Energy*. (**2018**), https://doi.org/10.1016/j.ijhydene.2018.05.100
[3] Zinatizadeh, A. A., Mirghorayshi, M., Birgani, P. M., Mohammadi, P., and Ibrahim, S. Influence of thermal and chemical pretreatment on structural stability of granular sludge for high-rate hydrogen production in an UASB bioreactor. *international journal of hydrogen energy*. (**2017**). *42*(32), 20512-20519.

Acknowledgements

The financial support received from PRODEP-México is highly acknowledged. Also much thanks are due to Dr Ruben García Braham who facilitated the TGA analysis.

067. BIOCHAR OBTAINED OF WATER HYACINTH AND WATER LETTUCE FOR ORR STUDIES

L. Morales S [1], B. Escobar [1,2], Mónica G. Ruiz-Salazar[1], L.C. Ordónez[1]

[1] Centro de Investigación Científica de Yucatán, Carretera Sierra Papacal – Chuburná Puerto, Km 5. Sierra Papacal, Mérida, 97302, Yucatán, México.
[2] CONACYT - Centro de Investigación Científica de Yucatán, Carretera Sierra Papacal – Chuburná Puerto, Km 5., Sierra Papacal, Mérida, 97302, Yucatán, México. Beatriz.escobar@cicy.mx

Biomass, due to its high carbon content and availability in the environment, is attractive for the production of doped carbons as catalysts for high-yield ORR [1]. Water Hyacinth and water lettuce (Eichhornia Crassipes and Pistia Stratiotes, respectively) are considerate high invasives floating plants that representing large amounts of organic matter. It has the ability to accumulate amounts of inorganic forms of nitrogen by grows in eutrophic water [2]. The plants were collected from Coatzacoalcos river and the leaves were crushed, washed and, dried in direct sunlight for a week. Then it was pulverized and impregnated with a KOH solution at room temperature in a 1:2 ratio. The activated samples were pyrolyzed at 730 °C nitrogen flow during 2 hours. An acid treatment, it was performed in previously reported [3]. The FT-IR, Raman and XRD measurements showed carbon turbostratic formation. Cyclic voltammograms and electrode disk rotating techniques were used to evaluate the catalytic activity in a 0.5 M KOH solution. The EC and PS samples are promising cathode material for fuel cells. It was obtained high surface area (2000 m2 g-1).

References

[1] Liu F, Peng H, You C, Fu Z, Huang P, Song H, et al. High-performance doped carbon catalyst derived from nori biomass with melamine promoter. Electrochim Acta 2014;138:353–9. doi:10.1016/j.electacta.2014.06.098.
[2] Liang J, Tang D, Huang L, Chen Y, Ren W, Sun J. High oxygen reduction reaction performance nitrogen-doped biochar cathode: A strategy for comprehensive utilizing nitrogen and carbon in water hyacinth. Bioresour Technol 2018;267:524–31. doi:10.1016/j.biortech.2018.07.085.
[3] Pérez-Salcedo KY, Alonso-Lemus IL, Quintana P, Mena-Durán CJ, Barbosa R, Escobar B. Self-doped Sargassum spp. derived biocarbon as electrocatalysts for ORR in alkaline media. Int J Hydrogen Energy 2018. doi:10.1016/j.ijhydene.2018.10.073.

Acknowledgments

The authors want to thank the Consejo Nacional de Ciencia y Tecnología (CONACYT) for the grants 253986, 254667 and 2266. The authors thank Martin Baas for technical support.

068. EFFECT OF HYDROGEN TO REMOVE NO_x OF EMISSIONS FROM DIESEL ENGINES USING A Pt-Ag/Al_2O_3-WO_x CATALYST

Naomi N. González [1], Marcos Pinto[1], J.L.Contreras[*1], Beatriz Zeifert[2], Gustavo A. Fuentes[3], Tamara Vázquez[1] and Ricardo López M[1].

[1] Departamento de Energía, Universidad Autónoma Metropolitana Azcapotzalco, A. Sn. Pablo 180, Col. Reynosa, Ciudad de México, Código Postal 02200, México
[2]ESIQIE, Instituto Politécnico Nacional. UPALM. Zacatenco, Ciudad de México, México.
[3] Departamento de IPH, CBI Universidad Autónoma Metropolitana-Iztapalapa.
**jlcl@correo.azc.uam.*

The nitrogen oxides (NOx) are considered the main pollutants in the atmosphere, as they are responsible for environmental problems such as photochemical smog, acid rain, tropospheric ozone, depletion of the ozone layer and even global warming caused by N_2O [1-2]. SCR is an effective technology that is widely used today to reduce NOx emissions from mobile sources, such as diesel vehicles [3].
Catalysts with Ag-Pt/γ-Al_2O_3-WOx were prepared to remove NOx from gas emissions of diesel engines using propane and H_2 as reducing agents. The Al_2O_3 was obtained by the precipitation method and ammonium tungstate ($(NH_4)_{12}W_{12}O_{40} \cdot 5H2O$) was added at 0.5%w by weight to achieve a higher thermal stability in the support. A mixture of polluting gases was prepared with commercial gas charges of CO_2, N_2, O_2 and a mix NO, CO and propane. The catalytic tests were carried out in a fixed-bed tubular reactor. We used a gas mixture of NO (500ppm), C_3H_8 (625ppm), CO (200ppm), H_2 (66ppm), O_2 (2% vol.) and N_2 as gas balance; with an SV of 160,000 ml / g ·h. The conversion of the NOx obtained from the catalytic evaluation showed values of 90% at 270 to 350°C.
The activity started at 100 ° C having a maximum at 145 ° C, decreasing the conversion due to H_2 depletion, and restarts the conversion again at 200 ° C due to the activation of propane. A decrease in catalytic activity of the catalyst is observed between 180 ° C to 210 ° C possibly due to the formation of nitrites and nitrates that could act as a poison on the catalyst surface.

References

[1] Ma L., Cheng Y., Cavataio G., McCabe R. W., Fu L., y Li J. (2013). Chemical Engineering Journal 225 (2013) 323–330.
[2] Twigg M. V. (2007). Appl. Catal. B Environ 70 (2007) 2-15.
[3] Ruggeri M. P., Novaa I., Tronconi E., Pihl J. A., Toops T. J. y Partridge W. P. (2015). Applied Catalysis B: Environmental 166–167 (2015) 181–192.

070. CATALYTIC ACTIVITY OF PtNi BIMETALLIC NANOPARATICLES SUPPORTED ON DIFERENT CARBON NANOMATERIALS

J.C. Ortiz-Herrera[1], H. Cruz-Martínez[1], M.M. Tellez-Cruz[2], O. Solorza-Feria[2] and D.I. Medina[1]

[1]Escuela de Ingeniería y Ciencias, Instituto Tecnológico y de estudios Superiores de Monterrey, Carretera Lago de Guadalupe Km. 3.5, Colonia Margarita Maza; Atizapán de Zaragoza, Estado de México, C.P. 52926. México
Teléfono: +52 (55) 5864 55 55, ext: 2448, e-mail: dora.medina@itesm.mx
[2]Departamento de Química, CINVESTAV, Av. Instituto Politécnico Nacional 2508, San Pedro Zacatenco, Gustavo A. Madero, Ciudad de México, C.P. 52926, México.
Teléfono: +52(55) 5747 3800, e-mail: osolorza@cinvestav.mx

PtNi bimetallic nanoparticles have demonstrated to be one of the most promising electrocatalysts for the oxygen reduction reaction (ORR) in polymeric electrolyte membrane fuel cells (PEMFCs) due to their high catalytic activity and efficient utilization of Pt. However, improvising the stability remains a significant challenge. Due to this, it is very important to increase the stability of these electro catalysts. In this sense, the support materials are fundamental to improve the durability of the electrocatalysts for the ORR. One of the most promising alternatives is to replace carbon black as support with novel carbon materials, such as Carbon Nanotubes (CNT), Carbon Nanofibers (CNF) or Graphene [1]. These nanostructured carbon allotropes are presumed to have essential support properties such as a large specific surface area, good electrical conductivity, and a relatively good stability in acid medium. Thus, in this work, the synthesis, physical characterization, and electrochemical evaluation of PtNi nanoparticles supported on different carbon materials (CNT, CNF and graphene) are analyzed for the ORR in an acid electrolyte. The physical properties of the electrocatalysts were investigated using XRD, EDXS-SEM, and TEM, while the catalytic properties were determined through CV, CO-stripping, and RDE electrochemical techniques.

References

[1] Song, Shuqin, et al. "Effect of pore morphology of mesoporous carbons on the electrocatalytic activity of Pt nanoparticles for fuel cell reactions.": Appl. Catal., B **(2010),** 98.3-4, 132-137.

Acknowledgments

H. Cruz-Martínez and J.C Ortiz-Herrera gratefully acknowledge to CONACYT for the postdoctoral and doctoral fellowship, respectively.

071. BULK NANOSTRUCTURED MAGNESIUM ALLOYS FOR HYDROGEN STORAGE

M. Osorio-García[1], R.Y. Hernández Jiménez[2], O. Hernández Silva[1], C. Casas Quesada[3], J.M. Cabrera[3], A. Tejeda Ochoa[4,5], J. M. Herrera-Ramírez[4], Y. Todaka[5], B. Zeifert [2], K. Suárez-Alcántara[6], J. L. Carrillo-Bucio[6], J. G. Cabañas Moreno[1]

[1] CINVESTAV-IPN, Cd. de México, México, mayara.osorio@cinvestav.mx
[2] ESIQIE-IPN, Cd. de México, México.
[3] Universitat Politècnica de Catalunya, Barcelona, España.
[4] CIMAV, Chihuahua, Chihuahua.
[5] Toyohashi University of Technology, Toyohashi, Japan.
[6] IIM-UNAM, Unidad Morelia, Michoacán, México.

Magnesium has been extensively studied because of its notable advantages as a hydrogen storage material, such as high capacity (7.6% by mass), light weight and low cost [1]. However, the hydrogenation and dehydrogenation processes of the Mg/MgH_2 system normally require temperatures higher than 300 °C [2]. Nanostructured materials intended for use as hydrogen storage materials is a very effective way to improve the kinetics of hydrogenation and dehydrogenation [3]. On the other hand, Mg and MgH_2 readily react with oxygen, moisture and carbon dioxide with the ensuing degradation of their hydrogen storage properties. This undesirable behavior is more damaging the finer the particle size and the larger the exposed surface area.

In our work, the powders of Mg, Ni and Nb_2O_5 are mixed by ball milling, with a nominal composition Mg-5wt.%Ni-2wt.%Nb_2O_5, and after that, the mixture is used to produce materials of nanostructured mass (BNM), in this way the reactivity of fine powders is avoided. These BNMs are manufactured by high pressure torsion (HPT). The material has been subjected to 10 or 20 turns in an HPT system to produce consolidated disks. The composition and structure of these HPT-processed alloys were then characterized by SEM, TEM, XRD and hydrogenation experiments at different temperatures. Our results show that the materials obtained have a remarkable improvement in the kinetics of hydrogenation compared to the initial powder mixtures, as a consequence of the HPT process. Additional experiments are under way to explore the hydrogenation behavior in repeated cycles at fixed temperatures.

References

[1] Amira, S.; Huot, J. Effect of cold rolling on hydrogen sorption properties of die-cast and as-cast magnesium alloys. J. Alloys Compd. **2012**, 520, 287-294.
[2] Zhang, Jiguang, et al. Controllable fabrication of Ni-based catalysts and their enhancement on desorption properties of MgH2J. Alloys Compd. **2017**, 715, 329-336.
[3] Xia, Kenong. Consolidation of particles by severe plastic deformation: mechanism and applications in processing bulk ultrafine and nanostructured alloys and composites. Adv. Eng. Mater. **2010**, 12, 724-729.

Acknowledgements.
This work is supported by CONACYT (FOINS grant 6072) and Cinvestav-IPN.

072. TGA STUDY OF HYDRIDED MAGNESIUM ALLOYS

M. Osorio-García[1], R. Y. Hernández Jiménez[2], C. Casas Quesada[3], J. M. Cabrera[3], A. Tejeda Ochoa[4,5], J. M. Herrera-Ramírez[4], Y. Todaka[5], N. Kametani[5], M. M. Tellez-Cruz[1], K. Suárez-Alcántara[6], J. L. Carrillo-Bucio[6], N. Torres[1], J. G. Cabañas Moreno[1]

[1]CINVESTAV-IPN, Cd. de México, México, mayara.osorio@cinvestav.mx
[2]ESIQIE-IPN, Cd. de México, México.
[3]Universitat Politècnica de Catalunya, Barcelona, España.
[4]CIMAV, Chihuahua, Chihuahua.
[5]Toyohashi University of Technology, Toyohashi, Japan.
[6]IIM-UNAM, Unidad Morelia, Michoacán, Méxco.

Magnesium hydride is considered a promising hydrogen storage candidate owing to its high hydrogen storage capacity (7.6 wt.%), good reversibility and low cost [1]. However, the use of MgH_2 is limited by the fact that it requires temperatures higher than 300 °C to release hydrogen. The thermodynamic stability is one of the main reasons impeding the decomposition of MgH_2 at low temperature. Additionally, due to a slow diffusion rate of hydrogen in MgH_2, its decomposition is usually sluggish. To overcome the kinetic barriers, the use of catalytic additives has been known to be an effective approach [2].
In our work, we use Ni and Nb_2O_5 as catalysts in a mixture with Mg powders. The powder mixture has been subjected to a high pressure torsion process (HPT). We made hydrogenation experiments to explore the kinetics of hydrogen capture at different temperatures.Thermogravimetric analysis (TGA) coupled with mass spectrometry (MS) of reactive grade MgH_2 (for calibration purposes) and hydrided HPT-samples was carried out to complement previous gas absorption experiments. We compare the results of TGA-MS and gas absorption and discuss the relationship between these independent measurements of hydrogen content in the hydrided materials.

References

[1] Huot, Jaques, et al. Mechanochemical synthesis of hydrogen storage materials. Prog. Mater. Sci. **2013**, 58, 30-75.
[2] Zhou, Chengshang; Fang, Zhigang Zak; Bowman JR, Robert C. Stability of catalyzed magnesium hydride nanocrystalline during hydrogen cycling. Part I: kinetic analysis. J. Phys. Chem. C. **2015**, 119, 22261-22271.

Acknowledgements. This work is supported by CONACYT (FOINS grant 6072) and Cinvestav-IPN.

074. HIGH STABILITY OF PtNiCu CATALYST SUPPORTED ON GRAPHENE OXIDE

Miguel Adrian Padilla-Islas[1], Miriam Marisol Tellez-Cruz[1], Omar Solorza-Feria[1]

[1] Química, CINVESTAV, Av. Instituto Politécnico Nacional 2508, Cuidad de México, C.P. 07360, México, adrianmapi@gmail.com

Nano-catalyst of NiCu is synthesized by two steps; reduction of non-noble metals as nuclei and decoration of platinum (shell) by galvanic displacement. New synthesis of catalysts for the reduction reaction of oxygen by the adequate amount of oleylamine and oleic acid and precursor salts of non-noble metals, Cu (acac)2 and Ni(acac)2 , and using morpholine borane as a reducing agent is present. The prepared NiCu@Pt octahedral core-shell were characterized by TEM, octahedral nanoparticles have narrow size distribution, with a measured average edge length of 30 ±5 nm. The EDX analysis by elemental mapping show that three elements were found homogeneously distributed throughout nanoparticles. The XRD pattern shows characteristic peaks, it suggests that CuNi is decorated whit Pt. The metallic core inherits the crystal structure of its composing elements, i.e., the face-centeredcubic (FCC) structure. The diffraction peaks at can be assigned to (1 1 1), (2 0 0), (2 2 0) and (311) crystallographic planes, respectively, which correspond to FCC phase. The electrochemical performance of NiCu decorate with Pt/C was evaluated by cyclic voltammetry, CO stripping and rotating disk electrode in HClO4 as electrolyte. NiCu@Pt/ shows better catalytic activity in terms of mass activity 311mA/cm2 and specific activity, which is 246 mA/cm2, respect to commercially available 20-wt% Pt/C-Etek® with mass activity of 105 mA/cm2 and specific activity of 184 mA/cm2 .
Therefore, this finding suggests a methodology for producing an oxide graphene supported octahedral nanocatalyst, which could be used as a cathode electrode in a PEM fuel cell.

References

[1] J. I. L.Hidrógeno y pilas de combustible: estado actual y perspectiva inmediata, Universidad Pontificia Comillas: Asociacion de Ingenieros del ICAI, 2010.
[2] S. M. Haile, «Fuel cell materials and components,» Acta Materialia, vol. 51, nº 19, pp. 5981-6000, 2003.
[3] K. E. Martin, «Status of fuel cells and the challenges facing fuel cell technology today. In Fuel Cell Chemistry and Operation,» American Chemical Society Symposium Series, vol. 1040, pp. 1-13, 2010. [4] V. R. Stamenkovic, «Trends in electrocatalysis on extended and nanoscale Pt-bimetallic alloy surfaces",» Nature materials, vol. 6, nº 3, pp. 241-247, 2007.
[5] J. S. Cooper., «Review and analysis of PEM fuel cell design and manufacturing,» Journal of Power Sources, vol. 114, nº 1, pp. 32-53, 2003.
[6] L. Thomas., «Alternative energy technologies,» Nature, vol. 414, nº 6861, pp. 332-337, 2001.

Acknowledgements:
To Dr Omar Solorza, PhD candidate Miriam Tellez and to proyect Conacyt-Sener No. 245920 for the financial support as well as all of members in a 47 labortory of chemistry deparment at CINVESTAV

075. PHOTOCATALYTIC ACTIVITY OF TiO_2-CoO AS MIXED OXIDE FOR IMPROVED H_2 PRODUCTION

A.Pérez-Larios[1,2,3], R. Gomez[2], R. Zanella[3]

[1] Universidad de Guadalajara, Centro Universitario de los Altos, Depto. Ingenierías, Av. Rafael Casillas Aceves 1200, Tepatitlán de Morelos, Jalisco, México. 47600.
[2] Universidad Autónoma Metropolitana-Iztapalapa, Depto. de Química, Av. San Rafael Atlixco No 189, D.F., México 09340.
[3] Instituto de Ciencias Aplicadas y Tecnologías, Universidad Nacional Autónoma de México (UNAM), 04510, Ciudad Universitaria, D.F. México.

TiO_2-CoO (metal load: 1.0, 3.0, 5.0, 10.0 wt. % Co) samples were prepared by the sol-gel method and were evaluated for the photocatalytic water splitting reaction for hydrogen production, using a mixture of methanol-water (1:1). The mixed oxide combination effectively increased the hydrogen production (~2400 □mol/h) obtained by 10.0 wt% Co. Were attributed to an enhancement of the electron charge transfer from TiO_2 to the CoO. The textural properties of the prepared materials shows that the metal (Co) content has a significant effect on the textural properties of TiO_2 increasing BET specific surface areas from 64 to 156 m^2/g for all the samples. The powder XRD patterns show the formation of anatase as the unique titania phase formed. The anatase phase (101) peak intensity at $2\Theta=25.4°$ and hence the crystallite size diminishes when the amount of Co increases. The diffractograms show peaks denoting the presence of Co or CoO. This result suggest that Co was incorporated to the titania network or that it is present as nano CoO conglomerates highly dispersed on the titania surface.

References

[1] N.I. Panwar, S.C. Kaushik, S. Kothari, Renew. Sust. Energy Rev. 15 (2011) 1513-1524
[2] M. Cargnello, A. Gasparotto, V. Gombac, T. Montini, D. Barreca, P. Fornasiero, Eur. J. Inorg. Chem. 2011 (2001) 4309-4323
[3] Tarek A.Kandiel, Ralf Dillert, Lars Robben, Detlef W.Bahnemann. Catalysis Today 161 (2011) 196–201.
[4] M. Ni, M.K.H. Leung, K. Sumathy, Renew. Sust. Energy Re. 11 (2007) 401-425.

Acknowledgements

Perez-Larios Thanks the postdoctoral fellowship ICAT-UNAM.

076. MODIFICATION OF CARBON MATERIALS FOR APPLICATIONS IN A BIOELECTROCHEMICAL REACTOR FOR ELECTRICITY AND HYDROGEN PRODUCTION

César Morales, Bibiana Cercado

Centro de Investigación y Desarrollo Tecnológico en Electroquímica S.C. (CIDETEQ), Querétaro, Mexico), cperez@cideteq.mx

Microbial electrolysis cells (MEC) are a potentially attractive green technology to cope with global warming and the energy crisis. The MECs can simultaneously eliminate organic pollutants and produce biohydrogen [1]. In the MECs the presence of electroactive microorganisms is critical since they enable electron transfer to the electrodes, have the capacity to oxidize substrates (organic or inorganic) and convert them into protons, CO_2 and electrons [2]. The electrode material plays an important role for improving the bioelectrode performance by acting as a bacterial support and as an electron exchange site [3]. Commonly, electrode materials must present a good conduction, chemical stability, high mechanical resistance and low cost [4]. Recently, modifications on the surface of the electrodes have been used to improve bacterial adhesion and electron transfer from the bacterium to the surface of the electrode [4]. Several studies have been conducted on anode materials which has allowed the identification of strategies to improve the exchange of electrons [3]. Among the materials tested are zeolites which have been used as surface coating material for electrodes to improve their properties (physical-chemical, conductivity and electron transfer) [5, 6].
Therefore, in this investigation will be evaluated the generation of energy and the elimination of organic pollutants using carbon felt electrodes modified with zeolites in MECs fed with different types of wastewater. Materials that allow a greater removal of organic pollutants and generation of electric current will be identified, performing biological tests (Suspended Solids, total COD and soluble COD), physicochemical (pH, conductivity, temperature) and electrochemical (Chronoamperometry, Cyclic Voltammetry). The first results show that carbon felt electrodes produced 702 Coulombs in 7 cycles.

References

[1] Cardeña, R., Cercado, B., y Buitrón, G. Microbial Electrolysis Cell for Biohydrogen Production, in: Pandey, A., Venkata, S., Chang, J., Hallenbeck, P.C., y Larroche, C (Eds.), Hydrog. Int.J.Hydrogen Energy (2019) 159-185.
[2] Saratale, R., Saratale, G., Pugazhendhi, A., Zhen, G., Kumar, G., Kadier, A., y Sivagurunathan, P. Microbiome involved in microbial electrochemical systems (MESs): A review. Chemosphere, 177 (2017) 176-188.
[3] Wu, X., Tong, F., Yong, X., Zhou, J., Zhang, L., Jia, H., Wei, P.Effect of NaX zeolite-modified graphite felts on hexavalent chromium removal in biocathode microbial fuel cells. Journal of Hazardous Materials. 308 (2016) 303-311.
[4] Wei, J., Liang, P., y Huang, X. Recent progress in electrodes for microbial fuel cells. Bioresource Technology. 102 (20), (2011) 9335-9344.
[5] Wu, X., Tong, F., Yong, X., Zhou, J., Zhang, L., Jia, H., Wei, P. Effect of NaX zeolite-modified graphite felts on hexavalent chromium removal in biocathode microbial fuel cells. Journal of Hazardous Materials. 308 (2016) 303-311.
[6] González, T., Ureta, M. S., Marco, J. F., y Vidal, G. Effect of Zeolite-Fe on graphite anode in electroactive biofilm development for application in microbial fuel cells. Applied Surface Science. 467-468 (2019) 851-859.

Acknowledgements

The financial support provided by the Fondo de Sustentabilidad Energética SENER-CONACYT (Mexico) through the Cluster Biocombustibles Gaseosos, project number 247006, is acknowledged.

077. ELECTROCHEMICAL CHARACTERIZATION AND KINETIC ANALYSIS OF Ru-Sn-Sb-O, Ir-Sn-Sb-O AND Ru(x)-Ir(y)-O CATALYST

Nicté J. Pérez-Viramontes[1], Ismailia L. Escalante-García[1,2],Sergio M. Durón-Torres[1,2] *

[1]Doctorado en Ciencias de la Ingeniería, Unidad Académica de Ingeniería Eléctrica, Universidad Autónoma de Zacatecas, Zacatecas, Zac., México, serduro@yahoo.com
[2]Unidad Académica de Ciencias Químicas, Universidad Autónoma de Zacatecas, Zacatecas, Zac., México

Water electrolysis is a route for energy storage as chemical energy in form of hydrogen. Nevertheless an energy excess for this process is required due to Oxygen Evolution Reaction (OER). In acidic media the use of oxides of precious metals with rutile structure as RuO_2 and IrO_2 is common.[1] Due to the high cost an low stability of this catalyst, it´s necessary mix them with a more stable and cheaper materials known as supports. Typical supports for electrochemical applications are vulcan carbon, carbon nanotubes, SnO_2, TiO_2, etc.[2] Actually the research in sinthesys methods focus in the sinthesys method for the obtention of cheaper catalyst and with better stability than single catalyst. In the present work RuO_2, IrO_2, Ru(25)-Ir(75), Ru(75)-Ir(25), Ru(40)-Sn(57)-Sb(3) and Ir(40)-Sn(57)-Sb(3)oxides mixtures were prepared by simple thermal decomposition of clorhides. The number in brackets represents the atomic proportion of the metal in the synthesis step. All the electrochemical measurements were conducted in a typical three electrode cell employing an aqueous solution 0.5 M of H_2SO_4. Cyclic voltametry (CV) analysis shows the presence of the typical shape for RuO_2 and IrO_2 for these catalyst, likewise in CV can be observed that onset potential for OER in all materials and are close to 1.42 V NHE. This result was corroborated by Linear scan voltammetry (LSV), were onset potential were close to 1.40 V vs NHE. Afther ohmic drop correction Tafel plots were constructed for the obtenition of kinetic parameters. Tafel Slope of 60 mV dec^{-1} and transfer coefficient (α) of 0.5 were obtained for IrO_2 catalys and Tafel slope of 40 mV dec^{-1} and α of 1.5 for everyone else. The results indicate that OER follows a electrochemical oxide pathway mechanism.[3] The influence of the temperature on OER was evaluated, showing a decrease on the onset potential for all the materials. It can also see a dependence of the Tafel Slope with the temperature, observing a decrease as the temperature increase. The α increase with the temperature and the results suggest that the enthalpic contribution is despicable compared with entropic contribution of this parameter. The apparent activation energy was obtained, close to 100 kJ mol^{-1} for IrO_2 and RuO_2 catalyst, close to 60 kJ mol^{-1} for Ru-Sn-Sb-O and Ir-Sn-Sb-O catalyst and close to 10 kJ mol^{-1} for Ru(x)-Ir-(y)-O catalyst. The presented results propose that Ru-Sn-Sb-O and Ir-Sn-Sb-O as effective catalyst for OER in acidic media.

References
[1] Marshall A. T., Haverkamp R.G., Electrochim. Acta, **2010**, 55, 1978.
[2] Xu J., Li Q., Hansen M.K. Chistensen E., García A.L.T., Liu G., Wang X., Bjerrum .J., Int. J. Hydrogen Energy, **2012**, 37, 18629.
[3] Suermann M., Schmidt T.J., Büchi F. N., Electrochim. Acta, **2018**, 281, 466.

Acknowledgements
The authors acknowledge to the Universidad Autónoma de Zacatecas for all the facilities to carry out this investigation. N.J.P.V thanks to CONACyT throughout the SENER Sustentabilidad Energética 2017 program for the scholarship awarded to accomplish her Ph.D. studies.

078. METAL-FREE ELECTROCATALYSTS FROM ASCOPHYLLUM NODOSUM FOR ALKALINE OXYGEN REDUCTION REACTION

Perez-Salcedo, K.Y.[1]; Shi, X.[2]; Kannan, A. M.[2]; Vayssieres, L.[3]; Escobar, B.[1]*

[1] Centro de Investigación Científica de Yucatán. Carretera Sierra Papacal– Chuburná Puerto, Km. 5, Sierra Papacal, Mérida, 97302, México.
[2] Fuel Cell Laboratory, Arizona State University, Mesa, Arizona, 85212, USA
[3] International Research Center for Renewal Energy, Xi'an Jiaotong University. Xi'an, 710049, China.

N-doped porous carbon (NPC) is a potential candidate as low cost metal-free electrocatalyst for oxygen reduction reaction (ORR) and catalyst support for low temperature fuel cells. In recent years, seaweeds have become a serious economic threat as well as an environmental disaster due to its fast growing.
High surface area NPC catalysts were synthesized by thermochemical treatments (pyrolysis, activation and doping) from Ascophyllum nodosum. The raw sample was activated with KOH (AKPH) and doped with N2H4 (AKPHD). Electrocatalysts physicochemical properties were determined by nitrogen adsorption analysis by the Brunauer-Emmett-Teller method (BET), scanning electron microscopy (SEM), elemental analysis (CHNS), Raman spectroscopy, X-ray spectroscopy (XPS) and X-ray diffraction (XRD). Electrochemical experiments demonstrated the great potential of NPC as a low cost alternative for widespread fuel cells commercialization and as an alternative for disposal of seaweed in the Mexican Caribbean.

Acknowledgements (10 pt)
The authors thank Martin Baas, Tanit Toledano, Wilian Cauich and Mónica Ruiz for technical support.

079. STABILITY OF Pd CLUSTERS SUPPORTED ON PRISTINE, B-DOPED, AND DEFECTIVE GRAPHENE QUANTUM DOTS, AND THEIR REACTIVITY TOWARD OXYGEN ADSORPTION: A DFT ANALYSIS

F. Montejo-Alvaro[1], H. Cruz-Martínez[2]

[1]Cinvestav Unidad Saltillo, Av. Industria Metalúrgica 1062, Parque Industrial Ramos Arizpe, Coahuila, C.P. 25900, Mexico, fmontejo@cinvestav.mx
[2]Tecnologico de Monterrey, School of Engineering and Sciences, Atizapán de Zaragoza, Estado de México, C.P. 52926, Mexico, hcruzm@tec.mx

Abstract

A DFT-based study was carried out to investigate the ground-state structures and properties of Pd_n (n = 3–10) clusters, the stability of Pd_n (n = 3–10) clusters supported on pristine ($C_{96}H_{24}$), B-doped ($C_{95}H_{24}$:B), and defective ($C_{95}H_{24}$) graphene quantum dots (GQDs), and their reactivity of the Pd n (n = 8–10) on GQDs toward oxygen adsorption. The calculated ground-state structures and properties for the Pd n (n = 3–10) clusters are consistent with the previous studies. The stability of Pd_n (n = 3–10) clusters adsorbed on GQDs presents the following trend: $C_{95}H_{24}$ > $C_{95}H_{24}$:B > $C_{96}H_{24}$, which demonstrates that defective GQDs is promising for its application as a support material in electrocatalysis. In general, the reactivity of the palladium clusters is not significantly modified by being supported on the $C_{96}H_{24}$, $C_{95}H_{24}$:B, and $C_{95}H_{24}$ GQDs. However, in some cases, the reactivity toward oxygen reduction reaction (using an oxygen atom as a catalytic predictor) is slightly improved (e.g., $Pd_8/C_{96}H_{24}$, $Pd_8/C_{95}H_{24}$:B, $Pd_9/C_{95}H_{24}$:B, and $Pd_{10}/C_{95}H_{24}$ composites).

Acknowledgements
F. Montejo-Alvaro thanks CONACYT for the doctoral scholarship. H. Cruz-Martínez thanks CONACYT for the doctoral and postdoctoral fellowship. The authors acknowledge the computational resource provided by the ABACUS-I supercomputer from CINVESTAV.

080. ELECTROPHORETIC CO-DEPOSITION OF SnO_2-Zn NANOPARTICLES ON CONDUCTIVE GLASS SUBSTRATE AS ANODE FOR DYE SENSITIZED SOLAR CELL

O. Rico-Martínez[1], M.G. Joaquín-Morales[2], J.A. Rodríguez-García[1], W.J. Pech-Rodríguez[1*]

[1] Universidad Politécnica de Victoria, Av. Nuevas Tecnologías 5902, Parque Científico y Tecnológico de Tamaulipas, Ciudad Victoria, Tamaulipas, C.P. 87138.
[2] Programa de Ingeniería cerámica y metalúrgica, CINVESTAV unidad Saltillo, Av. Industria Metalúrgica 1062, Parque Industrial Ramos Arizpe. Ramos Arizpe, Coahuila, C.P. 25900, México
**E-mail: wpechr@upv.edu.mx*

In this research, electrophoretic co-deposition of tin oxide (SnO_2) and Zinc (Zn) was developed onto conductive substrates as anode for third generation of solar cells. Taguchi orthogonal array was used to optimize the main electrodeposition parameters. The levels of the deposition time, powder concentration, applied voltage and wave form of the electrical signal was optimized according to the current density delivered by the fabricated solar cell.

The deposited layers were characterized by Scanning Electron Microscopy with energy dispersive X-ray spectroscopy, Fourier-Transform Infrared Spectroscopy, and optical microscopy. On the other hand, the electrical parameters of the fabricated cells were determined by V-I and electrochemical impedance spectroscopy. From the V-I curves was observed that the incorporation of Zn into the SnO_2 structure enhance the efficiency of the solar cell. Hence, the electrophoretic deposition is a feasible process to develop and scale anodes for dye sensitized solar cell.

Acknowledgements

We thank CONACYT for the master scholarship provide to O. Rico-Martínez.

081. A PREGNANCY TEST POWERED BY A PAPER-BASED MICROFLUIDIC FUEL CELL USING THE URINE SAMPLE AS FUEL

C. Romero-Camacho[1], J. Gamboa[2], S. Ríos-Ugalde[1], J. M. Olivares-Ramírez[1], D. Ortega-Díaz[3], A. Dector[4], D. M. Amaya-Cruz[5], D. Dector[6]

[1] Universidad Tecnológica de San Juan del Río, San Juan del Río, Querétaro, México
camachocass15@gmail.com
[2] Instituto Tecnológico de Estudios Superiores de Coatzacoalcos, Coatzacoalcos, Veracruz, Mexico
[3] Instituto Tecnológico de San Juan del Río, San Juan del Río, Querétaro, Mexico
[4] CONACYT – Universidad Tecnológica de San Juan del Río, Querétaro, Mexico
[5] Universidad Autónoma de Querétaro, Querétaro, Querétaro, Mexico
[6] Centro de Investigación en Materiales Avanzados, Chihuahua, Chihuahua, Mexico

The lateral flow assays (LFA´s) are a quick alternative for a medical diagnostic [1]. Researches directly to the integration of paper-based microfluidic fuel cells (paper-based µFC´s) towards the creation of autonomous lateral flow assay have called attention [2]. This can be possible to use the test sample that contains the anolyte i.e. human blood [3], sweat [4] or urine [5]. In this work a paper-based microfluidic fuel cell was developed and powered by human urine and integrated in a pregnancy test. During pregnancy test evaluation, a paper-based µFC was testing; this obtained a voltage, a maximum power density and a maximum current density of 0.9 V, 0.37 mW cm^{-2} and 1.42 mA cm^{-2} respectively, using the same human urine sample as fuel, TiO_2-Ni as an anode and Pt/C as cathode. On the other hand, The paper-based µFC showed a constant current density for 20 mins, this time was determinated on the drying of the urine. Finally, a 4cell-stack paper-based µFC was evaluated with the aim of evaluating the pregnancy test. The results of this work demonstrated that a paper-based µFC could be integrated in a pregnancy test and usefulness as a possible power supply to employ the urine sample.

References

[1] Yager P, Edwards T, Fu E, Helton K, Nelson K, Tam MR, et al. Nature 2006;442:412-418.
[2] Dector A, Galindo-de-la-Rosa J, Amaya-Cruz DM, Ortíz-Verdín A, et al. Int. J. Hydrogen Energy 2017;42:27979-27986.
[3] Eskandarifar A, Rasouli MA, Mansouri M, Moosavi S, Fotoohi A. Diabetes & Metabolic syndrome: Clinival Research & Reviews 2019;13:464-466.
[4] Tur-García EL, Davis F, Collyer SD, Holmes JL, Barr H, et al. Sens. Act. B: Chem 2017:242;502-510.
[5] Bielecki Z, Stacewicz T, Wojtas J, Mikolajczyk J, Szabra D, Prokopiuk A. Opto-Electron. Review 2018;26:122-133.

Acknowledgements

Authors want to thank to CONACYT and CONCYTEQ through projects: Cátedra CONACYT project 513 and Nuevos Talentos 2019 CONCYTEQ, respectively.

082. GREEN SYNTHESIS OF PLATINUM NANOPARTICLES AND CARBON FROM *SARGASSUM SPP*. FOR ELECTROCHEMICAL APPLICATIONS

D. Rosas[1], B. Escobar[1]

[1] Centro de Investigación Científica de Yucatán, Carretera Sierra Papacal – Chuburná Puerto, Km 5. Sierra Papacal, Mérida, 97302, Yucatán, México. beatriz.escobar @cicy.mx

The aim of this paper is the development of a new carbon based with platinum nanoparticles catalyst for PEM fuel cells, obtained through a process of pyrolysis of the waste biomass Sargassum spp. then adding the previously green synthesized platinum nanoparticles with the same waste biomass, the final product is a carbon based catalyst with 5% load of platinum in form of nanoparticles. Given the troublesome waste biomass deposited in the Caribbean beaches Sargassum spp. which generates tons of organic decomposing material thus affects the tourist sector and the ecosystem [1] so it seems imperative the proper use of this waste. The nanoparticles were synthesized with a sample of Sargassum spp. through a process of drying, milling and sieve, then boiled in deionized water and put in reaction with a solution of $PtCl_4$, the nanoparticle formation was confirmed with a UV-vis analysis. Aside a sample of the milled and sieved Sargassum spp. was activated with KOH and then pyrolyzed in a nitrogen atmosphere; the resulting carbon has a surface area of 2289 $m^2\ g^{-1}$. As shown in the figure 1: the nanoparticles where deposited on the carbon via ultrasound bath in an ethanol solution, the crystal formation of the nanoparticles where characterized with a DRX analysis which showed a crystal size between 9-10 nm using Scherrer equation, a TEM analysis showed a very well dispersed nanoparticle formation on the carbon and an average nanoparticle size of 3nm. Finally the newly synthesized electrocatalyst was characterized with a cyclic voltammetry in acidic media delivering a current density up to 30 mA cm^{-2} superior than with the commercial catalyst of 20%Pt-Vulcan XC72, then the kinetic reaction was calculated using the Koutecky-Levich equation in several linear voltammetry using a rotating disk electrode at different rotation speeds which showed that with the 5% load of synthesized nanoparticles it has an average electron transfer rate of 2.9 electrons.

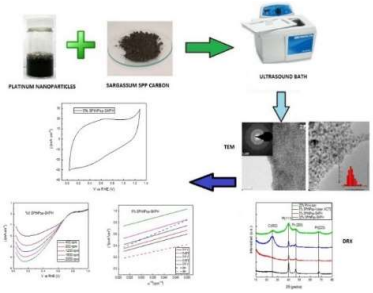

Figure1. Synthesis and characterization of electrocatalyst.

References

(1) Van Tussenbroek, B. I.; Hernández Arana, H. A.; Rodríguez-Martínez, R. E.; Espinoza-Avalos, J.; Canizales-Flores, H. M.; González-Godoy, C. E.; Barba-Santos, M. G.; Vega-Zepeda, A.; Collado-Vides, L. Severe Impacts of Brown Tides Caused by *Sargassum Spp*. on near-Shore Caribbean Seagrass Communities. *Mar. Pollut. Bull.* **2017**, *122* (1–2), 272–281.

083. NANOSTRUCTURED MATERIALS OF Ir-Sn-Sb-O WITH CARBON FOR OXYGEN EVOLUTION REACTION

Alberto Ruíz-Ramos[1], Nicté J. Pérez-Viramontes[2], Ma. Luisa García-Betancour[3] Sergio M. Durón-Torres[1,2], Ismailia L. Escalante-García[1,2*]

[1] Unidad Académica de Ciencias Químicas, Universidad Autónoma de Zacatecas, Zacatecas, Zac., México, ileg@uaz.edu.mx
[2] Doctorado en Ciencias de la Ingeniería, Unidad Académica de Ingeniería Eléctrica, Universidad Autónoma de Zacatecas, Zacatecas, Zac., México
[3] Centro de Investigaciones Químicas, Universidad Autónoma del Estado de Morelos, Cuernavaca, Mor., México

The hydrogen generation by water electrolysis is limited by the oxygen evolution reaction (OER), for this reason, stable electrocatalysts, with high catalytic and selective activity are necessary at the anode of a PEM water electrolyzer. RuO_2 and IrO_2 are electroactive materials that have shown good electrocatalytic activity for this reaction. Nevertheless, these metals are unstable at E >1.4 V and expensive. However, the use of a catalyst support could help to overcome these issues. SnO_2, TiO_2 among others have been investigated as material supports. Recently, the synthesis of Ir, Sn and Sb mixture oxides in a single-step has been reported as a catalyst-support system with an enhanced electrocatalytic activity towards OER than the IrO_2 [1]. In this work, it has been proposed that the preparation of Ir-Sn-Sb-O with N-doped Carbon Nanotubes (N-CNT) in a single-step by a thermal decomposition synthesis improves the electrical conductivity and the metal active phase dispersion to enhance the kinetics of OER. Scanning electron microscopy (SEM) was performed to study the morphology, particle distribution and size. Cyclic voltammetry (CV) and linear sweep voltammetry (LSV) were performed to evaluate the electrochemical profile and the electroactivity towards OER in aqueous acidic media, H_2SO_4 0.5 M. Preliminary SEM results show that Ir-Sn-Sb-O-CNT composite exhibited heterogeneous micrometric agglomerations of small spherical particles. Ir-Sn-Sb-O-CNT exhibited a similar behavior to the thermally oxidized IrO_2 films by CV. Also, Ir-Sn-Sb-O-CNT exhibited an acceptable activity for the OER as compared to IrO_2/C, thus, the Ir-Sn-Sb-O-CNT system show possibilities as possible anode electrocatalyst for PEM Water Electrolyzer.

References

[1] Perez-Viramontes, N. J.; Escalante-Garcia, I. L.; Guzman-Martinez, C.; Galvan-Valencia, M.; Duron-Torres, S. M. J. Appl. Electrochem. **2015,** 45, 1165.

Acknowledgements

The authors acknowledge to the Maestría en Ciencia y Tecnología Química at the Universidad Autónoma de Zacatecas for all the facilities to carry out this investigation. N.J.P.V thanks to CONACyT throughout the SENER Sustentabilidad Energética 2017 program for the scholarship awarded to accomplish her Ph.D. studies.

084. STUDY OF ANODE POTENTIAL UNDER DIFFERENT ELECTRICAL RESISTANCE VALUES IN A MICROBIAL FUEL CELL WITH LIVING HYDROPHYTES

Salinas-Juárez, M.G.[1], Luviano, V.J.[2], Cruz-Martínez, H.[3], Solorza-Feria, O.[2]

[1]Facultad de Estudios Superiores Zaragoza–UNAM. E-mail:maria.salinas@outlook.com
[2]Centro de Investigación y de Estudios Avanzados del IPN
[3]Tecnológico de Monterrey, Escuela de Ingeniería y Ciencias

Nowadays, it is possible to generate power from the microbial activity of microorganisms with reduced greenhouse gas emissions. A microbial fuel cell with living hydrophytes is an electrochemical cell composed by a plant, whose roots are located over the anode, where microorganisms oxidize the organic compounds released by roots. Electrons, protons and CO_2 are released from oxidation. Electrons are transferred to the cathode by means of an external electric circuit and protons pass through the medium to the cathode, where react with the electrons and oxygen to form water. Anodic microorganisms are the responsible of electron transfer to the anode, but they required specific conditions to grow. According to Torres et al., 2009 [1], the best condition of anode potential for anode-respiring bacteria growth is -150 mV vs SHE. Furthermore, the microbial biomass is influenced by the electrode potential [s]. In this work, the study of electrodes potential (anode and cathode) is carried out by connecting different electrical resistance values under different periods (from 20KΩ to 500 Ω). Four fuel cells were constructed using plastic containers (2L). Anode and cathode were made of graphite felt, and a stainless-steel plate was used as current collector. The support material for plant consisted of volcanic slag, which works as support for the vegetal species *Phragmites australis*. Electrodes were externally connected by means of an electrical resistance. Anode potential, cathode potential, voltage, and current were measured. In addition, current and power density was calculated and plotted. Although a voltage of 605 mV was achieved, a power density of 4.5 mW/m_2 was reached at the first stage, with an external resistance of 21.8 kΩ, in which the anode potential remained of -185±60 mV vs SHE. In the next stages of the experiment, other external resistances will be connected to the electrochemical cell in order to stabilize the anode potential.

References

[1] Torres et al, Environ. Sci. Technol., **2009**, 43 (24), pp 9519–9524.
[2] Carmona et al. Bioelectrochemistry., **2013**, 93, pp 23-29.

085. DESIGN AND CONSTRUCTION OF AN ALKALINE ELECTROLIZER WITH HYDROGEN OXYGEN SEPARATION

San Pedro L.[1], Casillas Reyes A. T.[1], Escalante Soberanis M.A.[1], Herrera-Romero J.V.[2], A. Bassam[1], Colorado-Garrido D.[3]

[1]Facultad de Ingeniería, Universidad Autónoma de Yucatán, Av. Industrias no contaminantes por periférico norte, col. Cordemex. Apdo. Postal 150, Mérida, Yucatán, México, mauricio.escalante@correo.uady.mx
[2]Facultad de Ingeniería, Universidad Veracruzana, Campus Coatzacoalcos, Av. Universidad km 7.5, Col. Santa Isabel, C.P. 96535, Coatzacoalcos, Veracruz, México.
[3]Centro de Investigación en Recursos Energéticos y Sustentables, Universidad Veracruzana, Av. Universidad km 7.5, Col. Santa Isabel, C.P. 9535. Coatzacoalcos, Veracruz, México.

Current alkaline electrolyzers present the main disadvantage of hydrogen impurity and the dangerous mixture of hydrogen and oxygen, typically called oxy - hydrogen. In this study, a prototype of an alkaline electrolyzer with hydrogen and oxygen separation is presented. A favorable performance is reported for the device at different electrolyte temperatures. The proposed design obtained a maximum 88.63% hydrogen purity using potassium hydroxide as electrolyte. It was observed a maximum purity of 80.21% with sodium hydroxide as electrolyte. These purities are higher than some results reported in selected literature [1]. The overall efficiency of the electrolyzer was 28.52% at an electrolyte temperature of 40°C for the potassium hydroxide, and 22.78% at the same temperature for the sodium hydroxide. On the other hand, the overall efficiency tends to decrease when the electrolyte temperature decreases. The total cost of the device construction was approximately $ USD 150.00, being significantly lower than the commercial ones.

References

[1] Bailón Martínez, A. *Desarrollo de un sistema de generación de Hidrógeno acoplado al tratamiento electroquimico de aguas superficiales utilizando energía solar*. Universidad Autónoma del Estado de México. **2013.**
[2] Dincer, I. (2011). Green methods for hydrogen production. *International Journal of Hydrogen Energy*, **2011,** *37*(2), 1954–1971.
[3] Dincer, I., & Acar, C. (2014). Review and evaluation of hydrogen production methods for better sustainability. *International Journal of Hydrogen Energy*, **2014,** *40*(34), 11094–11111.
[4] EERE. (2006). Central versus distributed hydrogen production. Retrieved October 19, **2017**, from https://energy.gov/eere/fuelcells/central-versus-distributed-hydrogen-production
[5]Ferrero, D., Lanzini, A., Santarelli, M., & Leone, P. A comparative assessment on hydrogen production from low- and high-temperature electrolysis. *International Journal of Hydrogen Energy*, **2013,** *38*(9), 3523–3536. https://doi.org/10.1016/j.ijhydene.2013.01.065

086. GRAPHENE OXIDE- POLYINDOLE HYBRID SUPPORT: NOVEL APPROACH TO INCREASE THE ORR ACTIVITY OF PT CATALYSTS IN ALKALINE MEDIA

N.M. Sánchez-Padilla[1], D. Morales-Acosta[1]*, R. Benavides[1], U. Sierra[2], S. Fernandez[2]

[1]Centro de Investigación en Química Aplicada, Blvd Enrique Reyna No. 140, Col. San José de los Cerritos, Saltillo, 25294; Coahuila, México.
[2]Laboratorio Nacional de Materiales Grafénicos, Blvd Enrique Reyna No. 140, Col. San José de los Cerritos, Saltillo, 25294; Coahuila, México.
** diana.morales@ciqa.edu.mx*

In order to enhance the catalytic activity for oxygen reduction reaction (ORR) by the improving dispersion and distribution of platinum nanoparticles (Pt NPs), three novel hybrid materials [1] were prepared and further used as supports for Pt NPs and evaluated in alkaline media. Polyindole (PIN, a conducting polymer) was in-situ grafted to graphene oxide sheets (GO) obtained by modified Hummer's method via oxidative polymerization of indole monomer. Three different percentage composition of PIN (10, 50 and 90 %) were considered in order to obtain three hybrid materials: GO_{90}-PIN_{10}, GO_{50}-PIN_{50}, GO_{10}-PIN_{90}. Pt NPs (20% wt.) deposition was carried out by polyol method obtaining Pt/rGO_{90}-PIN_{10}, Pt/rGO_{50}-PIN_{50}, Pt/rGO_{10}-PIN_{90}. For comparative purpose a Pt/rGO material was prepared and evaluated under the same conditions. FTIR and XRD results demonstrated the formation of hybrid materials by the grafting of PIN into the GO matrix. TGA analysis showed a close composition to the nominal value for that with highest GO content. TEM observations demonstrated that PIN in GO diminishes the crystallite size, from 3.5 nm (Pt/rGO) to 1.9 nm (Pt/rGO_{90}-PIN_{10}). Linear sweep voltammetry curves indicated that Pt/rGO_{90}-PIN_{10} has the highest onset potential (E_0= 1 V) and current density (j= 5 mA cm^{-2}), which is even higher than Pt/rGO (E_0= 0.95 V and j= 4 mA cm^{-2}). The higher activity of Pt/rGO_{90}-PIN_{10} is due to lower particle size and the improvement in the distribution and dispersion achieved in the hybrid support.

References

[1]Z. Gao, F. Wang, J. Chang, D. Wu, X. Wang, X. Wang, et al., **(2014)** Chemically grafted graphene-polyaniline composite for application in supercapacitor, Electrochim. Acta. 133 325–334.

087. INFLUENCE OF WO_3-ZrO_2-C AS ACTIVE SUPPORT FOR PLATINUM NANOPARTICLES: ENHANCEMENT OF ACTIVITY CATALYTIC OF NO_3^- and NO_2^- REDUCTION

C. R. Santiago-Ramírez[1,2], J. Soto-Hernánez[1], L.P.A. Guerrero-Ortega[1], E.Y. Cervantes-Aspeitia[1,2], A. Manzo-Robledo[1], M.L. Hernandez-Pichardo[2,*]

[1] Instituto Politécnico Nacional-ESIQIE, Laboratorio de Electroquímica y Corrosión, CDMX, 07738, México
[2] Instituto Politécnico Nacional-ESIQIE, Laboratorio de Nanomateriales Sustentables, CDMX, 07738, México, mhernandezp@ipn.mx

The electrochemical reduction of nitrate and nitrite anions was investigated on a new type of support for platinum. A nanobelt WO_3 with ZrO_2 (ZWC) composed by Vulcan Carbon (70 wt. %), WO_3 (25 wt. %) and ZrO_2 (5 wt. %) was synthesized by surfactant-assisted coprecipitation method [1]. A comparative study was performed to determine the catalytic activity of material different, the PtETEK commercial, PtC synthesized and the new material Pt/ZWC. The electrical conductivity of ZWC support and Vulcan Carbon were measured by a four-probe method. The electrocatalysts were characterized by X-ray diffraction (XRD), scanning electron microscopy (SEM), high-resolution transmission electron microscopy (HR-TEM) and X-ray photoelectron spectroscopy (XPS). The catalytic activity was evaluated on the NO_3^- reduction reaction (NO_3^-RR) and NO_2^- reduction reaction (NO_2^-RR) in alkaline media using cyclic voltammetry. In addition, the electrochemically active surface area was determined by the CO stripping technique. The results show that the electrocatalysts are stable in alkaline media under the experimental conditions employed, nitrate and nitrite were reduced on all materials with the occurrence of the hydrogen evolution. However, the Pt/ZWC material exhibited higher electrocatalytic activity for the NO_3^-RR and NO_2^-RR, in comparison to the reference Pt/C material and commercial Pt-Etek catalyst. This result could be attributed to the mixed metal oxide support (WO_3-ZrO_2-C) such as the high population of hydroxyl groups and hydrated state ($W(OH)_6$ [2,3], that checked by the hydrogen reduction reaction in alkaline media. Therefore, the oxide matrices are considered for good supporting and increasing the catalytic activity of the platinum nanoparticles.

References

[1] Catal. Commun. **2009**, 10 and 1828-1834.
[2] J. Phys. Chem. C. **2010**, 114 and 18298-18312
[3] Electrochim. Acta. **2019**, 210 and 575-587

Acknowledgements

CRSR thanks the financial support from CONACyT within Doctor Fellowship.

088. ANIONIC MEMBRANES FOR INTEGRATION IN HYDROGEN ALKALINE GENERATORS

Santos Fernández M.[1] *, Cortés Escobedo C. A. [1, *], González Huerta R de G.[2], Coutiño Cortés J.[2]

[1] Instituto Politécnico Nacional, CIITEC
[2] Instituto Politécnico Nacional, ESIQIE
** marianna.s.f@hotmail.com, phone number: +9221991228*

Anionic exchange membranes (AEM) were prepared and characterized for hydrogen alkaline generators system. AEM are composed by a main hydrocarbon chain and ionic interchange sites [1]. In this case polystyrene and quaternary ammonium groups were used as main hydrocarbon chain and ionic interchange groups, respectively. Polystyrene membranes were functionalized in four stages: nitration, amination, chlorination and quaternization. Obtained membranes were chemically characterized by Fourier transform infrared spectroscopy (FTIR), morphologycally by optical microscopy and water uptake were determined. Also, results of anionic conductivity in alkaline media compared with FUMATECH FAA-3-PE-30 commercially available membranes and characterization of the last one by X-Ray diffraction are presented, where detected phase, Gwihabaite is an potasium and ammonium nitrate mineral.

References

[1] Yanagi, H., & Fukuta, K. (**2008**). Anion exchange membrane and ionomer for alkaline membrane fuel cells (AMFCs). ECS transactions, 16(2), 257-262

Acknowledgements

Authors acknowledge Instituto Politécnico Nacional through project SIP 20190119, Centro de Investigación e Innovación Tecnológica and CONACYT for supporting this project.

089. HYDROGEN AND ELECTRICITY PRODUCTION IN A MICROBIAL FUEL CELL USING A RESIDUE FROM THE SYRUP INDUSTRY AS SUBSTRATE.

Héctor G. Sifuentes-Sánchez[1], Luis E. De la Cruz-Andrade[1], Lizeth A. Paredes-Peña[1], José G. Moreno-Cedillos[1], Angélica L. Ortiz-Cruz [1], Mónica Muñoz[1], Ileana M.M. Moreno-Dávila[1], Leopoldo J. Rios-González[1], Monica M. Rodríguez-Garza[1], Thelma K. Morales-Martínez[1], Miguel A. Medina-Morales[1], Silvia Y. Martínez-Amdor[2], José A. Rodríguez-de la Garza[1*]

[1]Department of Biotechnology, Facultad de Ciencias Quimicas, Universidad Autonoma de Coahuila,
*Corresponding author: Jose A Rodriguez-de la Garza. Email: antonio.rodriguez@uadec.edu.mx
(phone no.) +52-844-4155752
[2]Department of Botany, Universidad Autonoma Agraria Antonio Narro

The biggest challenges of our times are the depletion of fossil fuels, pollution and efficient development of renewable energy. The energy crisis encouraged researchers to investigate alternative energy sources. Microbial fuel cell is a promising technology, in which bacteria function as the catalyst, which has been developed to effectively generate bioelectricity from diverse organic wastes. The aim of the present study was to assess the hydrogen production in the anode compartment of a microbial fuel cell. The microbial fuel cell was configured with the anode compartment completely submerged in the cathode compartment. The electrodes of each compartment were made out of carbon cloth. A cationic exchange membrane (CMI-7000 International Membranes Inc.) was used to separate the anodic and cathodic compartments. A anaerobic granular sludge was used as inoculum and to eliminate hydrogen-consuming microorganisms (methanogens) and to favor hydrogen spore-formers mainly *Clostridium* species, the sludge was heated in a boiling water bath at 105 °C for 30 min, then cooled down and followed by an acid treatment that involved decreasing the pH of the sludge to 3.0 using 0.1 N HCl solution for 24 h. After this period, the pH was adjusted to 7.0 with a 0.1 N NaOH solution. Hydrogen production was determined by gas chromatography (GC FID). A residue from the syrup industry (mainly composed of sorbitol) was used as substratum for hydrogen production (3 g/L). Voltage generation in the microbial fuel cell was determined with a wireless data logger (HOBO Four-Channel Data Node and receiver). The maximum voltage (open circuit potential) generated during the operation of the MFC was measured with a data logger and reached 400 mv. Overall, this study demonstrated the potential of using microbial fuel cell for hydrogen and electricity production from residues.

References

[1] Bahareh Asefi, Shiue-Lin Li, Henry A. Moreno, Viviana Sanchez-Torres, Anyi Hu, ,Jiangwei Li, Chang-Ping Yu. 2019. Characterization of electricity production and microbial community of food waste-fed microbial fuel cells. Process Safety and Environmental Protection. 125: 83-91.

[2] Moreno-Dávila, I.M.M., Ríos-González, L.J., Rodríguez-de la Garza, J.A., Morales-Martínez, T.K., Garza-García, Y., 2019. Biohydrogen production from paper industry wastes by SSF: A study of the influence of temperature/enzyme loading. Int. J. Hydrogen Energy 4, 0–5.

Acknowledgements

The authors are grateful to the CGEPI of Autonomous University of Coahuila for the financial support.

090. SIMULTANEOUS CHARACTERIZATION OF POLYELECTROLYTIC MEMBRANES BY CYCLIC VOLTAMMETRY AND *IN-SITU* FTIR TECHNIQUE.

A. A. Siller-Ceniceros[1], L. Francisco-Vieira[1], D. Morales-Acosta[1], R. Benavides[1*], E. Cuara-Díaz[2] and L. Da Silva[1]

*[1]Centro de Investigación en Química Aplicada (CIQA). Blvd. Enrique Reyna H. 140, Saltillo, Coahuila, 25294, México *roberto.benavides@ciqa.edu.mx*

[2]Laboratorio Nacional de Materiales Grafénicos (LNMG). Blvd. Enrique Reyna H. 140, Saltillo, Coahuila, 25294, México

Nafion™ is the most used polyelectrolytic material as proton exchange membrane (PEM) in fuel cells due to its chemical characteristics [1]. Nevertheless, this membrane suffers degradation due to chemical attack from hydroxyl ($OH^{\bullet}$) and peroxyl ($HO_2^{\bullet}$) radical species, formed by the decomposition of hydrogen peroxide (H_2O_2) that take place at cathode and anode [2]. In the present work, is showed the spectroscopic and electrochemical studies by *In-situ* FTIR of Nafion 117 and Poly(styrene-co-butyl acrylate) (St-BuA) membranes with different sulfonation percentages, after hydration and a chemical degradation process. The later as material obtained from a previous work [3]. Nafion 117 or St-BuA solution was drop-casting on Pt electrode surface to obtain polymeric thin film (Pt/Nafion 117 or Pt/St-BuA). In the hydration experiment, polymer films were exposed to deionized water during 24 h and evaluated in acid media by cyclic voltammetry (VC) and *in-situ* FTIR reflectance. In the degradation process, the Pt/Nafion 117 and Pt/St-BuA were exposed to Fenton´s reagent during 24 h and evaluated at the same conditions of hydration procedure [4]. Moreover, the importance to use a sophisticated technique as *in-situ* FTIR coupled with CV is demonstrated through the high sensibility to detect simultaneously changes in the spectroscopic signals from the degraded polyelectrolytic membranes and differences in the catalytic activity of Pt electrode in acid media. This analysis is remarkable to evaluate in the future the performance and stability of this polyelectrolytic membranes in a PEMFC.

References

[1] Kanamura, K. Morikawa, H. Umegaki T. (**2003**) Observation of Interface Between Pt Electrode Nafion Membrane. J. Electrochem. Soc, 150, A193-A198.
[2] C. Fernandes, A. Ticianelli, E. A. (**2009**) A performance and degradation s tudy of Nafion 212 membrane for proton exchange membrane fuel cells. J. Pow. Sour, 193, 547-554.
[3] Francisco-Vieira, L. Benavides-Cantú, R. Cuara-Díaz, E. Morales-Acosta, D. (**2019**) Styrene-co-butyl acrylate copolymers with potential application as membranes in PEM fuel cell. Int. J. Hydrog. Energy, 44, 12492-12499.
[4] Kundu, S. Simon, L. C. Fowler, M. W. (**2008**) Comparison of two accelerated Nafion™ degradation experiments. Polym. Degrad. Stab. 93, 214-224.

091. NITROGEN-DOPED GRAPHENE OXIDE AS EFFICIENT METAL-FREE ELECTROCATALYST AND Pt NP'S SUPPORT FOR OXYGEN REDUCTION REACTION IN ALKALINE MEDIA

D. Morales-Acosta*, N. M. Sánchez-Padilla, R. Benavides-Cantú

*[1]Centro de Investigación en Química Aplicada (CIQA). Blvd. Enrique Reyna H. 140, Saltillo, Coahuila, 25294, México. *diana.morales@ciqa.edu.mx*

Platinum and group metal-free electrocatalysts are critical for the development of alkaline fuel cells (AFCs) [1,2]. In this work, Nitrogen-doped reduced graphene (N-rGO) was prepared by hydrothermal reaction of graphene oxide sheets with amitrole with a weight ratio of 15 %. Afterwards N-rGO was used as support for Pt nanoparticles (Pt NP's) deposition (20% wt.) by polyol method to obtain Pt/N-rGO. N-rGO and Pt/N-rGO were studied as electrocatalysts for oxygen reduction reaction (ORR) in alkaline media by rotating disk electrode linear sweep voltammetry (RDE-LSV). For comparative purpose, rGO and Pt/rGO catalyst were prepared and evaluated under the same conditions. The successful N doping and reduction of GO were confirmed by FTIR, XRD and RAMAN techniques, while XPS analysis showed that N composition in N-rGO was 10.5 wt. Pt crystal size varying from 3.6 to 4.4 nm for Pt/rGO and Pt/N-rGO. However, a superior thermal stability was observed for Pt/N-rGO compared Pt/rGO. LSV curves indicated that N-rGO catalyst has higher current density (j= 3.6 mA cm^{-2}) and lower onset potential (E_0= 0.85 V) compared to rGO (j= 2.4 mA cm^{-2} and E_0= 0.8 V). However, Pt/N-rGO showed a superior catalytic activity (j= 5 mA cm^{-2} and E_0= 1 V) even compared to Pt/rGO. Koutecky-Levich analysis confirmed that N-rGO catalyst undergoes a 4-electron transfer process during the ORR in alkaline media while rGO follows 2-electron transfer process. The superior performance observed for Pt/N-rGO suggesting a synergic effect Pt NP's and and N-rGO support.

References

[1] H. Tao, C. Yan, A.W. Robertson, Y. Gao, J. Ding, Y. Zhang, T. Ma, Z. Sun **(2017)**, N-Doping of graphene oxide at low temperature for the oxygen reduction reaction, Chem. Commun. 53, 873–876.

[2] Z. Li, Q. Gao, H. Zhang, W. Tian, Y. Tan, W. Qian, Z. Liu **(2017)**, Low content Pt nanoparticles anchored on N-doped reduced graphene oxide with high and stable electrocatalytic activity for oxygen reduction reaction, Sci. Rep. 7, 43352.

Acknowledgements

This work has been supported by the Mexican Council of Science and Technology (CONACyT) through grant CB 259010.

092. DESIGN OF AN ELECTRIC SUPPLY SYSTEM FROM AN ALTERNATOR TO AN OXYHYDROGEN REACTOR FOR A DIESEL ENGINE.

A. Wintergerst-Felipe[1], R de G. González-Huerta[2], E. A. Merchán-Cruz[1], J. M. Sandoval-Pineda[1]

Instituto Politécnico Nacional
[1]Escuela Superior De Ingeniería Mecánica Y Eléctrica U. Azcapotzalco
Sección de Estudios de Posgrado e Investigación
[2] Escuela Superior de Ingeniería Química e Industrias Extractivas, Laboratorio de Electroquímica y Corrosión. UPALM, CP 07738, Ciudad de México.

In this article the obtained results about the development and manufacture of an electric supply system of the alternator to Oxyhydrogen gas reactor, in an internal combustion engine, this is the purpose of not generating more energy consumption because the disadvantage is Its high consumption to generate it. Dual combustion (Oxyhydrogen - diesel) is proposed to reduce energy consumption and reduce polluting gases. The alternator delivers alternating current and the reactor works with direct current, that is, the system has a converter, plus a voltage booster (12 to 24v). The system is installed as a single assembly and not as parts of the entire engine, this in order to make the space more efficient, in conjunction with the Six Sigma scheme. The obtained results are the fuel reduction ratio of 10-15% are maintain, with the amperage delivered by the motor (80A), that is, at the foot of the motor load, it is not taken as excess power and therefore higher diesel consumption.

093. STUDY OF SINTERIZED POWDERS OF 316L STAINLESS STEEL WITH CONTROLLED POROSITY FOR HYDROGEN CELL APPLICATIONS

Victor Solorio[1], Julio C. Villalobos[1*], H. J. Vergara-Hernández[1], Gerardo M. Chávez-Campos[1], Luis Olmos-Navarrete[2], Octavio Vázquez-Gómez[1].

*[1]División de Estudios de Posgrado e Investigación, Instituto Tecnológico de Morelia, Avenida Tecnológico No.1500, Col. Lomas de Santiaguito, Morelia, Michoacán. julio.villalobos@uaem.mx**
[2]Universidad Michoacana de San Nicolás de Hidalgo, Avenida Francisco J. Múgica S/N, Ciudad Universitaria, Morelia, Michoacán.

Hydrogen evolution reaction (HER) on different metals in alkaline media is one of the most investigated reactions in the field of electrochemistry due to HER is the main reaction developed in alkaline water electrolysis, hydrogen-based fuel cells and during some industrial applications. The principal problems in these electrochemical processes is the large consumption of electrical energy caused by hydrogen over-voltage. The principal characteristics for catalytic materials are a low overpotential for HER, good catalytic activity, high stability and low cost [1]. 316L stainless steels have been widely used in industrial applications due to its low price compared with Ni and Pt electrodes and for its high corrosion resistance improved by Cr_2O_3 protective film. However, higher over-voltage required for hydrogen production can induce pitting corrosion, rupture of protective film and subsequent degradation of 316L electrodes. In order to improve a higher catalytic activity in 316L stainless steel electrodes is necessary to increase the active area of electrodes by inducing porosity [2]. The focus of this work is to produce porous compacts of 316L with different pore sizes by powder metallurgy technique and then, to evaluate the HER reaction as function of porous size. In addition, we report the study of the HER and corrosion rate of electrodes used in industrial electrolyzers of solid 316L, evaluated in different electrolytic solutions concentration: 0.5, 1.0 and 1.5 M NaOH. The electrochemical study of porous stainless steels in alkaline media was performed by cyclic voltammetry, and potentiodynamic curves to determine the HER efficiency at room temperature by Tafel slopes. The preliminary results showed that porous electrodes have a higher catalytic effect compared with solid stainless steel. However, the porous stainless steel showed a better response to hydrogen evolution reaction due to higher active area that increase the current density exchange.

References

[1] W. Yu, M. D. Porosoff y J. G. Chen, Chem. Rev., Vol. 112, pp. 5780-5817, 2012.
[2] Fariba Safizadeh, Edward Ghali y Georges Houlachi, Electrocatalysis developments for hydrogen evolution reaction in alkaline solutions – A review. Int. J. Hydrogen Energy, pp. 1-19, 2014.

094. BIFUNCTIONAL PT-BASED ELECTROCATALYSTS SUPPORTED ON BIOCARBON FUNCTIONALIZED WITH ORGANOMETALLIC RUTHENIUM COMPLEX TOWARD THE OXYGEN REDUCTION REACTION (ORR) AND THE OXYGEN EVOLUTION REACTION (OER).

M. P. Solórzano Alderete[1], M. Peralta Contreras[1], P.C. Meléndez González[2], J.C. Martínez Loyola[3], F.J. Rodriguez-Varela[2, 3] I.L. Alonso-Lemus[4*]

[1]Programa de Ingeniería en Energía, Universidad Politécnica de Aguascalientes, Calle Paseo San Gerardo No. 207, Fracc. San Gerardo. Aguascalientes, Ags., C.P. 20342, México.
[2]Programa de Nanociencias y Nanotecnología, Cinvestav Unidad Saltillo, Av. Industria Metalúrgica 1062, Parque Industrial Ramos Arizpe. Ramos Arizpe, Coahuila, C.P 25900, México.
[3]Programa de Sustentabilidad de los Recursos Naturales y Energía, Cinvestav Unidad Saltillo.
[4]CONACYT, Sustentabilidad de los Recursos Naturales y Energía, Cinvestav Unidad Saltillo.
**E-mail: ivonne.alonso@cinvestav.edu.mx*

Fuel cells are a promising clean energy devices. However, one of the main challenges for this technology lies in the development of catalysts for the oxygen reduction reaction (ORR), which has the slowest kinetics limiting the overall performance of the entire device. Recently, the study of organometallic compounds has attracted attention as it significantly improves the performance of the electrocatalyst. In this work, a novel Pt-based electrocatalysts supported on biocarbon (AB7) functionalized with a rutenium organometallic complex (Ru dim) has been synthetized and evaluated for the ORR and the Oxygen Evolution Reaction (EOR). AB7 is a biocarbon with high activity for the ORR obtained from waste leather [1, 2]; therefore, two diferents electrocatalysts have been synthetized and labelled as Pt/AB7$_{Rudim}$ and Pt/AB7-f. The last one has been functionalized by mild acid treatment [3]. The electrocatalysts has been obtained by convencional polyol method [4] and evaluated in alkaline media. They has been, as well, tested phisycochemicaly observing a chemical composition pretty closed to the desired of 20% Pt. The morfology observed is irregular pieces of carbon covered with Pt nanoparticles, with some aglomerations. The catalytic activity has been performed by the rotating ring-disk electrode technique (RRDE) showing that Pt/AB7$_{Rudim}$ is a promising bifunctional electrocatalysts for the ORR and the OER in alkaline media.

References:

I. L. Alonso Lemus, F. J. Rodríguez Varela, M. Z. Figueroa Torres, M. E. Sanchez Castro, A. Hernández Ramírez, D. Lardizabal Gutiérrez and P. Quintana Owen, "Novel self-nitrogen-doped porous carbon from waste leather as highly activemetal-free electrocatalysts for the ORR," *International Journal of Hydrogen Energy,* vol. 41, pp. 23409-23416, **2016.**

D. Lardizabal Gutiérrez, D. González Quijano, P. Bartolo Pérez, B. Escobar Morales, F. J. Rodríguez Varela and I. L. Alonso Lemus, "Synthesis of Self-Doped Metal-Free Electrocatalysts from Waste Leather with High ORR Activity," *Journal of The Electrochemical Society,* vol. 165, no. 10, pp. 2061-2068, **2015**.

J. Hyung Kim, J. Yeong Cheon, T. Joo Chin, T. Young Park and S. Hoon Joo, "Effect of the surface oxygen functionalization of carbon support on the activity and durability of Pt/C catalysts for the oxygen reduction reaction," *Carbon,* vol. 101, pp. 449-457, **2016.**

P. Meléndez González, E. Garza Duran, M. Salazar Oropeza, J. Serna Mata, F. Rodriguez Varela and I. Alonso Lemus, "Enhanced Catalytic Activity for the Oxygen Reduction Reaction Using 5 % Pt/OMCHS electrocatalysts," **2018.**

095 STUDY OF THE ELECTROCHEMICAL PERFORMANCE AND STABILITY OF NITROGEN-DOPED ORDERED MESOPOROUS CARBON HOLLOW SPHERES

J.C. Carrillo-Rodríguez[1], L. de la Torre-Sáenz[2], B. Escobar-Morales[3], A.M. Garay-Tapia[4], I.L. Alonso-Lemus[5], F.J. Rodríguez-Varela[1]

[1]Sustentabilidad de los Recursos Naturales y Energía, Cinvestav Unidad Saltillo, Av. Industria Metalúrgica, 1062, C.P. 25900, Ramos Arizpe, Coahuila, México, juan.carrillo@cinvestav.edu.mx
[2]Centro de Investigación en Materiales Avanzados S.C., Av. Miguel de Cervantes 120, Parque Industrial Chihuahua, C.P. 31109 Chihuahua, Chihuahua, México
[3]CONACYT, Centro de Investigación Científica de Yucatán, Calle 43 No. 130, Col. Chuburná de Hidalgo, Mérida, Yucatán, C.P. 97200, México
[4]Centro de Investigación en Materiales Avanzados S.C., Unidad Monterrey, Alianza Norte 202, Autopista Monterrey-Aeropuerto km 10, Parque PIIT, Apodaca, Nuevo León, C.P. 66628, México
[5]CONACYT, Sustentabilidad de los Recursos Naturales y Energía, Cinvestav Unidad Saltillo, México

Methanol-functionalized Nitrogen-doped Ordered Mesoporous Carbon Hollow Spheres (N-HWfs) are a novelty as high-performance metal-free electrocatalyst for the Oxygen Reduction Reaction (ORR) in alkaline media. In this works N-HWfs are synthetized by the silica template-based method, using resorcinol and formaldehyde as carbon source and two approaches of doping, using: i) 2-pyridinecarboxialdehyde (N1-HWf) and ii) pyrrole (N2-HWf) as nitrogen source. The functionalization is carried out with methanol solution (0.5 mol L^{-1}) with the aid of intermittent microwave heating. A non-doped Ordered Mesoporous Carbon Hollow Spheres (HW) electrocatalyst has also been synthetized following the same methodology. Its catalytic activity is compared with that of N1-HWf and N2-HWf.
The morphology of N1-HWf, N2-HWf and HW has been analyzed in a Field Emission-Scanning Electron Microscope (FE-SEM), resulting in highly rough hollow spheres for N1-HWf and HW. Meanwhile, N2-HWf shows hollow spheres with low roughness. Analysis of the electrocatalysts by X-Ray Diffraction (XRD) shows their amorphous structure with crystalline phases. Characterization by X-Ray Photoelectron Spectroscopy (XPS) shows the formation of pyrrolic, pyridinic, quaternary and oxide nitrogen species at N1-HWf and N2-HWf. The catalytic activity of the electrocatalysts for the ORR have been evaluated by the Rotating-Ring Disc Electrode (RRDE) technique. N2-HWf shows a higher performance than N1-HWf and HW, with an onset potential of the ORR (E_{Onset}) of 0.89 V, half-wave potential ($E_{½}$) of 0.82 V and a current density (j) of -1.86 mA cm^{-2} at 0.8 V (all potentials vs. RHE). However, its electron transfer number (n) is lower and its percent of H_2O_2 production ($\%H_2O_2$) is higher than N1-HWf and HW. Nevertheless, after accelerated degradation tests (3000 cycles, between 0.6 and 1.0 V), N2-HWf shows a high stability and improvement in catalytic activity compared to N1-HWf and HW, with E_{Onset}= 0.88 V, $E_{½}$= 0.81 V and j= -1.89 mA cm^{-2} at 0.8 V. Moreover n= 3.9 and $\%H_2O_2$ = ~1.5% at N2-HWf.
The catalytic activity for the ORR and the electrochemical stability of the N2-HWf electrocatalyst indicates that it is a potential candidate for Anion Exchange Membrane Fuel Cells (AEMFC) cathode applications.

Acknowledgements
The authors wish to thank CONACYT for financial support through grant 241526, 250632 and 253986.

096. $Zr(AlH_4)_4$ AS LOW-TEMPERATURE HYDROGEN STORAGE MATERIAL

Juan Rogelio Tena-Garcia, Karina Suarez-Alcantara

IIM-Morelia Unit of the National Autonomous Mexican University, karina_suarez@iim.unam.mx

A possible solution for the on-board hydrogen storage is the development of one-way low-temperature materials. Among the long list of possible materials, new-alanates can be of interest due to the high hydrogen storage capacity. In this work, $Zr(AlH_4)_4$ is presented as a one-way low-temperature material for hydrogen storage. This material was prepared by the metathesis reaction of $LiAlH_4$ and $ZrCl_4$ in cryogenic conditions by ball milling. Thermal desorption experiments demonstrated total dehydrogenation at about 50°C of near 4 wt. % for a mixture of $Zr(AlH_4)_4$ and LiCl (both products of metathesis). The characterization by X-ray diffraction and infrared spectroscopy is presented.

Acknowledgements
This work was founded by *CONACyT Ciencia Basica* proyect *Alanatos no convencionales para el almacenamiento de hidrógeno a baja temperatura. 251347*

097. GENETIC CHARACTERIZATION OF THE GENE HYDROGENASE OF *Scenedesmus Obliquus* AND ITS INTRA- AND INTER-SPECIFIC EVOLUTIONARY RELATIONSHIP WITH OTHER ALGAE.

Tamayo-Ordoñez M.C.[1], Tamayo-Ordoñez Y.J.[2], Ayíl-Gutierrez B.[3], Ruiz-Marin A.[4], Tamayo-Ordoñez F.A. [4], Moreno-Davila I.M.M.[1], Ríos-Gonzalez L.J.[1], Acosta-Cruz E.Y. [1] and Sosa-Santillán G.J.[1]

[1] Facultad de Química de la Universidad Autónoma de Coahuila. Saltillo, Coah. México.
mtamayo@uadec.edu.mx
[2] Unidad de Biotecnología. Centro de Investigación Científica de Yucatán, Mérida, México.
[3] CONACYT- Centro de Biotecnología Genómica-IPN, Reynosa, México.
[4] Facultad de Química, Dependencia Académica de Ciencias Química y Petrolera, Universidad Autónoma del Carmen, Carmen, México.

Hydrogen and electricity are attractive options in transportation and power generation for the world. The interconversion between these two forms of energy suggests the *in situ* use of hydrogen to generate electricity. In Mexico, 40% of H_2 production derives from the use of different biological processes and wastes, within these the use of microalgae as a source of H_2, is a viable option [1]. Since the sixties, the ability of green algae to produce H_2 was demostrated [2]. Unfortunately, in Mexico we are still developing knowledge for the generation of H_2 from algae. In this project we isolate and identify different genes encoding hydrogenases in *Scenedesmus obliquus* and through *in silico* analysis we study their evolutionary relationship with other hydrogenases reported in other genera of algae. The network construction of haplotypes, dendograms and 3D modeling of proteins, suggest that at least two functional groups of hydrogenase enzymes (Group I and Group II) are present and that possibly demonstrate a differential regulation in the presence of hygrogenase inducers. This enzyme could be applied in the future for the generation of H_2 through biocatalysis.

References

[1] Bhandari, R., Trudewind, C. A., & Zapp, P. (2014). Life cycle assessment of hydrogen production via electrolysis–a review. *Journal of cleaner production*, *85*, 151-163.Florin L., Tsokoglou A., Happe T. (2001). A novel type of iron hydrogenase in the green alga *Scenedesmus obliquuos* is linked to the photosynthetic electron transport chain. *J Biol Chem 276:*6125-6132.
[2] Torzillo, G., Scoma, A., Faraloni, C., & Giannelli, L. (2015). Advances in the biotechnology of hydrogen production with the microalga Chlamydomonas reinhardtii. *Critical reviews in biotechnology*, *35*(4), 485-496.

Acknowledgements. Thanks to UA de C, UNACAR, IPN-Centro de Biotecnologia genomica, for the infrastructure and financing granted for the development of these projects.

098. EVALUATION OF THE PERFORMANCE OF Pt_3Fe AS A CATALYST FOR THE RRO

M. M. Tellez-Cruz[1]*, M. A. Padilla-Islas[1], H. Cruz-Martinez[1], H.M. Alfaro-López[1], O. Solorza-Feria[1]*

[1] Departamento de Química, CINVESTAV. Av. Instituto Politécnico Nacional 2508, Cuidad de México, C.P. 07360, México, mtellez@cinvestav.mx, osolorza@cinvestav.mx

The synthesis of octahedral nanocatalyst of Pt_3Fe for oxygen reduction reaction (ORR) in acid media is presented. The catalyst was prepared through chemical reduction with a variable amount of oleylamine, oleic acid, dibenzyl ether (as solvent) and precursor salts $Pt(acac)_2$ and $Fe(acac)_3$. Subsequent, the catalyst was dispersing in a carbon matrix (Vulcan Carbon) previously thermally treated. XRD proved the presence of the alloy Pt_3Fe in the nanoparticles. STEM micrographs showed the morphology of the nanoparticles. The electrochemical performance of Pt_3Fe/C was evaluated by cyclic voltammetry, CO stripping and rotating disk electrode in $HClO_4$ as the electrolyte, showing best catalytic (mass activity and specific activity) than commercially available 20-wt% Pt/C-Etek® catalyst. The stability of the catalyst was evaluated, showing high resistance to corrosion. Finally the performance of the catalyst was evaluated as cathothe in a PEM fuel cell.

References

[1] M.Wang, et al., Journal of the American Chemical Society, 2015, 137 (44), 14027-14030.
[2] H. Wang, et al. International Journal of Hydrogen Energy, 2011, 36(1), 839-848.
[3] U.A. Paulus, et al., J Electroanal Chem, 2001 495:134–145.
[4] N. Markovic, et al. Fuel Cell, 2001, 1:105–116.
[5] K.J.J. Mayrhofer, et al., Electrochim Acta, 2008, 53:3181–3188

Acknowledgements

M.M.T.C. acknowledges CONACYT for the PhD fellowship and to Laboratorio Avanzado de Nanoscopía Electrónica (LANE). The authors are grateful for the financial support of the CONACyT-SENER-245920 project.

099. EFFECT OF EPITAXIAL GROWTH OF BIMETALLIC NANOCRYSTALS ON THE ACTIVITY OF ELECTROCATALYSTS IN THE OXYGEN REDUCTION REACTION

Francisco F. Tello Casas[1], Rosa de Guadalupe González Huerta[1], Martha L. Hérnandez Pichardo[2], Paz del Angel[3]

[1] Instituto Politécnico Nacional ESIQIE, Lab. de Electroquímica, Ed. Z-5, 3er piso, C.P. 07738, CDMX
[2] Instituto Politécnico Nacional ESIQIE, Lab. de Nanomateriales, Ed. Z-5, 2er piso, C.P. 07738, CDMX
[3] Instituto Mexicano del Petróleo, Eje Central L. Cárdenas 152, C.P. 07730, Ciudad de México
Email: rosgonzalez_h@yahoo.com.mx

The advantages of fuel cells are: high efficiency, do not generate pollutant emissions, low maintenance costs and wide ranges of energy. However, the high cost of noble metals has limited the application of fuel cells. To overcome this problem, the use of bimetallic nanoparticles has been proposed. In this work, bimetallic nanoparticles Pt-Pd were synthesized by surface oxide-reduction reactions and evaluated catalytically towards oxygen reduction reaction. Physicochemical characterization was performed, using analysis techniques such as X-ray diffraction, transmission electron microscopy (HRTEM and STEM), TGA. The rotating disk electrode in the bimetallic nanoparticles Pt-Pd with heat treatment have a more horizontal plateau which indicates a higher rate of oxygen reduction reaction, and also oxygen diffuses better on the surface of the electrode. A Tafel slope of 65.07 mV dec-1 in the bimetallic nanoparticles Pt-Pd with heat treatment was obtained, corresponds to first order kinetics, which shows a good catalytic activity towards the ORR.

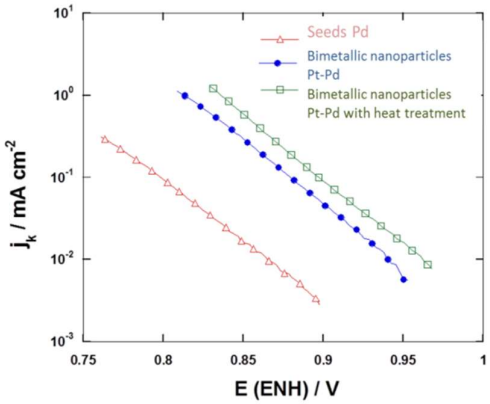

Fig. 1. Tafel slope. Result of electrochemical evaluation in acid medium of different syntheses. The bimetallic nanoparticles Pt-Pd with heat treatment had a better catalytic activity towards the oxygen reduction reaction

References

[1] Zhang, J., Miomir, B.,Ye, Xu., Mavrikakis, M., and Adzic, R., 2005. Controlling the Catalytic Activity of Platinum-Monolayer Electrocatalysts for Oxygen Reduction with Different Substrates. Weinheim. 117, 2170-2173.
[2] Selvarani, G., Pitchumani, S., and Shukla, A., 2009. A Methanol-Tolerant Carbon-Supported Pt-Au Alloy Cathode Catalyst for Direct Methanol Fuel Cells and Its Evaluation by DFT. J. Phys. Chem. 113, 7461-7468.

100. LOWERING OF DEHYDROGENATION TEMPERATURE OF $NaAlH_4$ BY USING $ZrCl_4$ AND $TiCl_4$

Juan Tena García, Karina Suárez Alcántara

Unidad Morelia del Instituto de Investigaciones en Materiales de la Universidad Nacional Autónoma de México. Antigua Carretera a Pátzcuaro No. 8701, Col. Ex Hacienda de San José de la Huerta, C.P. 58190, Morelia, Michoacán, México.
juanrogelio_tenagarcia@iim.unam.mx,

The alanates have been proposed as materials for storage of hydrogen [1]. Some of them, noted for their high hydrogen content and the possibility of having reversible storage, e.g., $NaAlH_4$ [2][3]. Other alanates, like those that contain elements of transition ($Ti(AlH_4)_4$ or $Zr(AlH_4)_4$) are practically unknown, with regard to their storage properties of hydrogen and their conditions of synthesis [4].
The cation substitution mechanism has been effective for the synthesis of materials with similar structures (borohydrides) [5]. In the present research work, mechanical milling was used at -197ºC (cooling with liquid nitrogen) to promote the formation of reactive mixtures with low dehydrogenation temperature.

References

[1] Naturwissenschaften **2004**, 91 (4), 157–172.
[2] J. Alloys Compd. **1997**, 253–254, 1–9.
[3] Inorg. Chem. **1967**, 5 (9), 1965–1967.
[4] Russ. Chem. Rev. **1968**, 37(2) 99-114
[5] J. Phys. Chem. C, **2012**, 116 (38), pp 20239–20245

Acknowledgements Research carried out thanks to the Basic Science project of CONACyT 251347: “Non-conventional alanates for hydrogen storage at low temperature”.

101. THE EFFECT OF STRUCTURE OF CO-ABSORBENT TO IMPROVE DYE SENSITIZED SOLAR CELL PERFORMANCE

Luciano da Silva[1]*, Harold Freeman[2]

[1] *Centro de Investigacion en Quımica Aplicada, Blvd. Enrique Reyna H. 140, Saltillo, Coahuila, 25294, Mexico.*
E---mail: luciano.dasilva@ciqa.edu.mx
[2] *Department of Textile Engineering,, Fiber and Polymer Science Program, North Carolina State University. E.mail: hfreeman@ncsu.edu*

ABSTRACT
Dye sensitized solar cell (DSSC) are important compared to the conventional solar cells such as monocrystalline, polycrystalline, and even amorphous silicon; basically due to its low manufacturing cost. However, the DSSC consists of many anode/cathode interfaces, such as semiconductor to dye and dye to electrolyte and electrolyte to platinum catalyst at the cathode. Therefore, the effect of charge recombination at dye-electrolyte interface is the most important role to cell efficiency. One of major implementations to alleviate the recombination effect could be efficiently solved by adding a hydrophobic co-adsorbent to dye solution. Such molecule will be anchored to a titanium dioxide semiconductor like dye and can be the barrier to protect the interface of the triiodide, dye and mesoporous titanium dioxide (TiO_2). In this study, N,N-diethyl-4-{[[4'-nitro-2'-tetrazoyl] phenyl]-diazenyl}aniline (LTz-1) and 5- (4-octhyloxy phenyl) tetrazole (LTz-2) were synthesized and used as the coadsorbent with HD-14 dye to prepare the photoanode for a dye-sensitized solar cell (DSSC), and its photovoltaic performance evaluated. The short-circuit current and the open-circuit voltage of the DSSC are increased for LTz-2 with the co-adsorption and reduced for LTz-1, comparing to deoxycholic acid (DCA) as co-adsorbent. The reason might be due to an observed negative direction shift in the conduction band (CB) for the co-absorbent LTZ-2, not seen for LTz-1. This can be associated to the ground state oxidation potential in SD-3, which is smaller than HD-14 while ground state oxidation potential in LTZ-2 is higher than HD-14. The energy conversion efficiency of the DSSC is 9.22 % to HD-14 - DCA, 9.21% to HD-14 – LTZ-2 and 7.49% to HD-14 – LTz-1, on the TiO_2 photoanode. For **LTz-1** co-adsorbent, the results can be attributed to the repellent effect of the long alkyl chain. For **LTz-2** coadsorbents, it is possible that the more compact layer was been formed with improves electron-injection efficiency into TiO_2.

ACKNOWLEDGMENTS
The authors gratefully acknowledges financial support by a scholarship from Conselho Nacional de Desenvolvimento Científico e Tecnológico (CNPq). The authors wish to thank Dr. Hammad Cheema for providing the sample of HD-14 used in this investigation.

102. ELECTROCATALYTIC EVALUATION OF THE SORBITOL ELECTRO-OXIDATION REACTION IN ALKALINE MEDIUM EMPLOYING Pd_x-Au_y/C NANOCATALYSTS.

L. J. Torres-Pacheco[1], L. Álvarez-Contreras[2], M. Guerra-Balcázar[3], and N. Arjona[1]*

[1]Centro de Investigación y Desarrollo Tecnológico en Electroquímica S. C., Parque Tecnológico Querétaro, Sanfandila, Pedro Escobedo, C.P. 76703, Querétaro, México.
[2]Centro de Investigación en Materiales Avanzados S. C., Complejo Industrial Chihuahua, Chihuahua, C. P. 31136, México.
[3]Facultad de Ingeniería, División de Investigación y Posgrado, Universidad Autónoma de Querétaro, Querétaro, C. P. 76010, México.
** Corresponding author: wvelazquez@cideteq.mx; noe.arjona@yahoo.com.mx*
Tel: +52 (442) 211 60 00 ext. 7874.

The development of new catalysts that allow a competitive use of alternative fuels is a major topic of concern in modern day. Sorbitol is a prominent candidate as fuel source, being possible to obtain through green chemistry approaches. Literature about the sorbitol electro-oxidation reaction (SOR) is scarse, with few works on platinum and gold alone materials in acid medium [1]; recently, our research group publiched a work on the SOR on alkaline medium with Pd, Au, and Pd-Au catalysts, showing the advantages of working with Pd-based catalysts and the viabillity of sorbitol as fuel, outperforming other alcohols like glucose and glycerol [2]. In the present work the effect of Pd_x-Au_y/C catalysts over the SOR was studied in alkaline medium at various sorbitol, KOH, and temperature conditions. The catalysts were characterized through XRD, XRF, HR-TEM, TGA, and electrochemical tests. XRD diffractograms revealed FCC metallic structures and TGA results showed metallic loads arround 20%. At 0.5 M sorbitol + 0.3 M KOH, Pd/C presented a peak potential of 0.14 V/NHE, while Au/C 0.56 V/NHE, with the bimetallics presenting potentials between those of the monometallics. Working at 0.5 M sorbitol + 3 M KOH, $Pd_{80}Au_{20}$/C and $Pd_{39}Au_{61}$/C presented the lower peak current potentials with 0.05 and 0.08 V/NHE, respectively. The lowering of peak potential of $Pd_{39}Au_{61}$/C at higher KOH concentrations is related to a better handling of reactions by-products, as is observed during the 500 cycles stabillity tests, where it maintained an i/i_2 relation above 100 % during all the cycles.

References

[1] Electrochim. Acta, 1989, 34, 391-97.
[2] Fuel, 2019, 250, 103-116.

Acknowledgements

The authors express their gratitude to CONACYT for the financial support granted for the development of this research. CONACYT SENER-Sustentabilidad Energética- INNOVATE UK Grant no. 269546. Acknowledgments to the laboratories of other institutions that contribute with CIMAV NANOTECH, LABMyN

103. HYDROGEN PRODUCTION BY ETHANOL STEAM REFORMING OVER Pt-*x*TiO$_2$/SBA-15: EFFECT OF THE TITANIUM CONTENT

N.L. Torres-Garcia[1], R. Huirache-Acuña[1], F. Fresno[2], V.A. de la Peña O'Shea[2]

[1] Facultad de Ingenieria Quimica, Universidad Michoacana de San Nicolas de Hidalgo, Francisco J. Mugica s/n, 58060, Morelia, Michoacan, Mexico. nidialibia.tg@gmail.com
[2] Unidad de Procesos Fotoactivados, IMDEA Energia, Av. Ramon de la Sagra 3, 28935, Mostoles, Madrid, España.

Hydrogen has been identified as an ideal energy carrier because it has been considered as the least polluting fuel that can be promisingly used in a fuel cell for electricity generation [1]. However, nearly 95% of hydrogen is currently produced from fossil-based feedstocks, being the steam reforming of methane the most used and nowadays the most economical option. In this process, carbon is released into the atmosphere as carbon dioxide, leading to global climate change [2]. In this mean, interest is focusing on search for effective alternatives to produce renewable hydrogen cleanly and safely. In particular, ethanol has shown good features for hydrogen production and it owns a series of advantages: a) high hydrogen content, b) good availability and low production costs, c) easy and save handling and transportation, d) non-toxicity and e) the possibility of distribution in a logistic net similar to the conventional fuel stations. In addition, ethanol could be bio-produced from a wide variety of biomass sources, including energy plants, waste materials from agroindustries or forestry residue materials, and therefore, it does not contribute to increase the greenhouse effect [3, 4].
In this work, semiconductor catalysts was supported on mesoporous silica SBA-15 were synthetized with different weight % (10, 20, 40, 60 and 80) and 0.5wt% Pt nanoparticles as co-catalyst. The catalysts have been tested in the ethanol steam reforming with a solution ethanol 1:10 by volume to 60°C and the light source was a 150W Xe lamp to simulate UV radiation. Ar flow (20ml/min) was employed to remove air from the reactor and as carrier for the reaction products. The gas was extracted to a quadrupole mass spectrometer (Pfeiffer OMNISTAR) for analysis. By means of different characterization techniques, it was possible to determine the interaction between the active phase, the metallic nanoparticle and the catalytic support. These studies indicate that the use of mesoporous silica SBA-15 as a support increases the dispersion of the active phase, resulting in an increase in the evolution of H_2.

References

[1] Zhang L, Li W, Guo C, Wang Y, Zhang J. Ethanol steam reforming reactions over Al_2O_3. SiO2-supported Ni-La catalysts. *Fuel* **2009**, *88*:511-8 .
[2] Vizcaíno AJ, Carrero A, Calles JA. Hydrogen production by ethanol steam reforming over Cu-Ni supported catalysts. *Int J Hydrogen Energy* **2007**, 32:1450-61.
[3] Fierro V, Akdim O, Proyendier H, Mirodatos C. Ethanol steam reforming over Ni-based catalysts. *J Power Sources* **2005**, 145:659-66.

Acknowledgements

The authors appreciate the support of CIC UMSNH 2019 Project, the CONACyT for the scholarship to NLTG (465563), the FotoArt-CM Project (S2018/NMT-4367) of Comunidad de Madrid, Spanish Government (ENE2016-79608-C2-1-R) and the European Research Council (contract number 648319)

104. ZEOLITES FROM GEOTHERMAL NANOSILICA AND ITS EVALUATION IN THE DEHYDRATION OF BIOETHANOL

J.A. Trejo García[1], A. Medina Ramírez[1*], B. Ruiz Camacho[1], J.I. Minchaca Mojica[1], C.M. López Badillo[2]

[1]Departamento de Ingeniería Química, División de Ciencias Naturales y Exactas, Universidad de Guanajuato, Campus Guanajuato. Noria Alta s/n, 36050, Guanajuato, Guanajuato, Mexico
**adriana.medina@ugto.mx*
[2]Facultad de Ciencias Químicas, Universidad Autónoma de Coahuila, Blvd. V. Carranza y José Cárdenas, 25280, Saltillo, Coahuila, Mexico

Investigations related to the bioethanol production from different kind of biomass has atracted the attention due to the bioethanol increase the octane number of gasoline, minimice the emissions, and it can reemplace some additives [1]. Additionally the biotehanol can be use in the fuel cells. Nevertheless the challenge in the production of biotehanol is that during fermentation process the bioethanol contains water, this generate inmiscible mixture of hydrocarbons affecting the performance of engine. Among different separations techniques the adsorption is a proper alternative and its effectivess depends of the adsorbent nature [2]. For these reasons in the present work zeolitic materials were synthesized from geothermal silica by hydrothermal method. The products were characterized by TEM, XRD and FT-IR. Solutions of water-ethanol of composition similar to bioethanol were used during adsorption trials. The content of ethanol was determined by UV-Vis spectroscopy. The XRD analysis allowed to identify the crystalline phases: zeolite type A and faujasite, the zeolites exhibited a cubic and octahedral morphology. Additionally the zeolites were stable in the medium and no significant structural changes were observed. The water adsorption capacity was influenced by the Si/Al ratio and the framework of the zeolites. According to the results the zeolites were able to adsorb the water reaching a alcohol concentration of 98% v/v, make them potentially useful to obtaining of fuel grade bioethanol.

References

[1] Frolkova A. K, Raeva V. M. Bioethanol Dehydration: State of the Art, Theoretical Foundations of Chemical Engineering, **2010**, 44, 545–556
[2] Hajilari M, Shariati A, Khosravi-Nikou M. Equilibrium adsorption of bioethanol from aqueous solution by synthesized silicalite adsorbents: experimental and modeling, Adsorption, **2019**, 25, 13-31

Acknowledgements

The authors acknowledge to DAIP-UG through the Convocatoria Institucional de Investigación Científica for the financial support of this work by the project "S*íntesis y caracterización de nanoadsorbentes para obtención de bioetanol grado combustible*"

105. EFFECT OF THE NATURE OF HYPO MATERIALS IN BIMETALLIC PD-M/C COMBINATIONS (M: MN, FE AND ZN) IN THE ELECTRO-OXIDATION OF CRUDE GLYCEROL IN ALKALINE MEDIUM

I. Velázquez-Hernández[1], V. Lair[2], L. Álvarez-Contreras[3], M. Guerra-Balcázar[4], and N. Arjona[1,*].

[1]Centro de Investigación y Desarrollo Tecnológico en Electroquímica, Sanfandila, Pedro Escobedo, Qro., C.P. 76703, México.
[2]Institut de Recherche de Chimie Paris, CNRS-Chimie ParisTech, 11 rue Pierre et Marie Curie,75005 Paris, France.
[3]Centro de Investigación en Materiales Avanzados S.C., Complejo Industrial Chihuahua, Chihuahua Chi., C. P. 31136, México. Facultad de Ingeniería, División de Investigación y Posgrado.
[4]Universidad Autónoma de Querétaro, Querétaro, Qro., C. P. 76010, México.
** Corresponding author: +52(442 211 60 00 EXT 7874) wvelazquez@cideteq.mx*

Crude glycerol as waste from the synthesis of biodiesel has been used in fuel cells to obtain electrical energy employing mainly Pt-based electrocatalysts. In the present work, nanoparticles of Pd, PdMn, PdFe and PdZn were synthesized and supported on Vulcan® carbon via green chemistry using the 2-hydroxyethylammonium formate ionic liquid. The synthesized materials were characterized by X-ray diffraction (XRD), X-ray fluorescence (XRF), thermogravimetric analysis (TGA), high-resolution transmission electron microscopy (HR-TEM) and cyclic voltammetry (CV). On the other hand, basic trans-esterification method was used to product biodiesel and crude glycerol. Moreover, the composition obtained by XRF revealed the composition of $Pd_{82}Mn_{18}$, $Pd_{84}Fe_{16}$ and $Pd_{88}Zn_{12}$, while TGA analyzes revealed mass compositions between 8 to 16% in metal-support content. The analysis by XRD revealed the materials show a face cubic centered structure (fcc). The electrocatalytic evaluation were performed by CV at 0.1, 0.5, 1 and 1.5 M of glycerol and crude glycerol in alkaline medium. PdMn/C exhibited a lower oxidation peak potential (0.0889 V vs. NHE) than the rest of the materials, this means PdMn/C required less energy to electro-oxidize glycerol resulting in a higher current density (84.49 mA mg^{-1}) with respect to PdZn/C and PdFe/C at a concentration of 0.5M analytical glycerol. In addition, in the electro-oxidation of crude glycerol PdMn/C had a 20% loss in terms of maximum current density. In summary, PdMn/C can be used as an alternative electrocatalysts for the efficient usage of crude glycerol as fuel for energy conversion applications.

Acknowledgements (10 pt)
The authors express their gratitude to CONACYT for the financial support granted for the development of this research. CONACyT SENER-Energy Sustainability- INNOVATE UK Grant no. 269546. Acknowledgments to the laboratories of other institutions that contribute with CIMAV NANOTECH, LABMyN.

106. SYNTHESIS OF Ni BASED ELECTROCATALYSTS BY USING INTERMITTENT MICROWAVE HEATING REDUCTION PROCESS FOR ETHANOL OXIDATION REACTION.

L.R. Vidales-Gallardo[1], Eddie N. Armendáriz-Mireles[1], E. Rocha-Rangel[1], W.J. Pech-Rodríguez[1]*

[1] Universidad Politécnica de Victoria, Av. Nuevas Tecnologías 5902, Parque Científico y Tecnológico de Tamaulipas, Ciudad Victoria, Tamaulipas, C.P. 87138.
**E-mail: wpechr@upv.edu.mx*

This work is focused on the design and development of Ni based electrocatalysts by using intermittent microwave heating polyol reduction process.
The electrocatalysts were synthesized under different sequences of irradiation time and Ni concentration in order to investigate the effects on the ethanol oxidation reaction.
The obtained electrocatalyst was physical and chemical characterized by X-ray diffraction, Scanning electron microscopy with energy dispersive X-ray spectroscopy and Fourier-Transform Infrared Spectroscopy. Meanwhile, their electrochemical activity for ethanol oxidation was studied by cyclic voltammetry, chronoamperometry and electrochemical impedance spectroscopy. The results indicated that the synthesized parameters play a key role into the electrochemical activity of the materials. Therefore, it is demonstrated that intermittent microwave irradiation is a promising method to synthetize in a short time and in large scale Ni based electrocatalyst.

Acknowledgements
We thank CONACYT for the master scholarship provide to LR. Vidales-Gallardo. Also, we are gratefully for the help we received from the doctors of the Polytechnic University of Victoria since the road so far has not been simple but thanks to their contributions, support and my effort this research has been carried out.

107. DESIGN OF BIPOLAR PLATES FOR DIRECT ALCOHOL FUEL CELL

I. Viera[1], M. Paredes[1], D. Pacheco[1], L.C. Ordóñez[1]

[1] Unidad de Energía Renovable, Centro de Investigación Científica de Yucatá.Parque Científico Tecnológico de Yucatán. Carretera Sierra Papacal – Chuburná Puerto, km 5. Sierra Papacal, Yucatán, México. C.P: 97302. E-mail: lcol@cicy.mx

Direct Alcohol Fuel Cells (DAFC) convert the alcohol chemical energy into electricity through electrochemical reactions. For their operation, these devices use auxiliary systems with the inevitable consume of part of the produced energy by the DAFC. The fuel pump and air supplies are the principal energy consumers [1]. Our objective was to develop a self-breathing (cathode) and self-pumping (anode) bipolar plate. We use computational fluid dynamics (CFD) to study the fluid regimens in both electrodes. Specifically, at anode we design a geometry that promotes the fuel supply by capillary and reduces or eliminate the auxiliary elements to improve the DAFC performance. A bipolar plate of 0.08 m high and 0.13 m long was proposed. The anode side consisted of conical channels. The open cathode has an architecture of circular pines (Figure 1). Simulations showed a capillary rise of 0.028 m which represents 70% of the height of the flow channel (Figure 2). A DAFC was manufactured and characterized.

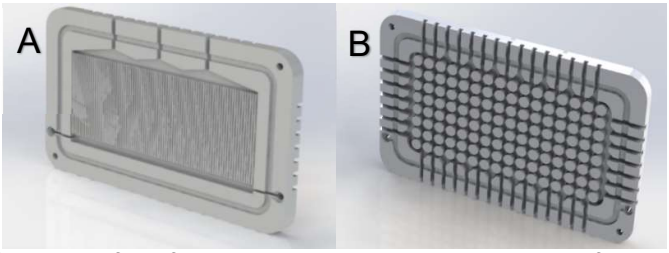

Figure. 1.-A) Structure of the flow channels in the anode B) Matrix of pins in the cathode.

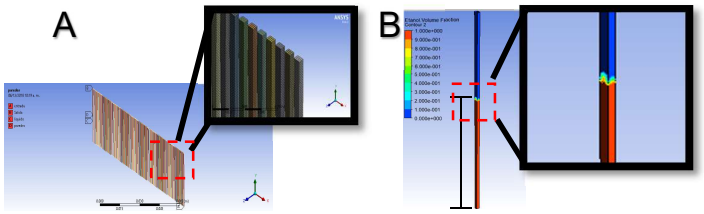

Figure. 2. - A) Definition of the domains and generation of the mesh of design. B) Result of the simulation of capillary rise in one of the flow channels.

References

[1] Zhu Y, Liang J, Liu C, Ma T, Wang L. Development of a passive direct methanol fuel cell (DMFC) twin-stack for long-term operation. J Power Sources 2009;193:649–55. doi:10.1016/j.jpowsour.2009.03.069.

Acknowledgments

The authors are grateful for the financing of the SENER-CONACYT-Energy Sustainability Project-254666.

108. BIOAUGMENTATION ON HYDROGEN PRODUCTION FROM FOOD WASTE

E. Villanueva, Y. Tarazona, I. Moreno-Andrade

[1]Laboratory for Research on Advanced Processes for Water Treatment, Unidad Academica Juriquilla, Instituto de Ingeniería, Universidad Nacional Autónoma de México, Blvd. Juriquilla 3001, 76230 Querétaro, Mexico. E-mail imorenoa@ii.unam.mx

Biohydrogen production using food waste as a substrate has been reported [1]. However, due to the substrate characteristics and different process variables, low H_2 production rates have been observed. Recently, the bioaugmentation (addition of specific microbial strains) into the reactor may accelerate the transformation of specific compounds, increasing the H_2 production [2]. The objective of this work was to evaluate the effect of the microorganisms that enhance the production of H_2 (*Clostridium beijerinckii, C. acetobutylicum, Bacillus subtilis,* and *Paenibacillus polymyxa*) in a batch test using food waste as substrate. The results indicated an increase in H_2 production due to the increase in the microorganisms added to the media (for all the species tested independently of the concentration evaluated). The H_2 generation increase from 46 to 149% for the case of *P. polymyxa and B. subtilis. Clostridium* species increase hydrogen production in more of 200%. The addition of the microorganisms is affected by the bacteria/inoculum ratio. The H_2 increases in 0.8 $\pm$ 0.5 $mLH_2/mL_{bacteria}$ in a bacteria/inoculum of 0.2 or lower. The increase of this ratio results in higher volumetric hydrogen production but a decrease in the specific hydrogen production (based in the mL of added bacteria), e.g., in Figure 1 for *P. polymyxa,* the volume of H_2 increase from 197 to 498 mL, but the rate decrease from 0.04 to 0.02 $mLH_2/mL_{bacteria\ added}/h$). The bioaugmentation not only improves hydrogen yields but also can be effective to overcome inhibition during H_2 production.

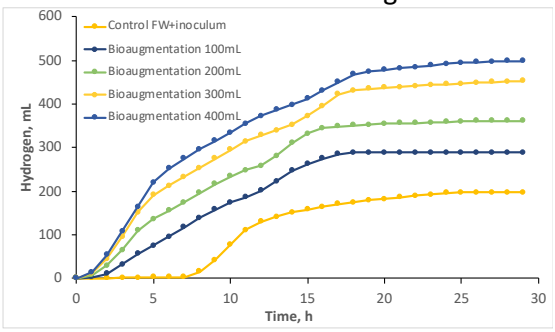

Figure 1. Hydrogen produción due to bioaugmentation by *P. polymyxa*

References

[1] Ramos C, Buitrón G, Moreno I, Chamy R **(2012)**. *Int. J. Hydrogen Energy*. 37, 13288-13295.
[2] Sharma P, Melkania U **(2018)**. *Int. J. Hydrogen Energy*. 43, 7290-7298.

Acknowledgements. Financial support by CONACYT Ciencia Básica 240087 is gratefully acknowledged. Gloria Moreno and Jaime Perez are acknowledged for their technical assistance. The support by "Fondo de Sustentabilidad Energética SENER-CONACYT (Mexico)"(project 247006 Gaseous Biofuels Cluster) is also acknowledged.

109. MODIFICATION OF CARBON NANOFIBERS WITH M-N (M=Co, Ni AND Fe) AS ELECTROCATALYSTS FOR THE OXYGEN REDUCTION REACTION WITH APPLICATIONS IN ENERGY STORAGE.

Deysi Gómez-Cholula[1*], Guadalupe Ramos-Sánchez[1,2], and Ignacio González[1]

[1] Departamento de Química, Área de Electroquímica, Universidad Autónoma Metropolitana-Iztapalapa, Avenida San Rafael Atlixco 186, Vicentina, 09340, Iztapalapa, CDMX, México.
[2] Conacyt Research Fellowship
deysigcholula@gmail.com

The ORR plays a vital role on the lifecycle and cost of several electrochemical systems, among them fuel cells[1]. This paper proposes new carbon-based electrocatalysts of the type M-N/CNFs (where M is Fe, Co, Ni and N/CNFs are N-doped carbon nanofibers) that allow improving the electrocatalytic activity of the ORR[2]. In this work, two modifications are investigated: metallic nanoparticles mechanically introduced in N-CNFs and the electrothreading[3] of M-N/CNFs with PAN (polyacrylonitrile)-DFM (dimethylformamide) and metallic phthalocyanines. Preliminary results have shown a slight improvement in the kinetics of ORR, however, further characterization is needed to determine the nature of the doping process taking place.

Additionally, DFT calculations are used to investigate the role of the inclusion of the metal into the carbonaceous structure.

References

[1] Yoo, H.D., Markevich, E., Salitra, G., Sharon, D., Aurbach, D., 2014. Biochem. Pharmacol. 17, 110–121.

[2] Wang, Z.L., Xu, D., Xu, J.J., Zhang, X.B., 2014. Chem. Soc. Rev. 43, 7746–7786.

[3] Zhang, L., Aboagye, A., Kelkar, A., Lai, C., Fong, H., 2014. J. Mater. Sci. 49, 463–480.

Acknowledgements

This project has been performed with the financial support from SECITI SECITI/080/2017.

110. AN OVERVIEW OF LMNO HIGH VOLTAGE LITHIUM-ION BATTERIES IMPLEMENTATION IN A HYBRID SOLAR-HYDROGEN SYSTEM. STUDY CASE "VIVIENDA SUSTENTABLE IPN®"

Jorge Olmedo-González[1], Guadalupe Ramos-Sánchez[2], Rosa de Guadalupe González-Huerta[1]

[1,2]Instituto Politécnico Nacional-ESIQIE, Electrochemistry and Corrosion Lab, UPALM, 07738, Mexico City, jorgeolmedog@outlook.com
[2]Universidad Autónoma Metropolitana- Iztapalapa, Chemistry Department, 09340, Mexico City

Energy storage technologies have a crucial role in variable renewable energies. Due to their natural intermittence or irregularity, it is necessary to control in indirect way electrical energy production. It is very important to develop new and better materials to store energy that can adapt to the requirements of energy production and consumption. High-voltage cathodes like $LiMn_{1.5}Ni_{0.5}O_4$ (LMNO) for lithium-ion batteries (LIB's) have proved to be a promising solution to avoid energy losses and have a better dynamic response time than lead acid batteries (PbAcB's), improving energy storage system cycle life. Therefore they could be an excellent option in electric vehicles and high-power applications[1].Vivienda Sustentable IPN® hybrid solar-hydrogen power system has proved that energy storage hybrid system (ESHS), PbAcB's and hydrogen system, is a reliable solution to increase autonomy in stationary applications with a proper energy management strategy[2]. However, cycle life PbAcB's have not been significative improved. In this work is studied the LMNO high voltage lithium-ion batteries implementation in ESHS. Household consumption profile, solar panels generation profile, maximum response time (dynamic charges) and energy management strategy (hydrogen system co-operation) are considered, power electronics influence it is not still full considered. Results indicate that LMNO batteries could be a proper option in the ESHS, especially when generation-consumption variations reduce in 400% and exceed in 20% respectively in periods of time up to pair of hours.

References

(1) Fang, X.; Ge, M.; Rong, J.; Zhou, C. Graphene-Oxide-Coated LiNi0.5Mn1.5O4 as High Voltage Cathode for Lithium Ion Batteries with High Energy Density and Long Cycle Life. *J. Mater. Chem. A* **2013**, *1* (12), 4083–4088. https://doi.org/10.1039/c3ta01534c.
(2) Yunes-Cano, A. Implementación de Un Sistema Híbrido Solar-Hidrógeno Para Producción de Energía Eléctrica Aplicado a Una Vivienda Sustentable, Instituto Politécnico Nacional, **2016**.

Acknowledgements

Authors thank to CEMIE-Océano 249795: Transversal Line I-LT1: Electrical grid integration and energy management resources, to the multidisciplinary project 2024 of Instituto Politécnico Nacional (IPN). Jorge Olmedo González thanks the scholarship granted by CONACYT-Mexico.

111. METAL-FREE ELECTROCALYST FOR ORR OBTAINED BY SOLAR PYROLYSIS OF AGAVE BIOMASS

D.C. Martínez-Casillas[1,2], G. Longinos Salazar[3], C. A. Campos Roldán[3], A. Ayala-Cortés[2], Rosa de Guadalupe González-Huerta[3], H.I. Villafán-Vidales[2], C.A. Arancibia-Bulnes[2], A.K. Cuentas-Gallegos[2].

[1] CONACYT-TecNM/ITD. Felipe Pescador 1803 Ote, Nueva Vizcaya, 34080 Durango, Dgo, Mexico, E-mail: dmartinez@itdurango.edu.mx
[2] IER-UNAM, Priv. Xochicalco s/n, Col. Centro, Temixco, CP 62580, Morelos, México.
[3] ESIQIE-IPN, Laboratorio de Electrocatálisis, UPALM Edificio 5, CP 07738, Ciudad de México.

In this work, the synthesis and the characterization of a novel metal-free electrocatalyst obtained by solar pyrolysis from alcoholic beverage industry waste is reported. The electrocatalysts was prepared using a sustainable process where concentrated solar energy is used as heat source. Agave biomass was processed in a glass spherical solar reactor at 500 °C with a heating ramp of 30°C min^{-1} in a inert atmosphere. From physical characterization we observed that our prepared metal-free electrocatalyst is an amorphous carbon, which have a macroporous structure with a surface area of 100 m^2 g^{-1}. The electrocatalyst was electrochemically evaluated by cyclic voltammetry and rotating disk electrode in 1M KOH using a three-electrode system, obtaining high performance as electrocatalyst for the Oxygen Reduction Reaction (ORR) in alcaline electrolyte. The metal-free electrocatalysts are a promising eco-friendly and scalable alternative as cathode materials for alkaline fuel cells. Our study provides a novel sustainable approach to use agricultural waste biomass to produce useful electrode materials for electrochemical energy devices using concentrated solar energy.

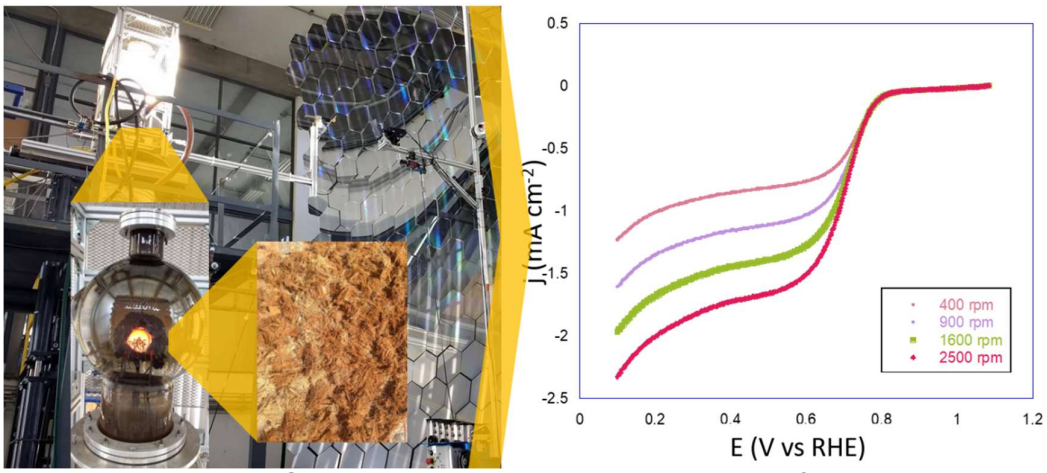

Figure 1. HoSIER, solar pyrolysis reactor and RDE performance.

Acknowledgements The authors acknowledge the technical support of J.J. Quiñones-Aguilar in the setup and operation of solar experiment. Financial support from DGAPA-PAPIIT-UNAM "Propiedades de Electrodos de Carbón producidos a partir de biomasa mediante concentración solar" and CEMIE-Sol "Combustibles solares y Procesos Industriales" (grants IG100217 and P-10, respectively).

112. CHARACTERIZATION AND ADAPTATION OF HYDROGEN OR OXYHYDROGEN RENEWABLE AND SUSTAINABLE COMBUSTION SYSTEM TO CONVENTIONAL HYDROCARBON COMBUSTION SYSTEM

F. A. Soriano Moranchel [1], J. M. Sandoval Pineda [1], R. Moreno Soriano [1], R. de G. González Huerta [2]

[1] ESIME UA – Instituto Politécnico Nacional, Sección de Posgrado e Investigación, Av. De las Granjas 682, C.P. 07738, CDMX, México, E-mail: fenix_alf105@hotmail.com
[2] ESIQIE – Instituto Politécnico Nacional, Laboratorio de Electroquímica, UPALM, C.P. 07738, CDMX, México.

The combustion of gases derived from conventional hydrocarbons has been used for centuries. The search for alternatives that reduce the emission of polluting gases, whether at the domestic or industrial level, has proved to be a challenge; the production and use of Hydrogen (H_2) in situ from renewable sources could reduce emissions of CO_2 and NO_X, increasing the efficiency of these combustion systems, in the long term [1]. Due to the high reactivity of H_2, there has always been a substantial interest in its application as a complement (enrichment) of hydrocarbonsm (methane, ethane and propane) in order to improve performance. H_2 can burn successfully in conventional combustion systems. In particular, with respect to systems based on premixed combustion technology, the unique characteristics of H_2 offer several advantages over combustible gases derived from hydrocarbons. The limits of flammability of H_2 are much wider than those of conventional hydrocarbons and their calorific value is higher than 298 K and 1 atm, 120 MJ / kg for H_2, while that of methane is 45 MJ / kg[2].

In this article will see topics related with the design and the integration in parallel of a renewable and sustainable combustion system based on gases obtained by alkaline electrolysis (Hydrogen and Oxyhydrogen) and applied on conventional hydrocarbon combustion system to reduce the use of this supplies [3].

References

[1] C. Echeverri-Uribe, et. al, “Numerical and experimental analysis of the effect of adding water electrolysis products on the laminar burning velocity and stability of lean premixed methane/air flames at sub-atmospheric pressures,” Fuel, vol. 180, pp. 565–573, 2016.
[2] C. Uykur, et. al , “Effects of addition of electrolysis products on methane/air premixed laminar combustion,” Int. J. Hydrogen Energy, vol. 26, no. 3, pp. 265–273, 2001.
[3] E. C. Okafor, et. al, “Effects of hydrogen concentration on premixed laminar flames of hydrogen-methane-air,” Int. J. Hydrogen Energy, vol. 39, no. 5, pp. 2409–2417, 2014.

Acknowledgements

To Concejo Nacional de Ciencia y Tecnología (CONACYT) and the Instituto Politécnico Nacional (IPN) in specific to Escuela Superior de Ingeniera Mecánica y Eléctrica Unidad Azcapotzalco (ESIME UA) and Escuela Superior de Ingeniera Química e Industrias Extractivas (ESIQIE) for the support provided.

113. AMMONIA BORANE STUDY AT LOW FREQUENCIES

R. Hinojosa N.[1, 2, 3*], E.V. Mejía-Uriarte[1], R Y. Sato-Berrú[1]

[1] Programa de Maestría y Doctorado en Ingeniería, Universidad Nacional Autónoma de México, Edificio Bernardo Quintana Piso 1, C.U., 04510 Coyoacán, CDMX, México.

[2] Instituto de Ciencias Aplicadas y Tecnología, Universidad Nacional Autónoma de México, Circuito Exterior S/N, Ciudad Universitaria, A.P. 70-186, Delegación Coyoacán, C.P. 04510 CDMX, México.

[3] Faculta de Ciencias, Universidad Nacional Autónoma de México, Av. Universidad 3000, Circuito Exterior S/N Delegación Coyoacán, C.P. 04510 Ciudad Universitaria, D.F. México.
hinro36@ciencias.unam.mx

Ammonia-borane ($H_3N{\cdot}BH_3$, AB) has been attracting a great deal of attention as a hydrogen storage medium [1]. The compound shows a phase transition from tetragonal to orthorhombic around 225 K [2]. Rotational nature of order−disorder has been proposed for this transition, with movement independent of -NH_3 and -BH_3 groups [3]. At present, the driving mechanism of the tetragonal-to-orthorhombic transformation is still unknown. Careful analysis of crystalline modes can surely help us understand the phase transition. In this work, the low-temperature experiment shows new modes at low frequencies. Therefore, so-called soft modes could be manifested [4]

There are information shows Raman signals from 100 cm^{-1}. Here, we study and present vibrational modes below 100 cm^{-1}. Figure 1 shows the modes related to the new crystalline structure.

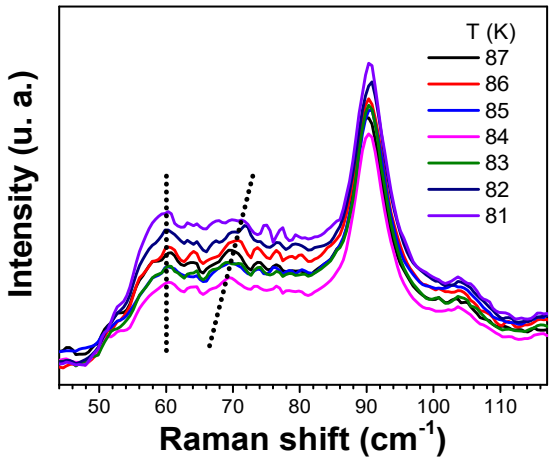

Figure 1. Raman modes around 59 and 69 cm^{-1}, at low temperature

References

[1] Frances H. S., Vincent P. and R. Tom B. The Royal Society of Chemistry. (2007), 2613–2626. DOI: 10.1039/b703053c.
[2] Nancy J. H., Mark E. B., Vencislav M., Chris M., Shawn M., Gregory K. and Autrey T. J. Chem. Phys. (2008) 128, 034508.
[3] Mark E. B., Graeme J. G. and Ward T. R. Aust. J. Chem. 2007, 60, 149–153.
[4] C. Ziparo, D. Colognesi, A. Giannasi, and M. Zoppi. J. Phys. Chem. A(2012), 116, 8827−8832.

Acknowledgements
This work has been supported by Project PAPIIT-IN108519, IN102917 and CONACYT.

114. PUBLIC POLICIES ON HYDROGEN IN MEXICO

Rosa de Guadalupe González Huerta[1*], Omar Solorza Feria[2], Juan Antonio Gutiérrez Rodríguez[3]

[1]Instituto Politécnico Nacional ESIQIE, Laboratorio de Electroquímica, Ed. Z-5, 3er piso, C.P. 07738, CDMX, México. Mail rosgonzalez_h@yahoo.com.mx
[2]Centro de Investigación y de Estudios Avanzados del IPN, Depto. Quíimica, C.P. 07360, CDMX.México
[3]Hazwo SA de CV, Tercera cerrada de calle 10, 212, Granjas San Antonio CP 09070, CDMX, México, mail

The inclusion of hydrogen technologies in energy portfolio of Mexico is a complex issue, since the entire 20th century was considered an oil country. Although there has been a level of growth within the field, ambitious goals and targets have been set by government officials. The Mexican government has set targets, to electric energy produccion from clean energy, of 25% by 2018, 30% by 2021, 35% by 2024, and finally an ultimate target of 50%by 2050. With these specific targets set, a tremendous amount of growth has occurred in order to keep up the demand. Public policy is the principled guide to action taken by the administrative executive branches of the state with regard to a class of issues, the foundation of public policy is composed of national constitutional laws and regulations. Clean energies are defined in the Electricity Industry Law [1], among which renewable energies (solar, wind, ocean etc.) are considered, and also the energy generated by hydrogen (combustion or use in fuel cells) is included. Today, there is a great opportunity for hydrogen technologies to grow within Mexico [2]. Hydrogen has become one of the most promising alternative energy carriers in the country, this in view to decentralize the today's energy production based on oil. Hydrogen versatility of new applications, high calorific value, and the fact that can be used as a clean fuel are some examples of the high potential in research and development activities. But the problem is the lack of an effective public policies in Mexico, which, despite the efforts to be placed on the boom of the hydrogen economy, that continues to legal bias and little social recognition. The great challenge facing Mexico in the energy transition goes beyond the effectiveness of government public policies; the change depends not only political area, but also legal, economic, technological, academic and social enviroment [3]

References

[1] SENER, 2014, Ley de la industria Eléctrica, http://www.diputados.gob.mx/LeyesBiblio/pdf/LIElec_110814.pdf (Last consultation 16 april 2019).
[2] López Ortiz A., Méndez Zaragoza M.J., Collins-Martínez V, Hydrogen production research in Mexico: A review, International Journal of Hydrogen Energy **(2016)** 41, 23363-23379.
[3] Avalos Rodríguez ML, Alvarado Flores JJ, Alcaraz Vera JV, Rutiaga Quinones JG, Espino Valencia J, The legal regulation of the H2 as a strategy for public policy in Mexico from the consolidation of the National Council of the hydrogen, Int J. hydrogen Energy **(2019)** in press.

Acknowledgements (10 pt)
Authors acknowledge to CONACYT CEMIE-Océano proyect 249795 and IPN Multidisciplinary Proyect SIP 2024, for the support provided for this academic research.

115. TEMPERATURE DEPENDENCE FOR HYDROGEN STORAGE IN METAL HYDRIDES $Mg_{1-x}M_x$ (M=Al, Zn, Ni, x=0.10, 0.12,..., 0.20)

O. Ramírez- Rodriguez[1], G. Ramírez-Dámaso[1].

[1] Escuela Superior de Ingeniería y Arquitectura "Unidad Ticomán" del Instituto Politécnico Nacional, Calz. Ticomán No. 600, Col. La Purísima Ticomán, C. P. 07340, Alcaldía Gustavo A. Madero, Ciudad de México, México. Email: omarod672@gmail.com

The purpose of this research work was the response of hydrogen, when it interacts on the surface of metals, magnesium base, at different temperatures. Calculations were performed with the help of computational molecular modeling software, Materials Studio 6.0, particularly with CASTEP and Dmol3 modules, based on the theory of electron density functional (DFT). The main objective is to find what alloys and at what temperatures these metal hydrides are more efficient to store hydrogen, whose potential use could be in transport. Molecular simulations of Magnesium-Aluminum, Magnesium-Nickel and Magnesium-Zinc alloys, in order to know the temperature dependence where greater adsorption of H2 molecules on the surface (110) of the metal alloy occurs.
The advantage of the use of metal hydrides, in the storage of hydrogen, would radically change the size of the containers and in the same way the level of safety would represent a real alternative.

References

[1] Vincent berube, M. S Dresselhaus, G. Chen. "Temperature dependence of the enthalpy of formation of metal hybrides characterized by an excess volume" **(2008)** 33: 5617-5628.
[2] K. Mark Thomas, "Hydrogen adsorption and storage on porous Materials" **(2006)** 120: 389-398.
[3] Andreasen A., "Hydrogenation properties of Mg-Al alloys. International Journal of Hydrogen Energy", **(2008)** 33: 7489-7497.
[4] Jeff Greeley, Manos Mavrikakis., "Surface and Subsurface Hydrogen: Adsorption Properties on Transition Metals and Near-Surface Alloys" J. Phys. Chem. B **(2005)**, 109: 3460-3471.
[5] Ming Chena, "Stability of transition metals on mg (0001) surfaces and their effects on hydrogen adsorption" **(2011)** 37: 309-317.
[6] L. Zaluzki, A. Zaluska, J.O. Strom-Olsen. "Structure, catalysis and atomic reactions on the nano-scale: a systematic approach to metal hybrids for hydrogen storage". Appl. Phys. A **(2001)** 72: 157-165.

Acknowledgements

Aknwledgement: G. Ramírez-Dámaso acknowledges the partial support provided through the project SIP-20181898, by Instituto Politécnico Nacional, MEXICO.

PART 2. Full-text works book

E001. INFLUENCE OF Er CONTENT ON THE ELECTRICAL PROPERTIES OF CeO_2 SOLID ELECTROLYTES OBTAINED BY MECHANOCHEMISTRY

D.E. Puente-Martínez[1], J.A. Díaz-Guillén[1], S.M. Montemayor[2], J.C. Díaz-Guillén[3], K.P. Padmasree[4], O. Burciaga-Díaz[1] and A.F. Fuentes[4].

[1]*Tecnológico Nacional de México, Instituto Tecnológico de Saltillo, 25280-Saltillo, Coahuila, México*
[2]*CIQA, Blvd. Enrique Reyna Hermosillo 140, 25294-Saltillo, Coahuila, México*
[3] *COMIMSA-Conacyt, Calle Ciencia y Tecnología 790, Saltillo 400, 25290 Saltillo, Coahuila, México*
[4] *CINVESTAV Unidad Saltillo, Av. Industria Metalúrgica 1062, Parque Industrial 25900-Ramos Arizpe, Coahuila, México*
* Dulce Esperanza Puente Martínez: (044) - 8441487831, dpuente@itsaltillo.edu.mx

ABSTRACT

Different researchers are looking to develop materials with high ionic conductivities at low temperatures (500°C) on views to be applied as solid electrolytes in Solid Oxide Fuel Cells (SOFCs). In this case, doped ceria systems, with general formula $Er_yCe_{1-y}O_{2-\delta}$ (y = 0.05 - 0.15) were synthesized by high energy mechanical milling (20 h) by using a planetary mill. Synthesized powders were then fired (800 - 1500 °C) and analyzed by XRD. Morphology and chemical composition of these materials were analyzed by Fe-SEM in uniaxially pressed and sintered pellets (1500°C). Electrical properties of these materials were analyzed by impedance spectroscopy as a function of temperature and frequency. Diffraction patterns of milled powders indicate the formation of solid solutions after 20 hours of milling, and also reveal a notorious positive effect of temperature on the crystallinity of these phases. Analysis of electrical properties corroborates the viability of these ceramics to be used in Intermediate temperature SOFC

Keywords: SOFCs, solid electrolyte, mechanical milling.

1. Introduction

Solid oxide fuel cells (SOFCs) are devices that can generate electrical energy in an alternative and clean way, from a reaction between hydrogen and oxygen, generating only pure water as a byproduct. Currently, the use of these technologies has increased due to the decreasing of

availability of fossil fuels, the increasing in their cost and the large amount of greenhouse gases produced by their combustion. In this sense, there are numerous efforts that looks to improve the efficiency and life of the SOFCs. One of the main problems that these cells present involves the thermal and chemical stability of the electrolyte, since the operating temperature is very high (600-1000 °C) [1], causing a decrease in the energy production of the cell, as well as insulating phases that can be harmful for its components [2-4]. Recent research looks to reduce the electrolyte operation temperature by the using of materials with high electrical (ionic) conductivity at lower temperatures (400-600 °C). The cerium oxide is a potential candidate to be applied as a solid electrolyte, since when atoms of its structure are replaced by atoms with different oxidation state, such as the lanthanide elements, the number of oxygen vacancies can increase, giving place to an increasing of the ionic conductivity [5-8]. A method that allows the synthesis of these materials is mechanical milling (mechanochemistry), which generates synthesized materials with a high structural disorder, which is beneficial for these applications. The present research involves the developing of materials based on Er-doped Ceria, of general formula $Er_yCe_{1-y}O_{2-\delta}$ (y = 0.05 - 0.15) for its use as solid electrolyte in SOFC, by the method of synthesis by mechanical milling. The structural and electrical analysis corroborates their viability to be applied as solid electrolytes in SOFC.

2. Materials and Methods

2.1 Method of Synthesis

The synthesis of phases $Ln_yCe_{1-y}O_2$ (Ln = Er, y = 0.05-0.15), was carried out by mechanical milling, using a planetary mill RESTCH model P100, where the starting powders were introduced in stoichiometric relation, using a yttria stabilized zirconia mortar, and balls of the same material as grinding media. The maximum milling time was 20 hours. The starting elements consisted of powders of the oxide elements involved, CeO_2 and Er_2O_3 of high purity 99.99% (Sigma-Aldrich) with particle size <5 µm, the compositions synthesized are presented in Table 1.

Table 1. Compositions of phases $Ln_yCe_{1-y}O_2$, milling time of 20 hours.

Sistem	Composition
Er-0.05	$Er_{0.05}Ce_{0.95}O_{2-\delta}$
Er-0.1	$Er_{0.1}Ce_{0.90}O_{2-\delta}$
Er-0.15	$Er_{0.15}Ce_{0.85}O_{2-\delta}$

2.2 Characterization

Evolution of the mixtures and the thermally treated powders were analyzed by means of an X-ray diffraction equipment Rigaku Model IV, using a wavelength Kα of Cu = 1. 54 A˚, a current of 30 mA

and a voltage of 40 kV, in a scanning range of 10 to 80 ° (2θ). Just milled powders were uniaxially pressed and sintered at different temperatures (800-1500 °C); morphology of these treated samples was analyzed by field emission scanning electron microscopy (FE-SEM).

2.3 Measurement of electrical properties

The measurement of the electrical properties was developed in uniaxially pressed pellets of 1 mm in thickness and approximately 9 mm in diameter (sintered at 1200 °C). Previous to the analysis of electrical properties, the pellets were coated with silver paint on both sides and dryed in a furnace at 400 °C for 6 hours. The analysis was performed in an impedance spectroscopy equipment of the Solatron brand, in a temperature range of 200-650 °C and frequencies form 0.1 Hz to 1 MHz.

3. Results and Discussion

3.1 Synthesis and Characterization

The diffraction pattern corresponding to the starting powders for the Er-0.1 system is presented in Figure 1. In the upper part, the pattern of the cubic erbium oxide is located (PDF 00-077-0777) and the lower part shows the cubic cerium oxide pattern. Additionally, the evolution of the mixtures of the same system with the milling time is showed in Figure 1b). Initially, it could be assumed that the Erbium oxide is incorporated into the CeO_2 phase in a substitutional solid solution as the milling time increases. The formation of such solid solution implies that part of Ce of CeO_2 is replaced by Er atoms and the above does not imply that cerium atoms have to be eliminated, but that initially they are added in a lesser proportion and complemented with erbium oxide for give rise to the stoichiometrically suitable phase.

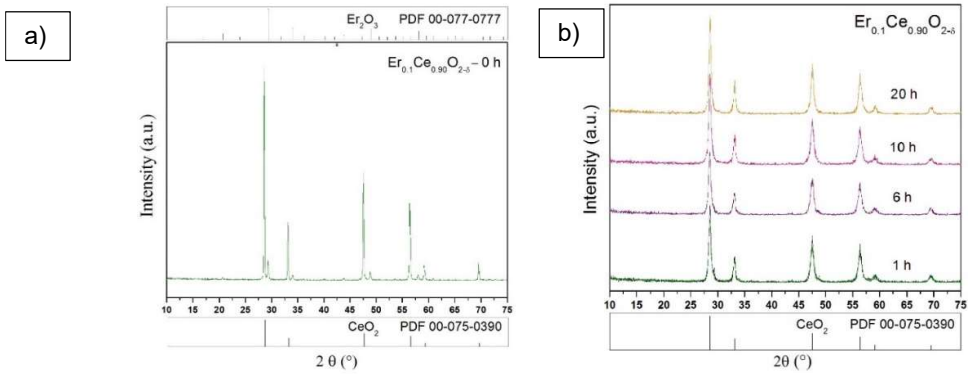

Figure 1. a) Diffraction patterns corresponding to the starting powders of the Er-0.1 system,b) Comparison of the diffraction patterns compared to the milling time of the Er-0.1 system.

3.2 Effect of temperatures of 800-1500 ° C in the structure

The diffraction patterns obtained from samples of the Er-0.1 system previously milled for 20 h and thermally treated at 800 -1500 °C for 6 h are presented in Figure 2. The temperature directly affects the crystallinity of the phases, it is observed that there is a behavior where the intensity of the reflections increases simultaneously with the temperature, this behavior is maintained until reaching 1200 °C, where there is a slight decrease in the intensity of the reflections, which is associated with a reduction reaction, where ceria presents loss of oxygen to give rise to the formation of vacancies [9,10]. The presence of new phases or starting reagents is not observed compared to the diffraction patterns of the starting powders.

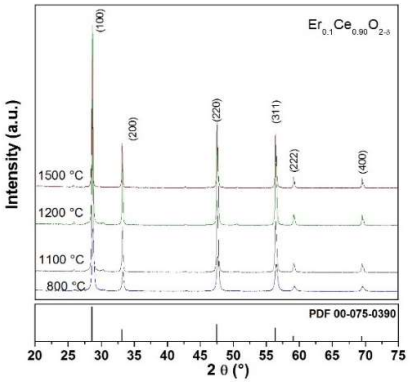

Figure 2. Diffraction patterns of samples milled for 20 hours and thermally treated 800 - 1500 ° C of the Er-0.1 system.

3.3 Effect of sintering temperature on morphology

3.3.1 Sintering at 1500 ° C

Figure 3 shows images of the morphologies obtained by scanning electron microscopy of these Er-0.1 systems. Well-defined borders between the grains, clean and without the apparent presence of impurities (without remains of unreacted oxides) are evident in both systems. Most of the shapes obtained from the grains were of the polygonal type with irregular sizes and with diameters less than 5 microns. It is observed that the grain size apparently does not vary with the increase in dopant concentration taking into consideration that dopant compositions were used in a range of 0.05-0.15, which implies a doping of between 5 and 15 mol% [11].

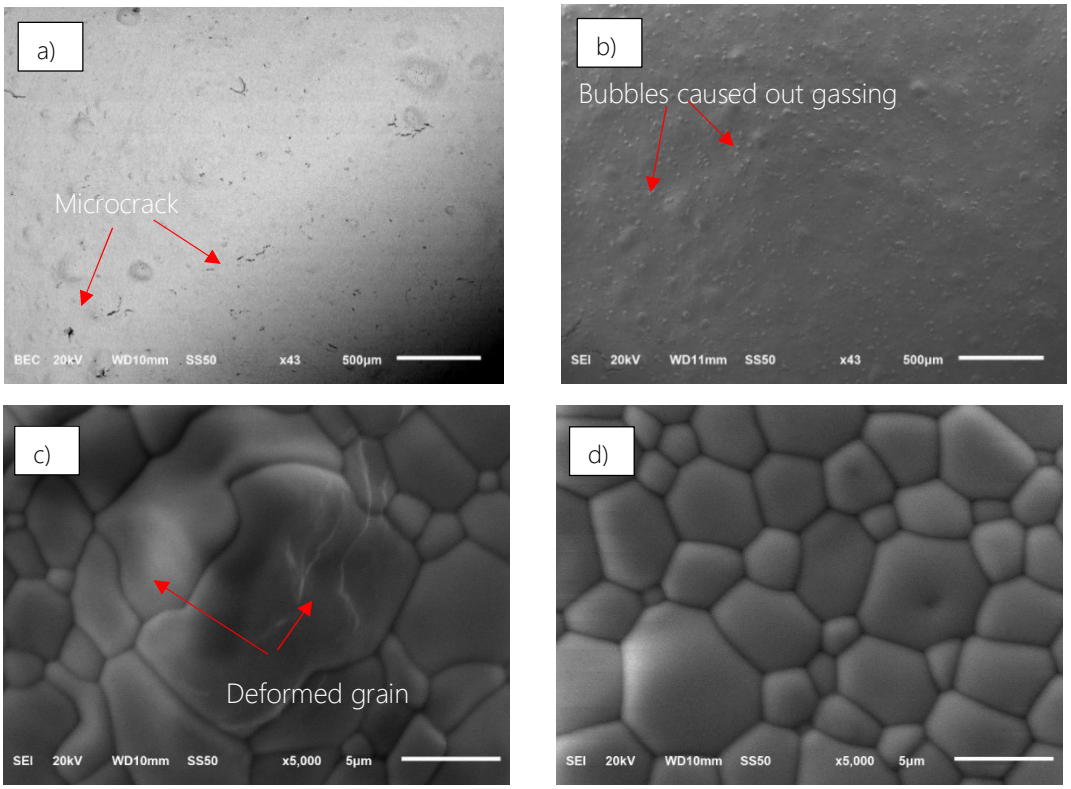

Figure 3. Photomicrographs taken by SEM of the main effects caused during the sintering at 1500 ° C of the Er-0.1 system. A) Microcrack in pellets sintered at 1500 ° C, b) Bubbles on the surface of pellets caused by gases during sintering, c) Photomicrograph of deformed grains taken at 5,000 magnifications and c) Morphology of pellets sintered at 1500 ° C taken at 5,000X.

3.3.2 Sintering at 1200 ° C

In Figures 4 a and b, morphology of samples milled for 20 h and sintered at 1200 °C for 6 h of the Er-0.1 system is presented. The grain size for these systems was less than 2 µm and with semiglobular morphologies. The percentage of densification of the pellets after sintering at 1200 °C, is lower than those obtained at temperatures of 1500 °C. In this case, many hollow spaces between each grain are observed, effect that is attributed to the fact that after 1200 °C, a reduction reaction begins where the ceria passes from CeO2 to Ce2O3, also this accompanied by the formation of oxygen vacancies for each pair of Ce^{+4}. The reduction of the sintering temperature allowed obtaining pellets in all the cases of study, without the presence of micro cracks and superficial bubbles, as in the case of those obtained at 1500 °C. The increasing in dopant content did not influence the sinterability, since as the

percentage of dopant was increased, this did not directly affect the morphology, so a similar morphology was obtained in all the study cases.

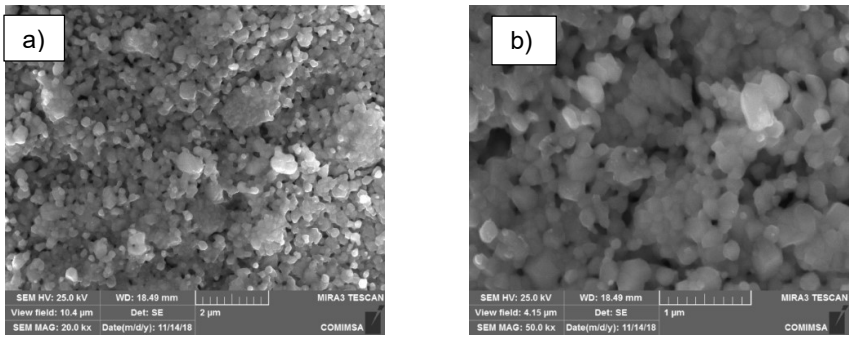

Figure 4. Morphology of samples milled for 20 h and treated at 1200 ° C for 6 h of the Er-0.1 system, a) Photomicrography taken with Field Emission Scanning Electronic Microscope (FE-SEM) at 2000 a, b) Photomicrography taken with Field Emission Scanning Electronic Microscope (FE-SEM) at 5000 magnifications.

3.4. Effect of dopant content on the structure and present phases of the $Er_{0.1}Ce_{0.90}O2_{-\delta}$ system

Figure 6 shows a comparison of the diffraction patterns, obtained from samples milled for 20 hours and treated at 1200 °C of ceria doped with Er (5-10 mol%). It can be seen that the behavior of the reflections present a tendency of displacement towards higher angles (2 theta), which is closely related to the increase of the volume of the cell (Figure 5 a). of lattice parameter for ceria systems doped with Er, presents a small decrease of 0.5397- 0.5394 nm [11].

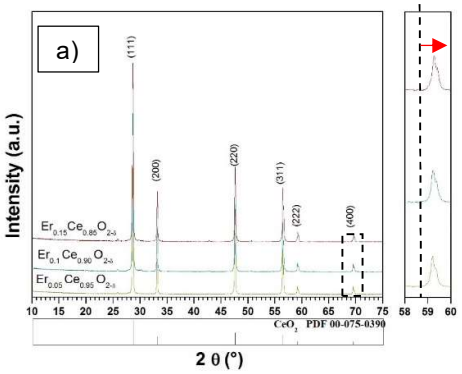

b)

Sistem	X_c (°)	$d_{(hkl)}$ (nm)	a (nm)
Er-0.05	28.6439	0.3116	0.5397
Er-0.1	28.6562	0.3115	0.5395
Er-0.15	28.6633	0.3114	0.5394

Figure 5. a) Comparison of the diffraction patterns of samples milled by 20 h and treated at 1200 ° of the $Ln_yCe_{1-y}O_2$ doped with Er, b) values obtained from the interplanar distance (d (hkl)) and lattice parameter (a) of the systems Er-0.05, Er-0.1 and Er-0.15.

3.5. Electric conductivity

Figure 6 a) shows the dependence of the real part of the conductivity as a function of the frequency (range of 0.1 Hz to 1 MHz) on a double logarithmic scale and of the temperature (measuring range of 200 - 700 ° C) of the system $Er_{0.1}Ce_{0.90}O_{1.95}$. It can be seen that in all cases of doped ceria, there is a dependence of the conductivity potential with the frequency at high frequencies and low temperatures, that is, at lower temperatures it can be seen that the conductivity values increase with frequency. This behavior is similar to that observed by A.K. Jonscher [13] in various materials with good electrical properties and that describes them as "Universal Dynamic Response" and that is represented by the following equation:

$$\sigma^*(\omega) = \sigma_{dc}[(1 + (j\omega/\omega_p)^n] \quad \text{ó} \quad \sigma^*(\omega) = \sigma' + \sigma'' \qquad 0 \le n \le 1 \tag{1}$$

Where the exponent n is related to the degree of interaction or correlation in the movement of the charge carriers and n is described as the crossover frequency and the opposite to this indicates the characteristic time of the conduction process ($\tau_p = 1/\omega_p$).For frequencies less than ω_p times greater than τ_p the ions are in a long-range motion regime, however when the frequencies are greater than ・p the ions are said to be jumping to neighboring positions, what he calls "local movements", which is reflected in the increase in conductivity mentioned. The previously mentioned describes the interaction that exists between mobile ions, which represents a remote response to what is described by the ideal Debye model of isolated dipoles. In these cases *dc* or bulk conductivity values in each temperature is represented as a plateau, where the conductivity value is independent of the frequency, in contrary way this effect does not happen in temperatures lower than 0 °C, due to that dc conductivity increases substantially as the frequency increases, leading to the region of potential dependence occurring at lower frequencies at lower temperatures. It can also be seen in the figures mentioned that increasing the temperature increases the dc (bulk) conductivity value and both the potential dependence region and the crossover frequency move at higher frequencies. For the measurement of the electrical conductivity previously it is necessary to obtain the value of the geometric factor that is given by the thickness and diameter of the sintered pellets. The geometric factor values obtained as well as the area of each chip are presented in Table 2. The conductivity versus frequency graphs for most of the samples are very similar to each other (systems $Er_{0.05}Ce_{0.95}O_{2-\delta}$ and $Er_{0.15}Ce_{0.85}O_{1.95}$, characterized by an increase in conductivity with the increase in temperature, which is explained if it is considered that sufficient energy is being added to favor the diffusion of ions through the network. greater diffusion and therefore greater conductivity The linear adjustment of the experimentally obtained data by means of thermal activation is observed in Figure 6b, what is obtained is usually a line whose slope is proportional to the activation energy associated with the process of long-range ionic conduction Edc. The dc conductivity values used were obtained

directly from the conductivity graphs (Table 3). It can be seen that the experimental values present a good fit using the Arrhenius equation, confirming that the conductivity was a thermally activated process. The dependence of dc conductivity varies with temperature and it is represented by the Arrhenius equation:

$$\sigma_{dc} = \sigma_0 e^{(-E_{dc}/K_B T)} \quad (2)$$

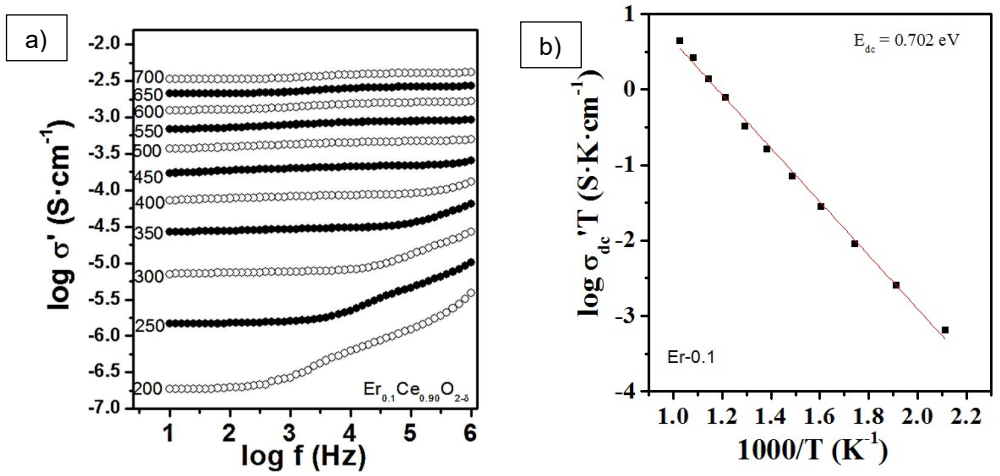

Figure 6. a) Real part of the conductivity as a function of the frequency at different system temperatures Er-0.1, b) logarithm of the dc conductivity versus 1000 / T in an Arrhenius type representation for the Er-0.1 system.

Table 2. Shows the dc conductivity values and the Edc activation energy for all doped ceria systems. The values obtained for dc conductivity were measured at 650 ° in accordance with the data of the previous table, It can be noted that the conductivity values dc are directly proportional to the activation energy Edc, that is, an increase in both values is observed. The values obtained in the system $Dy_{0.15}Ce_{0.85}O_{2-\delta}$ do not reveal a trend. Activation energy increases in all study cases as the percentage of the dopant increases (0.005-0.15%), because the ion needs more energy to move from one site to another. The obtained conductivities are similar to the works before reported, in addition to presenting a good performance at lower temperatures [14-17].

Table 2. Geometric factor and area of the pellets sintered at 1200 ° C for 6 h and used in the analysis of electrical properties.

Sistem	Area (cm^2) $(A = \pi r^2)$	Geometric factor $fg = \frac{thinkness\ pellets}{Area}$
$Er_{0.05}Ce_{0.95}O_{1.975}$,	0.187	0.187
$Er_{0.1}Ce_{0.90}O_{1.95}$	0.174	0.174
$Er_{0.15}Ce_{0.85}O_{1.925}$	0.187	0.187

Figure 7 shows the dc conductivity values obtained at 650 °C, with respect to the percentage of dopant (0.05-0.15 mol%) for each of the doped systems with Erbium, a slight increase in conductivity occurs when the percentage of lanthanide increases from 0.1-0.15%. The major conductivities are obtained in compositions $Er_{0.15}Ce_{0.85}O_{1.95}$ (1* $10^{-2.17}$ Scm^{-1}), in the same graph the activation energy values Edc are presented in addition to the percentage of the dopant. It can be seen that the activation energy increases directly proportional to the increase in the composition, which is associated with the charge carrier ions require a greater activation energy to get out of position and contribute to the long-range ionic conductivity, resulting in that, at higher concentrations, the movement of charged ions of charge becomes more difficult, as well as an accumulation of ions that causes an increase in the activation energy.

Table 3. dc conductivity values and Edc activation energy of ceria systems doped with Er.

Sistem	Conductivity *dc* Log (Scm^{-1})	Activation Energy E_{dc} (eV)
$Er_{0.05}Ce_{0.95}O_{1.975}$	-2.88	0.635
$Er_{0.1}Ce_{0.90}O_{1.95}$	-2.55	0.702
$Er_{0.15}Ce_{0.85}O_{1.925}$	-2.17	0.773

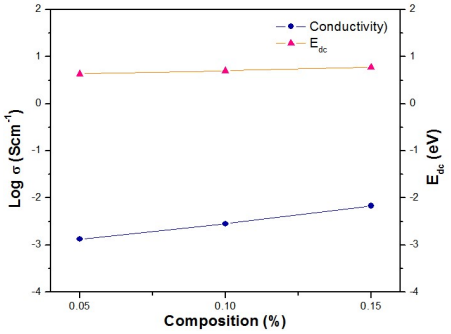

Figure 7. Comparison of the percentage of dopant in the systems Er-0.05, Er-0.1 and Er-0.15 vs the values of conductivity and activation energies.

4. Conclusion

The synthesis by mechanical milling caused a structural disorder in the materials obtained, and also allows the doping of ceria with erbium with a molar percentage of 0.05-.0.15%. The effect of temperature on the doped phases, favored the structural rearrangement of the phases milled for 20 hours and allows to adequately corroborate the formation of solid solutions. The sintering at 1500 ° C of samples of ceria doped with Er, promotes a high densification of the phases, however, a reduction reaction is promoted, causing the appearance of microcracks and gas liberation, giving place to microbubbles. The increasing in the percentage of the dopant in the ceria has no significant effect on the sinterability of the pellets. The sintering temperature of 1200 °C of the doped ceria systems, generates better surface conditions in the pellets (without microcracks, or bubbles). Dc conductivity increases with the doping percentage increasing. The system Er-0.15 shows the highest value of ionic conductivity in this study (1*10 $^{-2.17}$ Scm^{-1}). The activation energy increases when increasing the percentage of dopant associated with the mobility and accumulation of the charge carrying ions.

Acknowledgements

This work was financially supported by CONACYT CB- 166 995, and CV-860984.

References

[1] A. Boudghene Stambouli, E. Traversa, Solid oxide fuel cells (SOFCs): a review of an environmentally clean and efficient source of energy, Renewable and Sustainable Energy Reviews 6, (2002) 433–455.
[2] J.A. Labrincha, J.R. Frade, F.M. Marques, $La_2Zr_2O_7$ formed at ceramic electrode / YSZ contacts, Journal of Materials Science 28, (1993) 3809-3815.
[3] A. Mitterdorfer, L.J. Gauckler, $La_2Zr_2O_7$ formation between yttria stabilized zirconia and $La_{0.85}Sr_{0.15}MnO_3$ at 1773 °K, Journal of Solid State Chemistry of Inorganic Materials 453, (1997) 425-430.
[4] Y. Takeda, Y. Sakaki, H. Young, B. Phillipps, N. Imanishi, O. Yamamoto, Perovskite oxides for the cathode in solid oxide fuel cells, Electrochemistry 68, (2000) 764-70.
[5] Zili Wu, Steven H. Overbury, Catalysis by materials with well-defined structures, Elsevier (2015), 31-52.
[6] X. Guo and R. Waser, Electrical properties of the grain boundaries of oxygen ion conductors: acceptor-doped zirconia and ceria, Prog. Mater. Sci. 51 (2006), 151–210.
[7] K.C. Anjaneyaa, Mahander Pratap Singhb, Synthesis and properties of gadolinium doped ceria electrolyte for IT-SOFCs by EDTA-citrate complexing method" Journal of Alloys and Compounds 695, 25 (2017), 871–876.

[8] S.A. Muhammed Alia, Mustafa Anwara, Abdalla M. Abdallac, Mahendra Rao Somalua, Andanastuti Muchtar $Ce_{0.80}Sm_{0.10}Ba_{0.05}Er_{0.05}O_{2-\delta}$ multi-doped ceria electrolyte for intermediate temperature solid oxide fuel cells, Ceramics International, 43,1B, (2017), 1265–1271.
[9] Y.C. Zhou, Hydrothermal synthesis and sintering of ultrafine Ce_2O powders, Institute of Metals Research, 72.
[10] Chunwen Sun, Hong Liab, Liquan Chenab,Nanostructures ceria-based materials: synthesis, properties, and applications, (2012).
[11] D. Terribile, A. Trovarelli, J. Llorca, C. de Leitenburg and G. Dolcetti, The synthesis and characterization of mesoporous high-surface area ceria prepared using a hybrid organic/inorganic route J. Catal. 178, (1998) 299–308.
[12] Sameer Deshpande, Swanand Patil, Satyanarayana, Size dependency variation in lattice parameter and valency states in nanocrystalline cerium oxide.
[13] A. K. Jonscher, Dielectric relaxation in solids, Chelsea Dielectric London, (1983).
[14] Lingyao Li, Bin Zhu, Jin Zhang, Electrical properties of nanocube CeO_2 in advance solid oxide fuel cells, (2018).
[15] Thamyscira H. Santos, P. F. Grilo, Structure and densification and electrical properties of Gd^{3+} and Cu^{2+} co-doped ceria solid electrolytes for SOFC applications: Effects of Gd_2O_3 content, (2017).
[16] M. M. V. Chong, P. S. Lee, Physical and electrical properties of bilayer CeO_2/TiO_2 gate dielectric stack, Materials Science and Engineering B 210, (2016) 57-63.
[17] Ranran Peng, Changrong Xia, Qingxi Fu, Sintering and electrical properties of $(CeO_2)_{0.8}(Sm_2O_3)_{0.1}$ powders prepared by glycine-nitrate process, Materials letters 56 (2002) 1043-1047.

E004. IMPEDANCE MEASUREMENT ON A PEM FUEL CELL RUNNING ON A LOAD USING ALTERNATIVELY O_2 AND AIR AT THE CATHODE

C. M. Bautista-Rodríguez [1, 2,*] and P. Ozil † [1].

[1] Laboratoire d'Electrochimie et de Physico-chimie des Matériaux et des Interfaces (LEPMI). UMR 5631 CNRS-INPG-UJF, ENSEEG, BP 75, 38402 Saint Martin d'Hères, France.

[2] Actual address: Centro de Innovación Aplicada a Tecnologías Competitivas A.C. (CIATEC). Omega 201, Industrial Delta. CP. 37545, León Guanajuato, México.

* Corresponding author: cbautista@ciatec.mx ; (477) 710 0011 ext. 13003

ABSTRACT

In this work, an experimental study of the impedance response of H_2/O_2 and H_2/Air PEMFC was carried out with a single cell. A new method is proposed allowing a separate measurement for the anode and cathode impedances of a fuel cell running on a constant load. The results are analysed taking into account a different point at long of the performance curve for the PEMFC. The effect due to the reaction kinetics, mass transport limitations and ohmic losses are shown by the impedance spectres measurements at different potential values. The main conclusion is that, the impedance response for the anode cannot be neglected in comparison of the cathode impedance spectre measured when pure oxygen feeds the cathode compartment. In other way, if oxygen source is air, the impedance diagrams show that oxygen diffusion phenomena present in the cathode becomes a limiting step.

Keywords: PEMFC, Electrochemical Impedance Spectroscopy, Nafion membrane, MEA.

1. Introduction

Actuality, the Proton Exchange Membrane Fuel Cell (PEMFC) is an highly attractive energy conversion devices technology, particularly to be used as a power source for stationary and mobile application. However, some limitation steps are present in the PEMFC, and many electrochemical studies show a high cathode overpotential in to the oxygen reduction reaction and a strongly ohmic drop contributes to the high total efficiency losses.

The Electrochemical Impedance Spectroscopy (EIS), has been demonstrated to be a powerful experimental technique to examine the complexity of the different processes occurring in a PEMFC [1]. In early papers, ac impedance measurements were used mainly to determine the internal resistance of such systems, which is partly due to membrane resistance. They showed that membrane resistance is a function of the water content in to the membrane and the temperature imposed on the fuel cell [2].

More recently, EIS was used to study intraelectrode processes occurring in thin porous coating electrode or gas diffusion electrode in half cell [2-6] and later, some different suitable modelistic treatments were developed. Lastly, impedance techniques were used to investigate the response in a complete single cell [7-11]. Based on the thin film/flooded agglomerate model, a successful explanation was proposed by Paginin and co. [7] for impedance diagrams obtained in a PEMFC running. The main conclusions were about the important roles of water transport within the membrane and oxygen diffusion within the gas diffusion layer of the electrode, particularly when using air rather than pure oxygen. Freire and co. [8] studied the impedance response of a H_2/O_2 PEMFC under different working conditions and with several Nafion membrane thicknesses. Their results clearly highlighted that thinner membranes (<100 microns) offer better characteristics for water management, because of a much lower sensitivity to temperature and current density changes. The electrode structure and composition were optimised by Song and co. [9], using information from the cell current-potential and ac impedance measurements. Wagner and co. [10] simulated experimental impedance diagrams by using an equivalent circuit and taking into account electrode impedances and electrolyte resistance. Andreaus and co. [11] investigated the performance loss in a PEMFC operating at high current densities. They explain their experimental results from a shortage of water within the membrane, leading thus to a decrement in the membrane conductivity and a increment in the activation potential for hydrogen oxidation reaction. Such effects are due to a decrement in the number of active sites on the anode surface electrode.

In PEMFC, the hydrogen oxidation reaction is usually assumed to be a very fast reaction. Later, the impedance response is considered as negligible compared to cathode impedance diagram. Hence, the total impedance of the fuel cell, which is the sum of the cathode and anode impedances, is therefore supposed approximately equal to cathode impedance. Here the anode and cathode impedance responses were investigated owing to a new experimental method for the

impedance measurements makes on batteries and fuel cells [12-16] connected to a constant load. A platinum wire acts as "reference" electrode or more exactly comparison electrode, allowing thus recording both anodic and cathode impedances. This method has been previously tested and validated [15] for measuring the separated electrode impedances of a DMFC generator. The impedance of the single cell is measured with hydrogen pure at the anode compartment and oxygen pure or air at the cathode compartment. The aim of the present work is to propose a modelistic interpretation of the experimental impedance diagrams obtained in a PEMFC based on a previous published model devoted to a small PEMFC [17].

2. Materials and Methods

This study uses a pieces (10 cm^2) of Nafion® Membrane 117 (NM117) treated as following. NM117 was firstly boiled at 80°C in 3% Vol. H_2O_2 solution (Aldrich®) by hour, then in deionised water at same temperature and time, later in HNO_3 1 N solution (Aldrich®) by 2 hours. Finally, the sample was boiled three times in deionised water, until a volume swelling was reached corresponding to a 30% increase of the NM117 geometric area (thickness membrane was 180 μm under wetted conditions). About 5 cm^2 of active surface for the gas diffusion electrodes were assembled to the Nafion® membrane between holed gaskets by hot pressing at 135°C for 90 seconds. The platinum loads of Sorapec® electrodes were respectively 0.2 mg/cm^2 for anode and 0.32 mg/cm^2 for cathode. The MEA was finally set within a simple fuel cell stack (Figure 1). Hydrogen and oxygen gases were 99% pure (Air Liquid), for the H_2/O_2 fuel cells. Reconstituted air was used for the H_2/Air fuel cell.

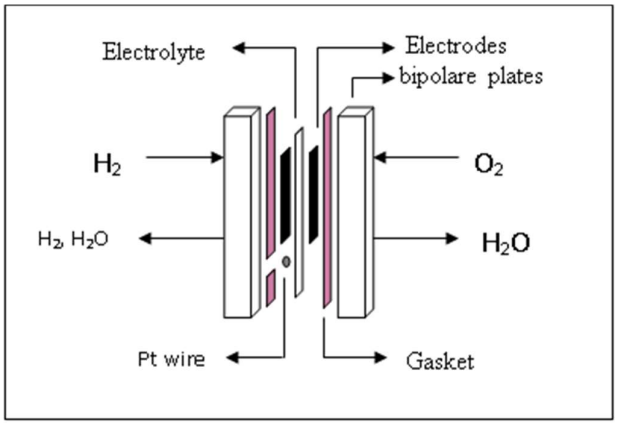

Figure 1. scheme of the PEMFC

Pure hydrogen was saturated with water contained in flasks and kept under controlled temperature, before entering the cell while neither oxygen nor air are humidified. Gases were supplied to the cell at different pressures with flowrates measured with a mass flow controller. The operating conditions are reported in table 1.

Table 1: Experimental conditions.

Experimental conditions	Anode part	Cathode part
Pressure (bar)	1	2
Flow (L h^{-1})	1.5	6.25
Hydration temperature (°C)	60	Without
Cell temperature (°C)	60	

Impedance measurements were carried out using a Solartron 1250 frequency response analyser coupled to a Solartron 1286 electrochemical interface. The ac signal amplitude was about 10 mA and frequency ranged from 10 mHz to 10 KHz covered by 8 or 10 points per decade.

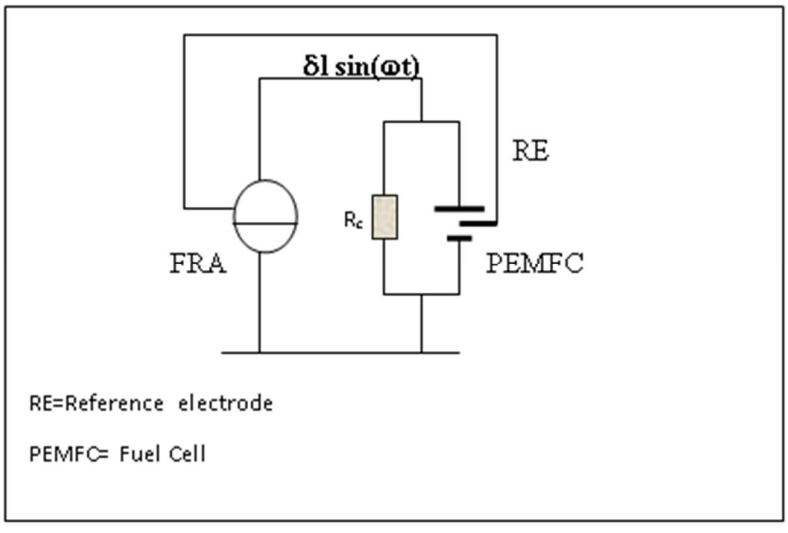

Figure 2. Connections used for the EIS study of the PEMFC running on a constant load.

Figure 2 shows the connection between the fuel cell and the EIS used in this study. The method used to measure EIS for a single cell of PEMFC running on a load was based on the technique developed by J-P. Diard and co. [12-16]. A platinum wire was located on the membrane in the anodic compartment surrounded by hydrogen to play the role of a "reference" electrode (déja détaillée plus haut). It enabled us to measure the anode and cathode impedances. The cell, anode and cathode impedances are then calculated from the theoretical method described by J.P. Diard [15].

3. Results and Discussion

Impedance diagrams were recorded along the steady state voltage (U) versus current density (i) for the PEMFC fed with pure oxygen or reconstituted air gas at cathode and with hydrogen at anode. Note that the PEMFC single cell is running on several resistors ranging from 1 Ω to 0.2 Ω. In order to separately determine anodic and cathodic impedances, a procedure as described by J.P. Diard [15] was applied to our PEMFC.

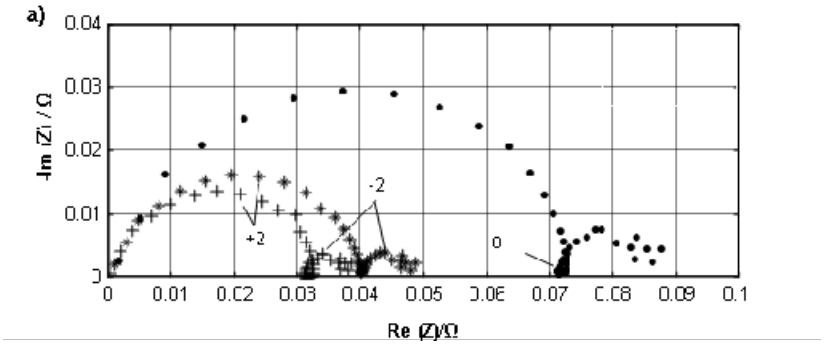

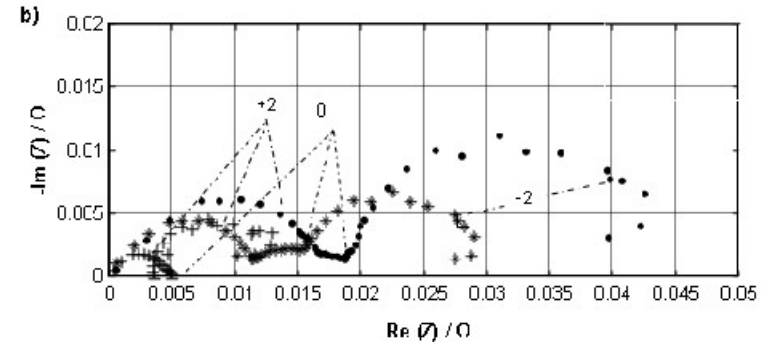

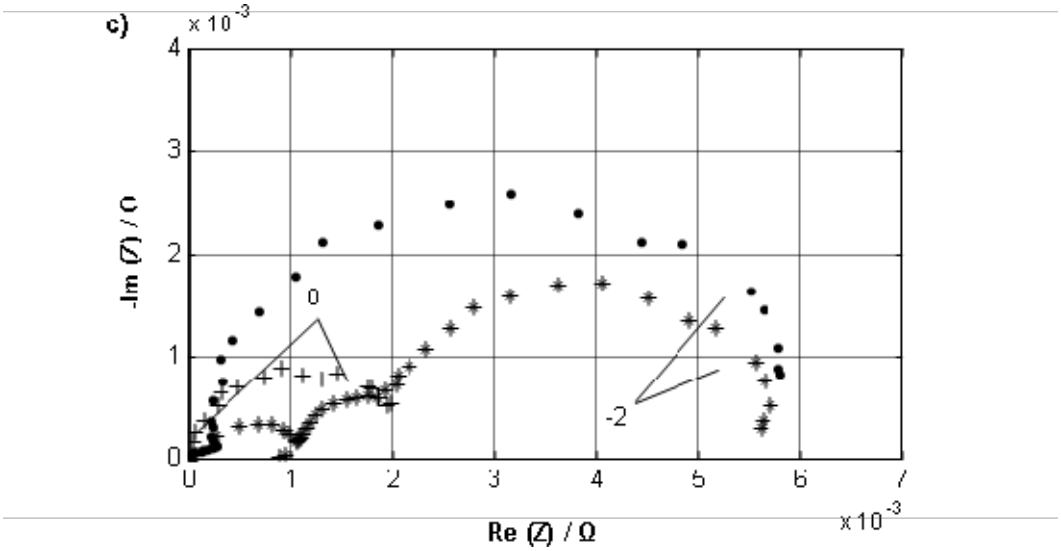

Figure 3: Impedance diagrams (Nyquist representation) measured for a single H_2/O_2 PEM fuel cell (●), cathode (∗) and anode (+) under galvanostatic conditions: (a): low current density (0.17 A cm^{-2}, U=0.75V) and b: moderate current density (0.43 A cm^{-2}, U=0.5 V). (plots corrected from the high frequency resistance).

The impedance diagrams in the Nyquist representation involve two or three capacitive arcs in the 10kHz – 10mHz range in figure 3. Impedance spectra of the single cell show a high frequency arc with a magnitude depending on potential. A second arc is also observed at low frequency. It is worth mentioning that this arc presents a smaller potential dependence. Nevertheless, an arc begins to appear in the middle frequency region for moderate and high current densities. The impedance diagrams for the cell present a shape in a good agreement with those plotted by Paganin and co. [7] and Freire and co. [8].

At low current density (figure 3.a), the anode and cathode impedance diagrams in he Nyquist representation are made up of two capacitive arcs respectively in the 10kHz-1Hz and 1Hz-10mHz frequency ranges, while a third capacitive arc appears at cathode for moderate current density. As expected, the sum of anode and cathode impedances is approximately equal to the fuel cell impedance at low and moderate current densities. Note that parasitic effects due to the location of the Pt wire at anode occur at high current density (i.e. >0.5 A cm^{-2}). Consequently the corresponding

impedance diagrams at high current densities are not reported. It is worth mentioning that the anode impedance modulus is quite similar to the cathode one at low current density (figure 3.a). On contrary, it becomes two times lower for moderate current density (figure 3.b). The total PEMFC impedance has roughly the same shape as cathode impedance but anode impedance is never negligible compared to cathode one. If assuming a Tafel kinetic, the rate of charge transfer resistance is given by b/2.3 i where b is the Tafel slope and i the current density. For a H_2/O_2 PEMFC, the anodic contribution to impedance response can become significant and the impedance response of the single cell cannot be thus assimilated to the one cathode impedance as classically assumed. In that case mass transport limitation at cathode remains rather small.

On the basis of previously available information [17], the impedance diagrams may be interpreted as follows. The capacitive arc in the 10kHz-1Hz frequency range, observed for both the electrodes and the fuel cell, depends on potential and is connected to the double layer capacitance of the electrode combined with the charge transfer resistance. At low current density, the rate-limiting step of the fuel cell is kinetics of both oxygen reduction and hydrogen oxidation. According to the modelistic interpretation of gas diffusion electrode [2-6,18], oxygen diffusion within the electrode may appear as a capacitive arc in the impedance spectra when increasing current density. The cathode impedance and thus the fuel cell one exhibit such behaviour at moderate current density. A third arc can be distinguished at intermediate frequency around 10 Hz (figure 3b). Nevertheless, charge transfer and diffusion processes appear as a combined capacitive arc owing to the large value of the double layer capacitance [19]. As previously discussed [8], the high value of the double layer capacity in supported catalysts partly masks the effect of oxygen or hydrogen diffusion within the electrode on the impedance response. Impedance diagrams also exhibit a small region of linear potential independent, in the high frequency limit that is superimposed to the lower frequency arc (≈100 Hz). Such behaviour bas been already analysed and could be attributed to the double layer charge and ionic transport that predominate in the overall electrode response at high frequencies for low ionic conductivity [4,5]. Finally the lowest frequency arc, previously reported by [7,8] is generally attributed to water transport in the membrane. In the case of PEMFC with Nafion® 115, these low frequency arcs are not observed [20], probably because a thinner membrane presents better back diffusion of water to the anode side [8].

Impedance diagrams for a steady state working point (0.43 A cm^{-2}, U=0.5 V) were recorded versus time (figure 4) to investigate mass transport limitation at cathode. On the diagrams, the third capacitive arc in the 100Hz-1Hz frequency range is appearing with time. Such effect could be related to the water accumulates in the cathodic compartment which is produced by the oxygen reduction reaction and transported from anode to cathode by the electroosmotic flow.

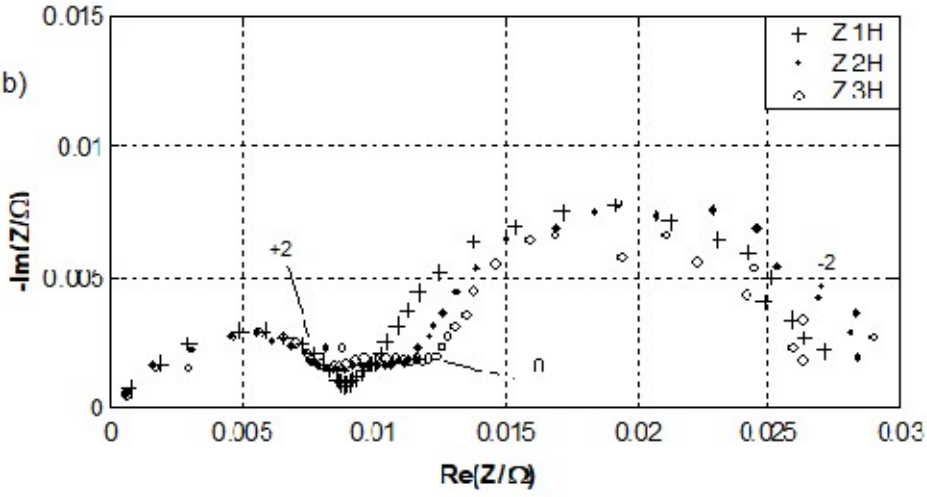

Figure 4: Impedance diagrams (Nyquist representation) measured for a single H_2/O_2 PEM fuel cell, under galvanostatic conditions at moderate current density (0.43 A cm^{-2}, U=0.5 V) versus the time: (+): 1 hour; (●): 2 hours; (O): 3 hours.

To analyse the membrane behaviour, Figure 5 respectively shows the high frequency resistance for the whole PEMFC and for each electrode versus the reference electrode as a function of the current density. As expected, the internal resistance of the PEMFC is the sum of anode and cathode internal resistances. A decrease of internal resistance is observed when current density increases. This experimental result has to be connected to water management. At higher current densities, an increase of water production at cathode occurs and consequently the water gradient is also increased. All these effects contribute to keep the membrane well hydrated by decreasing the membrane resistance. This effect is more important when oxygen is less humidified.

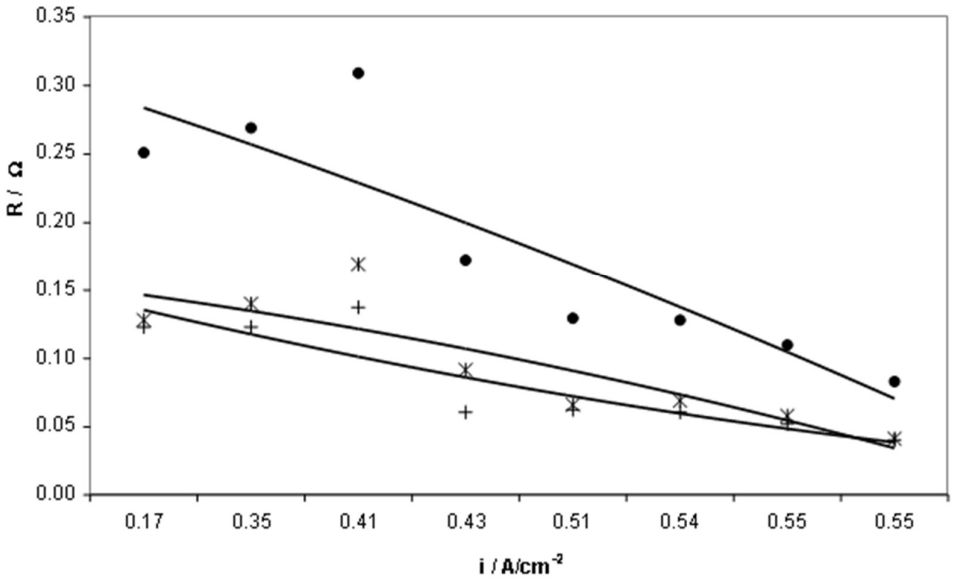

Figure 5: Dependence of the high frequency resistance with current density: whole H_2/O_2 PEMFC: (•); the cathode versus the reference electrode (*) and the anode versus the reference electrode (+).

Impedance diagrams of the single cell, anode and cathode were also recorded when air is used at cathode. Figure 6 shows the corresponding impedance diagrams for low and moderate current densities. As for the H_2/O_2 PEMFC, impedance diagrams are made up of two capacitive arcs: a first capacitive arc in the 2 KHz-1 Hz frequency zone and a second one in the 1 Hz-10 mHz zone. Contrarly to the first case, the impedance modulus becomes larger at cathode diagram than at anode at high current density, while both diagrams remains similar at low current density. In this second case, the shape of the fuel cell impedance is then similar to the cathode impedance at moderate and high current densities. These observations are in good agreement with literature [21,22], which considers that oxygen reduction reaction is the rate determining step mainly when air is used at cathode.

The shape of the impedance diagrams for the cathode in the 2kHz-1Hz range at moderate current density (figure 6), is quite similar in appearance to those obtained by Bultel and co. [19]. According to this work, the flattened capacitive arc in the 2KHz-1Hz frequency zone could be connected to the oxygen charge transfer coupled to the double layer capacitance and mass transport within both the active layer and gas diffusion layer at cathode.

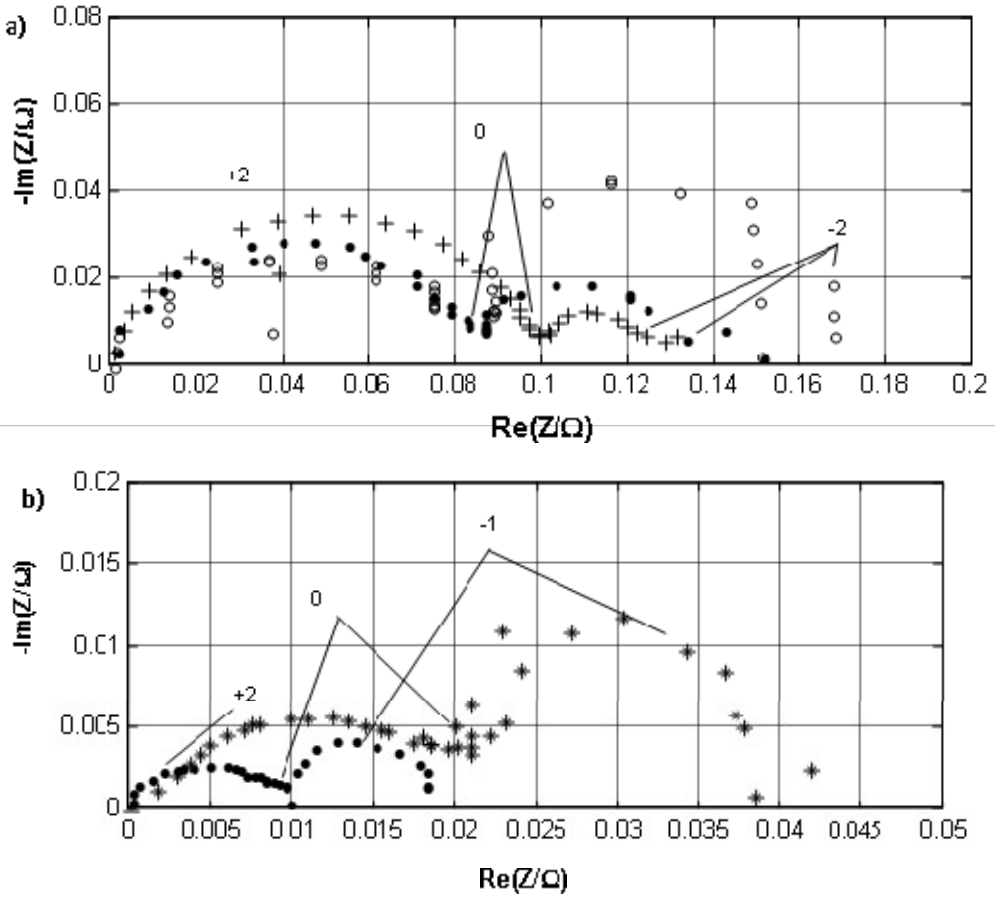

Figure 6: Impedance diagrams (Nyquist representation) measured for a whole, cathode and anode in a H_2/Air PEM fuel cell, under galvanostatic conditions: (a): low current density (0.08 A cm^{-2}, U=0.8V) and moderate current density (0.194 A cm^{-2}, U=0.4V). (plots corrected from the high frequency resistance).

4. Conclusion

Impedance measurement of a PEMFC was carried out using a modulated current method. Anode and cathode impedances were successfully recorded thanks to a platinum wire located on the membrane in the anode side surrounded by hydrogen. The comparison of the results validates the method, showing that it is a powerful tool for fuel cell electrochemical impedance spectroscopy characterisation under natural running conditions.

Based on previous published results, cell impedance can be split into electrode impedance and internal resistance. It has been shown that the capacitive arc for both anode and cathode can be separated into different parts corresponding to different reaction steps. A second capacitive arc at low frequency is also observed due to water transport through the membrane. Nevertheless, this mechanism is still unclear and has to be investigated. It has been determined that the performances of the PEMFC are mainly limited by oxygen reduction process when air is used at cathode, except at low current density. Oxygen diffusion may also be observed especially in the impedance response. Nevertheless, anode impedance response can not be neglected when pure oxygen is used. Thus the present study reveals the essential importance to measure the impedances of both anode and cathode for establishing an accurate diagnosis of PEMFC characterisation.

Acknowledgments

The authors would like to thank Pr. J.P. Diard and Pr. B. Le Gorrec for fruitful discussions.

References

[1] J.R Selman and Y.P. Lin, Electrochim. Acta 38 (1993) 2063.

[2] R.S. Chen. P.E. Stallworth, S.G. Greenbaum, J.J. Fontanella, and M.C. Wintersgill., Electrochimica Acta 40 (1995) 309

[3] A.V. Anantaraman, C.L. Garder., J. Of Electroanalytical Chemistry 414 (1996) 115

[4] M. Cappadonia, J. Wilhelm Erning, Seyedeh M. Saberi Niaki, Ulrich Stimming., Solid State Ionics 77 (1995) 65

[2] T.E. Springer, I. D. Raistrick, J. Electrochem. Soc. 136 (1989) 1594.

[3] T.E. Springer, T.A. Zawodzinski, M.S. Wilson, S. Gottesfeld, J. Electrochem. Soc. 143 (1996) 587.
[4] I. D. Raistrick, Electrochim. Acta 35 (1990) 1579.

[5] M. Eikerling, A.A. Kornyshev, J. Electroanal. Chem. 475 (1999) 107.
[6] O. Antoine, Y. Bultel, R. Durand, J. Electroanal. Chem. 499 (2001) 85.

[7] V.A. Paganin, C.L.F. Oliveira, E.A. Ticianelli, T.E. Springer, R.E. Gonzales, Electrochim. Acta 43 (1998) 3761.

[8] T. J. P. Freire, E. R. Gonzalez. J. Electroanal. Chem. 503 (2001) 57.

[9] J.M. Song, S.Y. Cha, W.M. Lee, J. Power Sources 94 (2001) 78.

[10] N. Wagner, J. Applied Electrochem. 32 (2002) 859.

[11] B. Andreaus, A.J. McEvoy, G.G. Scherer, Electrochim. Acta, 47 (2002) 2223.

[12] J.-P. Diard, B. Le Gorrec, P. Landaud, C. Montella, Electrochim. Acta 42 (1997) 3417.

[14] J.P. Diard, B. Le Gorrec, C. Montella, C. Poinsignon, G. Vitter, J. Power Sources 74 (1998) 244.

[15] J-P. Diard, N. Glandut, P. Landaud, B. Le Gorrec and C. Montella, Electrochim. Acta 48 (2002) 555.

[16] J-P. Diard, N. Glandut, B. Le Gorrec and C. Montella, J. Electrochem. Soc. 151 (12) (2004) A2193.

[17] M. Bautista, Y Bultel, P. Ozil, Chemical Engineering Research and Design, Part A 82 (A7) (2004) 907

[18] Y. Bultel, L. Genies, O. Antoine, P. Oil, R. Durand, J. Electroanal. Chem. 527 (2002) 143.

[19] Y. Bultel, K. Wiezell, F. Jaouen, P. Ozil and G. Lindbergh, Electrochim. Acta 51 (2005) 474.

[20] M. Bautista, Thesis, 2004, Grenoble

[21] E. Passalacqua, G. Squadrito, F. Lufrano, A. Patti, L. Giorgi, J. Applied Electrochem., 31 (2001) 449.

[22] J. Ihonen, M. Mikkola, G. Lindbergh, *J. Electrochem. Soc.*, 151(8) (2004) A1152.

E006. EFFECT OF LANTHANIDE DOPING ON THE ELECTRICAL PROPERTIES OF YPSZ SOLID ELECTROLYTES ON VIEWS TO THEIR USE IN SOFC

K.A. González-García[a*]; J.A. Díaz Guillén[a]; S.M. Montemayor[b]; J.C. Díaz-Guillén[c]; A.F. Fuentes[d]

[a] *Tecnológico Nacional de México, Instituto Tecnológico de Saltillo, 25280-Saltillo, Coahuila, México*

[b] *CIQA, Blvd. Enrique Reyna Hermosillo 140, 25294-Saltillo, Coahuila, México*

[c] *COMIMSA-Conacyt, Calle Ciencia y Tecnología 790, 25290 Saltillo, Coahuila, México*

[d] *CINVESTAV Unidad Saltillo, Av. Industria Metalúrgica 1062, Parque Industrial 25900-Ramos Arizpe, Coahuila, México*

* González García Karime Anaí: (044) - 4424 664472, kagonzalez86@gmail.com

ABSTRACT

In this research, samples of YPSZ were doped with different lanthanides and their electrical properties analyzed on views to be used as solid electrolytes in Solid Oxide Fuel Cells (SOFC). These solid solutions of general formula $Zr_{x-1}Y_{0.04}$ $Ln_xO_{2-\delta}$ (Ln = Sm, Nd and Gd, x = 0.05 - 0.2) were synthesized by mechanical milling, starting from high purity oxides of the involved elements. The synthesis consisted in 20 hours of milling in a planetary mill using zirconia containers and balls, followed by a firing at 1500°C. The samples before and after sintering were characterized by XRD to evaluate the effect of heat treatment in crystallization, as well as evaluating the polymorphic transitions on the powders. Milled powders were also uniaxially pressed to obtained pellets, which were sintered at 1500°C. Morphology and chemical composition were analyzed by FE-SEM and EDS. Finally, electrical properties were studied by impedance spectroscopy to evaluate the effect of doping on the ionic conductivity and activation energy of samples. Results revealed that the sintering to 1500 generates a combination of monoclinic-tetragonal and tetragonal-cubic phases in the samples, which influences their electrical properties, this phenomena is influenced by the thermodynamics that govern such systems, as well as metastable phases that are obtained by mechanical milling. Also these materials show electrical properties similar to some well-known ionic conductors, the conductivity values obtained were in a range of $1 \times 10^{-2.68}$ – $1 \times 10^{-2.98}$ Scm^{-1} and can be considered to be used as solid electrolytes in ceramic cells of the SOFC type.

Keywords: SOFC, YPSZ, mechanical milling, electrical properties, solid electrolytes

1. Introduction

The total world consumption of energy has presented a considerable increasing in recent years, due to most of the means of generating energy that are currently used, therefore, a large number of countries has boosted investment to the development and implementation of alternative energy sources. An example of this are fuel cells, and in particular those of solid oxide (SOFC: Solid oxide fuel cells), considered as the most efficient invented electrochemical devices, which transform chemical energy in electrical energy with the efficiency of oxidation of the fuel, while at the same time reducing the amount of oxidant, generating only pure water as a sub-product [1].

This technology is based on the combination of three active elements, a cathode made of a perovskite-type lanthanum and strontium manganite ($LaSrMnO_3$), a solid electrolyte, considered as the main and most important part of the cell, composed by zirconia (ZrO_2) stabilized with 8% mole of yttria (Y_2O_3) and an anode made of a cermet (yttria stabilized zirconia and Ni). Although it is considered as a promising technology, it still has several problems to overcome, since after certain periods of time at its high operating temperatures (700-1000 °C) there are chemical reactions between the components; that is, in the cathode / electrolyte interface, that decreases its efficiency, that is the reason why it is necessary to decrease the operating temperatures of SOFC´s, by using materials that have better properties than those currently used [2-4]. In this sense, we show the modification of properties of the YPSZ by partially replacing the Zr^{+4} atom with a lanthanide element such as Sm^{+3}, Gd^{+3} or Nd^{+3} and in this way improve its electrical properties; the most important from the point of view of its application as solid electrolyte. The use of mechanical milling is proposed as a synthesis route because it is a method little studied for this type of materials and has advantages over the conventional synthesis method. Finally, the development and innovation in these devices is of great importance at the global level, as this contributes to the progress in the production of more efficient SOFC and at lower cost, thus contributing both to the generation and use of alternative and low impact energies environment, which will lead to a better quality of life and technological development [5].

2. Materials and Methods

The starting materials used for the development of the mechanochemical synthesis were oxides ZrO_2, Y_2O_3, Gd_2O_3, Sm_2O_3 and Nd_2O_3, all with purity of 99.9% (Sigma Aldrich). The first step was to determine the stoichiometric composition of the proposed samples, which can be observed in Table 1, which lists the 4 different phases to be used for each lanthanide and the phase corresponding to 4% of doping of Y_2O_3 to stabilize the ZrO_2.

Table 1. Stoichiometric compositions of the proposed samples.

NAME OF THE PHASE	STOICHIOMETRIC COMPOSITION
Phase of YSZ 4%	$Y^{+3}_{0.04}\,Zr^{+4}_{0.96}\,O^{-2}_{2-\delta}$
Phase 1 Ln 0.05	$Ln^{+3}_{0.05}\,Y^{+3}_{0.04}\,Zr^{+4}_{0.91}\,O^{-2}_{2-\delta}$
Phase 2 Ln 0.10	$Ln^{+3}_{0.10}\,Y^{+3}_{0.04}\,Zr^{+4}_{0.86}\,O^{-2}_{2-\delta}$
Phase 3 Ln 0.15	$Ln^{+3}_{0.15}\,Y^{+3}_{0.04}\,Zr^{+4}_{0.81}\,O^{-2}_{2-\delta}$
Phase 4 Ln 0.20	$Ln^{+3}_{0.20}\,Y^{+3}_{0.04}\,Zr^{+4}_{0.76}\,O^{-2}_{2-\delta}$

The yttria content remained fixed at a value of 0.04 molar, varying only the lanthanide oxide Ln_2O_3 = 0.05, 0.10, 0.15 and 0.20 and ZrO_2. Also, chemical reactions were obtained for each system, following the form of the chemical reaction: $Ln_2O_3 + Y_2O_3 + ZrO_2$, and then the amount in grams to be used of each oxide to obtain the desired solid solutions. Then the starting oxides were introduced in a muffle in which a heat treatment was applied at 800 °C for 3 hours, in order to eliminate the possible presence of remnants of hydrates or carbonates of the involved elements. Once the above was done, we proceeded to weigh the different reactives in appropriate proportions for each system. The process of mechanochemical synthesis consisted of introducing the necessary amount of each of the oxides as well as the 6 balls in a steel mortar which has an internal coating of YSZ. This mortar was fixed, placed and secured in the planetary mill, by using YSZ balls as grinding media. The ratio of balls / weight of powder used was kept constant for all cases and was 10:1, that is, that 10 g of weight of the ball correspond to 1 g of sample, the milling speed parameters were 400 rpm.

Representative samples of each system were characterized by X-ray powder diffraction (XRD) to evaluate the evolution of the starting compositions with the milling time and with it the appropriate time of synthesis was determined. Based on this, results showed that the ideal time of synthesis was 20 hours of milling. At the end of the synthesis corresponding to the system with 20% of Ln and that of 4% YSZ, samples were thermally treated at 900, 1200 and 1500 °C for 6 hours. The powder samples were also analyzed by XRD to evaluate the effect of temperature on these

The just milled samples were also uniaxially pressed in order to obtain pellets, which were thermally treated at 1500 °C for 6 hours, using heating and cooling ramps of 2ºC / min.. Sintered pellets were characterized by FE-SEM to analyze the morphology of these in order to evaluate the effect of temperature on the densification of pellets. Subsequently, analysis of electrical properties was carried out in the sintered samples by impedance spectroscopy, to determine the ionic conductivity and the activation energy of these materials. The general procedure of the development of the mechanochemical synthesis, characterization and subsequent analysis of the properties of the different compositions, is shown graphically in the figure 1.

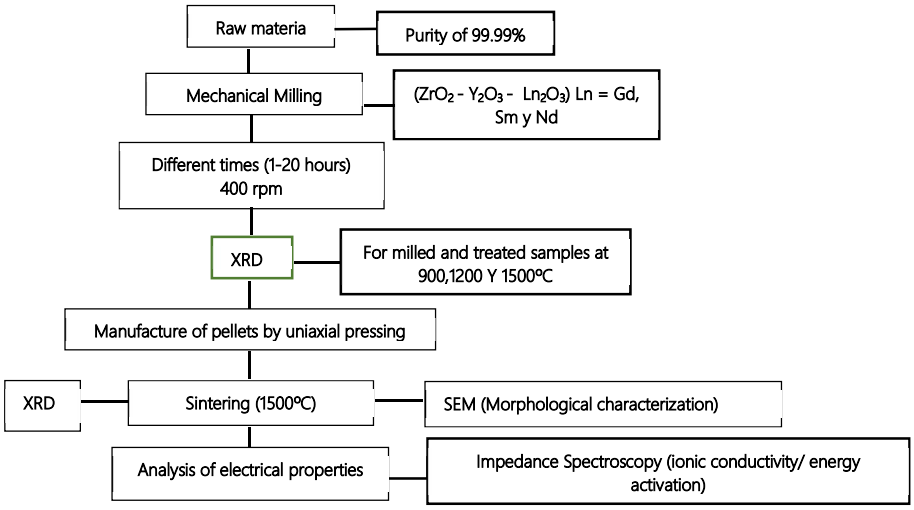

Fig.1. Shows a diagram of the experimental development.

3. Results and Discussion

Then, the results obtained with the characterization of the solid solutions synthesized are presented.

3.1 Synthesis and characterization by XRD

The synthesized samples were characterized by XRD to analyze the effect of mechanical milling in obtaining the proposed systems as shown in Figure 2.

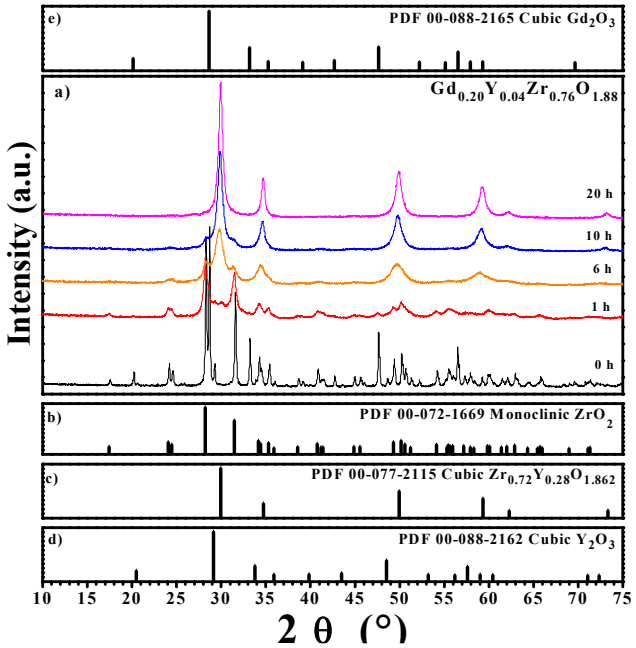

Fig.2. XRD patterns of $Gd_{0.20}Y_{0.04}Zr_{0.76}O_{1.88}$ at different milling times (a). Monoclinic ZrO_2 (b), cubic ZrO_2 (c), cubic Y_2O_3 (d) and cubic Gd_2O_3 (e) reported by the ICDD.

In the figure 2, can be observed the diffraction patterns obtained to evaluate the evolution of $Gd_{0.20}Y_{0.04}Zr_{0.76}O_{1.88}$ at different milling times; at zero and one hour of milling, the reflections coincide with the patterns reported by ICDD for de starting reactives; however, after 20 hours of synthesis the reactions of starting raw materials was carried out and the desired solid solution was obtained [6]. After 20 hours of synthesis, there are no changes in the stabilization of the phases obtained (tetragonal for all solutions with 5% and cubic for those doped with 10%, 15% and 20%).

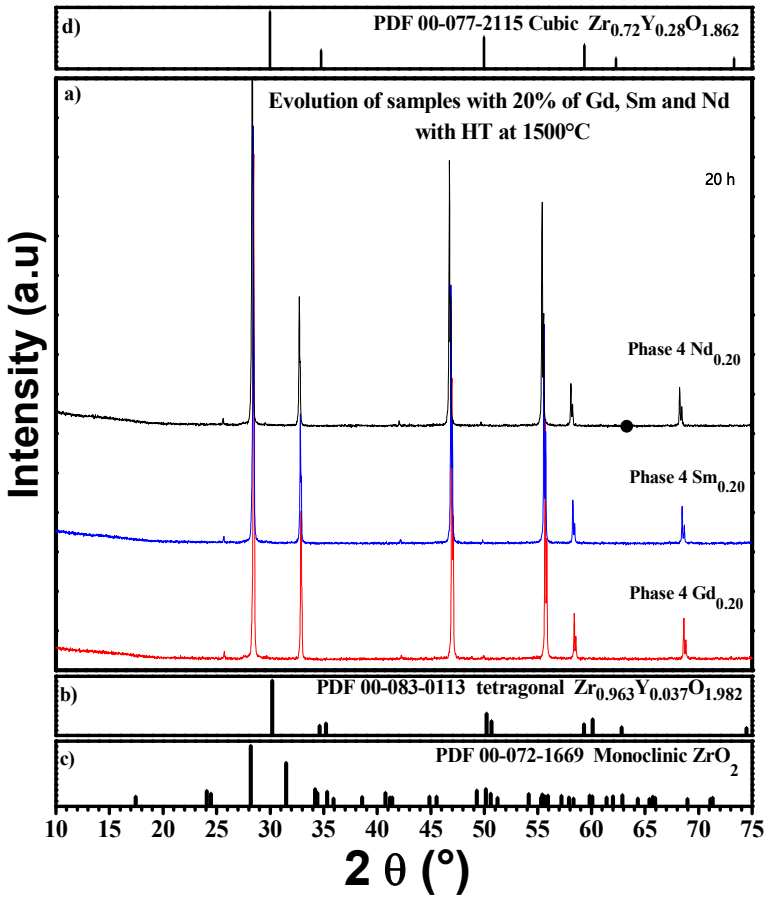

Fig.3. Diffraction patterns of $Gd_{0.20}$, $Sm_{0.20}$ and $Nd_{0.20}$ with heat treatment at 1500°C (a), tetragonal ZrO_2 (b), monoclinic ZrO_2 (c), and cubic ZrO_2 (d) reported by the ICDD.

The figure 3 (a) shows the diffraction patterns obtained for $Gd_{0.20}$, $Sm_{0.20}$ and $Nd_{0.20}$, where the effect of the thermodynamic equilibrium in the metastable phases [7] obtained was observed, because phase mixtures were obtained of zirconia in all systems; being monoclinic + tetragonal for percentages of 5 and 10% and tetragonal + cubic for 15% and 20%. Due to mechanical milling, metastable phases are obtained at room temperature [8,9].

The characterization by X-ray diffraction, allowed to determine the time of suitable milling, as well as the influence of temperature on the stabilization of the tetragonal and cubic phases obtained with the mechanical milling at room temperature after a sintering at 1500 ° C.

3.2 Microstructural characterization by FE-SEM

Pellets of each compositions were obtained, which were sintered at 1500 °C and a gold-palladium coating was placed to be able to characterize them by field emission scanning electron microscopy.

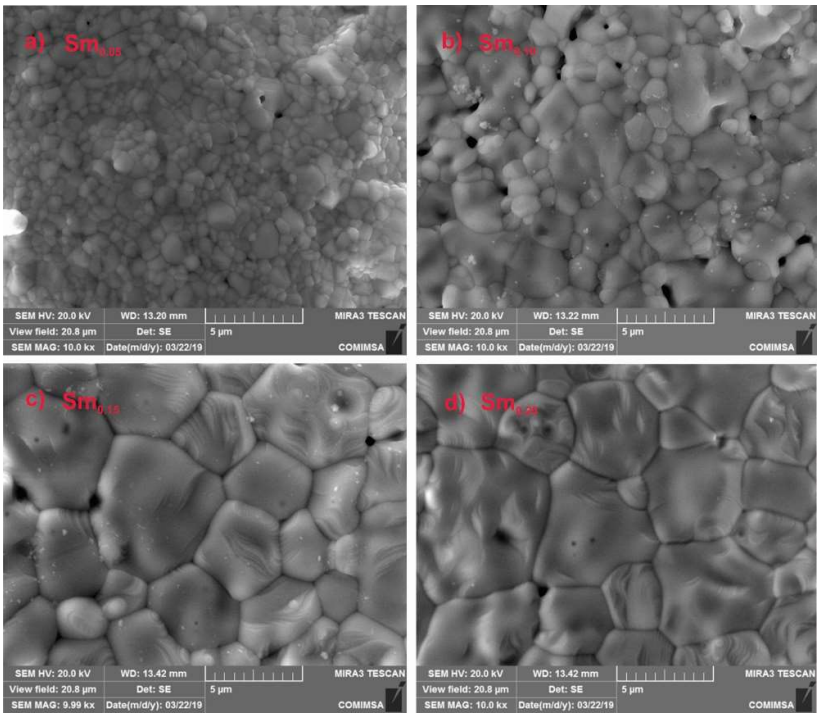

Fig.4. Micrographs obtained by EF-SEM at 10,000 magnifications of the 4 samarium phases: a) $Sm_{0.05}$, b) $Sm_{0.10}$, c) $Sm_{0.15}$ and d) $Sm_{0.20}$.

Figure 4 shows the micrographs obtained at 10,000 magnifications for solid samarium solutions. Grain size is increasing as the percentage of samarium increases; this phenomenon was constant for Gd and Nd [10]. In Figure 4b) a greater number of pores is observed. While for 4c) and 4d) the grain size increased with an average value of 4µm and the porosity decreased.

Recently, it has been reported that the metastable tetragonal ZrO_2 phase is stabilized by rare earth dopants (lanthanides); additionally, the grain size is directly related to the transformability of the tetragonal phase (t') and the ceramic tenacity, in addition to that the amount of stabilizer is the structure of the YSZ is directly related to an increase in grain size [11, 12].

The hypothesis that was raised regarding the influence of grain size on the electrical properties of these materials, was that to a larger size grain boundaries are smaller in quantity and this does not influence the diffusion of oxygen ions in the structure of the material, although there is still no point of agreement among several authors on what is the optimal size [13, 14].

The above, based on the fact that ionic conductivity is the main characteristic of a material to be considered as a solid electrolyte in a SOFC type cell.

3.2 Electrical properties by Impedance Spectroscopy

For electrical properties, a Solartron 1260 Impedance Analyzer was used in a 2-electrode configuration. The measuring cell consisted of two platinum electrodes attached to the sample,

previously painted on both faces with platinum paint. The systems were characterized at test temperatures of 325 °C - 700 °C in a tubular furnace, with temperature increases of 25 °C from 325 °C and up to 400 °C and increase of 50 °C from 400 °C to final measurement temperature.

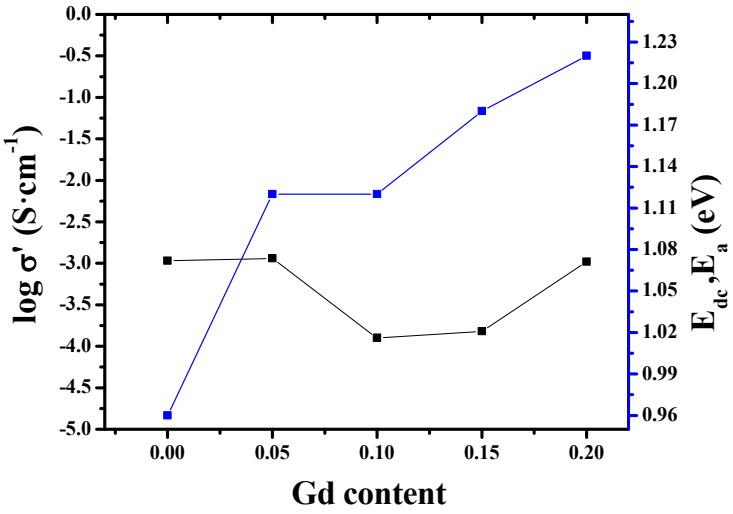

Fig.5. Values of activation energies E_{dc} and E_a and the conductivity of σdc at 700 °C as a function of the gadolinium content for the system $Gd_xY_{0.04}Zr_{1-(X+0.04)}O_{2-\delta}$.

The figure 5 shows the graph obtained for the gadolinium systems where it is appreciated how the values of conductivity and activation energy of each of the samples obtained vary depending on the percentage of this lanthanide with respect to the composition of 4YSZ, whose values correspond to the percentage zero of composition in the graph, where the activation energy of gadolinium systems increases with respect to YPSZ, and in the specific case of conductivity, it can be seen how the value increases lightly

As shown in the obtained results, conductivity of gadolinium systems ($1*10^{-2.94}$ Scm^{-1},$1*10^{-3.9}$ Scm^{-1}, $1*10^{-3.8}$ Scm^{-1} y de $1*10^{-2.98}$ Scm^{-1}) decreases as the percentage of lanthanide element increases, which can be related to reported data where it is mentioned that instead of a continuous increase in ionic conductivity by introducing dopant, the ionic conductivity usually reaches a maximum at a certain concentration of dopant and then decreases [15-17].

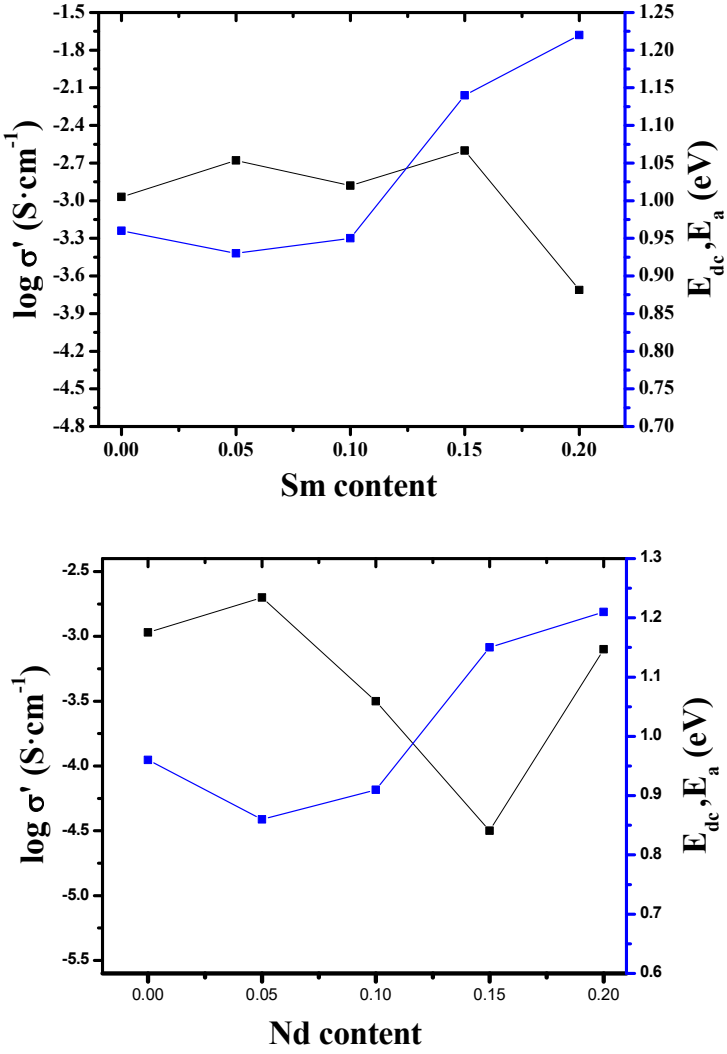

Fig.6. Values of the activation energies E_{dc} and E_a and the conductivity of σdc at 700 °C as a function of the samarium (a) and neodymium (b) content for the system $Ln_XY_{0.04}Zr_{1-(X+0.04)}O_{2-\delta}$.

Figure 6 (a) shows the conductivity and activation energy for Sm samples, where, as for Gd and Nd 6 (b), an increasing in the activation energy is observed at higher dopant contents. The black values corresponding to dc or bulk conductivity, this varies from 4YSZ $1 * 10^{-2.97}$ compared with solid samarium solutions which were $1 * 10^{-2.68}$, $1 * 10^{-2.88}$, $1 * 10^{-2.62}$ and $1 * 10^{-3.71}$ Scm^{-1} at 700 ° C, compared with those of neodymium of $1 * 10^{-2.7}$ Scm^{-1}, $1 * 10^{-3.5}$ Scm^{-1}, $1 * 10^{-4.5}$ Scm^{-1} and $1 * 10^{-3.10}$ Scm^{-1} . The conductivity values are in a range between $1 * 10^{-2.6}$ and $1 * 10^{-4.8}$ S.cm-1, with respect to this it is considered that the best compositions were Gd0.05, Gd0.20, Sm0.05, Sm0 .10 and Sm0.15, since they presented values of conductivity comparable with those reported at 800 °C [18-20], in addition to these were obtained at 700 ° C.

4. Conclusion

Mechanical milling is a suitable method to obtain this type of materials. The effect of the doping ion is related to the increase in grain size as well as in ionic conductivity. From the electrical properties, it is concluded that the solid solutions of $Gd_{0.05}$, $Gd_{0.20}$, $Sm_{0.05}$, $Sm_{0.10}$ and $Sm_{0.20}$ whose conductivity dc values are between a range of $1 * 10^{-2.6}$ to $1 * 10^{-2.9}$ Scm^{-1} and those of activation energy with variation between 0.93-1.22 eV at a temperature of 700 ° C, are the most viable to be used as materials for solid electrolytes in SOFC according to reported values.

Acknowledgements

This work was financially supported by CONACYT CB- 166 995, and CV-860984.

References

[1] U.S Energy Information Administration, International Energy Outlook 2017, https://www.eia.doe.gov/oiaf/ieo/highlights.html; 2017 [Access 20.03.2018].
[2] Zuo C, Liu M F, Liu M L. Solid Oxide Fuel Cells: From Materials to System Modeling. Springer 2013; 7: 8-12.
[3] Haile S M. Fuel cells materials and components. Acta Materialia 2003; 51: 5981-6000.
[4] Ramadhani F, Hussain M A, Mokhlis H, Hajimolana S. Optimization strategies for Solid Oxide Fuel Cell (SOFC) application: A literature survey. Renewable and Sustainable Energy Reviews 2017; 76: 460-487.
[5] Santori da Silva F, Souza T M. Review article novel materials for solid oxide fuel cell technologies: A literature review. International Journal of Hydrogen Energy 2017, 30:1-17.
[6] Sifuentes C A. Síntesis y propiedades eléctricas de circonatos de lantánidos con estructura tipo fluorita. Tesis para obtener el grado de Maestro en Ciencias en Materiales, Instituto Tecnológico de Saltillo: 2017.
[7] Eyring L. Progress in the science and technology of the rare earths. Pergamon press 1968; 2: 532.
[8] Lizer Sopicka M. Mechanochemical processing of nanopowders: introduction to mechanochemical processing. Woodhead Publishing 2014; 1-3.
[9] Baláz P. Mechanochemistry in nanoscience and minerals engineering. Berlin, Heidelberg: Springer; 2008.
[10] Suresh A, Mayo M J, Porter W D, Rawn C J. Crystallite and Grain-Size-Dependent Phase Transformations in Yttria-Doped Zirconia. Journal of the American Ceramic Society 2003; 86: 360-362.
[11] Basu B. Toughening of yttria-stabilized tetragonal zirconia ceramics. Journal of International Materials Reviews 2005; 50: 239-256.

[12] Chen W, Hu D L, Gu H, Quian P X, Vleugels J, Jiang Y. Bi-modal distribution of stabilizers to regulate the dual-phase microstructure and transformability in Nd_2O_3/Y_2O_3-doped zirconia ceramics. Journal of the European Ceramic Society 2019; 30.
[13] Fei L, Yanhuai L, Zhongxiao S, Kewei X, Dayan M, Bo G, Hong C. Grain growth characteristics of hydrothermally prepared Yttria Stabilized Zirconia nanocrystals during calcination. Journal of Rare Metal Materials and Engineering 2017; 46:899-905.
[14] Chih W K, Yun H S, Shaw B W, Huey L, Moo C W. Effect of Y_2O_3 addition on the crystal growth and sintering behavior of YSZ nanopowders prepared by a sol-gel process. Journal of Alloys and Compounds 2009; 472: 186-193.
[15] Young C G, Lee H Y, Yu W, An J, Cha W S. Optimization of Y_2O_3 dopant concentration of yttria stabilized zirconia thin film electrolyte prepared by plasma enhanced atomic layer deposition for high performance thin film solid oxide fuel cells. Energy 2019; 173: 436-442.
[16] Suciu C, Dorolti E, Hoffmann A C. Physico-chemical properties of nanocrystalline YSZ powders as a function of doping level and electrical properties after sintering. Material Science for Energy Technologies 2018; 1: 136-145.
[17] Perry N H, Harrington G F, Tuller H L. Electrochemical ionic interfaces. Metal Oxide Based-Thin Film Structures (Formation, Characterization and Application of Interface-Based Phenomena Metal Oxides). Solid State Ionics 2018; 1: 79-106.
[18] Díaz G J A. Efecto de diferentes iones dopantes en las propiedades eléctricas y térmicas del $Gd_3Zr_2O_7$. Tesis para obtener el grado de Doctor en Ciencias en Ingeniería Metalúrgica y Cerámica, Centro de Investigación y De Estudios Avanzados del Instituto Politécnico Nacional: 2011.
[19] Maeland D, Suciu C, Waernhus I, Hoffmann A C. Sintering of 4YSZ (ZrO_2 + 4 mol% Y_2O_3) nanoceramics for solid oxide fuel cells (SOFC´s), their structure and ionic conductivity. Journal of European Ceramic Society 2009; 29: 2537-2547.
[20] Salazar Z M, Díaz G J A, Acosta G O J, Díaz G J C, Martínez M S, Burciaga D O, Bazaldúa M M E, Fernández F A. Ionic conductivity of $Ln_4Zr_3O_{12}$ solid electrolytes synthesized by mechanochemistry. International Journal of Hydrogen Energy 2019; 44: 12500-12507.

E010. NOVEL PERIPLANETA AMERICANA DERIVED-BIOCARBON ELECTROCATALYSTS WITH HIGH CATALYTIC ACTIVITY FOR THE OXYGEN REDUCTION REACTION (ORR) IN ALKALINE MEDIA

J.-G. Alanís-Gutiérrez[1], J.-G. Bocarando-Chacon[1], B. Escobar-Morales[2], S. Garcia-Mayagoitia[3], F.-J. Rodríguez-Varela[3], I.-L. Alonso-Lemus[4]

[1]Universidad Tecnológica de Querétaro (UTEQ), Avenida Pie de la Cuesta # 2501, C.P. 76148 Querétaro, Qro., México.

[2]Centro de Investigación Científica de Yucatán (CICY), Calle 43 No. 130, Col. Chubumá de Hidalgo, Mérida, Yucatán, C.P. 31136, México.

[3]Sustentabilidad de los Recursos Naturales y Energía, CINVESTAV, Unidad Saltillo, Av. Industrial Metalurgia No.1062, Parque Industrial, Ramos Arizpe, Coahuila, C.P. 25900, México.

[4]CONACYT, Grupo de Sustentabilidad de los Recursos Naturales y Energía, CINVESTAV Saltillo, Av. Industrial Metalurgia No.1062, Parque Industrial, Ramos Arizpe, Coahuila, C.P. 25900, México.

*ivonne.alonso@cinvestav.mx

ABSTRACT

In this work, a novel metal free electrocatalysts were developed using *Periplaneta Americana* (most common cockroach specie in Mexico) as raw material for the synthesis of a biocarbon. In addition, the biocarbon was activated with potassium hydroxide in order to modify its textural properties and increase the active sites for the ORR. The most active electrocatalyst was labeled as N-aPAB (activated with KOH), which had an onset potential (E_0) of 0.86 V vs. RHE and a current density j = -2.74 mA cm^{-2} at 0.2 V vs. RHE. Furthermore, the hydrogen peroxide (% H_2O_2) and the electron number transferred (n) were calculated, where the %H_2O_2 was of ≈ 23.01 and n= 3.54. The electrochemical performance of N-aPBA electrocatalysts is comparable with commercial Pt-based electrocatalyst (E_0 = 1.00 V vs. RHE, j = -4.36 mA cm^{-2}, % H_2O_2 = 1.95 and n = 3.96). These results indicate that this novel electrocatalyst is a promising alternative for use in alkaline fuel cells cathodes.

Keywords: Electrocatalyst, Alkaline Fuel Cells, ORR, *Periplaneta Americana*.

1. Introduction

Energy plays a key role for the society progress, besides it is crucial and a determining factor related to the socioeconomic and sustainable development, therefore, it is very important to work in research of alternative energies. Low-temperature Fuel Cells (FCs) are promising and sustainable device for alternative for energy generation, because they convert chemical energy directly into electricity by the oxidation of a fuel and the reduction of oxygen [1]. In addition, FCs have high efficiencies and low/ zero emissions. FCs components are mainly three: anode, cathode and electrolyte. The oxidation of a fuel takes place at the anode, while at the cathode the the Oxygen Reduction Reaction (ORR) is carried out, which has the slowest kinetic limiting the overall performance of the FC. Finally, the electrolyte transports the ions generated by the redox reactions [2]. However, despite the advantages of this technology currently depends of the use of noble-metal electrocatalysts as platinum for that the redox reactions can be carried out, which is scarce and expensive. Therefore, the research of electrocatalysts for the ORR has been oriented to reduce or replace the platinum load maintaining the high catalytic activity [3].

Regarding to the above, recently metal-free electrocatalysts have been developed in order to reduce the FCs costs. These electrocatalysts was reported for first time in 2009 [4] increasing the interest of the scientific community in their study. These electrocatalysts are mainly composed by heteroatoms into the carbon lattice, which modifies the electron density of the neighbor's carbon atoms promoting the catalytic activity for the ORR. In addition, their large-scale production would not be a limitation due to the abundance of these elements.

An important source of carbon and heteroatoms is biomass, which can be from different sources such as animal, vegetable, industrial and forest. Metal-free electrocatalysts can be obtained from the carbonization and thermochemical treatments of biomass, which generate larger surface area and large pore volume improving the catalytic activity. An extensive review written by Kaur et. al. [5] mention at least 108 sources of biomass that have been studied to obtain metal-free electrocatalysts. Some of the most active *Sargassum spp.*-derived electrocatalyst for ORR has an E_0= 0.870 V vs RHE, j=-4.00 mA cm^{-2} and n= ≈3.5.

In this work, *Periplaneta Americana* (*P. Americana*) derived biocarbon has been synthetized and evaluated for first time as metal-free electrocatalysts for the ORR. This insect is the most common spice of cockroach in America, and its chemical composition (such as chitin, chitosan, cellulose, crude protein, fat, ash, carbohydrates, calcium, phosphorus, as well as amino acids and fatty acids) [6] makes it an attractive raw material for metal-free electrocatalysts synthesis. The blattodea has been subjected to eco-friendly thermochemical treatments in order to modify its physicochemical properties and provide it electrocatalytic activity.

2. Materials and Methods

2.1 Synthesis of metal-free electrocatalysts

Several specimens of *P. Americana* were collected in Saltillo, Coahuila, Mexico. First let it dry to grind and get cockroach powder. Then, the powder was placed into a porcelain crucible and carbonized in a Thermo Scientific tubular furnace at 700 ° C for 90 minutes in an inert atmosphere. Once the material was obtained, it was labeled as N-PAB (nitrogen-doped *Periplaneta Americana*-derived biocarbon). The activation process was carried out mixing N-PAB with KOH in a 2: 1 ratio until the material was homogenized the mixture was deposited in a crucible and heating at 750 °C for 90 min. Afterwards, the black powder was washed with a solution of hydrochloric acid and distilled water. This second metal-free electrocatalysts was labeled as N-aPAB (nitrogen-doped activated *Periplaneta Americana*-derived biocarbon).

2.2 Physicochemical characterization

The morphology of one *P. Americana* specimen was studied before and after the pyrolysis with an OLYMPUS SZ-CTV stereomicroscope connected to an INFINITY camera. In addition, in order to know the morphology of the electrocatalysts synthesized before and after each process, a microscopic analysis was performed by scanning electron microscopy of field emission (FE-SEM) with a Jeol 780F Prime microscope. A chemical mapping and composition were performed using the energy dispersion spectroscope coupled to the FE-SEM, the detector used was a Bruker's Quukax model.

2.3 Electrochemical Characterization

The electrocatalytic activity was evaluated using a bipotenciostat Bio-Logic model VSP-300 coupled to a rotating disc electrode system, (Pine AFMSRCE). All tests were carried out at room temperature in three cell electrodes: a glassy carbon electrode used as work electrode, an Ag/ AgCl reference electrode with a sodium hydroxide solution (3M NaOH) and a Pt wire as counter electrode. The electrolyte was an aqueous solution of potassium hydroxide (0.5 M KOH).

The cyclic voltammetry (CV) curves were obtained following the next protocol: for the activation the potential window was from 0 to 1.2 V vs the Reversible Hydrogen Electrode (RHE) at a scan rate of 100 mV s^{-1} during 50 cycles in a N_2 saturated electrolyte, subsequently, a CV curve was obtained in the same potential window at a scan rate of 20 mV s^{-1} during 3 cycles. The background current was determined in the same potential window at scan rate of 5 mV s^{-1} and a rotation rate of 2000 rpm. Afterwards, the electrolyte was saturated with O_2 in order to obtain the Linear Sweep Voltammetry (LSV) curves, which were performed in a potential window of 0 to 1.2 V vs RHE, at a scan rate of 5 mV s^{-1} at several rotations rates (400, 800, 1600, 2000 and 2500 rpm). From the obtained data, electrochemical parameters such as percentage of hydrogen peroxide and the electron number transferred were calculated (Equation 1 and 2).

$$\%H_2O_2 = \frac{200(I_r/N)}{I_d + (I_r/N)} \quad (1)$$

$$n = \frac{4 * I_d}{I_d + \frac{I_r}{N}} \quad (2)$$

where, I_d is the current detected in the disk, I_r is the current in the ring and N is the collection efficiency that is defined as the fraction of a completely stable species formed in the disk that is detected in the ring, the value is 0.37 for alkaline medium.

3. Results and Discussion

3.1 Morphology

Figure 1a shows a specimen collected for this experiment, as can be seen it is brown that is consistent with the *P. Amerticana* specie, the morphology of the legs and head is different from that of the wings. Figure 1b shows an image at greater magnification of the wings, where a system of veins homogeneously distributed can be seen. In figure 1c the specimen is observed after the carbonization process, it is observed that it maintains its shape, the above is confirmed observing figure 1d where the morphology of the wings of the *P. Amaericana* is preserved after the pyrolysis treatment.

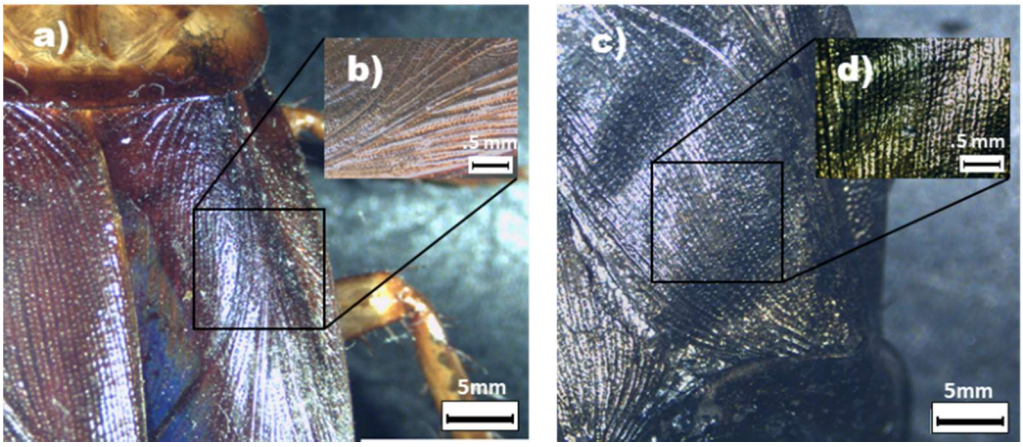

Figure 1. Images of P. Americana a) before carbonization, b) morphological structure of the wings, c) specimen after the pyrolysis process, d) wings morphology after the pyrolysis process.

Figure 2 shows the micrographs of the metal-free electrocatalysts. N-PAB (Figure 2a) has a heterogeneous morphology, with particles of very varied shapes and smooth and rough particle surface. On the other hand, Figure 2b shows the N-aPAB electrocatalyst which, although similar morphologies are observed, clearly shows a greater roughness, which indicates that the activation treatment modifies the carbon surface.

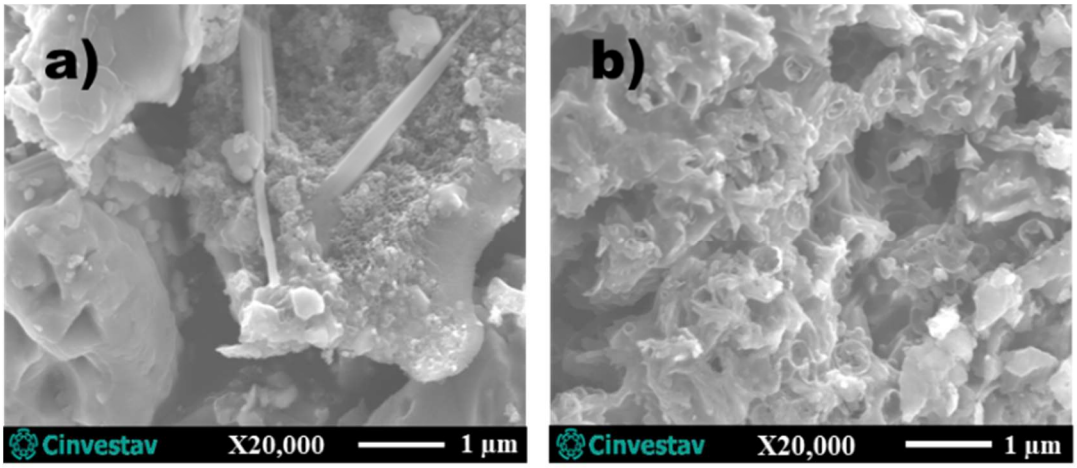

Figure 2. Secondary electrons FE-SEM images of samples a) N-PAB and b) N-aPAB.

3.2 Chemical Composition

Elementary analysis of all metal-free electrocatalysts was performed in 5 micro-areas at 500x. Table 1 shows the average of these 5 measures, the chemical composition of the electrocatalysts indicates that at lest 10 elements were detected. The main element is carbon (<67 wt.%), also heteroatoms such as nitrogen (between 3.5 and 4.8 wt%.), sulfur (≈ 0.80 wt. %) and phosphorous (≈ 0.80 wt. %) were detected, which provide catalytic activity for the ORR according with some reports [7]. As can be seen, the chemical composition of N-aPAB is slightly modified after the activation treatment, decreasing the concentration of calcium and potassium and removing silicon. The concentration of oxygen decreases up to 50%, maybe by the removal of potassium, calcium and silicon oxides.

Table 1. Elemental analysis by EDS in 5 zones at 500x, the reported results are the averages of the zones.

Electrocatalyst		
	N-PAB	N-aPAB
Element	wt. %	wt. %
Carbon	67.27	75.60
Nitrogen	4.87	3.75
Oxygen	9.83	3.99
Aluminum	0.22	0.2
Sulfur	0.80	0.61
Phosphorous	1.78	1.52
Silicon	0.43	ND
Chlorine	1.56	4.00
Potassium	5.01	4.85
Calcium	7.83	4.66
No detected= ND		

Additionally, elemental mapping of N-PAB is showed in Figure 3. The distribution of carbon, oxygen and some heteroatoms can be observed. In these images it is possible to appreciate that the C and N are distributed in the same zone, while O, S and P are distributed together in another zones, which may indicate that these elements are forming compounds. Moreover, the fact that the carbon and

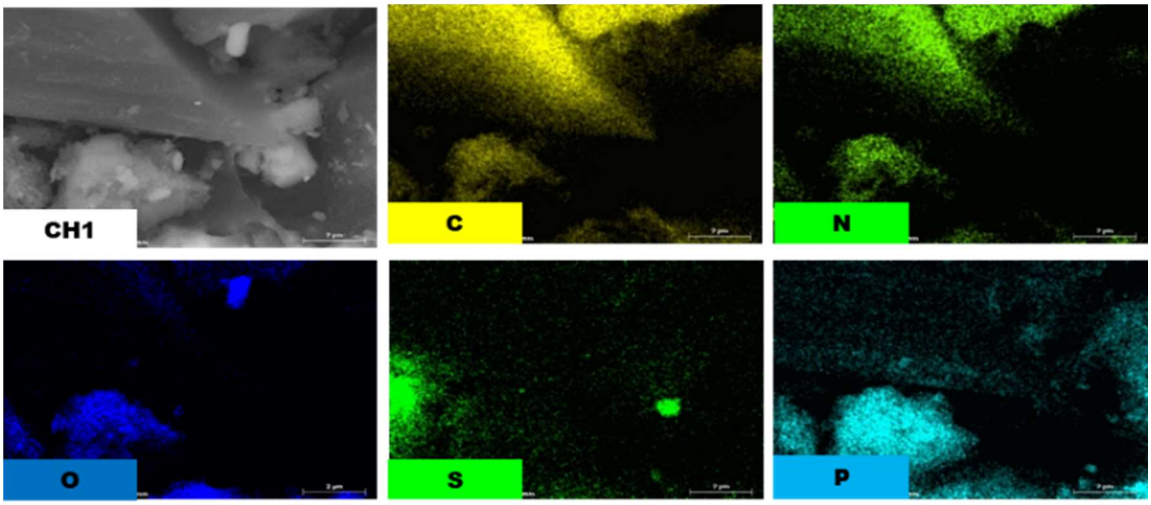

nitrogen are in the same zone suggests that at least this heteroatom is incorporated into the carbon lattice and it is distributed homogeneously in the carbon particles.

Additionally, figure 4 show the elemental mapping for the N-aPAB electrocatalyst. The images demonstrate that the activation treatment has an effect on the elemental distribution of this electrocatalyst. For example, C, N and O are distrusted in the same zone, maybe due at the oxidation of carbon surface after the treatment with KOH [8 and 9]. However, the homogeneous distribution of N on the C particles has been not modified. Moreover, the elemental distribution of S and P heteroatoms improves after activation treatment.

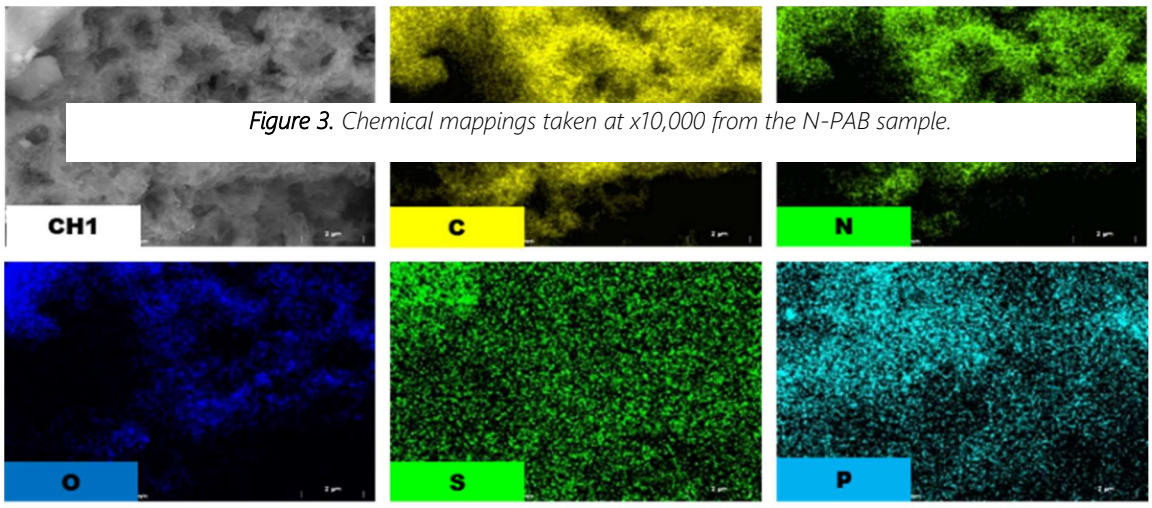

Figure 3. Chemical mappings taken at x10,000 from the N-PAB sample.

3.3

Figure 4. Chemical mappings taken at x10,000 from the N-aPAB sample.

Electrochemical Properties

Figure 5a shows the CV curves of the electrocatalysts N-PAB and N-aPAB. As can be seen, area of CV curve increases due to the activation treatment, also increasing the effect of the electrochemical double-layer. In addition, the current density of N-aPAb is greater than N-PAB, maybe due to the increase in the surface area, since, as has been widely reported, KOH treatment increases the surface area in carbonaceous materials, therefore, the electrode-electrolyte interface increase generating higher

current densities. On the other hand, figures 5b and c show the LSV curves of the N-PAB and N-aPAB respectively. The current density of both electrocatalysts increases as the rotation rate increases, as expected. The N-PAB electrocatalyst show a two-step LSV curve (dotted red line box), which indicates that the ORR is carried out by combined 2 and 4 electrons pathway [6]. Also, N-aPAB has a higher current density than N-PAB, which indicate a higher catalytic activity for the ORR.

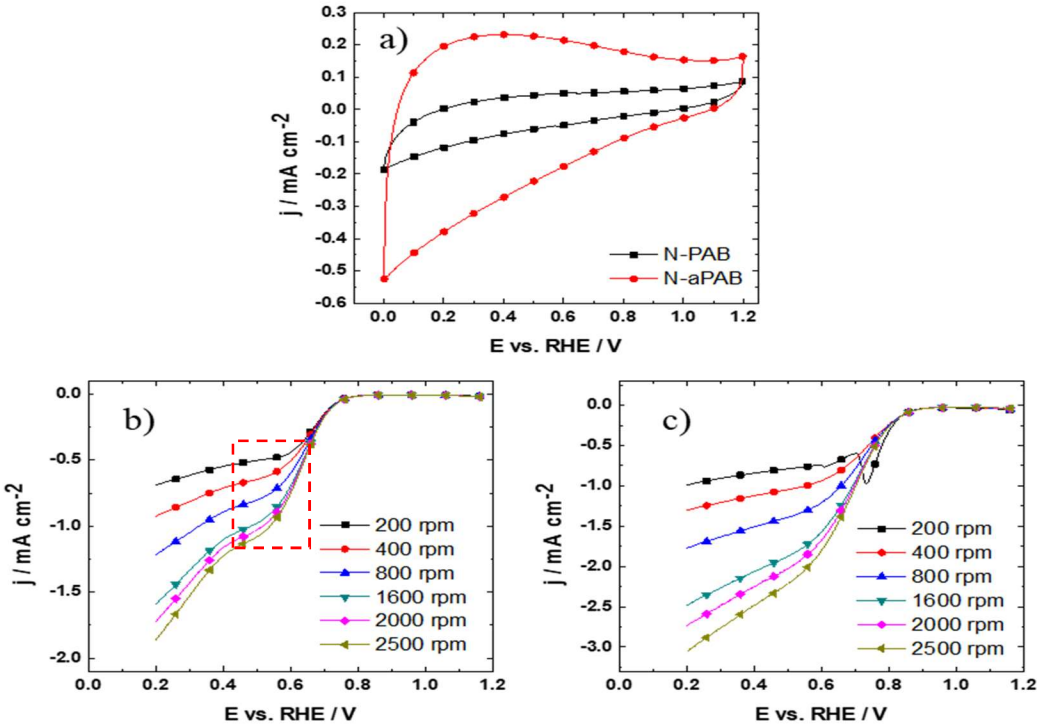

Figure 1. a) Voltammograms, b) y c) polarization curves of the electrocatalysts N-PAB y N-aPAB.

In order to determine the catalytic activity of the ORR of these electrocatalysts, electrochemical parameters such as onset potential (E_0), current density at 0.2 V vs. RHE (j), hydrogen peroxide production (H_2O_2%) and the electron number transferred (n) were calculated from the LSV curve performed at 2000 rpm. The N-aPAB has better electrochemical performance (E_0= 0.86, j=-2.74 mA cm^{-2}, H_2O_2% ≈ 23.01 and n=3.54) than N-PAB (E_0 = 0.79, j=-1.72 mA cm^{-2}, H_2O_2% ≈ 34.91 and n=3.30). These results are comparable with other reports of biomass-derived electrocatalysts Sargassum spp. (E_0= 0.870 V vs RHE, j=-4.00 mA cm^{-2} and n= ≈3.5) and (j=-3.55 mA cm^{-2}, % H_2O_2 ≈ 11 and n= ≈ 3.66) [5].

4. Conclusion

Novel metal-free electrocatalysts was obtained using *P. Americana* as raw material. This abundant biomass source currently it is not fully exploited. In this work the physicochemical properties of the *P. Americana* were modified by environmentally friendly treatments in order to obtain biocarbons with high catalytic activity for the ORR in alkaline media. The most active P. Americana-derived biocarbon was N-aPAB, which was activated with KOH. The electrochemical parameter calculated for this electrocatalysts are an E_0= 0.86, j=-2.74 mA cm^{-2}, H_2O_2% ≈ 23.01 and n=3.54. However, although N-aPAB does not exceed the electrochemical performance of commercial Pt-based electrocatalysts (20% Pt/C), it is a novel and promising catalysts for this application, which could be improved in the future to increase its performance. In addition, this catalyst could have the potential to solve the issue of the large-scale production faced by platinum catalysts.

References

[1] Ramos P. M. J., Bashiri B. N. (2013). *Renewable Energy and Sustainable Development*. España. Estudios de Economía Aplicada. Vol. 31-1. pp. 7-34.

[2] Rodríguez-Varela J., Solorza-Feria y O., Hernández-Pacheco E. (2010). *Celdas de Bombustible*. Canadá: Charleston, SC. Cap.1-pag 1-16.

[3] Banham D., S. Ye. Current Status and Future Development of Catalyst Materials and Catalyst Layers for Proton Exchange Membrane Fuel Cells: An Industrial Perspective. ACS Energy Letters. 2 (2017) 629-638.

[4] L. Yang, Y. Zhao, S. Chen, Q. Wu, X. Wang, Z. Hu. A mini review on carbon-based metal-free electrocatalysts for oxygen reduction reaction. Chinese Journal of Catalysis. 34 (2013) 1986-1991.

[5] Kaur, P., Verma, G., Sekhon, S.S., Biomass derived Hierarchical Porous Carbon Materials as Oxygen Reduction Reaction Electrocatalysts in Fuel Cells, Progress in Materials Science (2018), Recovered from: https:// doi.org/10.1016/j.pmatsci.2018.12.002

[6] Kulma M., Plachý V., Kouřimská L., Vrabec V., Bubová T., Adámková A. and Hučko B. (2016). Nutritional value of three Blattodea species used as feed for animals. Recovered from:

https://www.researchgate.net/publication/311752142_Nutritional_value_of_three_Blattodea_species_used_as_feed_for_animals.

[7] Wang D.-W., D. Su. Heterogeneous nanocarbon materials for oxygen reduction reaction. Energy & Environmental Science. 7 (2014) 576.

[8] Vázquez B., Sánchez del Campo A. y Salas D. (2005). Obtención de carbón activado por método de activación con etapa de lixiviación. Tecnología Química. XXV No. 3, pp. 74-86.

[9] Carvalho M. (2013). Preparación de carbones activados con KOH a partir de residuos de petróleo. Adsorción de hidrogeno. Alicante, España. Recovered from: https://rua.ua.es/dspace/bitstream/10045/33258/1/tesis_mateuscarvalho.pdf

[10] Dai L., Xue Y., Qu, L., Choi H., Baek J. (2015). Metal-Free Catalysts for Oxigen Reduction Reaction. Review of the American Chemical Society. 115, 48234892. Recovered from: https://pubs.acs.org/doi/10.1021/cr5003563

E012. SYMMETRY STUDIES OF $La_{0.7}Sr_{0.3}Cr_{0.4}Mn_{0.6}O_{3-\delta}$ PEROVSKITE FOR SOLID OXIDE FUEL CELLS

José Juan Alvarado Flores[1,*], María Liliana Ávalos Rodríguez[2], José Guadalupe Rutiaga Quiñones[1], Jaime Espino Valencia[3] and Jorge Víctor Alcaraz Vera[4]

[1]Facultad de Ingeniería en Tecnología de la Madera, Universidad Michoacana de San Nicolás de Hidalgo. Santiago Tapia 403, CP 58000, Morelia, Michoacán, México.

[2]Centro de Investigación en Geografía Ambiental, Universidad Nacional Autónoma de México. Antigua Carretera a Pátzcuaro No. 8701, C.P. 58190, Morelia, Michoacán, México.

[3]Facultad de Ingeniería Química, Universidad Michoacana de San Nicolás de Hidalgo. Francisco J. Mújica S/N, Col. Felicitas del Rio, C.P. 58000, Morelia, Michoacán, México.

[4]Instituto de Investigaciones Económicas y Empresariales, Universidad Michoacana de San Nicolás de Hidalgo. Francisco J. Mújica S/N, Col. Felicitas del Rio, C.P. 58000, Morelia, Michoacán, México.

* Corresponding author: doctor.ambientalista@gmail.com

ABSTRACT

This paper focuses on a review of advances in research on nanocrystalline solid oxide fuel cell synthesis and characterization (SOFC) anodes of $La_{0.7}Sr_{0.3}Cr_{0.4}Mn_{0.6}O_{3-\delta}$ (perovskite-type) with Nickel, Copper and Copper-nickel compounds. All nanocomposites impregnated have been synthesized by ethylene glycol modified sol–gel method to get a porous cermet electrode. The phase transitions and crystal structure of $La_{0.7}Sr_{0.3}Cr_{0.4}Mn_{0.6}O_{3-\delta}$ composites were studied by time resolved x-ray diffraction, Rietveld, and high-resolution transmission electron microscopy. Electrical and structural characterization by four-point probe method for conductivity. Composite powders were compressed into 10-mm diameter discs with 25–75 wt% Ni, XCu (x = 25-45%) and $XCu_{0.75}Ni_{0.25}$ (x = 25-75%). Symmetry-breaking by phase transition from high temperature has been identified and confirmed. it has been detected a cationic inter-diffusion between Cu and Ni interphase crystals during this reduction process. Only some perovskite compositions are viable for use as anodes in intermediate temperature solid oxide fuel cells (SOFC-IT).

Keywords: composite materials; sol–gel growth; electrical conductivity; crystal symmetry

1. Introduction

Hydrogen represents one of the greatest potentials as an energy vector for renewable energies. In this case, greater efficiency can be achieved through fuel cell technology [1]. Fuel cells are devices that combine oxygen and hydrogen to produce electricity, heat, and water. Solid oxide fuel cells (SOFCs) operating at high temperatures (around 1000°C) can achieve efficiencies of more than 60% if waste heat is used in cogeneration [2]. There has been much interest in the development of new cermet materials to enhance the hydrocarbon fuel electro-oxidation and reduce the catalyzing of C–C formation using electro-catalyst as Ni, Cu/GDC, and Ni-doped perovskite [3]. Nowadays, studies have been oriented to lower operation temperature (below 800°C) and intermediate temperature IT-SOFC (400–700 ◦C) [4,5]. Significant attention has been focused on methane electro-oxidation by using anodes with different electrocatalysts including Cu, Ni, Co–CeO_2, Ni/$Ce_{1-x}Gd_xO_{2-\delta}$, Ni–Co/YSZ, Ni–Cu/YSZ, Cu/YSZ [6] and Ni–perovskite materials as $La_{0.6}Sr_{0.4}Fe_{0.8}Co_{0.}2O_3$ with nickel additions [7]. Ni [8], XCu [9] and XCuXNi [10] - doped perovskite catalysts have been studied for hydrocarbon oxidation; attention has been especially focused on $La_xSr_{1-x}Cr_yMn_{1-y}O_{3-\delta}$ (LSCM), which shows suitable chemical stability but poor electrochemical performance at intermediate temperatures. In general, this perovskite offers low resistance of polarization and good stability in hydrocarbon-based fuels. It is important to mention that the LSCM compound is a P-type conductor with a conductivity value equal to 38 Scm^{-1} at an oxygen partial pressure of 10^{-10} atm and a temperature of 900°C [11]. However, the electrical conductivity of this perovskite is much lower in reducing atmospheres (1.5 Scm^{-1} with 5% H_2) [12]. In this sense, the addition of an electrically conductive phase, e.g. copper (Cu) or nickel (Ni, more expensive), can greatly improve the electrical conductivity of the electrode.

On the other hand, it is well known that the properties of ceramics are affected by the characteristics of their powders, such as particle size, morphology, purity and chemical composition; these characteristics change according to the synthesis method used, which is very sensitive to experimental parameters such as temperature, pH, chemical composition, reactant concentration and nature of the solvent. The sol-gel method has been shown to be efficient in controlling the morphology and chemical composition of prepared powders, compared to other non-chemical methods, such as solid state reaction [13], which presents certain drawbacks such as lack of homogeneity, irregular morphology, large particle sizes, high temperatures (1,300-1,600°C) and long periods of calcination [14].

2. Materials and Methods

Three types of perovskites were synthesized using the sol-gel method.

First, series of the perovskite-type $La_{0.7}Sr_{0.3}Cr_{0.4}Mn_{0.6}O_{3-\delta}$–Ni compounds with concentrations ranging from 25 to 75 wt% Ni. Stoichiometric amounts of nickel acetylacetonate, lanthanum acetylacetonate, strontium acetate, chromium(III) acetylacetonate and manganese (II) acetylacetonate, were used to obtain six cermets. Precursors were dissolved in "deionized water–nitric acid, ethanol, deionized water, and butanol respectively to form homogenous, steady and transparent sol solutions at 60°C. Dissolved ion solutions were mixed homogenously by stirring, reflux and heating at the same temperature. Ethylene glycol was added to each sol for the enhancement of salt dissolution. The solution pH value was tuned to 3 by adding ammonia solution. Hydrolysis and condensation reaction were accomplished by refluxing the mixed solution for 12 h. Gels were obtained by slow evaporation at 70°C until dried gel was formed. The gel was dried at 120 ◦C during 12 h and then calcined at 800°C for 1 h in air.

Secondly, XCu cermets were prepared. Where the content of copper (X) used as an additive was 25, 35 and 45% by weight. For the perovskite phase $La_{0.8}Sr_{02}Cr_{05}Mn_{0.5}O_3$ (LSCM) the precursors used were the same as mentioned above. To obtain the LSCM+ Cu cermets, the copper precursor $CuN_2O_{6\text{-}2.5}$ was dissolved under the same conditions as the LSCM perovskite. Subsequently, and maintaining the agitation of the copper solution, the perovskite powders impregnated it to form each of the compositions of LSCM-XCu. The resulting gels were dried under the same conditions as the LSCM compound and then calcined in an alumina crucible at 450°C for 1 h in air atmosphere. The LSCM-XCu powders were mixed with 6% graphite (pore former) and polyvinyl alcohol (PVA) as a binder, then ground in an agate mortar for 1 h and then unidirectionally pressed at 1 ton of pressure for 15 seconds. Finally, the resulting pellets with 25, 35 and 45% Cu in the perovskite $La_{0.8}Sr_{02}Cr_{05}Mn_{0.5}O_3$ were sintered in a platinum crucible. at 1200 ◦C for 75 minutes with a heating rate of and cooling of 3 and 5°C, respectively.

Finally, the $La_{0.7}Sr_{0.3}Cr_{0.4}Mn_{0.6}O_{3\text{-}\delta}$ + $XCu_{0.75}Ni_{0.25}$ perovskites with concentrations ranging, X from 25 to 75 % $Cu_{0.75}Ni_{0.25}$. The same procedure was considered as in the two previous cases. Ethylene glycol as an esterification agent was added in order to improve the ion solution. In order to obtain LSCM–$Cu_{0.75}Ni_{0.25}$ compositions, copper nitrate and nickel nitrate, with stoichiometric amounts were dissolved in distilled water through continuous stirring, reflux, and heating at the same LSCM temperature to form homogenous and transparent sol solutions. Afterward, LSCM nanometric powders were milled in an agate mortar for 1 h and impregnated with this solution to form LSCM– $XCu_{0.75}Ni_{0.25}$ compositions. Gels were dried under the same LSCM conditions and then, calcined in an alumina crucible at 450°C for 1 h in air atmosphere.

The XRD technique allows us to verify the degree of symmetry, crystallinity of the prepared compounds and to evaluate the purity of the phases. All the samples and porous cermets were analyzed by XRD using a diffractometer PANalytical model XPert'PRO, with Cu Kα (kα = 1.5456 A°) monochromatic radiation and θ–2θ geometry. XRD patterns were obtained from 20 to 80° 2θ angle range using step-scanning mode with a step of 0.01° and 100s of step counting time. Experimental crystal structure data parameters were refined by using the FullProof 2K [15] program. In situ reduction and cermet time reduction were obtained by collecting an individual diffraction pattern each 20 min, in periods of 8 h each by using a PSD-50m MBRAUN.

3. Results and Discussion

The results of the three perovskites synthesized by sol-gel are illustrated below. In the first instance crystal structure formation of the sintering samples in air at 1365°C for 1 h shows essentially crystallographic planes of the crystal family hexagonal perovskite $La_{0.7}Sr_{0.3}Cr_{0.4}Mn_{0.6}O_{2.85}$ (ABO_3) and NiO cubic structure (see figure 1). However, and after raising the temperature to 1050°C, the perovskite $La_{0.7}Sr_{0.3}Cr_{0.4}Mn_{0.6}O_{2.85}$. This perovskite was treated at a higher temperature of 1050°C, and during the first 2 hours no change in the symmetry of its crystalline structure was observed, however, after this incubation period exhibits symmetry breaking; perovskite crystallographic planes then begin to disappear and simultaneously crystallographic planes for tetragonal $La_{0.7}Sr_{0.3}Cr_{0.4}Mn_{0.6}NiO_{3.95}$ appear without diffraction features for an intermediate suboxide crystal structure (A_2BO_4) after this time tetragonal structure remains unchanged. This crystal structure transformation by splitting of the hexagonal (1 1 0) reflection into (1 1 0)/(1 0 3) tetragonal structure doublet can be due to the relative stability of the Mn^{3+} on the surface (first layer) and subsurface (second layer) regions of (0 0 l) hexagonal structure.

Concerning perovskite with copper additions ($La_{0.8}Sr_{02}Cr_{05}Mn_{0.5}O_3$ + XCu, X = 25, 35 and 45%), sintered at a temperature of 1200°C and reduced to hydrogen at 600°C it was observed that these samples have the same crystalline structure as the $La_{0.75}Sr_{0.25}Cr_{0.5}Mn_{0.5}O_3$ perovskite obtained by other authors [16]. In contrast to the previous perovskite (LSCM) with nickel, this perovskite exhibited no rupture of symmetry. In the diffractogram of figure 2, it is distinguished that the change of intensity in the crystallographic planes has a direct relation with the variation of the quantity of Cu in the composites, because when the quantity of LSCM decreases, the plane $(-111)_C$ of Cu increases but the plane of the perovskite $(104)_P$ decreases, which is proportional to the level of impregnation with Cu. In the lower part of the figure 2, it is observed that a single stable phase type $La_{0.8}Sr_{02}Cr_{05}Mn_{0.5}O_3$ without Cu impregnation has been

successfully formed, and subsequently the other phases of the perovskite are shown with the 25-45% Cu impregnation by weight. Clearly there is no evidence of secondary phase formation i.e. the structure of the perovskite remains unchanged.

In relation to perovskite $La_{0.7}Sr_{0.3}Cr_{0.4}Mn_{0.6}O_{3-\delta}$ (perovskite-type) nanocomposites impregnated with $XCu_{0.75}Ni_{0.25}$ (X = 25-75%), it was found that crystal symmetry of CuO and NiO nanoparticles have monoclinic *C*12/*c* and cubic Fm3m symmetry, respectively, but after sintering at 1,200°C and reducing the temperature to 600°C, it's transformed into a new $Cu_{0.75}Ni_{0.25}$ intermetallic solid solution without secondary phase. We have detected a cationic inter-diffusion in Cu and Ni interphase crystals during this reduction process; however, when sintering time exceeds 2 h at 1,200°C this reaction mechanism is interrupted by a sublimation phenomenon; which causes Cu_2O cubic structure segregation from monoclinic CuO structure. This leads to Cu precipitation from the $Cu_{1-x}Ni_x$ solid solution $Cu_{0.75}Ni_{0.25}$ inhibits the LSCM perovskite-type grain growth approximate to 220 nm. Figure 3 shows $La_{0.7}Sr_{0.3}Cr_{0.4}Mn_{0.6}O_{3-\delta}$– $XCu_{0.75}Ni_{0.25}$ powder XRD patterns after sol–gel synthesis and annealing at 1,050°C for 6 h. A single $La_{0.7}Sr_{0.3}Cr_{0.4}Mn_{0.6}O_{3-\delta}$-type phase is shown at the bottom (Fig. 3) without and with impregnation from 25 to 75 % $Cu_{0.75}Ni_{0.25}$. XRD patterns were indexed in a rhombohedral(hex)-type perovskite structure [17]. After the reduction process, it was observed that the oxides of copper and nickel were successfully transformed into a $Cu_{1-x}Ni_x$ (x = 0.25) intermetallic solid solution Therefore, there is a cationic inter-diffusion in the Cu and Ni interphase boundary crystals during the reduction process; this assertion is feasible according to the reaction mechanisms proposed by other authors [18]. However, when sintering time exceeds 2 h, this reaction mechanism is interrupted by a sublimation phenomenon; which causes Cu_2O cubic structure segregation from monoclinic CuO crystal structure (before reduction). $La_{0.7}Sr_{0.3}Cr_{0.4}Mn_{0.6}O_{3-\delta}$ perovskite structure cell volume is not altered by $Cu_{0.75}Ni_{0.25}$ (%) amount (before reduction). There is not evidence of volume increase by $Ni3^+$ partial substitution (0.56 angstrom, sixfold coordination) in $Cr3^+$ (0.61 angstrom, sixfold coordination), this indicates that the material has a high-stabilization perovskite phase because volume does not decrease. Therefore, there is no chemical reactivity by H_2–N_2 atmosphere incorporation.

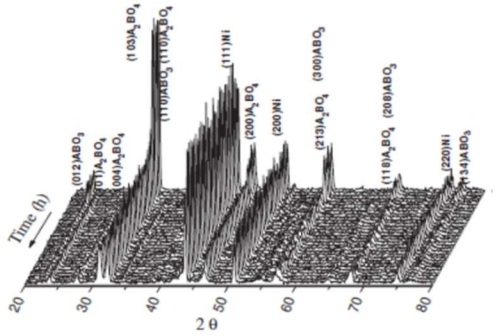

Fig. 1. Symmetry rupture of perovskite type ABO_3 to A_2BO_4.

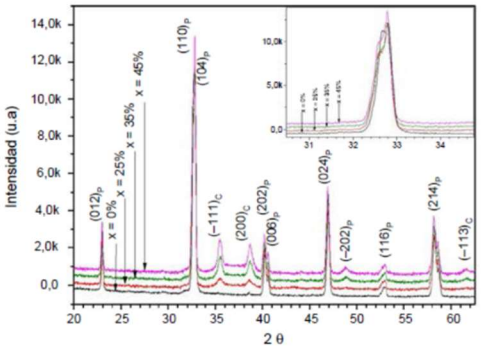

Fig. 2. X-ray diffraction patterns of perovskite LSCM (P) + XCu(c).

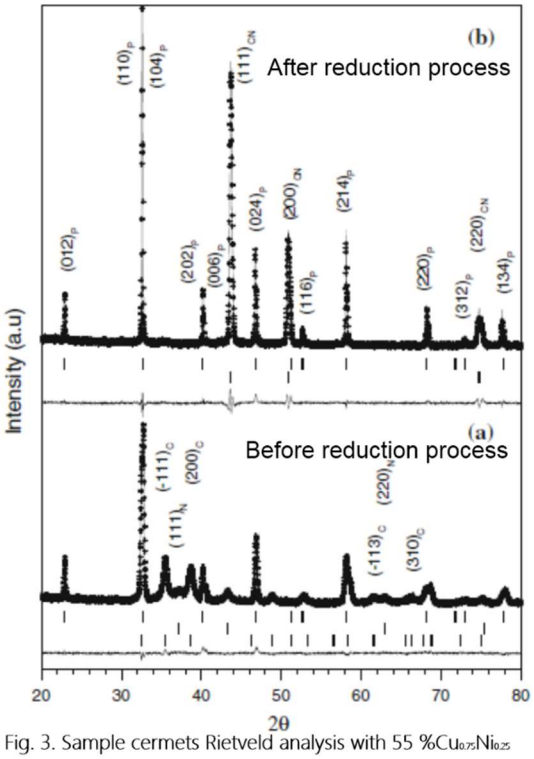

Fig. 3. Sample cermets Rietveld analysis with 55 %$Cu_{0.75}Ni_{0.25}$

4. Conclusion

An analysis of the symmetry of the crystalline structure of the perovskite $La_xSr_{1-x}Cr_yMn_{1-y}O_{3-\delta}$ with additions of nickel, copper and copper-nickel has been performed. In the case of cermets $La_{0.7}Sr_{0.3}Cr_{0.4}Mn_{0.6}O_{2.85}$ + Ni (25-75%) follows a high and low profile reduction while hexagonal perovskite particles are surrounding and then reduction process is obstructed, therefore there is a diffusion problem. When increasing the temperature to above 1050 ◦C, the symmetry breaking defect can be produced by introducing Ni^{2+} cations in the perovskite solid solution, but only after an induction period. In the $La_{0.8}Sr_{0.2}Cr_{0.5}Mn_{0.5}O_{2.85}$-XCu cermets (25-45%) no change of structure or origin of secondary phases was observed when the reduction of hydrogen in atmosphere at 800°C was performed. In relation to perovskite $La_{0.7}Sr_{0.3}Cr_{0.4}Mn_{0.6}O_{3-\delta}$ (perovskite-type) nanocomposites impregnated with

$XCu_{0.75}Ni_{0.25}$ (X = 25-75%), $La_{0.7}Sr_{0.3}Cr_{0.4}Mn_{0.6}O_{3-\delta}$ perovskite-type is highly stable, because a cell volume increase was not identified by partial substitution of Ni^{3+} in Cr^{3} and symmetry change from R3c to Pm3m space group. Therefore, there is no chemical reactivity by H_2–N_2 atmosphere incorporation. Finally it can be concluded that perovskite is stable and maintains its crystalline structure when impregnated with XCu (25-45%) or also with $XCu_{0.75}Ni_{0.25}$ (X = 25-75%). However, when synthesized only with XNi (X = 25-75%), the perovskite changes its symmetry from ABO_3 to A_2BO_4 at a temperature greater than 1000°C.

References

[1] Cano-Castillo U. La relevancia de desarrollar tecnologías de hidrógeno y celdas de combustible en México. *Boletín IIE* 2008; 143-51.

[2] Martinez AS, Brouwer J, Samuelsen GS. Comparative analysis of SOFC–GT freight locomotive fueled by natural gas and diesel with onboard reformation. Appl energ 2015; 148:421-38.

[3] Brunaccini G. Faro ML, La Rosa D, Antonucci V, Aricò AS. Investigation of composite Ni-doped perovskite anode catalyst for electrooxidation of hydrogen in solid oxide fuel cell. Int J Hydrogen Energ 2008; 33:3150-52.

[4] Baral AK, Sankaranarayanan V. Electrical study and dielectric relaxation behavior inánanocrystalline $Ce_{0.85}Gd_{0.15}O_{2-\delta}$ material at intermediate temperatures. App Phys A 2010; 98:367-73.

[5] Wang FY, Jung GB, Su A, Chan SH, Hao X, Chiang YC. Porous Ag–$Ce_{0.8}Sm_{0.2}O_{1.9}$ cermets as anode materials for intermediate temperature solid oxide fuel cells using CO fuel. J Power Sources 2008:185:862-66.

[6] Li Y, Guo Y, Xue B. Catalytic combustion of methane over M (Ni, Co, Cu) supported on ceria–magnesia. Fuel Process Technol 2009: 90:652-56.

[7] Faro ML, La Rosa D, Nicotera I, Antonucci V, Aricò AS. Electrochemical investigation of a propane-fed solid oxide fuel cell based on a composite Ni–perovskite anode catalyst. App Catal B-Environ 2009; 89:49-57.

[8] Reyes-Rojas A, Alvarado-Flores J, Esparza-Ponce H, Esneider-Alcala M, Espitia-Cabrera I, Torres-Moye E. Symmetry breaking and electrical conductivity of $La_{0.7}Sr_{0.3}Cr_{0.4}Mn_{0.6}O_{3-\delta}$ perovskite as SOFC anode material. Mater Chem Phys 2011; 126:773-79.

[9] Flores JJA, Cabrera IE, Valencia JE, Rojas AR. Impregnación de la perovskita $La_{0.8}Sr_{0.2}Cr_{0.5}Mn_{0.5}O_{3-\delta}$ como ánodo en celdas SOFC. Bol Soc Esp Ceram V 2015; 54:198-08.

[10] Alvarado-Flores J, Bocanegra-Berna MH, Espitia-Cabrera I, Torres-Moye E, Reyes-Rojas A. Synthesis, crystal stability, and electrical behaviors of $La_{0.7}Sr_{0.3}Cr_{0.4}Mn_{0.6}O_{3-\delta}$–$XCu_{0.75}Ni_{0.25}$ for its possible application as SOFC anode. J Mater Sci 2012; 47:8118-27

[11] Tao S, Irvine JT. Synthesis and Characterization of $(La_{0.75}Sr_{0.25})Cr_{0.5}Mn_{0.5}O_{3-\delta}$, a Redox-Stable, Efficient Perovskite Anode for SOFCs. J electroche Soc 2004; 151:A252-59.

[12] Wan J, Zhu JH, Goodenough JB. $La_{0.75}Sr_{0.25}Cr_{0.5}Mn_{0.5}O_{3-\delta}$+Cu composite anode running on H_2 and CH_4 fuels. Solid State Ionics 2006; 177:1211-17.

[13] Gaikwad SP, Dhesphande SB, Khollam YB, Samuel V, Ravi V. Coprecipitation method for the preparation of nanocrystalline ferroelectric $CaBi_2Ta_2O_9$. Mater Lett 2004; 58:3474-76.

[14] Murugan AV, Samuel V, Navale SC, Ravi V. Phase evolution of $NiTiO_3$ prepared by coprecipitation method. Mater lett 2006; 60:1791-92.

[15] Rodriguez-Carvajal J Wfp2k Rietveld Program, versión 2011. Laboratorie Leon Brillouin (CEA-CNRS) 2011.

[16] Chanquía CM, Montenegro-Hernández A, Troiani HE, Caneiro A. A bottom-up building process of nanostructured $La_{0.75}Sr_{0.25}Cr_{0.5}Mn_{0.5}O_{3-\delta}$ electrodes for symmetrical-solid oxide fuel cell: Synthesis, characterization and electrocatalytic testing. J Power Sources 2014; 245: 377-88.

[17] JCPDS-International Centre for Diffraction Data, Copyright (c) JCPDS-ICDD 2008, card 01-070-8672.

[18] Cangiano MDLA, Ojeda MW, Carreras AC, González JA, Ruiz MDC. A study of the composition and microstructure of nanodispersed Cu–Ni alloys obtained by different routes from copper and nickel oxides. Mater Charact 2010; 61:1135-46.

E018. IMPROVING PERFORMANCE OF ZNO DYE SENSITIZED SOLAR CELL BY INCORPORATION OF GRAPHENE OXIDE BY HIGH ENERGY MILLING

X. Atanacio-Sánchez[1], W.J. Pech-Rodríguez[1], Eddie N. Armendáriz-Mireles[1], P.C Meléndez-González[2], E. Rocha-Rangel[1*]

[1] Universidad Politécnica de Victoria, Av. Nuevas Tecnologías 5902, Parque Científico y Tecnológico de Tamaulipas, Ciudad Victoria, Tamaulipas, C.P. 87138. México.
[2]Programa de Nano ciencias y Nanotecnología, Cinvestav Unidad Saltillo, Av. Industria Metalurgia 1062, Parque Industrial Ramos Arizpe. Ramos Arizpe, Coahuila, C.P. 25900, México
* Corresponding author: 834 166 8789; erochar@upv.edu.mx

ABSTRACT

At today great interest has been paid to hydrogen production by water electrolysis due to their simplicity and low cost. Solar cells have been studied as promising renewable source for electrical power generation. They can be interconnected in order to obtain the necessary voltage to cause water electrolysis. Among the developed solar cells, dye sensitized solar cell are promising devices as renewable electrical power source to achieve water electrolysis because they possess high theoretical efficiency compared with Si based solar cells. In this research, ZnO photo catalyst was modified with graphene oxide (GO) by means of high energy ball milling and then was thermal treated at 420 °C for 2 h. The anode of the flexible dye-sensitized solar cell (FDSSCs) was fabricated by using the well know electrophoretic deposition process. The suspension for electrophoretic deposition consisted in a mixture of the as prepared photo catalyst dispersed in 2-propanol with magnesium oxide as charge agent. Meanwhile, the contra electrode was obtained by electrodeposition of Pt nanoparticles layer onto the flexible electrode. The synthetized materials were characterized by FTIR, XRD and SEM-EDS. The efficiency of the ZnO-GO was estimated from the VI curve, measured under simulated sunlight. The obtained results demonstrate that ZnO-GO have higher efficiency compared with the ZnO. The latter can be explained by the better dispersion of ZnO that enhance the dye adsorption onto the fabricated anode. Therefore, the efficiency of FDSSC can be enhanced by incorporation of GO into de ZnO matrix and in this manner more power energy will be available to carry out water electrolysis.

Keywords: Zinc Oxide, Graphene Oxide, Electrophoretic Deposition

1. Introduction

In recent years, renewable energy technology has been studied extensively in order to mitigate the environmental pollution and the depletion of fossil fuels. Therefore it is necessary to develop renewable energy and more accessible for example solar energy, specifically dye-sensitized solar cells (DSSC), as they have great benefits over other technologies, such as low cost materials, a simple manufacturing process, environmentally friendly [1].

Among semiconductor materials used in the fabrication of these DSSC, they have metal-oxides like titanium oxide (TiO_2), zinc oxide (ZnO), tin oxide (SnO_2), amount others, due to its physical and chemical properties [2]. However, these properties will be affected by the change in morphology and particle size of the nano-structures. TiO_2-based materials has been the most researched semiconductor to manufacture photo anodes in DSSC, but they suffer from poor photovoltaic efficiency caused by insufficient dye absorption and low energy value in the conduction band [3]. Therefore, the conversion efficiency based on TiO_2 is difficult to achieve due to its low electron mobility[4]. On the other hand, ZnO has been found to be an alternative, because it increase electron mobility, has wide band gap (3.3 eV), better stability against photo corrosion[5], and shows on improvement in dye adsorption compared to TiO_2 [6, 7].

On the other hand, polymeric flexible substrate are a current replacement of the glass material used in conventional solar cells, these flexible substrates are a good way to increase flexibility and reduce the weight of the substrates, these material can be polyethylene terephthalate (PET) and polyethylene naphthalene (PEN) [8], a comparison of glass substrates that are developed by methods were high temperatures are used, flexible substrates require methods where a low temperature is used to manufacture semiconductors [9], the low temperature methods used are press method, lift-off method, electro position and chemical tuning [8], as already mentioned due to the nature of the flexible substrate, the deposition of the material will be carried out by means of electrophoretic deposition which is very accessible, by which suspended particles are deposited when an electric field is applied, the particles move and adhere forming a layer on the electrode [10].

This work develops a simple and affordable procedure to activate pure ZnO and ZnO nano particles with graphene oxide (GO) for manufacturing FDSSC anodes using electrophoretic deposition, results

revealed that the structure of the ZnO was not affected in spite of incorporation, but there is a notable difference with respect to I –V.

2. Materials and Methods.

The development of semiconductors materials ZnO and ZnO-GO, was obtained by the activation of these in a planetary mill. Subsequently the powders are used in the manufacture of the FDSSC

2.1 Synthesis of ZnO and ZnO-GO photocatalysts

The ZnO-GO photocatalyst was synthesized as follows: first, 400 mg of commercial ZnO (Jalmek) powder and 1 mg of GO was grounded in a mortar. Then, the obtained sample was further mixed by using high-energy ball milling for 6 hours in a Retsch model PM 100 at 300 rpm. After that, the obtained powders were thermal treated at 420 °C with a heating ramp of 1 °C/min for 2 h. For comparison ZnO powder was also summited at the same treatment that ZnO-GO.

2.2 Manufacturing of FDSSCs

Flexible dye sensitized solar cell (FDSSC) was fabricated by using Poly-ethylene terephthalate (PET) doped with Indium Tin Oxide (ITO) from SOLARONIX. The obtained ZnO and ZnO-GO was used as photoanode semiconductor. The anode was fabricated by electrophoretic deposition (EPD) as follows: 40 mg of the obtained semiconductors was mixed by ultrasonication with 40 mL of isopropyl alcohol by 15 min, and then diluted magnesium oxide (MgO) in isopropyl alcohol was added as charge agent. Thereafter, the EPD was accomplished by applying 60 V between the PET electrode and a graphite counter electrode. The obtained sample was submitted to thermal treatment at 120 °C for 30 min and then was immersed in ethanolic solution of 0.5 mmol L^{-1} of N719 for 2 hours. On the other hand, the counter electrode was fabricated by electrodeposition of Pt nanolayer. The electrodeposition was carried out in a three electrode cell setup were the working electrode was the conductive PET and the counter electrode and reference electrode was graphite bar and Ag/AgCl electrode, respectively. 0.1 mmol L^{-1} chloroplatinic acid hexahydrate (Sigma-Aldrich) in 0.1 mol L^{-1} H_2SO_4 was used to achieve the electrodeposition of Pt layer.

The FDSCC was assembled in a typical sandwich configuration by using thermoplastic sealing of 60 µm thicknesses, heated at 120 °C for 2 minute on each side. The electrolyte solution, Iodolyte HI/30, was

injected in the small hole previously perforated of the counter electrode to fill the space between the photo anodes and counter electrode.

2.3. Physical and chemical characterization

The obtained ZnO and ZnO-GO was characterized by X-ray measurements in order to determine the crystal structrure, lattice parameter and crystallite size. X-Ray measurements were performed on a Phillips-X´Pert diffractometer using Cukα radiation (λ= 0.15406 nm) source, working voltage of 40 kV. The morphology of the synthesized powders was studied by field emission scanning microscopy. Meanwhile, FTIR measurement was performed in a WQF-510A FTIR Rayleígh instrument.

3. Results and Discussion

3.1. X-ray diffraction (XRD)

Figure 1 display the XRD patterns of the synthesized materials, they have reflections peaks attributed to a hexagonal wurzite crystal structure (according to JCPDS card No 36-1451), with the planes (100), (001), (101), (102), (110), (103), (200), (112) and (201) respectively [11]. It can be seen at first glance that no changes in the pattern is observed when graphene oxide was added.

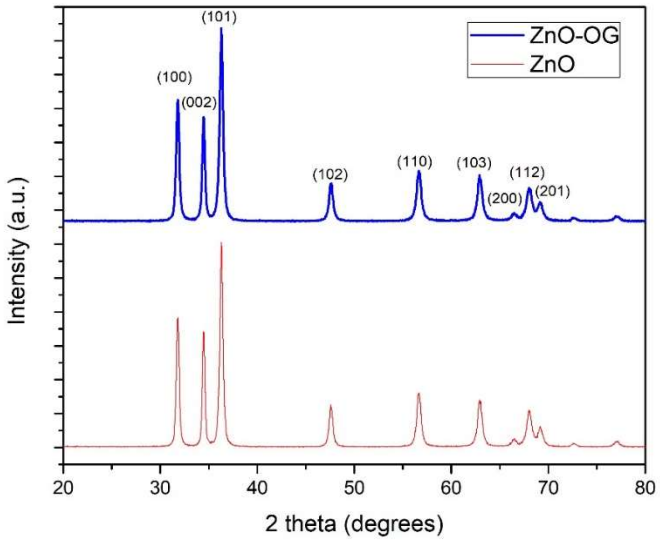

Fig. 1 X-ray diffraction of ZnO-GO and ZnO

Crystallite size was determined by using the well know Debye-Scherrer equation (1).

$$D = \frac{0.9\lambda_{K\alpha}}{\beta_{2\theta}cos\theta} \quad (1)$$

Where D is the crystallite size, 0.9 is the shape factor, λ radiation wavelength (0.15406 nm), $\beta_{2\Theta}$ the maximum width at half maximum and Θ is the diffraction angle of Bragg for each of the planes [12]. The obtained results are shown in table 1. On the other hand, other structural characteristics were also evaluated, such as the lattice parameter Eq. (2) [13], the theoretical density Eq. (3) and the surface area (S.A.) Eq. (4) [14].

$$sin^2\theta = \frac{\lambda^2}{4}\left[\frac{4}{3}\left(\frac{h^2+hk+k^2}{a^2}\right)\right] \quad (2)$$

$$\rho = \frac{nA}{V_c N_A} \quad (3)$$

Of the equation 2 has that ρ is the theoretical density, *n* is the number of atoms per unit cell, *A* is the atomic weight, V_c is the volume of the unit cell and N_A is the number de Avogadro.

In equation 3, *SA* is the surface area, *ρ* is the density of the sample and *d* is the crystallite size calculated by the equation of Scherrer.

$$SA = \frac{6X10^3}{\rho d} \quad (4)$$

Table 1 shows the data obtained for each of the equations mentioned above.

Tabla 2 Calculated physical parameters for ZnO and ZnO-GO

Sample	Average crystallite size (nm)	Lattice constant (Å)	Theoretical density (g cm^{-3})	Superficial area (m^2 g^{-1})
ZnO	20.7467	a=b=3.249110 c=5.205516	5.67829	50.93
ZnO-GO	19.5359	a=b=3.249060 c=5.205783	5.678055	50.090

3.1.2 Scanning Electron microscope (SEM)

The general morphology of ZnO and ZnO-GO was characterized by FESEM. Figure 2a shows the micrograph for ZnO, where very fine powders in the nonmetric range are observed. On the other hand, it is clearly observed that ZnO-GO (Figure 2b) has a better particle distribution.

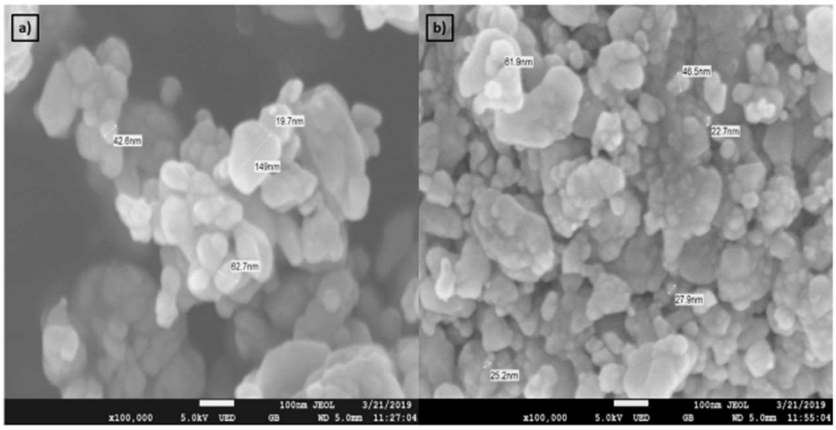

Fig. 2 Micrographs, a) ZnO and b) ZnO-GO

3.1.3 Energy Dispersive X-Ray Spectroscopy (EDS)

EDS analysis confirms the presence of chemical elements, see Figure 3 a-b. The samples present the peak relates to Zn and O and in the case of ZnO-GO the signal due to C element is also observed.

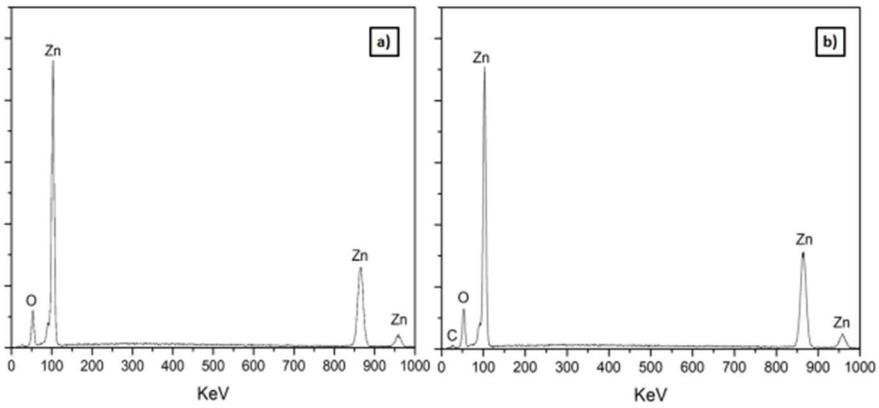

Fig. 3 Elementary distribution of samples

3.1.4 FTIR Characterization

The analysis was performed in order to identify the chemical bonds in the synthesized photocatalyst. Figure 3 shows the comparative spectra for ZnO and ZnO-GO, the strong perturbation in the range of 400-600 cm^{-1} can be assigned to the stretching vibration of ZnO [15, 16], A broad band is observed in 1080 cm^{-1} related to the C-O-C stretching vibration of some residual chemical agent in the ZnO and in the ZnO-GO as part of its nature [17], that is why in the ZnO-OH is shown more pronounced the stretching vibration, in addition as can be seen with the naked eye, the ZnO-GO shows a more intense downward disturbance than the ZnO, this disturbance is due to more energy being absorbed and this may be due to the particle size resulting in a higher surface area.

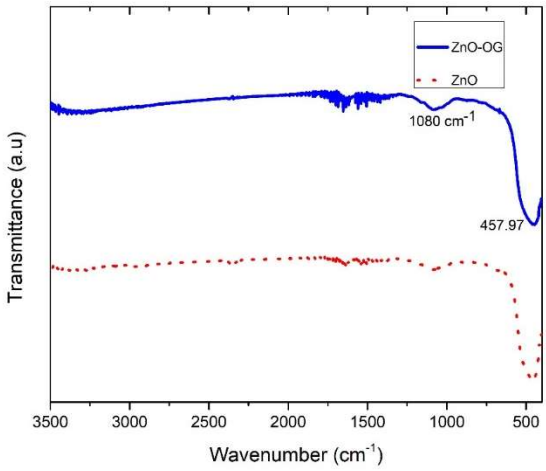

Fig. 4 FTIR spectra for the ZnO and ZnO-GO.

3.2 Electrical Characterization

The electrical characterization of current and voltage for the FDSSC, with ZnO and ZnO-GO, subject to the same methodology explained above, is shown below.

A solar simulator was used AM1.5 (sunLite model 11002, Abet Technologies) with a simulated light of 100 mW cm^{-2} and a potentiostat Gill AC (ACM instruments Ltd, Cumbria UK).

3.2.1 Current – Voltage Characterization

Fig. 4 shows the current –voltage curves for the FDSSC based on ZnO and ZnO-GO samples. It is observed that the short circuit current (J_{sc}) for the ZnO was 1.19 mA cm^{-2} with an open circuit voltage (V_{oc}) is at 0.558 V while for the ZnO-GO J_{sc} was 1.51 mA cm^{-2} with a V_{OC} of 0.51 V.

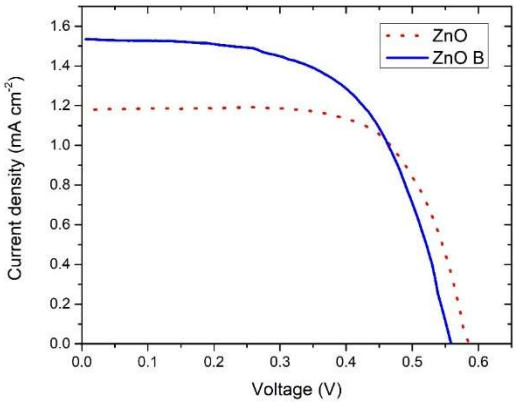

Fig. 5 J-V curves, comparison between ZnO and ZnO-OG

Table 3 shows the electrical parameters of the FDSSC, the efficiency was obtained from the equation (5).

$$\eta = \frac{P_{max}}{V_{max} J_{max}} \tag{5}$$

The efficiency for ZnO-OG is higher, just as the values of J_{sc} and V_{oc} are better.

Tabla 3 Characteristic parameters obtained for FDSSC prepared with ZnO and ZnO-GO

Sample	J_{sc} (mA cm^{-2})	V_{oc} (mv)	η (%)
ZnO	1.19	0.58	0.44
ZnO – GO	1.51	0.56	0.552

4. Conclusion

The use SEM, EDS, XRD allows to know the training the powder and check out that has been incorporated OG in the ZnO, with respect FTIR shows more absorbed energy, this is due to the smaller particle size, which results in a higher surface area and thanks to this, the collection of photons has been better in comparison with the sample containing only ZnO, it is for this reason that greater efficiency is achieved in FDSSC with ZnO-OG.

Acknowledgements

Xochitl Atanacio Sánchez thanks Conacyt for the scholarship granted for the completion of his master's studies.

References

E019. THE NEED FOR A PROYECT OFFICIAL MEXICAN STANDARD IN THE MANAGEMENT OF HYDROGEN

María Liliana Ávalos Rodríguez[1]*, José Juan Alvarado Flores[2], Jorge Víctor Alcaraz Vera[3]

[1] Centro de Investigación en Geografía Ambiental, Universidad Nacional Autónoma de México. Antigua Carretera a Pátzcuaro No. 8701, C.P. 58190, Morelia, Michoacán, México.

[2] Facultad de Ingeniería en Tecnología de la Madera, Universidad Michoacana de San Nicolás de Hidalgo. Santiago Tapia 403, CP 58000, Morelia, Michoacán, México.

[3]Instituto de Investigaciones Económicas y Empresariales, Universidad Michoacana de San Nicolás de Hidalgo. Francisco J. Mújica S/N, Col. Felicitas del Rio, C.P. 58000, Morelia, Michoacán, México.

* Corresponding author: +52 (443) 34095944; lic.ambientalista@gmail.com

ABSTRACT

Currently there is a global interest in the management of H_2 as an effective energy alternative that dissociates the dependence on fossil fuels, however, several studies have observed that resistance to H_2 prevails, especially in developing countries, the dangers and risks that its management represents. Despite this, there are a large number of publications that promote the sustainable management of H_2 and point out the advantages of its use in anthropogenic systems, which several countries with recognized technological advances, such as Germany, Spain, Canada, the United States and China, Japan, South Korea, among others, have not hesitated to promote the management of H_2 and incorporate the activities that arise from it, in a legal framework. It has been observed that, in Mexico, there is no legislation with respect to H_2, which promotes sustainable management, because energy dependence on fossil fuels still prevails. In the same way, it has been observed that there are no Official Mexican Standards that establish rules and specifications on H_2 management. In this context, this study aims to analyze the need to build, promote, publish and disseminate a Draft Official Mexican Standard (NOM) on H_2 management, based on the existing legal needs and absences. The main findings show that there is a legal feasibility in the promulgation of a NOM on H_2 management, which should consider, among other things: minimum safety requirements in the design, construction, operation and maintenance of H_2 storage terminals; as well as, the rules for obtaining and distributing the H_2.

Keywords: coercible; rule; risk; hydrogen management.

1. Introduction

Hydrogen (H_2) has been considered the fuel of the future because the only by-product is water [1], in addition to the fact that, unlike coal or oil, it cannot be extracted like fossil resources in general, despite its abundance in the universe [2], however, it is necessary to produce it from other raw materials that involve transformative actions, storage, transport and use that would allow the beginning of the H_2 era in the sense that energy needs would have no pollutants.

In addition to the above, H_2 can become inexhaustible, which has been an essential part of the new economic vision based on technological advances to avoid polluting gases. The so-called "hydrogen economy" is the reflection of this position and although it has been based on electrolysers and fuel cells invented in the 19th century, before the internal fuel engine was invented and the discovery of oil [3], it is until the last decade that the interest in hydrogen has been present in the technological advances of first world countries, such as the United States (USA), Canada, China, Iceland, some European countries, Holland, Sweden, Germany, Denmark, Japan, among others. In the same way, in the academic field, studies have been elaborated within the framework of H_2, such as Peschka, 1992; Lovins and Williams, 1999; National Research Council, 2004: Hoffmann, 2001; Rifkin, 2002; Wald, 2004; Service, 2004; Keith and Farell, 2003; Romm, 2004; Kreith and West, 2004; among others [4, 5, 6, 7, 8, 9, 10, 11, 12, 13].

The main challenges with the H_2, have been the conditions of storage, transport and use around the risks, dangers and damage that these activities could cause. Added to this are the regulatory obstacles that create legal, economic, social and technological barriers to the use and exploitation of H_2.

The economic cost of managing H_2 should not be forgotten; however, in quantification, it should be considered that the use of fossils will, in the short term, represent a greater cost both to the environment and to society, undermining development conditions.

Despite this, it has been estimated that the energy transition of H_2 will take between 30 and 50 years [3], so it is important to accelerate the pace to promote technological innovations that compensate for the efficient use of H_2.

However, in this transition it is pertinent to consider the energy access gap associated with the distribution of wealth faced by some countries, such as Mexico. In addition, there is currently a centralized political barrier in refineries that will limit, in the short term, the adoption of technological advances over H_2.

Added to the above is the absence of regulation regarding the use of H_2, from the storage, transport, management and use of H_2 as an alternative energy and not properly renewable. That is to say, in Mexico there is support for renewable energies such as wind in 2%, thermoelectric in 69%, geo thermoelectric in 6%, hydroelectric in 1%, dual in 12%, carboelectric in 7% and nucleoelectric in 6% [14].

In Mexico, the legislation in force that sustains energy matters is the Political Constitution of the United Mexican States (1917); Law of Geothermal Energy (2014); Law of Energy for the Countryside (2002); Law of the Regulatory Bodies Coordinated in Energy Matters (2014); Ley de Promoción y Desarrollo de los Bioenergéticos (2008); Ley de Transición Energética (2015); Ley que Declara Reservas Mineras Nacionales los Yacimientos de Uranio, Torio y las demás Substancias de las cuales se Obtengan Isótopos Hendibles que puedan Producir Energía Nuclear (1950); as well as various regulations such as the Geothermal Energy Law (2014); the Field Energy Law (2003); the Public Electric Energy Service Law on Contributions (1998); the regulation of the Law that Declares National Mining Reserves the Uranium, Thorium and other Substances from which Hendible Isotopes that can Produce Nuclear Energy are Obtained (1952).

As well as various complementary provisions such as the statute of the Professional Career Service of the Energy Regulatory Commission (2019); the statute of the Human Capital Management System of the Energy Regulatory Commission (2018); the Organic statute of the National Energy Control Center (2018); the Manual of Criteria for the Dispatch and Disaggregation of Energy for Jointly Owned Units in the Wholesale Electricity Market (2018); the manual of provisions relating to the supply and sale of electric energy intended for public service (2013); the Short-Term Energy Market manual (2016); the General Organization manual of the National Commission for the Efficient Use of Energy (2011); the General Organization manual of the National Energy Control Center (2018); among others.

For this reason, it is to be assumed that there are great challenges in Mexico, not only technological, but also political and legal, that allow the scientific advances proposed at the international level to be aligned with local social, cultural and technological conditions.

Therefore, the purpose of this study is to understand the regulatory advances that have regulated the storage, transport and use of H_2, in order to highlight the importance of developing a Mexican Official Standard (NOM) that requires certain conditions in the handling and management of H_2 in Mexico.

To this end, the study is divided into two sections, the first refers to the international context of H_2 regulations and the second to the essential guidelines to be covered by the NOM in Mexico, in order to promote the environmental, economic, technological and social use of H_2.

2. Materials and Methods

The study is carried out from a review of the literature on the main contributions in normative matter of H_2, comparing its content with the scopes of the existing normative dispositions, with the purpose of having the theoretical bases that sustain the importance of a NOM in the management of H_2 in Mexico.

3. Results and Discussion

3.1 International H_2 regulatory context

The results show that there is a clear need to move towards the H_2 economy, based on our own regulation in order to overcome the technological barrier [15 and 16].

There are studies that have emphasized the use of H_2, its extraction, its storage and its application, however, there is little research that talks about the importance of regulating the management of H_2, due to the constant concern of the risks, damages and dangerous that its management represents.

In the last decade there have been efforts to develop technical standards governing the handling of H_2, particularly in the USA, the European Union, Canada, Japan and China [15], focusing on requirements for the design, type of material, manufacture and testing of H_2 container cylinders. Leaving aside the next phase, the transport and use of the same.

In 1988 the ISO/TC 197 Technical Committee was created to develop standards for systems and devices for the production, storage, transport and use of H_2, of which the following stand out:

- ISO TR 15916 Basic Considerations for the Safety of Hydrogen Systems;
- ISO 14687-2 Hydrogen Fuel - Product Specification, Part 2: PEM fuel cell applications for road vehicles;
- ISO TC197 Working Group 9 (ISO 16110-2) Hydrogen Generators Using Fuel Processing Technologies Part 2: Test Method for Performance;
- IEC 60079-29-2 Explosive atmospheres, and

- ISO/TS 19881

ISO/TR 15916:2015 provides guidelines for the use of hydrogen in its gaseous and liquid forms as well as its storage in either of these or other forms (hydrides). It identifies the basic safety concerns, hazards and risks, and describes the properties of H_2 that are relevant to safety. Detailed safety requirements associated with specific hydrogen applications are treated in separate International Standards.

ISO 14687-2:2012 specifies the quality characteristics of hydrogen fuel in order to ensure uniformity of the hydrogen product as dispensed for utilization in proton exchange membrane (PEM) fuel cell road vehicle systems.

ISO 16110-2:2010 provides test procedures for determining the performance of packaged, self-contained or factory matched hydrogen generation systems with a capacity less than 400 m3/h at 0 °C and 101,325 kPa, referred to as hydrogen generators, that convert a fuel to a hydrogen-rich stream of composition and conditions suitable for the type of device using the hydrogen (e.g. a fuel cell power system, or a H_2 compression, storage and delivery system).

IEC 60079-29-2 Explosive atmospheres – Part 29-2: Gas detectors - Selection, installation, use and maintenance of detectors for flammable gases and oxygen.

ISO/TS 19880-1:2016 which standardizes H_2 charging stations and the creation of infrastructure for H_2. This international standard covers from the production and supply of H_2 considering the storage and fuel supply of an H_2 vehicle.

In 2018 ISO 19881:2018 (E) [17] is published containing requirements for the material, design, manufacture, marking and testing of serially produced refillable containers intended solely for the storage of compressed hydrogen gas for the operation of land vehicles.

Other norms of some countries stand out as:

- Commission Regulation (EU) No 406/2010 of 26 April 2010 implementing Regulation (EC) No 79/2009 of the European Parliament and of the Council on type-approval of hydrogenpowered motor vehicles, Promulgated by The European Union;

- GB/T 35544-2017 Fully-wrapped carbon fiber reinforced cylinders with an aluminum liner for the on-board storage of compressed hydrogen as a fuel for land vehicles, promulgated by General

Administration of Quality Supervision, Inspection and Quarantine of the People's Republic of China and Standardization Administration of the People's Republic of China.

- SAE J2579-2018 standard for fuel Systems in fuel cell and other hydrogen vehicles, promulgated by SAE international in United States.

In spite of this, the main findings show that current regulations, whether called laws, codes or norms, are an obstacle to the management of H_2 [16] because they are international standards that have not been taken to local regulation to make their scope effective, in addition to the fact that these international standards are voluntary, which allows for the continuation of the fossil-based energy backlog.

This is the case of Mexico, which, lacking mandatory standards, continues to focus energy satisfaction on oil-based energy and leaving aside advances in energy from H_2.

3.2 Normative provisions in Mexico on H_2

The results show that in Mexico the legal provisions on energy focus their attention on fossil fuels and in a little relevant way on renewable energies, despite the fact that it has been recognized that it is prevailing in the country to emphasize alternative energies starting from H_2 [14, 18, 19].

The Secretary of Labour and Social Security (STPS by its acronym in Spanish) currently has NOM´S which outlines safety provisions, such as NOM-026-STPS-2008, on colours and signs of safety and hygiene, and identification of risks from fluids conducted in pipelines and NOM-018-STPS-2000 on the system for the identification and communication of dangers and risks from dangerous chemical substances in workplaces. On the other hand, the Mexican norm (not mandatory) stands out: NMX-R-019-SCFI-2011on the harmonized system of classification and communication of dangers of chemical products.

This makes it possible to suppose that it is necessary to create an NOM with a mandatory condition that regulates the handling of H_2 in its different phases of handling, under the notions of risk, danger and environmental, economic, social and technological damage.

The literature suggests that risk is considered from the probability of causing harm; the harm is considered as loss or impairment and the danger will be the condition or situation of causing harm, i.e. it depends on the levels of risk [16].

In Mexico, this must be aligned with the provisions of the Federal Environmental Liability Law which alludes to the conditions of damage, its repair and compensation.

Therefore, it is suggested that according to the provisions of the Federal Law on Metrology and Standardization and under the context of the provisions of the Political Constitution of the United Mexican States (1917); the Law of Geothermal Energy (2014); the Law of Energy for the Field (2002); the Law of the Regulatory Bodies Coordinated in Energy Matters (2014); the Law for the Promotion and Development of Bioenergy (2008); the Energy Transition Law (2015); the Law that Declares National Mining Reserves the Uranium, Thorium and other Substances from which Hendible Isotopes that can Produce Nuclear Energy are Obtained (1950); the Federal Law for Environmental Responsibility (2013), as well as various regulations, statutes and manuals, create the NOM on the management of H_2.

The first approach in the regulation of gas storage is observed in the Official Mexican Standard Project PROY-NOM-013-SECRE-2012, which addresses safety requirements for the design, construction, operation and maintenance of liquefied natural gas storage terminals that include systems, equipment and facilities for reception, conduction, vaporization and delivery of natural gas; However, it can be assumed that this NOM is centralized to petroleum products and only in its section on "Dangers of internal origin that are not specific to liquefied natural gas" refers to services and chemicals from compressed gases, nitrogen and hydrogen, among others.

This allows us to assume that the safety of H_2 is limited to the possible risks involved in its manipulation by human beings, based on an effect on it, focusing its attention on the STPS; therefore, it may be thought that other environmental, economic and technological factors are absent; Hence the need to consider the preparation and publication of a NOM from the Ministry of Energy (SENER by its acronym in Spanish) with the support of the Ministry of the Environment and Natural Resources (SEMARNAT by its acronym in Spanish) and even the participation of the STPS and the Ministry of Communications and Transport (SCT by its acronym in Spanish), to encompass the actions of handling H_2, from its procurement, storage (ventilation conditions, materials of storage cylinders, detection of leaks, characteristics of condensation and entry of fluids, among others), as well as its transport and use.

Under this argument and considering that H_2 presents an extreme inflammability in air compared to other gases, physiological, physical and chemical risks must be considered, establishing a section in the NOM on the main risks associated with the handling of H_2 from leaks, dispersion, failures in storage cylinders, failures in the opening and closing systems of the cylinders, purging, failures in the vaporization systems, air condensation, leaks and explosions; risks due to freezing, respiratory diseases and asphyxia.

Likewise, the proposed NOM should consider the characteristics regarding the containment, detection and ventilation of H_2, according to the storage area, the conditions of storage away from combustible material, indirect heating, ventilation in the event of the loss of H_2, ensuring continuous renewal of the air to avoid concentrations of H_2, avoiding electrical sources of ignition, among others.

Finally, a risk study should be requested due to the H_2 management activity and all relevant measures should be taken for a highly risky activity, of federal competence.

These considerations go beyond the risks that any person faces when managing H_2, because it is necessary to consider the environmental conditions in order to minimize the dangers, the risks and, therefore, the damages that can not only be social but also environmental.

4. Conclusion

H_2 as any gas represents a risk, however, it has been observed that it is not toxic, it spreads quickly which means less damage than an explosion based on other fuel because the area of explosion is smaller than the area of other fossil fuels. This allows us to suppose that the environmental damage could be less (in expansion), but the conditions to be produced are different from fossil fuels, which is why it is necessary to have an NOM that obliges those who handle H_2 in terms of environmental and social security.

Acknowledgements

To the Research Center in Environmental Geography of the National Autonomous University of Mexico, Campus Morelia; to the National Council of Science and Technology (CONACYT) and a special thanks to all the people involved for their contributions, corrections and suggestions.

References

[1] Bennaceur, K., Clark, B., Orr Jr, F. M., Ramakrishnan, T. S., Roulet, C., & Stout, E. (2005). El hidrógeno: ¿Un futuro portador energético? Gas, 25(20.1), 15-3.

[2] Hortal, M. A., & Barrera, A. L. M. (2012). El hidrógeno: fundamento de un futuro equilibrado. Ediciones Díaz de Santos.

[3] Berry, G. D., & Aceves, S. M. (2006). La economía del hidrógeno como solución al problema de la estabilización del clima mundial. Acta universitaria, 16(1), 5-14.

[4] Peschka, W. (1992). Liquid Hydrogen: Fuel of the Future, New York, Springer.

[5] Lovins, A.B., y Williams, B.D. (1999). A Strategy for the Hydrogen Transition. Proceedings of the 10th Annual US Hydrogen Meeting, National Hydrogen Association, Vienna, VA.

[6] National Research Council and National Academy of Engineering. (2004). The Hydrogen Economy: Opportunities, Costs, Barriers and R&D Needs. The National Academies Press, Washington, DC.

[7] Hoffmann, P. (2001). Tomorrow's Energy. MIT Press, Cambridge, MA.

[8] Rifkin, J. (2002). The Hydrogen Economy: The Creation of the Worldwide Energy Web and the Redistribution of Power on Earth. New York, Tarcher/Putnam. [9] Wald, M.L. (2004). Questions About a Hydrogen Economy. Scientifi c American. 290(5) 66-73

[10] Service, R.F. (2004). The Hydrogen Backlash. Science, 305, August 13, pp. 958- 961, publicado como parte de una sección especial "Toward a Hydrogen Economy," Editado por Coontz, R., y Hanson, B., pp. 957-976.

[11] Keith, D.W., y Farrell, A.E. (2003). Rethinking Hydrogen Cars. Science. 301, July 18, pp. 315-316.

[12] Romm, J.J. (2004). The Hype about Hydrogen: Fact and Fiction in the Race to Save the Climate. Island Press, Washington. [13] Kreith, F., y West, R. (2004). Fallacies of a Hydrogen Economy: A Critical Analysis of Hydrogen Production and Utilization. Journal of Energy Resources Technology. 126 (2)249-257

[14] Vásquez, A. L. (2015). Desarrollo y prospectivas de energía renovable en México. Revista Economía Informa, 390, 132-153.

[15] Wang, D., Liao, B., Zheng, J., Huang, G., Hua, Z., Gu, C., & Xu, P. (2019). Development of regulations, codes and standards on composite tanks for on-board gaseous hydrogen storage. International Journal of Hydrogen Energy.

[16] Mair, G. W., & Hoffmann, M. (2014). Regulations and research on RC&S for hydrogen storage relevant to transport and vehicle issues with special focus on composite containments. International Journal of Hydrogen Energy, 39(11), 6132-6145.

[17] ISO 19881:2018 Gaseous hydrogen - Land vehicle fuel containers, promulgated by International Organization for Standardization.

[18] Flores, J. J. A., Valencia, J. E., & Rodríguez, M. L. Á. (2015). La necesidad de incorporar el hidrógeno como potencial fuente alterna de energía en la legislación mexicana. Revista Catalana de Dret Ambiental, 6(1).

[19] Sánchez, B. F., (2016) Plan Nacional de Hidrógeno: Alternativa Energética, https://petroquimex.com/PDF/SepOct16/Plan_Nacional_de_Hidrogeno.pdf [accessed 01.07.19].

E020. MOF 253-Pt A VIABLE OPTION FOR HYDROGEN PRODUCTION VIA PHOTOCATALYSIS

V. Ávila Vázquez[1] *, J. N. Pérez Viramontes[2], I.L. Escalante-García[2], V. H. Collins Martínez[3] , S.M. DurónTorres[2].

[1] Instituto Politécnico Nacional - Unidad Profesional Interdisciplinaria de Ingeniería Campus Zacatecas. Calle Circuito del Gato 202, Ciudad Administrativa, 98160 Zacatecas, Zac

[2]Universidad Autónoma de Zacatecas, Área de Ciencias Químicas, Carretera Zacatecas-Guadalajara km 6, Ejido "La Escondida", Edificio 6, C.P. 98160, Zacatecas, Zac.

[3]S.C. Depto. de Ingeniería y Química de Materiales, Centro de Investigación en Materiales Avanzados, Miguel de Cervantes 120, Complejo Industrial Chihuahua, 31190 Chihuahua, Mexico.

* Corresponding author: vav_taba@hotmail.com

Metal–Organic Frameworks (MOFs) have attracted increasing attention for the creation of solid-state platforms for catalysis applications, the MOFs are solid materials formed by metal ions (or clusters) coordinated to multidentate organic molecules [1]. The use of sunlight for the direct conversion of water into fuel is envisioned as essential process for sustainable production of hydrogen [2]. This work presents the results the physicochemical characterization of MOF 253 using Pt as metal ion for Hydrogen production from water. The material was synthesized by microwave methods, the specific surface of the particles ranged from 4 m^2/g. Their composition was studied by means of X-ray diffraction. The widths of band gaps were examined using UV-VIS spectroscopy. The E_g values of MOF 253-Pt were 3.27 eV. The photocatalytic activity of the samples prepared was tested on hydrogen production 128 µmol in 8 h with catalytic load of 10 mg compared with produced one by TiO_2 of 223 µmol de H_2 with catalytic load of 50 mg. MOF 253-Pt represents a viable option for the production of H_2 via photocatalysis.

1. Introduction

Metal-organic frameworks (MOFs, also known as porous coordination polymers or PCPs) are an emerging class of porous materials constructed from metalcontaining nodes (also known as secondarybuilding units, or SBUs) and organic linkers [3]. MOF crystals are produced by a process of self-assembly, which allows (under the proper conditions) for the spontaneous formation of ordered lattices. This bottom-up approach enables the growth of beautiful hybrid crystals with complex supramolecular architectures [4]. As a result, MOFs have shown remarkable capabilities in application áreas where the accessible surface area is a critical feature, such as in gas storage[5,6] separation [7], catalysis [8], sensing [9], microelectronics[10,11], pollutant sequestration [12-14]. This article present the result of use MOF 253-Pt for the photocatalytic production of molecular hydrogen and copared with TiO_2 showing that the MOF 253-Pt present advantage in the productión of H_2.

2. Materials and Methods

2.1. Synthesis of MOF 253-Pt

Pt based MOF-253 materials as the electrocatalyst precursor were synthesized in two steps according to the reported procedure [15]. For the microwaves synthesis the procedure was followed with the time change: to synthesize MOF-253 (first step), 151 mg of $AlCl_3$:$6H_2O$ was dissolved in DMF (10 mL), followed by the addition of 153 mg of 2,20-bipyridine-5,50-dicarboxylic acid (bpydc). The obtained mixture was then placed in a Teflon capped vial and heated at 120 °C for 6 min in microwaves. The resulting white microcrystalline powder was then filtered and washed with DMF. To obtain fully desolvated framework, this powder was subsequently washed with methanol in microwaves for 5 min, then collected by filtration and finally dried at 180 °C under dynamic vacuum for 12 h [16,17]

In order to introduce Pt atoms (second step), 500 mg of the desolvated MOF-253 was mixed with 386 mg of $PtCl_2$ $(CH_3CN)_2$ and acetonitrile (15 mL). This mixture was then heated at 85 °C in a Teflon-capped vial for 5 min. The resulting solid was collected by filtration and immersed in acetonitrile (15 mL). The total immersion time was three days and the solvent was replaced with fresh acetonitrile after each 24 h. Finally, the product (hereafter referred to as Pt-MOF and Ru-MOF) was collected by filtration and dried at 150 °C for 12 h under vacuum [16, 17].

2.2. Phisicochemical characterization

The phase identification and crystallinity of the synthesized MOF 253-Pt was determined by X-ray diffraction (XRD) using a Panalytical XpertPRO diffractometer with Cu Ka radiation (λ = 1.5406 Å). Phase recognition was obtained by comparison to Joint Committee on Powder Diffraction Standards (JCPDS) files. The BET specific surface areas (SBET) was calculated from the isotherm analysis in the relative pressure range, where a linear BET plot with positive C constant was obtained. The transmission electron microscopy (TEM) images were obtained using NANOTECH CIMAV modelo JEM-2200FS operated at 200 kV. Diffuse reflectance UV/VIS spectra were measured using Agilent, Cary 5000 spectrometer, the band gap energy values of the materials were determined from their UV absorption spectra in the reflection mode. According to the Kubelka-Munk theory, the band gap was obtained by plotting $[F(R\infty)\cdot E]^{1/2}$ vs. energy of the exciting light (E) assuming that materials showed direct allowed transition[18]

2.3 Testing of photocatalytic activity

Into the photoreactor **For each experiment** containing 100 ml of EtOH and 100 ml of destilled water and 50 mg of TiO_2 or 10 mg of MOF 253-Pt. The suspension was stirred and irradiated for 8 h. The radiation wavelength range was 254 nm. The gaseous products (H_2) of water/methanol photolysis were analysed on a gas chromatograph (GC-TCD (Thermo Scientific, TRACE GC Ultra).

3. Results and Discussion

The MOF 253 –Pt was chosen as a prototype because it exhibits high surface area, high chemical and thermal stability as well as a rigid framework structure (Figure 1). In MOF-253, one-dimensional chains of hydroxide-bridged, octahedrally coordinated Al^{3+} cations are linked via bpydc 2- ligands to give a three-dimensional framework with rhombic channels [19]. According to the previous observations upon insertion within the framework, the Pt atom is expected to fit the usual square planar geometry, with two Cl- ions and two N atoms from bpydc [19].

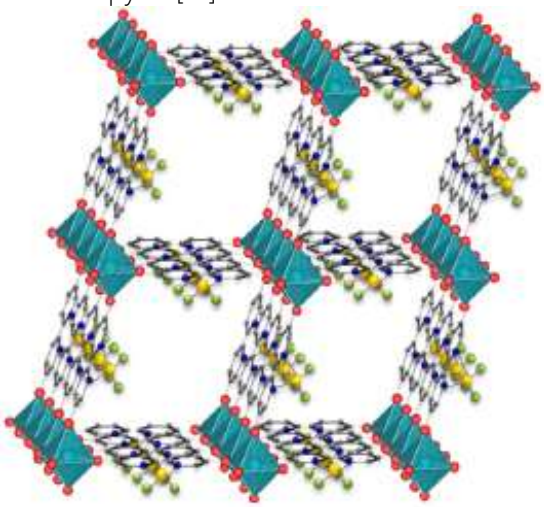

Figure 1. Structure of Pt-MOF. Al atoms (cyan octahedra), yellow, green, red, blue, and gray spheres stand for Pt, Cl, O, N, and C atoms, respectively; H atoms are omitted for simplicity [17].

As shown in Figure 2 XRD pattern of a) Pt and MOF 253 -Pt, sintetized in this work b) MOF 253 and MOF 253-Pt exhibits similar diffraction peaks to that of the synthesized MOF-253[20]. The diffraction peaks observed at around 2θ =39.8°, 46.28° y 67.53°, were attributed to Pt (1 1 1), (2 0 0), (2 2 0) crystalline planes, representing typical crystalline Pt face-centered cubic (fcc) structure. It can also be seen from Fig. 2 b) that Al although present in high content is not XRD visible. In addition, the XRD patterns did not show any trace of Pt oxide phases.

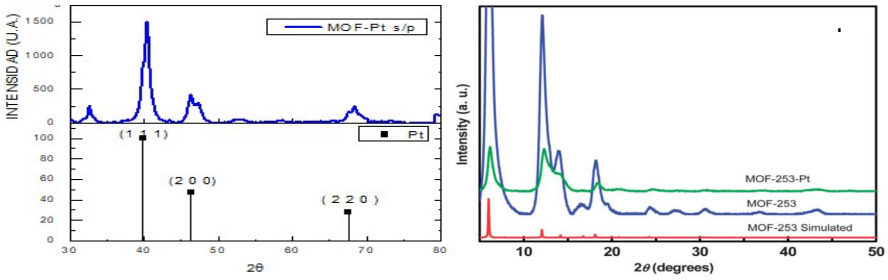

Figure. 2 Powder X-ray diffraction patterns a) Pt and MOF 253-Pt, b) of simulated MOF-253, methanol/exchanged MOF-253 and MOF-253-Pt[20]

TEM images (Figure 3) of the a) MOF 253 show nanometric particles b) MOF 253-Pt present dark areas related to the presence of metal (Pt) and nanometric particles similary a MOF 253.

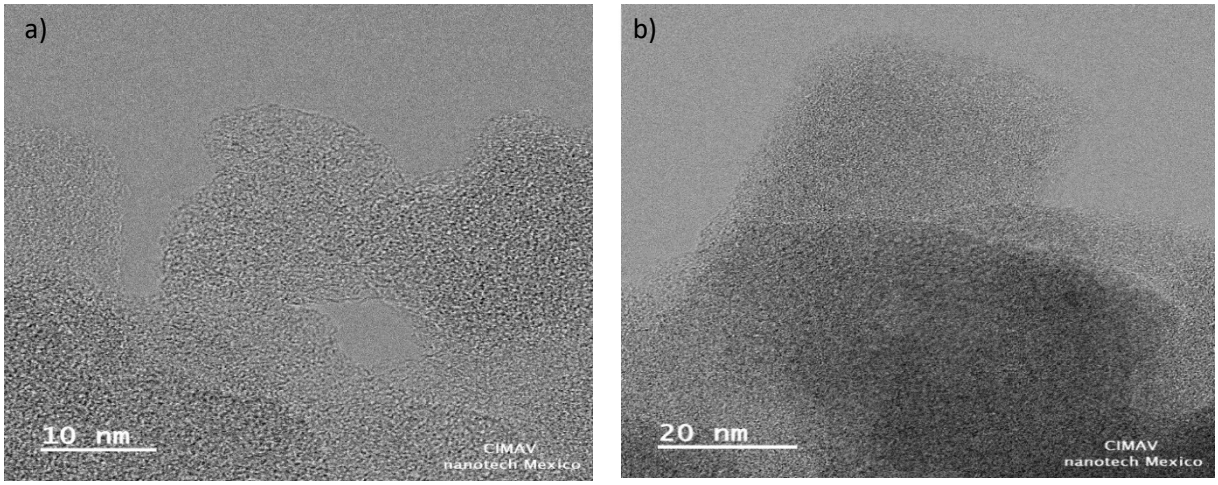

Figure 3 TEM images of a) MOF, b) MOF 253-Pt.

The Table 1 shows the specific surface area, the área decrease when the Pt is added may be due to the restructuration betwen Pt and MOF.

Table 1. BET specific surface area particle of MOF materials.

Sample	S BET (m^2 gr^{-1})

MOF 253	81
MOF 253-Pt	4

In Fig. 4, compared to an absorption edge at 310 nm of TiO_2, the absorption edge of MOF 253-Pt is obviously purple-line. Furthermore, in agreement with its bright yellow color, MOF 253-Pt shows an extra absorption band centered at about 410 nm with the absorption edge extended to around 550 nm. These features are attributed to the binding of PtCl2 to bipyridine. The low-energy absorption in MOF-253-Pt is due to the metal-to-ligand (Pt^{II} → bipyridine π^*) charge transfer (MLCT) transition [20].

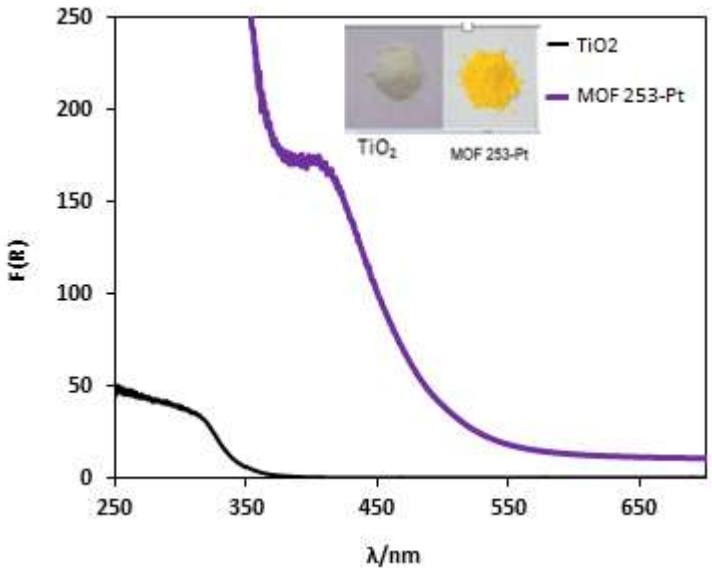

Figure. 4 UV-vis spectra of TiO2 and MOF 253-Pt. The inset shows the colors of the samples.

In the Table 2 show the band gap of TiO_2 y MOF 253-Pt from UV–Vis spectroscopy, shows that the band gap energy of is MOF 253-Pt less when is used photocalyst for production of H_2, which represent an energy reduction for reaction.

Table 2. Band gap energy of Materials sintetized.

Materials	E_{bg} /eV
TiO_2	3.32
MOF 253 -Pt	3.10

The photocatalytic activity of MOF 253-Pt for H_2 evolution was evaluated using ethanol as a sacrificial electron donor in water under visible-light irradiation (4400 μW/cm^2). Figure 5 shows that H_2 production increased stepwise with time upon light irradiation, and better results when use the MOF 253 –Pt. The literature

report that the evolution rate significantly depends on the concentration of Pt inserted in MOF-253-Pt and the results suggest that the rate may also depend on the extent of photon absorption by MOF[20].

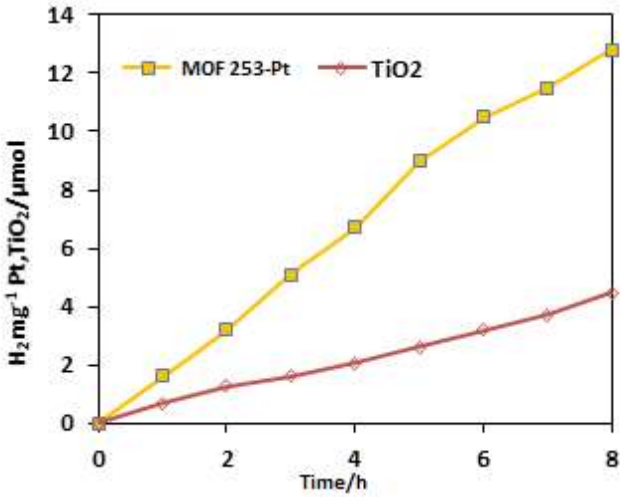

Figure 5 . Photocatalytic hydrogen evolution rate from a 50% v/v water–ethanol mixture, in the presence of TiO_2 and MOF 253-Pt

4. Conclusion

In conclusion, the MOF 253- Pt is a photosensitizer and a photocatalytic H_2 evolution catalyst. Although the precious metal was employed, importantly, we realized that the photocatalytic H_2 evolution can occur without an additional co-catalyst and photosensitizer over such a bifunctional MOF obtained. This work also demonstrates that the concept of inserting metal salts in a porous framework can be employed successfully as a strategy for designing and constructing new types of photocatalysts for H_2 production.

Acknowledgements

The authors wish to thank the Mexican CONACyT for financial support of this work and the SMH and XVII International Congress of the Mexican Hydrogen Society.

References

[1] Sonja Pullen, Sascha Ott , Photochemical Hydrogen Production with Metal–Organic Frameworks, Top Catal, 2016, 59:1712–1721.

[2] Olivier Rosseler, Muthukonda V. Shankar 1, Maithaa Karkmaz-Le Du, Loïc Schmidlin, Nicolas Keller, Valérie Keller, Solar light photocatalytic hydrogen production from water over Pt and

Au/TiO2(anatase/rutile) photocatalysts: Influence of noble metal and porogen promotion, Journal of Catalysis, 2010, 269, 179–190

[3]Hong-Cai Joe, Zhou, Susumu Kitagawa, Metal–Organic Frameworks (MOFs), Chem. Soc. Rev., 2014; 43, 5415-5418.

[4] Paolo Falcaro, Raffaele Ricco, Cara M. Doherty, Kang Liang, Anita J. Hill, Mark J. Styles, MOF positioning technology and device fabrication, Chem. Soc. Rev., 2014; 43, 5513-5560

[5] K. Sumida, D. L. Rogow, J. A. Mason, T. M. McDonald, E. D. Bloch, Z. R. Herm, T.-H. Bae and J. R. Long, Carbon dioxide capture in metal-organic frameworks. Chem. Rev., 2012, 112, 724-781.

[6] M. P. Suh, H. J. Park, T. K. Prasad and D.-W. Lim, Hydrogen storage in metal-organic frameworks Chem. Rev., 2012, 112, 782-835.

[7] J.-R. Li, J. Sculley and H.-C. Zhou, Metal–Organic Frameworks for Separations, Chem. Rev., 2012, 112, 869-932.

[8] M. Yoon, R. Srirambalaji and K. Kim, Homochiral Metal–Organic Frameworks for Asymmetric Heterogeneous Catalysis, Chem. Rev., 2012, 112, 1196-1231.

[9] L. E. Kreno, K. Leong, O. K. Farha, M. Allendorf, R. P. Van

Duyne and J. T. Hupp, Metal-organic framework materials as chemical sensors, Chem. Rev., 2012, 112, 1105-1125.

[10] A. A. Talin, A. Centrone, A. C. Ford, M. E. Foster, V. Stavila,

P. Haney, R. A. Kinney, V. Szalai, F. E. Gabaly, H. P. Yoon,

[11]F. Le´onard and M. D. Allendorf, Tunable electrical conductivity in metal-organic framework thin-film devices, Science, 2014, 343, 66-69.

[12] C. M. Doherty, E. Knystautas, D. Buso, L. Villanova, K. Konstas, A. J. Hill, M. Takahashi and P. Falcaro, Magnetic framework composites for polycyclic aromatic hydrocarbon sequestration,

J. Mater. Chem., 2012, 22, 11470-11474.

[13] C. M. Doherty, G. Grenci, R. Ricco`, J. I. Mardel, J. Reboul,S. Furukawa, S. Kitagawa, A. J. Hill and P. Falcaro, Combining UV lithography and an imprinting technique for patterning metal-organic frameworks, Adv. Mater., 2013, 25, 4701-4705.

[14] S.-H. Huo and X.-P. Yan, Facile magnetization of metal-organic framework MIL-101 for magnetic solid-phase extraction of polycyclic aromatic hydrocarbons in environmental water samples. Analyst, 2012, 137, 3445-3451.

[15] Ge L., Yang Y., Wang L, Zhou W., Dre M. R. , Chen Z., Zou J, Zhu Z., High activity electrocatalysts from metal–organic framework-carbon nanotube templates for the oxygen reduction reaction, Carbón, 2015:82, 417-424.

[16] Yin F., Li G., Wang H., Hydrothermal synthesis of α-MnO2/MIL-101(Cr) composite and its bifunctional electrocatalytic activity for oxygen reduction/evolution reactions, Catal. Commun. 2014:54, 17-21.

[17] F. Afsahi, H. Vinh-Thang, S. Mikhailenko, y S. Kaliaguine, «Electrocatalyst synthesized from metal organic frameworks», J. Power Sources, 2013;239: 415-423.

[18] López R, Gómez R, Band-gap energy estimation from diffuse reflectance measurements on sol–gel and commercial TiO2: a comparative study. J Sol Gel Sci Technol , 2011, 61:1–7.
[19] E.D. Bloch, D. Britt, C. Lee, C.J. Doonan, F.J. Uribe-Romo, H. Furukawa, J.R. Long, O.M. Yaghi, Metal Insertion in a Microporous Metal– Organic Framework Lined with 2, 2′-BipyridineJ. Am. Chem. Soc. 2010, 132: 14382-14384.
[20] Tianhua Zhou, Yonghua Du, Armando Borgna, Jindui Hong, Yabo Wang, Jianyu Han, Wei Zhang Rong Xu, Post-synthesis modification of a metal–organic framework to construct a bifunctional photocatalyst for hydrogen production, Energy Environ. Sci., 6:3229-3234.

E021. CONVERSION OF CRUDE GLYCEROL TO PYOCYANIN FROM *Pseudomonas aeruginosa* NEJ01R FOR USE IN BIOELECTROCHEMICAL SYSTEMS

Francisco Javier Bacame-Valenzuela[1,2], Antonia Sandoval-González[1,2], Jovita Valdez-Paz[1], Maria Guadalupe Cruz-Hernández[1], Yolanda Reyes-Vidal[1,2*]

[1]Centro de Investigación y Desarrollo Tecnológico en Electroquímica, Parque Tecnológico Querétaro s/n Sanfandila, Pedro Escobedo, Querétaro, México. C.P. 76703

[2]CONACYT-Centro de Investigación y Desarrollo Tecnológico en Electroquímica, Parque Tecnológico Querétaro s/n Sanfandila, Pedro Escobedo, Querétaro, México. C.P. 76703.

* Corresponding author: Email: mreyes@cideteq.mx; Phone: +52 442 211 6000 ext. 7818

ABSTRACT

Different options to the demand for obtain renewable feedstocks and green energy sources are biofuels, being the most widely used biodiesel and recently bioelectricity. However, in the production process, crude glycerol is generated as a principal by-product, which contains 50-60 % of crude glycerol, 12-16 % of alkalis, 15-18 % of methyl esters, 8-12 % of methanol and 2-3 % of water. Other elements present in this waste are Ca, Mg, P or S. Crude glycerol can be used as a carbon source. It has been reported that some bacteria, as *Citrobacter*, *Klebsiella*, *Clostridium*, *Lactobacillus*, metabolize this substrate. *Pseudomonas aeruginosa* species can use complex substrates as a carbon source. This microorganism is characterized for being a producer of phenazine-derived compounds, mainly pyocyanin, a molecule known for its diverse biological activity and its ability as mediator for transfer extracelullar electrons. Therefore, the objective of this work was to use crude glycerol for pyocyanin synthesis by *P. aeruginosa* NEJ01R and use in bioelectrochemical systems. It demonstrates that *P. aeruginosa* NEJ01R at a concentration of 1 % crude glycerol, pH 10, 30 °C and 76 rpm, produces 1 µg/mL of pyocyanin. Using the above-mentioned conditions in a double chamber microbial fuel cell, the production of a maximum current density of 52 µA/cm^2 and power density of 2.6 x 10^{-2} mW/cm^2 were achieved. The capacity of *P. aeruginosa* NEJ01R to use a by-product as a carbon source in the production of a redox metabolite, useful for transfer electrons to produce bioelectricity was demonstrated.

Keywords: glycerol crude; *Pseudomonas aeruginosa*; pyocianyn; microbial fuel cell

1. Introduction

Currently the concern about the effects of climate change due to the excessive use of fossil fuels and their supply is the main concern that has driven the development and discovery of new alternative energy sources [1]. One option to this problem are the biofuels that have turned out to be an excellent option that contributes to the development of a sustainable chemical industry [2]. The most widely used biofuels today is biodiesel, a good option to counteract the serious negative effects of the use of fossil fuels, in addition to biodiesel can be obtained from renewable sources [3]. By means of the transesterification reaction between fatty acid esters and alcohol, using as a catalyst a strong base, biodiesel synthesis is carried out. In this way, biodiesel is the final product of interest, however, different byproducts are produced, such as crude glycerol, seed/pod/shell covers, dried pasta, wash water, etc. [4, 5]. Crude glycerol is the most important by-product because it is produced in a greater proportion, it contains between 50 to 60 % of crude glycerol, 12 to 16 % alkalis, 15 to 18 % methyl esters, 8 to 12 % methanol, 2 to 3 % water, may also contain elements such as Ca, Mg, P or S [6]. It is estimated that the production of biodiesel in 2016 was 37 billion gallons, with an annual growth of 42 %, which indirectly produces 4 billion gallons of crude glycerol as a byproduct. This is due to the fact that 10 Kg of crude glycerol is produced per 100 Kg of biodiesel [7].

In obtaining value-added products by fermentation, glucose is the carbon source by choice. However, crude glycerol is a source of lower cost carbon and a greater degree of reduction, in addition it must be taken into account that glucose competes directly with the production of food and feed. Therefore, there are a high range of products synthesized from the reduction of glycerol. Compared with glucose, the conversion of glycerol generates double amount of reducing equivalents. As an example, the fermentation of glycerol to produce ethanol and formic acid allows obtaining twice the overall yield as glucose fermentation, because half of the glucose is lost as carbon dioxide during the bioconversion of glucose [7]. In addition, glycerol is easily metabolized by aerobic and anaerobic microorganisms and has a wide variety of industrial applications as raw material, so the crude glycerol obtained from the biodiesel process has great potential for the generation of fermentation products [8]. Crude glycerol is used as a carbon source by several genera of bacteria such as *Citrobacter*, *Klebsiella*, *Clostridium*, *Lactobacillus*. A microorganism with the capacity to use crude glycerol as a carbon source is *Clostridium pasteurianum*, to produce butanol, 1,3-propanediol, ethanol, butyrate, acetate, lactate, CO_2 and H_2 as byproducts [9]. On the other hand, the production of 1,3-propanediol from crude glycerol is analyzed by the fermentation of facultative anaerobic bacterium *Lactobacillus brevis* N1E9.3.3 with a yield of 0.89 g 1,3-PDO/g glycerol at pH 8.5 and anaerobic conditions [9]. However, the presence of

impurities in crude glycerol is the main obstacle to the use of crude glycerol as a carbon source for microorganism.

Pseudomonas aeruginosa has been shown that it is capable of using complex substrates as a carbon source. This bacterium is characterized as a producer of compounds derived from phenazines, mainly pyocyanin, which is known for its diverse biological activity. It has been shown that PYO is an inhibitor of the growth of phytopathogenic fungi, anti-vibriosis, antiprotozoal, in addition to an antimicrobial effect against *Staphylococcus aureus* strains resistant to vancomycin and methicillin, *Corynebacterium spp*., *Moraxella catarrhalis*, *Candida albicans*, *Candida tropicalis*, *Candida glabrata* and *Candida parapsilosis* [10, 11]. The PYO molecule is also known for its redox capacity to transfer electrons from the cell membrane to an electrode [12]. Therefore, *Pseudomonas aeruginosa* is known as an exoelectrogenic microorganism which has application in bioelectrochemical systems, which are capable of generating electrical energy by electron transfer. [13]. A study showed that there is a synergy between *Klebsiella variicola* and *Pseudomonas aeruginosa* in microbial fuel cells, since a current density was obtained 3 times that obtained in the culture separately, as well as an increase in the production of PYO. In this way, the objective of this work was to evaluate the crude glycerol generated as a byproduct of the biodiesel industry as a carbon source for the PYO production of *Pseudomonas aeruginosa* NEJ01R and generation of electric energy in a microbial fuel cell.

2. Materials and Methods

2.1 Strain

The strain was identified as *Pseudomonas aeruginosa* NEJ01 and deposited in the collection of Center for Research and Technological Development in Electrochemistry S.C. in Querétaro, México.

2.2 Culture medium

All culture media were sterilized in an autoclave at 121 °C for 15 minutes. Incubation conditions were 30°C, 76 rpm, 48 h. For the determination of the optimal concentration of crude glycerol in the culture medium, it was tested at 1,2,3,4 and 5 %, as a positive control Luria Bertani medium (LB) containing casein peptone (10 g/L), yeast extract (5 g/L) and sodium chloride (0.5 g/L). The optimum pH was determined in a range of 5 to 11.

2.3 Determination of biomass

The biomass was determined by dry weight method, aluminum dish adjusted to constant weight were used in a drying oven at 100 °C for 1 h, and their initial weight was recorded. Afterwards 48 h, cultures were centrifuged at 7500 rpm (10 min), supernatant was separated, pellet was transferred to aluminum dish and these were placed in a drying oven at 100 °C (1 h).

2.4 Determination of PYO

The separated supernatants in the determination of biomass were used for the determination of PYO by a liquid-liquid extraction, taking a volume of 3 mL to which, an equal volume of chloroform was added to be vigorously vortexed. The organic phase (blue) was separated to add a similar volume of 0.2 N HCl, vigorously stirred in a vortex and the aqueous phase (red) was separated to read it in a spectrophotometer at 520 nm. The absorbance obtained was multiplied by the factor of 17.1 to obtain µg/mL of PYO [12].

2.5 Experimental setup in bioelectrochemical system

Testing on bioelectrochemical systems was analyzed in a two chambers type H cell joined with a saline agar bridge, on both sides carbon felt electrodes (2 x 2 x 0.5 cm) were used. The anodic chamber consisted of 1 % v/v of crude glycerol at pH 10, from biodiesel production and 1 ml of *P. aeruginosa* NEJ01R culture (48 h), related with production of electricity and oxidation of glycerol molecule. 50 mM of potassium chloride was used in the cathodic area. 350 ml of volume was used in each chamber. Before carry on the experiments all materials and reactive were sterilized or sanitized. Current-Potential curves were analyzed with a Biologic VSP-300 potentiostat/galvanostat. All experiment was carrying on environmental temperature.

3. Results and Discussion

Figure 1 shows the effect of the concentration of crude glycerol on the production of biomass and PYO of *P. aeruginosa* NEJ01R. It can be observed that in the treatment with 1% of crude glycerol a higher concentration of PYO was obtained, being 55 % of the concentration of PYO that is produced with the LB medium. The concentration of PYO was decreasing as the concentration of crude glycerol was increased. This suggests that glycerol and the impurities present in crude glycerol have a negative effect on the induction of PYO production. This negative effect is proportional to the concentration of glycerol

present in the culture medium, highlighting that treatment with 3 % crude glycerol completely inhibits the production of PYO. A similar result is shown in the production of biomass, since the treatment of 1 % of crude glycerol produces the highest concentration of biomass with respect to others treatments where the concentration of glycerol was increased, also demonstrating the toxic effect of glycerol and the impurities for the growth of *P. aeruginosa* NEJ01R, because in the positive control it was possible to produce more than twice as many biomass as in the treatment with lower concentration of crude glycerol (1 %). According the results, it is demonstrated that *P. aeruginosa* NEJ01R can use the crude glycerol by-product of the biodiesel industry as a carbon source to produce secondary metabolites.

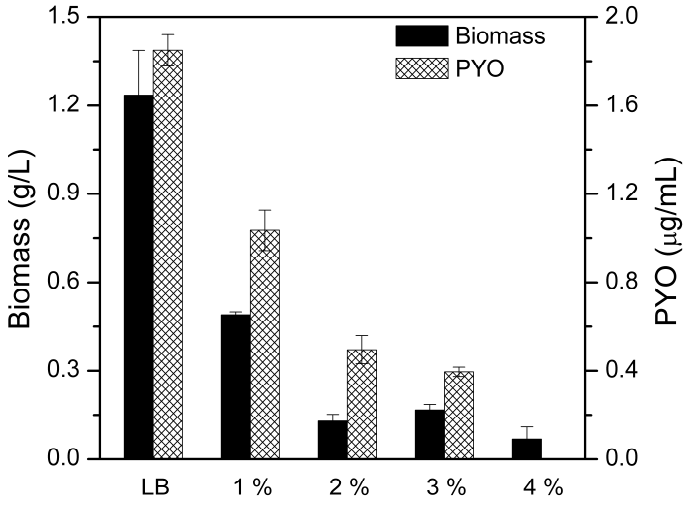

Fig. 1. Effect of glycerol crude concentration (%) in biomass and PYO production by *Pseudomonas aeruginosa* NEJ01R.

It is reported that it is possible that using glycerol as carbon source can obtain higher yields compared to those obtained with carbohydrates such as glucose or xylose due to the degree of reduction by carbon (k) that is significantly high for glycerol ($C_3H_8O_3$: k = 4.67), for glucose ($C_6H_{12}O_6$: k = 4) and for xylose ($C_5H_{10}O_5$: k = 4) [14]. Glycerol can be used as sole carbon source to produce rhamnolipids by *P. aeruginosa*, 30 g/L of pure glycerol produce 15.4 g/L of rhamnolipids [15] y another study reports that 3 % of crude glycerol produce 3.9 g/L of rhamnolipids [16]. Using the same crude

glycerol concentration as in this study (1 %) it was reported that two different strains of *P. aeruginosa* produce 2.16 g/L and 0.69 g/L of rhamnolipids [17, 18]. The differences in concentrations of glycolipids obtained could be related with impurities concentrations. In this work, *P. aeruginosa* NEJ01R produce more than 50 % of PYO compared to the positive control (LB medium) using 1 % of glycerol crude, considering that impurities had not negative effect or *P. aeruginosa* NEJ01R is a tolerant strain to these impurities.

The effect of pH on the PYO production by *P. aeruginosa* NEJ01R are presented in Figure 2. It is observed that in a range of 5 to 7 there is no difference in the PYO production. However, in alkaline pH range (8 - 10) the concentration of PYO was increased, obtaining the maximum concentration at pH = 10. An opposite effect occurs when the pH is adjusted to 11, obtaining a decrease in PYO production. This result is favorable in the use of crude glycerol as a carbon source, because the pH of this effluent was 11, probably related with impurities. Thus, a minimum conditioning must be given to the effluent for to use as a culture medium. This is a relevant aspect in cost of production of this metabolite by study strain.

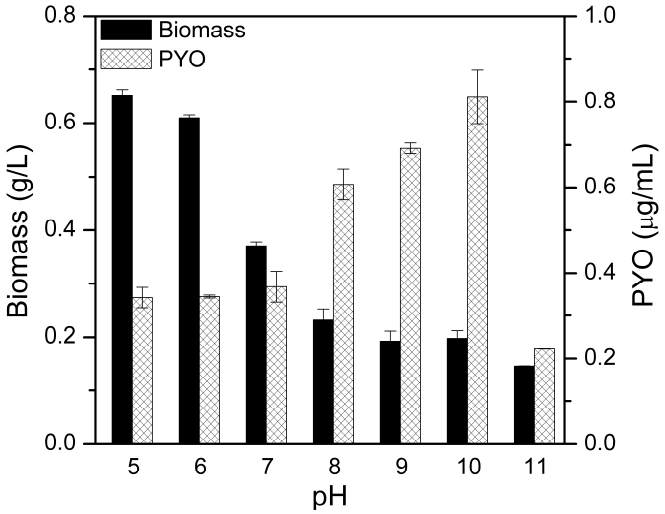

Fig. 2. Effect of pH in PYO and biomass production by *P. aeruginosa* NEJ01R (Crude glycerol, 1 %).

According to results, the strain *P. aeruginosa* NEJ01R can be considered as an alkalotolerant, since it can be used for the consumption of substrates that have a pH lower than 10, considering that

alkalotolerant microorganisms are those that tolerate a higher pH to 9 [19]. Regarding the production of biomass, a maximum of production is achieved at a pH = 6, decreasing when the pH was 7, for a pH range 8 - 11, the lowest biomass concentration remains constant. Thus, it is demonstrated that to produce PYO by *P. aeruginosa* NEJ01R an alkaline pH could be the best condition while for biomass production an acidic pH is more efficient.

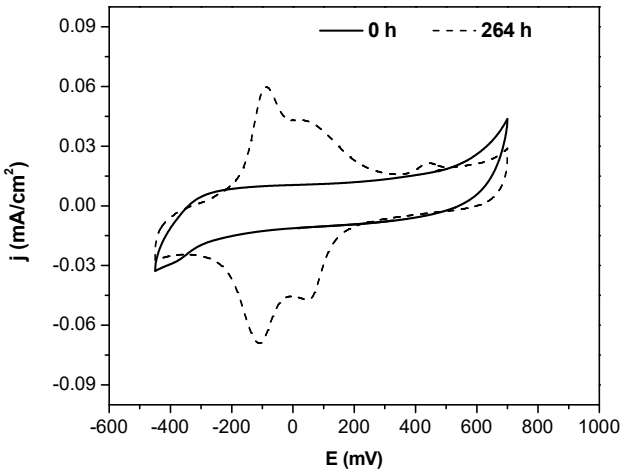

Fig. 3. Cyclic voltammogram of crude glycerol oxidation from -450 to 700 mV, at 10 mV/s. (Experimental time = 264 hours).

Figure 3 shows the cyclic voltammetry of crude glycerol oxidation. At the start of the electrochemical system (0 h), the carbon felt has a typical carbon cyclic voltammogram. After, a biofilm of *P. aeruginosa* NEJ01R grows on the electrode surface and pyocyanin (a redox mediator) was produced. This metabolite is important for the electron transfer of the system [20, 21]. After, it was observed the pyocyanin presence in the redox peaks -76.1/-106.2 mV, 65.33/56.79 mV and 445 mV (cyclic voltammetry, 264 h). These potentials depending on the time it takes the system to operate [22, 23]. It was observed that due to the pyocyanin presence and other metabolites the pH of the anolyte decreased from 10 to 5.9.

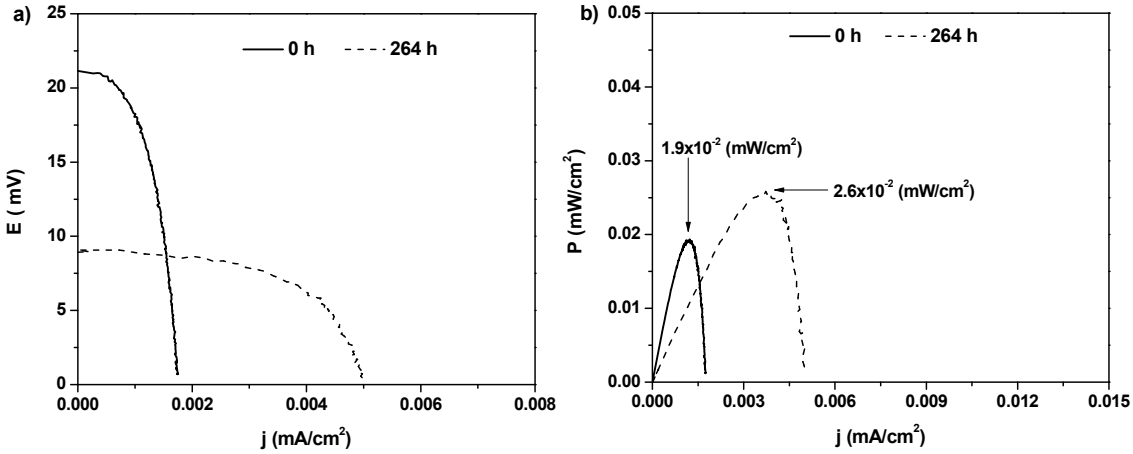

Fig. 4. a) Polarization and b) power density curves for 1 % v/v crude glycerol in a bioelectrochemical system. (Experimental time = 264 hours).

Figure 4a shows polarization curve in bioelectrochemical system, indicating that open circuit potential (OCP) initial was approximately 20.5 mV with a maximum current density (j_{max}) of 2 µA/cm^2. After, OCP drops sharply to 8.96 mV and j_{max} = 52 µA/cm^2. Figure 4b expose maximum power density (P_{max}), with values of 1.8 x 10^{-2} mW/cm^2 (0 h) and 2.6 x 10^{-2} mW/cm^2 (264 h). This abrupt decrease in potential could be related to the decrease in pH. In order for *P. aeruginosa* NEJ01R was able to oxidize the crude glycerol as a carbon source and in turn generate bioelectricity, it needs to maintain the same pH all times. In addition, crude glycerol had 60 % of pure glycerol, and others compounds may be also contributing to a loss of potential due to reactions competition.

4. Conclusion

The crude glycerol obtained from the biodiesel production process is efficient for the production of redox metabolites of *P. aeruginosa* NEJ01R, in turn also this effluent can be used for the production of bioelectricity in a microbial fuel cell. In this way, an efficient application of industrial effluent is proposed, which has repercussions on a possible system for the disposal and use of crude glycerol.

Acknowledgements

Authors thank CONACYT-SENER-Sustentabilidad Energética (246052) and CONACYT-SEP Ciencia Básica (258159) funds. Authors thanks to FORDECYT, Consorcio del Agua, Project 297116.

References

[1] Sarma S, Ortega D, Minton N, Kumar V, Vijayan D, Moholkar S. Homologous overexpression of hydrogenase and glycerol dehydrogenase in *Clostridium pasteurianum* to enhance hydrogen production from crude glycerol. Bioresour Technol 2019;284:168–177.

[2] Gonzalez A, Gonzalez M, Guillen G. High-Value Propylene Glycol from Low-Value Biodiesel Glycerol: A Techno-Economic and Environmental Assessment under Uncertainty. ACS Sustain Chem Eng 2017;5:5723−5732.

[3] Franca R, Souza P, Lima E, Costa A. An extended techno-economic analysis of the utilization of glycerol as an alternative feedstock for methanol production. Clean Techn Environ Policy 2017;17: 1855–1865.

[4] Kumar H, Chanakya H, Siddiqha A, Thomas C, Mukherjee N, Janardhana N. Anaerobic digestion of the inedible oil biodiesel residues for value addition. Sustain Energy Techn 2017;22:9–17.

[5] Tacias V, Rosales A, Torrestiana B. Evaluación y caracterización de grasas y aceites residuales de cocina para la producción de biodiésel: un caso de estudio. Rev Int Contam Ambie 2016;32:303-313.

[6] Maru BT, López F, Kengen SW, Constantí M, Medina F. Dark fermentative hydrogen and ethanol production from biodiesel waste glycerol using a co-culture of *Escherichia coli* and *Enterobacter* sp. Fuel 2016;186:375–384.

[7] Garlapati V, Shanka U, Budhiraja A. Bioconversion technologies of crude glycerol to value added industrial products. Biotechnol Rep 2016:9;9–14.

[8] Krasnan V, Plza M, Marr A, Markosová K, Rosenberga M, Rebros M. Intensified crude glycerol conversion to butanol by immobilized *Clostridium pasteurianum*. Biochem Eng J 2018;134:114–119.

[9] Vivek N, Pandey A, Binod P. Biological valorization of pure and crude glycerol into 1,3-propanediol using a novel isolate *Lactobacillus brevis* N1E9.3.3. Bioresour Technol 2016;213:222–230.

[10] Patil S, Nikama M, Patil H, Anokhina T, Kochetkov V, Chaudhari A. Bioactive pigment production by *Pseudomonas* spp. MCC 3145: Statistical media optimization, biochemical characterization, fungicidal and DNA intercalation-based cytostatic activity. Process Biochem 2017;58:298–305.

[11] Xu L, Zeng J, Jiang C, Wang H, Li Y, Wen W, Li J, Wang F, Ting W, Sun Z, Huang C. Isolation and determination of four potential antimicrobial components from *Pseudomonas aeruginosa* extracts. Int J Med Sci 2017;14:1368–1374.

[12] El-Fouly MZ, Sharaf AM, Shahin AA, El-Bialy HA, A.M.A. Omara AM. Biosynthesis of pyocyanin pigment by *Pseudomonas aeruginosa*. J Radiat Res Appl Sc 2015;8:36–48.

[13] Adnan NA, Suhaimi SN, Abd-Aziz S, Hassan M, Phang L. Optimization of bioethanol production from glycerol by *Escherichia coli* SS1. Renew Energ 2014;66:625–633.

[14] Doi Y. Lactic acid fermentation is the main aerobic metabolic pathway in *Enterococcus faecalis* metabolizing a high concentration of glicerol. Appl Microbiol Biotechnol 2018;102:10183–10192.

[15] Zhan Y, Sheng B, Wang H, Shi J, Cai D, Yi L, Yang S, Wen Z, Ma X, Chen S. Rewiring glycerol metabolism for enhanced production of poly-γ-glutamic acid in *Bacillus licheniformis*. Biotechnol Biofuels 2018;11:306.

[16] Bharali P, Singh P, Dutta N, Bora L, Debnathc P, Konwara B. Biodiesel derived waste glycerol as an economic substrate for biosurfactant production using indigenous *Pseudomonas aeruginosa* RSC Advances 2014;73.

[17] Eraqui WA, Yassin AS, Ali AE,Amin MA. Utilization of crude glycerol as a substrate for the production of rhamnolipid by *Pseudomonas aeruginosa*. Biotech Res Int 2016:1–9.

[18] Santa Anna LM, Sebastian GV, Menezes EP, Alves TLM, Santos AS, Pereira Jr. N, Freire DMG. Production of biosurfactants from *Pseudomonas aeruginosa* PA1 isolated in oil environments. Braz J Chem Eng 2002;19:159-166.

[19] Horikoshi K. Alkaliphiles: Some applications of their products for biotechnology. Microbiol Mol Biol Rev 1999;63:735-750.

[20] Rabaey K, Boon N, Siciliano SD, Verchaege M, Verstraete W. Biofuel cells select for microbial consortia that self-mediate electron transfer. Appl Environ Microb 2004;70:5373-5382.

[21] Zhou S, Huang S, He J, Li H, Zhang Y. Electron transfer of *Pseudomonas aeruginosa* CP1 in electrochemical reduction of nitric acid. Bioresour Technol 2016; 218:1271-1274.

[22] Sismaet HJ, Pinto AJ, Goluch ED. Electrochemical sensors for identifying pyocyanin production in clinical *Pseudomonas aeruginosa* isolates. Biosens Bioelectron 2017;97:65-69.

[23] Bellin DL, Sakhtah H, Rosenstein JK, Levine PM, Thimot J, Emmett JK, Dietrich LEP, Shepard KL. Integrated circuit-based electrochemical sensor for spatially resolved detection of redox-active metabolites in biofilms. Nat Commun 2014;5:3256 DOI:10.1038/ncomms4256.

[1] Wang H, Wang B, Yu J, Hu Y, Xia C, Zhang J, et al. Significant enhancement of power conversion efficiency for dye sensitized solar cell using 1D/3D network nanostructures as photoanodes. Scientific Reports. 2015;5.

[2] Makhal A, Sarkar S, Bora T, Baruah S, Dutta J, Raychaudhuri AK, et al. Role of Resonance Energy Transfer in Light Harvesting of Zinc Oxide-Based Dye-Sensitized Solar Cells. The Journal of Physical Chemistry C. 2010;114:10390-5.

[3] Szostak R, Morais A, Carminati SA, Costa SV, Marchezi PE, Nogueira AF. Application of Graphene and Graphene Derivatives/Oxide Nanomaterials for Solar Cells. 2018:395-437.

[4] Marimuthu T, Anandhan N, Thangamuthu R, Mummoorthi M, Ravi G. Synthesis of ZnO nanowire arrays on ZnO TiO 2 mixed oxide seed layer for dye sensitized solar cell applications. Journal of Alloys and Compounds. 2016;677:211-8.

[5] Golsheikh AM, Kamali KZ, Huang NM, Zak AK. Effect of calcination temperature on performance of ZnO nanoparticles for dye-sensitized solar cells. Powder Technology. 2018;329:282-7.

[6] Lee C-P, Lin J-C, Wang Y-C, Chou C-Y, Yeh M-H, Vittal R, et al. Synthesis of hexagonal ZnO clubs with opposite faces of unequal dimensions for the photoanode of dye-sensitized solar cells. Physical Chemistry Chemical Physics. 2011;13:20999-1008.

[7] Rokesh K, Pandikumar A, Jothivenkatachalam K. Dye Sensitized Solar Cell: A Summary. Materials Science Forum. 2013;771:1-24.

[8] Dong P, Rodrigues M-TF, Zhang J, Borges RS, Kalaga K, Reddy ALM, et al. A flexible solar cell/supercapacitor integrated energy device. Nano Energy. 2017;42:181-6.

[9] Li G, Sheng L, Li T, Hu J, Li P, Wang K. Engineering flexible dye-sensitized solar cells for portable electronics. Solar Energy. 2019;177:80-98.

[10] Chávez-Valdez A, Herrmann M, Boccaccini AR. Alternating current electrophoretic deposition (EPD) of TiO2 nanoparticles in aqueous suspensions. Journal of Colloid and Interface Science. 2012;375:102-5.

[11] Xie Y, Zhou X, Mi H, Ma J, Yang J, Cheng J. High efficiency ZnO-based dye-sensitized solar cells with a 1H,1H,2H,2H-perfluorodecyltriethoxysilane chain barrier for cutting on interfacial recombination. Applied Surface Science. 2018;434:1144-52.

[12] Hsu HY, Tongol BJ. Electrochemical and surface characteristics of carbon-supported PtSn electrocatalysts for ethanol electro-oxidation: possible application for inkjet ink formulations. Advances in Natural Sciences: Nanoscience and Nanotechnology. 2013;4:015012.

[13] Cullity BD, Stock SR. Elements of X-Ray Diffraction: Pearson New International Edition: Pearson Education Limited; 2013.

[14] Velazquez C, Eddie Nahúm A-M, Pech-Rodríguez WJ, González-Quijano D, Rocha-Rangel E. Improvement of dye sensitized solar cell photovoltaic performance by using a ZnO-semiconductor processed by reaction bonded2019.

[15] Moussawi RN, Patra D. Modification of nanostructured ZnO surfaces with curcumin: fluorescence-based sensing for arsenic and improving arsenic removal by ZnO. RSC Advances. 2016;6:17256-68.

[16] Salavati-Niasari M, Mir N, Davar F. ZnO nanotriangles: Synthesis, characterization and optical properties. Journal of Alloys and Compounds. 2009;476:908-12.

[17] Joseph S, Mathew B. Microwave-assisted green synthesis of silver nanoparticles and the study on catalytic activity in the degradation of dyes. Journal of Molecular Liquids. 2015;204:184-91.

E022. HYDROGEN PRODUCTION BY WATER PHOTOCATALYSIS

J. D. Becerra-Ruiz[1*], J. C. Jáuregui-Correa[2], I. Rangel-Vazquez[3], G. Del Angel-Montes[3]

[1]Faculty Chemistry, Autonomous University of Querétaro Cerro de las Campanas S/N. Z.C. 76010. Querétaro, Qro. México.
[2]Faculty Engineering, Autonomous University of Querétaro Cerro de las Campanas S/N. Z.C. 76010. Querétaro, Qro. México.
[3]Autonomous Metropolitan University - Iztapalapa Unit, Chemical Dept., Av. San Rafael Atlixco 186. Z.C. 09340. Ciudad de México. México.
* Corresponding author: 442 109 09 14 and jbecerra29@alumnos.uaq.mx

ABSTRACT

In this work we report the results obtained in hydrogen (H_2) production by water decomposition using TiO_2 photocatalysts modified graphene oxide (GO) using a UV light source. The synthesis of TiO_2 was carried out using sol-gel method (TiO_2 FL) and as reference TiO_2 Degussa P25. The addition of GO in different proportions by weight (0.5, 2 and 4%) using photoimpregnation method. The DRX and Raman spectra show mixture of crystalline phases of anatase and brookite in synthesized TiO2, while in P25 mixture of anatase and rutile phases. From diffuse reflectance spectra and applying Kubelka - Munk transform to FL - GOx compounds, E_g values were found between 2.92 and 3.12 by addition of GO to TiO_2. The highest production of H_2 was given in following order, first FL-GO 4% with 24.15 $x10^3$ µmol, followed by TiO_2 FL with 23.81 x 10^3 µmol and FL-GO 2% with 23.64 $x10^3$ µmol, after six hours of reaction. The addition of GO to TiO_2 shows a slight increase in H_2 production, despite the above, higher H_2 production was obtained than reported in some articles. This can be explained due to presence of small crystals of TiO_2 FL (observed in SEM) on GO sheets by improving the photocatalytic properties of synthesized sol-gel material, in addition to GO acting as an electron acceptor reducing the rate of recombination of e^- / h^+ photogenerated pairs in TiO_2; in addition, the mixed phases (anatase-brookite) of TiO_2 and obtaining of reduced GO (rGO), lead to an optimal composition to obtain the best performance of water division.

Keywords: hydrogen, titanium dioxide, graphene oxide, photocatalysis

1. Introduction

In recent years, it has become very important to look for new sources of energy that are economical, abundant, environmentally friendly and renewable. This is due to the growing global demand for energy for all domestic and industrial uses, among others. The energy supplies must meet the growing global demand, which is why we have been looking for new alternatives such as use of solar, wind, hydraulics,

geothermal and biofuels. Of the latter there are various investigations for production of bioethanol, biodiesel, bioturbosin and hydrogen (H_2). The H_2 considered as the fuel of future since its combustion produces only water vapor [1,2]. In addition, H_2 is very abundant in earth's crust, but it is not found in its pure state, it is combined with other chemical elements. The latter is disadvantage of H_2 since it is necessary to extract it, being the main sources of H_2 oil, natural gas and water [3,4]. Using oil or natural gas is to continue using fossil energy sources, so water becomes an option. To water splitting into H_2 and oxygen (O_2) can be done by electrochemistry, biochemistry, photoelectrochemistry, and photocatalysis. Being the photoelectrochemistry and photocatalysis could be promising that could get to use the spectrum of sunlight to water separate [5]. In this work, it focuses on photocatalysis of water for production of H_2. Photocatalysis uses photocatalysts, which are materials sensitive to light. One of these materials that has been extensively researched is Titanium Oxide (TiO_2), which is abundant in earth's crust, economically, chemically stable, sensitive in ultraviolet (UV) region, among other qualities. [6]. In addition, TiO_2 has three crystalline phases, Anatase, Brookite and Rutile. The Anatase and Rutile phases are most studied and best photocatalytic properties. According to studies brookite has a band gap (E_g) between 3.1 to 3.4 eV [7]. These values depend on method of preparation and content of metamorphosis phase present in samples [6]. The physical properties of brookite can be changed by calcination at different temperatures [8–12]. Unfortunately TiO_2 has a disadvantage which is recombination speed of electron / hollow pairs (e^- / h^+) which is practically instantaneous [13]. To reduce recombination rate of pairs e^- / h^+, TiO_2 is modified by doping to addition with metals or oxides. One of these oxides is Graphene Oxide (GO) which has been studied in recent years, which also has the maximum peak of light absorption in UV region.

Some works on water splitting using TiO_2 and GO, like that of Fan et al. 2011 in their work indicate that TiO_2 - GO is a good material for water photo-splitting [14]. On the other hand Faraldos and Bahamonde conclude in their work of 2017 that proportion of GO should not be greater than 5%, since it inhibits the photocatalytic activity of TiO2 [15]. Some works on the production of H_2 from water like that of Zhang, et al. 2010 who using 100 mg of photocatalyst composed of TiO_2 and Graphene (Gr) in different proportions on weight, obtained 86 µmol/h with visible light [16]. It should be mentioned that GO is Gr functionalized with carbon functional groups. On the other hand, Cheng et al. 2011, tested with 100 mg of photocatalyst also of TiO_2 - Gr with UV light source obtained 668 µmol/h of H_2 [17]. Finally Xiang et al. 2011, worked with 50 mg of photocatalyst of TiO2 - Gr using UV light obtained 736 µmol/h of H_2 [18]. It is important to mention that in these works TiO2 was used in anatase or anatase phase with rutile (Degussa P25). In this work, it propose H_2 production from water splitting under UV light, using nanoparticles (np) of TiO_2 phase Anatase / Brookite (synthesized in the laboratory by sol-gel method) impregnated with GO in different proportions (0.5, 2 and 4% by weight); in comparison with TiO2 (Degussa P25).

2. Materials and Methods

The photocatalyst of TiO_2 was synthesized by sol-gel method, the precursor being titanium (IV) isopropoxide Ti $[OCH(CH_3)_2]_4$ (Sigma Aldrich). The precursor was dissolved in isopropanol (Sigma-Aldrich) regulating the pH to 3 with nitric acid (J.T. Baker), the mixture was kept under reflux with stirring for 24 h. Subsequently, deionized water and isopropanol were added in a proportion of 4:16 and maintained at reflux for a further 24 h. The solvent was removed by filtration using filter paper with 40 nm pores. The solid was then washed with deionized water and dried at 120° C in oven. Finally, the solid (TiO_2 FL) was calcined at 400° C for 4 h.

For GO synthesis, the modified Hummers method was used, which consists of oxidizing graphite powder (Sigma-Aldrich) in sulfuric acid solution (JT Baker), phosphoric acid (Meyer) and potassium permanganate (Meyer). This mixture is stirred and heated between 50-70° C. Deionized water and 30% hydrogen peroxide (Sigma-Aldrich) are then added as a reducing agent. It is reheated between 50-70 ° C. The solid is washed with deionized water and ethanol until pH ≈ 7. It is then placed in ultrasonic bath in order to separate the GO layers, achieving a packing of 4 to 9 sheets. Finally, the material is dried in oven at 50-70° C for 12 h.

For preparation of photocatalysts of TiO_2 added with GO was made by photoimpregnation method, incorporating 0.5, 2 and 4% by weight. The FL-GOx impregnated photocatalysts (x = weight percentage of GO 0.5, 2 and 4%) were compared against TiO_2 Degussa P25. For photoimpregnation, the following procedure was carried out: TiO_2 FL was mixed in absolute ethanol (JT Baker) and placed in ultrasonic bath and then placed in 200 ml reactor to be irradiated with Hg UV lamp with power 45 W and temperature between 50-70° C with agitation. On the other hand, the GO synthesized in laboratory is placed in ultrasonic bath in mixture with distilled water. Then both solutions are mixed and then continue with UV lamp illumination, agitation and heat. To separate the solid from solution, it is dried in oven at 50° C for 24 hours. All photocatalysts were prepared with the same method. All reagents used are of high purity.

2.1. Characterization

X-ray diffraction analysis was performed on a Bruker D8 Advance with CuKα radiation detector and 2θ sweep of 38.4 min^{-1}. To calculate the approximate size of the crystal, the Williamson-Hall approximation was used and, to calculate the size of GO packaging the Debye-Scherrer equation was used (Table 1). The Raman spectra were measured with a DRX2xi brand Thermo Scientific with a sweep of 0.96 cm^{-1} in Raman shift, using green laser with wavelength of 532 nm. For Uv-vis diffuse reflectance

spectra, they were performed on Cary-100 Varian using integration sphere with scanning speed of 0.25 nm from 190 to 900 nm at room temperature. To calculate E_g of samples was done using the modified Kubelka-Munk transform [$(F(R) \times h\nu)^{1/2}$ vs $h\nu$], extrapolating the reflectance to "x" axis for y = 0. The surface area specificity was determined by the Brunawer-Emmet-Teller (BET) method at 77 K. The adsorption isotherms of nitrogen adsorption were measured at -196° C in Micromerttics of TriStar II Series. For physisorption measurements, a previous degassing was carried out at 200° C for 6 h. The thermogravimetric analysis (TGA) was carried out in TGA Q500 brand TA Instruments in temperature range of 30 to 900° C with a ramp of 10° C/min in nitrogen (N_2) atmosphere. The microscopy was performed by SEM in JEOL model JSM-6490LV. For evaluation of photocatalytic activity, it was used in 200 ml glass reactor at constant temperature. The reaction was carried out at room temperature and atmospheric pressure; for each experiment 50 mg of photocatalyst mixed in water-methanol solution (J.T. Baker) was used at a ratio of 1:1, the latter as sacrificial agent. The solution was degassed in presence of N_2 bubbles (1 ml/s) for 10 minutes and then irradiated with UV light with a mercury lamp (λ = 254 nm) of Pen-Ray brand and 45 W, also a quartz tube. The mixture was stirred to ensure uniform exposure of suspension during the process. The experiment was also maintained in N_2 atmosphere with the aim of preventing the corrosion of TiO_2. The reaction was monitored every hour using a Shimadzu GC-2014 gas chromatograph to analyze H_2 production; the experiment lasted 6 h and carrier gas was N_2.

3. Results and Discussion

The diffraction patterns are shown in Fig. 1. The Figs. 1a, 1b and 1c of pure materials (GO, TiO_2 P25 and TiO_2 FL). Figs. 2d to 2f the diffraction patterns of FL-GO compounds (0.5, 2 and 4%) respectively. Fig. 1a corresponding to diffractogram of GO shows the main peak corresponding to plane (001) at 2θ = 11° [19]. The pure TiO_2 were compared with crystallographic cards of International Center for Diffraction Data (ICDD), PDF 021-1272 (anatase), PDF 021-1276 (rutile) and ICDD 03-0380 (brookite). In the case of commercial TiO_2 P25, manufacturer indicates that anatase phase has a higher proportion than rutile phase (85 and 15% respectively), this is verified by presence of five peaks corresponding to rutile phase in the sample. The TiO_2 synthesized sol-gel TiO_2 FL shows characteristic peaks corresponding to anatase and brookite phases. Using deconvolution method of the diffractogram peaks of TiO_2 FL, approximate proportions of anatase and brookite phases were calculated, resulting in proportions of 66% anatase and 34% brookite. Figs. 1d to 1f correspond to FL-GO compounds (0.5, 2 and 4%), the intensity of X-ray diffraction peaks is similar to that of pure material (TiO_2 FL), no significant change in diffractograms of compounds, only by presence of a peak in 2θ = 18° that could be inherent to GO since it is only found in compounds with GO. On the other hand, the planes of anatase phase (101) and brookite (120) are present in all compounds.

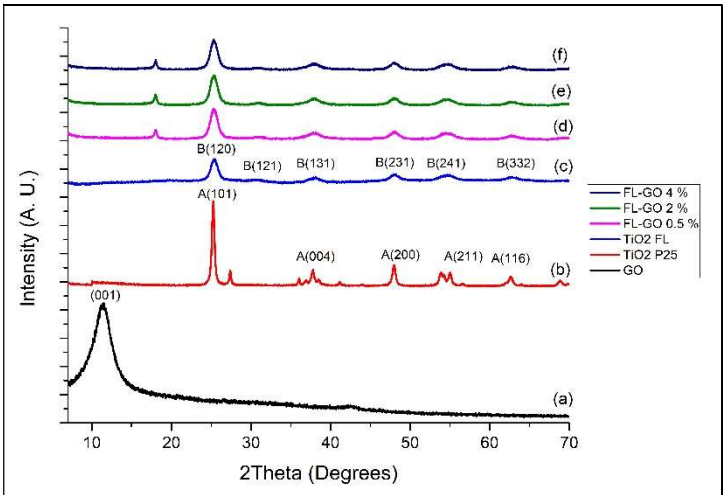

Fig. 1. DRX (a) GO, (b) TiO_2 P25, (c) TiO_2 FL, (d) FL – GO 0.5%, (e) FL – GO 2% y (f) FL – GO 4%.

The Raman spectrum of GO vibrational modes were observed at 1358 cm^{-1}, 1580 cm^{-1}, 2672 cm^{-1} and 2945 cm^{-1} corresponding to bands D, G, 2D and D + G respectively [20,21]. In reference to bands (2D and D+G), observed shape similar to a hill indicates the possible presence of GO. The band G provides information on vibration of sp^2 carbon atoms which indicates the characteristics of all sp^2 carbon forms, while the D band implies presence of sp^3 defects [22,23]. The ratio of intensities between bands D and G (I_D/I_G) provides information on presence of disorders that occur in GO or reduced Graphene Oxide (rGO), indicating defects associated with vacancies, grain boundaries and the amorphous carbon [24]. If this ratio between the band intensities the result is approximately 1, it could indicate presence of rGO [25]. In particular case of GO synthesized the result of ($I_D/I_G = 0.77$), which indicates that there is no presence of rGO. The Raman spectra of TiO_2 P25 and TiO_2 FL appreciate the vibrational modes of anatase phase and brookite phase, in the case of rutile phase it is not possible to

observe by ratio. On the other hand, in synthesized sol-gel TiO_2 FL presents the vibrational modes of both anatase phase and brookite, this corroborates what is found in diffractograms of these same materials [26]. In addition, in both spectra the vibrational modes of OH groups between 2500 and 3100 cm^{-1} are observed. While all FL-GO compounds between 1000 and 3500 cm^{-1} the vibrational modes of D and G bands (between 1000 and 1750 cm^{-1}) are observed, as well as 2D and D+G bands (2500 to 3100 cm^{-1}). To know if there is rGO or GO in compounds in Table 1, the intensity ratio of D and G bands (I_D/I_G) is shown. Some works have shown that rGO benefits water splitting.

Table 1. Ratio of intensities between bands D and G. E_g values of pure photocatalysts (GO, TiO_2 P25 and TiO_2 FL) and FL-GO compounds. BET specific area. Pore volume. Pore size. Average size of crystal.

Material	I_D/I_G Ratio	[1]Eg (eV)	BET Area ($m^2\ g^{-1}$)	Pore Volume ($cm^3\ g^{-1}$)	Pore size (nm)	[2]Crystal size (nm)
TiO_2 P25	-	2.95	53	0.013	15.19	15.86
TiO_2 FL	-	3.05	128	0.052	8.01	6.61
GO	0.77	2.32	35	0.006	12.53	[3] 2.6
FL – GO 0.5 %	1.08	3.12	74	0.037	7.67	6.57
FL – GO 2 %	1.06	2.92	100	0.029	7.66	6.76
FL – GO 4 %	0.98	2.98	107	0.033	7.64	6.59

[1] Eg using Kubelka-Munk transform.
[2] Determined by Williamson-Hall method.
[3] Average collection of GO sheets, determined by Debye-Scherrer.

From Diffuse Reflectance UV-vis (DRS) spectra applying the modified Kubelka-Munk transform $[F(R)h\upsilon))^{1/2}$ vs hυ] to obtain from these E_g of each material, which are shown in Table 1. TiO_2 P25 has E_g in values close to those reported for TiO_2 in anatase phase (3.0-3.2 eV) [18]. For TiO_2 synthesized sol-gel, the E_g values are close to both anatase phase (3.0-3.2 eV) and brookite (3.1-3.4 eV) reported [7]. The FL-GO compounds presented E_g between 2.92 and 3.12 eV, by adding the GO, some compounds moved their E_g to border of visible region. In Table 1, the BET surface areas are observed for all materials. The TiO2-P25, has an area of 53 m^2g^{-1}, while synthesized sol-gel material TiO_2 FL has area greater than 128 m^2g^{-1}, this due to preparation method. When GO is added to TiO_2 FL, the area decreases by approximately half (FL-GO 0.5%), as addition of GO increases (2 and 4%) the area increases, but it remains below area of pure material; this is due to higher content of GO over TiO_2. The isotherms that showed all materials are Type IV, which is corresponding to both TiO_2 and GO. With this it is concluded that materials are classified as mesoporous with pore sizes between 2 and 50 nm; this can be seen in Table 1, where the pore size values are between 2.64 to 15.19 nm. While the hysteresis cycles are different, for TiO_2 P25 the cycle is Type H3 and for TiO_2 FL and FL-GO compounds (0.5, 2 and 4%)

present hysteresis cycles Type H1. This is explained by pore size since for TiO_2 P25 the pore size is 15.19 nm, while TiO_2 FL materials and FL-GO compounds (0.5, 2 and 4%) pore sizes are between 7.66 a 8.01 nm; when the GO was added, no change was observed in hysteresis cycles, nor was type of isotherm. In the case of GO, it has area of 35 m^2g^{-1}.

From thermogravimetric analysis it is obtained that GO presents abrupt fall in weight in 200° C, caused by functional groups of carboxyl and hydroxyl [27,28]. TiO_2 (P25 and FL) are stable throughout the temperature range since they have virtually no weight loss [18,29]. The FL-GO compounds (0.5, 2 and 4%) show stability up to 400° C when they start to lose weight, but at approximately 525° C there is a very sharp drop in weight; this is due to presence of GO and hydroxyl and carboxyl functional groups. With these results it can be said that composite photocatalysts (FL - GO) are stable until before 400° C.

Fig. 2 presents micrographs of materials TiO_2 P25, TiO_2 FL and GO, as well as Energy Dispersive X-ray (EDS) analysis of elementary percentage. Fig. 2a shows SEM micrograph of TiO_2 P25, in which size of crystals and clusters formed is observed, which confirms the size of crystal is greater than TiO_2 FL; this reaffirms the calculation of crystal size (Table 1). Fig. 2b is EDS analysis of TiO_2 P25 in which average elemental (Table 2) percentage is approximately the expected of 33 and 66% titanium and oxygen respectively. Fig. 2c shows micrograph of TiO_2 FL where smaller size of crystal is appreciated compared to TiO_2 P25. Fig. 2d corresponds to EDS analysis of TiO_2 FL calculated averages (Table 3) of elementary percentage are similar to TiO_2 P25. Finally, Fig. 3e shows micrograph of GO, in which the stacking of GO sheets is observed.

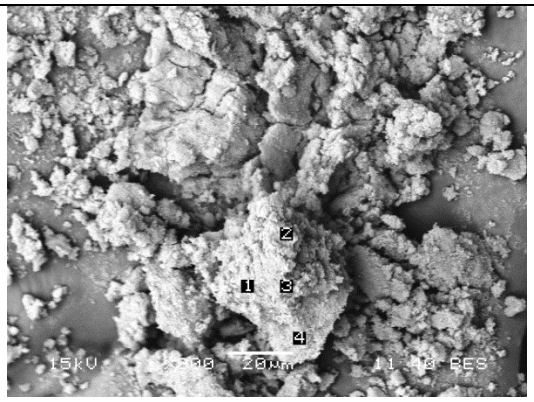

(a)

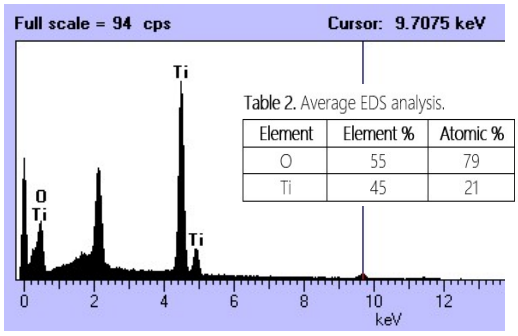

Table 2. Average EDS analysis.

Element	Element %	Atomic %
O	55	79
Ti	45	21

(b)

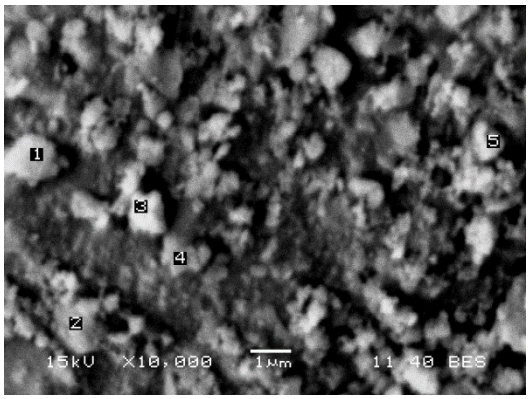

(c)

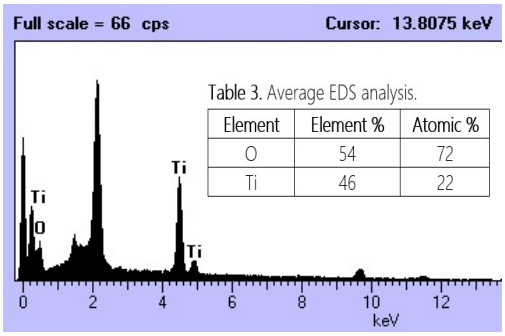

Table 3. Average EDS analysis.

Element	Element %	Atomic %
O	54	72
Ti	46	22

(d)

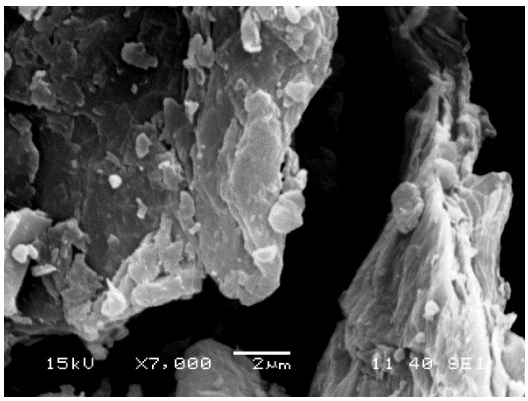

(e)

Fig. 2. SEM micrographs and EDS analysis. (a) TiO_2 P25, (b) EDS TiO_2 P25, (c) TiO_2 FL, (d) EDS TiO_2 FL and (e) GO.

Fig. 3 shows the results in H_2 production against time (6 h), using UV lamp, 50 mg of photocatalyst (P25, FL, GO, FL-GO 0.5, 2 and 4%), water, methanol, temperature 25° C, stirring and atmosphere of N_2. The catalytic photoactivity of pure TiO_2 was as follows: TiO_2 P25 produces 17.9 x 10^3 µmol, TiO_2 FL synthesized sol-gel produces 23.8 x 10^3 µmol. This difference could be due to differences in crystal size, crystalline phases among others due to different preparations. Regarding the materials with GO, only with FL-GO 4% present a slight higher production, while rest (FL-GO 0.5 and 2%) presented a lower production than TiO_2 FL. The addition of GO produces a modification in behavior with respect to pure TiO_2 material. GO has been reported as an acceptor material because of its bidimensional structure of conjugation π. In counterpart, TiO_2 P25 had lowest production; this is explained by rapid recombination of e^-/h^+ pairs, whereas materials composed by presence of GO the photo-excited electrons of TiO_2 are transferred to GO conduction band by percolation process, this produces separation of pairs e^-/h^+,

added to mixture of phases of TiO_2 (anatase/brookite), crystal size and differences in content of defects by vacancies of oxygen. La diferencia entre el material de mayor producción de H2 (FL – GO 4%) contra el de menor producción (TiO2 P25) es un factor de 1.3 veces. It is also important to consider that GO in composite materials is a mixture of GO with rGO and it has been reported that the amount of rGO affects the water splitting [17]. At the same time the displacement of E_g towards red, which is to say at a higher wavelength at absorption edge (FL - GO 2%) indicates that this band narrowed in interval 2.92 eV. This is associated with the strong interaction between rGO and TiO_2 FL sheets [17].

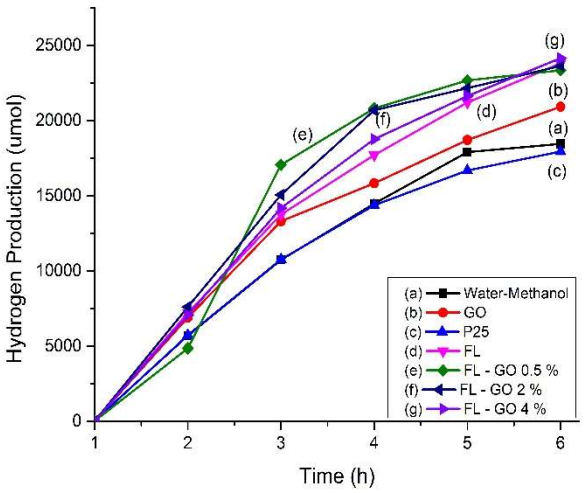

Fig. 3. Hydrogen production by photocatalyst and photolysis.

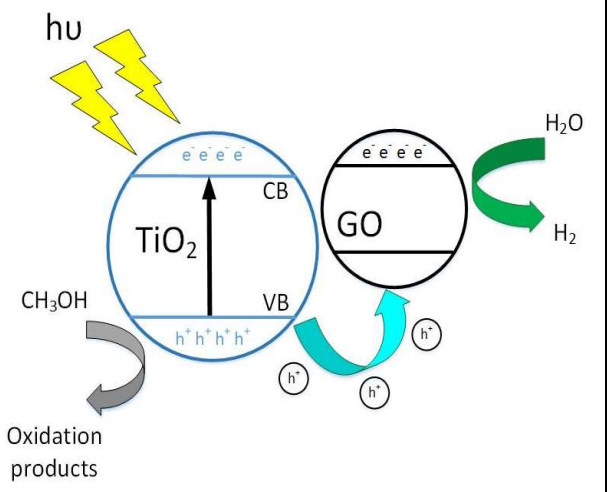

Fig. 4. Electron transfer diagram from CB when irradiated with UV light for FL-GOx compounds.

In Fig. 4 the diagram of H_2 production under UV illumination is shown. When TiO_2 is irradiated with UV light, the electrons of valence band (VB) are photoexcited towards the conduction band (CB), which generates gaps in VB and remain there. What causes the generation of superoxide radicals. In the case of pure TiO_2 charge carriers recombine rapidly. When GO is adhered to TiO_2, the photo-induced electrons are transferred from VB to GO. It has been mentioned in studies that the GO is an excellent acceptor of charge carriers; so it reduces the proton to produce H_2 molecules [18]. This causes slowdown of recombination rate and increases the H_2 production.

4. Conclusion

When adding GO to TiO_2 FL did not produce a great difference when producing H_2, it is probable that mixture of anatase (66%) / brookite (34%) / GOx produces a certain inhibition of photocatalytic

properties of material; however, there was greater production of H_2 than TiO_2 P25, GO and, same photolysis. This is due to addition of GO to TiO_2 since GO is very good acceptor of charge carriers when irradiated with UV light; which produces reduction in recombination rate of pairs e^-/h^+.

The highest production of H_2 was achieved by compound FL-GO 4% (24.15 x 10^3 µmol), followed by TiO_2 FL (23.81 x 10^3 µmol) and, thirdly compound FL-GO 2% (23.63 x 10^3 µmol) . On the other hand, the worst production of H_2 was obtained by TiO_2 P25 with 17.94 x 10^3 µmol.

The FL-GO 2% catalyst had displacement from E_g to visible region (2.92 eV), in addition the crystal size of materials with TiO_2 FL (FL-GOx) are smaller compared to crystal size of TiO2 P25. The thermal stability of composite materials is much lower (less than 400 ° C) than TiO_2, however it is greater than thermal stability of GO (200° C). This allows these materials to be used in processes with a higher temperature than environment. Regarding the superficial areas of materials with low percentage of GO, the value of area is affected almost by half, but as percentage of GO increases, it practically returns to initial values. It was detected that GO was reduced to rGO, although this material was reported as favorable for division of water, no difference was achieved with respect to TiO_2 FL. But even so H_2 production by these photocatalysts prepared in this way is greater than reported by some works.

As future work it would be possible to synthesize materials by adding a third material in order to produce more H_2 and produce a greater displacement of E_g to visible region of light.

Acknowledgements

Thank you for maintenance grant CONACyT-SENER 631485 and national mobility grant CONACyT-SENER. To UAM - Iztapalapa for facilities to carry out this project. We also recognize CONACYT for the support of project SEP-CONACYT CB-2013-01-220191.

References

[1] Zeng K, Zhang D. Recent progress in alkaline water electrolysis for hydrogen production and applications. Progress in Energy and Combustion Science 2010;36:307–26. doi:10.1016/j.pecs.2009.11.002.

[2] Fayaz H, Saidur R, Razali N, Anuar FS, Saleman AR, Islam MR. An overview of hydrogen as a vehicle fuel. Renewable and Sustainable Energy Reviews 2012;16:5511–28. doi:10.1016/j.rser.2012.06.012.

[3] Tour JM, Kittrell C, Colvin VL. Green carbon as a bridge to renewable energy. Nature Materials 2010;9:871–4. doi:10.1038/nmat2887.

[4] Tang C, Zhang Y, Huang Z. Progress in combustion investigations of hydrogen enriched hydrocarbons. Renewable and Sustainable Energy Reviews 2014;30:195–216. doi:10.1016/j.rser.2013.10.005.

[5] Tahir M, Amin NS. Recycling of carbon dioxide to renewable fuels by photocatalysis: Prospects and challenges. Renewable and Sustainable Energy Reviews 2013;25:560–79. doi:10.1016/j.rser.2013.05.027.

[6] Bellardita M, Di Paola A, Megna B, Palmisano L. Absolute crystallinity and photocatalytic activity of brookite TiO2 samples. Applied Catalysis B: Environmental 2017;201:150–8. doi:10.1016/j.apcatb.2016.08.012.

[7] Di Paola A, Bellardita M, Palmisano L. Brookite, the Least Known TiO2 Photocatalyst. vol. 3. 2013. doi:10.3390/catal3010036.

[8] Kominami H, Ishii Y, Kohno M, Konishi S, Kera Y, Ohtani B. Nanocrystalline brookite-type titanium(IV) oxide photocatalysts prepared by a solvothermal method: Correlation between their physical properties and photocatalytic activities. Catalysis Letters 2003;91:41–7. doi:10.1023/B:CATL.0000006316.45620.30.

[9] Zhang J, Yan S, Fu L, Wang F, Yuan M, Luo G, et al. Photocatalytic degradation of rhodamine B on anatase, rutile, and brookite TiO2. Cuihua Xuebao/Chinese Journal of Catalysis 2011;32:983–91. doi:10.1016/S1872-2067(10)60222-7.

[10] Bakardjieva S, Stengl V, Szatmary L, Subrt J, Lukac J, Murafa N, et al. Transformation of brookite-type TiO 2 nanocrystals to rutile: Correlation between microstructure and photoactivity. Journal of Materials Chemistry 2006;16:1709–16. doi:10.1039/b514632a.

[11] Li Z, Cong S, Xu Y. Brookite vs anatase TiO2 in the photocatalytic activity for organic degradation in water. ACS Catalysis 2014;4:3273–80. doi:10.1021/cs500785z.

[12] Tomić N, Grujić-Brojčin M, Finčur N, Abramović B, Simović B, Krstić J, et al. Photocatalytic degradation of alprazolam in water suspension of brookite type TiO<inf>2</inf> nanopowders prepared using hydrothermal route. Materials Chemistry and Physics 2015;163:518–28. doi:10.1016/j.matchemphys.2015.08.008.

[13] Ozer RR, Ferry JL. Investigation of the photocatalytic activity of TiO2-polyoxometalate systems.

Environmental Science and Technology 2001;35:3242–6. doi:10.1021/es0106568.

[14] Fan W, Lai Q, Zhang Q, Wang Y. Nanocomposites of TiO2 and reduced graphene oxide as efficient photocatalysts for hydrogen evolution. Journal of Physical Chemistry C 2011;115:10694–701. doi:10.1021/jp2008804.

[15] Faraldos M, Bahamonde A. Environmental applications of titania-graphene photocatalysts. Catalysis Today 2017;285:13–28. doi:10.1016/j.cattod.2017.01.029.

[16] Zhang X, Li H, Cui X, Lin Y. Graphene/TiO2 nanocomposites: synthesis, characterization and application in hydrogen evolution from water photocatalytic splitting. Journal of Materials Chemistry 2010;20:2801. doi:10.1039/b917240h.

[17] Cheng P, Yang Z, Wang H, Cheng W, Chen M, Shangguan W, et al. TiO 2 e graphene nanocomposites for photocatalytic hydrogen production from splitting water. International Journal of Hydrogen Energy 2011;37:2224–30. doi:10.1016/j.ijhydene.2011.11.004.

[18] Xiang Q, Jaroniec M. Nanoscale Enhanced photocatalytic H 2 -production activity of graphene-modified titania nanosheets 2011:3670–8. doi:10.1039/c1nr10610d.

[19] Minitha CR, Lalitha M, Jeyachandran YL, Senthilkumar L, Rajendra Kumar RT. Adsorption behaviour of reduced graphene oxide towards cationic and anionic dyes : Co-action of electrostatic and p e p interactions. Materials Chemistry and Physics 2017;194:243–52. doi:10.1016/j.matchemphys.2017.03.048.

[20] Zhang Y, Wang F, Zhu H, Zhang D, Chen J. Elongated TiO2nanotubes directly grown on graphene nanosheets as an efficient material for supercapacitors and absorbents. Composites Part A: Applied Science and Manufacturing 2017;101:297–305. doi:10.1016/j.compositesa.2017.06.026.

[21] Dubey PK, Tripathi P, Tiwari RS, Sinha ASK, Srivastava ON. Synthesis of reduced graphene oxide-TiO2nanoparticle composite systems and its application in hydrogen production. International Journal of Hydrogen Energy 2014;39:16282–92. doi:10.1016/j.ijhydene.2014.03.104.

[22] Dresselhaus MS, Jorio A, Hofmann M, Dresselhaus G, Saito R. Perspectives on carbon nanotubes and graphene Raman spectroscopy. Nano Letters 2010;10:751–8. doi:10.1021/nl904286r.

[23] Lu J, Yang J, Wang J, Lim A, Wang S, Loh KP. One-Pot Synthesis of Fluorescent Carbon Graphene by the Exfoliation of Graphite in Ionic Liquids. ACS Nano 2009;3:2367–75.

doi:10.1021/nn900546b.

[24] Naumov V, Gavrilko T, Fedorenko L, Kshnyakin V, Shymanovska V, Kernazhitsky L, et al. Room temperature photoluminescence of anatase and rutile TiO2 powders. Journal of Luminescence 2013;146:199–204. doi:10.1016/j.jlumin.2013.09.068.

[25] Allen NS, Mahdjoub N, Vishnyakov V, Kelly PJ, Kriek RJ. The effect of crystalline phase (anatase, brookite and rutile) and size on the photocatalytic activity of calcined polymorphic titanium dioxide (TiO2). Polymer Degradation and Stability 2018;150:31–6. doi:10.1016/j.polymdegradstab.2018.02.008.

[26] Yadav HM, Kim JS. Solvothermal synthesis of anatase TiO2-graphene oxide nanocomposites and their photocatalytic performance. Journal of Alloys and Compounds 2016;688:123–9. doi:10.1016/j.jallcom.2016.07.133.

[27] Figueiredo J., Pereira MF., Freitas MM., Órfão JJ. Modification of the surface chemistry of activated carbons. Carbon 1999;37:1379–89. doi:10.1016/S0008-6223(98)00333-9.

[28] Botas C, Álvarez P, Blanco C, Santamaría R, Granda M, Ares P, et al. The effect of the parent graphite on the structure of graphene oxide. Carbon 2012;50:275–82. doi:10.1016/j.carbon.2011.08.045.

[29] Shakir M, Noor-E-Iram, Khan MS, Al-Resayes SI, Khan AA, Baig U. Electrical conductivity, isothermal stability, and ammonia-sensing performance of newly synthesized and characterized organic-inorganic polycarbazole-titanium dioxide nanocomposite. Industrial and Engineering Chemistry Research 2014;53:8035–44. doi:10.1021/ie404314q.

E025. INFLUENCE OF DOPING WITH NEODYMIUM ON Pt-Pd BIMETALLIC CATALYSTS SUPPORTED ON γ-ALUMINA FOR THE PRODUCTION OF HYDROGEN BY CATALYTIC DECOMPOSITION OF METHANE

M. Caballero-Díaz[1, 2 *]; G. Del Ángel Montes[2]; V. Tostado-Ramirez[1]; M. Barrios Cruz[1]

[1] Carrera de Ingeniería Química, UNAM, Facultad de Estudios Superiores Zaragoza, Batalla del 5 de mayo, Colonia Ejército de Oriente, Iztapalapa, C.P. 09230 México, Ciudad de México.
[2]Universidad Autónoma Metropolitana-Unidad Iztapalapa, Departamento de Química, Área de Catálisis, Av. San Rafael Atlixco No. 186, C.P. 09340, A.P 55-534. México D. F. México.
*Corresponding author: 55-20032433 and e-mail: marcabdi@yahoo.com.mx

ABSTRACT

In the present work the effect of the addition of neodymium to the Pt-Pd catalyst was studied inorder to obtain a greater selectivity to hydrogen in the methane thermal decomposition (TDM). Three Pd-Pt catalysts supported on γ-Al_2O_3 and γ-Al_2O_3-Nd_2O_3 at 1 and 10% by weight were synthesized, by wet impregnation of the supports with ($H_2PtCl_6$6 H_2O and $PdCl_2$) (Strem Chemicals, 99.99%) aqueous solution. The solids were left in stirring for 3 h, and then, the water is evaporated using a vacuum evaporator bath at 60 °C and vacuum of 72 millibars. The solids were dried in an oven at 120 ° C for 12 hours, then calcined at 500 ° C with air flow at 60 ml / min for 5 hours and finally the catalysts were reduced in a H_2flow at 60 ml/min and 500 ° C for 5 hours. Supports, and catalysts were characterized using different characterization methods such as X-ray diffraction, N_2 adsorption-desorption, X-Ray photoelectron spectrometry, Temperature Programmed Reduction, infrared of CO and Pyridine, High Resolution Transmission Electron Microscopy and Temperature Programmed Oxidation analysis. The decomposition reaction of the methane was carried out in a temperature range of 400 to 750 ° C with a previous activation with nitrogen (30 ml/min at 200 ° C) and the flow of the reagent (methane) was 2 ml/min. To achieve this, an electric furnace was used with a tubular quartz reactor with a porous plate inside to contain the catalyst (50 mg). For the analysis of the reaction products a gas chromatograph Shimadzu GC-2014 was used. The results that were obtained were the following: 1) The bimetallic Pt-Pd/A and of Pt-Pd/ANd1% showed higher conversion than the PtPd/ANd10% catalyst. 2) Whereas, the highest hydrogen production was obtained on PtPd/A catalyst. 3) The presence of Nd inhibits the selectivity towards hydrogen as the Nd increases (1 and 10 wt%). It is assumed that neodymium could interact stronger with the Pt-Pd bimetallic particles causing a high deposit of the coque on the metal sites, poisoning the active sites.

Keywords: neodymium; selectivity; characterization; decomposition;

1. Introduction

With the increase in world population, industrialization and urbanization, the demand for energy is increasing rapidly [1]. Currently, around 85% of the total energy in the world is obtained from non-renewable resources such as coal, natural gas and oil; this contributes to environmental problems (global warming), economic problems and political crises. These resources are finite and their reserves around the world are running out, resulting in an increase in prices. The depletion of finite fossil fuels is a critical problem that must be overcome for a sustainable energy future [2].

The application of thermal decomposition of methane (TDM) to natural gas to produce H_2 and solid carbon has been proposed as a potential technology for the period of transition to the H_2 economy [3]. An analysis of the life cycle of TDM [4,5] have revealed that it has a lower fossil energy consumption. One benefit of this is the exploitation of the current natural gas infrastructure, and therefore, could provide a short-term solution for the production of less polluting H_2. The decarbonisation of fossil fuels, and especially the treatment of natural gas by the thermal decomposition of methane (TDM), has been proposed as a potential technology in the transition to the H_2 economy [6]. The reaction equation for the endothermic TDM reaction is as follows [7]:

$$\Delta H°_r = +\ 76\ KJ / mol) \qquad CH_4 \rightarrow C + 2\ H_2$$

Methane is one of the most stable organic molecules, therefore, in order to obtain hydrogen through the thermal decomposition of methane is an attractive process, it is necessary to develop suitable catalysts. These must satisfy a series of requirements. The activity has to be high, as well as the selectivity towards the desired products, in this case, hydrogen. The catalysts used must also be thermally stable (because reactions are carried out up to 700 and 750 °C). In addition, due to the deactivation by coke, it is convenient to use supports that reduce their formation or that favor their elimination. On the other hand, one of the most important factors to assess is the cost.

A supported catalyst consists of an active phase dispersed on a support. The way to reduce or eliminate the thermal agglomeration of the particles is by fixing it to the surface of a thermally stable support.

In this way the thermal coalescence of the same is avoided, which would lead to a loss of active surface area and decrease the catalytic efficiency [8]. The degree to which the metallic particles are dispersed on the surface of the support depends on the following factors: the metallic charge, the nature of the support and the interaction force between the support and the metallic particles.

The Bimetallic catalysts often show a superior catalytic performance compared to their main metals and have been widely used in many catalytic processes. In comparison with the monometallic catalysts, the bimetallic catalysts have more complex structural surface, where the second metal is exposed on the surface, in the region near the surface or inside the support body.

2. Materials and Methods

The γ-Al_2O_3 support was prepared from the boehmite catapal B (CONDEA, high purity 99.99%, 74% AlOOH, 26% H_2O), dried at 120 °C for 12 hours. After the drying procedure, the solid was calcined in air flow of 60 mL / min for 24 hours using a temperature program of 25 to 650 °C with a speed of 2 °C / min. Finally, the system was cooled to room temperature, maintaining the air flow at 60 mL / min. The γ-Al_2O_3-Nd_2O_3 supports were prepared by impregnation with the neodymium precursor salt, these were prepared at 1.0 and 10% by weight of Nd.

The impregnation method consisted of adding a certain amount of water to the boehmite and stirring for a few minutes. On the other hand, the necessary amount of the precursor salt $Nd(NO_3)_3 6H_2O$ was dissolved with the minimum amount of water, this solution was added to the boehmite and left in agitation for 3 hours, after which time it was placed in a rotary evaporator. 60 °C and a vacuum of 110 millibars, and the remaining water is evaporated with vacuum. Subsequently, it was dried in an oven at 120 °C for 12 hours. The supports thus prepared were calcined at 650 °C in an air flow at a rate of 60 mL / min for 24 hours. In this way, the γ-Al_2O_3 phase doped with neodymium oxide was obtained.

Three Pd-Pt catalysts supported on γ-Al_2O_3 and γ-Al_2O_3-Nd_2O_3 were synthesized at 1 and 10% by weight, the support was placed in the flask with a small amount of water while preparing a solution of the precursor salt ($H_2PtCl_6 \cdot 6H2O$ and $PdCl_2$), dissolved in the minimum amount of water and this was added in the same flask where the support is and it was left stirring for 3 hours in the rotary evaporator, and evaporated using a 60 °C water bath; The solids were dried in an oven at 120 °C for 12 hours, then calcined at 500 °C with air flow at 60 ml / min for 5 hours and finally the catalysts were reduced in a flow of 60 ml / min. H_2 at 500 °C for 5 hours.

The catalytic activity was carried out in a fixed bed U-type quartz micro reactor of the same material at atmospheric pressure, with a catalyst mass of 0.05 g. Before each reaction, the catalyst was activated with a N_2 flow of 30 ml min-1 for 15 min at 200 °C. After activation, the reaction was carried out at the set temperatures (400, 500, 600, 700 and 750 °C) with a flow of 2 ml min^{-1} of CH_4.

The conversion of the production of CH_4 and H_2 as well as of other hydrocarbons such as C_2H_4 and C_2H_6 were controlled in a gas chromatograph.

3. Results and Discussion

All samples exhibited type IV adsorption isotherms, with H1 type hysteresis found in materials that exhibit a narrow range of uniform mesoporous.

The pore diameter of the catalyst is reduced compared to that of the supports and after reacting they have a slight increase but only the one that has 10% of neodymium decreases. The BET surfaces of the fresh catalysts and after the reaction are shown in tables 1 and 2.

It should be noted that the addition of bimetal generates the decrease in pore size, average diameter and pore volume, generating less nitrogen adsorption and therefore less BET area.

The Pt-Pd / A catalyst after reaction decreases its specific area and its pore volume, but the catalysts with neodymium remain almost constant at this change.

Table 1. Areas and average size of the Pt-Pd / A, Pt-Pd / ANd1%, Pt-Pd / ANd10% catalysts fresh.

Catalyst	Areas BET m^2/g	Pore volume (cc/g)	Pore diameter (nm)
Pt - Pd/ɣ- Al_2O_3	170.039	0.5445	4.0
Pt - Pd/ɣ- Al_2O_3-Nd1	139	0.4326	5.5
Pt - Pd/ɣ-Al_2O_3-Nd10	111.32	0.3146	4.6

Table 2. Areas and average size of the Pt-Pd / A, Pt-Pd / ANd1%, Pt-Pd / ANd10% catalysts after reaction.

Catalyst	Areas BET m^2/g	Pore volume (cc/g)	Pore diameter (nm)

Pt - Pd/ɣ- Al_2O_3	126.4	0.446	5.7
Pt - Pd/ɣ- Al_2O_3-Nd1	127.9	0.464	5.7
Pt - Pd/ɣ- Al_2O_3-Nd10	109.2	0.317	4.1

Carbon is not deposited in the metal of any catalyst but, as the increase in neodymium generates the carbon increase in the support that is more difficult to oxidize.The species of carbon deposited in the Pt-Pd/A catalyst are more active than those of the other two catalysts.

The total amount of CO_2 was used to calculate the relative amount of coke deposited on the catalysts after the reaction (Table 3).

Tabla. 3. Total amount of carbon in the catalysts after reaction.

Catalyst	Carbon (carbon mass/catalyst mass, %)
Pt-Pd/A	4.92
Pt-Pd/ ANd1%	6.61
Pt-Pd/ ANd10%	6.83

It can be seen that the catalysts do not have a conversion higher than 63% but in any case the conversion is always increasing.

Table. 4. Hydrogen production and methane conversion of bimetallic catalysts at different temperatures.

Pt-Pd A	Pt-Pd A Nd1	Pt-Pd A Nd10

T °C	%CH_4	H_2 PPM	T °C	%CH_4	H_2 PPM	T °C	%CH_4	H_2 PPM
400	44.75	2697.42	400	47.39	2360.35	400	43.91	0
500	47.95	7309.04	500	49.70	6671.96	500	46.91	212.63
600	49.73	9806.35	600	51.20	9308.13	600	49.65	4138.75
700	58.32	18065.34	700	58.68	16438.45	700	53.62	9140.45
750	62.78	23397.69	750	62.03	18338.74	750	56.94	9631.75

4. Conclusion

The effect of the addition of Nd_2O_3 (1 and 10% by weight) to Pt-Pd / γAl_2O_3 was studied for the production of hydrogen in the decomposition of methane in the temperature range of 400-750 °C. The supports and catalysts were prepared by impregnation of Nd $(NO_3)_3 6H_2O$, $H_2PtCl_6 \cdot 6H2O$ and $PdCl_2$. The Pt-Pd / A catalyst was the one that best produced hydrogen, the addition of neodymium in the bimetallic catalyst did not present the expected result because instead of increasing the production of hydrogen and decreasing the generation of coke, it did everything the opposite, since the catalyst with 10% by weight of neodymium generated much coke for the most part in the support.

Hydrogen could be produced at lower temperatures than in non-catalytic systems for the decomposition of methane (temperature is 1300 °C).

The effect of the neodymium on the catalyst also generated that at 400 °C the production of hydrogen was null, and its maximum production at 750 °C was not even half the production of the best catalyst (Pt-Pd/A).

In the stability it can be seen that the catalyst with 1% neodymium has a stable production (since without neodymium a high production can be seen, but with a rapid decrease), and that production is slowly decreasing, it can be consider using the bimetallic system with little weight percentage in neodymium, since 10% by weight of neodymium produced a very low production.

Acknowledgements

To the Support Program for Research Projects and Technological Innovation PAPIIT with Password: TA100518.

References

[1] M.H. Mahfuz, et al.Exergetic analysis of a solar thermal power system with PCM storage Energy Convers Manage, 78 (2014), pp. 486-492.

[2] Abdalla M.Abdalla, ShahzadHossain, Ozzan B.Nisfindy, Atia T.Azad, MohamedDawood, Abul K.Azad, Hydrogen production, storage, transportation and key challenges with applications: A review.

[3] N.Z. Muradov, T.N. VeziroğluFrom hydrocarbon to hydrogen-carbon to hydrogen economy Int J Hydrogen Energy, 30 (2005), pp. 225-237.

[4] J. Dufour, D.P. Serrano, J.L. Gálvez, J. Moreno, C. GarcíaLife cycle assessment of processes for hydrogen production. Environmental feasibility and reduction of greenhouse gases emissions Int J Hydrogen Energy, 34 (2009), pp. 1370-1376.

[5] J. Dufour, J.L. Gálvez, D.P. Serrano, J. Moreno, G. Martínez Life cycle assessment of hydrogen production by methane decomposition using carbonaceous catalysts Int J Hydrogen Energy, 35 (2010), pp. 1205-1212.¿

[6] L. Weger, A. Abánades, T. ButlerMethane cracking as a bridge technology to the hydrogen economy Int J Hydrogen Energy, 42 (2017), pp. 720-731.

[7] N.Z. Muradov CO_2-Free production of hydrogen by catalytic pyrolysis of hydrocarbon fuel Energy & Fuels, 12 (1998), pp. 41-48.

[8] Campanati, M.; Fornasari, G.; Vaccari, A. Fundamentals in the preparation of heterogeneous catalysts. Catalysis Today. 2003, 77:299-314.

E026. PRODUCTION OF HYDROGEN USING Pd/γ·Al_2O_3 CATALYSTS AND THE INFLUENCE OF NEODYMIUM ON THE CATALYTIC ACTIVITY AND STABILITY OF THE CATALYSTS.

M. Caballero-Díaz[1, 2]*; G. Del Ángel Montes[2]; E. Castillo Bravo[1]

[1] *Carrera de Ingeniería Química, UNAM, Facultad de Estudios Superiores Zaragoza, Batalla del 5 de Mayo, Colonia Ejército de Oriente, Iztapalapa, C.P. 09230 México, Ciudad de México.*

[2]*Universidad Autónoma Metropolitana-Unidad Iztapalapa, Departamento de Química, Área de Catálisis, Av. San Rafael Atlixco No. 186, C.P. 09340, A.P 55-534. México D. F. México.*

** Corresponding author: 55-20032433 and e-mail: marcabdi@yahoo.com.mx*

ABSTRACT

To obtain hydrogen from methane decomposition reaction, γ-Al_2O_3 and γ-Al_2O_3 doped supports with 1 and 10 wt% of neodymium were synthesized. Once the supports were prepared, the Pd/γ-Al_2O_3 and Pd/γ-Al_2O_3-Nd catalysts were obtained by wet impregnation method (1 wt% of palladium). Such materials were characterized using different techniques such as X-ray diffraction, N_2 adsorption-desorption, Transmission Electron Microscopy, X-Ray photoelectron spectrometry, Temperature Programmed Reduction, Infrared of Pyridine adsorption and CO and Temperature Programmed Oxidation analysis. The methane conversion was carried out at temperatures of 400, 500, 600, 700 and 750 °C to hydrogen production. For the analysis of the reaction products a gas chromatograph Shimadzu GC-2014 was used. Experiments were conducted using a quartz tubular reactor, electric oven, a type K thermocouple and a mass of 0.05 g of catalyst was employed.

The increase in area in the AND1% support with respect to the γ-alumina can be attributed to the fact that the neodymium does not block the pores and deposited on external surface of γ-alumina and for ANd10 support, neodymium is not fully dispersed and only partially blocks the pores of the γ-alumina. While the incorporation of neodymium (1 and 10 wt%) decreased the volume and the pore diameter with respect to the γ-alumina alone, this behavior would be due to deposition of Nd_2O_3 at the alumina pores mouth. After adding the Pd as active metal (1 wt. % nominal), the BET surface area, pore diameter and the pore volume decreased, which can be due to the pore blocking of the support after metal addition and the destruction of the mesoporous structure.

.

Keywords: Yield, xps, interaction, stability, selectivity,

1. Introduction

Hydrogen is an attractive fuel for the future. The application of this fuel considerably reduces greenhouse gas emissions compared to current methods of producing energy [1].

But it has the disadvantage of producing a significant amount of CO_2 gas as a by-product [2]. The separation of carbon dioxide from hydrogen and its subsequent sequestration are complex and increase the cost of the overall process. The alternative method of decomposition of methane has been proposed for hydrogen production [3-6].

Metal catalysts supported in the decomposition of hydrocarbons can be used to produce hydrogen at moderate temperatures [7-9]. During the process, CH_4 is adsorbed on the catalyst particle followed by breaking of four C-H bonds and forming to deposition of hydrogen and carbon.

The demand for pure hydrogen is increasing every year, either in quantity or in number of applications that require hydrogen free of carbon monoxide. Improve the economy of methane catalytic cracking, requires extensive research to improve the different parameters of the process. The use of a very active and stable catalyst, the optimization of operating conditions, and the development of suitable reactors are among the different areas that need to be addressed in methane cracking [10].

It is well known that supported Ni catalysts are effective for methane decomposition in the temperature range of 400–600 °C but are deactivated immediately at temperatures above 600 °C [11].

Recently, it was reported that Ni–Cu alloy catalysts showed higher activity and longer life for methane decomposition at 675 °C than Ni catalysts [12]. The maximum conversion of methane for Ni–Cu alloy catalysts reached ca. 35%. In addition, it was reported that Fe–M (M = Mo, Pd, and Ni) alloy catalysts showed high activities for methane decomposition at 700–800 °C [13].

Rare earth metal oxides, particularly neodymium oxide (Nd_2O_3), have recently attracted enormous interest for application in catalysts, UV absorbent, luminescent materials, protective coatings and magnets owing to their wonderful properties [14].

The purpose of the present study was to investigate the influence the addition of Nd (1 and 10 wt%) on the Pd/γ-Al_2O_3 catalysts in the activity, selectivity and catalytic stability for the CH_4 decomposition. The reaction was carried out at temperatures of from 400 to 750 °C.

The characterization by H_2-TPR, XPS, X-ray diffraction, N_2 adsorption-desorption, TEM, FTIR of CO adsorption, FTIR Pyridine of adsorption, HRTEM, TPO, catalytic activity and catalytic stability analysis, was performed.

2. Materials and Methods

2.1 Experimental procedure. Supports and catalysts preparation.

γ-Al_2O_3 support was prepared from Boehmite Catapal B (CONDEA, high purity 99,999%, 74% AlOOH, 26% de H_2O). Firstly, the Boehmite was dried to 120 °C for 12 h, then the solid was calcined in air flow of 60 ml/min for 24 h using a ramp of temperature from 25 °C to 650 °C.

The γ-Al_2O_3-Nd_2O_3 (loaded with 1 and 10 wt% neodymium) mixed oxides, were prepared by wet impregnation of the Boehmite with the necessary quantity of $Nd(NO_3)_3 \cdot 6H_2O$ (Strem Chemicals, 99.99%), the mixture was maintained in stirring for 3 h. Then, the solids were dried in an oven to 120°C for 12 h, after that, samples were calcined at 650 °C in airflow for 24 h.

The Pd catalysts were prepared by wet impregnation of the γ-Al_2O_3 and γ-Al_2O_3-Nd_2O_3 supports with the necessary quantity of $PdCl_2$ (Strem chemicals, 99.9%) to obtain 1 wt% of Pd, at a pH of about 1 to dissolve palladium precursor salt. The solids were left in stirring for 3 h, and then, the water is evaporated using a vacuum evaporator bath. Subsequently the solids were dried in an oven at 120 °C, for 12 h. The catalysts were calcined at 500 °C under airflow for 5 h, finally reduced in H_2 flow at 500 °C for 5 h. The Pd real percentage on the catalysts was obtained by atomic absorption technique. Catalysts were labeled as: PdANdX%, where: Palladium, as Pd, alumina as A, neodymium as Nd, X% is the concentration of Neodymium in wt%, AR the catalysts after reaction and ST stability test.

2.2. Catalysts Characterization

The TPR determinations were carried out in a Chembet-3000 (Quantachrome Co) apparatus using 0.2 g of catalyst by means of the following protocol: samples were heated at 300 °C under nitrogen flow for 30 min. Then, the samples were cooled dawn to room temperature and a mixed gas flow (5% H_2/95% N_2) was passed through the cell. The TPR profiles were recorded by heating the sample from room temperature up to 500 °C at a rate of 10 °C/min.

X-ray photoelectron spectroscopy (XPS) analyses were performed in an ultra-high vacuum (UHV) system Scanning XPS microprobe PHI 5000 VersaProbe-II with a Al Kα X-ray source (hυ= 1486.6 eV), and a MCD analyzer. The surface of the samples were etched for 5 min with 1 kV Ar^+ at 0.04 μA mm^{-2}. The

XPS spectra were obtained at 45º to the normal surface in the constant pass energy mode (CAE), E_0 = 100 and 10 eV for survey surface and high-resolution narrow scan, respectively. The binding energies (BE) were referenced to the Al 2p peak, the BE of which was fixed at 73.5 eV for γ-Al_2O_3. In this case, the position of the C 1s line was 284.8 eV. The intensities and integration of the peaks for each of the elements were estimated by subtracting the Shirley type background and peaks adjustment performed using a mixture of Lorentzian/Gaussian curves. The XPS spectra were fitted using the SDP v 4:1 program. The X-ray diffraction patterns of the different supports and catalysts were measured using a Bruker D-8 Advance equipment with a Cu Kα iradiation source in the 2θ range from 20 to 70 ° with a 0.02° step.

The Temperature programmed oxidation (TPO) study after reaction was performed to determine the amount of carbon deposited in the catalyst after reaction. The TPO determinations were carried out in a CHEMBET-3000 apparatus using a thermal conductivity detector (TCD), and 0.1 g of catalyst. In these experiments, the coke formed during the reactions was oxidized. A flow rate of 10 mL min^{-1} of the 5% O_2/95% He mixture was passed on the sample at a heating rate of 10 °C min^{-1}. Then, the spectra were recorded from room temperature to 900 °C and keeping it at this temperature for one hour. The equipment was calibrated by sending pulses of O_2 diluted in He.

3. Results and Discussion

In the profiles of the H_2-TPR for the PdA, PdANd1% and PdANd10%, for PdA catalyst is observed that the profile has an inverted peak of reduction around 69 °C, which is attributed to the hydrogen desorption on the palladium surface and to the decomposition of palladium hydride formed through hydrogen diffusion in the Pd crystallites. The peaks at 161, 168 and 174 °C in the different catalysts are attributed to the reduction of PdO species on the surface, increasing the reduction temperature as the neodymium content was increased.

The absorption peaks of H_2 at 370 and 381 °C in the catalysts of PdA and PdANd1% respectively are due to the stable species of PdO. The latter was attributed to the complex two-dimensional surface of PdO that is interacting with the suppor.

Another PdO reduction peak could be observed at 464 °C for PdANd1% samples, suggesting more intensive interaction occurred between PdO and the support.

No other reduction peak for PdANd10% in the range of 250-550 °C was detected because it probably moved at higher temperatures.

The XPS technique was used to determine the binding energies of the chemical species of the elements and the proportions on the surface of the fresh catalysts, after reaction (PdANd10%AR) and stability test (PdANd10%ST). To determine the stability test of the PdANd10% catalyst, the sample, was maintained in time on stream for 10 h at 750 °, the relative abundances and the binding energies of each element (Al 2p, Nd 4d, Pd 3d y O 1s) obtained from the deconvolution of the high-resolution spectra in which the different atomic sensitivity factors of each of the atoms were used. The binding energy associated to Al 2p and Al 2s core levels is in 73.70 and 118.85 eV for all catalysts. The binding energy of core level Nd 4d in the fresh and used PdANd10% catalyst is 118.55 eV and for the PdANd1% catalyst was not detected due to the detection limit of the equipment (around 100 ppm).

The different species found according to the deconvolution are associated with different species, the first species is associated with oxygen in the network (Olatt) located at 530.4 eV for all the catalysts and the second is associated with oxygen on the surface due to the adsorption of Water (-OHsurf).

The XRD patterns of the Pd catalysts after reduction at 500 °C for 5 h. The catalysts show the characteristic peaks of γ-alumina phase (JCPDS PDF 056-0457 Quality: Rietveld). The lines associated with Pd crystals (JCPDS 46-1043) were not observed. The diffraction cards for the Nd_2O_3 phase is the JCPDS PDF card 01-079-9858 Quality: Star (*)), for PdO JCPDS PDF 43-1024 and for PdO2 JCPDS PDF 34-1101, these crystalline phases were not detected by DRX. This is explained by a low Pd and Nd concentration and small particles of these elements, which could not be detected by the equipment. The increase in the broad is related with the reduction of the crystallite size as the concentration of Nd_2O_3 increases.

The textural analysis of the catalysts calcined at 650 °C showed, a type IV N_2 adsorption-desorption isotherms. On the other hand, the hysteresis for the catalysts can be type H1.

The N_2 adsorption-desorption isotherms showed that the hysteresis loop of the PdA catalyst formed at a relative pressure around 0.66, while the loop for the PdANdX catalysts was found at relative pressure lower than 0.60. It indicates that the promoted with Nd catalyst contains smaller mesoporous. The BET specific surface area, the increased surface area in the ANd1% support relative to γ-alumina can be attributed to the neodymium does not block the pores and deposited on surface of γ-alumina and for ANd10 support neodymium is not fully dispersed and only partially blocks the pores of the γ-alumina. While the incorporation of neodymium (1 and 10 wt%) decreased the volume and the pore diameter

with respect to the γ-alumina alone, this behavior would be due to deposition of Nd_2O_3 at the alumina pores mouth.

The concentrations of Pd on the catalysts were determined by atomic absorption. The nominal concentration of Pd was 1.0 wt%, the real concentrations were 0.77, 0.80 and 0.80 wt%, these values can be considered valid, in the error range.
The histograms of the distribution of particle size determined by TEM,, for PdA, PdANd1% and PdANd10% fresh catalysts, the catalysts shower low dispersion (25, 24.5 y 20 % respectively), with an important fraction of particles with mean diameter greater than 4 nm.
The adsorption of CO followed by FTIR was used to determine the dispersion of the Pd catalysts and compare with the results of TEM, there being a good agreement between the two techniques.
The results obtained by FT-IR spectroscopy adsorption of pyridine, allowed to elucidate the amount of Brönsted and Lewis acid sites present in the samples. The infrared spectra with adsorbed pyridine of the catalysts show only the presence of bands at 1448 and 1613 cm^{-1} corresponding to Lewis acid sites, while no adsorption band characteristic of Brönsted acid sites at 1540 cm^{-1} was observed.
Considering the high basicity of neodymium with respect to alumina, it can be inferred that the reduction of acid sites in materials with neodymium may be due to the high dispersion of the latter on the surface of γ-Al_2O_3, thus blocking the sites acids.

The HRTEM study of the PdANd10% catalyst, showed different crystallographic planes that were associated to a certain crystalline phase, as mentioned below: the interplanetary distances 1.39 and 1.97 Å correspond to the crystallographic planes (4,4,0) and (4,0,0) associated γ-Al_2O_3 with card number JCPDS 56-0457 Quality: Rietveld.

The PdANd10% catalyst showed the highest catalytic activity and long life for the decomposition of methane at 750 °C, since in 10 hours only 15.8% decreased the activity, while the PdANd1% catalyst was deactivated 26.7% and the PdA catalyst had a deactivation of 33.4%. The stability test at constant reaction temperature, the PdANd10% catalyst provided excellent stability, achieved the best CH_4 conversion of ~77.5% and the highest stability in comparison with the other catalysts, also indicated that the deactivation rate of the PdA catalyst was accelerated, due to the more carbon deposition over the surface.

The strong interaction between palladium and support in the PdANd10% catalyst would be other of the reasons why the catalyst showed high activity and long life for the decomposition of methane at high temperature.

The Temperature programmed oxidation (TPO) study, was performed to determine the amount of carbon deposited in the catalyst after reaction. In these experiments, the coke formed during the reactions was oxidized. A flow rate of 10 mL min^{-1} of the 5% O_2/95% He mixture was passed on the sample at a heating rate of 10 °C min^{-1}. Then, the spectra were recorded from room temperature to 900 °C and keeping it at this temperature for one hour.

TPO enables characterization of coke deposits through oxidation of the coke on the catalyst surface. The temperature at which oxidation occurs is determined by the location and chemical nature of the coke species. Since metals catalyze oxidation, the location is represented by the distance from the active metal. Moreover. Different forms of coke can thus be classified with respect to their chemical nature and location on the catalyst.

The TPO of carbon deposited on the PdA catalyst produced five peaks at about 350, 550, 660, 720 and 900 °C, PdANd1% catalyst showed three peaks around 600, another in 800 and one more in 900 °C, while in PdANd10% catalyst presented six peaks, four peaks between 600 and 700 °C, another around 800 ° C and finally another at 900 ° C. Therefore, deactivation patterns are directly related to the type of carbon deposited and the place where they were deposited.

The coke formation was greater on the PdA catalyst with 18.6%, followed by PdANd10% catalyst with 14.6%, and the catalyst with less coke formation was PdANd1% catalyst with 12.2%, due to the lower conversion of methane in this catalyst.

The strength of acidity decreased with the subsequent increase of neodymium in the support, which could benefit the active phase to inhibit the deposit of coke in the reaction.

Noble metal catalysts are more tolerant toward coking than conventional nickel catalysts.

4. Conclusion

The hydride formation capacity of Pd in the PdA catalyst could be related to the activity of the catalyst in which the hydride could serve as a source of active hydrogen during the reaction.

The amount of neodymium stabilizes the catalysts and favors the formation of the PdO species and avoids the formation of palladium chloride complexes $PdCl_2$ and $PdCl_4^{2-}$.

A larger metal particle size, lower acidity and a surface rich on neodymium oxide of PdANd10% catalyst favored a high catalytic activity and long life for methane decomposition at reaction temperature of 750 °C. PdANd10% showed the highest hydrogen yield among all of the catalysts tested.

The PdANd10% catalyst had a hydrogen selectivity of 100%, since there were no byproducts only unconverted methane. It was observed in the output stream, traces of C_2H_4 and C_2H_6 (less than 1%) and unconverted methane over PdA and PdANd1% catalysts.

The presence of a large proportion of oxidized species of Pd benefited the catalytic activity of the PdANd10% and PtANd1% catalysts due to a strong interaction between the metal and the support.

In addition, Pd increases the migration speed of carbons and evades carbon accumulation on the surface of catalyst during the reaction, which promotes the catalyst lifetime

Acknowledgements

To the Support Program for Research Projects and Technological Innovation PAPIIT with Password: TA100518.

References

[1] Nasir Uddin M, Wan Daud WMA, Abbas HF. Energy Convers Manag (2015);90:218–29.

[2] I. Dincer, Green methods for hydrogen production, Int. J. Hydrogen Energy. 37 (2012) 1954–1971.

[3] A. Abánades, C. Rubbia, D. Salmieri, Thermal cracking of methane into Hydrogen for a CO_2-free utilization of natural gas, Int. J. Hydrogen Energy. 38 (2013) 8491–8496.

[4] W. Yan, S. Kent Hoekman, Production of CO_2-free hydrogen from methane dissociation: A review, Environ. Prog. Sustain. Energy. 33 (2014) 213–219.

[5] N. (Florida S.E.C. Muradov, Thermocatalytic CO_2-Free production of hydrogen from hydrocarbon fuels, Proc. 2000 Hydrog. Progr. Rev. (2000) 1–14.

[6] N.Z. Muradov, CO_2-Free Production of Hydrogen by Catalytic Pyrolysis of Hydrocarbon Fuel, Energy & Fuels. 12 (2002) 41–48.

[7] T.J. Huang, C.H. Wang, Methane decomposition and self de-coking over gadolinia-doped ceria-supported Ni catalysts, Chem. Eng. J. 132 (2007) 97–103.

[8] N. Bayat, M. Rezaei, F. Meshkani, Methane decomposition over Ni-Fe/Al_2O_3 catalysts for production of CO_x-free hydrogen and carbon nanofiber, Int. J. Hydrogen Energy. 41 (2016) 1574–1584.

[9] A. Rastegarpanah, F. Meshkani, M. Rezaei, Thermocatalytic decomposition of methane over

mesoporous nanocrystalline promoted Ni/MgO·Al_2O_3 catalysts, Int. J. Hydrogen Energy. 42 (2017) 16476–16488.

[10] A.M. Amin, E. Croiset, W. Epling, Review of methane catalytic cracking for hydrogen production, Int. J. Hydrogen Energy. 36 (2011) 2904–2935.

[11] S. Takenaka, S. Kobayashi, H. Ogihara, K. Otsuka, Ni/SiO_2 catalyst effective for methane decomposition into hydrogen and carbon nanofiber, J. Catal. 217 (2003) 79–87.

[12] T. V. Reshetenko, L.B. Avdeeva, Z.R. Ismagilov, A.L. Chuvilin, V.A. Ushakov, Carbon capacious Ni-Cu-Al_2O_3 catalysts for high-temperature methane decomposition, Appl. Catal. A Gen. 247 (2003) 51–63.

[13] N. Shah, D. Panjala, G. Huffman, Hydrogen production by catalytic decomposition of methane, Energy & Fuels. 46 (2001) 1528–1534.

[14] C.R. Michel, A.H. Martínez-Preciado, N.L.L. Contreras, Gas sensing properties of Nd_2O_3 nanostructured microspheres, Sensors Actuators, B Chem. 184 (2013) 8–14.

E028. ZINC FERRITES FOR METHYL RADICALS FORMATION: A STUDY OF WATER ADSORPTION INFLUENCE

Lorenzo Antonio Cruz Santiago[1*], Ana Lidia Martínez Salazar[1], Benjamín Portales Martínez[2], Ana Adela Lemus Santana[2], Edilso Francisco Reguera Ruíz[2]

[1]Centro de Investigación en Petroquímica, Instituto Tecnológico de Ciudad Madero, Tamaulipas, México.
[2]Laboratorio Nacional de Conversión y Almacenamiento de Energía, Centro de Investigación en Ciencia Aplicada y Tecnología Avanzada - Unidad Legaría, IPN, CDMX, México.

**lacrus8@gmail.com*

ABSTRACT

The oxidative coupling of methane is a reaction that involves formation of methyl radicals via hydrogen abstraction from the methane by active surface oxygen available in some catalysts, such as iron oxides. Methane gas is a raw material of great energy importance, which could be transformed into other useful chemicals and release hydrogen during the process. In this work, $Fe(III)_{tet}[Zn_xFe(II)_{1-x}Fe(III)]_{oct}O_4^{2-}$ x=0.00,0.25,0.50,0.75,1 systems were synthesized through coprecipitation route. The $Zn(NO_3)_2$, $Fe(NH_4)_2(SO_4)_2$ and $FeCl_3$ precursors were mixed with constant stirring at 50°C until homogenization was achieved. In next step, a solution of NaOH was added dropwise to mixture. Then, temperature was increased to 65°C and mixture was kept under constant stirring for 2 hours. Washings were carried out in triplicate before drying step, which was carried out at 30°C for 24 hours. X-ray diffraction report of the synthesized samples matches well with 28664-ICSD (magnetite) and 76178-ICSD (zinc ferrite) cards. Through diffraction analysis, it is possible to observe the insertion of the zinc ion in the magnetite structure as its concentration increases, plane (311) shows that behavior. Infrared spectroscopy confirmed the ferrites presence, with bands in 300–650 cm^{-1} range that belong to Fe-O bond in Fe_3O_4. The identification of the functional groups present on the surface of the systems allow the assessment of their acidity (Brönsted and Lewis), and therefore, obtain an approach concerning their electronic affinity with water molecules. Study of the chemical environment in ferritic systems clarifies the possibility that these can be used in methyl radicals formation using Fenton's process.

Keywords: zinc ferrite; coprecipitation; infrared spectroscopy; X-ray diffraction

1. Introduction

Iron oxides have three different phases (maghemite, magnetite, and wustite) and transformation between these phases to be determined by distribution of Fe(II) and Fe(III) ions within the oxygen sublattice and electron transfer between the different Fe ions valences [1]. Magnetite (Fe_3O_4) is a black ferromagnetic mineral that belongs spinel group of minerals. The general formula for spinel mineral is AB_2O_4 where A and B represent divalent and trivalent metallic cations, respectively. The spinel-type structure contains all divalent cations on tetrahedral sites and all trivalent cations on octahedral sites. In inverse spinel structure, octahedral sites are occupied by divalent and trivalent cations. Magnetite is an inverse spinel with structural formula $Fe(III)_{tet}[Fe(II)\ Fe(III)]_{oct}O_4^{2-}$ [2]. Magnetite can be transformed into a mixed iron oxide MFe_2O_4, where M is divalent metal (i.e. Mn, Co, Ni, Zn). Mixed iron oxides attract considerable interest as materials for potential applications in different fields [3]. A commercially important mixed iron oxide is zinc ferrite, represented by the following formula $Fe(III)_{tet}[Zn_xFe(II)_{1-x}Fe(III)]_{oct}O_4^{2-}$. Zinc ferrite has been widely investigated due to its unique magnetic, electrical properties, microwave absorption and photocatalytic properties [4].

Among the range of possible applications of zinc ferrite, is its use as a catalyst in oxidative coupling of methane, since it can increase active sites compared to pure magnetite. At the surface level, the active sites of magnetite are both cations and anions and their exposure level depends on the planes preferentially shown by the crystal. The planes (111) are very stable for this structure and the Fe^{3+} cations, which behave like Lewis acids, are exposed in a monolayer 2x2 of 5.94 Å [5]. Similarly, oxygen atoms that are not fully coordinated act as Brönsted bases [6]. Therefore, both active sites (iron and oxygen atoms) are on the surface accessible to the substrates.

Magnetite particles are commonly produced by coprecipitation of ferrous and ferric ions in aqueous solution, thermal decomposition of an alkaline solution of Fe(III) chelate in the presence of hydrazine, and by sonochemical decomposition of hydrolyzed Fe(II) salt followed by thermal treatment [1]. Co-precipitation is an economically viable technique to prepare spinel ferrites at low temperatures, as it offers numerous advantages such as homogeneity, free from contamination and finer control over the particle size of the synthesized particles [7]. This method involves the mixing of a base with an aqueous mixture containing dissolved species of Fe(II) and Fe(III) at room temperature [2]. Below are the details of the synthesis of zinc ferrites by coprecipitation, as well as the chemical and structural studies of each proposed system.

2. Materials and Methods

2.1 Procedure

All chemicals used in the experiment were of analytical grade. Iron(III) chloride hexahydrate (99%), iron(II) ammonium sulfate hexahydrate (99%), zinc nitrate hexahydrate (99%), and sodium hydroxide (99%) as precipitating agent.

To prepare magnetite particles added 20 ml of $Fe(NH_4)_2(SO_4)_2{\cdot}6H_2O$ solution 0.2 M to 20 ml of $FeCl_3{\cdot}6H_2O$ solution 0.4 M and stir the solution continuously at 45 °C till complete dissolution is achieved. Then add 20 ml of sodium hydroxide solution 2 M drop by drop and allow the reaction to occur for around 120 minutes at 55 °C under constant stir. The resulting particles were then washed three times with deionized water. The precipitates were allowed to air dry and dried particles were ground in a mortar.

For the preparation of zinc ferrite particles, the above procedure is replicated by stoichiometrically replacing the iron precursor with zinc precursor according to following formula: $Fe(III)_{tet}[Zn_xFe(II)_{1-x}Fe(III)]_{oct}O_4^{2-}$. The x values for each sample are presented in **Table 1**.

***Table 1**. Samples of magnetite and zinc ferrite synthetized by co-precipitation method.*

Sample	x value
FZ00	0.00
FZ01	0.25
FZ02	0.50
FZ03	0.75
FZ04	1.00

The general chemical equation for synthesis of magnetite and ferrites is given by:

$$M^{2+} + 2Fe^{3+} + 8OH^- \rightarrow M(OH)_2{\cdot}2Fe(OH)_3$$

$$M(OH)_2{\cdot}2Fe(OH)_3 \rightarrow MFe_2O_4{\cdot}nH_2O + (4 - n)H_2O$$

where M represents a divalent cation.

2.2 Analysis of samples

Crystalline and phase formation of the samples has been obtained using X-ray diffractograms by Bruker D8 Advance instrument through CuKα radiation (λ= 1.5406 Å) in 2θ range 05–95°. Fourier Transform Infrared Spectroscopy analysis has been recorded using a Perkin Elmer spectrometer using a KBr pellet technique in the range of 2000–300 cm^{-1}.

3. Results and Discussion

3.1 X-ray diffraction

Zinc ferrites were analyzed by X-ray diffraction and corresponded to a face-centered cubic spinel structure. The XRD patterns of samples are shown in **Fig. 6**. The diffraction peaks match well with 28664-ICSD (magnetite) and 76178-ICSD (zinc ferrite) cards. Diffractograms were characterized by several well-defined peaks, the most intense occurs at 2θ=35.3º (311).

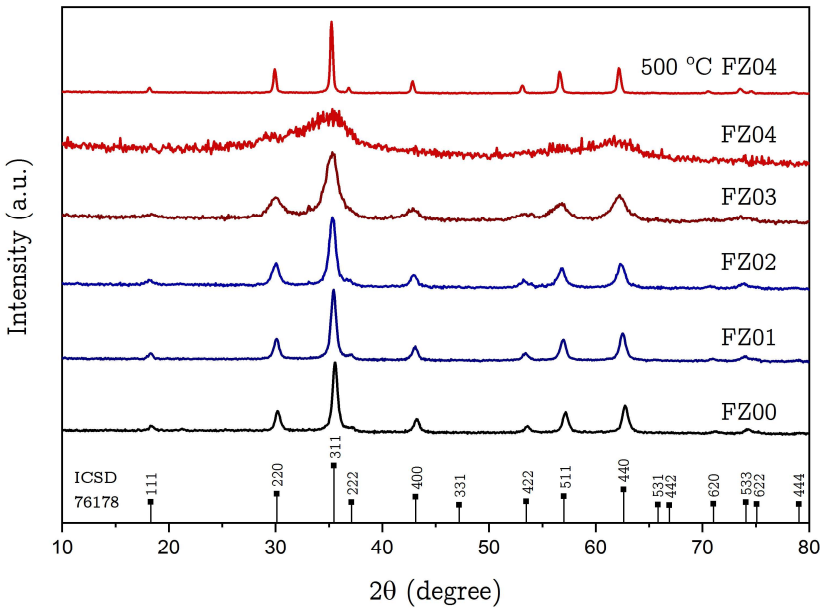

***Fig. 6**. XRD pattern of FZ00-FZ04 samples, synthesized by co-precipitation method, that indicate insertion of zinc ions into magnetite lattice.*

A widening of the most intense peak is observed as the concentration of zinc ions increases, this behavior is related to a decrease in the size of crystal in ferrites. By completely replacing the Fe^{2+} ions with Zn^{2+} the material loses crystallinity and needs to be subjected to thermal treatment, in this case, a temperature of 500 °C was used for one hour. The zinc incorporation into magnetite spinel confers purity to the phase, preventing the formation of a mixture of oxides. This statement is supported by disappearance of peak at 2θ=21.2° which is present in magnetite sample (FZ00).

3.2 Infrared Spectroscopy

FTIR spectra of samples FZ00-FZ04 are shown in **Fig. 7**. A bending vibration of OH^- groups in the range 1620-1640 cm^{-1} is observed. Very weak band at 635-710 cm^{-1} can be attributed to atmospheric CO_2. The band as a shoulder at 1474 cm^{-1} (v_3 asymmetric stretching), bands at 1128 (v_3 asymmetric stretching) and 890 cm^{-1} (v_2 out of plane bending) can be attributed to fundamental vibration bands of CO_3^{2-} group. Infrared spectra below 1050 cm^{-1} contains stretching vibration of Me–O in tetrahedral or octahedral positions, deformation vibration of metal–anion (v_2) bonds and libration vibration of water. Bands at around 570 cm^{-1} can be assigned to v_1(Fe–O) vibration for spinel ferrite structure at tetrahedral site. Fe–O bands are observed at 390-450 cm^{-1} on the infrared spectra of FZ00. In contrast, FZ01 to FZ04 samples presents a Fe-O single band at 380-400 cm^{-1} [8].

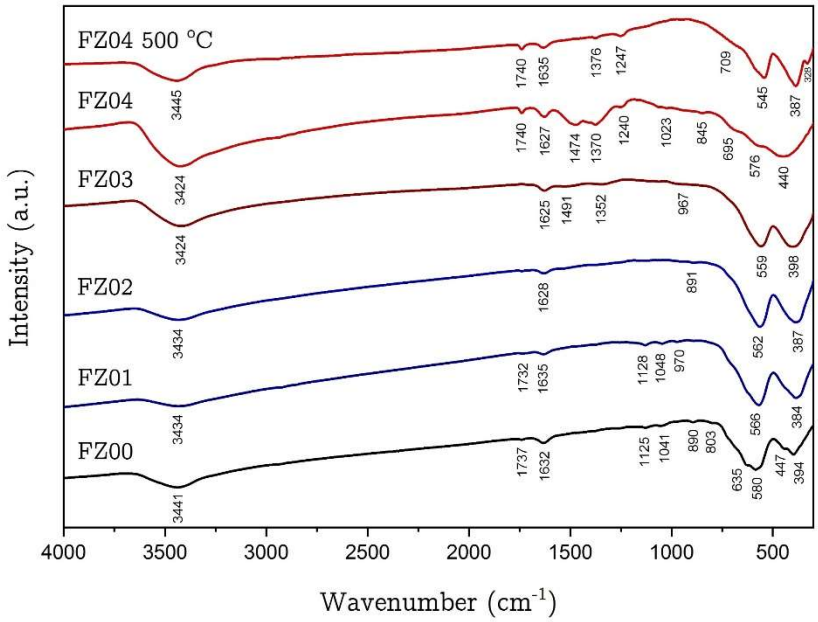

Fig. 7. FTIR analysis of the samples FZ00 to FZ04.

When comparing spectra of samples, displacement of fundamental vibration bands characteristic of ferrite (Fe-O) and bands decrease of CO_3^{2-} groups are observed. These behaviors can be attributed to incorporation of zinc ion in magnetite structure. The presence of CO_3^{2-} groups could be linked to an oxidation process of CO_2 adsorbed on surface.

We can infer that at surface level, the exposure level of active sites in the ferrites depends on planes preferentially shown by the crystal. Planes (111) are often very stable for this type of structure, and it is here that the cations (Zn^{2+}, Fe^{2+}, and Fe^{3+}) and anions (O^{2-}) interact with the substrates. Specifically, Fe^{3+} cations behave like Lewis acids, and likewise O^{2-} anions that are not fully coordinated act as Brönsted bases.

4. Conclusion

Although magnetite contains naturally active sites, it is possible to improve this property through the incorporation of divalent ions that replace Fe^{2+} in its structure. In the results by X-ray diffraction, it was possible to obtain a spinel-type structure that coincides with the characteristic structure of the $ZnFe_2O_4$ systems. The decrease in crystal size and the preference for the plane (111) in these materials allow anticipating a better catalytic activity. Besides, zinc ions have a preference for tetrahedral sites and therefore force Fe^{3+} ions to occupy octahedral sites, exposing them to surface level.

Regarding the chemical environment of samples, through infrared spectroscopy, adsorption phenomena with OH^- and CO_3^{2-} groups that support the behavior of Fe^{3+} ions as Lewis acids are observed. Thus, this interaction of the surface of the material with the surrounding medium is less evident in FZ02 sample corresponding to $Fe(III)_{tet}[Zn_{0.5}Fe(II)_{0.5}Fe(III)]_{oct}O_4^{2-}$ system.

Acknowledgements

We thank Instituto Politécnico Nacional for providing necessary resources to carry out the research.

We gratefully acknowledge the financial support of this work by Tecnológico Nacional de México; research project 5760.19-P.

References

[1] Hai HT, Kura H, Takahashi M, Ogawa T. Facile synthesis of Fe3O4 nanoparticles by reduction phase transformation from gamma-Fe2O3 nanoparticles in organic solvent. J Colloid Interface Sci 2010;341(1):194–9.

[2] Usman M, Byrne JM, Chaudhary A, Orsetti S, Hanna K, Ruby C et al. Magnetite and Green Rust: Synthesis, Properties, and Environmental Applications of Mixed-Valent Iron Minerals. Chem Rev 2018;118(7):3251–304.

[3] Biglari N, Nasiri A, Pakdel S, Nasiri M. Facile and reliable route for synthesis of zinc ferrite nanoparticles and its application in photo-degradation of methyl orange. J Mater Sci: Mater Electron 2016;27(12):13113–8.

[4] Qin M, Shuai Q, Wu G, Zheng B, Wang Z, Wu H. Zinc ferrite composite material with controllable morphology and its applications. Materials Science and Engineering: B 2017;224:125–38.

[5] Rim KT, Eom D, Chan S-W, Flytzani-Stephanopoulos M, Flynn GW, WEN X-d et al. Scanning tunneling microscopy and theoretical study of water adsorption on Fe3O4: implications for catalysis. J Am Chem Soc 2012;134(46):18979–85.

[6] YANG T, WEN X-d, CAO D-b, LI Y-w, WANG J-g, HUO C-f. Structures and energetics of H2O adsorption on the Fe3O4 (111) surface. Journal of Fuel Chemistry and Technology 2009;37(4):506–12.

[7] Vinosha PA, Mely LA, Jeronsia JE, Krishnan S, Das SJ. Synthesis and properties of spinel ZnFe2O4 nanoparticles by facile co-precipitation route. Optik 2017;134:99–108.

[8] Ilhan S, Izotova SG, Komlev AA. Synthesis and characterization of MgFe2O4 nanoparticles prepared by hydrothermal decomposition of co-precipitated magnesium and iron hydroxides. Ceramics International 2015;41(1):577–85.

E033. CHITOSAN-POLYPYRROLE MEMBRANE AS AN ALTERNATIVE FOR PEM TYPE FUEL CELLS.

A. Díaz Rivera[a]; C. Hernández Tenorio[a]; C. A. Cortes Escobedo[b]; M. Villanueva Castañeda[a]; H. Moreno Saavedra[a]; A. Tepale Cortes[a].

[a] División de Estudios de Posgrado e Investigación, Tecnológico Nacional de México/Instituto Tecnológico de Toluca, Av. Tecnológico s/n, Col. Agrícola Bellavista, CP 52149 Metepec, EdMx, México

[b]Centro de Investigación e Innovación Tecnológica, Instituto Politécnico Nacional, Azcapotzalco, Ciudad de México 02250, México

* Corresponding author: 7228409731 ing.alejandradr@gmail.com

ABSTRACT

The present work focuses on the study of chitosan doped with pyrrole (Py) by means of a luminescent plasma discharge in aqueous solution, in order to evaluate its application in fuel cells from its functional groups, morphology, proton conductivity and thermal resistance. Chitosan is a biodegradable polymer that contains a large number of -NH_2 and -OH groups attached to glucose units, resulting in a hydrophilic material that offers greater adsorption and selectivity than Nafion [1]. The synthesis of the membrane was carried out by evaporation and three plasma doping times were worked with 20, 40 and 60 minutes with concentrations of 0.1 M and 0.2 M of Py, 480 µm in thickness. The morphology showed that chitosan membranes have a smoother surface compared to those treated with pyrrole, which have a higher roughness improving proton conductivity [2]. The FTIR spectra show the presence of polypyrrole functional groups producing interactions between amines, hydroxyl groups and C-N bonds; resulting in water resistant and mechanically stable membranes. The thermogravimetric analysis showed a degradation in a range of 40 to 70% at a temperature of 200 to 400 ° C, confirming the thermal stability of the membranes and the proton conductivity significantly increased with the doping time in a range of 10^{-4} and 10^{-3} S / cm.

Keywords: Fuel cell; proton exchange membrane; chitosan-polypyrrole membrane; proton conductivity.

1. Introduction

The current demand for energy is growing at an alarming rate, and the main sources of electricity use fossil fuels which are limited and have important environmental consequences. A promising alternative to this problem are the fuel cells, which generate electrical energy from chemical reactions with hydrogen, producing energy that is economical and friendly to the environment [3].

The fuel cells convert the chemical energy of the reactions between hydrogen as a reducer, and oxygen as an oxidant. The classification of the cells is by the type of electrolyte between these is the proton exchange membrane fuel cell (PEMFC), operate at low temperatures of 60 to 80 ° C allowing a potentially faster start than the fuel cells that they operate at high temperatures [4].

The Nafion became a standard membrane for fuel cells type PEM, because it has a negative charge of SO3 (sulfonic acid groups), which works as an insulator since it does not allow the flow of electrons through the membrane [5]. The main feature of the Nafion membrane is high chemical stability and good proton conductivity, however, its high cost has stimulated the development of new polymeric materials.

The membrane of Chitosan-Polypyrrole is an alternative for fuel cells type PEM, because Chitosan is a biopolymer abundant in the environment therefore its cost is minimal [1]. Polypyrrole, on the other hand, is a semiconductor polymer with long-chain conjugated chemical bonds in its molecular structure, providing a proton transport channel [6]. The combination of these two materials allows obtaining a proton exchange membrane.

2. Materials and Methods

2.2 Synthesis of Chitosan membranes.

The synthesis of the Chitosan membrane was carried out by evaporation of the solvent in an acid medium, 3 g of chitosan (Sigma Aldrich) in 100 ml of an acetic acid solution (Sigma Aldrich, 99.7%) was dissolved by stirring. 1% v / v and glycerol (92.09 PM, 99.7%) 3% v / v for 8 hours. Subsequently, ethylene glycol diglycidyl ether (Tokyo Chemical Industry CO. LTD, 97%) was poured into the solution at 0.15% v / v, again stirring for a further 5 hours until a homogeneous solution was obtained, subsequently the solution was poured into a petri dish 17.5 x 12.5 cm at room temperature for 5 days, once dried, the membranes were cut into 3 x 3 cm squares.

2.3 Doping of the membranes of Chitosan.

For the doping of the membranes of chitosan with pyrrole (Py) was carried out by means of a luminescent plasma discharge (GDP) in aqueous solution. The electrolyte solution was prepared using two different concentrations of pyrrole (Sigma Aldrich, 98%) of 0.1 M and 0.2 M, in a solution of sodium sulfate (Fermont 99.6%) at 0.1 M in 100 ml of deionized water (pH 5.5 to 2.0 µS / cm). The doping times were 20, 40 and 60 minutes and at the end of the doping time the membranes were rinsed with deionized water and allowed to dry for 3 hours.

2.4 Sulphonation treatment of membranes

The chitosan membranes doped with pyrrole lack sulfonated groups in their structure, to add this group the sulphonation treatment was carried out, which consists of immersing the dry membranes in a sodium hydroxide solution (J.B.Baker, MW 40.0 g / mol) 2 M for 5 minutes to neutralize, then rinsed with deionized water and submerged again in a sulfuric acid solution (Fermont, 97.7%) at 0.5 M for 24 hours, in order to add the SO3H groups.

2.5 Characterization

2.5.1 Water uptake and swelling index

To calculate the percentage of water uptake, the dry membranes are immersed in deionized water for 24 h and weighed to know the amount of liquid retained in it. To know the swelling index, the thickness of the membranes before and after immersion in water is measured. Finally using the equations (1 and 2) the water uptake and swelling index is calculated.

$$\%\,\mathrm{WU} = \frac{W_h - W_s}{W_s} * 100 \quad (1)$$

$$\%S_W = \frac{e_h - e_s}{e_s} * 100 \quad (2)$$

Where WU is the water uptake by the membrane, W_h is the weight of the wet membrane, W_s is the weight of the dry membrane, S_W is the swelling index, e_h thickness of the wet membrane and e_s thickness of the dry membrane [1, 7, 8].

2.5.2 Proton conductivity analysis

The proton conductivity of the membranes is calculated by means of electrochemical impedance spectroscopy (EEI), using a biologic SP300 galvanostat potentiostat and a parallel plate device. The information provided by the ISS is interpreted through the Nyquist diagram where a semicircle is plotted representing the impedance at the measured membrane frequency. The following equation is used to calculate the proton conductivity of the membranes [9].

$$\sigma = \frac{l}{A * R} \quad (3)$$

Where σ is the conductivity (S / cm), l is the thickness of the sample in cm; A It is the area of the cross section of the membrane in cm^2 and R is the resistance to proton conduction Ω.

2.5.3 Scanning electron microscopy (SEM) and X-ray energy dispersion spectrometry (EDS) analysis

Using the scanning electron microscope JEOL JSM-6610LV was used to obtain structural information of the surface and the qualitative and semi quantitative analysis of the chemical elements contained in the structure of chitosan-polypyrrole membranes where an electron sweep was applied to a voltage from 20kV to 1000 magnifications.

2.5.4 Fourier transform infrared spectroscopy (FTIR)

The characterization by infrared spectroscopy was used an AGILENT brand FTIR model VARIAN 640-IR for the qualitative analysis of the functional groups and the types of bonds present, using samples of the chitosan-polypyrrole membrane in a range of width of band from 4000 to 500 cm^{-1}.

2.5.5 Thermogravimetric analysis (TGA)

To know the thermal stability of the chitosan-polypyrrole membranes, a thermogravimetric analysis was carried out using the LINSEIS STA TP1600 equipment, the heating was carried out with a ramp of 5 ° C / min in a range of 30 ° C to 800 ° C under an atmosphere of air.

3. Results and Discussion

3.1 Water uptake and swelling index

Figure 1 shows the water uptake index of the membranes (% WU) of chitosan-polypyrrole, Figure1A shows that the membrane that has a lower absorption capacity is treated for 60 min with a pyrrole concentration of 0.2 M and a thickness of 480 µm. Also, Figure 1B shows that the swelling index is 23.6% and has a greater dimensional stability.

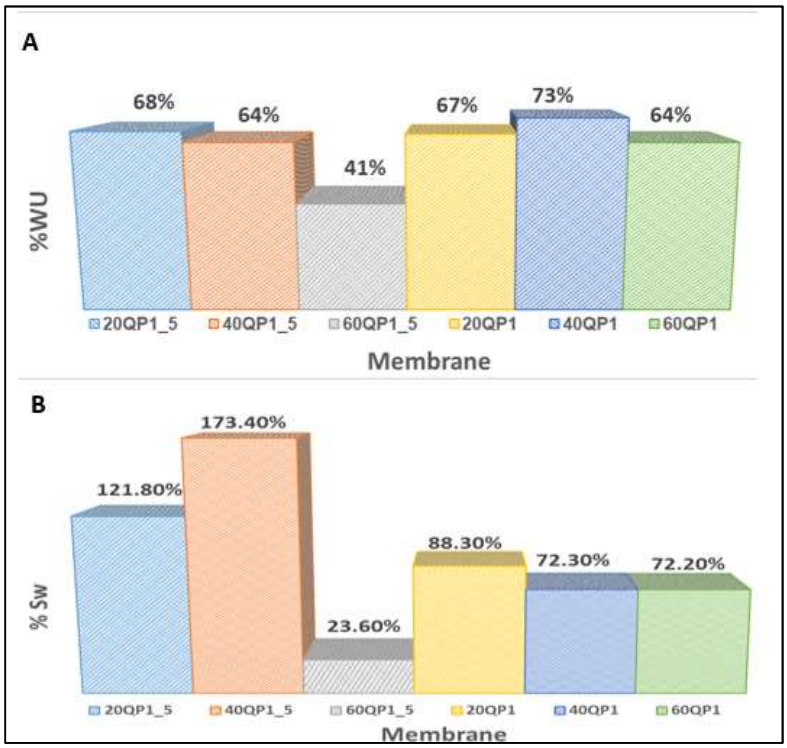

Fig. 1. Membranes of chitosan-polypyrrole A: Comparison of water uptake, B: Swelling index.

3.2 Proton conductivity analysis

By means of the Nyquist diagram obtained by the impedance electrochemical spectroscopy technique, the imaginary impedance (Zim) and real impedance (Zre) were calculated in a frequency range of 100 mHz -10 kHz. From the impedance data, the value of the proton resistance (R) corresponding to the cut point of the semicircle with the real axis of the impedances was calculated. Table 1 shows the relationship of the thickness of the film and the proton conductivity, it is observed that the proton conductivity improves as the concentration of the pyrrole used during the treatment with luminescent discharge plasma increases.

Table 1. Chitosan-polypyrrole membranes A: Water uptake (% WU), and Swelling index (% SW)

Membrane	Resistance (Ω)	Thickness (µm)	Area (cm^2)	Conductivity (S/cm)
20QP0.2M	99.35	712	1	7.17E-04
40QP0.2M	87	700	1	8.05E-04
60QP0.2M	18.77	476	1	2.54E-03
20QP0.1M	68.03	433	1	6.36E-04
40QP0.1M	87.12	398	1	4.57E-04
60QP0.1M	76.78	341	1	4.44E-04

According to the consulted data, the Nafión 115 membrane has a conductivity of 0.1 S / cm [Reference]. The experimental results of the membranes analyzed, shown in Table 1, the membrane with the highest proton conductivity corresponds to the membrane with a thickness of 480 µm with a proton conductivity of 2.54 $X10^{-3}$ S / cm.

3.3 Scanning electron microscopy (SEM)

Figure 2 shows the micrographs of chitosan-polypyrrole membranes at different concentrations and times of plasma treatment, Figure 2A belonging to the membrane with concentration 0.1 M shows greater porosity with respect to the 0.2 M of Figure 3B with treatment of 20 min. Figures 3C and 3D of the membranes of 0.1 and 0.2 M respectively with treatment time of 40 minutes, show a decrease in the pore size, while figures 3E and 3F belonging to the samples treated for 60 min show the sizes of much smaller pores, this allows to improve the mechanical properties of the membrane, which allows to improve the flexibility, and also prevents the hydrogen molecules from passing freely through it.

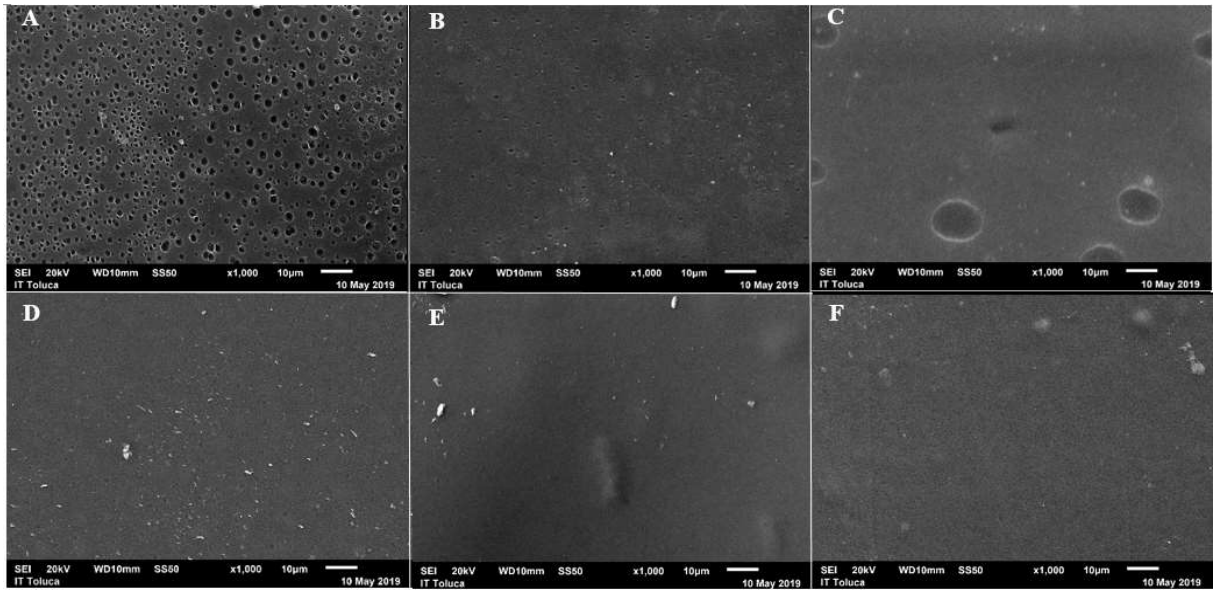

Fig. 2. Micrographics MEB x1000: Membranes of chitosan-polypyrrole, A) 0.1 M of pyrrole and 20 min of doping, B) 0.2 M of pyrrole and 20 min of doping, C) 0.1 M of pyrrole and 40 min of doping, D) 0.2 M of pyrrole and 40 min of doping, E) 0.1 M of pyrrole and 60 min of doping, F) 0.2 M of pyrrole and 60 min of doping.

3.4 Analysis of X-ray energy dispersion spectrometry (EDS)

MEB x1000 micrographs: Chitosan-polypyrrole membranes, A) 0.1 M pyrrole and 20 min of doping, B) 0.2 M pyrrole and 20 min of doping, C) 0.1 M pyrrole and 40 min of doping, D) 0.2 M of pyrrole and 40 min of doping, E) 0.1 M of pyrrole and 60 min of doping, F) 0.2 M of pyrrole and 60 min of doping.

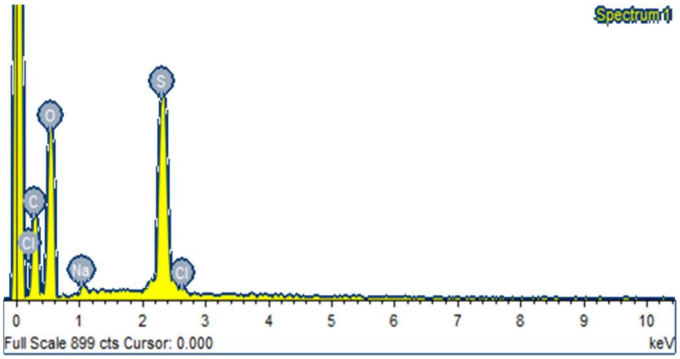

Fig. 3 EDS of chitosan polypyrrole membranes treated at 60 min and a thickness of 480 µm.

3.5 Fourier transform infrared spectroscopy (FTIR)

Figure 4 shows the FTIR spectra of the chitosan-polypyrrole membranes at a concentration of 0.1 M and 0.2 M respectively of three different doping times, the band 3330 cm^{-1} correspond to the stretching vibration of NH of the primary amines of the polypyrrole, the bands 2353 cm^{-1} represent the stretching vibrations = C =, in the band 1636-2637 cm^{-1} corresponds to the vibrations of stretching of carbon double bonds C = C due to the aromatic ring of pyrrole, the band 1536 cm^{-1} corresponds to the stretching vibrations of a nitric compound N- belonging to the basic structure of the polypyrrole, in the band 1380 cm^{-1} the vibrations of the sulfonic acid groups generated in the sulphonation treatment are presented in the band 1075 cm^{-1}, on the other hand, the absorption peaks for CN bonds that represent vibrations of amines of chitosan are presented.

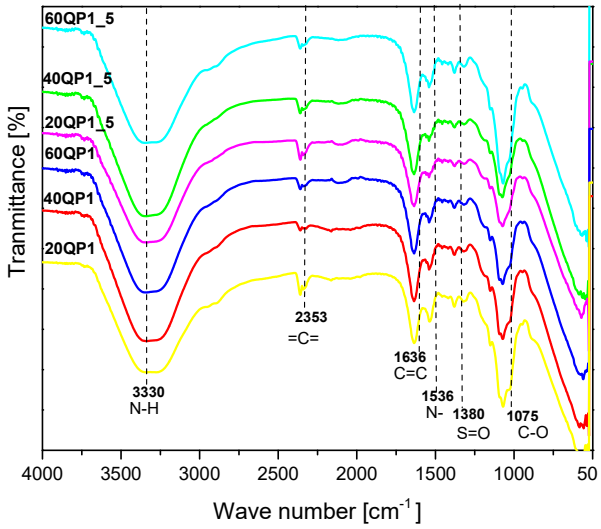

Fig. 4. FTIR of chitosan-polypyrrole membranes at a concentration of 0.1 and 0.2 M pyrrole at 20, 40 and 60 min of doping.

3.6 Thermogravimetric analysis (TGA)

Figure 5 shows the weight loss behavior of the sample with respect to the temperature increase in the range of approximately 20 to 100 ° C, three important events occur, where the first event between 20-100 ° C is related with the loss of water molecules present on the surface of the membrane. The second thermal event comprised between 170 and 220 ° C corresponds to the depolymerization reaction of the chitosan chains. Finally the third thermal event of the film present between 220 to 400 ° C, indicates the total degradation of all polypyrrole and chitosan particles.

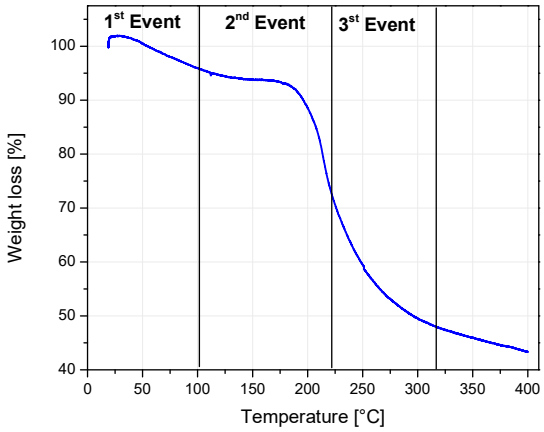

Fig. 5. TGA thermogram Chitosan-polypyrrole membranes of sample 60QP0.2M

4. Conclusion

The membranes of Chitosan-Polypyrrole do not present a significant variation in their composition of functional groups with respect to the treatment with plasma discharge, however, if a high percentage of oxygen is shown, which suggests a certain degree of oxidation. On the other hand, the presence of sulfur is verified as a result of the sulphonation technique, likewise, the thermogravimetric analysis describes three main events: moisture loss, depolymerization and degradation in an air atmosphere in a temperature range of 20-400 ° C. The morphology of the membranes reveals the presence of pores which decrease in size considerably as the doping time increases, which gives the membranes greater flexibility and mechanical resistance. Finally, the membranes show good water absorption and good dimensional stability generating greater protonic conduction in a range of 10-4 and 10-3 S / cm.

Acknowledgements

This research work was supported by Technological Institute of Toluca, Center for Research and Technological Innovation (CIITEC), National Polytechnic Institute (IPN), National Council of Science and Technology (CONACYT), SMH and XVII International Congress of the Mexican Hydrogen Society.

References

1] Kumar D, Dipak F, Subbiah A, Meenakshi S, Sri Abirami S, Alagumalai N. Investigating the usefulness of chitosan based proton exchange membranes tailored with exfoliated molybdenum disulfide nanosheets for clean energy applications. J Carbohydr. Polym 2019; 208: 504-512.

[2] Saad A, Yangben C, Muhammad A, Santosh K, Shiai Xu. Preparation and performance of nanoparticle-reinforced chitosan proton-exchange membranes for fuel-cell applications. J. Appl. Polym. Sci. 2018; 136:1-7.
[3] European Commission EUR 20719 ES. The energy of hydrogen and fuel cells, a vision for our future. Luxembourg: Office for Official Publications of the European Communities: 2003 - 32.
[4] EG & G Services, National Energy Technology Laboratory (U.S.). Fuel cell handbook. Morgantown, WV: U.S. Dept. of Energy, Office of Fossil Energy, National Energy Technology Laborator 2004; 3-1-23.
[5] S. J. Peighambardoust, S. Rowshanzamir, and M. Amjadi. Review of proton exchange membranes for applications in fuel cells. Int J Hydrogen Energy 2010; 35: 9349-9384.
[6] L. Fan, T. Gao. Applications of Nanoscale Polypyrrole Proton Exchange Membrane in Microbial Fuel Cells. Int J Electrochemical Science 2019; 14:470–480.
[7] M. S. Asgari, M. Nikazar, P. Molla Abbasi, M. Hasani Sadrabadi. Nafion/histidine functionalized carbon nanotube: High-performance fuel cell membranes. Int J Hydrogen Energy 2013; 38: 5894–5902.
[8] K. Pourzare, Y. Mansourpanah, and S. Farhadi. Advanced nanocomposite membranes for fuel cell applications: a complete review. J Biofuel Research 2016; 3: 496-513.
[9] R. Kuwertz, C. Kirstein, T. Turek, and U. Kunz. Influence of acid pretreatment on the ionic conductivity of Nafion membranes. J Membrane Science 2015; 500: 225-235.

E035. EFFECT OF THE PARTICLE ARCHITECTURE ON THE PALLADIUM CHARGE IN ELECTROCATALYSTS FOR PEM-FC

Eduardo Y. Cervantes-Aspeitia[1], C. R. Santiago-Ramírez[1], Martha L. Hernández-Pichardo[1], R.G. González-Huerta[2] and Paz del Ángel[3].

[1]*ESIQIE-Instituto Politécnico Nacional, Laboratorio de nanomateriales sustentables, Av. IPN s/n, Ciudad de México, 07738.*
[2]*ESIQIE-Instituto Politécnico Nacional, Laboratorio de electroquímica y corrosión, Av. IPN s/n, Ciudad de México, 07738.*
[3]*Caracterización de Materiales Sintéticos y Naturales, Instituto Mexicano del Petróleo, Eje Central L. Cárdenas 152, Ciudad de México, 07730.*
**mhernandezp@ipn.mx*

ABSTRACT

In this work, Au@Pd core-shell nanoparticles (NPs) supported on vulcan carbon were synthesized by the seed growth method in order to decrease the palladium charge, compared to the commercial Pd/C catalyst. The morphology, size and composition weres studied by of Au@Pd/C were investigated by transmission electron microscopy (TEM), X-ray diffraction (XRD), energy dispersive spectroscopy (EDX), EDX mapping, and scanning transmission microscopy (SEM). The electrochemical properties were investigated by cyclic voltammetry (CV) and linear sweet voltammetry (LSV). The Au@Pd/C catalyst shows a higher current density, with a difference of 0.15 mV with respect Pd/C. This effect is related to the rugosity that the Pd has on the Au, which generates a greater number of active sites and therefore greater activity towards the oxygen reduction reaction. The effect of the bimetallization shows an enhanced activity toward the oxygen reduction reaction (ORR) evaluated in acid medium, as well as the change of the architecture allows a synergic effect between Au and Pd, this allow decreasing the palladium charge percent, from 10% to 5%.

Keywords: core-shell nanoparticles, ORR, metallic charge.

1. Introduction

The main objective of fuel cells is to provide an efficient and clean mechanism for energy conversion, in recent years they have attracted great interest with the potential to become the most important power generating device in the future [1]. Proton exchange membrane fuel cells (PEMFC) show the most promising types already in the early commercialization stage, but those devices have been hindered by the sluggish reaction kinetics of the oxygen reduction reaction (ORR) [2–4]. Most of the research currently being conducted on ORR are the development of core-shell electrocatalyst [5,6]. The core-

shell catalysts are focused on two important features: the first one is the presence of a core, generally constituted by relatively low-cost metals and an the other one is the outer shell, where prevalent a noble metals to sustain the electrochemical conditions and which have been attracting particular interest because of their unique features, such as high electrical conductivity, large surface area, high stability, enhanced activity and optimizable surface electronic structure due to intimate interactions between the metal core and shell. The activity differences are explained via structural, charge transfer and electronic structure analyses. [7–9]. For many years the catalysts based on Pt have been used due to the excellent activity towards the ORR, but due to the high cost and few reserves of this metal, the possibility of decreasing the metal load used and better still replacing it with nonplatinum alloy compositions was studied. That offer catalytic activity like that of platinum, likewise the development of catalysts of two or more metals is sought that help to improve in a better way the mechanisms involved in the ORR [10]. Pd based catalyst are the main candidate to use like outer shell alloying elements M (M=Ag, Ir, Pt and Au) may be able to affect the electronic structures of the Pd segregated surface by lattice strain (strain effect) or electronic interaction (ligand effect) [11]. Additionally, some studies show that gold can improve electrocatalytic properties through synergistic effects [12]. Au@Pd catalysts present an enhanced catalytic activity and improved durable ability for ORR [13] and some studies are focused on the particle architecture due to present an enhanced catalytic activity, those activity differences are related with shape and size changes [14,15].

Thus, in this work present the results of the study of core-shell nanoparticles and the effect of architecture on the oxygen reduction reaction. We evaluated the metal content of Au@Pd/C compared with Pd/C commercial catalyst.

2. Materials and Methods

2.1. Chemicals and Materials. Cetyltrimethylammonium bromide, cetyltrimethylammonium chloride, $NaBH_4$, $HAuCl_4{\cdot}H_2O$, trisodium citrate, $PdCl_2$, ascorbic acid, Nafion (5%) were all purchased from Sigma-Aldrich and HCl (Fermont). The Pd/C catalyst (10% Pd mass loading containing 5−6.5 nm Pd NPs) and carbon vulcan XC 72 was obtained from Fuel Cell Store. Ultrapure deionized water was used for all solution preparations.

2.2 Synthesis of Au@Pd/C core-shell nanoparticles. A three-step synthesis method was followed for the preparation of Au@Pd nanoparticles [16]. Seeded growth Au nanoparticles with 5 ± 0.8 nm

diameter: The seeded growth Au nanoparticles were prepared similarly to a previous report by Jana et al. [17] with some variations, In a conical flask was added 300 µL of $HAuCl_4$ (10 mM) and 2 ml of trisodium citrate ($2.5x10^{-4}$ M). Next, 0.6 mL of ice-cold, freshly $NaBH_4$ (0.1 M) solution was added to the solution while stirring. The solution was kept under slow stirring for 3 h to assure the total decomposition of $NaBH_4$. Octahedral Au nanoparticles: To obtain Au-truncated octahedral NPs, 200 µL of $HAuCl_4$ (10 mM), 5 mL of CTAB (0.1 M) and 2 mL ascorbic acid (0.1 M) were diluted to 35 ml of Milli-Q water. After, 0.3 mL of seeded growth Au nanoparticles solution was added, mixed for 3 minutes and left undisturbed overnight. Au@Pd core-shell nanoparticles. Two solutions were prepared, 4 ml of Octahedral Au nanoparticles was mixed with 32 ml of Milli-Q water, moreover 5 ml of CTAC was mixed with 400 µL of H_2PdCl_4, those solutions were mixed and stirring for 3 minutes, after this 0.1 ml of ascorbic acid was added, the solution was mixed for 10 minutes and left undisturbed overnight. The supported NPs on carbon vulcan were prepared mixed a carbon vulcan ethanol solution and Au@Pd NPs solution, obtaining a Pd charge of 5%.

2.3. NPs Characterization. X-ray diffraction (XRD) patterns were collected on a Bruker AXS D8 diffractometer with Cu Kα radiation (λ =1.5418 Å). Transmission electron microscopy (TEM) images were acquired on a JEOL 2200-FS operating at 200 kV. Scanning transmission electron microscopy (STEM) analyses were carried out with a FEI TITAN 80-300 (300 kV) with a Cs corrector. Samples for TEM and STEM analysis were prepared by depositing a single drop of diluted NPs dispersion in isopropanol on amorphous carbon coated copper grids.

2.4 Electrochemical measurements. The electrocatalytic activity was evaluated on the oxygen reduction reaction (ORR) in 0.1 M $HClO_4$. The electrocatalytic ink for two samples Au@Pd/C and commercial Pd/C were prepared as follows: 5 mg of powder catalyst were mixed with 750 µL of isopropanol, 250 µL of Milli-Q water and 70 µL of Nafion® and sonicated for 45 min. Then, 9 µL of this suspension were dropped on a glassy carbon electrode (0.196 cm2) previously polished at mirror-finish. Finally, the glassy carbon electrode was dried by rotating at 500 rpm at room temperature. For all electrochemical measurements a standard tree-electrode glass cell by using a potentiostat Autolab Modelo PGSTAT302N. A Pt mesh and a reversible hydrogen electrode (RHE) were used as counter and reference electrode, respectively. A Pt mesh and a reversible hydrogen electrode (RHE) were used as counter and reference electrode, respectively. The electrolyte was 0.1 M $HClO_4$. The electrochemical measurements were carried out at 25° C. Cyclic voltammetry (CV) and linear sweep voltammetry (LSV) techniques were carried out in Ar and O_2-saturated, respectively. The CV profiles were recorded from 0.05 to 1.2 V vs.

RHE, at 50 mV s^{-1}.LSV polarization curves were obtain from open circuit potential (OCP) to 0.20 V vs. RHE, at 5mV s^{-1}, with a rotation speed of 100, 200, 400, 900, 1600 and 2500 rpm and 25° C.

3. Results and Discussion

3.1 Structural and compositional characterization.

In Fig. 1, the XRD reflection peaks suggest the formation of core-shell nanoparticles, showing distinct Au and Pd crystalline components, according to JCPDS no. 04-0784 and JCPDS no 46-1043, respectively. The reflections peaks at 40.1°, 46.5°, and 68° correspond to (111), (200) and (220) planes in the Pd fcc structure. For Au XRD reflection peaks at 38.2°, 44.5°, 64.89° and 77.56° correspond to (111), (200) and (220) planes in the Au fcc structure.

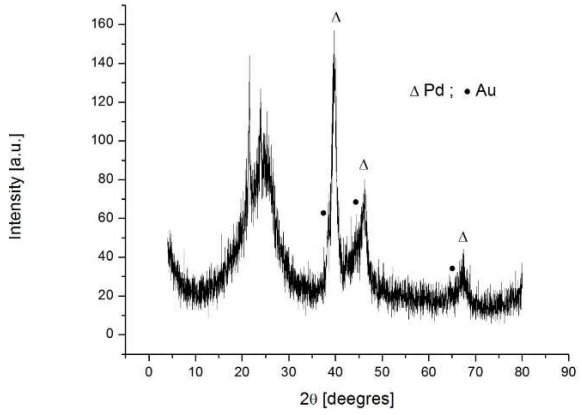

Fig. 1. XRD patterns of Au@Pd/C.

A three steps synthesis method was following by TEM. Fig. 2(a) shows the formation of Au seeds. It is observed a uniform distribution of nanoparticles with an average size of 5 nm and HRTEM micrography, by fast Fourier transform (FFT) it is possible to define the zone axis [2 0 -2]. Fig. 2(b) shows a growth to truncated octahedral Au nanoparticles with an average size of 20 nm and HRTEM micrography, by fast Fourier transform (FFT) it is possible to define the zone axis [2 0 -2], and Fig. 2(c) shows the formation of Au@Pd core-shell nanoparticle.

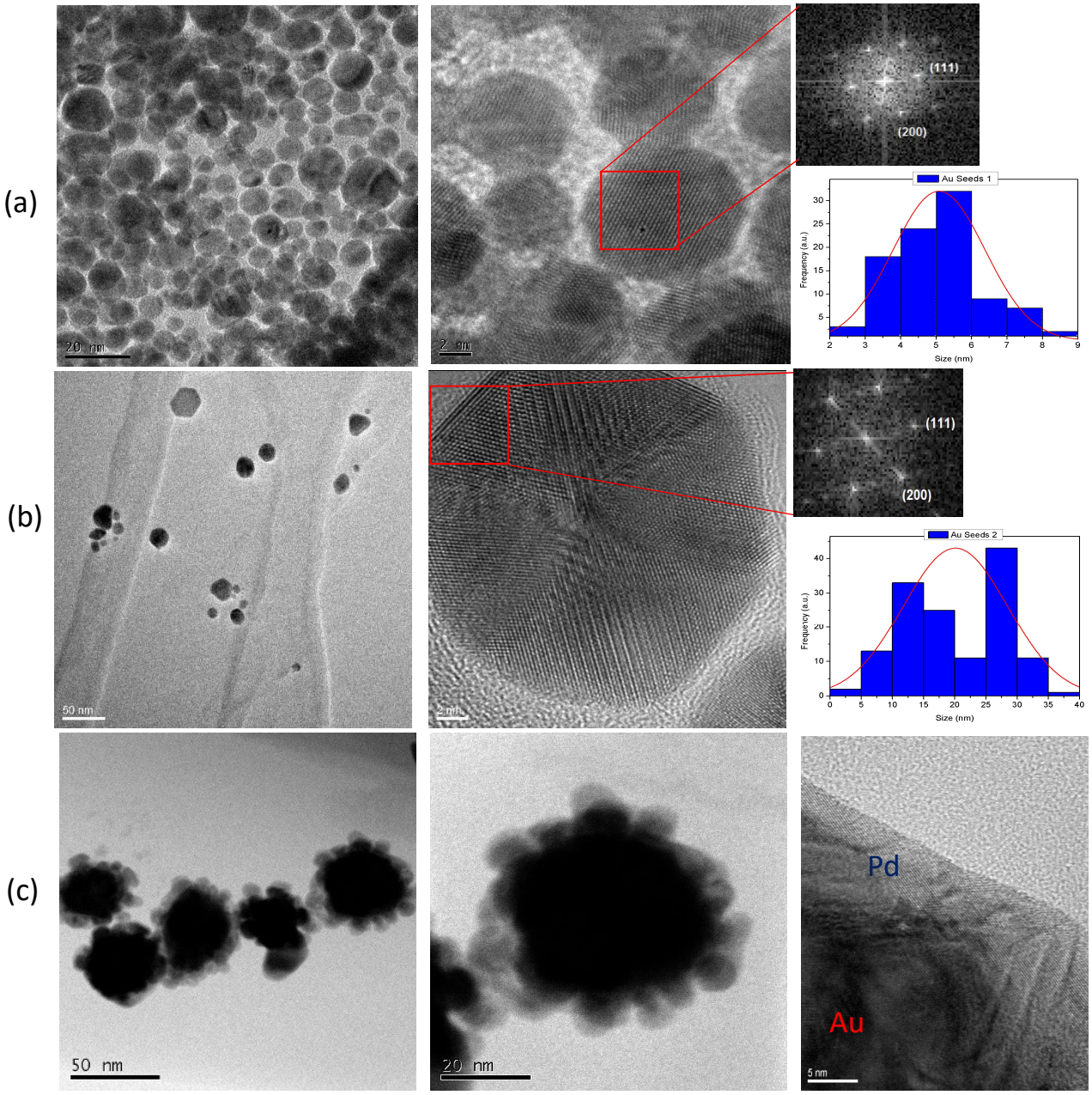

Fig. 2. Three step synthesis following by TEM and HRTEM micrographs. (a) Au Seeds, (b) Au truncated octahedral and (c) Au@Pd core shell formation.

In order to identify the structural components, the HAADF-STEM, EDX elemental mapping patterns and EDX line scanning profiles were obtained. In Fig. 3(a) the HAADF-STEM image shows a difference of luminance contrast between the inner Au core and the outer Pd shell because the atomic density of Au is much higher than that of Pd.

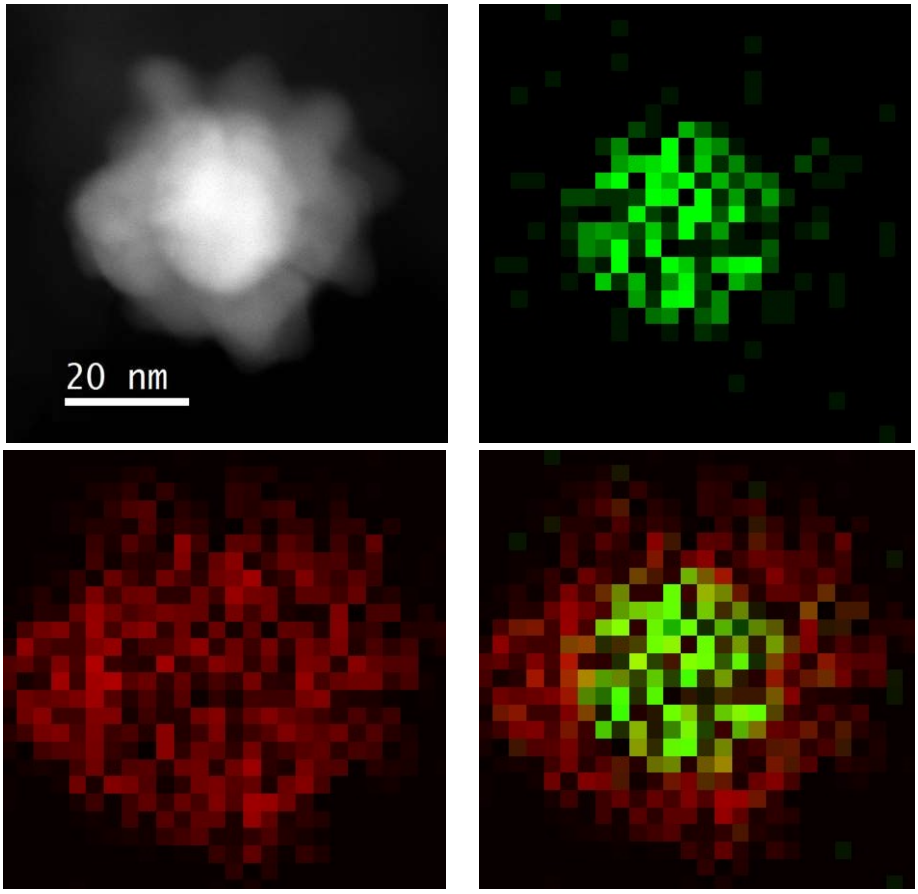

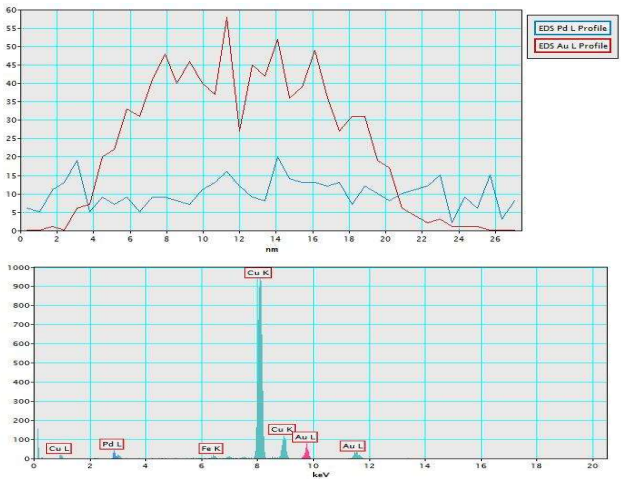

Fig. 3. (a) HAADF-STEM micrography of the Au@Pd nanoparticle. (b1)-(b3) EDX elemental mapping patterns, (c) EDX line scanning profiles of the Au@Pd nanoparticle and (d) EDX spectrum of the Au@Pd nanoparticle.

The corresponding EDX elemental mapping (Fig.3(b)) show the formation of an Au–Pd core shell nanostructure consisting of an Au core and a porous Pd shell. The EDX line scanning profiles of a single nanoparticle further confirm that the Au@Pd are composed of a Au core and Pd-rich boundary (the thickness of the Pd shell is about 7-10 nm) (Fig. 3(c)). EDX analysis show the presence of Au and Pd.

3.2 Electrochemical activity tests

Fig.4(a) shows a Cyclic voltammetry (CV) measurements show a typical Pd profile where the hydrogen adsorption-desorption region well defined at low potential (0.17-0.25 V vs RHE) and the reduction peak at 0.65 and 0.69 V vs RHE for commercial Pd/C and Au@Pd/C, respectively, showing a 30 mV shift. Typical ORR polarization curves for the Au@Pd/C and commercial Pd/C are shown in Fig. 4(b). The current densities were normalized with reference to the geometrical area of the glassy carbon electrode. The half-wave potentials ($E_{1/2}$) show at 0.75 V vs. RHE for both samples, apparently, the electrocatalytic activity of the Au@Pd/C is not significantly higher than that of commercial Pd/C, but doing a comparison between the Pd contents were 5% and 10% Pd content for the Au@Pd/C and commercial Pd/C, respectively.

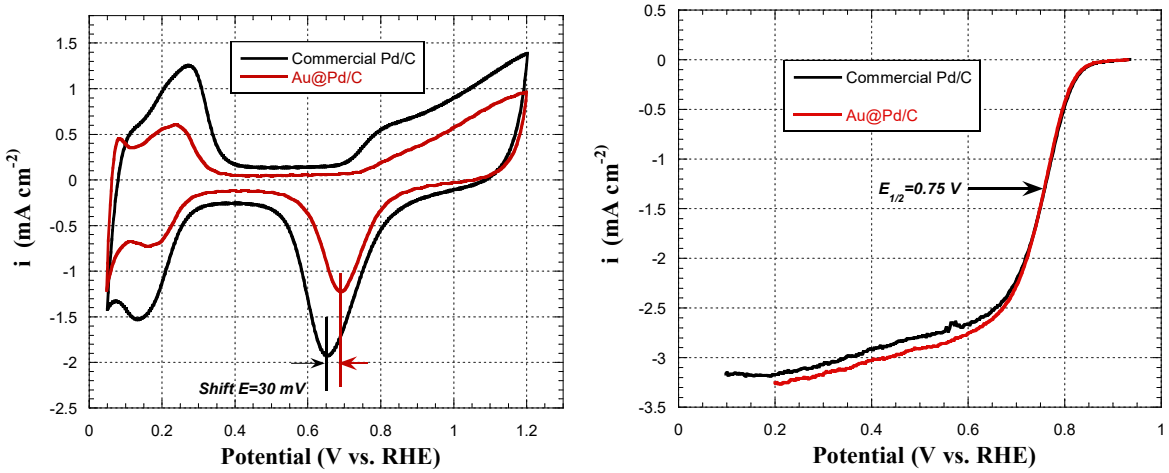

Fig. 4. (a) CVs for the Au@Pd/ and commercial Pd/C in Ar_2 saturated 0.1 M $HClO_4$ solution at a scan rate of 50 mVs^{-1}, (b) ORR polarization curves for the Au@Pd/ and commercial Pd/C in Ar-saturated 0.1 M $HClO_4$ solution at a scan rate of 50 mVs^{-1} and rotation rate of 1,600 rpm.

Au@Pd/C show a competitive electrocatalytic activity for the ORR. The improved ORR activity of the Au@Pd/C may be ascribed to its unique porous surface structure and synergistic effects between the Au core and Pd shell, trough the surface porous structure facilitates the electron transport and O_2 diffusion[18].

4. Conclusion

Well-defined Au@Pd/C core–shell nanoparticles have been synthesized by a seeded growth method synthesis. The formation of the Au@Pd core– shell structure presented a porous and irregular morphology of the nanostructures. The Au@Pd/C exhibited a comparative ORR activity to the commercial Pd/C in alkaline media, decreasing the Pd content from 10% to 5% and presenting the synergistic effects between the Au core and the Pd shell. Au@Pd/C structure and the decrease of Pd content is a promising material for using as a cathode electrocatalyst in PEM Fuel Cells.

Acknowledgements

This study was supported by the Instituto Politécnico Nacional through the projects SIP-20195668 and SIP-20195399. EYCA thanks the financial support from CONACyT within Ph.D fellowship.

References

[1] Sharaf OZ, Orhan MF. An overview of fuel cell technology: Fundamentals and applications. Renewable and Sustainable Energy Reviews 2014;32:810–53.

[2] Song C, Zhang J. Electrocatalytic Oxygen Reduction Reaction s/f.

[3] Si F, Zhang Y, Yan L, Zhu J, Xiao M, Liu C, et al. Electrochemical Oxygen Reduction Reaction. Elsevier B.V.; 2014.

[4] Hamnett A. Kinetics of electrochemical reactions 2010:1–5.

[5] Peng Y, Chen S. Electrocatalysts Based on Metal@Carbon Core@Shell Nanocomposites: an Overview. Green Energy and Environment 2018.

[6] Wang L, Gao W, Liu Z, Zeng Z, Liu Y, Giroux M, et al. Core – Shell Nanostructured Cobalt – Platinum Electrocatalysts with Enhanced Durability 2018.

[7] Liu W, Herrmann AK, Bigall NC, Rodriguez P, Wen D, Oezaslan M, et al. Noble metal aerogels-synthesis, characterization, and application as electrocatalysts. Accounts of Chemical Research 2015;48:154–62.

[8] Nair AS, Pathak B. A Computational Screening for ORR Activity of 3d Transition Metal Based M @ Pt Core-Shell Clusters A Computational Screening for ORR Activity of 3d Transition Metal Based M @ Pt Core-Shell Clusters 2019.

[9] Wu L, Xi Z, Sun S. Well-Defined Metal Nanoparticles for Electrocatalysis. vol. 177. 1a ed. Elsevier B.V.; 2017.

[10] Ferna L, Raghuveer V, Manthiram A, Bard AJ. Pd - Ti and Pd - Co - Au Electrocatalysts as a Replacement for Platinum for Oxygen Reduction in Proton Exchange Membrane Fuel Cells 2005:13100–1.

[11] Ou L. Design of Pd-Based Bimetallic Catalysts for ORR: A DFT Calculation Study 2015;2015.

[12] Binbin Jiang, Zeyuan Tang, Fan Liao, Haiping Lin, Shunkai Lu, Youyong Li MS. Powerful synergy: efficient Pt-Au-Si nanocomposites as state-of-the-art catalyst for electrochemical hydrogen evolution. Journal of Materials Checmistry A 2017;0:1–3.

[13] Hsu C, Huang C, Hao Y, Liu F. Electrochemistry Communications Au / Pd core – shell

nanoparticles for enhanced electrocatalytic activity and durability. Electrochemistry Communications 2012;23:133–6.

[14] Wang W, Zhang J, Yang S, Ding B, Song X. Au @ Pd Core – Shell Nanobricks with Concave Structures and Their Catalysis of Ethanol Oxidation 2013:1–8.

[15] Fu G, Liu Z, Chen Y, Lin J, Tang Y, Lu T. Synthesis and electrocatalytic activity of Au @ Pd core – shell nanothorns for the oxygen reduction reaction 2014;7:1205–14.

[16] Fan F, Liu D, Wu Y, Duan S, Xie Z, Jiang Z. Epitaxial Growth of Heterogeneous Metal Nanocrystals : From Gold Nano-octahedra to Palladium and Silver Nanocubes 2008:6949–51.

[17] Jana NR, Gearheart L, Murphy CJ, Carolina S. Seeding Growth for Size Control of 5 - 40 nm Diameter Gold Nanoparticles 2001:6782–6.

[18] Sun S, Zhang G, Geng D, Chen Y, Li R, Cai M. A Highly Durable Platinum Nanocatalyst for Proton Exchange Membrane Fuel Cells : Multiarmed Starlike Nanowire Single Crystal ** 2011:422–6.

E037. EFFECT OF SULFONATION DEGREE ON POLY(ETHER-ETHER-KETONE) FOR FUEL CELL MEMBRANE APPLICATIONS

P.C. Flores-Escareño, D. Morales-Acosta*, R. Benavides Cantú*, L. DaSilva

Centro de Investigación en Química Aplicada, Bvld. Enrique Reyna No. 140, Col. San José de los Cerritos, 25290. Saltillo, Coahuila, México

* Tel: +52844-4389830 E-mail: diana.morales@ciqa.edu.mx; roberto.benavides@ciqa.edu.mx

ABSTRACT

Proton exchange membrane fuel cells (PEMFC) are known to be environment friendly devices to convert chemical energy of a fuel (e.g. hydrogen, methanol) directly into electrical energy with high efficiency, particularly for portable and transport application systems. Polymer electrolyte membrane (PEM) is one of the main components of a PEMFC, with capability to promote proton diffusion from the anode to the cathode. The current focus of research for PEM is, the development of novel sulfonated aromatic hydrocarbon polymers as alternatives to conventional perfluorinated polymers. In this work, a series of sulfonated poly (ether ether ketone) (SPEEK) was prepared by aromatic electrophilic substitution with concentrated sulfuric acid as sulfonating agent, where the variation of temperature (70-90 °C) and reaction time (1-5 h) were considerated. Membranes were cast from SPEEK solutions in DMAc. The effects of sulfonation time and reaction temperature on the ability to form a membrane were evaluated. The effective insertion of SO_3H groups in SPEEK structure (PEEK-SO_3H) was confirmed by FTIR, while the thermal stability and degree of sulfonation of SPEEK was evaluated by thermogravimetric analyses (TGA), Water Uptake (WU), Ion-Exchange Capacity (IEC) and sulfonation degree (DS) calculated from IEC values and TGA traces. Results indicated IEC values in the range between of 1.2-2.27 meq/g are directly related with DS, which is several times higher than that of NAFION ®117 (0.91 meq/g). WU values varied from 11-84%, but most of the membranes also exhibited higher WU over the corresponding NAFION (WU=13%). DS values calculated from the IEC results agree with those obtained from TGA traces. The above results indicate that SPEEK with a DS between 38-80% are promising materials to be used as membranes in PEMFC applications.

Keywords: Membranes, SPEEK, Fuel Cells.

1. Introduction

The increase in the demand for energy has been generated, from domestic devices to various means of transport, generates the need to develop further research to find alternative and clean sources of power generation to meet global demand. Fuel cells (FC) are electrochemical devices that have a particular attention for their high power density for stationary of mobile applications; and also because they generate less impact on the environment[1–3]. It should be emphasized that the proper perfomance of the FC depends to a largely extent on the polymer exchange membranes (PEM), wich is responsible of protons transport from the anode to the cathode. Traditionally in proton exchange fuel cells (PEMFC), the most commonly used membrane is the commercially known as the NAFION^{TM}. Sulfonated poly(ether ether ketone) (SPEEK) has been widely employed during the last decade to fabricate membranes operating in the range from 90-120ºC. The degree of sulfonation (DS) is defined as the number of sulfonic acid groups per repeat unit and can be controlled by conditions reactions. In this work, the sulfonation of PEEK was carried out at different temperatures (70-90°C) and reaction times (1-5h), to obtain SPEEK with a high level of sulfonation and film forming capacity. The sulfonated polymers were characterized by FTIR and TGA, The effect of sulfonation degree in polymer solubility and film formation capacity were evaluated, as well as the ion exchange capacity and water uptake properties were also evaluated.

2. Materials and Methods

Poly (ether-ether-ketone) with Mw= 20,800 was acquired from Aldrich in the form of pellets, Sulfuric Acid (H_2SO_4 98-99%) and dimethylacetamide (DMAc 98%). Were purchased from Aldrich.

2.2 Sulfonation reaction

The sulfonation of PEEK was carried out using concentrated sulfuric acid as sulfonating agent. PEEK powder was dissolved in concentrated sulfuric acid with a PEEK/H_2SO_4 ratio of 1:10 w/v. Subsequently the solution was heated at a specific (70,80, 90ºC during fix time 1, 2, 3, 4 and 5h) under a nitrogen atmosphere and reflux conditions. The reaction was stopped by pouring the sulfonated polymer solution into a beaker with distilled water immersed in an ice bath. The solid sulfonated polymer was washed several times with distilled water until neutral pH was reached and subsequently dried in a vacuum oven at 60°C for 48 h, to remove residual water. The samples were labelled SPK-X-Y (X=70, 80 and 90 ºC and (Y= 1, 2, 3, 4, 5 h) [4].

2.3 Membrane preparation

The sulfonated PEEK membranes were prepared by the casting method using DMAc as solvent. 0.2g of SPEEK o were dissolved in 20mL of solvent, wich was then poured into a flat glass container. The casted membranes were dried at 50ºc in a vacuum oven at 50 ºC for 24 h, to remove residual solvent.

2.4 Characterization of polymers and membranes

FTIR measurements were performed in an instrument Bruker Vertex-70 infrared spectrometer, with a nominal resolution of 4 cm^{-1} in the 4000-500 cm^{-1} region. Thermal stability was determined by TGA analysis, using an equipment TA Instruments model Q500 under nitrogen atmosphere and a heating rate of 10 °C/min^{-1}, from 30°C to °600 C. Water uptake (WU) measurements of the SPEEK membranes were conducted by immersing the membrane samples into distilled water at room temperature for 24h for full equilibrium. Then, the membrane surface was wiped off with a tissue paper and weighed immediately in order to obtain the wet weight (Wwet). Membranes were dried at 80°C in a vacuum oven for 2h and later weighed to determine the dry weight (Wdry). The percentage of water uptake is calculated by differences between dry/wet weights (in gr), according to the equation[5]:

$$WU\% = \frac{Wwet - Wdry}{Wdry}.100 \qquad (1)$$

The ion exchange capacity (IEC) and degree sulfonation of the sulfonated PEEK membranes were determinated by acid-base titration method using a potentiometric titrator from Metrohm. The dried membrane was immersed into a 1M HCl solution for 24h; then, they were rinsed and immersed into deionizer water. Finally, the membrane was rinsed with into 1M NaCl solution for 24h and the resultant solution was titrated with 0.005M of NaOH. The IEC and sulfonation degree of SPEEK were calculated using the following equations[6]

$$IEC = \frac{V_{NaOH} \cdot N_{NaOH}}{W_{dry}} \qquad (2)$$

$$DS(\%) = \frac{IEC.Mw(polìmero)}{1-(IEC.MwSO3H)}.100 \qquad (3)$$

where V_{NaOH} (mL) and N_{NaOH} (mL) is the volume consumed and concentration of NaOH (mmol·mL^{-1} ~meq·mL^{-1}), Wdry is the dry weight of the polymer membrane, MwPEEK (gr·mol^{-1}) is the molecular weight of the polymer (PEEK or SPEEK) and Mw SO_3H (gr.mol^{-1}) is the molecular weight of the sulfonic group [3]. DS was also calculated from the TGA analysis, using the following equation:

$$DS(\%) = \frac{MwPEEK}{\left\{\left(\frac{m}{\Delta m - 1}\right)\right\}.MSO3H}.100 \qquad (4)$$

where m is the molecular mass of the SPEEK , **Δ**m is the first loss in weight in the thermograms of the sulfonated polymers, corresponding to the weight loss by the decomposition of the sulfonic groups [7,8].

3. Results and Discussion

3.1 Sulfonation reaction

The different conditions during sulfonation reactions allowed us to obtain differences in products. At the lowest temperature (70°C) it was possible to obtain precipitate polymer for all temperature conditions evaluated. However, for 80°C only at 1 and 2 h some materials were obtained. For the higher temperature 0f 90 °C only the first hour of reaction allowed to obtain solid material precipitated. Figure 1 shows images of the products obtained after of the sulfonation reaction.

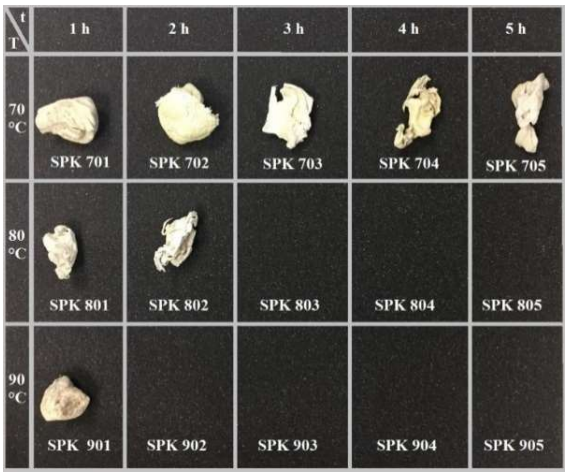

Fig.1 Polymers obtained from sulfonation reactions of PEEK at different time and temperature conditions.

FTIR spectroscopy was carried out to observe chemical differences among polymer sulfonated at different conditions. The PEEK resin before sulfonation (Figure 2), presents its characteristic absorption bands. The band observed at 1649 cm^{-1} corresponds to the elongation C=C. The band at 1490 cm^{-1} is due to the stretching vibration of the C-C from the main chain and the band at 1223 cm^{-1} wich is the presence of the C-O-C.

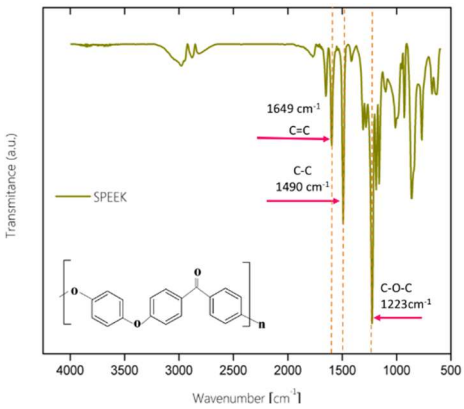

Fig. 2. FTIR spectrum of PEEK polymer

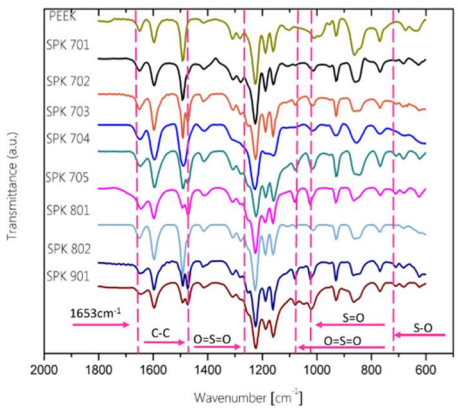

Fig. 3. FTIR spectra of the sulfonated materials

The precipitated materials that precipitated demonstrated the presence of the functional groups to identify the sulfonation, like the following bands: 1. The C-C stretching band (1490 cm^{-1}) is affected, basically due to the reduced symmetry from the sulfonic acid groups influencing their vibration frequencies [9,10]. As a consequence, the band is affected in intensity and even divided. Between 1090 cm^{-1} and 1020 cm^{-1} there are bands attributed to symmetric and asymmetric vibrations between oxygen-sulfur O=S=O bonds and vibrational stretches of S-O at 709 cm^{-1} (figure 3). One of the most important characteristics to verify the sulfonation of the material is through the appearance of the broad band in the range of 3450-3430 cm^{-1} [11] with corresponds to the O-H vibration of the sulfonic group. Figure 4 shows the spectra of the materials, specifically in the O-H and the C-C intervals.

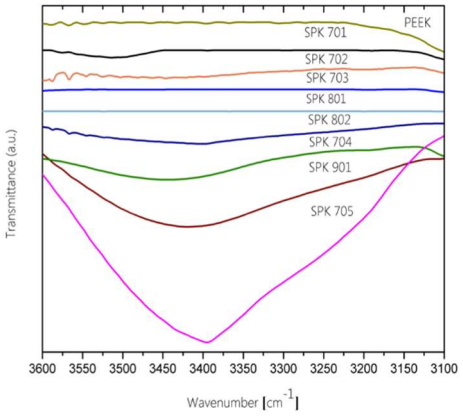

Fig. 4. Sulfonated materials in the O-H region

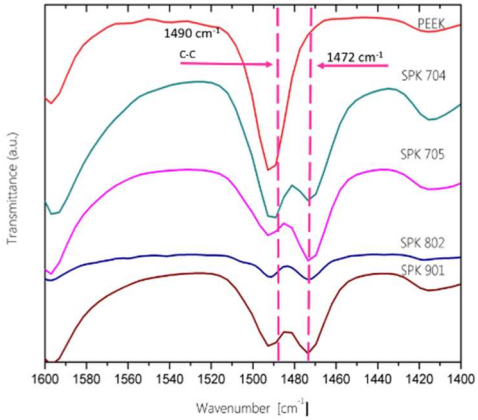

Fig. 5. Spectra of sulfonated materials in the region of 1490 and 1472 cm^{-1}

The OH bands is clearly higher for more sulfonated materials, like in 70ºC with 4 and 5 hours and the 80 and 90ºC. On the other hand, the effect of the C-C splitting into a second band at 1472 cm^{-1} [12] (figure 5), corroborates the effect of higher levels of sulfonation, since such behavior is observed fot the same time and temperature conditions. Basically identify the need of 4-5 hour of sulfonation reaction at 70ºC of 2 hours for 80ºC and 1 hour for 90ºC to have a noticeable sulfonation level in the PEEK.

3.2 Thermogravimetric Analysis.

The TGA analyses were carried out in order to observe the effect caused by the sulfonation in the thermal stability of the sulfonated polymers. The thermograms obtained for the PEEK and different SPEEKs are shown in figure 6.

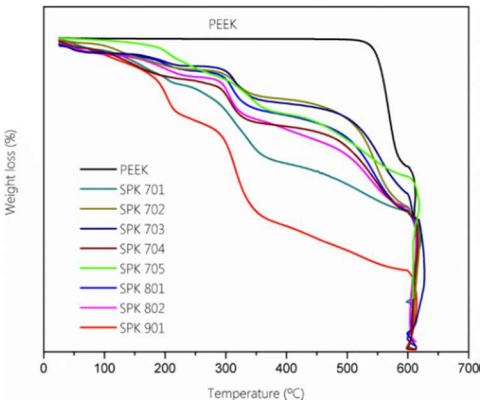

Fig. 6. TGA thermograms of the precipitated Materials

The thermogram for the PEEK indicates an excellent stability above 500°C and after the degradation of the main chain suffers decomposition. The sulfonated polymers, in general, show weight loss as a function of temperature in three stages. The first step around of the 100°C is due to the loss of the water from the samples, since PEEK becomes hygroscopic after sulfonation and most of the water comer from the neutralization process, after the sulfonation reaction of the polymers. The second loss, between 200-300°C can be attributed to the loss of the SO_3H groups and the last step occurring around 500°C is attributed to the structural decomposition of the SPEEK backbone [7,13]. The above indicates that the thermal properties of sulfonated PEEK is suitable for use in fuel cells.

3.3 Membrane preparation

The SPEEK membranes were obtained by casting from solutions of DMAc and SPEEK. The SPK 703 was capable to form film, although physically was not considered as convenient to follow characterization; however, materials SPK 704, 705, 802 and 901 were capable to form membranes and convenient to follow. Figure 7 shows images of the membranes obtained with the DMAc solvent.

Fig. 7. Membranes obtained with the solvent DMAc

3.4 Water uptake (WU) and Ion Exchange Capacity (IEC).

Figure 8 shows the result of WU for the membranes and as a comparison the one evaluated for the NAFION reference membrane is included. The evaluation of this parameter shows an increasing tendency of the WU as the sulfonation time increases for sulfonated membranes at 70ºC. however, at the temperature of 80°C, the highest value of all the materials is obtained at only 2 h of sulfonation. Surprisingly, the sulfonated material at 90°C greatly reduces its water absorption capacity, although it remains above the NAFION. On the other hand, IEC is related to the number of sulfonic groups present, which turn are responsible for the proton transportation (H^+) through the membranes. Figure 9 shows the ion exchange capacity (IEC), for each of the membranes evaluated. In general, a similar tendency to increase the IEC value is clearly observed as the sulfonation time/temperature condition but the highest value was obtained for the 70ºC/5h membrane.

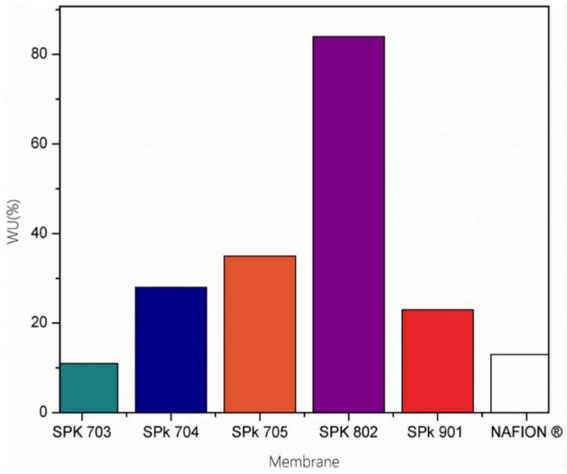

Fig. 8. Water retention of sulfonated membranes

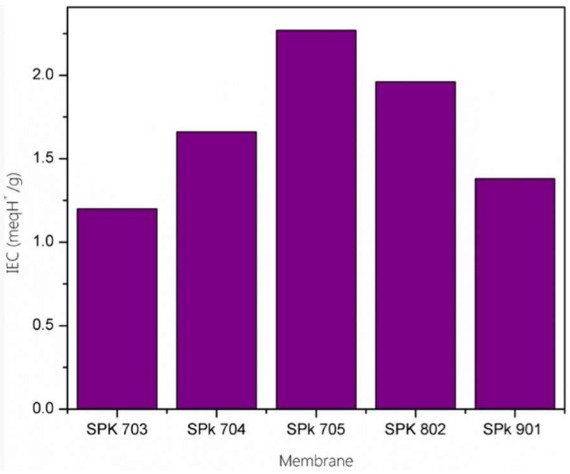

Fig. 9 IEC values for membranes

It is important to note that, even though the SPK802 membrane has greater water absortion. It does not exceed the value of the SPK705. The above suggest that even higher temperature promotes greater water absorption, it does not mean this absorption is due to a higher level of sulfonation; it is probable that this temperature causes greater opening of the molecular structure to allow the entry of water, even it does not have a high level of sulfonation.

3.5 Degree of Sulfonation from the Ionic Exchange Capacity (IEC) and Thermogravimetric Analysis. The

Sulfonation Degree (DS) was calculated for each membrane obtained from both TGA and IEC values. The same trend is observed, in general, for values calculated from both techniques: however, a certain deviation from tendency is observed for SPK 705 and SPK 802 membranes. The later membranes are precisely the ones were a specific combination between water uptake an IEC values are observed, which most surely will need more specific tests to properly explain the reason. Even though, the highest DS value from IEC reached 80% and 68% from the TGA traces (figure 10).

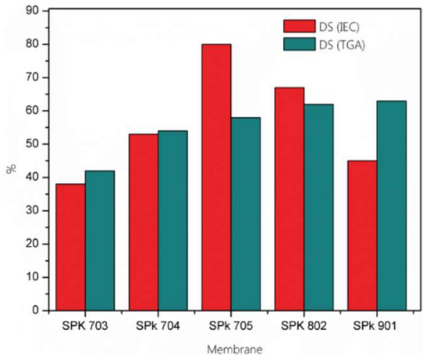

Fig. 10. Comparison of the Degree of Sulfonation obtained by IEC and TGA.

4. Conclusions

The sulfonation reaction was successful to modify PEEK as FTIR and TGA corroborate. The DMAc was defined as the organic solvent for the preparation of membranes from the sulfonated. materials High water absorption was obtained for the SPK802 membrane, although the rest of the membranes absorbed similar levels to the NAFION reference membrane. Contrary to expectations, membrane SPK705 presented the highest IEC VALUE (2.27 meq/g), even not having the highest WU value, being a considerably higher than that reported for the NAFION (0.92meq/g).

Acknowledgements

This work has been supported by the Mexican Council of Science and Technology (CONACyT) through grants 259010. PCFE thanks CONACyT for the support through the PhD scholarship. The authors also grateful to the SMH and XVVII International Congress of the Mexican Hydrogen Society for accepting the presentation of this work.

References

[1] Stambouli AB. Fuel cells: The expectations for an environmental-friendly and sustainable source of energy. Renew Sustain Energy Rev 2011:4507–20.

[2] Afolabi AS, Fungura N, Mokrani T, Mateescu C. The Realities and Economic Benefit of the Utilization of Fuel Cells as an Alternative Source of Energy: A Review AU - Abdulkareem, A. S. Energy Sources, Part B Econ Planning, Policy 2015;10:404–11.

[3] Basile A, Paturzo L, Iulianelli A, Gatto I, Passalacqua E. Sulfonated PEEK-WC membranes for proton-exchange membrane fuel cell: Effect of the increasing level of sulfonation on electrochemical performances. J Memb Sci 2006;281:377–85.

[4] Yee R, Zhang K, Ladewig B. The Effects of Sulfonated Poly(ether ether ketone) Ion Exchange Preparation Conditions on Membrane Properties. Membranes (Basel) 2013;3:182–95.

[5] Khanh Ngan T. Do DK, Department. Synthesis and Characterization of Homogeneously Sulfonated Poly(ether ether ketone) Membranes: Effect of Casting Solvent Khanh. J Appl Polym Sci 2008;110:1763–70.

[6] Li Z, Xi J, Zhou H, Liu L, Wu Z, Qiu X, et al. Preparation and characterization of sulfonated poly(ether ether ketone)/poly(vinylidene fluoride) blend membrane for vanadium redox flow battery application. J Power Sources 2013;237:132–40.

[7] Knauth P, Hou H, Bloch E, Sgreccia E, Di Vona ML. Thermogravimetric Analysis of SPEEK Membranes: Thermal Stability, Degree of Sulfonation and Cross-linking Reaction. J Anal Appl Pyrolysis 2011;92:361–5.

[8] Banerjee S, Kar KK. Impact of degree of sulfonation on microstructure, thermal, thermomechanical and physicochemical properties of sulfonated poly ether ether ketone. Polymer (Guildf) 2017;109:176–86.

[9] Zaidi SMJ. Polymer Sulfonation – A Versatile route to prepare proton-conducting membrane material for advanced technologies 2003;28:183–94.

[10] Jin X, T. Bishop M, S. Ellis T, E. Karasz F. A sulphonated poly(aryl ether ketone). vol. 17. 1985.

[11] K. Nakanishi. Infrared Absorption Spectroscopy. Science (80-) 1963;140:648.

[12] Pretsch Ë. Structure Determination of Organic Compounds. 2009.

[13] Inan TY, Doğan H, Unveren EE, Eker E. Sulfonated PEEK and fluorinated polymer based blends for fuel cell applications: Investigation of the effect of type and molecular weight of the fluorinated polymers on the membrane's properties. Int J Hydrogen Energy 2010;35:12038–53.

E041. Pt AND Pt-Sn AS ELECTROCATALYSTS FOR METHANOL OXIDATION REACTION

P. J. Pérez-Díaz[1*], B. Ruiz-Camacho[1], A. Medina-Ramírez[1]

[1] Department of Chemical Engineering, University of Guanajuato, DCNE, Col. Noria Alta s/n, C.P. 36050, Guanajuato, Gto., Mexico

* Corresponding author: +52 1 2282515360 pperezdiaz01@gmail.com

ABSTRACT

A zeolite-carbon composite with ratio 3:1 was prepared and used as supports of Pt and Pt:Sn in ratio 1:1 nanoparticles as electrocatalysts for methanol oxidation reaction (MOR). Additionally, Pt supported on carbon Vulcan was synthesized, with the objective of test the effect of the support in the electrocatalytic activity for MOR in acidic medium. Sonication was used as a simple method to obtained Pt nanoparticles. The zeolite-carbon composite was obtained by sol-gel method. It was demonstrated that the presence of zeolite in the composite Pt/zeolite-C increase the current density in the MOR in comparison with the conventional Pt/CV catalyst. XRD results showed the crystalline structure of the materials synthesized. The tin presence favors the methanol direct oxidation generating less intermediary, also this addition diminishes the final cost of the electroctalyts. Even though the decrease of the platinum in the electrocatalyst reduced the generated conductivity, the Pt/zeolite X-C catalyst presented the major stability in the chronoamperometry test.

Keywords: Fuell cell; methanol oxidation; composite; zeolite X; Pt:Sn.

1. Introduction

Fuel cells are galvanic cells, which are devices capable of generating electric power in a direct and clean way, capable of substituting the conventional batteries even the engines. In these devices the free energy of a chemical reaction is converted into electrical energy [1], it has been demonstrated that they are a clean, silence and efficiency source energy, among which proton exchange membrane fuel cells (PEMFCs) are the most promising mechanisms [2]. The direct methanol fuel cells (DMFC) are a type of PEMFCs, using the methanol as fuel which is fed directly to the cell. The methanol is a good option as fuel due to it is found naturally in the liquid form, this makes the methanol easy to manage and store; it is relatively cheap, and it is easily available due to it can be produced from natural gas or renewable biomass [3]. This kind of fuel cell generates electric energy through the methanol oxidation reaction (MOR), which can proceed in two pathways: the first is a direct path to form CO_2, and the seconds correspond to an intermediate path where intermediaries as CO are produced [4]. The reactions that happen in a DMFC are as follow:

Anode (Oxidation): $CH_3OH + H_2O \rightarrow CO_2 + 6H+ + 6e-$
Cathode (Reduction): $\frac{3}{2} O_2 + 6H+ + 6e- \rightarrow 3H_2O$
Global reaction: $CH_3OH + \frac{3}{2} O2 \rightarrow CO_2 + 2H_2O$

It has been demonstrated that catalyst based on Pt are essential for Fuel Cells for both for performance and durability [4]; but this has implications for the cost due to the high price of the precious metal. From the material point of view, the Pt charge can be reduced by improving the catalytic activity or the electrochemical active surface area (EASA). Pt supported on the large electroactive area of the carbon (Vulcan X-72) is one of the most used catalysts in PEMFC and DMFC [5]. Nevertheless, the carbon as Pt support trends to degrade under the reference electrode operation conditions affecting the Pt electrochemical surface and therefore dismissing the electrodes useful life [6-7]. For this reason, it is necessary a material that gives support and stability to electrocatalysts, in that order, the zeolite Faujasite NaX (zeolite X) type is proposed as material that will offer those characteristics.

Zeolites as the second catalyst can accelerate the alcohols oxidation [8, 9]. The zeolites are compounds of crystalline aluminosilicate of Si, Al y O with a tetrahedral structure, which ones have four oxygen atoms around a cation [10-12]; this property will allow enhancing the Pt dispersion and nucleation [13]. Due to Pt as electrocatalyst is very expensive, several Pt-X materials have been research in order to reduce cost; the addition of a second metal modified the electronic and bifunctional mechanism of Pt to oxide the methanol. For example, zeolite Y combined with Ru, Pd, Pt, Ni has been tested as electrocatalyst for methanol, ethanol and formic acid oxidation in acid electrolytes showing a reducing

of the onset potential and an increasing the electrochemical activity by zeolite presence [14-16]. Moreover, a problem in the fuel cells is the intermediary formation (CO) due to the "Pt poisoning" [1], to attend this issue a bimetallic catalyst of Pt-Sn was proposed with the aim to decrees the intermediary formation and increases the MOR until CO2.

The aim of this work was the study of the catalytic effect in the methanol oxidation reaction of different catalysts of Pt supported on zeolite X-carbon composite with ratio 3:1 and Carbon Vulcan, also a catalyst of Pt:Sn supported on zeolite X-carbon composite with ratio 3:1 was tested.

2. Materials and Methods

2.1. Materials

Fly ash was used as the precursor for zeolite X synthesis, the details and the properties are reported in Medina et al. [17]. Aluminum hydroxide (J. T. Baker) was used for the support zeolite-carbon synthesis. Hexacloraplatinic acid (H2PtCl6·6H2O), isopropyl alcohol, methanol, sulfuric acid, and 5 wt.% solution of Nafion were purchased from Sigma Aldrich analytical grade. Distilled water was used as solvent.

Synthesis of zeolite X-C supports.

The support of zeolite X-Carbon was prepared with ratio of wt. % 3:1. First, the zeolite X was added to distilled water and it was stirred for 10 min. Then, the corresponding amount of carbon was added, the suspension was kept under stirring for 10 minutes more. After that, the mixture was put into an ultrasonic bath and the aluminum hydroxide was added. This mixture was stirred for 24 h. Following this time, it was filtered under vacuum and the recovered solid was dried in an oven at 80° C for 24 h. Subsequent, the powder obtained was submitted to heat treatment in a furnace at 300° C for 3 h in air atmosphere.

Preparation of the electrocatalyst Pt/zeolite X-C, Pt/C and Pt:Sn/zeolite X-C

The preparation of Pt nanoparticles by reduction method was previously reported Ruiz-Camacho et al [18]. Briefly, 85 mg of the previously prepared zeolite-carbon support plus were added to 50 mL of 0.5 mM solution of hexachloroplatinic acid. 60 mL of isopropyl alcohol was added as reducing agent to the previous suspension and put it in an ultrasonic bath (42 kHz) for 2 h. Finally, the solvent was removed by evaporation. The electrocatalysts obtained, following this technique, were (1) Pt/C, (2) Pt:Sn/zeolite X-C and (3) Pt/zeolite X-C

2.4 Physical characterization

The X ray diffraction patterns of the samples were characterized using a PANalytical Model X-ray diffractometer with a Cu K α radiation source (λ = 1.5406 Å) in the range of 10-80° 2θ. The study of the morphology and structural properties of the samples was performed by TEM using a TEM JEOL 1010 field emission microscope, operated at 80 kV, each one.

Electrochemical characterization

A potentiostat/galvanostat GAMRY Instrument reference 1000 T was used to determinate the electrocatalytic activity of the materials synthesized through cyclic voltammetry (CV) and chronoamperometry (CA) techniques. The CV technique was tested using two electrolytes: i) H_2SO_4 0.5 M and ii) H_2SO_4 0.5 M plus CH_3OH 0.5 M in a nitrogen-saturated atmosphere. 25 cycles of CV were performed to stabilize the current-potential signal a scan rate of 50 mV s^{-1}. Electrocatalytic tests were performed using the three-electrode system, which consists of a counter electrode of graphite, a reference electrode of standard saturated Calomel electrode (SCE = 0.246 V) and a working electrode (5 mm diameter) of glassy carbon disk. The catalytic ink was prepared with 6 mg of the catalyst powder, which was dispersed by ultrasonic bath for 2 hours in 500 µL of an isopropanol solution and 50 µL of a 5 wt.% Nafion solution. 11 µL of the ink was deposited on the surface of the working electrode. Potentials measurements in this work were referred to the normal hydrogen electrode (NHE).

3. Results and Discussion

Fig. 1. Shows the physical characterization of XRD for a) bimetallic catalyst and (b) Pt/C and Pt/zeolite X-C catalyst. Both images show the crystalline face-centered cubic structure (fcc) of platinum at 2θ values of 39.85°, 46.35°, 67.66° corresponding to the planes (111), (200) and (220), indicated with a diamond (JCPDS 01-087-0642). In Fig 1 a), bimetallic catalyst smaller diffraction peaks of Pt than the Pt peaks of Fig. 1. b). This is the effect of have the half of Pt metal in the bimetallic catalyst. In other hand, Pt/Zeolite X-C shows the crystalline structure of zeolite X, indicated with a circle.

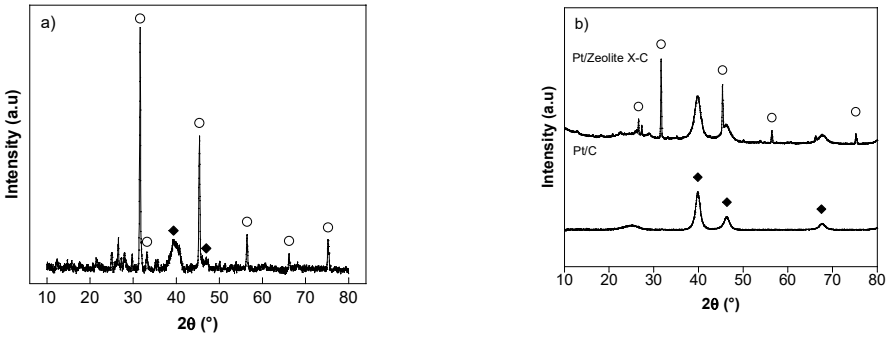

Fig. 1. XRD patterns of (a) Pt:Sn\zeolite X-C. (b) Pt supported on zeolite X-C and Carbon Vulcan.

Fig. 2. shows the TEM images of the (a) Pt/zeolite X-C, (b) Pt-Sn/zeolite X-C and (c) Pt/Carbon Vulcan. The particle size and dispersion varies according to the type of substrate. For example, a smaller Pt particle size and greater dispersion were obtained on the bimetallic composite, compared to zeolite X-C composite and Pt/C. Furthermore, a core-shell morphology between Pt and Sn is observed in Fig. 2b.

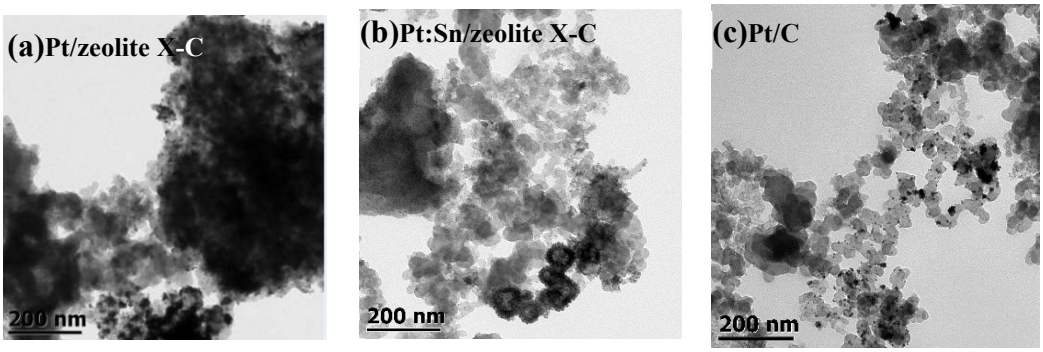

Fig. 2. TEM images of Pt catalysts supported on (a) C-zeolite X, (b) Pt:Sn/zeolite X-C and (c) carbon Vulcan.

Fig. 3. corresponds to the CVs of Pt:Sn/zeolte X-C and Pt synthesized supported on the different substrates. Fig 3a shows the CVs in acid medium, the curves show the typical characteristic of Pt nanoparticles identified by three regions: I) the adsorption and desorption hydrogen region (H^+) around 0.05 to 0.3 V/NHE, which allow us to estimate the electrochemically active surface area (EAS) of the catalysts, II) the double layer region around 0.3 to 0.6 V, and III) the oxide region between 0.6 to 1.2 V [19]. In Fig. 3 (a) it is observed throughout the range of study potential that the response of the bimetallic

catalyst presents a higher intensity of current compared to monometallic samples, which can be associated with the presence of Sn. In Fig. 3. (b) the CVs in acid electrolyte plus methanol. The MOR curves are observed using the Pt and Pt: Sn samples on the same zeolite-carbon substrate and Pt/C. In this graph we observed two peaks, the first is associated with methanol oxidation while the second is related to the electro-oxidation of intermediaries. The maximum MOR peak obtained was presented with the material of Pt/zeolite X-C, which is found at14.19 $mAcm^{-2}$ of current density while for Pt: Sn/zeolite X-C was obtained at 9.24 mA cm^{-2}. However, when making a comparison against the peaks of the curve representing the formation of methanol intermediates in each catalyst, it is observed that the electro oxidation peak of Pt/zeolite X-C is greater than that of methanol oxidation (16.11 mA cm^{-2}), while for bimetallic catalyst the oxidation peak is at the same level (9.24 mA cm^{-2}). In this way it is demonstrated that, although the presence of tin reduces the conductivity, it also reduces the formation of intermediates, favoring the complete oxidation of methanol.

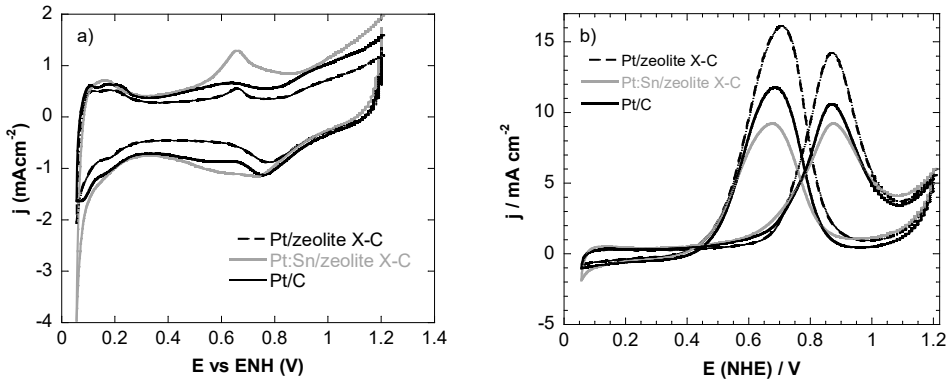

Fig. 3. (a) Cyclic voltammetry, scan rate 50 mV s^{-1} in H_2SO_4 0.5 M saturated atmosphere of N_2; (b) MOR in H_2SO_4 + CH_3OH 0.5 M saturated atmosphere of N_2 of Pt/zeolite X-C, Pt:Sn/zeolite X-C and Pt/C.

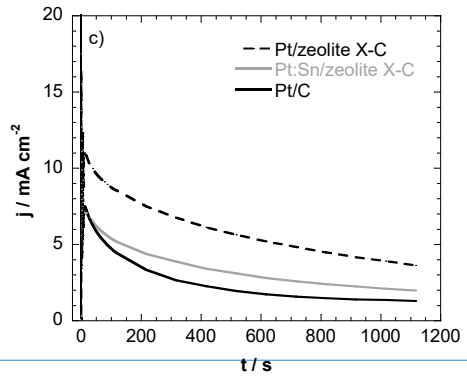

Fig. 4. Chronoamperometry at 0.79 V/NHE results of Pt/zeolite X-C, Pt:Sn/zeolite X-C and Pt/C.

Fig. 4. presents the chronoamperometry results obtained from catalyst of Pt/zeolite X-C, Pt:Sn/zeolite X-C and Pt/C, representing the real-time response of the variation of the current against time at a potential pulse of 0.55 V, which was carried out during 1800 s in a medium of sulfuric acid plus 0.5 M methanol. The comparison shows that the catalyst Pt/zeolite X-C is stabilized before the other, and that it has a higher current density of 3.59 mA cm^{-2} at 1117 second against the current density of Pt: Sn/zeolite X-C and Pt/C at 1.98 and 1.27 mA cm^{-2}, respectively.

4. Conclusion

In summary, the synthesis of Pt and Pt:Sn catalysts supported on a zeolite X-C were tested in the MOR. The electrochemical activity was compared with Pt/CV synthesized at same conditions. This work showed that the electrocatalyst of Pt/zeolite X-C has the best electrochemical performance for MOR. Additionally, this material showed the higher stability and current density at 1800 s obtained at 0.55 V during the chronoamperometry analysis. In other hand, the presence of Sn reduces the amount of Pt, favoring the direct oxidation of methanol to CO_2, achieving a less formation of intermediates, such as CO, also, the addition of this second metal decrease the final cost of the electrocatalyst. By X-ray diffraction results, the crystalline structure of Pt, zeolite and carbon was corroborated.

Acknowledgements

The authors are grateful for University of Guanajuato through the DAIP office for providing financial support for the present research. We also thank Lourdes Palma Tirado (Neurobiology Institute-UNAM) for TEM characterization. Finally, we thank SMH and XIX International Congress of the Mexican Hydrogen Society for providing a space where to present this work.

References

[1] Daas BM & Ghosh S. Fuel cell applications of chemically synthesized zeolite modified electrode (ZME) as catalyst for alcohol electro-oxidation - A review. J Electroanal Chem 2016;783:308–315.

[2] Arvia, A.J., & Giordano, M. C. (1983). Introducción a la electrocatalisis-Monografía.

[3] Antolini E. Catalysts for direct ethanol fuel cells. J Power Sources 2007;170:1–12.

[4] Moghaddam RB, Shahgaldi S & Li X. A facile synthesis of high activity cube-like Pt/carbon composites for fuel cell application. Front Energy 2017;11:245–253.

[5] Kinoshita K. Electrochemical Oxygen Technology. New York: Wiley-Interscience Pubilications; 1992.

[6] Vogel W, Timperman L, Alonso-Vante N. Probing metal substrate interaction of Pt nanoparticles: structural XRD analysis and oxygen reduction reaction. Appl Catal A 2010;377:167-173.

[7] Dhanushkodi SR, Tam M, Kundu S, Fowler MW, Pritzker MD. Carbon corrosion fingerprint development and deconvolution of performance loss according to degradation mechanism in PEM fuel cells. J Power Sources 2013;240:114-121.

[8] Wang Y, Ren JW, Deng K, Gui LL, Tang YQ. Preparation of tractableplati- num, rhodium, and ruthenium nanoclusters with small particle size in organic media. Chem Mater 2000;12:1622–1627.

[9] G Fernanda, Medeiros RS, Jean GE, Lucia GA. Active sites for ethanol oxidation over SnO2-supported molybdenum oxides. Appl Catal A Gen 2000;193:195–202.

[10] Coombs DS, Recommended nomenclature for zeolite minerals: report of the sub- committee on zeolites of the International Mineralogical Association. Can Mineral 1997;35:1571–1606.

[11] Rolison DR. Zeolite-modified electrodes and electrode-modified zeolites. Chem Rev 1990;90:867–878.

[12] Sun T, Seff K. Silver clusters and chemistry in zeolites. Chem Rev 1994;94:857–870.

[13] Mojovic Z, Bankovic P, Jovic-Jovicic N, Milutinovic-Nikolic A, Rabi-Stankovic AA, Jovanovic D. Electrocatalytic behavior of nickel impregnated zeolite electrode. Int J Hydrogen Energy 2011;36:13343-13351.

[14] Samant PV, Fernandez JB. Enhanced activity of Pt (HY) and Pt-Ru (HY) zeolite catalysts for electrooxidation of methanol in fuel cells. J Power Sources 2004;125:172-177.

[15] An-Ya L, Chin-Te H, Ningya Y, Cheng-Tzu K, Shang-Bin L. Synthesis of carbon porous materials with varied pore sizes and their performances as catalyst supports during methanol oxidation reaction. Appl Energy 2012;100:66-74.

[16] Medina Ramírez A, Ruiz Camacho B, Villicaña Aguilera M, Galindo Esquivel IR, Ramírez-Minguela JJ. Effect for different zeolite as Pt supports for methanol oxidation reaction. Appl Surf Sci 2018;456:204-214.

[17] Medina A, Gamero P, Almanza JM, Vargas A, Montoya A, Vargas G, Izquierdo M. Fly ash from a mexican mineral coal I: mineralogical and chemical characterization. J Hazard Mater 2010;181:91-104.

[18] Ruiz-Camacho B, Martínez Álvarez O, Rodríguez-Santoyo HH, López Pérez PA, Fuentes-Ramírez R. Mono and bi-metallic electrocatalysts of Pt and Ag for oxygen reduction reaction synthesized by sonication. Electrochemm Comm 2015;61:5-9.

[19] Rouquerol J, Rouquerol F, Sing K. Adsorption by powders and porous solid, principles, methodology and applications. 1st ed. Academic Press: London, UK; 1999, p. 439-442.

E042. EFFECT OF THE TiO2 CONTENT OVER THE ELECTROCATALYTIC BEHAVIOR OF Pt/C-TiO2 CATALYSTS ON THE OXYGEN REDUCTION REACTION

Reyes-Tapia N.K.[1], García-de la Cruz Ariane[1], Cervantes-Aspeitia Eduardo Y.[1,2], González-Huerta Rosa de Guadalupe[2], Hernández-Pichardo M.L.[1,*], Paz del Ángel[3].

[1]Laboratorio de Nanomateriales Sustentables, ESIQIE-Instituto Politécnico Nacional. Av. IPN s/n, Ciudad de México 07738.
[2]Laboratorio de Electroquímica y Corrosión, ESIQIE-Instituto Politécnico Nacional. Av. IPN s/n, Ciudad de México 07738.
[3] Caracterización de Materiales, Instituto Mexicano del Petróleo, Eje Central L.C. 152, Ciudad de México, 07730,
* *mhernandezp@ipn.mx

ABSTRACT

Platinum catalysts are excellent materials for electrochemical reactions; however, these solids have some disadvantages such as their high price and poor stability against carbon corrosion, which leads to the detachment of metal nanoparticles and a loss of the electrocatalytic activity. Thus, in this work, Pt/C-TiO2 catalysts were prepared with different contents of TiO2 in order to increase the stability and the catalytic activity of these samples by increasing the interaction between the metallic particles and the support. The samples were characterized by DRX, HRTEM, and XPS. The catalysts were evaluated on the oxygen reduction reaction, and we found that by using this synthesis method, the highest catalytic performance was found by using low TiO2 contents (3-5 % wt.).

Keywords: TiO_2, Pt nanoparticles, ORR.

1. Introduction

Among the fuel cells, polymer electrolyte membrane fuel cells (PEMFC) are presently the most suitable devices for mobile and stationary power applications [1]. However, durability, the slow kinetics, and high overpotentials associated with the performance of the catalyst are the most critical issues to be solved in these systems [2]. Platinum supported on carbon are, up to now, one of the best catalysts for electrochemical reactions. However, these solids have some disadvantages such as the high price of platinum and poor stability against carbon corrosion, especially in the cathode where the catalyst works at low pH, high potential, and high temperatures. Those several conditions lead to the corrosion of the

carbon and the detachment of metal nanoparticles and, consequently, to the loss of the electrocatalytic activity. Then, the development of a robust catalyst support is a crucial factor for the commercialization of fuel cell systems. One approach to solving these challenges is to use modified carbon materials using metal oxides such as WO3, TiO2, or SiO2 [3,4]. Among these oxides, titanium dioxide (TiO2) has gained considerable attention in fuel cell applications due to their stability in acidic and oxidative environments, which promotes excellent corrosion resistance [4–9]. Also, TiO2 properties might modify the so-called strong metal-support interaction (SMSI) and, hence, the electrocatalytic behavior of TiO2-supported catalysts [10]. Recently, Vante et al. have proved that it is possible to reduce the amounts of the catalyst when platinum atoms interact with titanium oxide for the ORR [4]. Thus, in this work, we prepare Pt/C-TiO2 catalysts in order to study the effect of the SMSI on the electrocatalytic activity of these materials.

2. Materials and Methods

2.1 Chemicals and Materials. Titanium terbutoxide, isopropanol, $PtCl_6 \cdot 6H_2O$ and Nafion (5% wt.), were all purchased from Sigma-Aldrich, H_2SO_4 from Fermont and Pt/C Etek and carbon vulcan XC-72 was obtained from Fuel Cell Store. Ultrapure deionized water was used for all solution preparations.

2.2 Synthesis of Pt/C-TiO2 catalysts. Pt/C-TiO_2 catalysts with different titanium dioxide contents were prepared by photo-deposit similarly to the method reported by Vante et al. [4]. Briefly, Vulcan carbon was mixed with titanium terbutoxide in isopropanol on adequate concentrations for each catalyst. The mixture was ultrasonically dispersed by 2 h and then treated at 400 °C under nitrogen for 4 h. Then 1 mL of water was added, and finally, the sample was dried at 110 °C by 16 h. For platinum incorporation, an aqueous solution of $PtCl_6 \cdot 6H_2O$ was added, and the sample was treated in a photoreactor by 3h, using a Xe lamp of 250W. Three catalysts were prepared with different contents of TiO_2 (3,5, and 10% wt.). For comparison, a Pt/C catalyst synthesized without TiO_2. The samples were labeled as PtCT3, PtCT5, PtCT10, and PtC, respectively.

2.3 *Catalysts characterization*. For the characterization, XPS spectra of the catalysts were recorded on a K-Alpha Thermo Scientific 180 apparatus after excitation with a monochromatic Al K radiation. Calibration of the energy position of an XPS peak was performed by using the binding energy of adventitious carbon 1s peak at 284.8 eV. The X-ray diffraction patterns were obtained in a Siemens D500 diffractometer, using a step size = 0.02 degree and step time of 10 s and CuKα radiation. The samples were studied by high-resolution transmission electron microscopy (HRTEM), the micrographs were obtained in a TITAN 80-300 with Schottky type field emission gun operating at 300 kV. The point

resolution and the information limit were better than 0.085 nm. HRTEM digital images were obtained using a CCD camera and Digital Micrograph Software from GATAN.

For the electrochemical analyses, a conventional single three-electrode test electrochemical cell was used. All the electrode potentials in this work are related to a normal hydrogen electrode (NHE) in a 0.5 M H_2SO_4 aqueous solution. The electrochemical measurements were performed at room temperature using a Potentiostate AUTOLAB. The working electrode was a glassy carbon disk with a 5 mm diameter (0.19 cm^2). The counter electrode was a graphite bar, and the reference electrode was Hg/Hg_2SO_4/0.5 M H_2SO_4 (MSE ¼ 0.680 V/NHE). The catalytic ink was prepared by dispersing 1 mg of catalyst in 8 mL of Nafion®, 40 mL of water, and 60 mL of ethyl alcohol in an ultrasonic bath for 30 min. A drop containing 8 mL of catalyst ink was deposited onto the working electrode surface and dried at atmospheric conditions. The Pt loading on the glassy carbon was 38 mg Pt cm^{-2} having concentrations of 10 wt% Pt on support. The electrodes were activated in an oxygen-free electrolyte, by scanning the potential in a region between 1.2 V/NHE to 0.0 V/NHE at 100 mV/s for 30 cycles, until a steady state voltamperogram was reached. Finally, two cycles were performed at 50 mV s^{-1} in the same potential range to analyze the oxide-reducing signals on the catalyst surface. Thereafter, the electrolyte was saturated with pure oxygen for 30 min and maintained on the electrolyte surface during the rotating disk electrode (RDE) experiments from 100 to 2500 rpm at 5 mV/s. The current density was normalized for a geometric area of 0.196 cm^2.

3. Results and Discussion

3.1 *Electrochemical characterization of Pt/C and Pt/C-TiO_2 catalysts.* Four electrocatalysts were studied: Pt/C, PtCT3, PtCT5, and PtCT10 with 0, 3, 5 and 10% wt. of TiO_2, respectively. The cyclic voltammetry characterization of electrodes prepared with these samples is shown in Fig. 1a. These electrodes present adsorption-desorption hydrogen region (Hupd) in a potential region of about 0 to 0.3 V/NHE, which is characteristic in polycrystalline noble metals.

The analysis at a more positive potential, corresponding to the anodic region, also shows a well-defined hydroxide-adsorbed peak with slight differences in the current magnitude, which indicates the capacity of these materials for anion adsorption. The cathodic scan shows the signals corresponding to the reduction of the oxides formed during the anodic sweep. The reduction peaks of PtCT3 and PtCT5 catalysts show a slight displacement to positive potential compared to the sample without TiO_2 (PtC). So it is evident the positive effect of the incorporation of TiO_2 to the carbon substrate. On the other hand, PtCT10 catalyst shows a remarkable difference in the current magnitude in all potential scan. This

electrode presents a low electrochemically active area in the hydrogen region as well as low oxygen reduction activity. It could be the result of the TiO_2 migration on the Pt surface, covering the active sites.

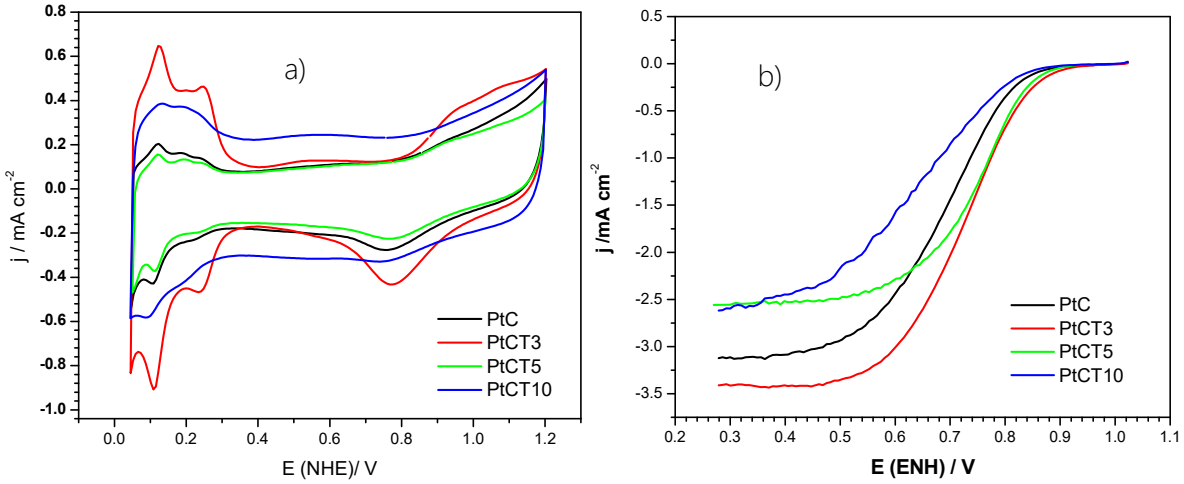

Fig. 1. a) Cyclic voltammetry of Pt/C, PtCT3, PtCT5, and PtCT10 catalysts, in O_2 free 0.5 M H_2SO_4 solution; b) Polarization curves of the electrocatalyst at a rotating speed of 1600 rpm at 25 °C, in 0.5 M H_2SO_4 in O_2-saturated electrolyte.

Fig. 1b shows the comparison of a representative set of polarization curves for the ORR for all the electrocatalyst in 0.5 M H_2SO_4 at 25 °C in O_2-saturated electrolyte. It is observed well-defined kinetic currents (0.85-0.98 V/NHE) for the samples with low TiO_2 content (3 and 5 % wt.), as well as mixed-diffusion limiting currents (0.85-0.60 V/NHE) and diffusion limiting currents (jL) (0.3-0.5 NHE) are observed in polarization curves. It is also noted that the ORR response is more favorable in the PtCT3 and PtCT5 electrodes than in the PtCT10 electrode, and even better than in the PtC electrode.

The mass transfer corrected Tafel plots deduced from the rotating disk electrode (RDE) measurements for the three catalysts are shown in Table 1. Comparable Tafel slope values between 87 and 89 mV dec^{-1} were obtained for the at a low current density at 25 °C. These values indicated a mechanism where the first electron transfer rate Tafel is the determining step.

Table 1. *Kinetics parameters for the Pt/C and Pt/C-TiO_2 catalysts.*

CATALYST mV dec-1	b mV dec-1	α	J_0 mV dec-1

PtC	96.5	0.613	1.68×10^{-7}
PtCT3	88.9	0.665	1.64×10^{-5}
PtCT5	87.6	0.675	1.08×10^{-5}
PtCT10	104.8	0.565	1.55×10^{-5}

3.2 *Phisicochemical characterization results* . X-ray diffraction patterns of all the samples are shown in Fig. 1. It shows mainly the characteristics peaks of the Vulcan XC-72R carbon in 2θ of 25° (002) and 43° (101) two-theta, indicating that the carbon is a polycrystalline material. Also, the presence of the TiO_2 phase is inferred not only for the significant intensity decrease in the diffraction patterns of the samples prepared with this oxide, but also for the small peaks at the positions in 2θ of about 36.4° and 48°, 53.8 °, and 62.5 °, that refer to the (004), (200), (105), and (204) planes of TiO2 in the anatase form [11]. Interestingly, there are no XRD peaks for platinum metal, indicating that the particles are lower than 3 nm, which is the detection limit for this technique. HRTEM images of PTCT3 catalyst (Figure 3), show that the Pt and the TiO_2 are homogeneously dispersed on carbon Vulcan whit particles only detected by EDS. These results partially explain the higher activity of the samples with low content of TiO_2, since it is well known that in the TiO_2 anatase phase the electrons can move faster than in another form of titanium oxide, due to the indirect band gap that enables excited electrons to stabilized itself at lower level in conduction band leading to higher mobility [12]. Moreover, it has been found that the amount of electron density transferred to the metal is found critically and inversely proportional to the metal cluster's size: this being 0.5 electrons per metal atom for a cluster size smaller than 2.0 nm [13].

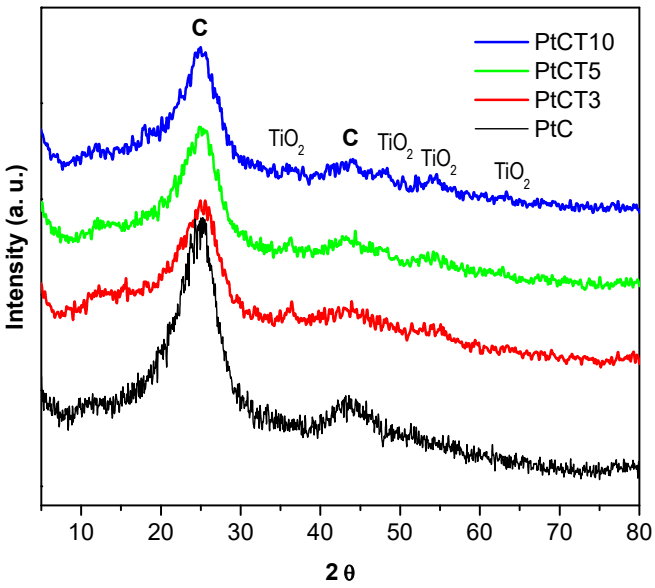

Fig. 2. XRD patterns for Pt/C and PtCT3, PtCT5, and PtCT10 catalysts.

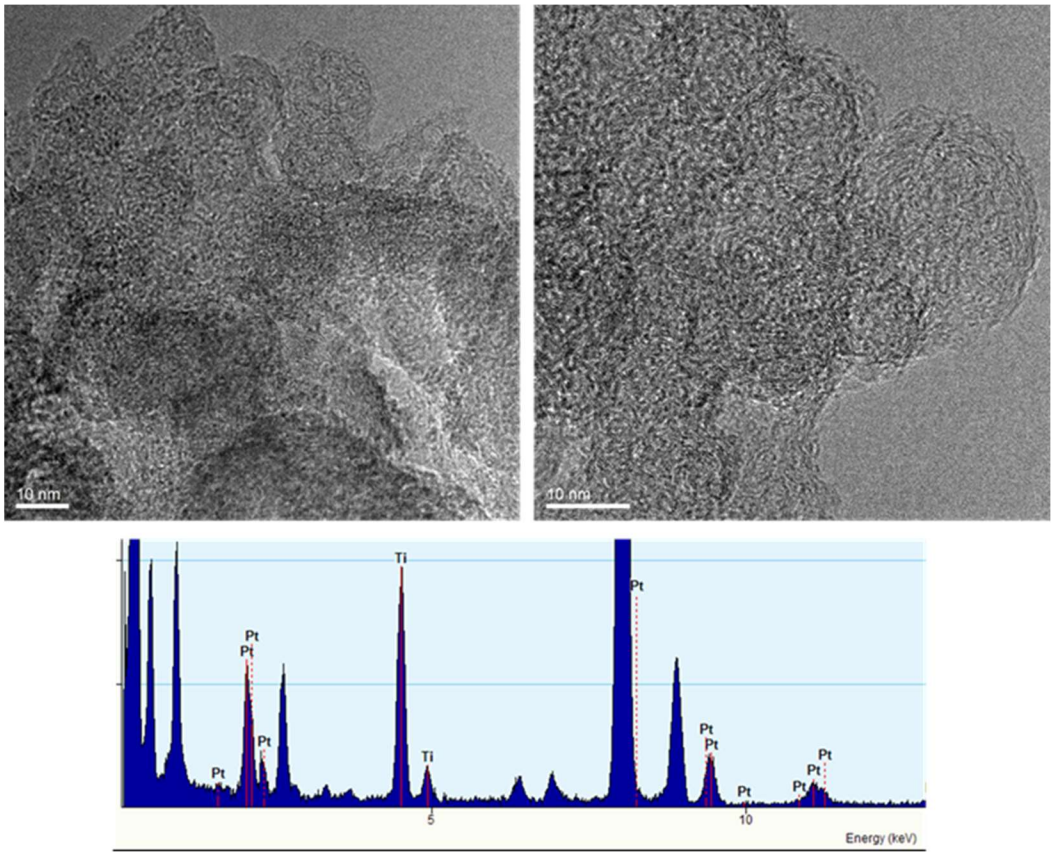

Fig. 3. HRTEM and EDS spectrum for the PtCT3 sample (Pt/C-TiO_2 3% wt.).

Finally, XPS analyzes were XPS carried out to investigate the chemical composition and surface binding states of the Pt/C and Pt/C-TiO_2 catalysts. In Fig. 4, the general XPS survey for the samples show peaks of C 1s, O 1s, Ti 2p, Pt 4d, and Pt 4f, in accordance with the EDS measurement (Fig. 3). Also striking is the presence of Cl 2p that comes from the residues of the Pt precursor, which would indicate that not all platinum is in a metallic state.

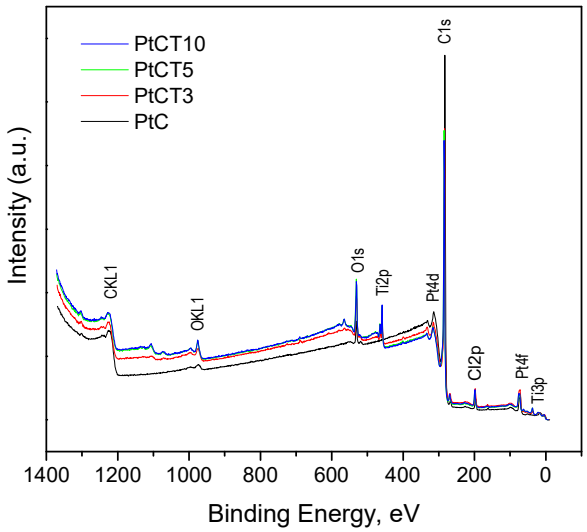

Fig. 4. General XPS survey for the samples PtC, PtCT3, PtCT5 and PtCT10.

High-resolution spectra in the Pt 4f region are shown in Figure 5. It can be seen that the high-resolution spectra of Pt 4f are composed of distinct peaks around 71.8 eV and 81.4 eV for all catalysts, which correspond well with the signals of Pt0, Pt2+, and Pt4+, respectively [14] . The above is an indication that the time spent in the synthesis during the photoreduction process was not enough to reduce all platinum to its zero-valent state. It is also observed that for the catalyst without TiO_2 (Pt/C) the signals of Pt 4f7/2 and Pt 4f5/2 were identified in 71.85 and 75.19 eV, respectively. On the other hand, these same signals were found between 72.2 and 72.38 eV for Pt 4f7/2 and between 75.6 and 75.85 eV for Pt 4f5/2 respectively. This shift towards higher binding energies in the titanium samples suggests the electronic interaction of Pt with other species in the sample, in this case with TiO_2, carbon, and oxygen. The ORR is kinetically limited by slow electron transfer between the surface of catalyst and adsorbed O_2 molecule. Then, the incorporation of TiO_2 may help to the electron transfer in these samples.
On the other hand, Fig. 6 shows the high-resolution spectra in the Ti2p region for catalysts with different TiO_2 contents. The binding energy of the Ti $2p_{1/2}$ and Ti $2p_{3/2}$ levels are observed at approximately 458.6 and 464.3 eV with ~5.7 eV maximum separation, confirming the status of Ti^{4+} in the TiO_2 anatase [15].

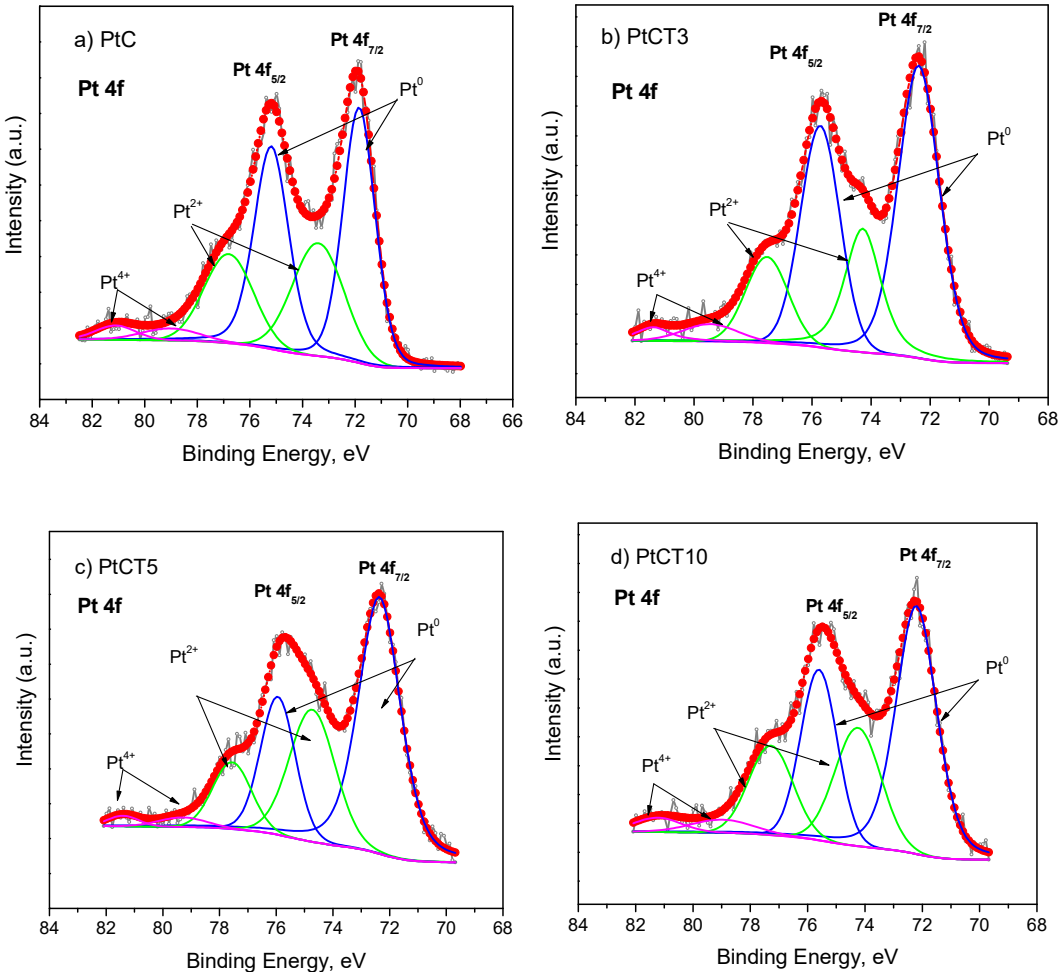

Fig. 5. High resolution XPS spectra of the samples: a) PtC, b) PtCT3, c) PtCT5 and d) PtCT10 in the Pt 4f region.

Analysis of peaks fitted to the O1s region of the various samples provided information complementary to that from the Pt4f and Ti2p spectra. The O1s signal (Figure 7) reveals different surface oxygenated species, which strongly depend on the substrate. It is observed that for Vulcan carbon only C=O (O2:~533.64 eV) and C–O (O3:~532.28 eV) signals are observed [16]. Then when platinum is incorporated a new signal appears at about 531.35 eV assigned to the platinum-oxygen binding. And finally, the samples prepare with TiO_2 present a forth peak at about 530.01 eV associated with the lattice oxygen in the TiO_2 [17]. When the content of TiO_2 is increased, the oxygen related to the M-O appears more in the surface.

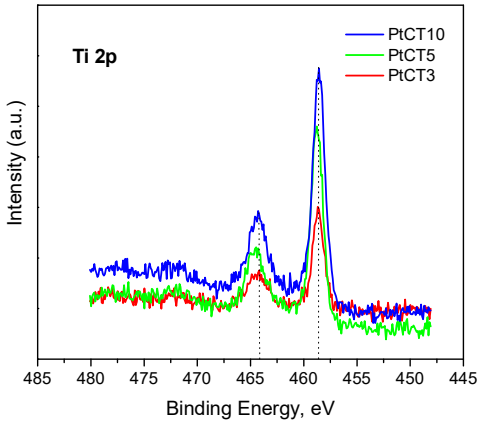

Fig. 6. High-resolution XPS spectra of the TiO_2 samples in the Ti 2p region.

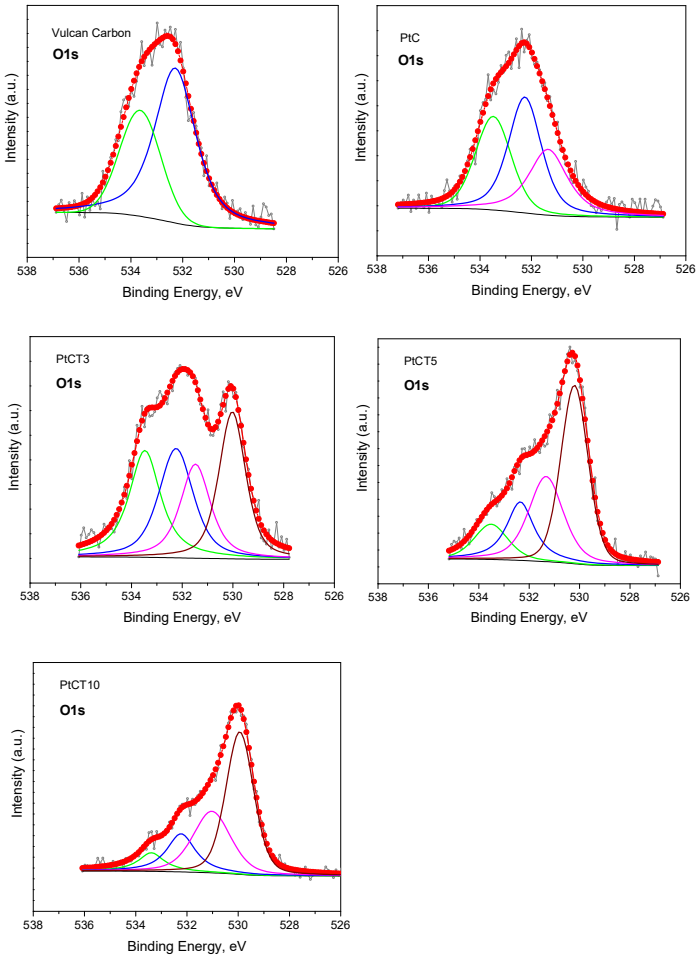

Fig. 7. High-resolution XPS spectra of Vulcan carbon, PtC, PTCT3, PTCT5 and PTCT10 catalysts in the O1s region.

4. Conclusion

The synthesis of Pt/C-TiO_2 by the photodeposit method allows the formation of nanoparticles smaller than 3 nm well dispersed on the C-TiO_2 substrate. This intimate contact with the support allows the SMSI effect and an increase in the catalytic activity for the ORR for the catalysts prepare with titanium oxide, as a result of an electron transfer between Pt, O and Ti atoms.

Acknowledgements

This study was supported by the Instituto Politecnico Nacional through the projects SIP-20195668 and SIP-20195399.

References

[1] J. Wang, G. Yin, Y. Shao, S. Zhang, Z. Wang, Y. Gao, Effect of carbon black support corrosion on the durability of Pt/C catalyst, 171 (2007) 331–339.

[2] G.R. Mirshekari, C.A. Rice, Effects of support particle size and Pt content on catalytic activity and durability of Pt/TiO2 catalyst for oxygen reduction reaction in proton exchange membrane fuel cells environment, J. Power Sources. 396 (2018) 606–614.

[3] M.L. Hernández-Pichardo, R.G. González-Huerta, P. del Angel, M. Tufiño-Velazquez, L. Lartundo, The role of the WO3 nanostructures in the oxygen reduction reaction and PEM fuel cell performance on WO3–Pt/C electrocatalysts, Int. J. Hydrogen Energy. 0 (2015) 1–9.

[4] L. Timperman, Y.J. Feng, W. Vogel, N. Alonso-Vante, Substrate effect on oxygen reduction electrocatalysis, Electrochim. Acta. 55 (2010) 7558–7563.

[5] T.T. Huynh, H.Q. Pham, A. Van Nguyen, L.G. Bach, V.T.T. Ho, Advanced Nanoelectrocatalyst of Pt Nanoparticles Supported on Robust Ti0.7Ir0.3O2 as a Promising Catalyst for Fuel Cells, Ind. Eng. Chem. Res. 58 (2019) 675−684.

[6] J. Ma, E. Valenzuela, A.S. Gago, J. Rousseau, N. Alonso-Vante, Photohole Trapping Induced Platinum Cluster Nucleation on the Surface of TiO 2 Nanoparticles, J. Phys. Chem. C. 118 (2014) 1111−1117.

[7] B.R. Camacho, C. Morais, M.A. Valenzuela, Enhancing oxygen reduction reaction activity and stability of platinum via oxide-carbon composites, Catal. Today. (2012).

[8] B. Ruiz Camacho, M. A. Valenzuela, R. G. Huerta, N. Alonso- Vante, Preparation and Characterization of Pt/C and Pt/TiO2 Electrocatalysts by Liquid Phase Photodeposition, Top. Catal. 54 (2011) 512–518.

[9] L.A. Estudillo-Wong, Y. Luo, J.A. Díaz-Real, N. Alonso-Vante, Enhanced oxygen reduction reaction stability on platinum nanoparticles photo-deposited onto oxide-carbon composites, Appl. Catal. B Environ. 187 (2016) 291–300. [10] L. Timperman, A. Lewera, W. Vogel, N. Alonso-Vante, Nanostructured platinum becomes alloyed at oxide-composite substrate, Electrochem. Commun. 12 (2010) 1772–1775.

[11] L. Timperman, A.S. Gago, N. Alonso-Vante, Oxygen reduction reaction increased tolerance and fuel cell performance of Pt and Ru x Se y onto oxide – carbon composites, J. Power Sources. 196 (2011) 4290–4297.

[12] Y. Ji, Y. Jeon, C. Lee, D. Park, Y. Shul, Environmental Design of active Pt on TiO2 based nanofibrous cathode for superior PEMFC performance and durability at high temperature, Appl. Catal. B, Environ. 204 (2017) 421–429.

[13] C. Pan, M. Tsai, W. Su, J. Rick, Tuning/exploiting Strong Metal-Support Interaction (SMSI) in Heterogeneous Catalysis, J. Taiwan Inst. Chem. Eng. 74 (2017) 154–186.

[14] M.A. Matin, E. Lee, H. Kim, W.S. Yoon, Y.U. Kwon, Rational syntheses of core-shell Fe@(PtRu)

nanoparticle electrocatalysts for the methanol oxidation reaction with complete suppression of CO-poisoning and highly enhanced activity, J. Mater. Chem. A. 3 (2015) 17154–17164.

[15] L. Yu, Y. Shao, D. Li, Direct combination of hydrogen evolution from water and methane conversion in a photocatalytic system over Pt/TiO2, Appl. Catal. B Environ. 204 (2017) 216–223.

[16] S.M. Senthil Kumar, J. Soler Herrero, S. Irusta, K. Scott, The effect of pretreatment of Vulcan XC-72R carbon on morphology and electrochemical oxygen reduction kinetics of supported Pd nano-particle in acidic electrolyte, J. Electroanal. Chem. 647 (2010) 211–221.

[17] M. Ratova, L. Tosheva, P.J. Kelly, B. Ohtani, Characterisation and properties of visible light-active bismuth oxide-titania composite photocatalysts, Sustain. Mater. Technol. 22 (2019) e00112.

E045. REDUCTION AND OXIDATION KINETICS OF $NiWO_4$ AS AN OXYGEN CARRIER FOR HYDROGEN STORAGE BY CHEMICAL LOOPING PROCESS.

P.E. González-Vargas[1]; J.M. Salinas-Gutiérrez[1]; M.J. Meléndez-Zaragoza[1]; V. Collins-Martínez[1]; A. López-Ortiz [1, *]

[1]*Centro de Investigación en Materiales Avanzados, S.C., Miguel de Cervantes 120, Complejo Industrial Chihuahua*

Chihuahua, Chih. México. C.P. 31136

** Tel: +52 6144394815; e-mail: alejandro.lopez@cimav.edu.mx*

ABSTRACT

Chemical looping process (CL) have been used for various purposes, one is the hydrogen storage using metal oxides (MeO) as the only source of oxygen (oxygen carriers) to produce water ($MeO + H_2 = Me + H_2O$) and regenerating the metal oxide with a steam oxidizing atmosphere for the hydrogen release ($Me + H_2O = MeO + H_2$). It was previously proved the potential capacity of $NiWO_4$ as an oxygen carrier to be used on CL process, to confirm these a kinetic study was performed on the involved redox reactions and their kinetic parameters are presented. In order to evaluate the nickel tungstate ($NiWO_4$) oxidation and reduction kinetics, this was thermogravimetrically tested (TGA) in three redox cycles in a temperature range of 730 to 870°C and reductive atmosphere from ca. 2 to 5 v% of H_2/Ar, while oxidation employed concentrations from ca. 0.8 to 2.2 v% H_2O/Ar. For the kinetic study, the data corresponded to the second cycle reduction or oxidation period for each experimental condition. Results indicate a global first order reaction for the reduction of the material (n = 1), while an order reaction of n = 0.7 for the oxidation reaction. Activation energies of 84 and 18 kJ/mol for the reduction and oxidation reactions were found, respectively. A process simulation employed the obtained kinetics parameters to evaluate the theoretical potential application of $NiWO_4$.

Keywords: $NiWO_4$; kinetics; chemical hydrogen storage; chemical looping.

1. Introduction

Although it is difficult to determine energy consumption in a precise way in the future, it is a fact that it will increase significantly in the coming decades. The constant growth of the human population, which in turn demands the consumption of diverse natural resources to satisfy basic needs. Such is the case of the use of fossil fuels, mainly used to obtain electricity, transport and for artificial air conditioning of buildings. It is due to the decrease of these fuels and the environmental impacts that they generate that a large number of researchers around the world find themselves searching for alternative energy sources and sustainable raw materials [1].

In recent times, hydrogen (H_2) has been of great interest, since it is considered as raw material for a wide variety of processes. For example, with nitrogen in the synthesis of ammonia, with CO and CO_2 to produce methanol, in the manufacture of medicines, production of hydrogen peroxide, in the electronics and petrochemical industries and to produce numerous chemical products in various syntheses [1-3]. Moreover, hydrogen is considered a clean source of energy because it has been reported to be a key element in the generation of clean and sustainable energy systems. Virtually any source of fuel, whether renewable or non-renewable, containing in its molecular structure hydrogen atoms (H) can be used for the generation of hydrogen as a gas (H_2). Due to its high energy efficiency (122 kJ/g), hydrogen has great potential to reduce dependence on oil and reduce GHG emissions, with an energy yield 2.75 times higher than that of hydrocarbons. Currently, hydrogen production accounts for around 2% of primary energy demand [4]. Nevertheless, it is necessary to develop better technologies, such as storage and transportation, to make it a more feasible source of energy [4].

Nowadays, various physical and chemical methods for hydrogen storage have been proposed. Such as high-pressure and cryogenic-liquid storage, adsorptive storage on high-surface-area adsorbents, chemical storage in metal hydrides and complex hydrides, storage in boranes, carbon materials, and metal organic frameworks [5, 6]. However, each storage method has its advantages and difficulties due to safety, size, weight, cost and efficiency requirements [7].

To overcome the difficulties presented by many methods of hydrogen storage, recently, the use of redox reactions with metal oxides (MeO) under a chemical looping (CL) reaction scheme has been proposed. This principle of hydrogen storage is based on reactions (1) and (2) [5].

$$Me_xO_y + yH_2 \rightarrow xMe + yH_2O \qquad (1)$$

$$xMe + yH_2O \rightarrow Me_xO_y + yH_2 \qquad (2)$$

In order to be used in CL process, MeO species must be thermally stable to withstand the temperature gradients which are subjected during the process, to be able to store and release lattice oxygen at reaction conditions, and have good availability and affordable costs [8]. The most common MeO reported is iron oxide in its different oxidation states (Fe_3O_4, Fe_2O_3) and this process is commonly known as the steam-iron process. This process consists in the reduction of the iron oxide with H_2 for the H_2 storage, and the subsequent liberation of the H_2 when oxidizing the Fe with steam [9-11]. The theoretical maximum storage capacity of H_2 in this process is 4.8 wt% of Fe [5], i.e., based on the Fe as the only reactive solid. However, most of the processes suggested in various research works propose the impregnation and/or support on different materials of the iron oxide to improve the storage capacity and to avoid the material sintering [5, 9, 11-14], which causes generation of an additional inert load to the reactors, which in turn causes the reduction of up to 3 times the storage capacity of H_2 based on the total solids in the reactive species (including Fe).

In other studies related to the chemical looping partial oxidation of methane (CLPO), it has been reported that some mixed metal oxides used as oxygen carriers (OC), such as perovskites and ilmenites (ABO_3), are resistant to high temperatures [15, 16]. These investigations attribute the thermal resistance of the material to the cation A, while high valence B cations would contribute to the catalytic action. An example of these materials is ilmenite ($FeTiO_3$) that is reported by Schwebel et al. [17] as an OC for H_2, CO and CH_4 as reducing gases, finding kinetics similar to previously reported, with the exception of the reaction with CH_4, which was lower due to limitations in the surface area. These materials are reported without the addition of inert solid species for their operation, a feature that may be of advantage in CL storage of H_2.

The cobalt tungstate ($CoWO_4$) proposed by De Los Ríos et al. [8, 18], doped with nickel (Ni) as a catalyst, reported that is highly stable before cyclic redox tests. In subsequent work, it is reported that this same material is capable of carrying out redox cycles at temperatures below 800°C and thermal efficiencies comparable to the literature [19]. This type of materials present a high thermal resistance, are stable to cyclic redox conditions due to the phenomenon of the solid diffusional reactive barrier [20] and theoretically, are capable of requiring lower temperatures compared to other mixed metal oxides.

Based on the principles and features of mixed metal oxides in CLPO processes, the nickel tungstate ($NiWO_4$) was selected in the present work to evaluate its thermal stability and its ability to store and release lattice oxygen through redox cycles using H_2 as the reductive and steam as oxidative atmospheres as well as to determine the kinetic parameters involved on each reaction step to study its

performance as a H_2 storage material. The involved CL redox reactions of $NiWO_4$ with H_2 and H_2O are the following:

$$NiWO_4 + 4H_2 \rightarrow Ni + W + 4H_2O \quad (3)$$

$$Ni + W + 4H_2O \rightarrow NiWO_4 + 4H_2 \quad (4)$$

2. Methodology

2.1. Synthesis

The $NiWO_4$ was synthesized by the precipitation of solutions method at room temperature with constant agitation, as was done by Song et al. [21], where the formation of crystals with a diameter of ca. 30 nm. 100 mL of 0.7 M precursors salts $Na_2WO_4{\cdot}2H_2O$ and $Ni(NO_3)_2{\cdot}6H_2O$ solutions were mixed. Once precipitate was obtained, it filtered and washed repeatedly with deionized water and then dried at 100°C for 2 hours. After dried, it was calcined at 600°C for 5 hours and allowed to cool at room temperature.

2.2. Characterization

Characterization of the calcined sample was examined to study its crystalline structure, surface area, morphology and microanalysis composition by X-ray diffraction analysis (XRD), BET surface area, scanning electron microscopy (SEM), and energy dispersive X-ray spectroscopy (EDS), respectively.

The XRD, SEM and EDS analyzes were performed on the sample before and after three redox cycles, in order to establish the stability of the material.

2.3. TGA Hydrogen Storage Performance Evaluation and Global Kinetic Study

The redox behavior of the $NiWO_4$ powder was followed by a conventional thermogravimetric analysis (TGA) system, following the weight change (%w) signal respect to time. All redox experiments were carried out at atmospheric pressure, the total reactive gas flowrate was 100 mL/min and the amount of $NiWO_4$ samples were of ca. 20 mg placed in a platinum-made sample holder.

A first experiment of redox cycle at a constant temperature of 700°C using respectively 5 v% H_2/Ar and ca. 5 v% H_2O/Ar for reduction and reoxidation was carried out to evaluate the hydrogen storage potential of the material, then it was compared with other oxygen carriers reported previously in the literature.

In order to evaluate the oxidation and reduction kinetics, different experimental conditions of temperature and concentrations of reductive and oxidative atmospheres were used. Table 1 shows 18 experimental conditions for the global kinetic study. The data corresponded to the second cycle reduction or oxidation period for each experimental condition.

Table 2. TGA tests for the global kinetic study.

Reactant atmosphere	Temperature								
	730 °C			800 °C			870 °C		
H_2/Ar	2.0%	3.4%	5.0%	2.0%	3.4%	5.0%	2.0%	3.4%	5.0%
H_2O/Ar	0.8%	1.5%	2.2%	0.8%	1.5%	2.2%	0.8%	1.5%	2.2%

Prior to the reactions, the sample was heated up in an inert atmosphere (Ar) to the targeted experimental temperature (730, 800 or 870 °C) and then isothermally treated under a reducing or oxidizing flow. Before switching from reduction to oxidation atmosphere and vice versa, the remaining reactive gases were removed by an argon flush flow for ca. 5 min.

For the reduction process, different H_2/Ar flowrates (ca. 2, 3.4 and 5 v%) were used. The duration of this step was determined in order to achieve a complete reduction of $NiWO_4$ to Ni and W, i.e., ca. 20.9% of weight loss.

For the reoxidation of the sample, mixtures of water vapor and argon were supplied by water saturation of an Ar flow at room temperature, with concentrations of ca. 0.8, 1.5 and 2.2 v% H_2O/Ar. The duration of this step was determined in order to complete de reoxidation of Ni and W back to $NiWO_4$ (until no mass change could be detected).

Once kinetic parameters were obtained, a process simulation using Aspen Plus was carried out in order to confirm the viability for a potential application of the material in a CL hydrogen storage process.

3. Results and Discussion

3.1. Characterization

Figure 1a shows the XRD pattern of the synthesized material. The obtained crystallographic phase was indexed with the Match! Software, which is in agreement with the nickel tungstate diffractogram ICSD collection code 015852 [22].

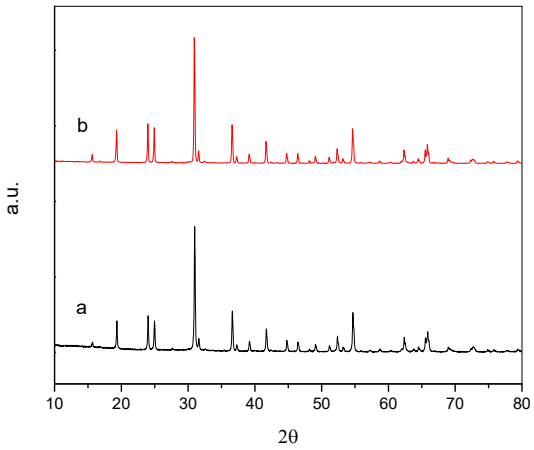

Figure 1. X-Ray diffraction pattern of the fresh sample (a) and after the three redox cycles (b).

Figure 1b shows the XRD pattern from the sample after being exposed to three redox cycles in a TGA. The obtained crystallographic phase was indexed (as in Figure 1a) with the nickel tungstate diffractogram ICSD collection code 015852, i.e., the same crystallographic phase was present at the beginning and at the end of the redox cycles. This thermal stability can be explained based on what was reported by De Los Ríos et al. [23] that established that when the $CoTiO_3$ is exposed to H_2/Air redox cycles, during the reoxidation process, the cobalt returns to form the perovskite phase of titanate and cobalt, which inhibits the nucleation and migration of Co particles, thus considerably reducing the sintering process.

Table 3. BET surface area and crystallite size of the sample

Sample	BET (m^2/g)	Fresh crystallite size (nm)	Crystallite Size – Three redox cycles (nm)
$NiWO_4$	4.25	47.2	56.6

Table 2 shows results of BET surface area analysis and crystallite sizes of the $NiWO_4$ before and after of being exposed to three redox cycles. The crystallite size was determined through the characteristic signal from the samples crystalline structures and the Scherrer equation [24]:

$$\beta = \frac{0.95\lambda}{L\text{Cos}\theta} \qquad (5)$$

Where, β is the width of the peak at half maximum intensity of a specific phase (hkl) in radians, K is a constant (0.95), λ is the wavelength of incident x-rays (0.1541 nm), θ is the center angle of the peak and finally L is the crystallite length (nm).

According to Table 2, BET analysis results indicate a surface area within the range of other mixed metal oxides. As the mixed Fe-CeZr oxides doped with Ni reported by Sosa et al. [25] that report surface areas between 1.8 and 8.2 m^2/g.

The fresh crystallite size matches the size reported by De Los Rios et al. [20] for the $CoWO_4$ doped with Ni of 47.6 nm. This change in the size of the sample was expected, due to its exposure to the redox cycles at high temperatures as also reported by De Los Rios et al. [8] for the $CoWO_4$ after four redox cycles.

Figure 2 presents the SEM images and the EDS analysis results of the sample before and after the redox cycles. In these images, it can be observed that the fresh $NiWO_4$ sample is composed of sphere like particles whose sizes vary between 0.1 and 0.4 μm and forming agglomerates. In the sample after the redox cycles, it can be observed sphere like polygonal particles with an increase in particle size that ranges between 0.2 and 0.6 μm and also forming agglomerates with slight signs of sintering.

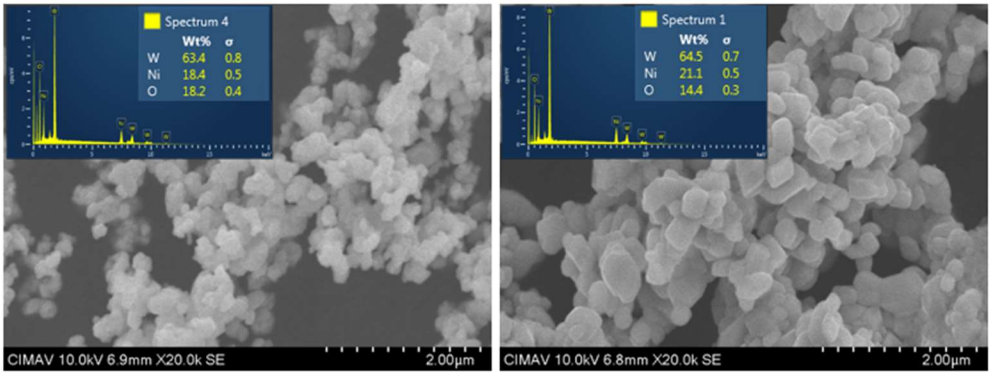

Figure 2. SEM micrographs and EDS analysis of the fresh NiWO4 (left) and after the redox cycles (right).

This change in morphology is due to the exposure of the material to the constant temperature of 700°C during the redox cycles. However, the signs of sintering of the material agree well with those reported by De Los Rios et al. [8], where these changes are reported to be considered not significant compared to other processes where the particle size can exceed up to one thousand times the original size after redox cycles [26]. In addition, this can be confirmed by observing that the cyclic behavior (Figure 3) and the weight composition (EDS results in Figure 2) of the material are not importantly affected within the performed cycles.

3.2. Hydrogen Storage Performance Evaluation

Evaluation of the storage and release of H_2 performance by TGA during three redox cycles can be observed in Figure 3. This test provides the behavior of the $NiWO_4$ during reduction using 5 v% H_2/Ar and reoxidation with ca. 5 v% H_2O/Ar at a constant temperature of 700°C. In this figure the weight change percentage is plotted as a function of time. The corresponding theoretical weight changes (%) from $NiWO_4$ (100%), the reduced metals W and Ni (79.1%), and the possible intermediate species $NiO*WO_2$ and $Ni*WO_3$ (94.8%) are represented by horizontal dotted lines. In this figure it can be observed that the material presents a high thermal stability during the redox cycles. It is also possible to observe that $NiWO_4$ is progessively adapting to each cycle since the reduction and oxidation times are decreasing as the number of cycles is increased. For example, in the case of the first cycle compared to the third, there is a time decrease during reduction from 85

to 60 minutes; and a decrease time during oxidation from 132 to 123 minutes. Moreover, there is a close agreement of the sample weight loss of 20.7% with respect to the theoretical value of 20.9% corresponding to the reduction of $NiWO_4$ to Ni and W according to reaction equation (3). Whereas, the experimental weight gain by oxidation was of approximately 20.7% compared to the theoretical 20.9%, corresponding to the reoxidation of Ni and W to $NiWO_4$ in agreement with reaction equation (4).

These results obtained also revealed a presumable oxidation mechanism of the reduced metals (Ni + W) that follows two oxidation stages, first W is either oxidized to WO_3 or WO_2 and secondly, Ni is oxidized by any of the previous tungsten oxide forms. The latter is because it is thermodynamically impossible to oxidize Ni with steam (see reaction equation 6, Gibbs free energy). Therefore, the only source of oxygen capable of regenerating the oxide must be through two reaction paths that involved the formation of WO_2 or WO_3 as intermediate species. The first path deals with the formation of WO_2 by the oxidation of W with steam and followed by the reaction of WO_2 with Ni and H_2O to form $NiWO_4$ according to reactions (7) and (8), respectively.

$$Ni + H_2O \rightarrow NiO + 2H_2 \qquad \Delta G_{700°C} = 43.3\ kJ/mol \qquad (6)$$

$$W + 2H_2O \rightarrow WO_2 + 2H_2 \qquad \Delta G_{700°C} = -23.93\ kJ/mol \qquad (7)$$

$$Ni + WO_2 + 2H_2O \rightarrow NiWO_4 + 2H_2 \qquad \Delta G_{700°C} = 6.92\ kJ/mol \qquad (8)$$

$$WO_2 + H_2O \rightarrow WO_3 + 2H_2 \qquad \Delta G_{700°C} = 14.25\ kJ/mol \qquad (9)$$

$$W + 3H_2O \rightarrow WO_3 + 3H_2 \qquad \Delta G_{700°C} = -9.68\ kJ/mol \qquad (10)$$

$$Ni + WO_3 + H_2O \rightarrow NiWO_4 + H_2 \qquad \Delta G_{700°C} = -7.33\ kJ/mol \qquad (11)$$

It is clear that this reaction path is not feasible, due to the fact that the reaction (8) will not thermodynamically occur because its ΔG is positive at reaction conditions (700°C). Furthermore, the formation of WO_3 from WO_2 and H_2O through reaction (9) is also not feasible ($\Delta G_{700°C}$ = 14.25kJ/mol). Therefore, the second reaction path, which consists in the formation of WO_3 by the reaction (10) followed by the formation of $NiWO_4$ through reaction (11) is presumably the most likely reaction path to obtain the desired initial oxide condition.

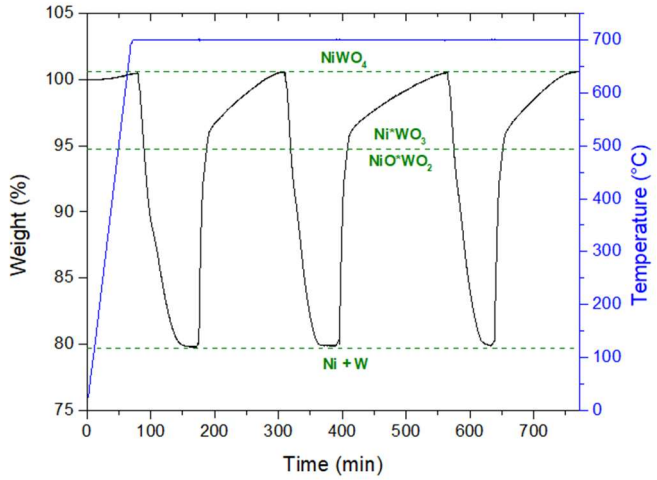

Figure 3. TGA monitoring results of redox cycles for the sample of NiWO4 at 700 °C.

A comparative H_2 storage capacity based on the total reduced solids between different previous research works can be observed in Table 3. The theoretical maximum H_2 storage capacity of $NiWO_4$ is 3.3 W% corresponding to a Ni/W stoichiometric ratio, which is a low capacity compared to iron oxides (4.8 W% maximum theoretical). However, it is worth to notice that this proposed material is not mixed with any inert materials such as supports or dopants to improve the redox reactions and/or to prevent sintering, which makes the net loading of solids to the reactor totally reactive and the storage capacity of H_2 with respect to total solids is higher than several other Fe-based materials reported in the literature, where their capacity is reduced up to 1.4 W%.

Table 4. Comparative H2 storage capacity of various metal oxides.

Sample	H_2 storage capacity based on Total solids (W%)	Reference
$NiWO_4$	3.3	-
$Fe_2O_3/Al_2O_3/SiO_2$	3.4	[5]
Cu-Fe/Ce/Zr	1.8	[11]

Cu/Fe/YSZ	1.8	[12]
Fe_2O_3/YSZ-GDC-Zr-Ce	1.4	[27]
Fe_2O_3/Mo/Al	4.6	[28]

3.3. Kinetic Study

3.3.1. Initial reaction rate

From the TGA signal response in %W vs time (minutes), the slope obtained (Δw/Δt) is proportional to the initial reaction rate. Initial reaction rates were evaluated for each one of the 18 tests that were described previously in the Table 1.

According to what is widely used in the literature [29], this reaction can be studied by a usual model of a gas-solid reaction rate according to the following expression:

$$-r_A = kC_A{}^n \quad (12)$$

where *k* is the reaction rate constant, C_A is the H_2 concentration in molar fraction and *n* is the global reaction order with respect to the H_2.

3.3.2. Reaction order

The reaction order for the $NiWO_4$ oxygen carrier reduction during the second cycle with respect to the methane concentration at experimental conditions previously described is shown in Figure 4. The logarithm of the reaction rate vs the logarithm of the hydrogen concentration is plotted in this figure. A linear equation results from the analysis at each temperature condition, where the ordinate axis intersect represents the logarithm of the reaction rate constant (*k*) and the slope (*n*) the reaction order at a specific temperature.

A reaction order between 0.87 and 1.01 was obtained. Therefore, it can be concluded that the global reduction reaction of $NiWO_4$ is first order (n = 0.94) with respect to the hydrogen concentration during the second cycle.

Abad et al. [30] studied the reduction of an ilmenite structure-type mineral ($FeTiO_3$) in a chemical looping process with hydrogen and they found also a global first order reaction rate. Furthermore, $NiWO_4$ reduction with hydrogen has not been widely reported in the literature so far. More than 30 years ago, Albiston and Sale [31] reported that nickel tungstate presents a thermochemical stability during its reduction with hydrogen similar to that of cobalt tungstate in a temperature range of 600-900 °C, thus reducing completely to a mixture of metallic nickel and tungsten. In a more recent study, Kang et al. [32] were focused in the reduction of WO_3 and NiO-WO_3 powders with hydrogen to study this reaction and its sintering behavior to synthesize a consolidated W-Ni powder. They did not report a reduction rate order; however, they obtained activation energies values as well as other kinetic parameters. Other studies found a global first order reaction of the mixture of NiO-WO_3 with hydrogen in a fluidized bed reactor [33, 34].

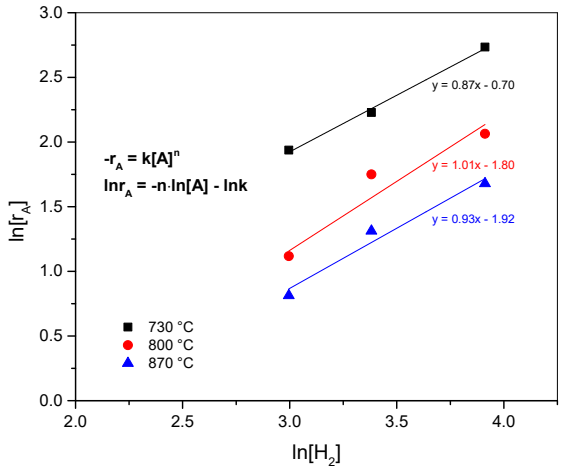

Figure 4. Global reaction order plot for the reduction of $NiWO_4$ with respect to H_2 concentration.

Otherwise, the reaction order for the regeneration of the metal oxide with steam during the second cycle with respect to the H_2O concentration at the experimental conditions is shown in Figure 5.

A reaction order for the material between 0.70 and 0.73 was obtained. Thus, a value of 0.71 was assumed for the global reaction order with respect to the H_2O concentration in the second cycle. Aspinall [35] previously reported an order of 0.8 for the W oxidation with steam in a temperature range between 1960-2290 K. The fractional reaction order obtained presumably indicates that the reaction proceeds in

several elementary steps, such as the reaction mechanism previously proposed. Therefore, according to the kinetics behavior of the oxidation step we proposed that the H_2O diffusion through the outer oxide external layer (WO_3) to the inner unreacted tungsten of the reacting particle presumably determines the reaction (11) rate as reported by Sabourin and Yetter [36], and this can be attributed to be the rate-determining step.

Moreover, Chen et al. [37] suggest that there is a strong interaction between Ni and WO_x species during the reduction reaction with methane and the oxidation with oxygen and the global activity can be directly affected by lattice oxygen diffusion and surface reaction rate, which in the case of the reaction between Ni and WO_3 will promote the formation of $NiWO_4$.

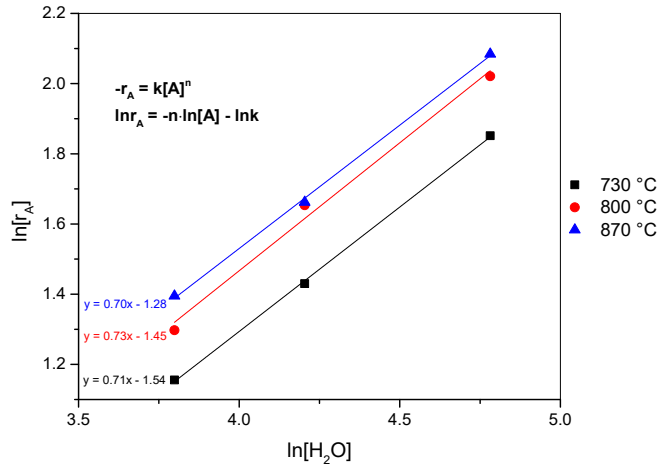

Figure 5. Global reaction order plot for the regeneration of $NiWO_4$ with respect to H_2O concentration.

3.3.3. Reaction constant

Reaction constants were obtained from the intersection of the linear trend with the abscissa generated for each temperature, *i.e.* $\ln r_A = \ln k + n \ln [H_2]$ and $r_A = \ln k + n \ln [H_2O]$ for the reduction and oxidation steps, respectively. Reaction rate constants for the second cycle are shown in Table 4. The reaction rate constant offers a simple way to associate reaction rates at different temperatures, *e.g.*, according with the results, for the reduction reaction the increase in temperature from 730 to 870 °C represents an enhancement in rate constant of about 3.4 times and only 1.1 times faster from 800 to 870 °C. However,

for the oxidation reaction an increase of rate constants is obtained with an increment of 1.3 times from 730 to 870 °C. This relatively small increment in oxidation rate constant, confirms that this reaction rate is mass transport limited (water diffusion). This behavior explains the fact that these reaction constants are not that sensitive to a temperature increment compared to an equivalent increment in temperature over the reduction reaction rate constants.

Table 5. Reaction rate constant values for reduction and oxidation reactions ($k=min^{-1}$)

	730 °C	800 °C	870 °C
Reduction	2.01	6.08	6.82
Oxidation	0.21	0.23	0.28

Ahmed et al. [34] divide the hydrogen reduction reaction of NiO-WO_3 in three stages and calculate the reaction rate constants for each stage by a theoretical model from 700 to 1000 °C and these values agreed well with their experimental reaction rate constants. In these data, it can be observed that over the same temperature range, the reaction rate constant has an increase of about 2.3, 3 and 2.9 times in the first, second and third stages, respectively. These values agree well with data for the global reduction step determined in the present study.

3.3.4. Global activation energy

The reaction rate constant (temperature-dependent), is represented by the Arrhenius law [29]:

$$k = k_0 e^{-E/RT} \tag{13}$$

Where k_0 is the pre-exponential factor or frequency factor, E is the global activation energy of the reaction, R is the universal gas constant and T is the temperature. This expression is considered as a very good approximation to the true temperature dependence of a reaction.

From the linearization of the Arrhenius equation, the following expression is established:

$$\ln k = -\frac{E}{RT} + \ln k_0 \tag{14}$$

Thus, the resulting slope of plotting 1/T against ln *k* corresponds to the activation energy divided by the universal gas constant [8]. Results indicate a global activation energy of 84.4 kJ/mol for the reduction of $NiWO_4$ with H_2, which is consistent with reported values for similar reactions of other metal oxides [32]. Ahmed *et al.* reported activation energies of 47.2 and 91.4 kJ/mol for NiO and $NiWO_4$ in early stages of hydrogen reduction, and they attributed these values to the surface reaction that includes the chemical reaction itself as well as other physical phenomena [33].

In the case of steam oxidation reaction, the global activation energy obtained was 17.64 kJ/mol. This value is consistent with a transport limited reaction kinetics, since it is well established that activation energy values approximately lower than 20 kJ/mol [38] are indication of diffusional limitations of H_2O through the outside external layer of the reactive particle

According to results obtained in this research, the global kinetic expressions for the reduction and oxidation reactions are respectively as follows:

$$-r_A[NiWO_4] = 10.9e^{(-\frac{84.4}{RT})}y_{H_2}$$

$$r_A[NiWO_4] = 0.5e^{(-\frac{17.6}{RT})}y_{H_2O}$$

3.4. Process Simulation

The proposed process simulation scheme is shown in Figure 6, which describes the metal oxide hydrogen reduction and the metal oxide regeneration under a chemical looping concept. The reactor's model employed under Aspen Plus was RBatch. In the first one (RED reactor) the hydrogen reduction of $NiWO_4$ as an oxygen carrier is carried out, while in the second (REGEN reactor) tungsten and nickel reoxidation reactions take place in the presence of steam, thus regenerating nickel tungstate and producing hydrogen. 4 kmol/hr of hydrogen and 1 kmol/h of $NiWO_4$ are fed to the first reactor. A Redlich-Kwong-Aspen thermodynamic system equation of state was used in the simulation, which is aimed for processes that involve hydrocarbons and their mixtures with polar components for medium and high pressures [39]. Cyclones CYC1 and CYC2 are used to separate the solid and gaseous products resulting from both reactors.

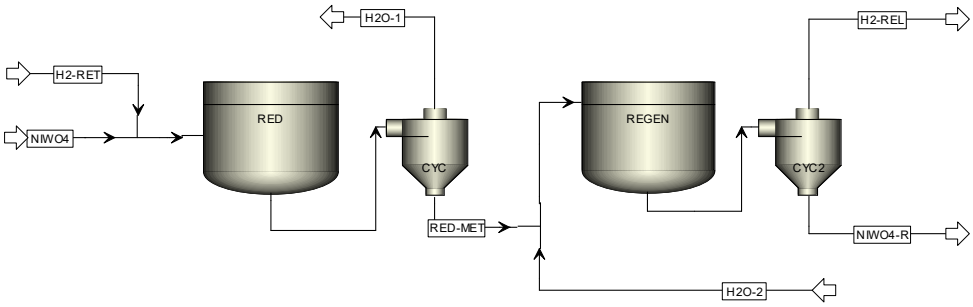

Figure 6. Process simulation flowsheet.

Simulation results are shown in Table 5. These results show a global mass balance that confirms a complete conversion of the hydrogen (H2-RET) $NiWO_4$ (NiWO4) streams to reactor RED into H_2O (stream H2O-1) and a mixture of Ni and W. These solid products in stream RED-MET react with stoichiometric steam from H2O-2 stream and the products from reactor REGEN obtained are divided in a solid stream NIWO4-R (containing only the regenerated $NiWO_4$) and a gas H2-REL stream (released H_2), thus closing the loop to the initial conditions. A successful hydrogen storage chemical looping process employing the experimental kinetic parameters previously obtained can be proposed. These findings clearly show that the $NiWO_4$ have a good potential as an oxygen carrier for this chemical looping process. Results from Table 5 clearly show that 4 kmol/h of H2 are possible to be stored and released by this process. Further research involving the thermal stability of this oxygen carrier for several reduction-oxidation cycles at proposed reaction conditions is needed in order to experimentally assessed the real potential of $NiWO_4$.

Table 6. Simulation results.

Stream name	H2-RET	NIWO4	H2O-1	RED-MET	H2O-2	H2-REL	NIWO4-R
Temperature (°C)	25.00	25.00	800.00	800.00	100.00	800.00	800.00
Pressure (atm)	1.00	1.00	1.00	1.00	1.00	1.00	1.00
Mole Flow (kmol/hr)	4.00	1.00	4.00	2.00	4.00	4.00	1.00
H_2	4.00	-	-	-	-	4.00	-
H_2O	-	-	4.00	-	4.00	-	-
$NiWO_4$	-	1.00	-	-	-	-	1.00
Nickel	-	-	-	1.00	-	-	-
Tungsten	-	-	-	1.00	-	-	-

It should be noted that the process simulation was limited, because this is only aimed to evaluate the theoretical potential application of the studied material under the chemical looping hydrogen storage process and did not take into account other important aspects such as engineering details, physical properties of the compounds, among other important design features.

4. Conclusions

Hydrogen storage and release characteristics of pure $NiWO_4$ using TGA redox cycles were studied. Characterization of the material (XRD, BET surface area and SEM) before and after the redox cycles shown slight signs of sintering. However, TGA evaluation indicates that these changes do not significantly affect the performance of $NiWO_4$ as a hydrogen storage material. The isothermal redox test yield to a hydrogen storage capacity of 3.3 wt% based on Ni/W reduced metals, which is competitive with current materials reporter in the literature. Furthermore, TGA tests revealed an oxidation mechanism of the reduced metals (Ni + W) that follows a reaction path, which consists in the formation of WO3 by the oxidation of W with steam, followed by the formation of $NiWO_4$. This reaction path was confirmed by the kinetic parameters that indicate several steps during the oxidation mainly due to diffusion of H_2O into the reactant particle.

Process simulation carried out using the experimental kinetic parameters confirmed the potential of the $NiWO_4$ as an oxygen carrier for the proposed hydrogen storage chemical looping process and showed that 4 kmol/h of H_2 are possible to be stored and released.

Despite the limitations of the process simulation, it can be confirmed that the $NiWO_4$ has good potential for use as an oxygen carrier material for the hydrogen storage in chemical looping process.

Further research involving the thermal stability of this oxygen carrier for several reduction-oxidation cycles at proposed reaction conditions is needed in order to experimentally assessed the real potential of $NiWO_4$.

Acknowledgements

The authors of this paper wish to thank the Mexican Society of Hydrogen for accepting the proposed research for dissemination and discussion during its XIX International Congress, as well as the scholarship. We thank equally to CONACYT for the scholarship awarded to the student involved in the project.

References

[1] Sunny A, Solomon PA, Aparna K. Syngas production from regasified liquefied natural gas and its simulation using Aspen HYSYS. Journal of Natural Gas Science and Engineering. 2016;30:176-81.
[2] De Los Ríos T, Collins Martinez V, Delgado Vigil MD, López Ortiz A. Synthesis, characterization and stability performance of CoWO4 as an oxygen carrier under redox cycles towards syngas production. International Journal of Chemical Reactor Engineering. 2007;5.
[3] Collins-Martinez V, Escobedo Bretado M, Meléndez Zaragoza M, Salinas Gutiérrez J, Ortiz AL. Absorption enhanced reforming of light alcohols (methanol and ethanol) for the production of hydrogen: Thermodynamic modeling. International Journal of Hydrogen Energy. 2013;38:12539-53.
[4] da Silva Veras T, Mozer TS, da Costa Rubim Messeder dos Santos D, da Silva César A. Hydrogen: Trends, production and characterization of the main process worldwide. International Journal of Hydrogen Energy. 2017;42:2018-33.
[5] Zhong M, Rui X, Huiyan Z. Montmorillonite-Supported Iron Oxide for Hydrogen Storage by Chemical Looping. Energy Technology. 2017;5:1399-406.
[6] Eberle U, Felderhoff M, Schueth F. Chemical and physical solutions for hydrogen storage. Angewandte Chemie International Edition. 2009;48:6608-30.
[7] Niaz S, Manzoor T, Pandith AH. Hydrogen storage: Materials, methods and perspectives. Renewable and Sustainable Energy Reviews. 2015;50:457-69.

[8] De los Ríos Castillo T. Óxidos Metálicos Mixtos como Portadores de Oxígeno para Procesos REDOX a partir de Metano Chihuahua, México: CIMAV; 2010.
[9] Hacker V, Vallant R, Thaler M. Thermogravimetric investigations of modified iron ore pellets for hydrogen storage and purification: the first charge and discharge cycle. Industrial & engineering chemistry research. 2007;46:8993-9.
[10] Hui W, Takenaka S, Otsuka K. Hydrogen storage properties of modified fumed-Fe-dust generated from a revolving furnace at a steel industry. International journal of hydrogen energy. 2006;31:1732-46.
[11] Kim H-S, Cha K-S, Yoo B-K, Ryu T-G, Lee Y-S, Park C-S, et al. Chemical hydrogen storage and release properties using redox reaction over the Cu-added Fe/Ce/Zr mixed oxide medium. Journal of Industrial and Engineering Chemistry. 2010;16:81-6.
[12] Kim H-S, Lee D-H, Kim H-S, Park C-S, Kim Y-H. Hydrogen storage and release properties of a Cu-added Fe/YSZ redox system. Journal of Nanomaterials. 2013;2013:8.
[13] Kim YH, Je HS, Kang EJ, Lee SG, Park CS. Hydrogen storage and release by redox reaction of iron oxide medium with Mo and Zr additives. Advanced Materials Research: Trans Tech Publ; 2012. p. 3317-20.
[14] Kim YH, Kang EJ, Lee SG, Kim HS, Park CS. Effect of Mo and Ce additives on redox behavior for hydrogen storage and release of iron oxide mediums. Advanced Materials Research: Trans Tech Publ; 2012. p. 616-9.
[15] Mihai O, Chen D, Holmen A. Catalytic consequence of oxygen of lanthanum ferrite perovskite in chemical looping reforming of methane. Industrial & Engineering Chemistry Research. 2010;50:2613-21.
[16] Rydén M, Leion H, Mattisson T, Lyngfelt A. Combined oxides as oxygen-carrier material for chemical-looping with oxygen uncoupling. Applied Energy. 2014;113:1924-32.
[17] Schwebel GL, Sundqvist S, Krumm W, Leion H. Apparent kinetics derived from fluidized bed experiments for Norwegian ilmenite as oxygen carrier. Journal of Environmental Chemical Engineering. 2014;2:1131-41.
[18] De los Ríos Castillo T, Salinas Gutiérrez J, López Ortiz A, Collins-Martínez V. Global kinetic evaluation during the reduction of CoWO4 with methane for the production of hydrogen. International Journal of Hydrogen Energy. 2013;38:12519-26.
[19] López-Ortiz A, González-Vargas PE, Meléndez-Zaragoza MJ, Collins-Martínez V. Thermodynamic analysis and process simulation of syngas production from methane using CoWO 4 as oxygen carrier. International Journal of Hydrogen Energy. 2017.
[20] De Los Ríos-Castillo T, Palacios LC, De los Ríos SA, Vigil DD, Salinas J, Gutiérrez ALO, et al. Study of CoWO4 as an Oxygen Carrier for the Production of Hydrogen from Methane. Journal of New Materials for Electrochemical Systems. 2009;12:55-61.
[21] Song Z, Ma J, Sun H, Wang W, Sun Y, Sun L, et al. Synthesis of NiWO4 nano-particles in low-temperature molten salt medium. Ceramics International. 2009;35:2675-8.
[22] Match!©. Calculated from ICSD using POWD-12++ 1997. p. 238

[23] De los Rios T, Lardizabal Gutierrez D, Collins Martínez V, López Ortiz A. Redox Stabilization Effect of TiO2 in Co3O4 as Oxygen Carrier for the Production of Hydrogen through POX and Chemical Looping Processes. International Journal of Chemical Reactor Engineering2005.
[24] Patterson A. The Scherrer formula for X-ray particle size determination. Physical review. 1939;56:978.
[25] Vázquez MS, Vigil MD, Gutiérrez JS, Martínez VC, Ortiz AL. Synthesis gas production through redox cycles of bimetallic oxides and methane. Journal of New Materials for Electrochemical Systems. 2009;12:029-34.
[26] S. T, V. S, K. O. Stotage and supply of pure Hydrogen from methane mediated by modified Iron Oxides Energy & Fuels. 2004;18:820-9.
[27] Kosaka F, Hatano H, Oshima Y, Otomo J. Iron oxide redox reaction with oxide ion conducting supports for hydrogen production and storage systems. Chemical Engineering Science. 2015;123:380-7.
[28] Hui W, Xiaoqiong F, Xiaofang W, Sanping C, Shengli G. Hydrogen production by redox of bimetal cation-modified iron oxide. international journal of hydrogen energy. 2008;33:7122-8.
[29] Levenspiel O. Ingeniería de las reacciones químicas: Reverté; 2002.
[30] Abad A, Adánez J, Cuadrat A, García-Labiano F, Gayán P, de Diego LF. Kinetics of redox reactions of ilmenite for chemical-looping combustion. Chemical Engineering Science. 2011;66:689-702.
[31] Albiston JN, Sale FR. Thermogravimetric studies of the hydrogen reduction of nickel tungstate. Thermochimica Acta. 1986;103:175-80.
[32] Kang H, Jeong Y-K, Oh S-T. Hydrogen reduction behavior and microstructural characteristics of WO3 and WO3-NiO powders. International Journal of Refractory Metals and Hard Materials. 2019;80:69-72.
[33] Ahmed HM, Seetharaman S. Isothermal dynamic thermal diffusivity studies of the reduction of NiO and NiWO4 precursors by hydrogen. International Journal of Materials Research. 2011;102:1336-44.
[34] Ahmed HM, El-Geassy A-HA, Viswanathan NN, Seetharaman S. Kinetics and mathematical modeling of hydrogen reduction of NiO–WO3 precursors in fluidized bed reactor. ISIJ international. 2011;51:1383-91.
[35] Aspinall S. Principles governing the behavior of solid materials in severe high temperature environments. UNION CARBIDE RESEARCH INST TARRYTOWN NY; 1965.
[36] Sabourin JL, Yetter RA. High-temperature oxidation kinetics of tungsten-water reaction with hydrogen inhibition. Journal of Propulsion and Power. 2011;27:1088-96.
[37] Chen S, Zeng L, Tian H, Li X, Gong J. Enhanced Lattice Oxygen Reactivity over Ni-Modified WO3-Based Redox Catalysts for Chemical Looping Partial Oxidation of Methane. ACS Catalysis. 2017;7:3548-59.
[38] Froment GF, Bischoff KB, De Wilde J. Chemical reactor analysis and design: Wiley New York; 1990.
[39] Mathias PM. A versatile phase equilibrium equation of state. Industrial & Engineering Chemistry Process Design and Development. 1983;22:385-91.

E047. HEAT SOURCES IN A PEMFC STACK: A NUMERICAL STUDY BASED ON CFD TECHNIQUES.

C. E. Hernández-Herrera[1]; S.J Figueroa-Ramirez[1]; H.J. Mandujano-Ramirez[1]; L. C. Ordóñez[2]; J. M. Sierra[1*]

[1]Facultad de Ingeniería, Universidad Autónoma del Carmen, Mundo Maya, Cd. Del Carmen C.P. 24115, México.

[2]Unidad de Energía Renovable, Centro de Investigación Científica de Yucatán, Ctra. Sierra Papacal-Chuburna, C.P.97302, Mérida Yucatán,

* Corresponding author: Juan Manuel Tadeo Sierra Grajeda, Phone: +52 777 184 35 85 and E-mail: juanmsg@live.com.mx

ABSTRACT

In this paper a Computational Fluid Dynamics (CFD) study in a proton exchange membrane fuel cell (PEMFC) is presented. The purpose of this study is focused on heat transfer produced in a fuel cell aerostack (10 cells) as well as evaluate an active cooling system "Cooling Channels" to decrease the overpotentials and thus increase the efficiency of the PEMFC. The heat generated in a PEM fuel cell may represent 50% of the total energy produced in these devices. The sources of heat generation are produced mainly for three reasons: the entropic heat of reactions, heat from the ohmic resistance (joule effect) and heat from the vapor condensation (latent heat and mass flow rate) in the fuel cell. The understanding of these sources of heat generation provide useful information to solve the problems of hot zones in the PEMFC which results in the degradation of the membrane and the catalyst, the dehydration or overhydration of the membrane, among others. Conventional designs of flow fields for the anode and cathode in an Aero-Stack were considered: flow channels in serpentine form and parallel channels, respectively. The governing equations were solved using a commercial code of Computational Fluid Dynamics (CFD) and normal operating conditions of pressure and temperature were set. Distributions contours of temperature, species, current density and volumetric heat sources were obtained in this study. Numerical results showed that there is a close relationship between the current density and temperature increase in the fuel cell. However, it was observed that at high potentials the gradient of temperature in the aerostack is approximately 5 degrees. The increases in the current density causes a tendency exponential in the temperature that show gradients than higher to 50 degrees. By adding cooling channels in the PEMFC with flow fields in the reverse direction to the cathode, it was

possible to decrease the temperature and heat sources. Thus, the efficiency of the fuel cell was increased up to 20%. The results were validated by polarization curves and experimental data reported in the literature.

Keywords: Heat transfer; PEMFC Fuel Cell; Cooling-Channels; CFD*

1. Introduction

The indiscriminate use of fossil fuels (natural gas, oil, among others) has driven to the search for new ways to process and obtain electricity. To satisfy our energy requirements has caused society to seek the renewable energy sources (solar, wind, geothermal, biomass and hydroelectric) and clean technologies; however, among the different clean technologies that exist we can find the PEM fuel cells (PEM, is the acronym for Proton Exchange Membrane). Fuel cells have attracted the attention of many scientists and engineers due to their low operating temperature, high efficiency, modularity and zero emissions. The PEMFC uses hydrogen as fuel and oxygen as oxidant (some devices use "air"). Their advantages have made them a leading technology that can replace the internal combustion engines in transportation and batteries in portable applications [1]. The operation of a fuel cell is illustrated in Fig. 1. In the anode, the fuel (H_2) is oxidized releasing electrons and producing protons. The free electrons flow to the cathode, through an external circuit, where the protons combine with the dissolved oxidant (O_2), the electrical circuit is complemented by the transfer of protons from the anode to the cathode through a solid electrolyte (membrane). The reaction at the anode and cathode is given by the following equations:

$$2H_2 \rightarrow 4H^+ + 4e^- \quad (1)$$

$$O_2 + 4H^+ + 4e^- \rightarrow 2H_2O(+Heat) \quad (2)$$

In the PEM fuel cells, in addition to electricity, deionized water is obtained as a result of electrode reactions, which is displaced outside of the system along with the rest of the oxidant that failed to react. Thus, the operating of a fuel cell is simple, hydrogen and oxygen are supplied separately to the cell and they react electrochemically to generate electricity, the only products obtained are water and heat.

The heat generated in the fuel cell is one of the main problems in the cell because this affects the membrane and the performance of the fuel cell, which may represent 50% of the total energy produced in these devices [1]. These sources of heat generation are produced mainly for three reasons: the entropic heat of reactions, heat from the ohmic resistance (joule effect) and heat from the condensation

of water vapor (latent heat and rate of mass change) in the fuel cell. Proper management of these mechanisms are a critical problem to solve. To understand these processes different experimental studies and numerical methods have been employed to study the physical phenomenon within a fuel cell such as mass, heat and energy transport, electrode kinetics and potential fields.

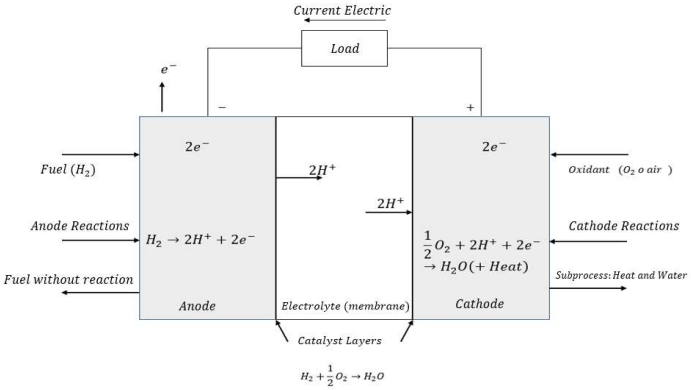

Figure 1: Operating principles of a PEM fuel cell.

Wang and Ouyang [2] developed a 3D model for an air-breathing PEMFC using non-dimensional heat/mass transfer coefficients. The Navier Stokes and energy equations were solved using a commercial CFD tool STAR-CD. The model was built considering assumptions including steady state and non-isothermal conditions. The anode and cathode channels were arranged in intercross flow mode. However, disadvantages of their model were the assumptions of a solid membrane, ohmic resistance in the bipolar plates and the neglect of the ohmic heating. S. Didierjean [3] proposed a 2D numerical study of heat transfer in a PEMFC to understand the main phenomena that govern the performance of a fuel cell. The proposed model takes into account gas dissusion in the porous electrodes, water diffusion and the electro-osmotic transport through the polymeric membrane, and heat transfer in both the membrane/electrode assembly (MEA) as in the bipolar plates. However, the heat generation occurs due to water absorption or desorption, which can be important in the absence of electrical current when there is a big difference between partial pressure of water in hydrogen and air (oxidant). Therefore, the important difference between the temperatures in the MEA and the temperature of the cooling circuit should be emphasized. F.C. Chen in 2003 [4] developed a Computational Fluid Dynamics (CFD) study in 3D model for a PEM fuel cell. This work propose to investigate the cooling process between the solid plate and a refrigerant flow for the optimization of a stack. The mass flow rate of cooling liquid as well as the distribution of the cooling channels were varied. Also, it is proposed to remove the excess of heat

generated in a PEM fuel cell by means of cooling plates as well as demonstrate that serpentine design is a considerably better than the parallel design due to the poor distribution of cooling fluid.

In this regard, a Computational Fluid Dynamics (CFD) study in a proton exchange membrane fuel cell (PEMFC) is presented. The purpose of this study is focused on heat transfer produced in a fuel cell Aero-Stack (10 cells) that use hydrogen and air as fuel/oxidant, respectively. Also, this work is intended to evaluate an active cooling system to decrease the overpotentials and increase the efficiency of the PEMFC. Furthermore, the understanding of these sources of heat generation provide useful information to solve the problems of hot zones in the PEMFC which result in the degradation of the membrane and the catalyst, the dehydration or over hydration of the membrane, among others. Conventional designs of flow fields for the anode and cathode in an Aero-Stack are mainly; flow channels in serpentine form and parallel channels, respectively. This conventional design of Aero-Stack were evaluated to understand these issues: 1) how the temperature is distributed inside the fuel cells, 2) which components showing more heat generation on PEMFC, 3) how much heat remove effectively the cooling channels in the PEM fuel cell, and 4) how much performance can be improved in Aero-Stack. To achieve these goals the first analysis consisted of studying the temperature variation as function of the current density, as well as the temperature distribution through the membrane/electrode assembly (MEA) in the Aero-Stack without cooling channels. The second analysis was to identify the main heat sources affecting the fuel cell efficiency. The third analysis was done to evaluate the cooling channels placed in the cathode and the water as coolant.

2. Description of the computational model.

The computational models evaluated in this work consist of two PEM fuel cell stacks (Fig. 2): (a) a stack without cooling system, (b) a stack with cooling channel´s/cathode. The fuel cell models include gas diffusion layers (GDL), catalyst layers (CL), membrane (MEM) and monopolar and bipolar plates (MP and BP). The flow fields for both the anode and cathode had different design; serpentine form with 3 flow channels and parallel channels, respectively. The area covered by the flow fields in the MEA was 30.78 cm^2. The flow fields were oriented such that the reagents were fed perpendicularly. The dimensions of the components are specified in Table 1.

In the order to establish the accuracy of the results and to ensure that they were independent of the grid, previous simulations were performed. The reference parameter used to do the analysis was the average current density. The final mesh (Fig. 2 and Fig. 3) and dimensions used in the models had the

following intervals as is observed in the table 1. The mesh elements obtained in the models was about 16 million. The computational time calculated per each polarization curve was about 147 hrs., in a workstation; CPU XEON Gold 3.4 Ghz and 64Gb of the RAM memory.

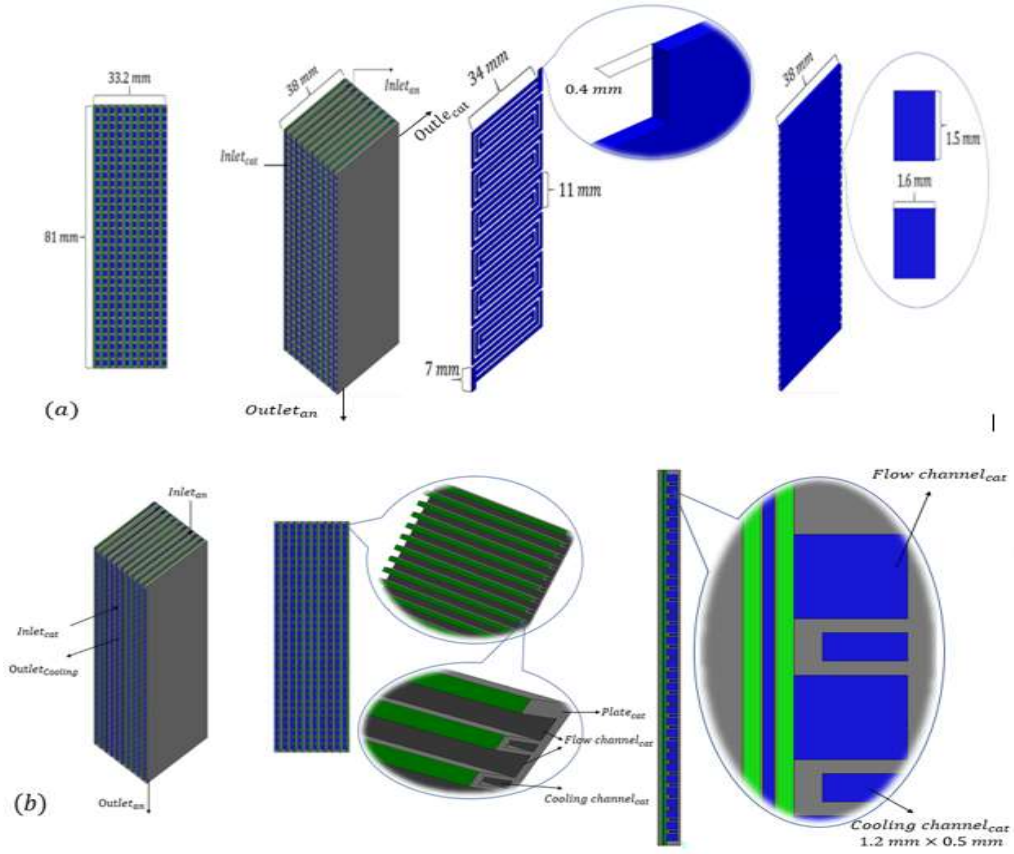

Figure 2: (a) Geometry and dimensions of the Aero-Stacks; (b) Model of the Aero-Stack with cooling channels in the cathode.

For the aero-stack model 10 cells were considered, for each cell a flow field with 32 straight channels in parallel form for the cathode was included. Dimensions of the cooling channels are showed in Figure 1. The grid interval used in the component of a PEMFC Aero-Stack with cooling channels were the same as the previous ones, except the cooling channels has intervals of 0.25 and 0.4 in the transversal section.

Table 7. Mesh dimensions and intervals for the subdomains.

Zone	Dimensions ($Height \times Width \times Thickness$)	Mesh: Body sizing/ edge size.
Gas Diffusion Layer (GDL's)	$38\ mm \times 81\ mm \times 0.25\ mm$	$0.25\ mm \times 0.0625\ mm$
Membrane (MEM)	$38\ mm \times 81\ mm \times 0.18\ mm$	$0.25\ mm \times 0.045\ mm$
Catalyst Layer (CL's)	$38\ mm \times 81\ mm \times 0.02mm$	$0.25\ mm \times 0.005\ mm$
Flow Channel anode	$N/A \times 1\ mm \times 0.4\ mm$	$0.25\ mm \times 0.1\ mm$
Flow channel cathode	$N/A \times 1.5\ mm \times 1.6\ mm$	$0.25\ mm \times 0.4\ mm$
Plate anode	$38\ mm \times 81\ mm \times 0.6\ mm$	$0.25\ mm \times 0.1\ mm$
Plate cathode	$38\ mm \times 81\ mm \times 2\ mm$	$0.25\ mm \times 0.4\ mm$
Cooling Channels	$38\ mm \times 1.2\ mm \times 0.5mm$	$0.25\ mm \times 0.4\ mm$

The assumptions considered to carry out the numerical simulation of the computational models were the following: (a) steady state conditions, (b) laminar flow in the channels, (c) isotropic porous zones, (d) electrochemical reactions take place on the catalyst layer surface, (e) transport of species in the gas phase, (f) transport of liquid water in the membrane is controlled by diffusion mechanisms and electro-osmic drag, and (g) the heating caused by the resistance of materials and the entropic reactions.

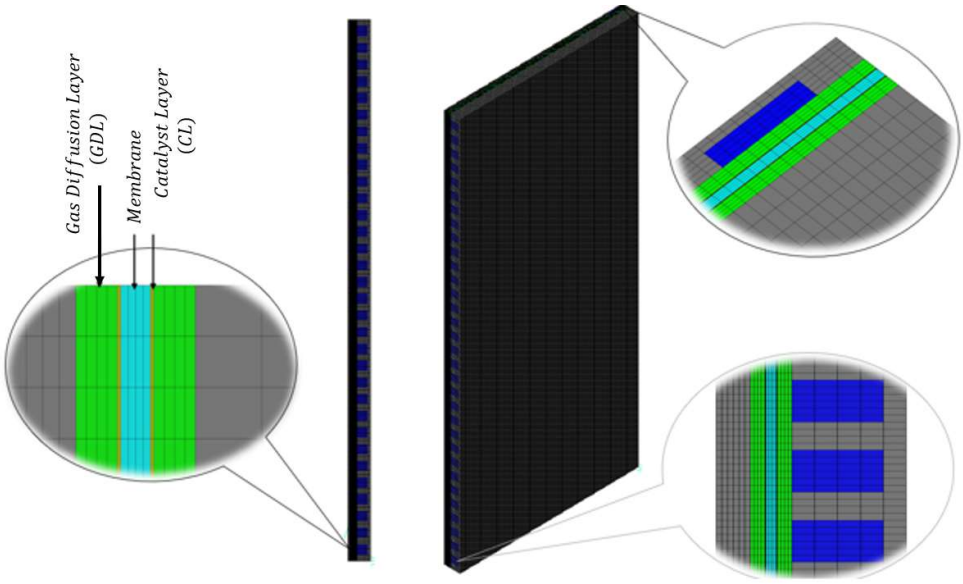

Figure 3: Design of hexaedric mesh for two models of Aero-Stacks.

3. Mathematical Model

Transporting phenomena occurring inside a PEM fuel cell are represented by the governing equations of mass conservation, momentum, energy, species and charge transport. These equations are described below.

3.1.1 Continuity equation

The continuity equation represents the mass conservation for all transport processes that take place in the fuel cell, such as fluid flow, mass diffusion, phase change and electrochemical reactions. This equation is written in a simplified form (steady state) as:

$$\nabla \cdot (\rho \vec{v}) = s_m \tag{3}$$

where $\boldsymbol{\rho}$ is the fluid density, $\vec{\boldsymbol{v}}$ is the vector velocity and $\boldsymbol{S_m}$ is the source term for the species balance.

3.1.2 Species transport

The species transport equation represents the mass conservation for each individual species of a gas. To determine the local mass fraction of each species y_i, the following equation is used:

$$\nabla \cdot (\rho \vec{v} y_i) = -\nabla \cdot \vec{J}_i + S_i \quad (4)$$

where S_i is the source term for each phase, $\vec{J}_i$ is the flux diffusion for the species i, which is calculated for a laminar flow as:

$$\vec{J}_i = -\rho D_i \nabla \cdot y_i \quad (5)$$

where D_i is the diffusion coefficient for the species i.

3.1.2 Momentum transport

The momentum transport equation in a steady state is described by:

$$\nabla \cdot (\rho \vec{v} \vec{v}) = -\nabla p + \nabla \cdot \left(\mu^{eff} \nabla \vec{v}\right) + S_p \quad (6)$$

where p is the static pressure, μ^{eff} is the average viscosity of the mixture and S_p is a source term that contains the physical characteristics of porous media and it is defined as:

$$S_p = -(\mu/k)\vec{v} \quad (7)$$

where μ is the gas viscosity ($kg/m \cdot s$), k is the permeability (gas diffusion layers and catalyst layers), and $\vec{v}$ is the superficial vector velocity at the porous media (m/s) [6].

3.1.4 Energy

The energy equation for steady state is expressed by:

$$\nabla \cdot [\vec{v}(\rho E + p)] = \nabla \cdot \left(k_{eff} \nabla T - \sum_i h_i \vec{J}_i\right) \quad (8)$$

where E is the total energy, k_{eff} is the effective conductivity and $\vec{J}_i$ is the flux diffusion for the species i.

3.1.5 Electrochemical model

The fluid dynamics equations preceding this section are coupled to the electrochemical model implemented in Ansys-Fluent®. This set of equations allows to solve the transport phenomena and electrochemical processes occurring in the PEM fuel cell. The electrochemical model used in this work was reported by J.M. Sierra, et al. [7].

Table 8. Operating conditions used for the 3D simulation.

Parameter	Symbol	Unit	Value
Pressure	P	atm	1
Cell temperature	T_c	K	300
Flow temperature	T_{flow}	K	300
Mass fraction H_2	X_{H_2}	-	0.9
Mass fraction H_2O anode	X_{H_2O}	-	0.1
Mass fraction O_2	X_{O_2}	-	0.21
Mass fraction H_2O cathode	X_{H_2O}	-	0
Mass flow H_2O anode	$\dot{M}_{H_2}$	$kg \cdot s^{-1}$	3.21×10^{-7}
Mass flow O_2 anode	$\dot{M}_{O_2}$	$kg \cdot s^{-1}$	1.05×10^{-7}

The operating conditions and the electrochemical parameters used in the simulation were taken from experimental data and literature data [5, 7]. These values are shown in Table 2 and 3.

Table 9. Electrochemical parameters for a numerical study in CFD.

Parameter	Symbol	Unit	Value
Ref. exchange current density (anode)	$j_{ref,an}$	$A\ cm^{-2}$	7,500
Ref. exchange current density (cathode)	$j_{ref,cat}$	$A\ cm^{-2}$	20
Charge transfer coefficient (anode)	α_{an}	-	2
Charge transfer coefficient (cathode)	$\propto_{cat}$	-	2
Concentration exponent (anode)	γ_{an}	-	0.5
Concentration exponent (cathode)	γ_{cat}	-	1
$CL's$ porosity	ε_{CL}	-	0.12
$CL's$ viscous resistance	VR_{CL}	m^{-2}	1.3×10^{12}
$GDL's$ porosity	ε_{GDL}	-	0.4
$GDL's$ viscous resistance	VR_{GDL}	m^{-2}	1.59×10^{09}

3. Results and Discussion

Distribution contours were obtained at the anode and cathode interfaces of the PEM fuel cell. In addition, it is observed that there is a close relationship between the current density and the temperature increase presented by the PEMFC (Fig. 4; section b). However, the high potentials (0.9 V to 0.75 V) the gradient of temperature in the aero-stack is approximately 6 degrees but as the potential decreases, the current density increases, being able to observe an exponential tendency of the temperature gradients of up to 50 degrees. The polarization curve of the Aero-Stack and the model with cooling channels are shown in Fig. 4.

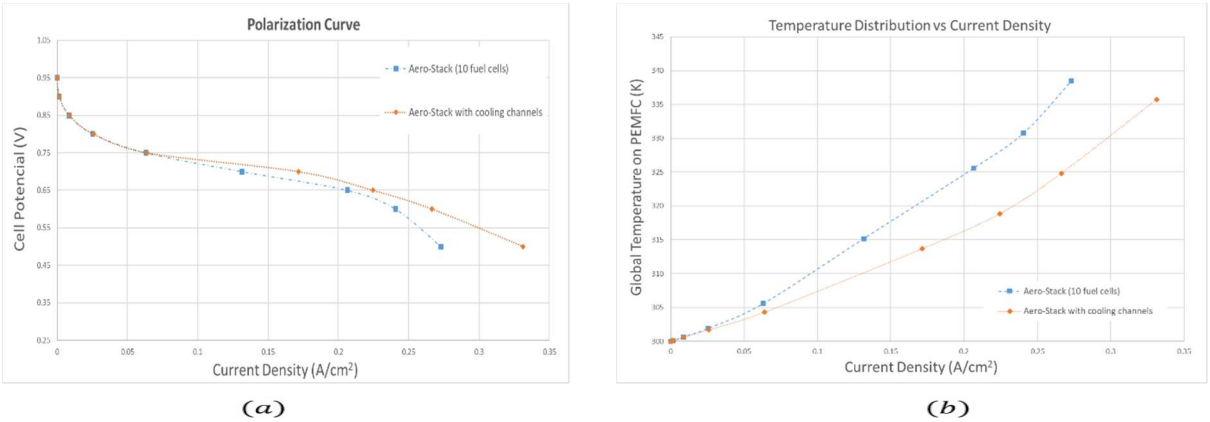

Figure 4: (a) Polarization curve of the Aero-Stack and PEMFC stack with cooling channels; (b) Temperature distribution and current density for a PEMFC with cooling channels.

The temperature distribution is not uniform throughout the fuel cell, higher temperature values are showed in the lower part, top and near to the cathode outlet. However, the temperature distributions and sources heat are presented between fourth and seventh cell of the aero-stack.

The heat generated for the entropic reactions are observed in greater intensity in the cathode catalyst layers and the ionic resistance of the membrane strongly represent the joule heating (heat for the resistance of materials). The joule heating is the predominant form in the temperature distribution (Fig. 5). Moreover, it was observed that in the cathode compartment, the temperature is always higher than anode compartment. In the catalyst layer can be observed the higher temperature due that present the three heat sources. It proposes a cooling system design by parallel channels with reversed flow fields to the cathode (Fig. 2; section b). The temperature distributions in the fuel cell with cooling system show that a decrease exists (10 Celsius degrees) temperature near of the lower part, top, and cathode outlet flow versus the first aero-stack model.

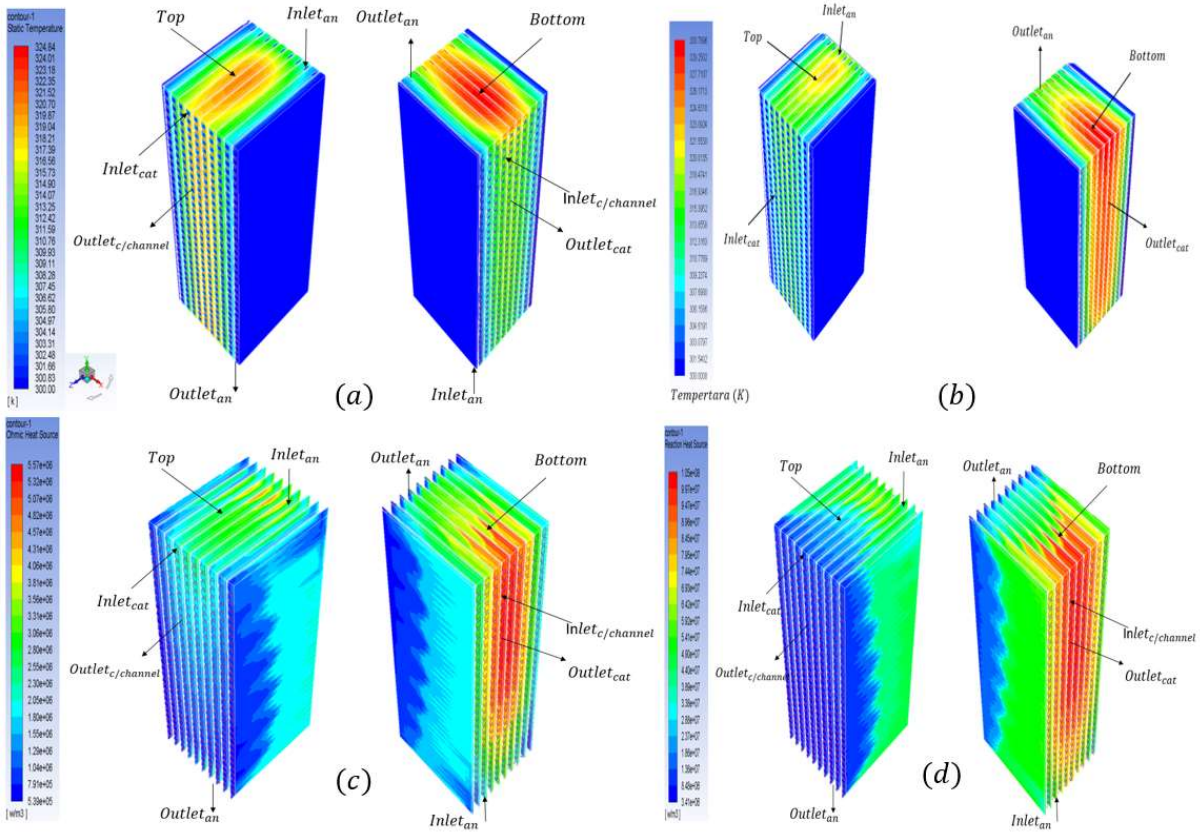

Figure 5: (a) Temperature distributions in isometric view from Aero-stack with cooling channels; (b)Temperature distributions in isometric view from Aero-Stack; (c) Contours of the ohmic heat source on solid electrolyte (membrane); (d) Contours of reaction heat source in the catalyst layers.

4. Conclusion

A 3D numerical study of heat transfer in a PEMFC was presented in this work. From this study was demonstrated that temperature is directly related to the current density of the fuel cell. The higher temperature in the first model from an aero-stack are show to the lower part, at top and near to the cathode outlet flow, this is due to water distribution in the fuel cell. If an active cooling system is implemented to reduce the heat generation on aero-stack it is possible to decrease down to 25% due to remotion of latent heat in the fuel cell. Also from the simulation result was demonstrated that heat generated by the electrochemical reactions and ohmic heating is removed due the convection mechanism through channels.

Acknowledgements

The authors gratefully acknowledge to UNACAR for the granted support to perform the numerical simulations in their computing equipment and the use of Ansys ® software license. In addition, the author gratefully acknowledges CONACyT for the master's scholarship and the financial support from the project 254667 "Consolidación del Laboratorio de Energía Renovable del Sureste (LENERSE)".

References

[1]. F. Barbir, PEM Fuel Cells – Theory and Practice, Academic Press, Elsevier, 2005.

[2]. Ying Wang. Mingao Ouyang. Three-dimensional Heat and Mass Transfer Analysis in an Air-breathing Proton Exchange Membrane Fuel Cell. Journal of Power Sources 2007; Volume: 164: pp. 721-729.

[3]. J. Ramousse, J. Deseure, O. Lottin, S. Didierjean, and D. Maillet, "Modelling of Heat, Mass and Charge Transfer in a PEMFC Single Cell", Elsevier, Journal of Power Sources (2005), Volume: 145; pp. 416-427.

[4]. F.C. Chen, Z. Gao, R. O. Loutfy, and M. Hecht, "Analysis of Optimal Heat transfer in a PEM Fuel Cell Cooling Plate", Fuel Cells, Wiley-VCH Verlag GmbH & Co. KGaA, Weinheim (2003), Volume: 3 No. 4; pp. 181-188.

[5]. J.M. Sierra, J. Moreira, P.J. Sebastian, Numerical analysis of the effect of different gas feeding modes in a proton exchange membrane fuel cell with serpentine flow-field. J. Power Sources 2011; Volume: 196; pp 5070-5076.

[6]. Ansys Manual 15.0. 20013.

[7]. J. M. Sierra, S. J. Figueroa Ramírez, S.E. Díaz, J. Vargas, P. J. Sebastian, Numerical evaluation of a PEM fuel cel with conventional flow fields adapted to tubular plates. Int. Journal of Hydrogen Energy 2015; Volume:39: pp.16694 - 16705.

E054. CATALYTIC ACTIVITY EVALUATION OF $La_{0.5}Sr_{0.5}CoO_3$ PEROVSKITE FOR METHYL ORANGE DYE DEGRADATION UNDER DARK

L.E. Verduzco[1], A.I. Martínez[1], R. Almanza Salgado[2], F. Méndez-Arriaga[2,4] S.A. Lozano-Morales[3], M. Avendaño[4], K.P. Padmasree[1*]

[1]Cinvestav Unidad Saltillo, Parque Industrial Saltillo-Ramos Arizpe, Ramos Arizpe, Coahuila, 25900, México
[2]Instituto de Ingeniería, Universidad Nacional Autónoma de México, Circuito Ext. S/N, Cd. Universitaria, C. P. 04510, CDMX, México
[3]CONACYT-Centro de Investigación en Química Aplicada, Blvd. Enrique Reyna No. 140, Saltillo, 25294, Coahuila, México
[4]Instituto de Ciencias Aplicadas y Tecnología, Universidad Nacional Autónoma de México, Circuito Ext. S/N, Cd. Universitaria, C. P. 04510, CDMX, México
E-mail: padmasree@cinvestav.edu.mx Tel: 844 438 9600(8521)

ABSTRACT

The pollution in water bodies caused by the discharge of organic dyes from textile industries has been a major concern as these organic dyes negatively affect our environment. Metal oxides such as perovskites or perovskite related phases have received attention as catalysts for the degradation of textile dyes. In this study, perovskite oxide $La_{0.5}Sr_{0.5}CoO_3$ was synthesized by the Pechini method and evaluate its catalytic activity for the degradation of methyl orange dye pollutant under dark condition. The prepared sample was characterized by X-ray diffraction, scanning electron microscopy, thermal analysis, specific surface area BET, X-ray photoelectron spectroscopy and UV-vis diffuse reflecance spectroscopy. The $La_{0.5}Sr_{0.5}CoO_3$ sample crystallized in a rhombohedral phase with a $R\bar{3}C$ space group symmetry. The catalytic activity under different catalyst concentration and pH values was evaluated under dark condition. The kinteic study shows the degration rate was 90% in 20 min under dark and reusabilty study shows the sample is reusable for further degradation. Under dark conditions the generation of electrons from the oxidation of Co^{2+} to Co^{3+} and breaking of the azo groups played an important role in the formation of hydroxyl radicals ($OH^{\bullet}$) for the degradation of methyl orange. The result shows the $La_{0.5}Sr_{0.5}CoO_3$ catalyst is an efficient alterative material for the degrdation of pollutant dyes in waste water treatmet plants.

Keywords: catalytic activity; perovskites; dark conditions; dye degradation

1. Introduction

Many industries related to textile, cosmetic, paper, rubber and plastic use dyes in various processes and a high amount of wastes from different dying processes are discharged into the waterbodies everyday [1]. This causes serious environmental problems such as increase of toxicity in the environment, color to the waste water, chemical oxygen demand etc. Dyes usually have poor biodegradability and good resistance to UV or visible light irradiation. Hence, different physical, chemical and biological processes are used to treat dye containing wastewater. These include adsorption, electrochemical oxidation, fenton like reaction, ozonation, microbiological fuel cell, photocatalysis etc. [2]. These technologies basically need some external inputs like light illumination, pH adjustment, chemical additives, electricity etc. However, these processes are economically unachievable or limited in terms of operating conditions. Therefore, the development of simple, effective and fast methods to remove the organic dyes from the dye polluted wastewaters is of vital environmental importance. Recently, another promising method to degrade organic pollutants in the waste water is through catalytic process without the use of external input [2].

Aromatic azo dyes with azo group (–N=N–) constitute about a half of global dye production and about 15% of the azo dyes end up in waste water. These azo dye compounds were recognized as potential carcinogens. Azo dye effluents are highly resistant to microorganisms so that the biological treatments for their degradation is generally ineffective. Methyl orange (MO) is an example of an azo dye which is chemically stable and difficult to degrade and is taken as a representative organic pollutant to evaluate its degradation in this study. The sulfonic group in the methyl orange structure is responsible for the high solubility of this dye in water. Similarly, methyl orange is an anionic dye and its adsorption is favored in acidic conditions [3].

Recently perovskite structured metal oxides have been studied as a heterogeneous catalyst for the degradation of textile dyes under dark and visible light [4]. Perovskites are crystalline ceramics described by the general formula ABO_3 where the partial substitutions with other cations at A and B site are possible, where A site can be rare-earth or alkaline earth elements and B site can be transition metal elements. $LaCoO_3$ perovskite has been studied as a promising catalyst for the degradation of organic pollutants from waste water under dark conditions without the need of external stimulants and energy [5]. Thus, the degradation under dark conditions reduces the operating cost by providing the need of catalytic stimulants such as peroxides in the heterogenous Fenton-like reaction or energy in photocatalysis using UV or visible light irradiation [6-8]. The catalytic property of $LaCoO_3$ can be

increased by doping Ba^{2+} or Sr^{2+} on the La^{3+} site. In this work we investigate the catalytic effect of strontium doped $LaCoO_3$ perovskite oxide, $La_{0.5}Sr_{0.5}CoO_3$ for the degradation of methyl orange dye with different catalyst concentrations and pH values under dark condition.

2. Materials and Methods

The $La_{0.5}Sr_{0.5}CoO_3$ perovskite oxide was prepared via Pechini method.The stoichiometric amounts of the analytical grade lanthanum nitrate hydrate $La(NO_3)_3.6H_2O$, cobalt nitrate hydrate $Co(NO_3)_2.6H_2O$, strontium nitrate $Sr(NO_3)_2$ (Sigma Aldrich) were dissolved in a solution of citric acid and ethylene glycol (Sigma Aldrich). The solution was stirred well using magnetic stirrer and heated to about 80 °C to form a gel. Afterwards, the gel was dried at 120 °C until polymerization has occurred. To remove all the organic composition, the obtained material was then fired at 500 °C for 4 h in air. The solid material was then crushed to fine powder in an agate mortar and heated at 1000 °C for 12 h in air. Methyl Orange (MO) was obtained from Merck and used without further purification.

The crystal structure of the synthesized powder sample was analyzed by X-ray diffraction (XRD) in a Philips X'Pert diffractometer using Ni-filtered CuKα radiation of wavelength, λ=1.5418 Å. The JEOL-JSM-6300 scanning electron microscope was used to characterize the morphology of the synthesized powder. Thermogravimetric analysis (TGA) data were recorded with TA instruments SDT-Q600. Surface area was determined by the multipoint BET method (Quantachrome model AS-1CT-8 apparatus). X-ray photoelectron spectroscopy (XPS) analysis was carried out using a Model K-Alpha, Thermo Scientific instrument with a monochromatized Al Kα radiation (E=1486.68 eV) and the spectra recorded with an overall resolution of 0.1 eV. The absorbance spectrum of the sample was taken with a Perkin-Elmar Lambda 365 spectrophotometer with an integrating sphere of Spectralon in the range 200-1100 nm.

The catalytic activity of the $La_{0.5}Sr_{0.5}CoO_3$ sample under dark condition was analyzed by using methyl orange as a model dye. For this, 100 mL of the methyl orange solution (20 ppm) at several concentrations of $La_{0.5}Sr_{0.5}CoO_3$ and was magnetically stirred in a Pyrex glass vessel and kept under stirring for 5 min to establish the adsorption/desorption equilibrium. After that, 1.5 mL of the samples was withdrawn at several times until the color disappeared and then centrifuged at 15,000 rpm for 20 min to separate the catalyst from solution. The pH value of the solution was adjusted with HCl 1 *M* or NaOH 1 *M* to desired values to evaluate the pH influence on the degradation of methyl orange. The absorbance of each sample was determined with a UV–Vis UNICO SQ-4802 spectrophotometer at the maximum absorption λ_{max} =506 nm and converted to the concentration through the standard curve of methyl orange. The degradation efficiency (DE) of methyl orange was obtained from the following equation as follows:

$$DE\ (\%) = \frac{C_0 - C_t}{C_0} \times 100 \quad (1)$$

where C_0 is the initial concentration of methyl orange and C_t is the concentration at several reaction times (min).

The reusability of the $La_{0.5}Sr_{0.5}CoO_3$ sample was investigated by carrying out five experiments under conditions described as follows. 10 mg of $La_{0.5}Sr_{0.5}CoO_3$ was put in 25 mL of the 20 ppm of methyl orange into the centrifuge tube and kept under stirring under dark conditions. After 1 h of the contact, the final solution was centrifuged to obtain the catalyst. The obtained material was washed several times with ethanol and deionized water carefully and then dried at 100 °C for 24 h. Afterwards, a fresh solution of methyl orange was mixed with the used catalyst to perform the next cycle until to reach 5 cycles. The concentration was obtained in the same manner as described above.

3. Results and Discussion

The X-ray diffraction analysis was performed on the $La_{0.5}Sr_{0.5}CoO_3$ powder and is shown in Fig. 1. The XRD pattern shows sharp peaks indicating good crystallinity. The three prominent crystalline peaks at 33°, 47.5° and 59° (2θ) attributed to the crystal planes of the rhombohedral structure of $La_{0.5}Sr_{0.5}CoO_3$ perovskite with $R\bar{3}C$ space group symmetry. There is no additional peak in the X-ray spectrum indicating the phase purity of the synthesized material.

Fig. 1. X-ray diffraction pattern of the $La_{0.5}Sr_{0.5}CoO_3$ sample

The average values of the surface area, total pore volume and average pore diameter of the catalyst obtained from the BET analysis are 1.357 m^2/g, $4.0x10^{-3}$ cm^3/g and, 11.81 nm, respectively. The BET nitrogen gas absorption-desorption isotherm exhibits a hysteresis loop in the range of 0.71 to 1.0 relative pressure, which is typical for the mesoporous (< 50 nm) structured materials. The

thermogravimetric analysis curve of $La_{0.5}Sr_{0.5}CoO_3$ sample from room temperature to 900 °C are shown in Fig. 2. TGA curve shows three steps of weight loss at different temperatures and an overall weight loss of 4.5%. The weight loss observed in the range 180–286 °C are attributed to the elimination of physisorbed water from the oxide. The temperature region (394–641°C) could be associated with the decarbonization process accompanying with the formation of perovskite structure. The major weight loss observed at 750 °C is attributed to the removal of the lattice oxygen and crystallization of the perovskite phase [5].

Fig. 2. Thermogravimetric analysis plot of the $La_{0.5}Sr_{0.5}CoO_3$ sample.

The morphology of the $La_{0.5}Sr_{0.5}CoO_3$ sample after calcination at 1000 °C is shown in Fig. 3. The SEM image shows agglomerated particles with non-homogeneous shape and sizes. During calcination up to 1000 °C, many smaller particles are interconnected to form large particles. For catalytic applications, large pore dimensions are more suitable for the adsorption process in a liquid phase. The bandgap energy (E_g) of $La_{0.5}Sr_{0.5}CoO_3$ sample was estimated from the Kubelka-Munk function and the obtained value of E_g is 1.6 eV. This value shows a strong photo absorption property in the UV-Vis-NIR region as this sample exhibits potential application also as a photocatalyst for dye degradation under visible and UV irradiation.

The oxidation state of the surface metal species of the $La_{0.5}Sr_{0.5}CoO_3$ catalyst was confirmed by XPS measurements. The XPS spectrum in the range of 820-870 eV present two main peaks identified as 3*d* core-level spectrum. The existence of La^{3+} ions in the $La_{0.5}Sr_{0.5}CoO_3$ sample was confirmed by the peaks $La3d_{5/2}$ (830-839 eV) and $La3d_{3/2}$ (851-858 eV) respectively (Fig. 4a). Similarly, we can

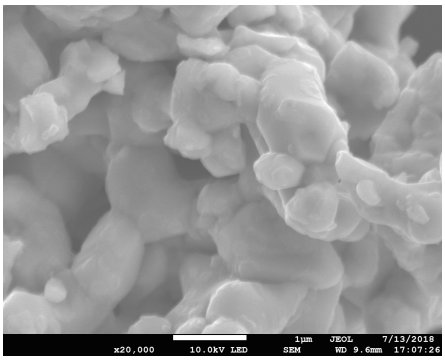

Fig. 3. SEM image of the $La_{0.5}Sr_{0.5}CoO_3$ sample after calcination at 1000 °C.

observe the bulk (lattice) Sr ions are located at lower binding energy around ~131.67 eV and 133.4 eV and the surface Sr ions are found to be at higher binding energy (136.4 eV and 135.46 eV) (Fig. 4b). The Co 2*p* region exhibits two mains peaks centered at 794.71eV (not shown here) and 779.61 which are attributed to the Co $2p_{1/2}$ and Co $2p_{3/2}$ spin-orbit peaks respectively (Fig. 4c). The oxidation state of cobalt may be mainly attributed to Co^{3+} since the spin-orbit splitting between $2p_{1/2}$ and $2p_{3/2}$ peaks in $La_{0.5}Sr_{0.5}CoO_3$ was found to be 15.1 eV. The deconvolution of the Co $2p_{3/2}$ (Fig. 4c) showed the existence of Co^{2+} and Co^{3+} at higher and lower binding energy. The peak observed at 528.24 eV

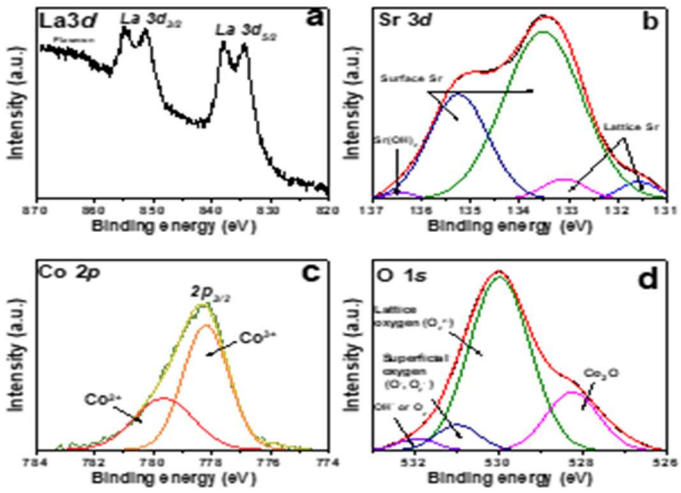

Fig.4. XPS spectra of LSCO sample

is assigned to the lattice (bulk) oxygen ($O_{lattice}$) ions present in the $La_{0.5}Sr_{0.5}CoO_3$ perovskite crystalline structure. Likewise, the peak at 529.98 eV arise from the perovskite lattice termination layer such as O_2^{2-} /O^- . The O_2^{2-} and O^- species are strongly electrophilic reactants, which will be beneficial for attacking organic molecule in the region of its highest electron density in the organic dyes.

The pH of the solution is an principal parameter to control a catalytic reaction. For determining the effect of the pH of an initial solution on the methyl orange dye removal efficiency by $La_{0.5}Sr_{0.5}CoO_3$, different values of pH are changed from 1 to 10 using an initial concentration of 20 mg L^{-1} of methyl orange and 0.02 g of $La_{0.5}Sr_{0.5}CoO_3$ under dark condition. Fig. 5 shows the maximum absorption of methyl orange at acidic pH occurred at 506 nm and the peak decreased quickly with the treatment time due to the decreasing concentration of methyl orange. Similarly, a new absorbance peak formed concomitantly at 248 nm during dye treatment which may be the result of the cleavage of the azo bond (–N=N–) and the formation of new degradation products [8].

Fig. 5. UV-Vis spectra of methyl orange in dark conditions: [MO] = 20 ppm, [LSCO] = 0.2 g L^{-1}, pH = 2.5, room temperature and constant stirring.

The degradation rate with time for different pH values are shown in Fig.6a and the degradation rate at different pH values are shown in Fig. 6b. At basic conditions (pH 6.3 and 10), the degradation percentage was minimal and can be neglected. For pH values 2.5 and 1.8, degradation rate increases significantly (98 and 97%) even at lower reaction times. At acidic conditions, the absorption/ desorption equilibrium was obtained even a contact of only 5 min. Under dark conditions, the methyl orange degradation

decreases with the increase of the initial pH. The highest degradation rate is observed for the lower pH of 2.5. Therefore, $La_{0.5}Sr_{0.5}CoO_3$ catalyst resulted to be an effective material in breaking the conjugation of the methyl orange molecules, particularly the azo bonds. The breakdown of azo bonds generates electrons which has a tendency to form the superoxide anion radical in aqueous solutions with concomitant further reactions involving the generation of hydroxyl radicals ($OH^{\bullet}$) [6].

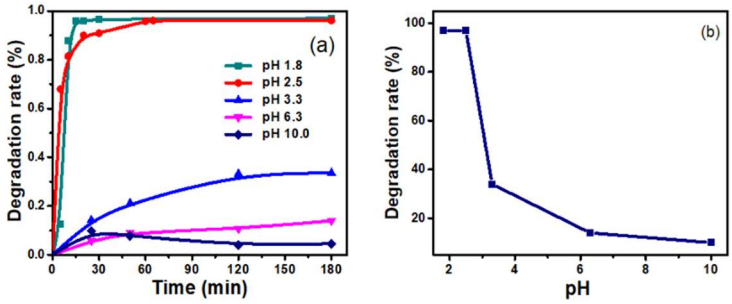

Fig.6. (a) Degradation percentage of methyl orange with time and (b) Degradation rate with different pH varying initial pH from 2 to 10 ([MO] = 20 ppm, [LSCO] = 0.2 g L^{-1}, room temperature and constant stirring).

Fig. 7a shows the methyl orange degradation kinetics with time as a function of catalyst dosage under dark conditions. The effect of catalyst dose on the degradation of methyl orange at pH 2.5 and the behavior obtained shows a pseudo-first-order kinetics as shown in Fig. 9b. The catalytic activity increases with the increase of the catalyst dosage from 10 to 25 mg L^{-1} in steps of 5 mgL^{-1}. This is due to the formation of reactive oxygen species on the catalyst surface. Similarly, the rate constant increases from 0.122, 0.141, 0.161, 0.241 respectively, for the increase in the concentration of catalysts 10 ,15, 20 and 25 mgL^{-1}.

The catalytic surface properties of the $La_{0.5}Sr_{0.5}CoO_3$ was attributed to the methyl orange degradation under dark conditions [5]. It is expected that under dark conditions, methyl orange degradation happens through the two electrons transfer mechanism. In the first case, the generation of electron is due to the contact of methyl orange on the catalyst surface of $La_{0.5}Sr_{0.5}CoO_3$ catalyst which results in the degradation at the azo bonds of methyl orange. Second is due to the oxidation of Co^{2+} and the presence

of Co^{2+} and Co^{3+} can be confirmed from the XPS data. The electrons released through these mechanisms react with the available dispersed O_2 in the methyl orange solution to form superoxide anion radials $O_2^{\bullet-}$ and following reactions results in the formation of hydroxyl radicals ($OH^{\bullet}$). The formation of hydroxyl radicals in metal oxide catalysts is responsible for the degradation of azo dyes under dark conditions has been reported [5,6].

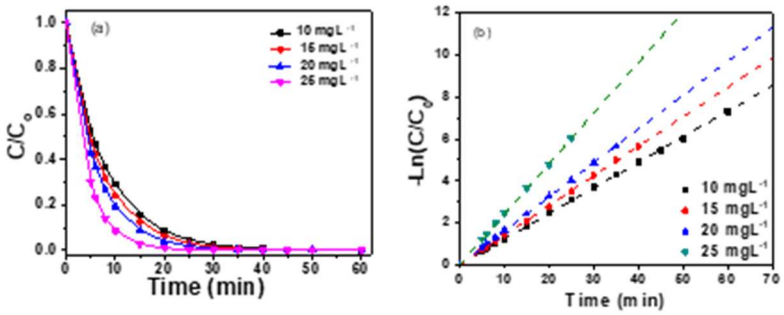

Fig. 7. (a) Methyl orange degradation kinetics as a function of catalyst dosage under dark conditions. (b) the pseudo first order kinetics of methyl orange decolorization.

The reusability of the $La_{0.5}Sr_{0.5}CoO_3$ catalyst was checked for 5 cycles (not shown here). The results show the degradation capacity of $La_{0.5}Sr_{0.5}CoO_3$ catalyst decreases in following cycles. In the fifth cycle degradation capacity decreases by 15%. This is because of the poisoning of the cleaved organic molecule formed on the catalytic surface. The change in degradation rate is very less up to 4 cycles, because the thermal treatment eliminates the possible organic species adsorbed on the $La_{0.5}Sr_{0.5}CoO_3$ catalyst after each cycle. The reusability and catalytic activity shown by the $La_{0.5}Sr_{0.5}CoO_3$ catalyst support its potential for dye degradation applications in wastewater treatment plants.

4. Conclusion

In this work, the perovskite oxide $La_{0.5}Sr_{0.5}CoO_3$ was successfully prepared by Pechni method. The $La_{0.5}Sr_{0.5}CoO_3$ exhibited higher catalytic activity for degradation of methyl orange dye in the acidic conditions and short reaction times at different catalytic dosage. With the increase of catalyst dosage, the degradation percentage increases and follows a pseudo-first order kinetic pathway. The generation of electrons from the breaking of the azo group and oxidation of cobalt ions played a significant role in the generation of hydroxyl radicals ($OH^{\bullet}$) which is responsible for degradation of methyl orange.

Acknowledgements

This research was supported by CONACYT Mexico for the financial support (grant number CB-84267) and Secretaria de Ciencia Tecnología e Innovación CDMX, grant number SECITI-048/2016.

References

[1] Verduzco LE, Garcia-Diaz R, Oliva J, Martinez AI, Gomez-Solis C, García CR, Fuentes AF, Padmasree KP. Enhanced photocatalytic activity of layered perovskite oxides $Sr_{2.7-x}Ca_xLn_{0.3}Fe_2O_{7-\delta}$. Ceram. Int. 2018;44:17079-17086.

[2] Obaidulah Md, Miah MJ, Kayes MdN, Suzuki N, Hossain MdM. Effect of transitional metal ions on photodegradation of remazol black B (RBB) in the aqueous suspension of ZnO under solar light irradiation. J. Adv. Chem. Sci. 2017;3:445-448.

[3] Chen H, Motuzas J, Martens W, Diniz da Costa JC. Surface and catalytic properties of stable Me(Ba, Ca and Mg)SrCoO for the degradation of orange II dye under dark conditions. Appl. Surf. Sci. 2018;450:292-300.

[4] Sun M, Jiang Y, Li F, Xia M, Xue B, Liu D. Dye degradation activity and stability of perovskite type $LaCoO_{3-x}$ (x= 0-0.75). Mater. Trans. 2010;51:2208-2214.

[5] Chen H, Motuzas J, Martens W, Costa JC. Ceramic metal oxides with Ni^{2+} active phase for the fast degradation of Orange II dye under dark ambiance. Ceram. Int. 2018;44:6634–6640

[6] Chen H, Motuzas J, Martens W, Costa JC. Degradation of orange II dye under dark ambient conditions by MeSrCuO (Me=Mg and Ce) metal oxides. Sep. Purif. Tecnol. 2018;205:293–301.

[7] Fu S, Niu H, Tao Z, Song J, Mao C, Zhang S, Chen C, Wang D. Low temperature synthesis and photocatalytic property of perovskite type $LaCoO_3$ hollow spheres. J. Alloy Compd. 2013;576:5-12.

[8] Ghiasi M, Malekzadeh A. Solar photocatalytic degradation of methyl orange over $La_{0.7}Sr_{0.3}MnO_3$ nano-perovskite. Sep. Purif. Technol. 2014;134:12-19.

E058. SYNTHESIS AND CHARACTERIZATION OF $IrRuO_X/TiO_2$ AS ELECTROCATALYST FOR THE OXYGEN EVOLUTION REACTION.

Abissaid Martínez[1,2*], Miguel Ángel Valenzuela[1], Rosa de Guadalupe González[2] and Ricardo Zenteno[2]

1 Lab.Catálisis y Materiales, ESIQIE-Instituto Politècnico Nacional. Zacatenco, 07738, CDMX abissaid@hotmail.com

2 Laboratorio de Electroquímica y Corrosión, ESIQIE-Instituto Politècnico Nacional, Ed. Z-5, 3er piso, UPALM, C.P. 07738, México DF

* Corresponding author: 5546216704, abissaid@hotmail.com

ABSTRACT

Currently, hydrogen has been proposed as a viable energy vector. The most efficient and cleanest method for the production of high purity hydrogen is electrolysis by proton exchange membrane (PEM) electrolysers. However, this production methodology involves high costs due to the use of highly expensive materials such as Ir and Pt for the catalytic layers. In this research work, $IrRuO_x$ supported in TiO_2 was obtained by impregnation. The electrocatalyst obtained contains a total nominal amount of 40 Ru % w and 10 Ir % w. This electrocatalyst was chemically and structurally characterized by X-ray fluorescence (XRF), X-ray diffraction (XRD), electron scanning microscopy (SEM) and energy dispersive spectroscopy (EDS). In order to quantify the activity and electrocatalytic stability, were made cyclic voltammetry from 0 to 1 V vs NHE as well as linear voltammetry from 1 to 1.68 V vs NHE in 0.5 M H_2SO_4. The electrocatalyst had the same electrochemical stability than a 1:3 IrO_2-RuO_2 commercial mechanical mixture (CMM) and showed higher mass activity (89 mA/mg_{metal}) than CMM (60 mA/mg_{metal}). These results are due to a high dispersion of the active phase of Ir-Ru on the support of TiO_2, it was corroborated by the chemical and structural analyses. Membrane-electrodes assembly (MEA) was manufactured. The synthetized electrocatalyst was anodic coating of the test electrolyzer where the oxygen evolution reaction is carried out. Deionized water (≥18 MΩcm) was used. The performance curve was obtained using a controlled current from 0.025 to 0.5 A cm^{-2}. MEA performance whit $IrRuOx/TiO_2$ electrocatalyst anode was lower (5 V @ 0.5 A cm^{-2}) than MEA performance with CMM of IrO_2-RuO_2 (3 V @ 0.5 A cm^{-2}). This lower performance is attributed to the electrical resistance of the material, because of TiO_2 is a semiconductor that generates resistance to the electrons transfer and probably pores of TiO_2 particles do not contain IrO_2-RuO_2.

Keywords: PEM electrolysis; Oxygen Evolution Reaction; Supported Catalyst; Ruthenium Oxide

1. Introduction

Since the industrial revolution, humanity has been using fossil fuels such oil and its derivatives, as well as natural gas and coal. These energy sources produce a high rate of pollution and are not renewable. Therefore, there is an immediate need to develop alternative energy sources renewable and which a minimal pollution. A viable alternative is hydrogen, since it has a great advantage over fossil fuels, due to its greater energy density (33 kWh kg^{-1}) and its combustion process has as chemical by-products water vapor and a small amount of nitrogen oxides which do not significantly impact the environment as a result of their low concentrations. [1] [2] [3]

Electrochemical processes for the generation of hydrogen are viable for industrial and domestic applications using renewable energy sources. Currently, there are three types of electrolysers: alkaline, proton exchange membrane (PEM) and solid oxide. The PEM electrolysers (PEME) are more compact than alkaline and solid oxide electrolysers since these can work with a current density five times higher (~2A cm^{-2}), its solid electrolyte (polymeric membrane) gives a response time of less than one second and it can produces high purity hydrogen (~99.99% w) [4] [5] [6]. The commercial catalysts for this type of electrolyzer is made of compounds based on noble metals such as IrO_2-RuO_2 for the oxygen evolution reaction (OER) for the anode and Pt/C for the hydrogen evolution reaction (REH) for the cathode side since these noble metals have the best catalytic activity and electrochemical stability in the acidic medium in which the reaction occurs as a consequence of the proton exchange membrane is generally composed of sulphonated polymers, which gives it an acid character. [7] [8] [9] [10]

Consequently of the noble metals used in PEME, the economic price of PEME is higher than alkaline electrolysers therefore, the need arises to develop new electrocatalytic materials not based on noble metals or, failing that, considerably reduce the amount of them. For OER, several alternative catalytic materials have been synthesized, for example: $IrRuCoO_x$ [11] and $IrSnO_2$ [12] to reduce the amount of noble metals by adding a transition metal or, on the other hand, IrO_2/ATO [13] and IrO_2/SnO_2 [14] catalysts have also been developed, in which the metallic phase was dispersed on a support with a specific high area to increase the active area with respect to the metallic load. The catalyst exposed in this work belongs to the second type. The performance of $IrRuO_x/TiO_2$ obtained by impregnation is presented in this work. [15]

2. Materials and Methods

2.1 Synthesis of $(IrRuO)_x/TiO_2$ electrocatalysts

A range of catalysts (Table 1) were synthesized with the percentage in weight of Ru and Ir in relation to TiO_2 a mechanical mixture of commercial catalysts was evaluated for comparative purposes. The precursors $IrCl_3$, $RuCl_3$ were dispersed by ultrasound during 5 minutes in 200 ml of deionized water; this solution was transferred to a rotavapor flask where vacuum impregnation took place, the temperature was controlled at 70 ° C for 3 hours. After impregnation, the resulting material was subjected to an oxidative heat treatment in an air atmosphere at 450°C for 4 hours in order to obtain the $IrRuO_x$ spices. Then, 5 washes were made using deionized water with the purpose of separate the remains of $RuCl_3$ and $IrCl_3$.

Table 1. Composition and key to the range of synthesised catalysts

Key	%wRu	%wIr
I25	25	0
I50	50	0
I4010	40	10
Comercial Electrocatalyst Sigma-Aldrich®		
C7525	75	25

2.2 Physico-chemical characterization.

Elemental analysis of the electrocatalysts with the best electrocatalytic performance was performed by X-ray fluorescence using a Rigaku device model Supermini 200 equipped with a 200 W Pd anode coupled to RX25 and LiF crystals with a Zr filter and a proportional P-10 gas flow meter to know the elemental species present on the surface of the material.

The morphology of this electrocatalyst, was obtained using a Hitach SU3500 scanning electron microscope (SEM), in addition, with the same equipment a compositional quantitative mapping of the present elements was carried out by X-ray energy dispersive spectroscopy (EDS) and this results were compared with the results obtained by X-ray fluorescence (XRF).

2.3 Electrochemical Characterization

The electrochemical tests were performed on a potentiostat/galvanostat Autolab Differentia Electrometer Amplifier PGSTAT12/30/302, the software used was the Nova version 1.11. The linear scanning voltammetry were performed in a double-walled glass cell using a three-electrode arrangement. 10 µL of a dispersion composed of 5 mg catalyst, 400 µL of ethyl alcohol, 100µL of

deionized water and 30 µL of Nafion® was deposited on a glassy carbon electrode with the purpose of generate an ultra-thin layer, a sulphates electrode was used like reference electrode (Hg/Hg_2SO_4, E= +0.68 V/NHE) and as counter electrode, a Pt mesh was used. The electrolyte was a 0.5M H_2SO_4 solution previously saturated with Ar. Linear scanning voltammetry was performed in a potential range of 1.0 to 1.68 V/NHE.

2.4 Test Electrolyzer

Once the electrocatalyst with the best performance and experimental stability was found, a membrane-electrode assembly (MEA) with an active area of 4 cm^2 was manufactured. This electrocatalyst was the anodic coating of the assembly where the REO is carried out, the proton exchange membrane used as a solid electrolyte made of Nafion® 115 having a thickness of 127 µm, for the cathodic part a commercial carbon cloth electrode was used containing a Pt coating supported on Vulcan Carbon at 40% w in order to catalyze the HER, the mechanical mixture of commercial catalysts was used as well as anodic coating in another MEA for comparison proposes. The MEA's were tested using a power source Matrix® model MPS-3003LK-3 a current density sweep from 0 to 0.5 $A*cm^{-2}$ in step increments of 0.0025 $A*cm^{-2}$ was made recording the potential response.

3. Results and Discussion

3.1 Physico-chemical characterization

Figure 1 shows the elemental X-ray fluorescence analysis for the I4010 electrocatalyst, which has the characteristic Ir signals underlined in green and Ru in red. The Table 2 shows the mass concentration. There is a slight deviation between the nominal quantity of Ti and Ru, however for the Ir, this difference is significant, the analysis shows a lower concentration (2.5% w) than the nominal concentration (10% w), this loss is attributed to the synthesis process, the fraction of Ir could remains on the surface of the rotavapor flask since it is not completely chemically reduced due to temperature, rotation speed and impregnation time. In future works, these variables will be optimized to avoid high Ir loss.

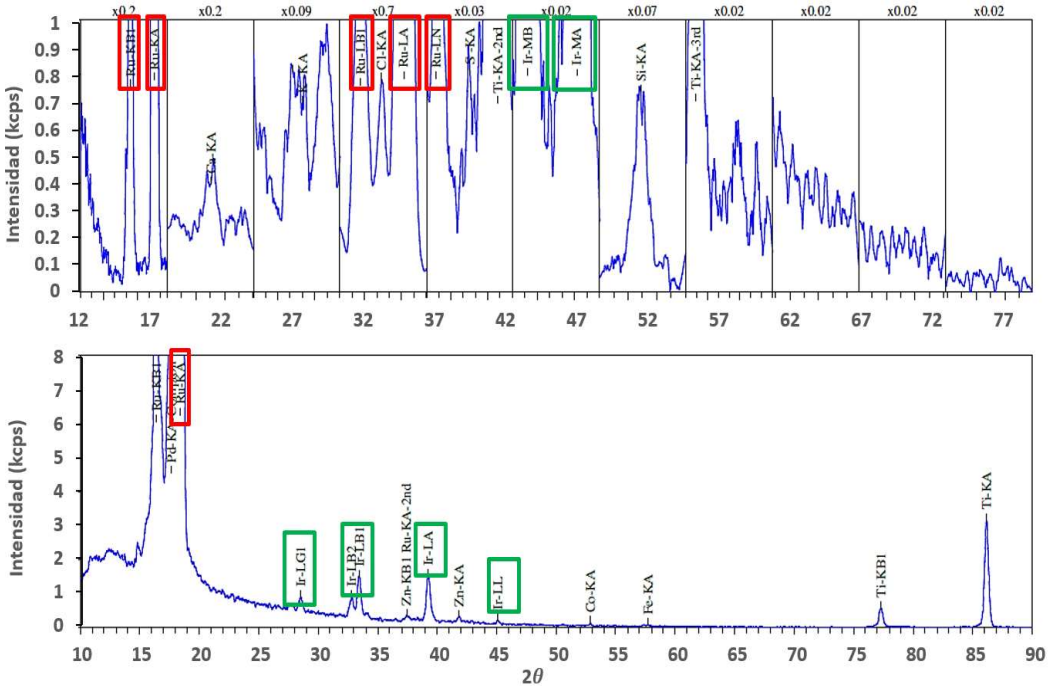

Figure 1. XRF patterns of I4010

Table 2. Elemental composition of I4010 (without O) determined by XRF

Element	Intensity	%Weight
Ti	9.132	46.416
Ru	0.382	50.511
Ir	0.062	2.574
K	0.108	0.123
Co	0.026	0.1719
Si	0.087	0.1994
Total		99.996

Figure 2 corresponds to the SEM micrography of the I4010 electrocatalyst, is observable a little porous with some agglomerations of material that form macroparticles and microparticles, attributable to the equipment resolution (~ 125 nm per pixel) These agglomerations should not affect the electrochemical performance of it since in the preparation of the catalytic ink used for electrochemical tests, the material

is dispersed by ultrasound which destroys these algomerations and homogenizes the particle size. From dispersive energy spectroscopy of secondary electrons (EDS) was obtained a mapping of the elemental composition of the I4010 electrocatalyst, the composition is homogeneous, this is not accordance with the nominal and from XRF, composition as is shown in Table 3 owing to EDS is punctual qualitative technique while XRF is a bulk compositional analysis, so we used composition from XRF technique.

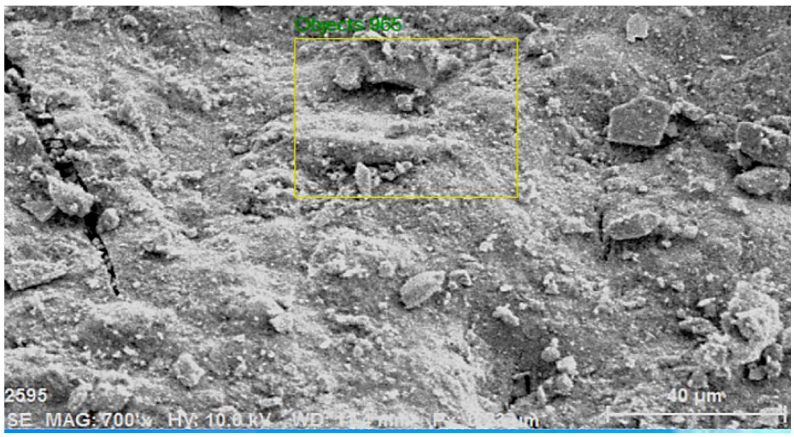

Figure 2. SEM micrography of I4010

Table 3. Elemental composition of I4010 (without O) determined by EDS

Element	AN	Series	%Weight
Ti	22	K-series	70.76
Ru	44	L-series	25.17
Ir	77	M-series	4.07
Total			100.00

3.2 Electrochemical characterization

Figure 3 belongs to the linear voltammetry of I4010, which obtained the best performance towards the REO in the potential interval from 1 V to 1.68 V/ENH, the potential at which the generation of oxygen starts is at 1.48 V/ENH, coinciding with the potential of the commercial electrode, at 1.6 V/ENH reaches a current density of 20 mA cm^{-2} being 20% lower than that of the commercial electrocatalyst obtained by mechanical mixing, the electrode with the synthesized catalyst I4010, presented a better stability since it does not show a significant reduction of its catalytic activity after 5 cycles.

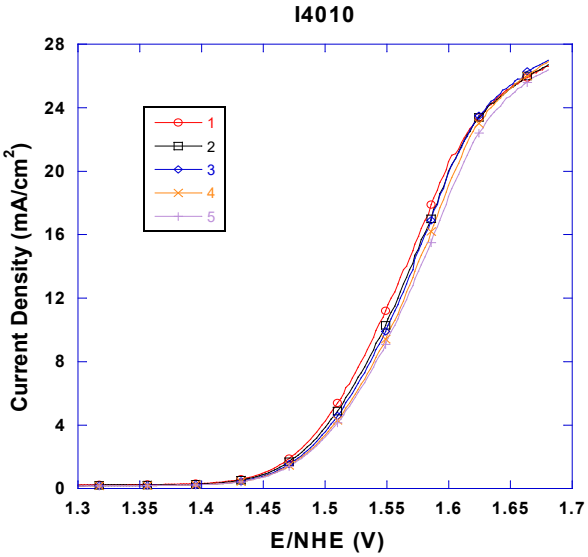

Figure 3.Linnear sweep voltammetry of I4010

Figure 4 shows the catalytic activity normalized like electrode mass activity (mA/$mg_{Ru,Ir}$).The I4010 has a current mass density superior than the mechanical mixture C75Ir25 of commercial catalysts, which is an indication that the I4010 has an active area comparable to that of the C75Ir25 with a lower metallic load (50%) due to the dispersion of the active phases of RuO_2 and IrO_2 on the catalytic support (TiO_2). The I4010 shows high electrocatalytic activity (89 mA/$mg_{Ru,Ir}$ @ 1.6V/NHE) compared to commercial reference electrocatalysts (65 mA/$mg_{Ru,Ir}$ @ 1.6V/NHE).

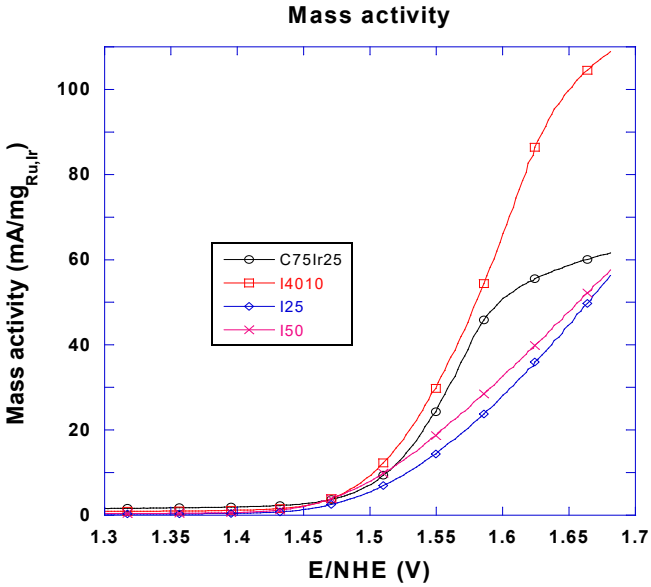

Figure 4. Mass electrochemical activity

3.3 Test electrolyzer

Once the membrane was properly impregnated, the test electrolyzer was assembled and the current sweep was performed as described in section 2.1 obtaining the applied current density vs. voltage curve, the results are shown in Figure 5 which also shows the performance obtained by a previous design of the test electrolyzer using a membrane with catalytic layers of commercial catalysts.

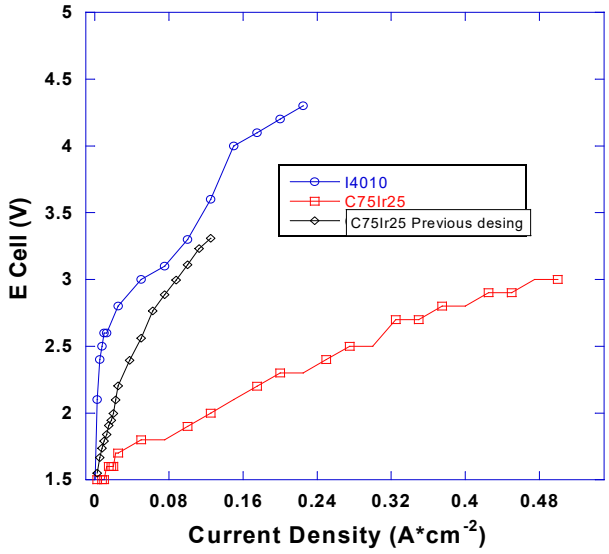

Figure 5 . MEA aTest electrolyzer performance.

The I4010 catalyst had a lower performance, namely 66% compared to the commercial C75Ir25 when used as an anodic electrocatalyst for the REO in the test electrolyzer, since at a current density of 0.25 A cm-2 there is a cell potential of 5V for the membrane with the I4010 coating, while for the membrane with the C75Ir25 coating the cell potential is 3 V. The lower performance is attributed to the generation of considerable resistance due to the fact that the pores of TiO_2 particles which do not contain IrO_2 or RuO_2 species are in contact with other empty TiO_2 pores increase the transfer of electrons resistance since TiO_2 is a semiconductor with high electronic resistance which affects the performance of the electrolyzer since several layers of catalyst are deposited on the surface of the membrane of the anodic side.

4. Conclusion

The (10%Ir40%Ru)O_x/TiO_2 catalysts called I4010, obtained by impregnation, showed the highest electrocatalytic activity in mass and stability compared to the average 1:3 mechanical mixture of commercial IrO_2-RuO_2 electrocatalysts. Instead, the catalysts prepared by photodeposit showed a lower electrocatalytic activity than the mechanical mixture of commercial electrocatalysts.

The performance of the test electrolyzer when using a MEA with an anodic catalyst catalyst layer (10%Ir40%Ru)O_x/TiO_2 was 66% lower than when using the same test electrolyzer with a MEA with an anodic catalytic layer with a commercial mixture of 25%IrO_2-75%RuO_2 (C75Ir25) electrocatalysts due to the generation of considerable resistance on the membrane's surface.

Acknowledgements

The authors would like to thank IPN multidisciplinary project 2014 and CONACYT CEMIE Oceano-249795, transversal line I-LT1.

References

[1] W. Vielstich, Handbook of fuel cells: Fundameltals, technology and applications, Chichester, England; New York: Wiley, 2003.

[2] T. Reier, „Electrocatalytic Oxygen Evolution Reaction in Acidic Environments-Reaction Mechanisms and Catalysts," *Advance Energy Materials*, pp. 1601275-, 2017.

[3] M. Carmo, „A comprehensive rewiew on PEM water electrolysis," *International Journal of Hydrogen Energy*, Bd. 38, p. 4901, 2013.

[4] S. Siracusano, „Electrochemical characterization of single cell and shrot stack PEM electrolyzers based on a naonsized IrO2 anode electrocatalyst," *International Journal of Hydrogen Energy*, Bd. 35, p. 5558, 2010.

[5] P. Strasser, „Lattice strain control of the activity in dealloyed core shell fuel cell catalysts," *Nature Chemistry*, Bd. 6, p. 454, 2010.

[6] J. Russell, „Hydrogen generation by solid plymer electrolyte water electrolysis," *American Chemical Society Division of Fuel Chemistry*, Bd. 18, pp. 24-40, 1973.

[7] J. Polonsky, „Tantalum carbide as a novel support material for anode electrocatalysts in ploymer electrolyte membrane water electrolysers," *International Journal of Hydrogen Energy*, Bd. 37, p. 2173, 2012.

[8] R. Kotz, „XPS studies of oxygen evolution on Ru and RuO2 anodes," *Journal of the Electrochemical Society*, Bd. 130, p. 825, 1983.

[9] M. Miles, „Periodic variations of overvoltages for water electrolysis in acid solutions from cyclic voltametric studies.," *Journal of the Electrochemical Society*, Bd. 123, p. 1459, 1976.

[10] D. R. Lide, Handbook of Chemistry and Physics, 87 Hrsg., Florida: CRC Press, 2006.

[11] J. L. Corona-Guinto, „Performance of a PEM electrolyzer using RuIrCoOx electrocatalysts for the oxygen evolution electrode," *International Journal of Hydrogen Energy*, Bd. 38, pp. 12667-12673, 2013.

[12] E. Mayousse, „Synthesis and characterization of electrocatalysts for the oxygen evolution in PEM water electrolysis.," *International Journal of Hydrogen Energy*, Bd. 36, pp. 10474-10481, 2011.

[13] K. Puthiyapuram-Vinod, „Physical and electrochemical evaluation of ATO supported IrO2," *Journal of Power Sources*, Bd. 269, pp. 451-460, 2014.

[14] J. Xu, „The electrocatalytic properties of an IrO2/SnO2 catalyst using SnO2 as a support and assisting reagent for the oxygen evolution reaction," *Electrochemical Acta*, Bd. 59, pp. 105-112, 2012.

[15] A. Mills, „A simple, novel method for preparing an effective water oxidation catalyst," *Chemical Communication*, Bd. 46, p. 2397–2398, 2010.

E060. STUDY OF A CATALYTIC BED REACTOR FOR THE PRODUCTION OF HYDROGEN FROM BIOETHANOL

I. R. Martínez[a], J.L.Contreras*[a], J. Salmones[b], B. Zeifert[b], T. Vázquez[b]

1 Departamento de Energía, Universidad Autónoma Metropolitana Azcapotzalco, A. Sn. Pablo 180, Col. Reynosa, Ciudad de México, Código Postal 02200, México

2ESIQIE, Instituto Politécnico Nacional. UPALM. Zacatenco, Ciudad de México, México.

* Corresponding author: 5591911047 and jlcl@correo.azc.uam.mx

ABSTRACT

In this work, a catalyst has been developed for the ethanol steam reforming reaction (ESR) based on a bimetallic Ni-Co-Hydrotalcite-WOx catalyst that has shown high selectivity to H2. As a tool for the design of the reactor a two-dimensional mathematical model has been proposed, based on the conservation equations of matter and energy, with the objective of obtaining the conversion and temperature profiles in an integral reactor delimiting the problem by initial and contour conditions. The resolution of the system of parabolic partial differential equations was discretized by a variant of the implicit methodology, called the Crank-Nicholson method. Subsequently, an encoding was implemented in the Wolfram Mathematica® software for mathematical resolution. A series of models have been obtained from the literature that allows obtaining the numerical values of the transport properties required in the simulation. To validate the proposed model, the experiment was carried out in a tubular reactor, packed with catalytic material (PBTR). Composition analyzes were performed through the length of the reactor. The reaction of ESR is endothermic, presenting high energy demand. Therefore the heating was carried out externally using an electric furnace, isolated to eliminate the loss of heat with the outside.

Keywords: Hydrogen, Ni-Co-Hydrotalcite-WOx, mathematical, model

1. Introduction

Hydrogen is an ideal energy vector, since it can be transformed into heat, mechanical energy, or electrical energy [1]. The clean and innovative technology of hydrogen is obtained from renewable sources such as bioethanol in the presence of metal catalysts [2]. Currently we have developed a catalyst

for the process of ethanol steam reforming with water vapor (ESR) based on Ni-Co-Ex Hidrotalcita-WOx catalyst that has shown high selectivity to H_2 using a ratio H_2O / ethanol = 4, with low selectivity to CO and that it has been shown to be stable for times of more than 3 h at high temperature of 550 °C [3]. This contribution help to solve the conversion of ethanol and temperature along the axial and radial axis of the fixed bed reactor.

2. Materials and Methods

This catalyst was prepared and acquired a cylindrical shape by compaction at 205 kg/cm^2 giving dimensions of 1/8x1/8 in, in diameter and length respectively, to be evaluated later in a reactor with 13 cm (5.11 in) length of packed bed with 3/4 in diameter in 316 stainless steel.

The reaction of ethanol steam reforming is endothermic which makes it extremely demanding of energy [4], the heating was carried out externally by means of an electric furnace so that the reaction is carried out in a fixed bed. In order to determine the mathematical model of the conversion profile (mass balance) and temperature (energy balance) along the packed reactor, we start from the conservation equations applied to a control volume as shown in the Figure 1.

By realizing the material balance with respect to the limiting reagent through the control element, and according to the flux in the axial direction z, diffusion in the radial direction and losses by reaction, the two-dimensional model of mass balance [5] is obtained by the Equation 1.

$$\partial x/\partial z - De/u\ ((\partial^2 x)/\partial r^2 + 1/r\ \partial x/\partial r) - (\rho_B\ rP)/(G/PM\ y_{A0}) = 0 \qquad (1)$$

The equation of energy is obtained analogously. (Equation 2)

$$\partial T/\partial z - Ke/(G\ Cp)\ ((\partial^2 T)/\partial r^2 + 1/r\ \partial T/\partial r) + (\rho B)\ \Delta HrP)/(G\ Cp\ ) = 0 \qquad (2)$$

Where the transport properties such as, the effective diffusivity was calculated according to the model proposed by Brokaw [6] for binary mixtures with participation of polar components. In the case of effective thermal conductivity, the two phases involved in the reactor were used. The first belongs to the gaseous phase fed and the second one based on the catalytic bed belonging to the solid phase [5,6].

For the resolution of partial differential equations the finite difference method was used. Within the latter are both explicit and implicit methods, where the problem was addressed by the Crank-Nicholson method as a variant of the implicit methodology [7]. The above increase accuracy and precision in the calculations, since it requires a higher number of nodes with respect to the explicit for example, a more complex meshing. Finally, the series of equations that are generated must be solved simultaneously for each node [8]. The physical interpretation of the reactor provided the boundary conditions and initial values. The Wolfram Mathematica® software has been applied to calculate the phenomena present in the reactor of ethanol steam reforming towards the production of hydrogen.

Among the considerations made was to simulate the reactor symmetrically giving way to a short list of boundary conditions, or three geographical zones in the reactor: reactor center or the middle, reactor wall and intermediate points between these two borders [9].

Fig. 1(a). Fixed bed reactor and Fig. 1(b) Border conditions, to solve the equation (1)

Several parts of the fundamental section and in the simulation are: the operating conditions, the thermodynamic values of the reaction, the kinetic expression [10], effective dimensions of the reactor

(internal diameter), physical properties of the catalyst, as well as the distribution and number of increases of the radial and axial axis. Table 1 show the operating conditions used in the simulation.

Table 1. Operating conditions used in the reactor for reforming Ethanol under pressure of 1 atm and temperature of 500 ° C in the feed. (See the units at the end of the manuscript)

Operating condition Values	Value
Surface speed (G)	100
Volumetric flow (V_o)	1
Feed Temperature (°C)	500
Wall Temperture (°C)	510
Effective Diffusivity (D_E)	$5.08x10^{-7}$
Effective Thermal Conductivity (K_E)	0.955765
Density of the catalytic bed (ρ_B)	580
Linear feed speed (u)	0.1
Number of points on the radial axis	18
Number of points on the axial axis	100
Initial composition of the limiting reagent	0.2

The method of preparation of the catalysts was by coprecipitation of the precursors $Ni(NO_3)_2$, $Co(NO_3)_2$, Ammonium tungstate, for the hydrotalcite (HT) was precipitated from $Mg(NO_3)_2$ and Al $(NO_3)_3$ in aqueous solution. The precipitate was left at rest to crystallize. The suspension was left at 70°C at a

pH of 11 with stirring for 18 h, and the solid was washed several times with demineralized water and then dried at 110°C for 18 h, finally calcined at 450°C for 5 h . The catalyst was mixed with 10% boehmite as a binder and again dried at 110 ° C for 12 h to form 1/8 x 1/8 in cylinders using a stainless steel mold and pressing the compactor material up to 250 lb/in^2.

The evaluation of the bimetallic catalyst was carried out under a flow of 1 ml/s in a micro-reaction installation with two water and ethanol saturators driving the molar ratio of 4 moles of water to one of ethanol. The temperatures that were handled during the reaction were: 450, 480, 510 and 540 ° C.

3. Results and Discussion

It was observed in Figure 2, that the conversion in the reactor increases by 91% during the first 6 cm of the catalytic bed, and only by 8% in the next second half section of the reactor. It is probable that in the first section of the reactor the greater amount of H_2 is generated because in the feed of the reactor the highest molar ratio of water vapor / ethanol is due to the reaction.

$$CH_3CH_2OH + 3H_2O \rightarrow 6\ H_2 + 2\ CO_2 \qquad (3)$$

A decrease in temperature was observed in the center of the reactor using the Eley Rideal kinetic equation (Fig. 3) and a minimum temperature value of 468°C was calculated. In the case of using a kinetic equation of power law, the minimum value calculated was 523° C.

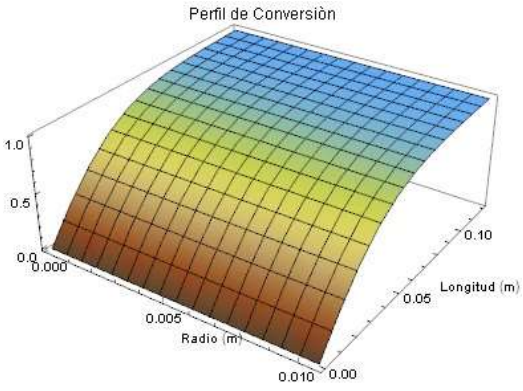

Fig. 2. Two-dimensional conversion profile using Eley Rideal reaction rate [10] at 550 ° C.

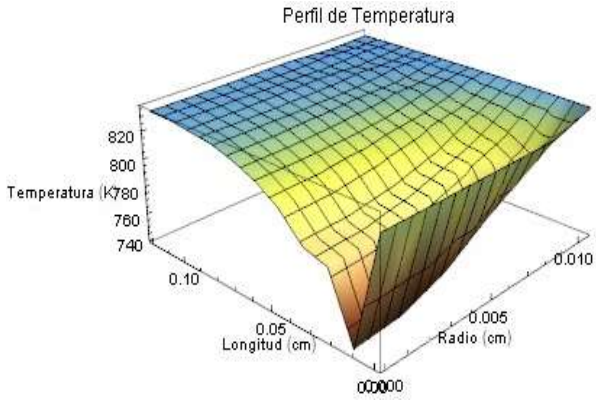

Fig. 3. Two-dimensional temperature profile using Eley Rideal reaction rate [10] at 550 ° C.

The calculation of the average conversion (Figure 4) was observed as the catalytic reaction temperature increases to 550°C and the difference in conversion of the calculated and experimental results decreases compared to the conversions calculated at a lower temperature (450°C) using the same kinetic equation.

The average temperature calculated of the catalytic bed, in the center (Figure 5) was observed from 2 cm a percentage of error very small in comparison to the experimental temperature, having its better coincidence to 9.5 cm of catalytic bed which was very similar to the values analyzed at 500 ° C.

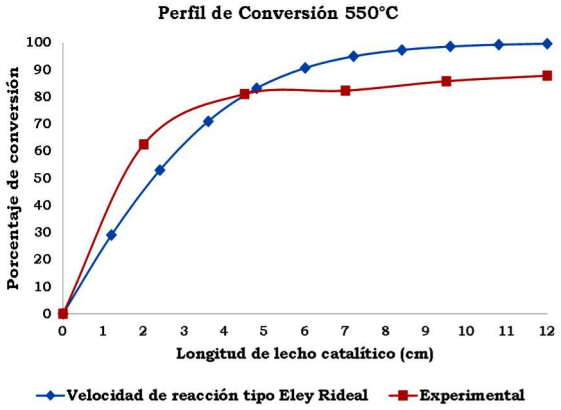

Fig. 4 Average conversion profile using reaction rate of the Eley Rideal type [10] at 550 ° C.

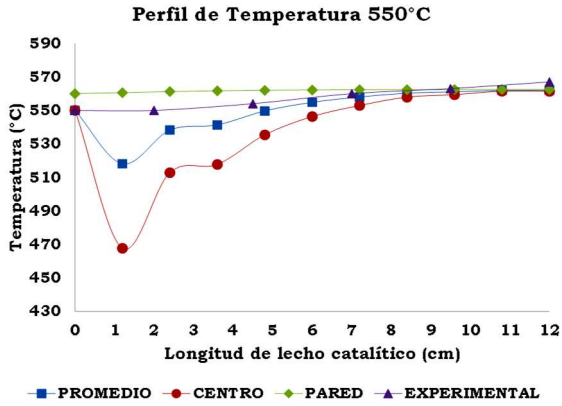

Fig. 5 One-dimensional temperature profile using Eley Rideal reaction rate [10] at 550 ° C.

The analysis on the conversion profiles and temperature according to the reaction rate equation was carried out with constant operating values, such as: density of the catalytic bed, flow and surface feed and initial composition, as well as the respective temperature-dependent transport properties, using the finite difference method to solve the pair of partial differential equations generated from the mass and energy balance.

The methodology implemented in our case study and developed by Crank-Nicolson (CN), defines that the stability is not altered by the existing relationship by the radial and axial step size, that is to say when performing the iterations of the equations algebraic it is possible to find simultaneous solution of each internal node.

In order to obtain percentages of average absolute error less than 15% for the conversion profile and temperature respectively, the step size in the radial and axial axis was reduced. It was observed that the conversion and temperature profiles exhibited similar behaviors as the temperature and mathematical simulation were increased to 450, 500 and 550 °C, showing better coincidence of the numerical and experimental results with an reaction equation of the type Eley Rideal, so it was selected to make changes in radial and axial pitch size.

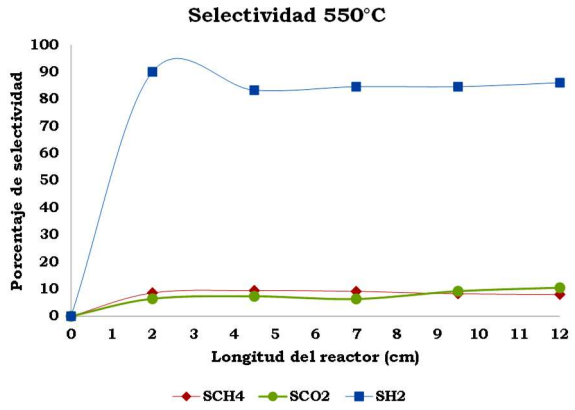

Fig. 6 Hydrogen selectivdy along its reactor length.

Table 2. Average error between experimental and calculated Temperatures.

		Absolute error %		
Port	*L (cm)*	*Conversion*	*Temperature*	
			Average	*Middle*
-	0.0	0	0	0
1	2.0	31.02	3.09	9.01
2	4.5	6.73	1.30	4.55
3	7.0	11.91	0.64	1.73
4	9.5	13.23	0.51	0.89
5	12.0	12.72	0.96	1.08
% average error		12.60	1.08	2.88

4. Conclusion

A mathematical model of a fixed-bed catalytic reactor for the ethanol steam reforming reaction to H_2 was developed describing the conversion and temperature profiles along the fixed-bed reactor of ¾ in internal diameter by 5.11 in of length using a Ni-Co-Hydrotalcite-WOx catalyst in the form of tablets of 1/8 x 1/8 in. The transport properties such as diffusivity and effective conductivity were calculated while the reaction rate equations were taken from the literature.

It was observed, that the conversion in the reactor, increases by 91% during the first 6 cm of the catalytic bed, and only increases again in the 8% of the next second half section of the reactor. The radial difference of the conversion in three axial sections of the reactor (1.2, 6 and 12 cm) was relatively

small since it was not greater than 0.56% of the conversion, when 1080 algebraic equations were solved. The Eley Rideal rate equation is best adjusted, after analyzing the numerical and experimental results at 450, 500 and 550°C. The highest percentage of error was observed in the conversion results and the lowest error value in conversion (11.35%) was determined at a reaction temperature of 500°C. The greatest radial difference in temperature was located 1.2 cm from the length of the catalytic bed and decreases as a smaller step size is used. The presence of CO, CH_3CHO and $CH_2 = CH_2$ were not observed through the catalytic bed. There were very low deviations in the validation of the model because low values of temperature errors (1.3%), were found especially from 4 to 12 cm in length.

Acknowledgements

The authors are grateful for the financial support of this research to the Universidad Autónoma Metropolitana-Azcapotzalco. The M. in C. Iván F Martinez is grateful for the CONACYT scholarship for his master in Process Engineering and support for a stay with the Dr. Hugo de Lasa, of the Chemical Reactor Engineering Center (CREC) of the University of Western Ontario, Canada.

References

[1] M. N. Barroso, Manuel F. Gomez, Luis Arrúa, M. Cristina Abello, "Hydrogen production by etanol Reforming over NiZnAl catalysts" Appl. Catal. A: General, 2006,304, 116-123.

[2] J. L. Contreras, M. A. Ortiz, G. A. Fuentes, M. Ortega, "Catalysts for H2 production using the ethanol steam reforming (A review)", Int. Journal of Hydrogen Energy, 2014,39,1835-1853.

[3] A. Figueroa A., "Síntesis de catalizadores Ni-Co/Hidrotalcitas para la producción de hidrógeno a partir de bio-etanol", Tesis de Licenciatura. Universidad Autónoma Metropolitana, México, 2014.

[4] Alessia Santucci, Maria A., Fabio B., Luigi M., Martina R., Silvano T., "Oxidative steam reforming over a Pt/Al2O3 catalyst in a Pd-based membrane reactor", Int. Journal of Hydrogen Energy, ,2011, 36,1503-1511.

[5]J. M. Smith, "Chemical Engineering Kinetics", Mc Graw-Hill, México,1991.

[6] Bruce E. Poling, John M. Prausnitz, John P. O´Connell, "The Properties of Gases and Liquids", Mc Graw-Hill, Mexico,2001.

[7] John H. Mathews, Kurtis D. Fink, "Numerical Methods using MATLAB", Prentice Hall, Mexico,2002.

[8] V. G. Jensen, G. V. Jeffreys, "Mathematical Methods in Chemical Engineering", Mc Graw-Hill, Mexico,2001.

[9] Stanley M. Walas, "Modelling with Differential Equations in Chemical Engineering (Butterworth-Heinemann Series in Chemical Engineering)", Prentice Hall, Mexico, 2002.

[10] Abayomi A., Ahmed A., Raphael I., Ajay D., "Kinetic modelling of hydrogen production by the catalytic reforming of crude ethanol over a co-precipitated Ni-Al2O3 catalyst in a packed bed tubular reactor", Int. Journal of Hydrogen Energy,2006, 31,1707-1715.

NOMENCLATURE

D_e	Effective diffusivity, $\frac{m^2}{s}$
u	Lineal feed speed, $\frac{m}{s}$
ρ_B	Density of the catalytic bed, $\frac{Kg}{m^3}$
r_p	Reaction rate, $\frac{Kmol}{h \cdot Kg\ cat.}$
G	Surface speed, $\frac{Kg}{h \cdot m^2}$
P.M.	Average molecular weight of the mixture fed, $\frac{Kg}{Kmol}$
y_{Ao}	Percentage fraction of limiting reagent in the feed, Adimensional
K_e	Effective thermal conductivity, $\frac{W}{m \cdot K}$
K_m	316 stainless steel thermal conductivity, $\frac{W}{m \cdot K}$
C_p	Heat capacity of the mixture fed, $\frac{KJ}{Kg \cdot K}$
ΔH	Reaction Enthalpy, $\frac{KJ}{Kmol}$
m	Number of points on the radial axis, where it starts from 0 and must be an integer value.
n	Number of points on the axial axis, where it starts from 0 and must be an integer value.
Δz	Value of the increase in the axial axis,
Δr	Value of the increase in the radial axis,
r_{ext}	External reactor radio, m
r_{int}	Radio interno del reactor, m
V_o	Volumetric flow in the feed $\frac{ml}{s}$

E061. MODELLING OF A TUBULAR REACTOR TO OBTAIN HYDROGEN FROM DRY REFORMING OF ETHANOL

Iván Ramos[1], Jose L. Contreras[1], Alberto Hernández[2], Israel Pala[3], Arturo Pallares[1], Jennipher Pérez[1]

[1] Universidad Autónoma Metropolitana–Azcapotzalco, CBI-Energía Av. San Pablo 180, Col. Reynosa, 02200 México D. F.

[2]Universidad Autónoma Metropolitana - Iztapalapa, Departamento de Energía e Hidraúlica Av. San Rafael Atlixco 186, Leyes de Reforma 1ra Secc, 09340 México D.F.

[3] Instituto Politécnico Nacional, ESIQIE, UPALM Col. Lindavista, Gustavo A. Madero, 07738 México, D.F.

Contact: 5529658232 , Email: irs.90@hotmail.com

ABSTRACT

The dry reforming of ethanol (DRE) reaction has been studied, with the purpose of obtain H_2 mainly from ethanol and CO_2. This was posible by the synthesis of an Hydrotalcite (HDT) catalyst with 10%Ni-4.5%Co as an active precursor obtained by the copreciration method. The mechanical properties of cataylst particles were given by the addition of a mixture of H_2SiO_3 and $Al(OH)_3$. This blending allowed the catalyst keep its textural properties and excellent mechanical properties. Characterization of the catalyst was necessary to confirm the correct synthesis and porous structure. Differential reactor tests were performed to obtain a power law reaction mechanism, to obtain a reaction rate without resistance to mass and heat transport, and subsequently obtain the effectiveness factors. The mass and energy transport parameters were calculated to be inserted into the equations. The transport parameters were Effective Diffusion and Thermal Conductivity. The Thermodynamic effects were important and, the equilibrium conversion had to be calculated to see the maximum temperature reaction an conversion that can be reached at these conditions. Due to the nature of the DRE reaction (endothermical), the reaction were carried up in a range of 600 to 800°C. Mass and energy balances were developed in a differential element into the reactors bed. The remaining partial differential equations were discretized bidirectionally, and solved by finite difference method to be solved algebraically to obtain temperature and conversion profiles along the reactors bed. This was achieved by using MATLAB. The numerical simulation results were compared with the experimental results in order to see how accurate were the mathematical modelling against the experimental procedure. The results were succesfull, because mechanical streght of catalysts pellets were about 15 to 30 psi. It was good enough to support the packed conditions into the reactor. Otherwise, the maximum conversion and energy transport were carried at 800 °C, And the accuracy of the mathematical method against experimental results shown deviation about 5%. Therefore, DRE was a good alternative to obtain H_2 and take advantage about CO_2 with the use of active and selective HDT catalysts.

Keywords: Hydrotalcite, NI, Co, Dry, reforming, ethanol, equilibrium, conversion, catalyst, power law, kinetics

1. Introduction

Different mitigation methods have been implemented for CO_2 handling and processing, including improving plant energy efficiency, optimization production processes, develop of biofuels, nuclear energy, renewable energies, the improvement of biological sinks, etc.[1]. Nowadays, hydrogen has been materialized as a possible solution for the emission of greenhouse gases, since it is a clean fuel, because its combustion product is only water, and it is a very important raw material for industry, which is used in several industrial processes. There are other ways to produce like water electrolysis, partial oxidation of some oils , coal gasification, wood pyrolysis, partial gas reform and oxidation, catalytic alcohol reforming, etc.

Most of the hydrogen obtained for industrial service comes from the catalytic reforming of natural gas, Currently, Scientific and Industrial community have had a great interest to obtain H_2 in this way, Due to the use of active and selective catalysts can reduce the reaction conditions. [2] Among the active metals used for the hydrocarbon reform process employ metals such as Pt, Ir, Rh, Os, Ru, Pd, etc. Most of them have some inconvenients, its high cost, and difficult extraction. However, there are some options such as Ni, Co, Cu, Fe, etc. These metals have been studied, by its good selectivity towards H_2 production. It is an attractive option to use CO_2 as a raw material in a chemical process, to obtain H_2 which has higher cost at an industrial level, and is a promising alternative against the use of fossil fuels.

The dry reforming of ethanol is the next, and its formation enthalpy indicates that is an extremely endothermic reaction:

$$C_2H_6O + CO_2 \leftrightarrow 3H_2 + 3CO \quad \Delta H^{\circ}_{298} = 296.8\ kJ/mol$$

Although this reaction would give good hydrogen yields, it could lead to undesirable reactions as follows:

$$C_2H_6O \rightarrow CH_3CHO + H_2$$
$$C_2H_6O \rightarrow C_2H_4 + H_2O$$

Even if the reaction produces Ethylene and acethaldehyde, after 700°C, these components become into Methane and Hydrogen as the following reactions [7]:

$$CH_3CHO \rightarrow CH_4 + CO$$
$$CH_3CHO + H_2O \rightarrow CH_4 + CO_2 + H_2$$
$$C_2H_4 + H_2O \rightarrow CH_4 + CO + H_2$$
$$C_2H_4 + 2H_2O \rightarrow CH_4 + CO_2 + 2H_2$$

The mesoporous materials of Hydrotalcite type (MMTH) were discovered in 1842 in Sweden. These are mineral clays that can be of natural or synthetic origin. These can be easily synthesized and possess high crystallinity. These have a wide range of applications such as water treatment, such as ion exchange resins, absorbent materials,

catalyst synthesis, pharmaceutical industry, etc. Its made of laminar double hydroxides (HDL) formed by aluminum and magnesium hydroxides.
The general formula for this type of structure is the following [6]:

$$\left[M^{2+}_{(1-X)}M^{3+}_{X}(OH)_2\right](A^{n-})_{X/n}\cdot mH_2O$$

Where:

M^{2+}= Bivalent metalic ions (Mg^{2+}, Fe^{2+}, Co^{2+}, Cu^{2+}, Ni^{2+} o Zn^{2+})

M^{3+}=Trivalent metalic ions (Al^{3+}, Cr^{3+}, Co^{3+}, Mn^{3+} o Fe^{3+})

A^{n-}=Interlaminar anion (Cl^-, NO_3^-, CO_3^{-2} o un anión orgánico)

X= Molar rate ($M^{2+}/(M^{2+}+M^{3+})$)

2. Materials and Methods

2.1. Catalyst synthesis

The procedure to synthesize Hidrotalcite catalyst is described in the following diagram:

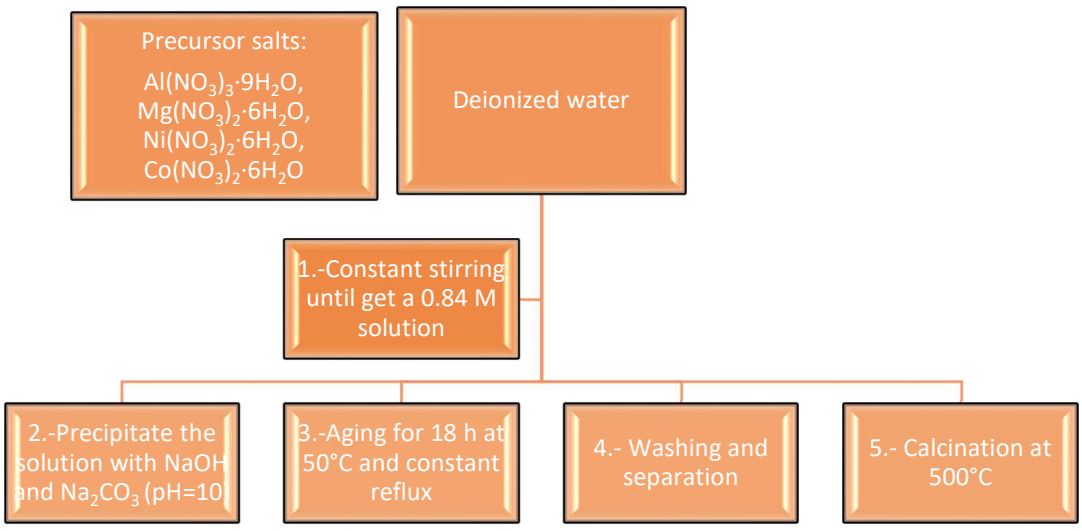

Fig. 2.1. Synthesis of catalyst Ni-Co-HDT [4]

After this procedure, the catalyst was sieved with a molecular mesh (100 mesh) and evaluated with a temperature between 600°C and 700°C, with a feed ratio CO2/C2H6Or of 1.5. This ratio is recommended by Olivieiria Vigier[3].

The operating pressure is equal to the atmospheric and a velocity space (GHSV) of 0.289. Also a CO2 flow of 60ml/min, and a catalyst weight of 1,000g. The reactor used is made of stainless steel, with 8mm in diameter and 35cm in length. The reaction products were analyzed by flame ionization gas chromatograph (Varian 3380®). and thermal conductivity detection (Gow Mac 550®).The purpose of these system is to obtain a power law kintetics. This was not the evaluation of the pellets.

The way to obtain the expression for reaction rate expression was the Gauss-Newton method to obtain a power-law model, using partial pressures and reaction rates as follows:

Table. 2.1. Reaction orders calculated from Gauss-Newton

Temperature (K)	K	A	B	R^2
773.15	0.2422	1.4277	0.2978	0.98
873.15	0.6603	1.7942	0.9281	0.9
973.15	1.5470	2.52	0.1991	0.89

$$-r_A = K\, p_{C_2H_6O}^{\alpha} p_{CO_2}^{\beta} \quad (1)$$

2.2. Binder synthesis

To get the enough mechanical strenght in catalyst , a mixture of Metasilicic Acid and Aluminum Hydroxide were prepared to form pellets for an integral reactor, in order to have similar conditions as industrial packed reactors. The synthesis route is divided into the synthesis of metasilic acid and the synthesis of aluminum hydroxide. The first one is described as follows:

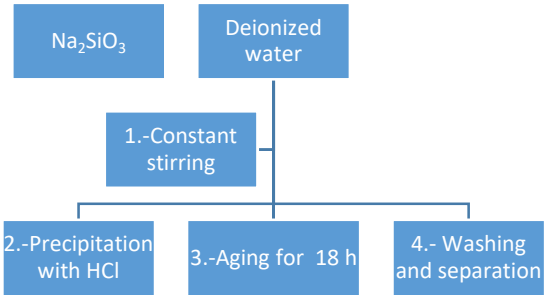

Fig. 2.2. Synthesis route for Metalisic Acid

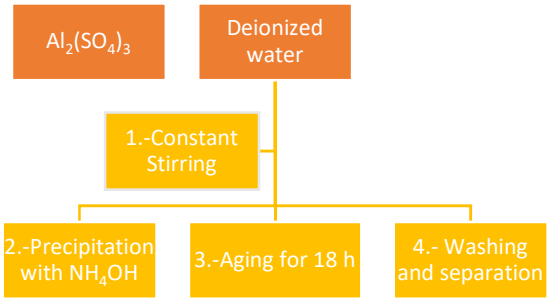

Fig. 2.3. Synthesis route for Aluminum Hydroxide

To get a correct mixture of these gels, it had to be tested certain concentrations of these substances and check the mechanical strength in the UNITED Modelo SSTM-1 equipment at UAM-Azcapotzalco.

2.3. Equilibrium conversion

It should be mentioned that for simplicity, only the main reaction for DRE was taken account to calculate some thermodynamic information as chemical equilibrium constant, and the equilibrium conversion. The reason was that the undesirable reactions almost disappeared, because the extreme conditions into reactors bed did not permit the emission of almost undesirable products (ethylene and acetaldehyde), except the carbon deposits. The next table show how the calculus were carried up:

Table. 2.2. Mass balance in terms of stoichiometric information

Component	ϑ	*ni*	n_R	*yi*
CO	3	0	3ξ	3ξ/4+4ξ
H_2	3	0	3ξ	3ξ/4+4ξ
C_2H_5OH	1	1	1-ξ	1-ξ/4+4ξ
CO_2	1	3	3-ξ	3-ξ/4+4ξ
		Nt	4+4ξ	

The next equations were used, first, to obtain the equilibrium constant, and to obtain the equilibrium conversion:

$$K_{eq} = \frac{y_{products}}{y_{reactives}} = \frac{{y_{CO}}^3 {y_{H_2}}^3}{{y_{C_2H_6O}}^1 {y_{CO_2}}^1} = \frac{\left(\frac{3\varepsilon}{4+4\varepsilon}\right)^6}{\left(\frac{1-\varepsilon}{4+4\varepsilon}\right)^1 \left(\frac{3-\varepsilon}{4+4\varepsilon}\right)^1} \quad (2)$$

$$\ln K_{eq} = -\frac{\Delta G_0^\circ}{RT} \quad (3)$$

$$x_{C_2H_6O} = \frac{n_{C_2H_6O,i} - n_{C_2H_6O,R}}{n_{C_2H_6O,i}} = \frac{1-(1-\varepsilon)}{1} = \varepsilon \quad (4)$$

2.4. Numerical modelling

The mathematical simulation was based on the principle of mass conservation. It mentions that for any reactor requires that the mass of the species i in a differential element of volume V in the reactor obey the following statement (Smith 1991) [5];

$$\left\{\begin{matrix}\textbf{Feed velocity for i}\\ \textbf{component}\end{matrix}\right\}-\left\{\begin{matrix}\textbf{Effluent velocity for i}\\ \boldsymbol{component}\end{matrix}\right\}+\left\{\begin{matrix}\textbf{Production velocity}\\ \boldsymbol{for\ i\ component}\end{matrix}\right\}=\left\{\begin{matrix}\boldsymbol{accumulation\ term}\\ \boldsymbol{for\ i\ component}\end{matrix}\right\}$$

One of the key features of this statement is the size of the volume element and its relationship to the production speed term. The element must be small enough for the concentration and temperature to be uniform in its entirety (Smith 1991). A differential element of volume of a catalytic reactor must be considered
Conservation mass and energy equations take the following form [6]:

$$\frac{\partial C_i}{\partial t}+(v\cdot\nabla C_i)=D_e\nabla^2C_i+\mathrm{r_{ij}} \quad (5)$$

$$\frac{\partial T}{\partial t}+(v\cdot\nabla T)=\frac{K_e}{\rho\,C_p}\nabla^2T-\frac{\Delta H}{\rho\,C_p}r_{ij} \quad (6)$$

Some considerations had to be applied to simplify the PDE system. These considerations were:

- The differential volume element has radius 'r', width 'Δr' and height 'Δz'
- The reactant fluid is isothermic.
- Radial and longitudinal diffusion can be expressed by Fick's law, $\left(D_{eff}\right)_r$ and $\left(D_{eff}\right)_L$. These are the effective diffusion coefficients based on the total area perpendicular to the direction of the diffusion, and due to the dimensions of the reactor, will be considered constants along the catalytic bed.
- The differential volume element ($\Delta v=2\pi r\,\Delta r\,\Delta z$) contains as many catalytic granules as the fluid that surrounds them.
- The concentration of the fluid phase is constant within the element and the total velocity is known in terms of this overall fluid concentration.
- The axial velocity of the reacting fluid may vary in radial direction. It will be described as a local surface flow rate, based on the total area (empty and non-empty) of the cross section

Applying these considerations and developing vector operators, the PDE system and its Boundary conditions are:

$$\frac{\partial x}{\partial z}-\frac{\mathcal{D}_e}{u}\left(\frac{\partial^2x}{\partial r^2}+\frac{1}{r}\frac{\partial x}{\partial r}\right)-\frac{\partial x^2}{\partial z^2}-\frac{\rho_B r_P}{\frac{G}{PM}y_{A0}}=0 \quad (7)$$

$$\frac{\partial T}{\partial z}-\frac{K_e}{G\,C_p}\left(\frac{\partial^2T}{\partial r^2}+\frac{1}{r}\frac{\partial T}{\partial r}\right)-\frac{\partial T^2}{\partial z^2}+\frac{\rho_B\,\Delta H\,r_P}{G\,C_p}=0 \quad (8)$$

$$x(r,0)=0,\qquad \boldsymbol{z=0}\quad En\quad \boldsymbol{0\le r\le R} \quad (9)$$

$$\frac{\partial x}{\partial r}(0,z)=0,\qquad \boldsymbol{r=0}\quad En\quad \boldsymbol{0\le z\le L} \quad (10)$$

$$\frac{\partial x}{\partial r}(R,z) = 0, \qquad \boldsymbol{r = R} \quad En \quad \boldsymbol{0 \le z \le L} \tag{11}$$

$$T(r,0) = T_0, \qquad \boldsymbol{z = 0} \quad En \quad \boldsymbol{0 \le r \le R} \tag{12}$$

$$\frac{\partial T}{\partial r}(0,z) = 0, \qquad \boldsymbol{r = 0} \quad En \quad \boldsymbol{0 \le z \le L} \tag{13}$$

$$U(T_w - T_s) = -K_{eff}\frac{\partial T}{\partial r}\Big]_W \qquad \boldsymbol{r = R_i} \quad En \quad \boldsymbol{0 \le z \le L} \tag{14}$$

3. Results and Discussion

Table 3.1. Mechanical strength of Ni-Co-HDT pellets

Composition	Rupture resistance (lb_f)
90%Binder – 10%Catalyst	41.8
80%Binder – 20% Catalyst	23.52
70%Binder – 30% Catalyst	14.12
60%Binder – 40% Catalyst	9.21
50%Binder – 50% Catalyst	7.66
40%Binder – 60% Catalyst	3.95

Fig. 3.1. Synthesis of Ni-Co-HDT pellets.

According to the figure 3.1, the resulting size of catalyst pellets are approximately of 1/8" of diameter, they were molded by hand, taking care of the amount of water that the pellets could lose while its molding and Drying. An important factor was the mechanical strength. The proportion of catalyst-binder was the one who offered the best mechanical strength, as it shown in Table 3.1.

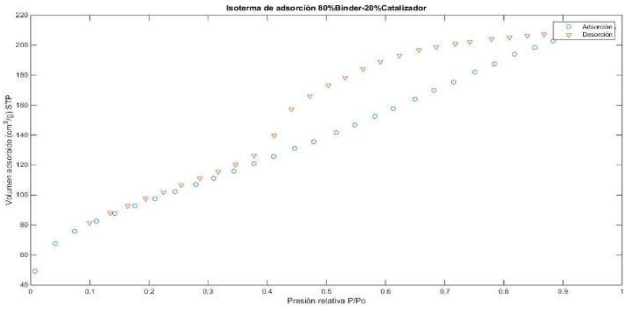

Fig. 3.2. BET Analysis results.

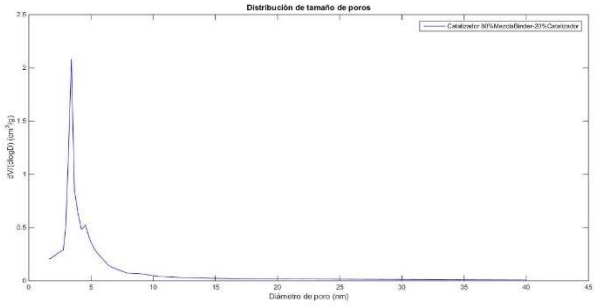

Fig. 3.3. Pore size distribution

Table 3.2. Textural and structural properties of Ni-Co-HDT pellets

Composition	Surface (m^2/g)	Total pore volume (cm^3/g)	Pore diameter (Å)
90%Binder – 10%Catalizador	366.7	0.3799	31.44
80%Binder – 20%Catalizador	350.5	0.3277	37.40
70%Binder – 30%Catalizador	331.0	0.3407	41.17
60%Binder – 40%Catalizador	323.2	0.3774	46.71

50%Binder – 50%Catalizador	309.8	0.3890	50.23
40%Binder – 60%Catalizador	312.5	0.4485	57.41

About Table 3.2 and figure 3.2, they explain how the areas depend of the Binder/Catalyst ratio vary. It was confirmed that the type of HDT Catalyst structure, that According to the BET isotherm, is a laminar material, and its pore distribution is in the order of mesoporous materials.

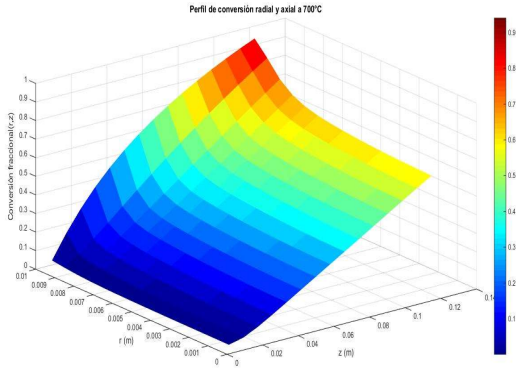

Fig. 3.4. Bidimensional conversion.

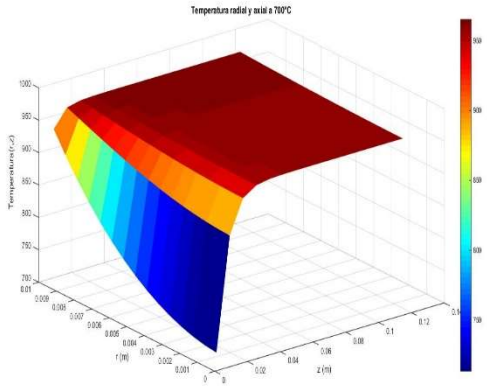

Fig. 3.5. Bidimensional temperature

The PDE system were solved by the finite difference method, with 100 iterations the solution was achieved. In the case of Figure 3.5, it is observed that the heat transfer in the reactor wall is very good, not showing temperature gradients axially or radially, except in the reactors center. For Figure 3.4 an axial gradient is seen in the conversion, perhaps due to the endothermal reaction, as it is benefited by the increament of temperature.

Table 3.3. Comparison between experimental and simulation results

Length (m)	Experimental conversion	Calculated conversion	%Error
2	0.04	0.06	33.33

4	0.12	0.16	25
6	0.21	0.27	8.6
8	0.367	0.38	3.4
10	0.63	0.68	7.3

4. Conclusion

On the center of the reactor when R-0, a decrease in temperature is observed indicating that in the center of the bed this condition is not maintained, perhaps due to the empty spaces within the bed, which decrease the transfer of energy. The conversion of ethanol is improved by the increase in temperature, and an excess of CO2 fed. However there is an axial temperature gradient that may be due to the consideration made that the extremeness and effective conductivity are constants along the bed. For simplicity, is assumed that the porosity of the bed is uniform, which is not entirely true. However, because of the relatively small dimensions of the reactor and the difficulty in obtaining porosity data along the length and width of the bed, they are taken into account.

Otherwise, mathematical simulation is a very effective tool to predict some properties or parameters in a system, in this case the temperature and conversion can be predicted with a high an accurate level. The problem could be in the development of the right model and the boundary conditions. No always is easy to obtain these solutions. They always depend of the geometry of the problem to apply certain methods. A better approximation could be reached, if a kinetic model type LHHW, Eley Rideal or another, would have been developed, because the effects off diffusion in reactors bed were not considered in this work.

Acknowledgements

The authors would like to thank to the Energy Department of Universidad Autonoma Metropolitana, for funding this work, and to the Instituto Mexicano del Petróleo for the support to do the catalyst characterization.

References

[1] Prog. Naciones Unidas para el Medio Ambiente (PNUMA), GEO-5, Cap. 2; Atmósfera pag. 32 (2011), Edit. Novo Art, S.A.

[2] T. LeValley, *"Development of catalysts for hydrogen production through the integration of steam reforming of methane and high temperature water gas shift"*, Energy (2015), pp. 261-27

[3] K. De Olivieiria-Vigier,*"Dry reforming of etanol in presence of 316 Stainless Steel cat."*,The C.J. of Chem. Eng, Vol. 83, 2005.

[4]T. LeValley, *"Development of catalysts for hydrogen production through the integration of steam reforming of methane and high temperature water gas shift"*, Energy (2015), pp. 261-274

[5]S. Sumrunronnasak, S. Tantayanon, *"Improved hydrogen production from dry reforming reaction using a catalytic packed-bed membrane reactor with Ni-based catalyst"* . J of chem. reactor eng., 12 (2010).

[6]S. Zhao, W. Cai, *"Syngas production from ethanol dry reforming over Rh/CeO2 catalyst"*, J. of Saudi Chemical Society (2017), 892.

[7]C. Crisafulli, S. Scirè, S. Minicò, L. Solarino "*Ni–Ru bimetallic catalysts for the CO_2 reforming of methane*" Applied Catal. , 225 (2002) pp. 98- 106

[8]J. Hunt, A. Ferrari,"*Microwave-Specific Enhancement of the Carbon–Carbon Dioxide (Boudouard) Reaction*". J. of Physical Chemistry, (2013), pp 26871-26880.

E065. BIOHYDROGEN PRODUCTION FROM CODIGESTION OF WASTE ACTIVATED SLUDGE AND FOOD WASTE

I. Moreno-Andrade, M. J. Berrocal-Bravo, I. Valdez-Vazquez

Unidad Academica Juriquilla, Instituto de Ingeniería, Universidad Nacional Autónoma de México, Blvd. Juriquilla 3001, 76230 Querétaro, Mexico.

* Corresponding author: E-mail imorenoa@ii.unam.mx

ABSTRACT

The codigestion of different organic waste has been proposed to increase the hydrogen (H_2) production rate in dark fermentation processes. One of the substrates with a high potential of hydrogen production is food waste. On another hand, the waste activated sludge (WAS) generated in wastewater treatment plants also can be used for the H_2 production, but due to its low carbohydrate content, the H_2 yields are not high. However, the addition of WAS to the food waste has been shown that can improve the biogas production rate, compared to that obtained with the substrates independently. Also, to increase the global energy production from this waste, the use of subproducts of hydrogen production (e.g., volatile fatty acid (VFA), lactic acid, ethanol, etc.) can be used subsequently in a methanogenic step for biogas (methane and CO_2) production. The objective of this work was to evaluate the productivity of hydrogen in a dark fermentation process and methane in methanogenic process by a codigestion of food waste and WAS in a discontinuous process. The results showed that there is a mixing ratio (90-10% food waste-WAS) that favors the production of H_2 above the other mixtures, in addition it can be observed that the addition of sludge facilitates the fermentation to the extent that the latency phase of the process decreases when compared to the case of 100% food waste, which turns into higher rates of hydrogen production. Carbohydrate removal was higher than 88% independently of the mixture evaluated. For the operation of the two-phase process, the highest concentration of H_2 in the biogas (37%) was obtained with an HRT of 16 h, while the highest removal of carbohydrates, volatile solids and COD were obtained with an HRT of 24h, producing the highest production of VFA. During CH_4 production, the biogas composition generated was 69% CH_4 - 29% CO_2, with productivities of 809 mL $CH_4/L_{reactor}/d$.

Keywords: Biohydrogen; Co-digestion; Organic Solid Waste; Waste Activated Sludge.

1. Introduction

The Waste Activated Sludge (purged sludge, PS) is an organic waste generated in wastewater treatment plants caracterized by a low carbohydrate content and poorly biodegradable characteristics [1]. In other hand, restaurant organic solid waste (OSW), mainly constituted by food waste, has been used as substrate for hydrogen (H_2) and methane (CH_4) production applying biological process, due to the high content of carbohydrates, resulting in an economically viable practice. Several studies of fermentation of food residues have been carried out, reporting yields of 50-150 mLH_2/gVS [2]. On the other hand, to increase increase the H_2 production rate, it has been proposed to combine different residues in a co-digestion since the addition of PS to the food waste as a co-substrate has been shown to improve the biogas production rate, compared to that obtained with the substrates independently [3]. In a two-step process, the fermentation can be the limiting step, because it has been reported that different parameters affect the hydrogen production including the HRT, temperature, pH and the organic loading rate [4].

The objective of this work was to evaluate the codigestion of purge sludge and organic solid waste of a restaurant in order to increase the productivity of hydrogen (H_2) in a dark fermentation process and methane in the methanogenic process.

2. Materials and Methods

The organic solid waste (OSW) was obtained from a cafeteria, and only the fermentable matter was preserved as feedstock for the experiments -20 °C. The waste acrivated sludge (PS) was obtained from an aerobic municipal wastewater treatment plant after its dewatering with a press. For hydrogen and methane potential production test, different combinations of OSW and PS (100, 90, 80, 70, 60, 50, 30, 0%) were tested in serum bottles of 160 mL with a working volume of 80 mL. Deoxygenated water was added to fill the total volume. For methane production test, the inoculum was anaerobic sludge blanket (UASB) reactor degrading wastewater from a brewery (5 gVSS/L) and pH value was adjusted at 7.

For hydrogen production test, the pH values in the experiments were adjusted to 5.5 using an organic buffer and were inoculated with heated pretreated microorganisms from the same UASB reactor from a brewery according to Ramos et al. [5]. Incubation was at a constant temperature of 36°C, and the content was mixed using an orbital shaking at 130 rpm. All experiments were run in triplicates, and the standard deviation values are reported. The ratio of OSW-PS with the best results for the H_2

production, was used in a two-phase process: Fermentative process in a Sequencing Batch reactor (SBR) for H_2 production (1.5L), and Methanogenic process (using the effluent of the fermentative step) in an SBR of 4L.

Hydrogen, carbon dioxide and methane were analyzed with a gas chromatograph (Agilent 6890 / TCD, column Supelco-Carboxen 1010 Plot). Volatile Fatty acids (acetic, propionic, butyric and iso-butyric acids), solvents (ethanol and acetone), were determined by gas chromatography (FID, flame ionization detector). Analytical analysis of Total solids, total and volatile suspended solids (TS, TSS, VSS), as well as Chemical Oxygen Demand (COD), were determined according to the Standard Methods. A kinetic analysis of cumulative hydrogen production was done using the modified Gompertz equation according to [5].

3. Results and Discussion

Table 1 showed the H_{max} (total amount of hydrogen produced), R_{max} (maximum hydrogen production rate) and is the lag time (λ) before the exponential hydrogen production in the fermentative process experiments. The results show that there is a mixing ratio (90-10% OSW-PS) that favors the production of H_2 (142 mL/L/d) above the other mixtures, in addition it can be observed that the addition of sludge facilitates the fermentation to the extent that the latency phase of the process decreases when compared to the case of 100% OSW; Which turns into higher rates of hydrogen production. It is interesting to note that in the 100% purge sludge test, hydrogen production was practically zero, due to the low amount of available carbohydrates (compared to OSW) reflected in a low biodegradability.

Table 1. Accumulated H2 production at various mixing ratios.

Mixture	λ (h)	R_{max} ($mLH_2/gVS/h$)	H_{max} (mLH_2/gVS)	$mLH_2/L_{reactor}/d$
100% OSW	17	2.5	53	115
90%OSW-10%PS	10	2.6	65	142
80%OSW-20%PS	6.5	1.7	45	115

70%OSW-30%PS	5.5	2.0	53	98
60%OSW-40%PS	5.0	1.8	41	90
50%OSW-50%PS	4.8	1.7	35	77
30%OSW-70%PS	3.0	0.4	6	13
100%PS	6.5	0.1	1	2

For the case of the methane production, the maximal methane production was obtained using OSW without a codigestion with PS. The raw PS produced 76 mLCH_4 after 300h, and the total methane production increase as result of the OSW addition. The methane production by the codigestion of these substrates not increased the methane potential of the OSW, but the methane production of PS. This can be an option when waste of PS need to be treated and an increase of methane are required in the process.

For the operation of the two-phases process, Figure 1 shows the variations in the concentration of the biogas obtained in the first stage (fermentative) during the three HRT evaluated conditions. The highest concentration of H_2 in the biogas (37%) was obtained with a HRT of 16 h, resulting in a productivity of 470 mlH_2/$L_{reactor}$/d.

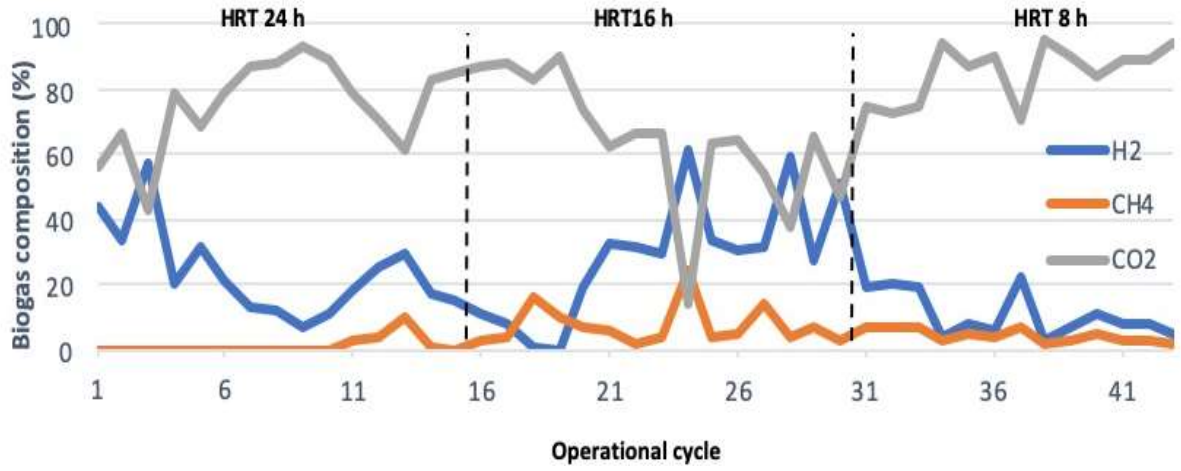

Fig. 1. Biogas composition during the operation of the bioreactor at different HRT.

Table 2 shows the physicochemical parameters evaluated in the two different stages, the highest removal of carbohydrates, volatile solids and COD were obtained with a HRT of 24h, producingthe highest production of VFA, available for methane production in the second stage.

During CH_4 production, the biogas composition generated was 69% CH_4 - 29% CO_2, with productivities of 809 ml $CH_4/L_{reactor}/d$. The operation with each HRT was maintained at least 10 days. The overall soluble COD removal of the system has remained between 78-85%.

Table 2. Physicochemical parameters of the reactors operation.

First step- H_2 production					
HRT (h)	**Hydrolisis (%)**	**Removal**			**mL$CH_4/L_{reactor}/d$**
		Carbohydrates (%)	**VS (%)**	**COD_{total} (%)**	
24	78 ± 17	75 ± 14	63 ± 10	55 ± 13	55 ± 13

16	49 ± 8	74 ± 13	53 ± 16	42 ± 12	42 ± 12
8	32 ± 9	45 ± 17	41 ± 0.3	34 ± 7	34 ± 7

Second step- CH_4 production				
HRT (d)	**COD_{total}**	**VS (%)**	**$mLCH_4/gDQOt$**	**$mLCH_4/L_{reactor}/d$**
8-10	89 ± 4	74% ± 9	288 ± 15	809± 80

4. Conclusion

For the hydrogen production, a codigestion of 90% OSW-10%PS presented the best results for H_2 production, showing that the addition of small amounts of PS improves the performance of H_2 fermentation from OSW. For the operation of the two-phases process, the highest concentration of H_2 in the biogas (37%) was obtained with a HRT of 16 h, while the highest removal of carbohydrates, volatile solids and COD were obtained with a HRT of 24h, producing the highest production of VFA, available for methane production in the second stage. During CH_4 production, the biogas composition generated was 69% CH_4 - 29% CO_2, with productivities of 809 mL $CH_4/L_{reactor}/d$.

Acknowledgements

The financial support granted by "Fondo de Sustentabilidad Energética SENER-CONACYT (Mexico)", through the project 247006 Gaseous Biofuels Cluster, is gratefully acknowledged. Angel Hernández, Gloria Moreno and Jaime Perez are acknowledged for their technical assistance. M. J. Berrocal-Bravo thanks to CONACYT for the award of scholarship.

References

[1] Lay JJ, Fan KS, Chang J, Ku CH. Influence of chemical nature of organic wastes on their conversion to hydrogen by heat-shock digested sludge. Int. J. Hydrogen Energy 2003;28: 1361-1367.

[2] Kim DH, Kim, SH, Kim HW, Kim MS, Shin HS. Sewage sludge addition to food waste synergistically enhances hydrogen fermentation performance. Bioresour Technol 2011;02:8501–8506.

[3] Liu X, Li R, Ji M, Han L. Hydrogen and methane production by co-digestion of waste activated sludge and food waste in the two-stage fermentation process: Substrate conversion and energy yield. Bioresour Technol 2013;146:317-323.

[4] Lin CY, Lay CH, Sen B, Chu CY, Kumar G, Chen CC, Chang JS. Fermentative hydrogen production from wastewaters: a review and prognosis. Int J Hydrogen Energ 2012;37:15632-15642.

[5] Ramos C, Buitrón G, Moreno-Andrade I,Chamy R. Effect of the initial total solids concentration and initial pH on the bio-hydrogen production from cafeteria food waste. Int J Hydrogen Energy 2012;37:13288-13295.

E068. EFFECT OF HYDROGEN TO REMOVE NOx OF EMISSIONS FROM DIESEL ENGINES USING A Pt-Ag/Al_2O_3-WOx CATALYST

N. González Hernández[1]; M. Pinto[1]; J. L. Contreras Larios[1*]; B. Zeifert[2]; G. A. Fuentes Zurita[3]; T. Vázquez[1]; R. López Medina[1].

[1]Universidad Autónoma Metropolitana Azcapotzalco, Av. San Pablo No. 180. Col. Reynosa Tamaulipas C.P. 02200. México.

[2]Instituto Politécnico Nacional, Av. Luis Enrique Erro S/N, Unidad Profesional Adolfo López Mateos, Zacatenco C.P. 07738. México.

[3]Universidad Autónoma Metropolitana Iztapalapa, Av. San Rafael Atlixco No. 186. Col. Vicentina C.P. 09340. México.

* Corresponding author: (55) 55 91 91 10 47; *jlcl@correo.azc.uam

ABSTRACT

The NOx are considered the main pollutants in the atmosphere, as they are responsible for environmental problems such as photochemical smog, acid rain, tropospheric ozone, depletion of the ozone layer and even global warming caused by N_2O. This research has focused on the study of pollution from the gases emitted by Diesel engines. The central analysis refers to the study of the NOx reduction with Ag-Pt/γ-Al_2O_3-WOx for the NOx SCR using H_2 as a reducer, coming from the reaction of ethanol reforming with Ni-Co/HDT. These catalytic materials were characterized by: texture and BET area, Scanning Electron Microscopy (MEB/EDS), hydrogen chemisorption to determine the amount of Pt and Ag dispersed on the support, DRX and UV-vis. Different species of Ag were found on the prepared catalysts which were evidenced by UV-vis spectroscopy. The effect of the presence of C_3H_8 and H_2 on the NOx reduction was studied using a representative mixture of pollutant gases similar to that emitted by a Diesel engine. The longevity of the Ag-Pt/γ-Al_2O_3-WOx catalyst was studied, varying the gas flows (GHSV of 30 000, 70 000 and 10 0000 h^{-1}) and the ratio of active sites of Ag and Pt on the NO conversion due to its importance during the oxidation of propane. The Ni-Co/HDT catalysts were evaluated at temperatures of 450,500,550 and 600°C, with the analyzes carried out by gas chromatography the presence of H_2, CO_2, CH_4, CO was confirmed and CH_3CH_2OH was not detected in the reaction products because a conversion was achieved total (x=1). The Ag-Pt/γ-Al_2O_3-WOx catalysts were found to be active in NOx reduction and the largest conversions were observed in the evaluations at 30 000 h^{-1}, while as the GHSV was increased the conversion was reduced.

Keywords: NOx, Ag-Pt/γ-Al_2O_3-WOx catalyst, H_2 production, ecological impact

1. Introduction

The NOx are considered the main pollutants in the atmosphere, as they are responsible for environmental problems such as photochemical smog, acid rain, tropospheric ozone, depletion of the ozone layer and even global warming caused by N_2O [1-2]. It is known that Diesel engines have a higher thermal efficiency compared to stoichiometric engines, that is, they reduce CO_2, CO and HC emissions, so Diesel combustion can be tuned to further increase thermal efficiency, however, such strategies usually produce high NOx emissions [3-4]. The selective catalytic reaction (SCR) is an effective technology that today is widely used to reduce NOx emissions from mobile sources, such as vehicles Diesel [5]. For this purpose, much attention has been paid to the HC-SCR. The SCR with hydrocarbons is able to overcome the disadvantages of the selective catalytic reduction with ammonium (NH_3-SCR), as is the complexity of the system, the additional cost due to the urea dosing system, the storage space and the freezing. In this system, hydrocarbons such as methane, propane, n-butane, propene and n-octane are used as reducing agents [6-7-8]. The present investigation has focused on the study of pollution from Diesel engines. The central analysis refers to the HC-SCR of NOx using H_2 as a reducing agent, generated from the steam reforming of ethanol with Ni-Co/HDT, as well as the obtaining of the catalyst Ag-Pt/Al_2O_3-WOx for the SCR-NOx.

2. Materials and Methods

The Ni-Co/Hydrotalcite-WOx catalyst was synthesized by the precipitation method and dried at 120°C for 18 h. Prior to its use; it was subjected to a thermal treatment at 450°C for 4.5 h. The Al_2O_3 was obtained by the precipitation method and $(NH_4)_{12}W_{12}O_{40}{\cdot}5H_2O$ was added at 0.5%wt by weight to achieve a higher thermal stability in the support. The material was dried at 110°C for 24 h and subjected to a heat treatment for 6 h at 500°C. Using the incipient humidity impregnation method, Pt and Ag were deposited on γ-Al_2O_3 from solutions of H_2PtCl_6 and $AgNO_3$. Subsequently synthesized materials were characterized by the following techniques. The texture and BET area were determined by N_2 physisorption (Micromeritics, ASAP-2460); the crystalline faces were obtained in a diffractometer (Bruker D8FOCUS). The morphology, as well as the qualitative and quantitative chemical analysis, was determined using SEM/EDS (JFM 6701, Jeol, SEM / EDS) and UV-vis spectroscopy. The production of H_2 was carried with steam reforming ethanol; the catalyst was activated for 1 h at 450°C. Four reaction temperatures (450, 500, 550 and 600°C) were studied using N_2 as the entrainment gas. The reaction

products were analyzed by gas chromatography with TCD detector. The SCR-NOx was carried out in a fixed-bed tubular reactor. A gas mixture similar to that emitted by a Diesel engine was used. In each evaluation, the GHSV varied from 30,000, 70,000 and 100,000 h^{-1} and a temperature sweep of 50 to 500°C was performed. The NOx conversion was evaluated in a CONSINO brand emissions analyzer, model FGA-4100.

3. Results and Discussion

3.1 Characterization of Ni-Co/Hydrotalcite-WOx

The textural properties of fresh and calcined materials have an average pore diameter between 192 and 310 Å, this contributes to the fact that the obtained samples turned out to be mesoporous. The catalyst, as well as the fresh support have a smaller area than the calcined materials, due to the collapse of the structure of the Hydrotalcite when this is subjected to a thermal treatment, this phenomenon agrees with Bellotto M. et al., who assumes that, during the decomposition of the Hydrotalcite, it brings about the increase of the surface [9]. The Fig.1 shows the diffraction patterns of fresh (a) and calcined HDT and NiCoHDT samples (b).

a) b)

Fig.1. X-ray diffraction patterns of HDT and NiCoHDT samples. Dry to 120°C (a) and calcined to 450°C (b).

The dry samples exhibited characteristic peaks of Hydrotalcite (PDF 89-0460) synthesized by the coprecipitation method, while in the calcined samples MgO was detected (PDF 04-0829), as the main crystalline phase [10].

In micrographs of NiHDT, CoHDT and NiCoHDT materials calcined at 450°C with approaches of 30,000X plate type morphology can be seen with the formation of holes, the plates are agglomerate of small particles hardly measurable (Fig.2), something similar was found by Hong- Yang Zeng in 2008 [11].

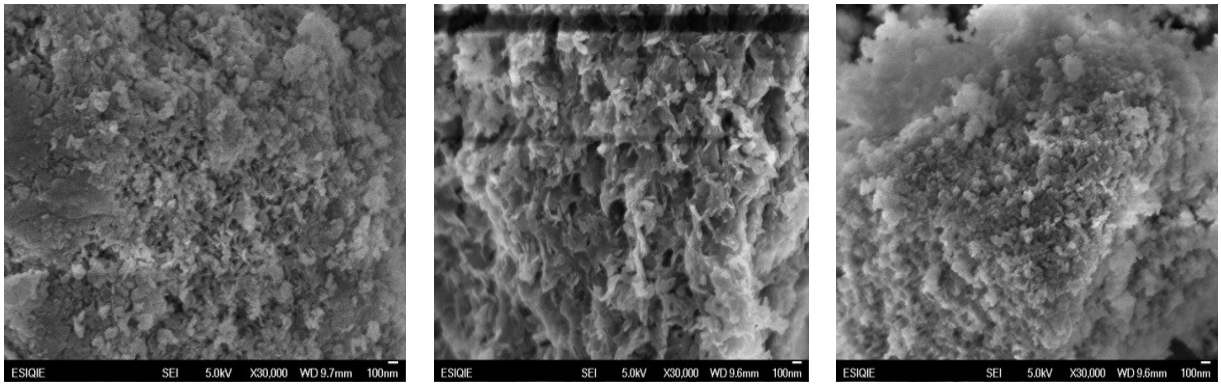

a) b) c)

Fig.2. Micrographs of the samples calcined at 450 ° C with increases of 30,000X. NiHDT (a); CoHDT (b); NiCoHDT (c).

3.2 Characterization of Pt-Ag/γ-Al_2O_3-WOx

The results of the textural analysis of the support and the catalysts of Pt-Ag are shown in Table 1. It is observed that the area of the support decreases when adding Pt and Ag, which may be due to the partial replacement of the alumina by Pt-Ag [12].

Table 1. Textural analysis of the support and catalysts based on Pt-Ag

Catalyst	BET área (m^2/g)	Pore volume (cm^3/g)	Pore diameter (nm)
$Al_2O_3$500°C	327.87	0.47	3.18
Pt$Al_2O_3$500°C	298.54	0.41	5.88
PtAg$Al_2O_3$300°C	245.75	0.35	4.94

The average pore diameter resulted between 32 and 59 Å, a convenient classification of the pores originally proposed by Dubinin M., and officially accepted by the IUPAC. This contributes to the fact that

the obtained samples turned out to be mesoporous, given that they are in the average pore range between 2 and 50 nm [13-14].

The X-ray diffraction patterns of the catalysts $PtAl_2O_3$-WOx, $AgAl_2O_3$-WOx and $PtAgAl_2O_3$-WOx (Fig.3) show the characteristic diffraction of the γ-Al_2O_3 phase [15-16]. The incorporation of platinum and silver does not lead to major changes in the recorded diffractograms.

Fig.3. X-ray diffraction patterns of the catalysts $PtAl_2O_3$-WOx, $AgAl_2O_3$-WOx and $PtAgAl_2O_3$-WOx

The Fig.4 shows the panoramic image of the catalyst $PtAgAl_2O_3$-WOx with an approximation of 10,000X and 30,000X, morphology of superficial nanoparticles can be seen.

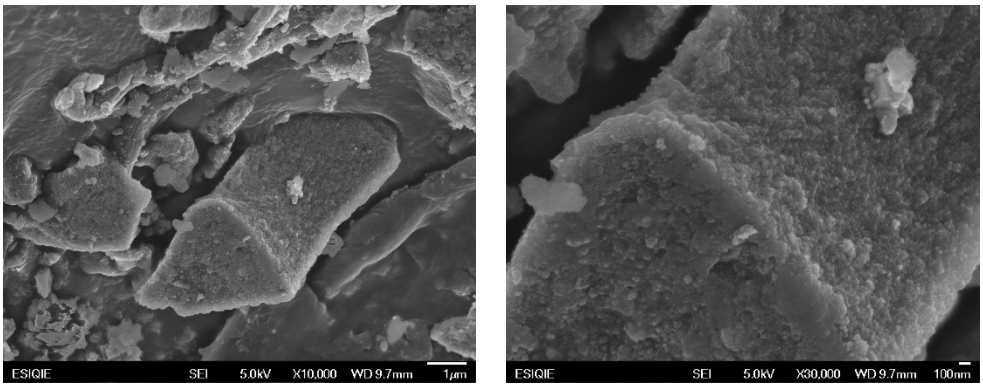

a) b)

Fig.4. Panoramic image of the catalyst $PtAgAl_2O_3$-WOx.
Approximation of 10,000X (a) and 30,000X (b).

The existence of different oxidation states of silver was demonstrated through the UV-vis technique (Fig.5). The spectra of the catalysts $AgAl_2O_3$-WOx and $PtAgAl_2O_3$-WOx show a band between 220-240 nm, a similar band was observed for the materials Ag/Al_2O_3 and Ag^+/H-ZSM-5 and was assigned to the Ag^+ ions or to the nanoparticles of Ag_2O highly dispersed in the support [16-17-18]. A shoulder at 350 nm was also observed which is believed to correspond to the oxidized silver clusters (Agn^+) [15-19] and a last band was observed at 425 nm, which the literature attributes to silver metal (Ag^0) [17].

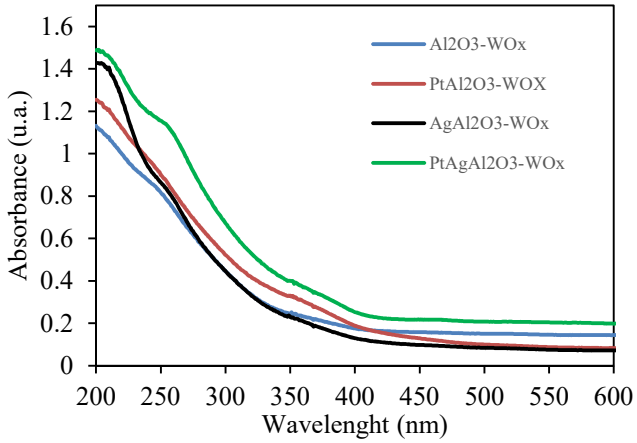

Fig.5. UV-vis spectra of the Pt and Ag catalysts supported in Al_2O_3-WOx

The textural bands LMCT of W=O (W^{6+}) in tetrahedral coordination and W-O-W located in 250 and 309 nm were found respectively. Bands were also found at 350 and 391 nm, attributed to species $[Pt(OH)xCly]_s$ and $[PtOxCly]_s$.

3.3 Catalytic evaluation of the catalysts

The Ni-Co/HDT-WOx catalysts were evaluated in the steam reforming reaction of ethanol at temperatures of 450, 500, 550 and 600°C, with the analyzes carried out by gas chromatography the presence of H_2, CO_2, CH_4, CO and CH_3CH_2OH was not detected (Fig.6) because a total conversion was reached (x=1).

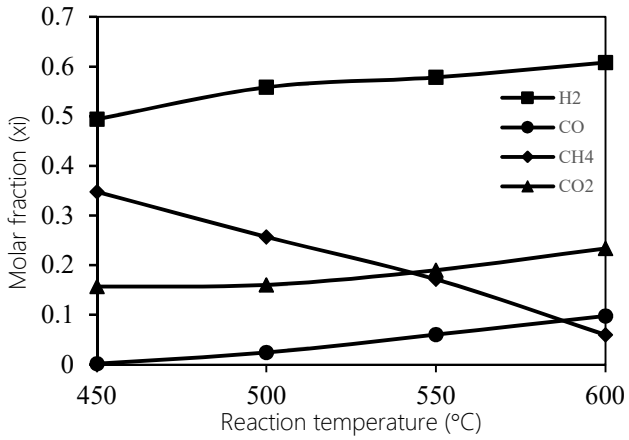

Fig.6. Molar fraction in the reaction with Ni-Co/HDT-WOx calcined to 450°C

The NOx conversion profiles obtained from the evaluations with the pollutant gas stream are shown in Fig. 7. A temperature sweep of 50 to 500°C was performed and these correspond to a different GHSV (30,000, 70,000 and 100,000 h^{-1}).

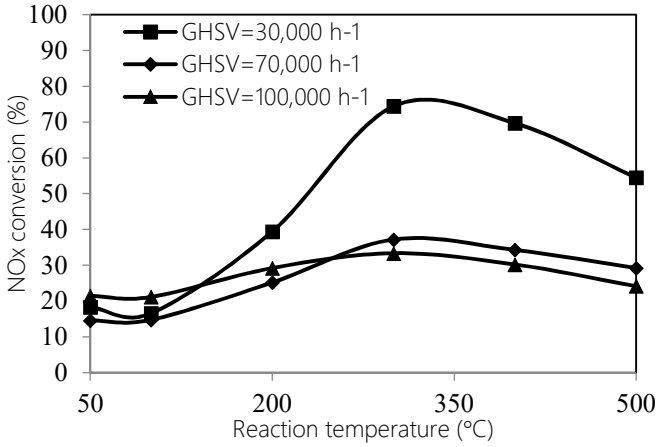

Fig.7. Selective catalytic reduction of NOx with the catalyst Pt-Ag/γ-Al_2O_3-WOx using C_3H_8 as reducing agent

The catalyst shows high conversions at 300°C (76%) in the evaluations at 30,000 h^{-1}, but as we increase the GHSV, NOx conversion decreases.

The conversion of the nitrogen oxides obtained from the catalytic evaluations using H_2 as a reducer is shown in Fig. 8. It started activity at 100°C having a maximum conversion at 145°C with 80%, later it presented a decrease in the activity between 180 and 210°C possibly due to H_2 depletion. Again, restart

the conversion at 200°C, maintaining 93% between 270 and 350°C, due to the activation of C_3H_8 since short-chain hydrocarbons need a higher temperature for activation [20].

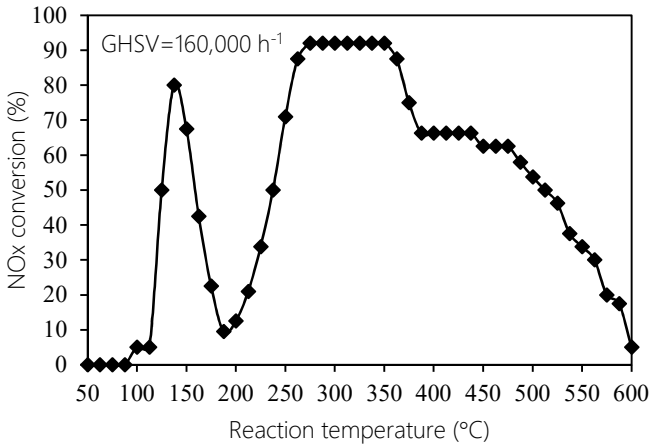

Fig.8. Selective catalytic reduction of NOx with the catalyst Pt-Ag/γ-Al_2O_3-WOx using C_3H_8 and H_2 as reducing

4. Conclusion

The use of H_2 and propane allowed the reduction of NOx (90%) at low temperatures (275°C) using the Ag-Pt/Al_2O_3-WOx catalyst. The NOx conversion of the Pt-Ag/Al_2O_3-WOx catalyst evaluated at a GHSV of 30,000h^{-1} was the highest with respect to those evaluated at higher GHSV. The distribution of the reaction products from the evaluation of steam reforming of ethanol with the catalyst NiCoHDT-WOx shows high selectivity (above 90%) for H_2 production. The method of obtaining the NiCoHDT-WOx and PtAgAl2O3-WOx catalysts produced mesoporous solids with a high specific area and thermal stability. γ-Al_2O_3-WOx showed a good dispersion of Pt, Ag on the support, and a homogeneous particle size which was evidenced by EDS microanalysis and elemental mapping performed by SEM. By UV-vis spectroscopy, Ag° species were found in the catalysts $AgAl_2O_3$-WOx and $PtAgAl_2O_3$-WOx.

Acknowledgements

First of all, I thank CONACYT. The authors acknowledgment for the joint collaboration of the Autonomous Metropolitan University units Azcapotzalco and Iztapalapa with the National Polytechnic Institute-ESIQIE for allowing the development of this research.

References

[1] Ma L., Cheng Y., Cavataio G., McCabe R. W., Fu L., y Li J. (2013). Characterization of commercial Cu-SSZ-13 and Cu-SAPO-34 catalysts with hydrothermal treatment for NH_3-SCR of NOx in Diesel exhaust. *Chemical Engineering Journal* 225 (2013) 323–330.

[2] Twigg M. V. (2007). *Appl. Catal. B Environ* 70 (2007) 2-15.

[3] Shrestha S., Harold M. P., Kamasamudram K., Kumar A., Olsson L. and Leistner K. (2016). Selective oxidation of ammonia to nitrogen on bi-functional Cu–SSZ-13 and Pt/Al_2O_3 monolith catalyst. *Catalysis Today* 267 (2016) 130–144.

[4] Luo J., Kisinger D., Abedi A., and Epling W. S. (2010). Sulfur release from a model Pt/Al_2O_3 Diesel oxidation catalyst: Temperature-programmed and step-response techniques characterization. *Applied Catalysis A: General* 383 (2010) 182–191.

[5] Praveena V. y Martin J. M. L. (2017). A review on various after treatment techniques to reduce NOx emissions in a CI engine. *Journal of the Energy Institute* xxx (2017) 1-17.

[6] Keshavaraja A., She X., Flytzani-Stephanopoulos M. *Appl. Catal. B Environ.* 27 (2000) L1-L9.

[7] Shimizu K., Satsuma A., Hattori T. (2002). *Appl. Catal. B Environ.* 25 (2002) 239-247.

[8] Abdulhamid H., Fridell E., Skoglundh M. (20049. *Catal. Today* 30/31 (2004) 161-168.

[9] Bellotto M., Rebours B., Clause O., Lynch J., Bazin D., Elkaïm E. (1996). Hydrotalcite decomposition mechanism: a clue to the structure and reactivity of spinel-like mixed oxides. *Journal of Physical Chemistry* 100 (1996) 8535-8542.

[10] Sánchez-Cantú M., Pérez-Díaz L.M., Hernández-Torres M. E., Cruz-González D. and Tepale-Ochoa N. (2009). MOX, un método sencillo y económicamente viable para la obtención de la Hidrotalcita. *Superficies y Vacío* 22(3) (2009) 1-5.

[11] Zeng H., Feng Z., Deng X. and Li Y. (2008). Activation of Mg-Al Hydrotalcite catalysts for transesterification of rape oil. *Fuel* 87(3071) (2008) 13-14.

[12] Yan Y., Yu Y. B., He H. and Zhao J. J. (2012). *J. Catal.* 293(2012) 13-26.

[13] Dubanin Zhur M. M. (1960). *Phys. Chem.* 34, 959(1960); *Chem. Rev.* 60, 235 (1960).

[14] Gregg S.J. and Sing K. S. W. (1982). Adsorption, surface area and porosity. 2ed. Academic Press (1982) 25.

[15] Xu G., Ma J., He G., Yu Y. y He H. (2017). An alumina-supported silver catalyst with high water tolerance for H_2 assisted C_3H_6-SCR of NOx. *Applied Catalysis B: Environmental* 207 (2017) 60–71.

[16] Hernández-Terán M. E. and Fuentes G. A. (2014). Enhancement by H_2 of C_3H_8-SCR of NOx using Ag/γ-Al_2O_3. *Fuel* 138 (2014) 91–97.

[17] Zhang R. and Kaliaguine S. (2008). Lean reduction of NO by C_3H_6 over Ag/Al_2O_3 derived from Al_2O_3, Al_2OOH an Al $(OH)_3$. Applied Catalysis B: Environmental 78(2008) 275-287.

[18] She X. and Flytzani-Stephanopoulos M. (2006). The role of Ag–O–Al species in silver–alumina catalysts for the selective catalytic reduction of NOx with methane. *Journal Catalysis* 237(2006) 79-93.

[19] Wichterlova B., Sazama P., Breen j. P., Burch R., Hill C. J., Capek L. and Sobalik Z. (2005). *Journal Catal*. 235(2005) 195-200.

[20] R. Lanza, E. Eriksson, L.J. Pettersson. NOx selective catalytic reduction over supported metallic catalysts. Catalysis Today (2009), 147S, S279–S284.

E071. BULK NANOSTRUCTURED MAGNESIUM ALLOYS FOR HYDROGEN STORAGE

M. Osorio-García[1*]; J. L. Carrillo-Bucio[2]; R.Y. Hernández Jiménez[3]; A. Tejeda Ochoa[4,5]; N. Torres[1]; O. Hernández Silva[1]; Y. Todaka[5]; K. Suárez-Alcántara[2]; C. Casas Quesada[6]; J.M. Cabrera[6]; J. M. Herrera-Ramírez[4]; B. Zeifert[3]; J. G. Cabañas Moreno[1]

[1]CINVESTAV-IPN, Cd. de México, México. [2] IIM-UNAM, Morelia, Michoacán. [3] ESIQIE-IPN, Cd. de México, México.

[4]CIMAV, Chihuahua, Chihuahua. [5]Toyohashi University of Technology, Toyohashi, Japan. [6] Universitat Politècnica de Catalunya, Barcelona, España.

* mayara.osorio@cinvestav.mx

ABSTRACT

Powders of Mg, Ni and Nb_2O_5, with a nominal composition Mg-5wt.%Ni-2wt.%Nb_2O_5, are mixed by ball milling and the mixture is used to produce bulk ultrafine grain and nanostructured materials (BNM) by high pressure torsion (HPT). In this way, the reactivity of fine powders is avoided. The powder mixture has been subjected to 10 or 20 turns in an HPT system at room temperature under a pressure of 3 or 5 GPa to produce consolidated disks of 10 mm diameter. The composition and microstructure of these HPT-processed alloys are then characterized by SEM, TEM, and hydrogenation experiments. Our results show a remarkable improvement in the kinetics of hydrogenation of the HPT materials compared to the initial powder mixtures. Additional experiments have been performed to explore the hydrogenation behavior in repeated cycles at different temperatures.

Keywords: hydrogen storage; ultrafine grain and nanostrucured Mg alloys; HPT

1. Introduction

Hydrogen is a promising alternative energy carrier because of its prominent advantages, such as high energy density and environmental friendliness. As a medium for hydrogen storage, Magnesium has been extensively studied because of its notable advantages, namely, high gravimetric capacity (7.6%

by mass), low density and low cost [1]. However, the hydrogenation and dehydrogenation processes of the Mg/MgH_2 system normally require temperatures higher than 300 °C, and the reactions are slow [2].

An improvement in the kinetics of hydrogenation / dehydrogenation reactions is possible with the use of catalysts, because the addition of catalysts favors the dissociation and recombination of the H2 molecule [3,4]. It has been shown that the hydrogen release rate from MgH_2 can be significantly improved by the introduction of small amounts of Ni and Nb_2O_5 [5-7]. Our group has been developing a material with a nominal composition of Mg-5wt.%Ni-2wt.%- Nb_2O_5.

The usual strategy to optimize the performance of systems based on Mg alloys has been the reduction of the grain size, which helps to destabilize the MgH_2 phase and shortens the diffusion routes. On the other hand, Mg and MgH_2 readily react with oxygen, moisture and carbon dioxide with the ensuing degradation of their hydrogen storage properties. This undesirable behavior is more damaging the finer the particle size and the larger the exposed surface area. The techniques of severe plastic deformation (SPD) are well known for their potential to produce consolidated materials with ultrafine grains for a variety of metal systems [8]. SPD describes a group of plastic deformation techniques in which very large deformations are imposed without introducing significant changes in the overall dimensions of the piece. By means of SPD techniques, it is even possible to obtain bulk nanostructured materials (BNM), in which the exposed surfaces are minimized, preventing the materials from reacting with the environment. The most common SPD techniques are high pressure torsion (HPT) [9] and equal channel angular pressing (ECAP) [10]. In this work we report results of material processed by HPT.

2. Materials and Methods

2.1. Powder mixtures

A mixture was prepared from powdered reagents of Mg (AlfaAesar, -325 mesh, 98%), Ni (Sigma-Aldrich, <100nm, avg, 99%) and Nb_2O_5 (Sigma-Aldrich, 99%). Mixture preparation was carried out using a planetary ball mill under N_2 atmosphere, with grinding bowls (250 mL) and balls (radius of 5 mm) made of stainless steel. A total amount of 30 g of powders was milled with 1 mL of methanol at 250 rpm for 60 minutes using a 5:1 ball-to-powder mass ratio. The mixture had a nominal composition of Mg-5wt.%Ni-2wt.% Nb_2O_5.

2.2 HPT processing

For the manufacture of BNMs, powders were initially cold compacted and subjected to 10 and 20 turns at 0.2 rpm under a compression stress of 3 and 5 GPa. We produced consolidated disks of approximately 10 mm in diameter and 1 mm in thickness.

2.3 Characterization

The composition and structure of all the materials used in this study were characterized by SEM, TEM and XRD. A Sievert-type measurement system was employed for the characterization of the hydriding and dehydriding properties of Mg-5Ni-2Nb_2O_5 [11]. The hydriding measurements were performed at 25 bar and different temperatures to explore the kinetics of hydrogen capture under these conditions.

3. Results and Discussion

3.1 Microstructure before the HPT process

Fig. 1 shows an SEM micrograph (BSE signal) of the Mg-5Ni-2Nb_2O_5 mixture after 1 h of milling. There are bright agglomerated particles in this field of view. The particle size is on average of approximately 1 µm for Ni and 100 nm for Nb_2O_5, sizes that correspond to that of the initial reagents. This is consistent with a short grinding time, since the goal was only to disperse these powders in the larger Mg particles (dark grains in Fig.1).

3.2 Microstructure after the HPT process

Fig. 2a shows an SEM micrograph (SE signal) of the surface of a sample of Mg-5Ni-2Nb_2O_5 after undergoing 20 turns under 3 GPa. From the X-Ray maps obtained from this area of the sample (Figs. 2b,c), it is shown that Ni and Nb_2O_5 are still agglomerated in the consolidated material. Lamella of about 5.7 x 3.3 µm were prepared by FIB from a sample that was subjected to 20 turns under 3 GPa.The lamellae were taken from two different locations on the sample: near the center and at about 1850 µm from the edge of the HPT disk. These lamellae were prepared to observe the size of the grains after HPT processing. At the center of the disk, Fig. 3a shows a microstructure characteristic of heavily

deformed grains of sizes in the range 100 to 200 nm. However, closer to the edge, it was possible to observe grains smaller than 100 nm, as seen in Fig. 3b.

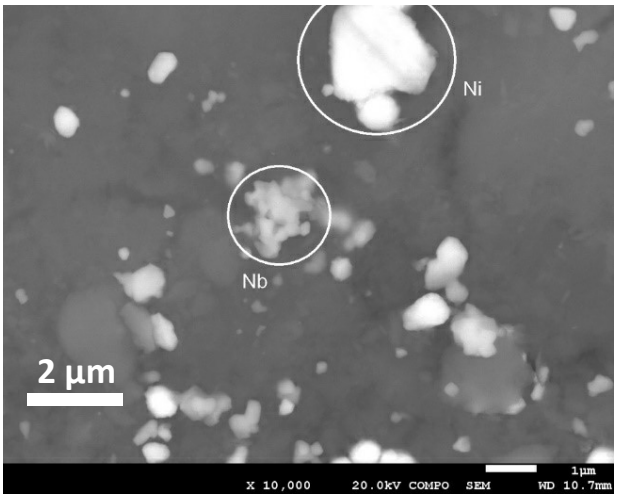

Fig. 1. SEM micrograph (BSE signal) of the Mg-5Ni-2Nb_2O_5 mixture after 1 h of milling.

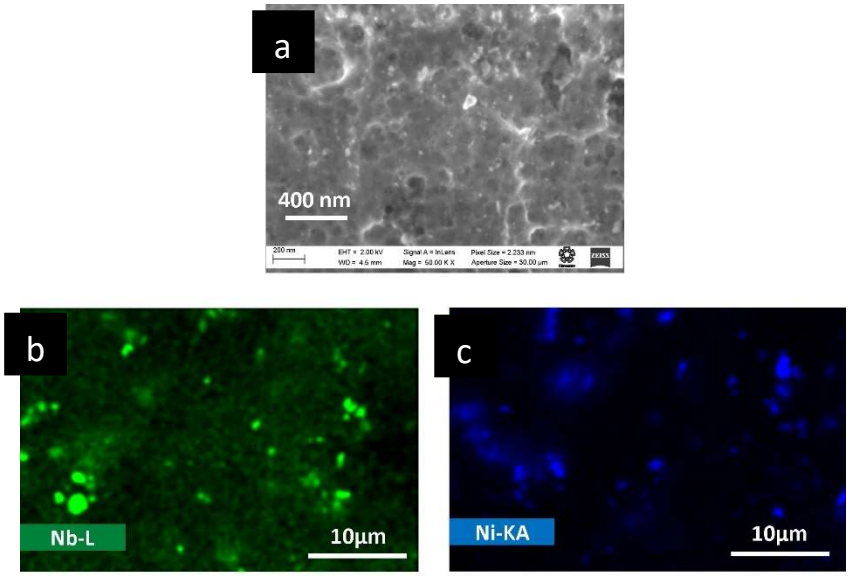

Fig. 2. (a) SEM micrograph (SE signal) and (b,c) X-Ray maps of the consolidated mixture after HPT processing (20 turns under 3 GPa).

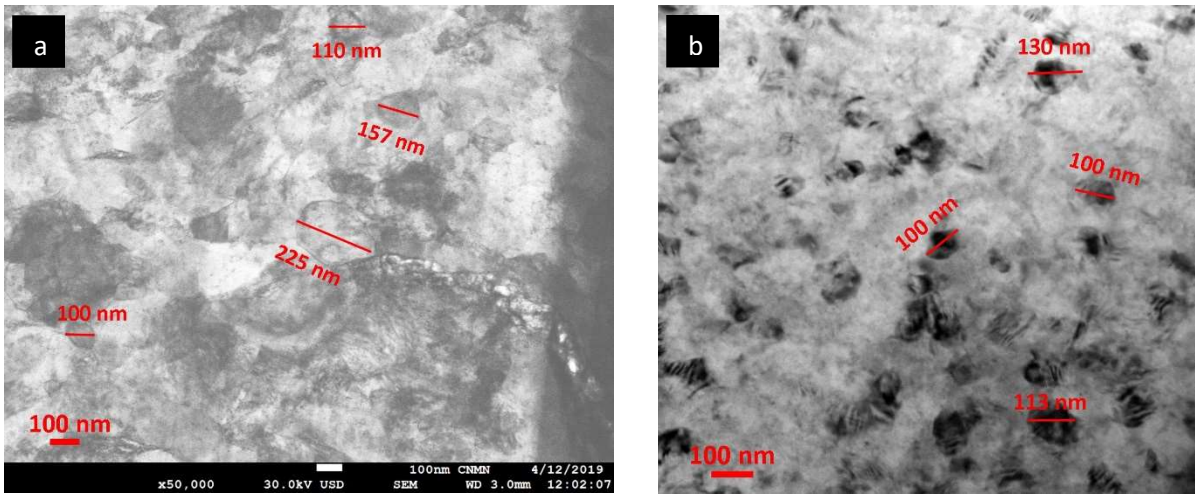

Fig. 3. (a) STEM image ,near the center of the HPT disk; (b) TEM image close to the edge of the HPT disk

3.3 Hydrogenation and dehydrogenation tests

The graphs presented in Figs.4 and 5 correspond to hydrogenation tests performed at different temperatures and a pressure of 25 bar H_2. In our protocol, tests start with a system initially under vacuum for 3 h, followed by an activation treatment at 375 °C under 25 bar of H_2. All dehydrogenation tests were performed at 350 °C and 1 bar (equilibrium pressure at 350 °C is 5 bar) [12], so that a complete release of H_2 from the material could be accomplished before further hydrogenation. Details of the dehydrogenation tests are not shown in this report.

Fig. 4a corresponds to the powder mixture; one can observe that as the temperature decreases from 350 °C to 100 °C the storage capacity decreases, from 5.3 to ~ 0.4 wt.% H_2. On the other hand, in the mixture processed by HPT (Fig. 4b) the maximum H_2 content is almost the same (~ 4.5%) for temperatures between 200 and 350 °C. In comparison with the as-milled powders, the HPT-processed alloys also show an improvement in hydrogenation kinetics. In the case of the HPT material, the maximum amount of H_2 capture is reached after ~40 min from the beginning of the hydrogenation experiments, while for the powder material (Fig. 4a) the maximum storage capacities are observed after ~120 min. In addition, it is important to mention that hydrogenation experiments with consolidated material could be performed down to 100 °C, with the material still displaying considerable storage capacity (3 wt.% H_2). This did not happen with as-milled powders (Fig. 4a).

Some hydrogenation experiments were carried out in repeated cycles at a fixed temperature of 200 °C in order to explore the cyclic behavior of the material and the results are reported in Fig. 4c. In this case, it is observed that after the 4th cycle the hydrogenation behavior is reproducible. Additionally, when comparing these curves with the one shown for 200 °C in Fig. 4b, a similar behavior is observed.

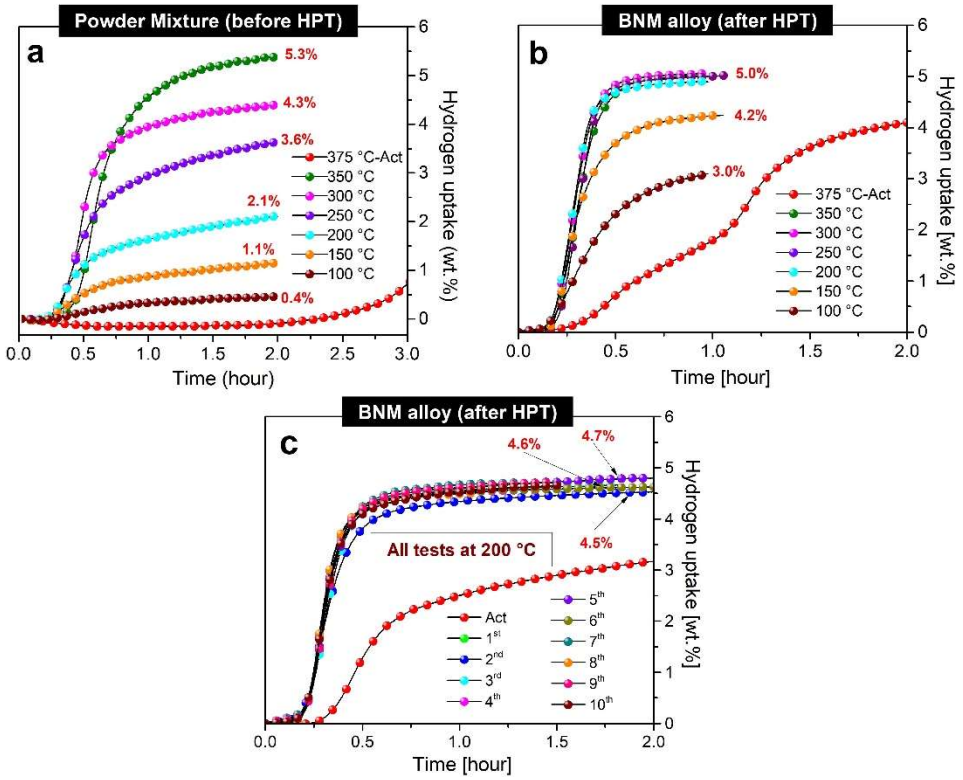

Fig. 4. Hydrogenation curves of (a) powder mixture and (b, c) after 20 turns under 3GPa.

Fig. 5a shows hydrogenation curves at temperatures from 350 to 100 ° C, while in Fig. 5b another set of curves are reported for temperatures of 300, 200 and 100 ° C, the latter corresponding to experiments done on the same sample *after* the tests shown in Fig. 5a. The results of Fig. 5b show that it is possible to recover storage capacity after several hydrogenation processes, even after experiments at low temperatures (which give lower capacities). Comparing both sets of data in addition to those shown in Fig. 4, it is evident that the storage capacity is basically a function of temperature in our samples.

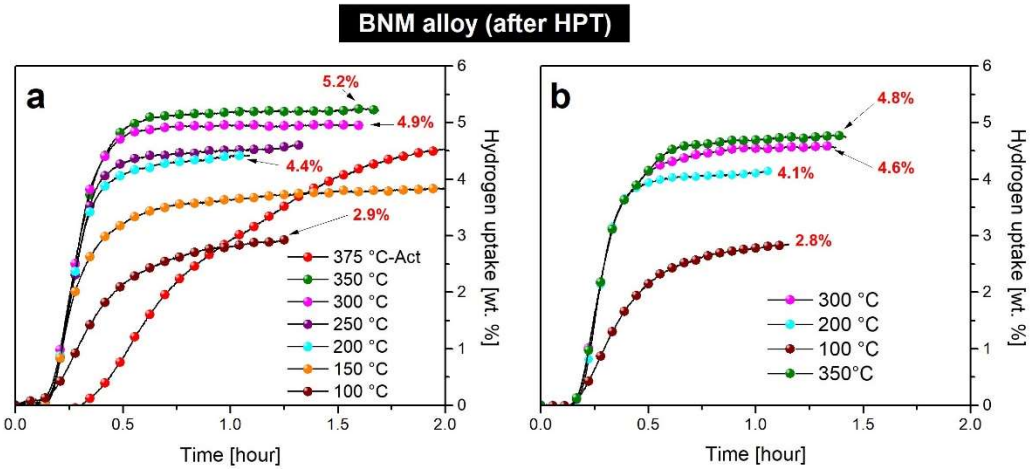

Fig. 5. Hydrogenation tests after 10 turns under 3 GPa. (a) Tests run from 375 to 100°C; (b) tests run after the experiments in (a).

4. Conclusions

The HPT-processed alloys show a improvement in hydrogenation kinetics when compared to the initial powder mixtures; this indicates an effect of the plastic deformation incurred during HPT processing. Hydrogenation at temperatures as low as 100°C has been recorded for the Mg alloys under study, although with maximum storage capacities of ~5wt.%, these capacities are only slightly greater than half the theoretical limit for these materials (7.6 %). Hydrogenation at temperatures as low as 100 °C has been recorded for the HPT-processed magnesium alloys under study. The storage percentage of H_2 seems to depend mainly on the temperature at which the material is hydrogenated and it is reproducible during cycling, at least at a fixed temperature of 200 °C. In addition, it is also possible to recover the capacity associated to a specific temperature after hydrogenation experiments at different temperatures.

Acknowledgements

This work is supported by CONACYT (grant 6072 and graduate scholarship CVU 710507) and Cinvestav-IPN. The HPT process was performed at Prof. Y. Todaka's lab in TUT (Japan). We are grateful

to Drs. H. Martinez and R. Borja from CNMN-IPN for support with SEM and TEM observations, and to Dr. A. Angeles from LANE-Cinvestav-IPN for FIB work. The hydrogenation experiments were performed at IIM-UNAM, Morelia campus.

References

[1] Amira S., Huot J. Effect of cold rolling on hydrogen sorption properties of die-cast and as-cast magnesium alloys. Journal of Alloys and Compounds 2012; 520: 287-294.

[2] Zhang, Jiguang, et al. Controllable fabrication of Ni-based catalysts and their enhancement on desorption properties of MgH_2. Journal of Alloys and Compounds 2017; 715: 329-336.

[3] Wang H., Lin H. J., Cai W. T., Ouyang L. Z., Zhu, M. Tuning kinetics and thermodynamics of hydrogen storage in light metal element based systems–a review of recent progress. Journal of Alloys and Compounds 2016; 658: 280-300.

[4] Webb C. J. A review of catalyst-enhanced magnesium hydride as a hydrogen storage material. Journal of Physics and Chemistry of Solids. 2015; 84: 96-106.

[5] Liu T., Zhang T., Qin C., Zhu M., Li, X. Improved hydrogen storage properties of Mg–V nanoparticles prepared by hydrogen plasma–metal reaction. Journal of Power Sources 2011; 196(22): 9599-9604.

[6] Lototskyy M., Sibanyoni J. M., Denys R. V., Williams M., Pollet B. G., Yartys, V. A. Magnesium–carbon hydrogen storage hybrid materials produced by reactive ball milling in hydrogen. Carbon 2013; 57: 146-160.

[7] Hong S. H., Kwon S. N., Bae J. S., Song, M. Y. Hydrogen-storage properties of gravity cast and melt spun Mg–Ni–Nb_2O_5 alloys. International journal of hydrogen energy 2009; 34(4): 1944-1950.

[8] Panda S., Toth L., Zou J., Grosdidier T. Effect of strain heterogeneities on microstructure, texture, hardness, and H-activation of high-pressure torsion Mg consolidated from different powders. Materials 2018; 11(8): 1335.

[9] Kusadome Y., Ikeda K., Nakamori Y., Orimo S., Horita, Z. Hydrogen storage capability of MgNi2 processed by high pressure torsion. Scripta Materialia 2007; 57(8): 751-753.

[10] Huot J., Skryabina N. Y., Fruchart D. Application of severe plastic deformation techniques to magnesium for enhanced hydrogen sorption properties. Metals 2012; 2(3):329-343.

[11] Carrillo-Bucio J. L., Tena-Garcia J. R., Armenta-Garcia E. P., Hernandez-Silva O., Cabañas-Moreno J. G., Suárez-Alcántara K. (2018). Low-cost Sieverts-type apparatus for the study of hydriding/dehydriding reactions. HardwareX 2018; 4: e00036.

[12] Abdessameud S., Mezbahul-Islam M., Medraj M. Thermodynamic modeling of hydrogen storage capacity in Mg-Na alloys. The Scientific World Journal 2014; 2014: 1-16.

E081. A PREGNANCY TEST POWERED BY A PAPER-BASED MICROFLUIDIC FUEL CELL USING THE URINE SAMPLE AS FUEL

C. Romero-Camacho[1], J. Gamboa[2], S. Ríos-Ugalde[1], J. M. Olivares-Ramírez[1], D. Ortega-Díaz[3], C. Goyes[4], D. Dector[3], A. Dector

[1]*Universidad Tecnológica de San Juan del Río, San Juan del Río, Querétaro, México*
[2]*Instituto Tecnológico de Estudios Superiores de Coatzacoalcos, Coatzacoalcos, Veracruz, Mexico*
[3]*Instituto Tecnológico de San Juan del Río, San Juan del Río, Querétaro, Mexico*
[4]*CONACYT – Universidad Tecnológica de San Juan del Río, Querétaro, Mexico*
[5]*Universidad Autónoma de Occidente, Valle del Lili, Cali, Colombia*
[6]*Centro de Investigación en Materiales Avanzados, Chihuahua, Chihuahua, Mexico*
andres_dector@live.com

ABSTRACT

Researches directly to the integration of paper-based microfluidic fuel cells (paper-based μFC´s) towards the creation of autonomous lateral flow assay have called attention. This can be possible to use electrodes that oxidise the test sample that contains the anolyte i.e. human blood, sweat or urine. In this work a paper-based microfluidic fuel cell was developed and powered by human urine and integrated in a pregnancy test. During pregnancy test evaluation, a paper-based μFC was testing; this obtained a voltage, a maximum current density and a maximum power density of ~ 1.6 V, 1.00 mA cm^{-2} and 0.37 mW cm^{-2} respectively, using the same human urine sample as fuel, TiO_2-Ni as an anode and Pt/C as cathode. The results of this work demonstrated that a paper-based μFC could be integrated in a pregnancy test and usefulness as a possible power supply to employ the urine sample.

Keywords: paper-based; microfluidic; evaluating; pregnancy

1. Introduction

The paper used for microfluidic systems has been recently incorporated [1] with application mainly in the area of chemical analysis for their versatility in material-type and design at a low cost. This device is lateral flow assay (LFA) type, which allows for capillary flow across the paper without needing an external device, for example, a pump or capillary electrophoresis. The main application of LFA is

biomedical systems for the detection of enzymes, nanomaterials, immunoassay, in the detection of foodborne contaminants and recently in fuel cells [2].

In this sense, the paper-based microfluídic fuel cells (PμFCs) are one of the emerging technologies in the development of devices at low cost, efficient, portable and simple construction for power generation [3]. Another major advantage is unnecessary to use pumps, allowing the autonomously flow to passive diffusion of fuel and oxidant solutions across fibers and pores in the paper, ensuring the laminar flow since the length of the paper resulting Reynolds number in the order of 10-3 [4].

Using PμFCs, interesting results have been reported by J.P Esquivel et al. in a paper-based fuel cell that uses abiotic catalyst and methanol as fuel, achieving an OCP of 0.52 and a current and power density of 15.5 mA cm^{-2} and 3.2 mW cm^{-2} respectively using 4 M methanol [3]. A similar system was reported by the working group of S. Chakrablory for formic acid as fuel, reporting an OCP maximum of 0.33 V and a current density of 660 mA cm^{-2}, highlighting the idea that in the cathode the oxygen is taken from air as the fuel cell type air-breathing [5]. On other hand, in biofuel cell (BFC) has been reported the use of cellulose paper-based microfluidic systems for immobilizing glucose dehydrogenase (GDH) in the anode and bilirubin oxidase (BOx) in the cathode on paper Toray obtaining an OCP of 0.62 V and a maximum current of 1 mA and power 0.08 mW mg-1 GDH using 100 mM glucose for a single BFC [6]. In this sense, the versatile design of the PμFCs, allows the coupling of external devices with low energy requirement for its functioning like has been reported for other fuel cells and within the PμFCs has the ability to integrate its a system of quantitative or semi-quantitative analysis colorimetric to a molecule of interest, similar in microfluidic paper-based analytical devices (μPADs), has been done for glucose, urine, pH, lactate, ammonium and uric acid.

In this work, we showed an original, simple and efficient paper-based microfluídic fuel cell of lateral flow that incorporates Toray paper as an electrode for deposition of TiO2-Ni in the anode and Pt/C in the cathode for urea oxidation using human urine as a fuel source, and that has been integrated into a pregnancy test. Demonstrating that the same sample for analysis could be used to provide power to some analytical devices.

2. Materials and Methods

Electrode fabrication

The anode and cathode electrodes consisted of pieces of Toray® porous paper electrode (Technoquip Co Inc. TGPH-120) with dimensions of 0.5 x 10 mm. The electrodes were covered with an ink containing

7 μL of Nafion® 5% (Sigma Aldrich), 73 μL of isopropyl alcohol (J. T. Baker) and 1 mg of TiO_2-Ni (synthesized in the working group) or commercial Pt/C (30 wt. % on Vulcan XC-72 from E-TEK), which were deposited using an airbrush with a final loading of 1 mg cm^{-2} over the entire surface.

Human urine sample preparation

The device used in this work was based on the oxidation of urea from human urine for energy production. Since the device included an air-breathing fuel cell, the limiting reagent participated in the reaction because it received ambient oxygen. Human urine sample was extracted from a male volunteer using a completely clean (sterile) container.

Paper-based micro fluidic fuel cell assembly process.

The paper-based microfluidic fuel cell was constructed with the use of a Clearblue digital pregnancy test. To modify this pregnancy device, the anode and cathode electrodes, both with a 5 x 5 mm contact area, were placed at the bottom and top, respectively, of the reaction paper strip to form a sandwich arrangement. In this case, the cathode was attached on the top to facilitate oxygen access.

The voltage and current were measured using a Zahner Zennium potentiostat/galvanostat. The reported current and power densities were calculated according to the planar geometric area of the electrodes exposed to the microchannel (0.25 cm^2). A set of polarisation and power density curves were created, and the one that best described the performance was shown.

3. Results and Discussion

TiO_2-Ni Characterization

One method used to determine the size of TiO_2/Ni particles was scanning electron microscopy (SEM). Two of the images obtained by this technique are shown in Figure 1.

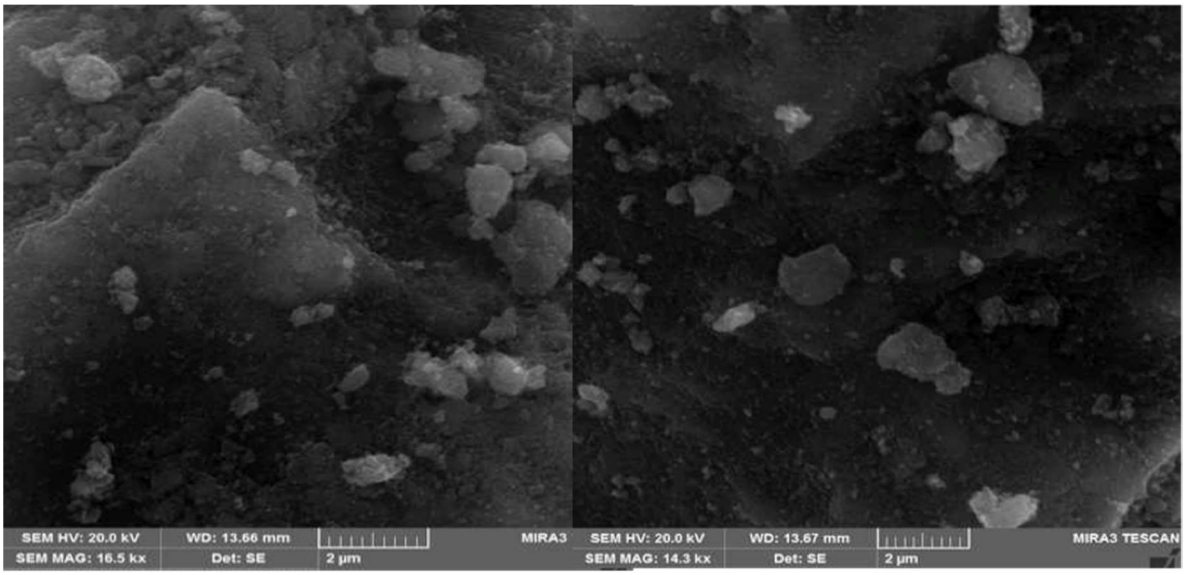

Fig. 1. Scanning Electron Microscopy (SEM) of TiO_2/Ni.

The images show particles with both spherical and elongated geometries with dimensions that are between 50 and 200 nm. This increase in particle size may be related to the formation of the composite, since the deposited Ni can serve as a bridge to join two or more TiO_2 particles, also with the process of drying the samples since it is known that the heating induces particle aggregation.

Anatase and brookite crystalline phases were identified in the synthesized TiO2/Ni nanoparticles by XRD analyses (Figure 2), these same crystallographic phases were identified for TiO_2 in a previously published article [7]. Interplanar spacing was estimated using JCPDS files 29-1360 (brookite) and 21-1272 (anatase). A detailed analysis of Figure 2 exposes a set of characteristic signals for 2θ at 36°, 38°, 40°, 48°, 54°, and 55°, which seem to be the anatase (103), (004), (112), (200), (105), and (211) crystallographic planes, respectively. Furthermore, the same review indicates another set of five characteristic signals localized at 2θ of 31°, 42°, 46°, 49°, and 57°, which should correspond to brookite planes (121), (221), (032), (132), and (113), respectively. Crystallite size determined for anatase and brookite by the Rietveld analysis were 11 and 16 nm, respectively. Additionally, an intense signal was localized at 2θ = 25°, which can be correlated with the overlapping of the diffraction planes (120) and (101), for brookite and anatase, respectively. Diffraction peak at 2θ = 59° belongs to the crystallographic plane (110) that can be indexed to the standard data of hexagonal $Ni(OH)_2$ (marked by a circle, JCPDS 14-0117), which confirmed the

successful fabrication of TiO_2/Ni. Also, crystallite sizes determined for $Ni(OH)_2$ by the Rietveld analysis were 5.2 nm.

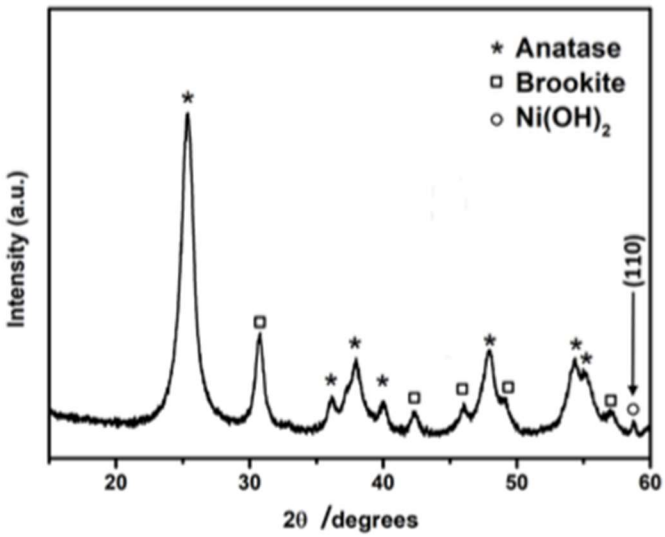

Fig. 2. XRD patterns for synthetized TiO_2-Ni nanoparticles. The peak at 59º represents the crystallographic plane (110) belonging $Ni(OH)_2$.

Electrochemical measurements

All fuel cell tests were performed using a micropipette with 15 µL for the urine. When the urine was deposited on the paper strip this showing the capillary action, at the time that the paper absorbs the urine, about 10 seconds, this make contact with both electrodes thus generating as shown the typical polarization curves for this paper-based micro fuel cell (Figure 3), which yielded an open circuit voltage and maximum power density around of 1.5 V and ~ 1.6 V, and 0.135 mW cm^{-2} and 0.37 mW cm^{-2}, for TiO_2 and TiO_2-Ni respectively; meanwhile the maximum current density was 0.5 mA cm^{-2} and 1.0 mA cm^{-2} (table 1).

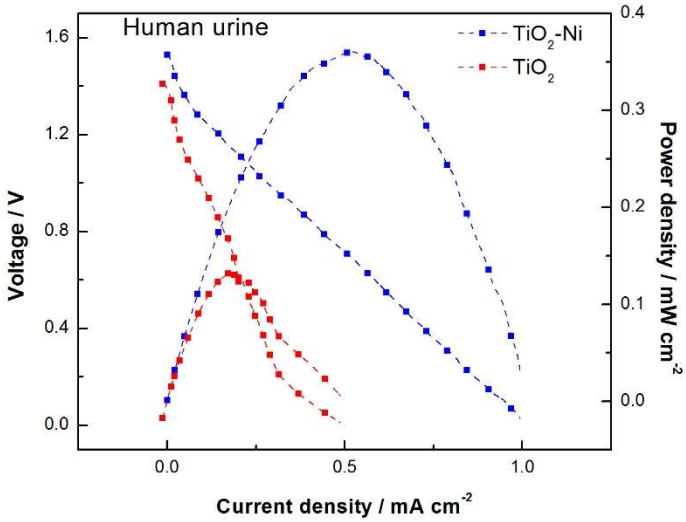

Fig. 3. Polarization and power density curves for the paper-based microfluidic fuel cell for pregnancy testing with a TiO_2-Ni anode and a Pt/C cathode in human urine at 25 ºC under atmospheric pressure.

Table 1. Paper-based microfluidic fuel cell performance using TiO2 or TiO2-Ni as anode for urine oxidation.

Anode	Cathode	OCP (Volt)	Current density (mA cm^{-2})	Power density (mW cm^{-2})
TiO_2	Pt/C			
TiO_2-Ni	Pt/C	~ 1.6	1.0	0.37

Finally, chronoamperometric studie was performed to demonstrate the stability of the paper-based microfluidic fuel cell (Fig. 4). The chronoamperometric measurement was carried out at 0.8 V (potential corresponding to the maximum power density, shown in Fig. 3) for the paper-based micro- fluidic fuel cell. The resultant curve indicates that the paper-based micro fluidic fuel cell performance decreased over time due to drying of the urine on the paper strip.

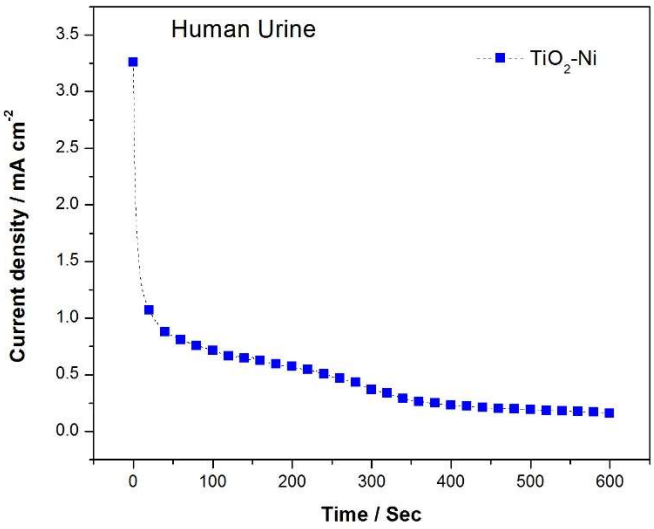

Fig. 4. Current density as a function of time at 0.30 V, for the paper-based microfluidic fuel cell with human blood transversal flow.

4. Conclusion

Present a brief conclusion of the main results obtained during your research highlighting the importance of the results. Avoid adding discussions of data obtained, if needed, an extra section including discussion can be placed before the conclusions.

The polarization curves demonstrated that the paper-based microfluidic fuel cell could generate power from urea available in the urine sample and operate with a single urine flow because oxygen is obtained from the atmosphere. Although, the generated power is insufficient for lighting a display, the combination of an appropriate number of connected electrodes to obtain the desired power in future designs is suggest.

Acknowledgements

Authors want to thank to CONACYT through project: Cátedra CONACYT project 513.

References

[1] Andres W. Martinez, Dr. Scott T. Phillips, Dr. Manish J. Butte, and Prof. George M. Whitesides. Angew Chem. *2014, Patterned Paper as a Platform for Inexpensive, Low Volume, Portable Bioassays*, Int Ed Engl ; 46 (8): 1318- 1320.

[2] Muhammad Sajid, Abdel-Nasser Kawde, Muhammad Daud. 2014, *Designs, formats and applications of lateral flow assay: Journal of Saudi Chemical Society.*. In Press, Corrected Proof.

[3]J. P. Esquivel, F. J. Del Campo, J. L. Gómez de la Fuente, S. Rojas and N. Sabaté. 2014, *Microfluidic fuel cells on paper: meeting the power needs of next generation lateral flow devices. Energy Environ. Sci.*, 7, 1744-1749.

[4] Osborn JL, Lutz B, Fu E, Kauffman P, Stevens DY, Yager P. Lab Chip. 2010 Oct 21; 10(20). Microfluidics without pumps: reinventing the T-sensor and H-filter in paper networks. Pp. 2659.65.

[5] Ravi Kumar Arun, Saurav Halder, Nripen Chanda and Suman Chakraborty. 2014, *A paper based self-pumping and self-breathing fuel cell using pencil stroked graphite electrodes*. Lab Chip, 14, 1661-1664.

[6] Gonza lez-Guerrero MJ, Del Campo FJ, Esquivel JP, Giroud F, Minteer SD, Sabate N. 2016, *Paper-based enzymatic microfluidic fuel cell: from a two-stream flow device to a single-stream lateral flow strip*. J Power Sources; 326:410e6.

[7] D. Ortega-Díaz, D. Fernández, S. Sepúlveda, R.R. Lindeke, J.J. Pérez-Bueno, E. Peláez-Abellán, J. 2018, Manríquez, *Preparation of nanoparticulate TiO2 containing nanocrystalline phases of anatase and brookite by electrochemical dissolution of remelted titanium components*. Arabian Journal of chemistry. DOI:10.1016/j.arabjc.2018.07.015.

E082. GREEN SYNTHESIS OF PLATINUM NANOPARTICLES AND CARBON FROM *SARGASSUM SPP.* FOR ELECTROCHEMICAL APPLICATIONS

D. Rosas Medellín[1], B. Escobar[2,*]

[1] Centro de Investigación Científica de Yucatán, A.C. Calle 43 No 130, Col. Chuburná de Hidalgo, C.P.97200, Mérida, Yucatán, México.

[2] Centro de Investigación Científica de Yucatán, A.C. Calle 43 No 130, Col. Chuburná de Hidalgo, C.P.97200, Mérida, Yucatán, México.

* 9993514293 beatriz.escobar@cicy.mx

ABSTRACT

Given the troublesome waste biomass deposited in the Caribbean beaches Sargassum spp. which generates tons of organic decomposing material thus affects the tourist sector and the ecosystem so it seems imperative the proper use of this waste. The aim of this work is the development of a new carbon based with platinum nanoparticles catalyst for PEM fuel cells, obtained through a process of pyrolysis of the waste biomass Sargassum spp. then adding the previously green synthesized platinum nanoparticles with the same waste biomass, the final product is a carbon based catalyst with 20% load of platinum nanoparticles. The nanoparticles were synthesized with a sample of Sargassum spp. through a process of drying, milling and sieve, then boiled in deionized water and put in reaction with a solution of PtCl4, the nanoparticle formation was confirmed with a UV-vis analysis. Aside a sample of the milled and sieved Sargassum spp. was activated with KOH and then pyrolyzed in a nitrogen atmosphere; the resulting carbon has a surface area of 2289 m^2 g^{-1}. The nanoparticles where deposited on the carbon via ultrasound bath in an ethanol solution, the crystal formation of the nanoparticles where characterized with a DRX analysis which showed a crystal size between 9-10nm using Scherrer equation, a TEM analysis showed a very well dispersed nanoparticle formation on the carbon and an average nanoparticle size near 3nm. Finally, the newly synthesized electrocatalyst was characterized with a cyclic voltammetry in acidic media delivering a current density up to 30mA cm-2 superior than with the commercial catalyst of 20%Pt-Vulcan XC72, then the kinetic reaction was calculated using the Koutecky-Levich equation in several linear voltammetry using a rotating disk electrode at different rotation speeds which showed that the 20% load has an average electron transfer rate of 4.2 electrons. Which is a very good efficiency compared with the commercial catalyst and also a cheaper alternative using waste biomass.

Keywords: Sargassum spp.; electrocatalyst; green synthesis; platinum nanoparticles

1. Introduction

Given the increasing need for renewable energy, one of the best means for this type of energy´s development is the use of waste biomass such as *Sargassum spp*. which is a type of brown macroalgae found to be a great problem in several beaches around the world given the massive amount of waste and odor, it has a direct impact on the tourist sector as well as in the ecosystem. It can be found in the Caribbean beaches since 2011 [1]. So it is imperative to find a proper use for this waste biomass so abundant in Mexico.

It has been proven that *Sargassum spp*. can produce a high surface area carbon up to 2289 m^2 g^{-1}, characterized as a good electrocatalyst in alkaline media [2] it hasn't been used as a support for electrocatalyst in acidic media for fuel cells such as PEMFC (Proton exchange membrane fuel cells) which are considered as promising sustainable energy conversion technologies given many advantages including a high energy conversion efficiency, quick start-up times and zero by-product emissions when operating [3], the main issue with this technology is its efficiency given by the oxygen reduction reaction (ORR) and the best catalyst for it is Platinum supported on high surface area carbon [4] however its high cost (up to 1520 USD/g of 50nm Pt) [2] makes a great deal of importance to develop new cheaper means of synthesis for this type of catalyst. The particle size of the platinum is of great importance to its efficiency in the ORR [5] and a lower cost way to achieve a smaller particle size is the new trending green synthesis of metallic nanoparticles using extract of biomass [6] such as: *Sargassum bovinum* [7], Sea grass (*Cymodocea serrulata*) [8], Mangrove plant (*Avicennia marina*) [9], *Boerhaavia diffusa* [10], *Sargassum myriocystum* [11], *Sargassum muticum* [12], *Cinnamimum camphora* [13]. In this matter we find that brown algae (the same family as Sargassum spp.) in an adequate candidate for bio reduction of ions into metallic particles given the high amount of OH ions present in this biomass, it could produce metallic nanoparticles between 5-10nm [7]. As well as the particle size, the structure and crystal planes of the platinum nanoparticles play a very important role in the catalyst behavior [14]. To our knowledge there is no know research of synthesis of platinum nanoparticles using *Sargassum spp*. extract

2. Materials and Methods

Sample

Sample of *Sargassum spp.* was obtained from the Caribbean beach of Playa del Carmen Mexico, firstly it was cleansed with sea water to remove large minerals and impurities after it was rinsed with

tapped water then with deionized water, dried for 16 hours in an oven at 80°C. Finally, it was grinded and sieved through a number 60 mesh (0.25mm).

Green synthesis of platinum nanoparticles

Using 10gr of the Sargassum spp. sample it was obtained an aqueous extract through boiling in 100ml of deionized water for 10 minutes, after cooling it was filtered and known as SE (Sargassum Extract). Then with 5ml of the SE sample and with 95ml of a solution 1mM of $PtCl_4$ mixed at 60°C with stirring for 1 hour, it was obtained the sample SPtNPs (Sargassum Platinum Nanoparticles) which were characterized with FTIR and UV-vis analysis to confirm the formation of nanoparticles, later the sample SPtNPs was dried at 80°C and put through a thermal treatment in a tubular oven at 400°C for 2 hours in a Nitrogen atmosphere after this the sample is known as SPtNPsp (Sargassum Platinum Nanoparticles powdered).

Synthesis of electrocatalyst

With the methodology described in the work of K. Y. Perez-Salcedo et al. [2] it was obtained the high surface area carbon from *Sargassum spp.* known as SKPH, then it was measured 16mg of the sample SKPH, 4mg of the sample SPtNPsp in order to obtain a 20% mass ratio, then they were mixed with 1ml of ethanol and put in a sonic bath for 2 hours, finally the sample was dried at 80°C over night and this sample its known as 20% SPtNPsp-SKPH this sample was characterized with a XRD analysis.

Then the sample 20% SPtNPsp-SKPH and 20mg of commercial catalyst 20%Pt-Vulcan XC72 were added each with 30 µL of Nafion® and 1ml of ethanol at 96% in order to obtain a catalyst ink which later were deposited in a RDE.

Physical-chemical characterization

Infrared spectra were measured with a Fourier transformed infrared spectrometer Tensor II Bruker. Ultraviolet spectroscopy analysis was carried out in a Cary 60 UV-Vis Aligent Technologies equipment. Morphological characteristics were measured by X ray diffraction analysis carried out in a Phaser 2 Bruker equipment from 10° to 80° with an increment of 0.01° every 0.5 seconds.

Electrochemical characterization

A three cell electrode cell with a Biologic VSP300 equipment was used, all measurements were performed in a 0.5M H_2SO_4 solution at 25°C, a rotating disk electrode made of glassy carbon (2mm Ø) as a working electrode, a saturated calomel electrode as a reference electrode and a platinum wire electrode as a counter electrode were used. After the ink preparation mention in the electrocatalyst section it was deposited 4.8µL of it in the working electrode. As an activation treatment, 40 cycles of cyclic voltammetry were performed from 1.2 V to 0.0 V vs. RHE at 50 mVs^{-1} then measurements were: 3 cycles of (CV) at 20 mVs^{-1} in an N_2 saturated 0.5M H_2SO_4 solution. ORR kinetics were studied by the rotating disk electrode (RDE) technique in the same electrolyte now saturated in O_2 for 25min prior the first measurement through several linear sweep voltammetry (LSV) at 5 mVs^{-1} from 1.2 to 0.0 V vs. RHE at different rotation rates (400, 800, 1200, 1600 and 2000 RPM).

3. Results and Discussion

Physical-chemical characterization

A UV-vis analysis carried out in aqueous dissolutions of the samples: SPtNPs5 (1:5), SE100 (1:100) y $PtCl_4$10 (1:10) in a sample: deionized water ratio, presented a significant peak of absorption at 265nm in the SE sample as shown in Fig. 1, which is not present in the $PtCl_4$ sample and it also disappears after the thermal treatment at 60°C in the sample SPtNPs5 which confirms the green synthesis and the formation of nanoparticles [15].

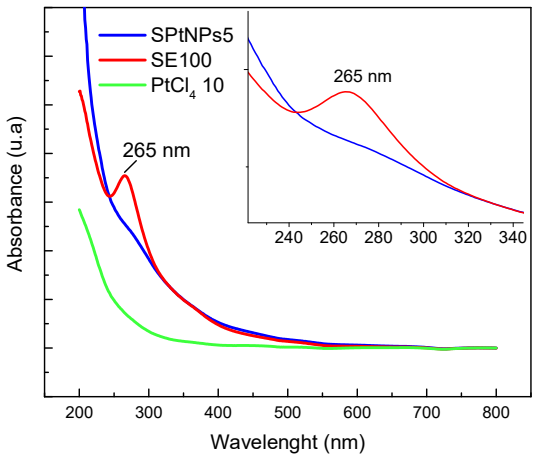

Fig. 1. UV visible spectra of SPtNPs5 (1:5), SE100 (1:100) and $PtCl_4$10 (1:10) samples.

An FT-IR was carried out to study the presence of molecules responsible of the reduction and stabilization of the synthesized PtNPs. In the Fig. 2a) it is shown the FTIR normalized spectra of the SE sample which shows main peaks at 3373.6cm^{-1} corresponding to OH groups, at 2929.8 cm^{-1} associated with sp2 C-H bonds [16], at 1586.9 and 1538.4cm^{-1} which might be from aromatic NO_2 groups and secondary anime respectively [7,16], at 1408.5cm^{-1} corresponding to C-H bonds [16], at 1258cm^{-1} related to S=O bonds, while the peak at 1076 cm^{-1} could be given by the presence of carbohydrates and polysaccharides. Finally, the peak at 617.9cm^{-1} could represent the presence of C-S and C=S bonds[17]. In the Fig. 2b) it is shown the FTIR normalized spectra of the SPtNPs sample which shows main shifts given by the formation of nanoparticles in the peak corresponding to OH groups at 3373.6 cm^{-1} in the SE sample with a shift to 3444.9 cm^{-1} which indicates that this chemical group was involved in the formation of NPs [16]. Another peak shift is found at 1586.9 cm^{-1} to 1076 cm^{-1} which shows the main responsible of the metallic reduction to polysaccharide sulfates. It is known that the same species as *Sargassum spp*. is rich in terpenoids, polyols and polysaccharides which give them the distinct aroma, and also are reported to be responsible for the reduction of metallic particles[7].

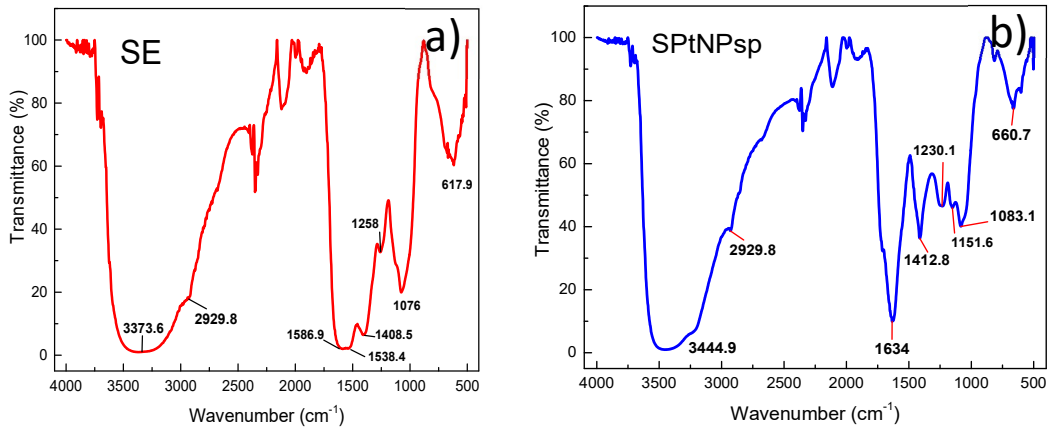

Fig. 2 FTIR Spectra of the samples: a) SE and b) SPtNPsp

An X ray diffraction analysis was carried out to determine the crystalline structure of the nanoparticles present in the sample 20%SPtNPsp-SKPH in Fig. 3a) which shows the same crystalline structure as the commercial catalyst 20%Pt-Vulcan in Fig 3b), both show well defined peaks at 40°, 46.2° and 67.7° which

correspond to the crystal planes (111), (200) and (220) respectively and it is consistent with a face cubic centered structure [18] and only for the commercial catalyst is found a peak at 25° corresponding to the

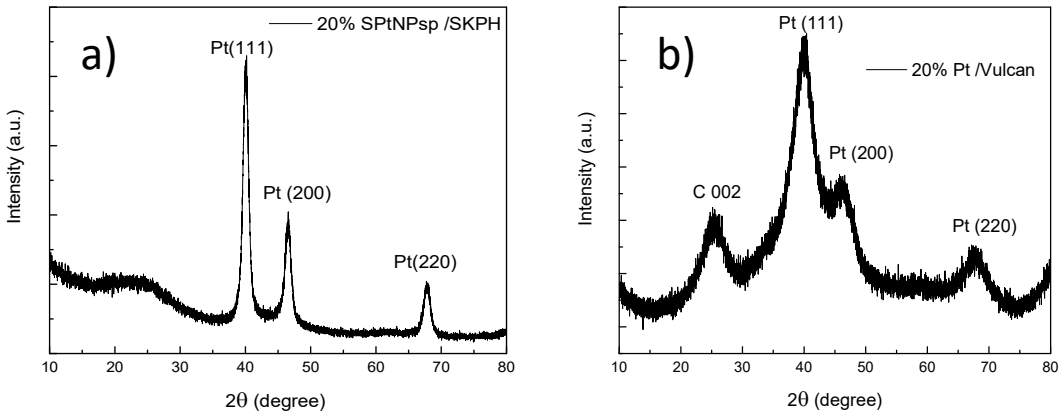

carbon crystal plane given by the carbon Vulcan XC72[18]. The crystal size was calculated using the Scherrer equation

$$D = K\lambda/\beta cos\theta \quad (1)$$

Where D is the average crystal size in Å, λ is the length of the X ray ($\lambda = 0.154056$), K is Scherrer constant ($K = 0.9$), θ is the angle at the highest point of the peak y β is the full width at half maximum [19]. The crystal size for the 20%SPtNPsp-SKPH sample was between 9.5 and 10nm and for the 20%Pt-Vulcan between 3 and 4nm.

Fig. 3. X ray diffraction spectra of the sample: a)20%SPtNPsp-SPKH and b) 20%Pt-Vulcan PDF (Pt)#00-004-0802, PDF (Graphite)#01-075-1621.

Electrochemical characterization

Cyclic Voltammetry

A cyclic voltammetry in a N2 saturated electrolyte is presented in Fig. 4a) for the commercial catalyst where it shows a couple of hydrogen absorption peaks in the potential range between 0 and 0.15V corresponding to the crystal plane (110) [20]. The ORR is present from 0.8 to 1.1 V given mainly by the

crystal plane (111) [21], and the ORR peak is consistent with the reported behavior for the commercial catalyst [19,22]. The sample 20%SPtNPsp-SKPH is presented in Fig. 4b) where different from the commercial catalyst the reduction potential range is from 0.4 to 1.1 V with a very broad peak, however it reaches up to a 30 $mAcm^{-2}$ current density in a rectangular shape which is associated with capacitance [23] and could be given by the SKPH sample which could be related to its high surface BET area (2289 $m^2\ g^{-1}$) [2,23].

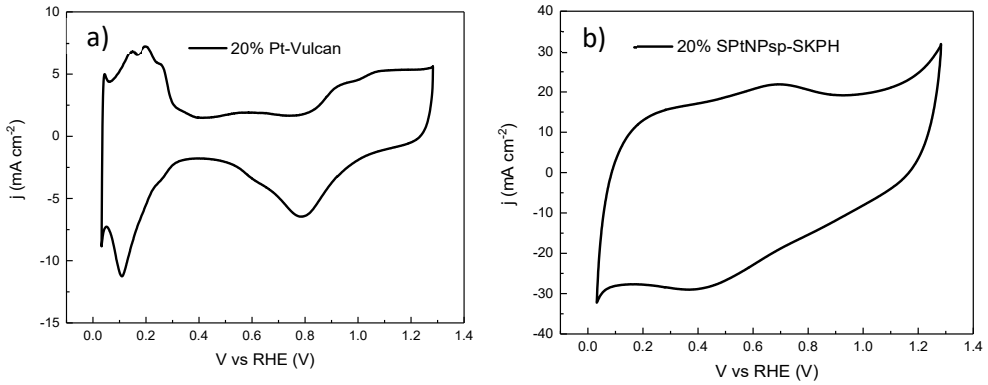

Fig. 4. Cyclic voltammetry in a 0.5 M de H_2SO_4 solution saturated with N_2 of the sample: a) 20% Pt/Vulcan. b) 20% SPtNPs-SKPH

Results should be clear and concise, avoid verbosity and repeated results. Please ensure Figures and Tables are placed next to the relevant text in the manuscript, rather than at the bottom or the top of the file. Ensure that each illustration and table has a caption. A caption should comprise a brief title (not on the figure itself) and a description of the item. Keep text in the illustrations themselves to a minimum but explain all symbols and abbreviations used.

Rotating Disk Electrode

The kinetics of the ORR was evaluated through the RDE technique using linear sweep voltammetry (LSV) at different rotation speeds in the same electrolyte saturated with O_2 shown in the Fig. 5a) for the sample 20%SPtNPsp-SKPH where it is found that the onset potential al 0.8V is different from the commercial catalyst and the limiting current density plummets from 30 to 5 $mAcm^{-2}$ which concurs with the

capacitive behavior shown in the cyclic voltammetry without speed. The number of electrons transferred in the ORR was calculated using the Koutecky-Levich equation

$$1/j = 1/jk + 1/(B\omega\text{^}(1/2)) \quad (2)$$

defined for the absolute current density value (j, mA cm-2) shown in the LSV, the kinetic current (j_k), the electrode rotation rate (w, RPM) and (B) correspond to the slopes of the Koutecky-Levich plots which are shown in Fig. 5b). B could also be defined as

$$B = 0.2nFAD\text{^}(2/3)\, v\text{^}(-1/6)\, C\text{^}0 \quad (3)$$

Where the electrons transferred number per O2 molecule is given by n, the Faraday constant by 96485 C mol^{-1}, the O2 diffusion coefficient for the 0.5M H_2SO_4 solution is $D = 1.7x10^{-5}cm^2 \cdot s^{-1}$,$C_0$ is the O2 global concentration $C_{O_2} = 1.1x10^{-6}mol \cdot cm^{-3}$and n is the electrolyte kinetic viscosity is $v = 9.87x10^{-3}cm^2 \cdot s^{-1}$ [19].The Koutecky-Levich plots were measured at a potential range between 0.65 a 0.45V and it was calculated an average n of 4.2 electrons, which indicates a direct reduction from O_2 to H_2O as well as the commercial catalyst which as an average n of 4 electrons, the slight higher electron average for the 20%SPtNPsp-SKPH sample could be given by another reaction that could be occurring simultaneously [24]. Further analysis might be required

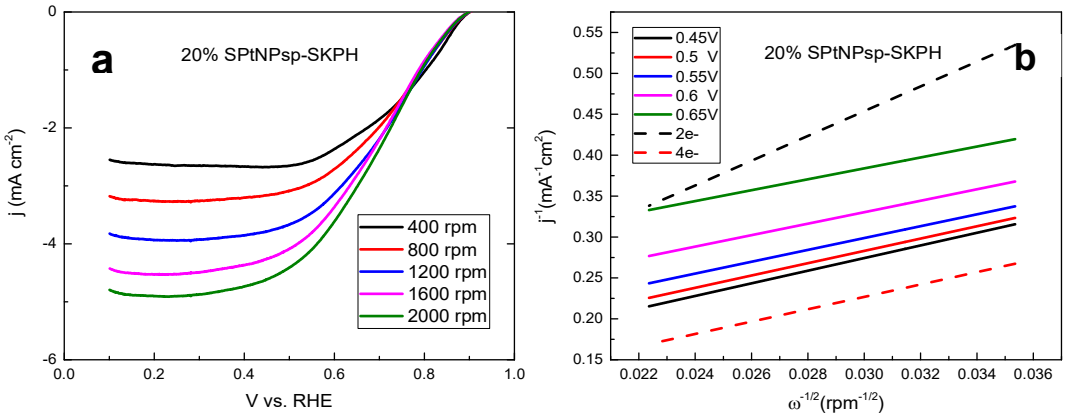

Fig. 5. a) LSV of 20%SPtNsp-SKPH at a scan rate of 5mV.s^{-1} at different rotation speeds. b) Koutecky-Levich plot of 20%SPtNPsp-SKPH

4. Conclusion

Sargassum spp. appears to be an excellent option for metallic reduction given the crystal size obtained through the green synthesis (9.5-10nm) as well as the same crystal planes as the highly cost commercial catalyst.

The newly synthesized catalyst delivers a much higher current density than the commercial catalyst with a very similar kinetic reaction, even with a different onset potential and high capacitive behavior this type of catalyst has great potential for electrochemical applications.

Acknowledgements

We thank LENERSE-254667 and Infraestructura 2015-253986 grants and also would like to acknowledge the technical support received from M.Sc. Martin Baas, C. Monica Ruiz and CONACYT LAB-2009-01-123913, 292692, 294643, 188345, 204822, 292692, and 294643

References

[1] J.M. Schell, D.S. Goodwin, Recent Sargassum Inundation in the Caribbean: Shipboard Observations Reveal Dominance of a Previously Rare Form, Oceanography. 28 (2015) 8–10. doi:10.5670/oceanog.2015.70.

[2] K.Y. Pérez-Salcedo, I.L. Alonso-Lemus, P. Quintana, C.J. Mena-Durán, R. Barbosa, B. Escobar, Self-doped Sargassum spp. derived biocarbon as electrocatalysts for ORR in alkaline media, Int. J. Hydrogen Energy. (2018). doi:10.1016/j.ijhydene.2018.10.073.

[3] Y. Wang, H. Luo, G. Li, J. Jiang, Highly active platinum electrocatalyst towards oxygen reduction reaction in renewable energy generations of proton exchange membrane fuel cells, Appl. Energy. 173 (2016) 59–66. doi:10.1016/j.apenergy.2016.04.019.

[4] S. Cherevko, N. Kulyk, K.J.J. Mayrhofer, Durability of platinum-based fuel cell electrocatalysts: Dissolution of bulk and nanoscale platinum, Nano Energy. 29 (2016) 275–298. doi:10.1016/j.nanoen.2016.03.005.

[5] S. Guo, S. Zhang, S. Sun, Tuning nanoparticle catalysis for the oxygen reduction reaction, Angew. Chemie - Int. Ed. 52 (2013) 8526–8544. doi:10.1002/anie.201207186.

[6] M. Kundu, G. Karunakaran, D. Kuznetsov, Green synthesis of NiO nanostructured materials using Hydrangea paniculata flower extracts and their efficient application as supercapacitor electrodes, Powder Technol. 311 (2017) 132–136. doi:10.1016/j.powtec.2017.01.085.

[7] S. Momeni, I. Nabipour, A Simple Green Synthesis of Palladium Nanoparticles with Sargassum

Alga and Their Electrocatalytic Activities Towards Hydrogen Peroxide, Appl. Biochem. Biotechnol. 176 (2015) 1937–1949. doi:10.1007/s12010-015-1690-3.

[8] P. Palaniappan, G. Sathishkumar, R. Sankar, Fabrication of nano-silver particles using Cymodocea serrulata and its cytotoxicity effect against human lung cancer A549 cells line, Spectrochim. Acta - Part A Mol. Biomol. Spectrosc. 138 (2015) 885–890. doi:10.1016/j.saa.2014.10.072.

[9] S. Balakrishnan, M. Srinivasan, J. Mohanraj, Biosynthesis of silver nanoparticles from mangrove plant (Avicennia marina) extract and their potential mosquito larvicidal property, J. Parasit. Dis. 40 (2016) 991–996. doi:10.1007/s12639-014-0621-5.

[10] P.P.N. Vijay Kumar, S.V.N. Pammi, P. Kollu, K.V. V Satyanarayana, U. Shameem, Green synthesis and characterization of silver nanoparticles using Boerhaavia diffusa plant extract and their anti bacterial activity, Ind. Crops Prod. 52 (2014) 562–566. doi:10.1016/j.indcrop.2013.10.050.

[11] T. Stalin Dhas, V. Ganesh Kumar, L. Stanley Abraham, V. Karthick, K. Govindaraju, Sargassum myriocystum mediated biosynthesis of gold nanoparticles, Spectrochim. Acta - Part A Mol. Biomol. Spectrosc. 99 (2012) 97–101. doi:10.1016/j.saa.2012.09.024.

[12] M. Mahdavi, F. Namvar, M. Ahmad, R. Mohamad, Green Biosynthesis and Characterization of Magnetic Iron Oxide (Fe3O4) Nanoparticles Using Seaweed (Sargassum muticum) Aqueous Extract, Molecules. 18 (2013) 5954–5964. doi:10.3390/molecules18055954.

[13] T. Odoom-Wubah, Z. Li, Z. Lin, T. Tang, D. Sun, J. Huang, Q. Li, Ascorbic acid assisted bio-synthesis of Pd-Pt nanoflowers with enhanced electrochemical properties., Electrochim. Acta. 228 (2017) 474–482. doi:10.1016/j.electacta.2017.01.107.

[14] G.A. Attard, A. Brew, Cyclic voltammetry and oxygen reduction activity of the Pt{1 1 0}-(1 × 1) surface, J. Electroanal. Chem. 747 (2015) 123–129. doi:10.1016/j.jelechem.2015.04.017.

[15] R. Venu, T.S. Ramulu, S. Anandakumar, V.S. Rani, C.G. Kim, Bio-directed synthesis of platinum nanoparticles using aqueous honey solutions and their catalytic applications, Colloids Surfaces A Physicochem. Eng. Asp. 384 (2011) 733–738. doi:10.1016/j.colsurfa.2011.05.045.

[16] V.S. Ramkumar, A. Pugazhendhi, S. Prakash, N.K. Ahila, G. Vinoj, S. Selvam, G. Kumar, E. Kannapiran, R.B. Rajendran, Synthesis of platinum nanoparticles using seaweed Padina gymnospora and their catalytic activity as PVP/PtNPs nanocomposite towards biological applications, Biomed. Pharmacother. 92 (2017) 479–490. doi:10.1016/j.biopha.2017.05.076.

[17] S. Kannan, FT-IR and EDS analysis of the seaweeds Sargassum wightii and Gracilaria corticata

(red algae), Int J Curr Microbiol Appl Sci. 3 (2014) 341–351.

[18] F. Hasché, Activity , stability , and degradation mechanisms of platinum and platinum alloy nanoparticle PEM fuel cell electrocatalysts, Dissertation. (2012) 155.

[19] H. Liu, J. Li, X. Xu, F. Wang, J. Liu, Z. Li, J. Ji, Highly graphitic carbon black-supported platinum nanoparticle catalyst and its enhanced electrocatalytic activity for the oxygen reduction reaction in acidic medium, Electrochim. Acta. 93 (2013) 25–31. doi:10.1016/j.electacta.2013.01.090.

[20] G. Fu, K. Wu, X. Jiang, L. Tao, Y. Chen, J. Lin, Y. Zhou, S. Wei, Y. Tang, T. Lu, X. Xia, Polyallylamine-directed green synthesis of platinum nanocubes. Shape and electronic effect codependent enhanced electrocatalytic activity, Phys. Chem. Chem. Phys. 15 (2013) 3793. doi:10.1039/c3cp44191a.

[21] M.D. Maciá, J.M. Campiña, E. Herrero, J.M. Feliu, On the kinetics of oxygen reduction on platinum stepped surfaces in acidic media, J. Electroanal. Chem. 564 (2004) 141–150. doi:10.1016/j.jelechem.2003.09.035.

[22] G. Jerkiewicz, G. Vatankhah, J. Lessard, M.P. Soriaga, Y.S. Park, Surface-oxide growth at platinum electrodes in aqueous H2SO4Reexamination of its mechanism through combined cyclic-voltammetry, electrochemical quartz-crystal nanobalance, and Auger electron spectroscopy measurements, Electrochim. Acta. 49 (2004) 1451–1459. doi:10.1016/j.electacta.2003.11.008.

[23] L. Deng, W. Zhong, J. Wang, P. Zhang, H. Fang, L. Yao, X. Liu, X. Ren, Y. Li, The enhancement of electrochemical capacitance of biomass-carbon by pyrolysis of extracted nanofibers, Electrochim. Acta. 228 (2017) 398–406. doi:10.1016/j.electacta.2017.01.099.

[24] L. Demarconnay, C. Coutanceau, J.M. Léger, Study of the oxygen electroreduction at nanostructured PtBi catalysts in alkaline medium, Electrochim. Acta. 53 (2008) 3232–3241. doi:10.1016/j.electacta.2007.07.006.

E092. DESIGN OF AN ELECTRIC SUPPLY SYSTEM FROM AN ALTERNATOR TO AN OXYHYDROGEN REACTOR FOR A DIESEL ENGINE.

A. Wintergerst-Felipe[1], R de G. González-Huerta[2], J. M. Sandoval-Pineda[1], E. A. Merchán-Cruz[1],

Instituto Politécnico Nacional

[1]Escuela Superior De Ingeniería Mecánica Y Eléctrica U. Azcapotzalco. Sección de Estudios de Posgrado e Investigación

[2] Escuela Superior de Ingeniería Química e Industrias Extractivas, Laboratorio de Electroquímica y Corrosión. UPALM, CP 07738, Ciudad de México.

SUMMARY

The use of hydrogen as fuel is growing, but not yet commercially on a large scale in Mexico, because there are still several limitations, such as hydrogen storage, that is why we choose to produce it in the same system where it will be occupied, but with that option, there is a limitation that is the question of energy supply, that is, the energy that is required to produce hydrogen or oxyhydrogen, which is why, in this article, a summary of the forms is presented that some authors have implemented to cover this limitation. In addition, it presents the proposals to be implemented for energy management and what are the other areas of opportunity that can improve the efficiency of the system.

1. INTRODUCTION

Nowadays, fuel consumption has grown as a source of energy that results in a higher rate of non-renewable fuel depletion, the search for alternative fuel has gained momentum. While diesel engines are the most reliable sources of energy in the transportation industry, due to strict emission standards and rapid depletion of oil resources, it has had a continuous effort to use alternative fuels. Hydrogen is one of the best alternatives for alternative fuels [1].

Of the various alternatives, hydrogen is one of those that offers the greatest potential as a complement to traditional fuels, either applied to hybrid cars or enriching natural gas lines in open combustion systems (at a transition stage), and as fuel autonomous to power internal combustion engines or combustible cells, which is projected as viable applications in the next two decades. Hydrogen generation can be done by means of an Alkaline Electrolyzer, which is an electrochemical device that produces hydrogen and oxygen (Oxyhydrogen Reactor) through electrical energy, which can be obtained; the car battery, alternator or a renewable source such as a photovoltaic panel. Alkaline electrolysers are a technology that can be adapted to different needs, since they are modular and do not have the use of noble metals in their electrodes [2].

Alkaline electrolysis is not a current process, it has about 200 years of study, currently it has had a greater development due to the research aspects of 21st century fuels, these for the implementation of totally clean energy systems, since photovoltaic systems or wind turbines can be joined for hydrogen production through alkaline electrolysis, thus having a fully sustainable system.

Hydrogen has its own benefits and limitations in its use as a conventional fuel in the automotive engine system, within those restrictions, it is the use of direct current for the electrolysis process, normal for an extra battery, this generates greater consumption of energy, and at a certain moment the efficiency of the system is affected.

Several articles study the implementation of hydrogen production systems in "diesel or gasoline" internal combustion engines, where hydrogen is a fuel enrichment, thus helping to improve combustion and reducing pollutant emissions. N. Saravanan (et al) mentions that, in a diesel engine, he made 2 combinations of fuel, hydrogen-diesel and diethyl hydrogen-ether, in both scenarios the reduction of polluting gases is notable, but in the test with diethyl hydrogen-ether he had a pounding greater than expected due to the high flammability of both [3].

In other articles it mentions the various experimentation versions that have been carried out with hydrogen, whether liquid, gaseous, or mixed with diesel, gasoline or natural gas, in all scenarios it is mentioned that the reduction of polluting gases is quite remarkable [4,5], but one point that most of the articles do not mention, is energy management, that is, the form of power supply to the hydrogen / oxyhydrogen reactors.

2. THEORETICAL BASES

2.1. Functions of an alkaline electrolyzer.

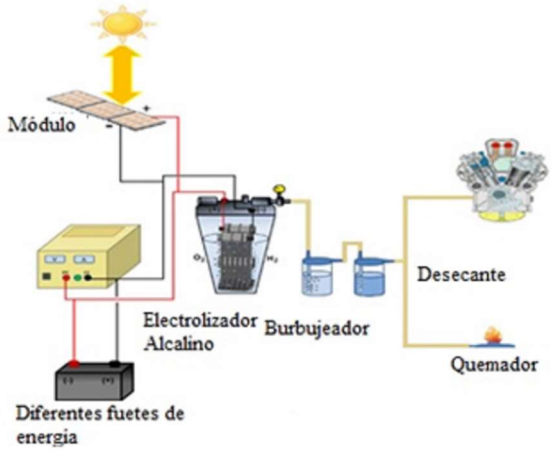

Figure 1. Alkaline electrolysis diagram.

The alkaline electrolysis process (Figure 1) is divided into 4 parts, which are listed below.

• Electricity supply (Batteries, energy sources, other renewable energies).

• Alkaline electrolyzer or oxyhydrogen gas reactor.

• Gas drying (bubbler, silica gel dryer)

• Use of gases (hydrogen or oxyhydrogen) for internal combustion engines or burners.

Electricity supply: An important part of the electrolysis process is the electricity that is applied to the cathode and flows through the electrolyte breaking the oxygen and hydrogen bonds. For this, direct current is needed, usually generated by batteries (occupied in cars), energy sources (deliver current and voltage according to what is required) or by renewable energy (solar panels, wind turbines, etc.).

Electrolyzer: An electrolyser can be dry cell or wet cell, but in both, it is a container in it is the cathodes and anodes, through which the electrical energy flows to the cathodes. In addition, the deposit is

submerged by the electrolyte (Distilled water H2O + Potassium Hydroxide KOH or Sodium Hydroxide NaOH). When the direct current is applied, the covalent bonds of the water are broken and the electrodes are heated (between 60 ° C / 80 ° C optimum operating temperature), generating the oxygen and hydrogen gases formed on the electrode surface.

Gas drying: Once the gases have already passed to this section, they first pass to a bubbler which traps any electrolyte particles that have passed, leaving pure hydrogen and oxygen gas. Later, the gas passes to a dryer, which contains silica gel, which traps any moisture that the gas can carry.

Gas utilization: when the oxygen and hydrogen gas have gone through the previous stages, it proceeds to procedures such as fuel, either as dual combustion for internal combustion engines or dual combustion for natural gas or LP burners.

2.2. Electrical system of a vehicle.

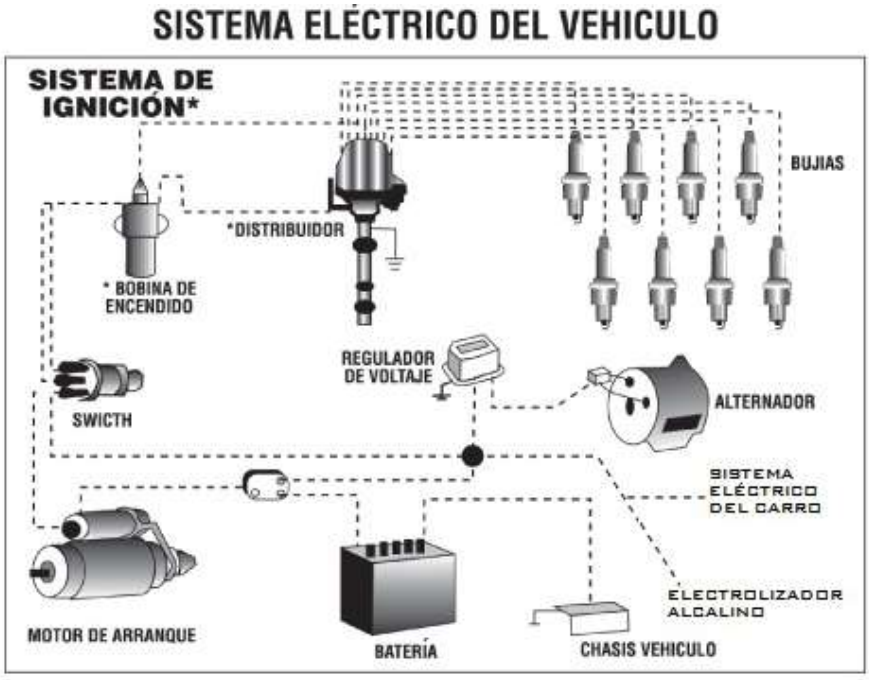

Figure 2. Electrical system of a vehicle.

The operation of the electrical system of a vehicle requires electrical energy so that the components that require energy work and the engine can start, this system consists of the following elements.

The battery provides power to the starting system, which moves the crankshaft until the engine runs automatically, that is, the distributor generates the current in each of the spark plugs sequentially to generate the spark and with this start the combustion inside the engine.

The ignition or swicth switch is where the key is inserted and has four positions: off, accessory power, starter ignition and ignition.

The starter motor converts electrical energy into mechanics and has a pinion that rotates the flywheel and thus transmits the movement to the motor to start its cycle.

The solenoid has two functions: attach the pinion to the flywheel and activate a switch to power the starter from the battery.

The charging system transforms part of the motor's energy into electricity to power the electrical parts in use, it also continually recharges the battery.

This consists of an alternator, which transforms the mechanical energy of the motor into electrical energy, by means of a diode bridge the alternating current is converted into direct current.

The voltage regulator keeps the output voltage generated by the alternator constant.

The battery is responsible for providing power to the starter motor to complement the demand for electric power when the alternator is not sufficient, that is, stabilize the voltage.

The electric current flows along the vehicle through a single cable, from the battery, to the last component being fed and returns to the battery through the metal body. This is because the body is connected to the battery ground terminal by a thick wire, thus closing the cycle. This type of circuit is called a ground return system and any part that is connected to the vehicle body is said to be grounded.

3. CASE STUDIES

Several authors mention in their articles the energy needs that exist, and how they are covered by hydrogen. Studies conducted in internal combustion engines mixing hydrogen or oxyhydrogen, focusing on the specific quantity part of the mixture, the viability of production and the reduction of gas emissions [6], but do not contemplate the energy management part, the what is the relation of the

necessary requirements for the production of hydrogen and the total efficiency that can affect us when using energy sources such as extra batteries or power supplies.

With the aim of analyzing the viability from the economic perspective and the impacts of all stages from the production, storage and distribution to the final use of hydrogen as a resource for mobility purposes. They compare hydrogen production not only with electrolysis and water use, but also with coal, biomass, natural gas, ethanol, among others using gasification methods, steam reformed respectively [7]. In each study carried out they analyze it from the current point of view and without making some possible improvements to the aforementioned processes, some more developed than others. In other words, energy management in its results was a negative factor that impacts the efficiency they show.

[8, 9] A photovoltaic panel system network is implemented, which will be the ones that will provide the electrolysis process, it is a good way to generate hydrogen since clean energy is being produced with the help of clean energy, seeing this from the ecological point of view it is very good, also thinking that it is for use in some station. In addition to taking electricity from the electricity network as a backup to operate and regulate the system if required. But it would be inefficient with current technologies, to be able to mount it in a vehicle, since the panels would not be able to meet the energy demand necessary for the electrolysis process and generate enough oxyhydrogen gas for mixing in the combustion chamber, this without count on the weather issues.

This article focuses more on an energy management system, which analyzes the uncertainties of load demand and energy production from renewable energy sources. The controller they developed controls the direct input current to the electrolyser, increasing the life of the electrolyser and increasing the production of hydrogen [10]. As such, the energy management part is covered from the point of view of direct current power quality, but not of the current itself.

4. CONCLUSIONS

In conclusion, as shown in Figure 3, the alternator generates 14V and 140A, of which, the car does not occupy 100% of this load, that is why the energy management system that is planned to be implemented will be supplied by the alternator within the relevant parameters, that is, not to exceed the maximum power of the alternator, in addition, it must be in an internal combustion vehicle to make the combination of the fuel with the oxyhydrogen gas generated by the electrolyser. For all the aforementioned, it is proposed that the system has the following characteristics:

Figure 3. Capacity of the alternator

• Do not generate more load to the engine.

• Do not use an extra battery, only for the electrolyzer.

• Do not reduce engine power efficiency.

• Do not reduce the efficiency of fuel / oxyhydrogen consumption.

• Be completely autonomous.

• Controller to decide where to take the load at the time required by the system.

With this it is intended that the energy management system can feed on the energy wasted by the vehicle, thereby increasing the final efficiency.

REFERENCES

[1] N. Saravanan, (et al). An experimental investigation on hydrogen as a dual fuel for diesel engine system with exhaust gas recirculation technique. Elsevier, Renewable Energy Vol 33, Pag. 422-427, 2008.

[2] Rosa de G. Gonzales (et al). Producción de Oxi-Hidrógeno para el enriquecimiento y ahorro de hidrocarburos: usos y retos. SMH, Vol. 1. 2015.

[3] N. Saravanan, G. Nagarajan, G. Sanjay, C. Dhanasekaran, K.M. Kalaiselvan. Combustion analysis on a DI diesel engine with hydrogen in dual fuel mode. Fuel, 87, 3591–3599, 2008.

[4] N. Saravanan, G. Nagarajan. An experimental investigation on manifold-injected hydrogen as a dual fuel for diesel engine system with different injection duration. International Journal of Energy Research, 33, 1352–1366, 2009.

[5] M.A. Escalante Soberanis, A.M. Fernandez. A review on the technical adaptations for internal combustion engines to operate with gas/hydrogen mixtures. International Journal Hydrogen Energy, 35, 12134-12140, 2010.

[6] Pierpaolo Polverino, Federica D'Aniello, Ivan Arsie, Cesare Pianese. Study of the energetic needs for the on-board production of Oxy-Hydrogen as fuel additive in internal combustion engines. Energy Conversion and Management. 179, 114–131, 2019.

[7] Tiago Sinigaglia, Felipe Lewiski, Mario Eduardo Santos Martins, Julio Cezar Mairesse Siluk. Production, storage, fuel stations of hydrogen and its utilization in automotive applications-a review. International journal of hydrogen energy, 42, 24597-24611, 2017.

[8] Sanae Dahbi, Abdelhak Aziz, Abdelhafid Messaoudi, Imane Mazozi, Kamal Kassmi, Naima Benazzi. Management of excess energy in a photovoltaic/grid system by production of clean hydrogen. International journal of hydrogen energy, 43, 5283-5299, 2018.

[9] Chrysovalantou Ziogou, Dimitris Ipsakis, Panos Seferlis, Stella Bezergianni, Simira Papadopoulou, Spyros Voutetakis. Optimal production of renewable hydrogen based on an efficient energy management strategy. Energy, 55, 58-67, 2013.

[10] Mauricio Higuita Cano, Kodjo Agbossou, Sousso Kelouwani, Yves Dubé. Experimental evaluation of a power management system for a hybrid renewable energy system with hydrogen production. Renewable Energy, 113, 1086-1098, 2017.

E099. EFFECT OF EPITAXIAL GROWTH OF BIMETALLIC NANOCRYSTALS ON THE ACTIVITY OF ELECTROCATALYSTS IN THE OXYGEN REDUCTION REACTION

Francisco F. Tello Casas[1], Rosa de Guadalupe González Huerta[1*], Martha L. Hérnandez Pichardo[2], Paz del Angel[3]

[1] Instituto Politécnico Nacional ESIQIE, Lab. de Electroquímica, Ed. Z-5, 3er piso, C.P. 07738, CDMX
[2] Instituto Politécnico Nacional ESIQIE, Lab. Investigación de Nanomateriales, Ed. Z-5, 2er piso, C.P. 07738, CDMX
[3] Instituto Mexicano del Petróleo, Eje Central L. Cárdenas 152, C.P. 07730, Ciudad de México
Phone number and email: 5529552955 rosgonzalez_h@yahoo.com.mx

ABSTRACT

The use of renewable energy is the best solution to stop the global warming and exhaustion of fossil fuels. The advantages of fuel cells are: high efficiency, do not generate pollutant emissions, low maintenance costs and wide ranges of energy. However, the high cost of noble metals has limited the application of fuel cells. To overcome this problem, the use of bimetallic nanoparticles has been proposed. The interaction of two or more metals at the nanometric level can form alloys, metal aggregates, core-shell nanoparticles with properties different.

In this work, bimetallic nanoparticles Pt-Pd were synthesized by surface oxide-reduction reactions and evaluated catalytically towards oxygen reduction reaction. Physicochemical characterization was performed, using analysis techniques such as X-ray diffraction, transmission electron microscopy (HRTEM and STEM), TGA. The rotating disk electrode in the bimetallic nanoparticles Pt-Pd with heat treatment have a more horizontal plateau which indicates a higher rate of oxygen reduction reaction, and also oxygen diffuses better on the surface of the electrode. A Tafel slope of 65.07 mV dec^{-1} in the bimetallic nanoparticles Pt-Pd with heat treatment was obtained, corresponds to first order kinetics, which shows a good catalytic activity towards the ORR.

1. Introduction

In Mexico, the combustion of energy is responsible for approximately 61% of the emissions of carbon dioxide (CO_2), and 46% of the greenhouse gases associated with the problem of climate change. It is evident that through the years Mexico contributes more to greenhouse gas emissions. Mexico generated at the beginning of the 1970s about 0.7% of international emissions, while in 2002 its contribution was 1.5% of the world total[1].

Research shows that pollutants in vehicle emissions damage lung tissue and can cause and aggravate respiratory diseases, such as asthma or cancer[2]. For this, alternatives have been sought to increase the production and use of cleaner energies, among which are: biofuels, solar cells and fuel cells. Fuel cells are electrochemical devices, which have a more efficient conversion process, chemical energy is converted directly into electrical energy.

Interest in fuel cells appeared in 1960 when NASA demonstrated some of its potential applications in energy supply during spaceflight [3]. One of the biggest problems in fuel cells is the high cost of their electrodes by noble metals[4]. In some way to overcome this problem, several approaches have been proposed, including the use of bimetallic nanoparticles. Bimetallic nanoparticles, composed of two different metallic elements, are of greater interest than monometallic ones. This is because bimetallization can improve the original catalytic properties of a single metal and create new properties, which cannot be found in monometallic catalysts[5]. The oxide-surface reduction synthesis technique was used in this work to synthesize bimetallic catalysts.

2. Materials and Methods

Pd seeds were placed in the reactor with nitrogen flow. A flow of hydrogen was used on the seeds of Pd in order to remain pre-absorbed on the seeds of Pd, and act as a reducer. Again a flow of nitrogen was used on the seeds of Pd to displace the hydrogen that was not pre-absorbed. At the same time a flow of nitrogen was also used on the dispenser that contained the salt of the second metal. The flow of nitrogen over the dispenser was stopped and gradually added to the seeds of Pd without stopping the flow of nitrogen over the reactor. Once the reaction was over, the solution was placed in the oven to dry. This synthesis is carried out by the following system. Figure 1.1:

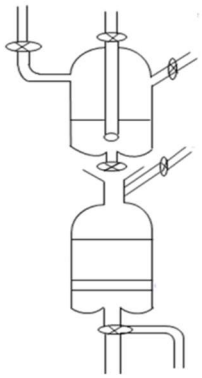

Figure 1.1 Reactor for synthesis of bimetallic materials

3. Results

Analysis by transmission electron microscopy (TEM)

Synthesis of Pd nanoparticles (seeds) supported on Vulcan carbon, reduced with hydrogen.

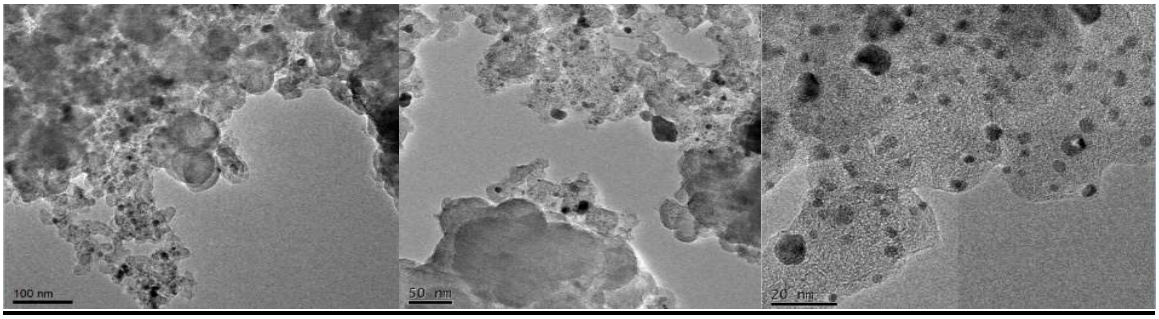

Figure. 1.2 TEM images of Pd nanoparticles

Synthesis of bimetallic nanoparticles Pt-Pd

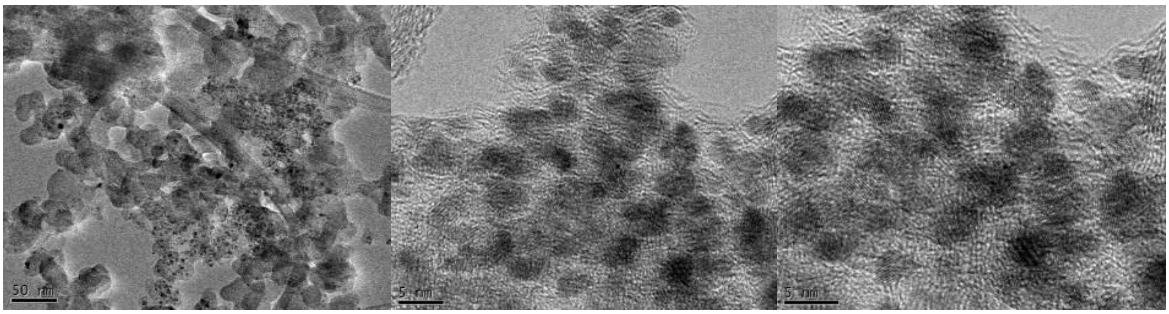

Figure. 1.3 TEM images of Pt-Pd nanoparticles

X-ray diffraction of Pt-Pd nanoparticles

In this analysis the NaCl phase was not found, this was due to the washes that were made in the seeds of Pd. The characteristic peaks of Pt and Pd do not distinguish between them since they are overlapping.

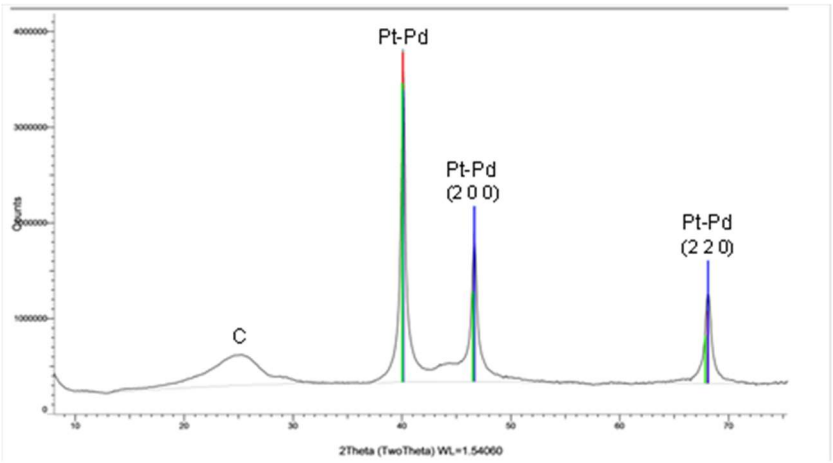

Figure. 1.4 X-ray diffraction pattern of Pt-Pd synthesis

Cyclic voltammetry

A comparison of 3 synthesis was performed, with better results the synthesis of Pt-Pd with heat treatment towards the oxygen reduction reaction (ORR)

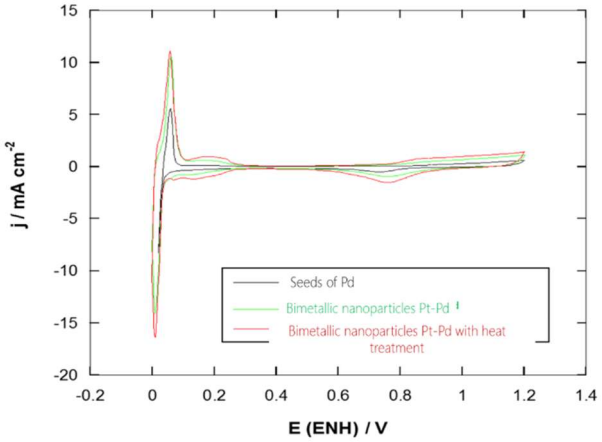

Fig. 1.5 Cyclic voltammetry of different synthesis in a 0.5 M H_2SO_4 solution at a scanning rate of 50 mV/s^{-1}

Rotating disk electrode (RDE)

In the diffusion zone, a more horizontal and better defined plateau is observed, which indicates that the ORR is carried at a higher speed and in a constant way.

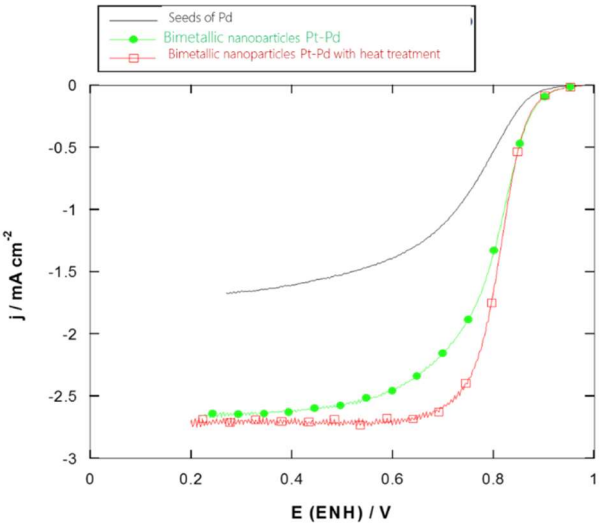

Fig. 1.6 Polarization curves at a speed of 900rpm in a 0.5 M H_2SO_4 solution

4. Conclusion

The seeds must be totally clean, without traces of any contaminant of the precursor used in the synthesis, reducer, stabilizer or any other material, this affects the deposit of the second metal. In the synthesis of Pd (monometallic), NaCl was forming and this directly affected the deposition of the Pt.

The NaCl acts as a contaminant that had not been identified in the syntheses performed, and for this reason the evaluations in the electrochemical tests were not as expected. By changing the synthesis method and performing the washes correctly, in addition to changing the precursor of the second metal, better results were obtained. And it was possible to deposit the Pt on the monometallic, this was demonstrated with the characterization techniques used.

References

1.- Alarco, T. Crecimiento económico y emisiones de CO_2 por combustión de energéticos en México, 2005-2030, vol. 15, 291-321, Economía Mexicana, Nueva época. (2006)

2.- Hinch, N. Air pollution, vol. 46, 93-95. Journal of chemical education. (1969)

3.- Sharon, T., and Zalbowitz, M. Fuel cells Green power, vol. 10, 2-5. Energy efficiency and renewable energy U.S. Department of energy. (1990)

4.- Shao, M., Chang, k., Dodelet, J., and Chenitz, R. Recent Advances in Electrocatalysts for Oxygen Reduction Reaction, vol. 116, 3594-3657. American chemical society. (2016)

5.- Yaldagard, M., Jahanshahi, M., and Seghatoleslami, N. Carbonaceous Nanostructured Support Materials for Low Temperature Fuel Cell Electrocatalysts—A Review, vol. 3, 121-153. Nano Science and Engineering. (2013)

E100. LOWERING OF DEHYDROGENATION TEMPERATURE OF $NaAlH_4$ BY USING $ZrCl_4$ AND $TiCl_4$

Juan Rogelio Tena García, Karina Suárez Alcántara*

Unidad Morelia del Instituto de Investigaciones en Materiales de la Universidad Nacional Autónoma de México. Antigua Carretera a Pátzcuaro No. 8701, Col. Ex Hacienda de San José de la Huerta, C.P. 58190, Morelia, Michoacán, México.

* karina_suarez@iim.unam.mx

ABSTRACT

The alanates have been proposed as materials for storage of hydrogen. Some of them are noted for their high hydrogen content and the possibility of having reversible storage, i.e., $NaAlH_4$. Other alanates, like those that contain elements of transition ($Ti(AlH_4)_4$ or $Zr(AlH_4)_4$) are practically unknown, despite their high content of hydrogen. In the present work, we present mixtures of $NaAlH_4/TiCl_4$ and $NaAlH_4/ZrCl_4$ milled at cryogenic conditions (-197ºC cooled with liquid nitrogen) to promote the formation of reactive mixtures with low dehydrogenation temperature. A detailed FT-IR and XRD characterization of the milled and dehydrogenated samples confirms the formation of reactive mixtures and the on-set dehydrogenation temperature of 60°C. This temperature is particularly low and is the result of the formation of the mixtures in cryogenic conditions.

Keywords: hydrogen storage, low temperature dehydrogenation, transition metals alanates

1. Introduction

Hydrogen storage is frequently identified as one of the main problems to be solved in order to implement hydrogen as fuel. Hydrogen storage in solid materials can be a suitable solution; there is a lot of families of materials, among them, the alanate family stands out. The alanates are complex compounds composed of covalent $[AlH_4]^-$ or $[AlH_6]^{-3}$ ions ionically bonded to a metal [1]. Among the alanates, $NaAlH_4$ stands out because of their reversibility of the hydrogenation/dehydrogenation reactions. The main drawback of the $NaAlH_4$ is the high dehydrogenation temperature, which is higher than the PEMFCs (polymer exchange membrane fuel cell) operational temperature, i.e., 150°C-250°C

vs. 80°C. The catalyst that makes the $NaAlH_4$ reversible also reduced significantly the dehydrogenation temperature, jet not as low as 80°C [2]. Other alanates can be of interest in the hydrogen storage area; in particular, our research group has interest in transition metals alanates of Zr and Ti. During the 1950 decade, for the first time, the synthesis of $Ti(AlH_4)_4$ [3] and $Zr(AlH_4)_4$ [4] (alanates of group IV) was reported. The $Ti(AlH_4)_4$ was synthesized by the metathesis reaction of $TiCl_4$ and $4LiAlH_4$ in ether solution at -110°C, and reported to start decomposing at -85°C [3]. Zr(AlH4)4 was prepared by the reaction between $LiAlH_4$ and $Zr(BH_4)_4$ in ether solution in He atmosphere, with further removal of solvent [4]. The white solid of $Zr(AlH_4)_4$ was unstable at room temperature producing a pyrophoric black solid. In 2008, $Zr(AlH_4)_4$ was claimed to be produced by the reaction between $LiAlH_4$ and $ZrCl_4$ in ether solution [5]. However, producing $Zr(AlH_4)_4$ was not the primary goal of the 2008 report, $Zr(AlH_4)_4$ was obtained instead as an intermediary stage for the production of surface passivated Zr-Al mixed metal-hydride nanoparticles [5]. On the other hand, the same reactives that can produce the new alanates, i.e., a stating alanate and particularly the $TiCl_4$ and $ZrCl_4$ have been used as catalysts to reduce the dehydrogenation temperature of different hydrogen storage materials. Thus, we use the $TiCl_4$ and $ZrCl_4$ to reduce the dehydrogenation temperature of $NaAlH_4$.

The mechanical milling is a preparation technique widely used in the hydrogen storage area. The mechanical milling allows for quick processing of materials and to reduce contamination by solvent residues as in other synthesizing techniques. The planetary and shaker mills are the most common machines used, yet other mills can be useful. In particular, in the present work, we used a cryogenic mill to process the studied materials. Cryomilling is similar to the typical milling by shaking, however, the difference is the cooling with liquid nitrogen. The cryomilling allows the processing of temperature sensible materials.

2. Materials and Methods

High purity $ZrCl_4$, $TiCl_4$ (97-99.99% purity) and $NaAlH_4$ (95% purity) were purchased from Sigma-Aldrich and used as received. Two mixtures were prepared: i) $1.6NaAlH_4 + 0.2ZrCl_4$, and ii) $1.6LiAlH_4 + 0.2TiCl_4$. 0.5 g of mixtures and 7.5 grams of zirconium yttrium stabilized balls were loaded together in a stainless steel milling vial. Then, the vial was closed in an argon atmosphere and transferred to a cryomill (Retsch). The milling vial was pre-cooled for 7 minutes, and then the mixtures were milled for 10 minutes. A frequency of shake of 25 Hz was presented in this work, accordingly to the best results in previous

mixtures and group experience. With the aim of a suitable comparison, a sample of pure $NaAlH_4$ was milled and testes in identical conditions as the mixtures.

The as-milled materials and dehydrogenated materials were characterized by X-ray diffraction (XRD), and Fourier transformed infrared spectroscopy (FT-IR). XRD was performed in a D2 Phaser diffractometer of Bruker. Cu $K\alpha$ (1.540598Å) wavelength was used. The powders were compacted in a dedicated sample-holder; then, they were covered with Kapton tape for protection against ambient oxygen and moisture. FT-IR characterization was performed in a Nicolet iS10 of Thermo Fisher Scientific. The studied materials were compacted in KBr pellets. The KBr was purchased from Sigma-Aldrich and dried just before the pellet preparation. About 2.5 mg of each material was dispersed in 50 mg of dry KBr. FT-IR data was collected in ATR mode with a 1 cm^{-1} resolution, 64 scans were averaged.

Temperature programmed dehydrogenation experiments were carried out in a Sievert´s type apparatus of own design and construction [6]. Samples were transferred to/from the Sievert´s-type reactor without oxygen contact employing a closing valve at the sample holder. Then, the system was cleaned by successive cycles of dynamic vacuum and argon. Calibration and operation details were performed as reported elsewhere [6]. The dehydrogenations were performed at 1 bar hydrogen (absolute) pressure and up to 250°C. The first step was to fix the initial pressure in the apparatus; then, the sample was heated at the test temperature with a heating ramp of 1°C/min. The hydrogen used during experiments was of chromatographic purity. After the experiment, the sample was cooled down. At room temperature, the remaining pressure was released. Then samples were recovered and characterized. All handling of materials was performed in a high purity argon atmosphere. Dehydrogenated materials are identified hereafter adding DHH to the name of the sample.

3. Results and Discussion

Two mixtures were prepared: i) $1.6NaAlH_4 + 0.2ZrCl_4$, and ii) $1.6LiAlH_4 + 0.2TiCl_4$. The stoichiometries were chosen to keep 0.8 mol of $NaAlH_4$, and to possible form 0.2 mol of $Zr(AlH_4)_4$ or $Ti(AlH_4)_4$ and 0.8 mol NaCl. Fig 1(a) shows the X-ray diffraction patterns of the two mixtures and the pure $NaAlH_4$. All the peaks correspond to $NaAlH_4$. No peaks of $ZrCl_4$. $TiCl_4$ or any product such as NaCl were found. Despite all samples were processed and tested under the same conditions; i.e., the reduction on the crystallite size (observed indirectly and the height of the diffraction peaks) is very different. The mixtures presented low height of the diffraction peaks, indicating that the milling was more efficient, perhaps by the

presence of the salts $ZrCl_4$ or $TiCl_4$. By its part, the infrared indicates the presence of some Na_3AlH_6 (i.e., the intermediary of the $NaAlH_4$) in all the samples. The mixtures presented a clear decrease of the Al-H stretching zone; and a small shift of the peak positions. Based on the characterization of the mixtures, the formation of reactive mixtures is feasible.

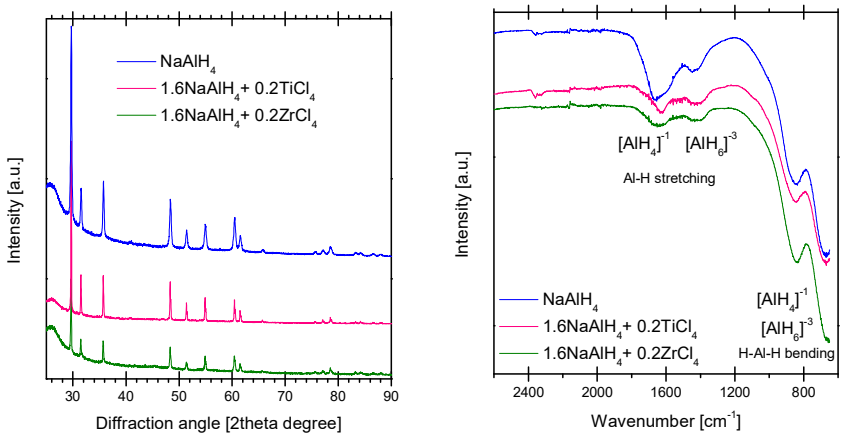

Fig.1 (a) X-ray diffraction and (b) infrared spectroscopy characterization of the mixtures of $NaAlH_4$, $TiCl_4$ and $ZrCl_4$.

Figure 2 presents the dehydrogenation curves of the mixtures and $NaAlH_4$ pure as reference. This last material presents the characteristic two dehydrogenation steps corresponding to the typical reactions:

$$NaAlH_4 \rightarrow 1/3Na_3AlH_4 + 2/3Al + H_2 \quad (1)$$

$$1/3NaAlH_4 \rightarrow NaH + 1/3Al + 1/2H_2 \quad (2)$$

These reactions occur into the typical temperature ranges; thus, no effect of the cryogenic milling is observed in this material.

By its parts, the mixtures of $NaAlH_4/TiCl_4$ and $NaAlH_4/ZrCl_4$ indeed presented an important reduction on the dehydrogenation temperature. The on-set of the dehydrogenation temperature is about 60°C, meeting the range of PEMFC operational temperature. The shape of the dehydrogenation curve of the mixtures reveals a change in the dehydrogenation reactions from the equations (1) and (2). The last change in the shape of the curve, at 175°C, corresponds to the second dehydrogenation of $NaAlH_4$ (eq. (2)). This can be explained as the part of $NaAlH_4$ of the mixtures that did not react with $ZrCl_4$ or $TiCl_4$. The total hydrogen released was 5.4 wt.% of the 5.6 wt.% of pure $NaAlH_4$ and 4.0 wt. % and 3.6 wt.% for the samples of $NaAlH_4/ZrCl_4$ and $NaAlH_4/TiCl_4$, respectively.

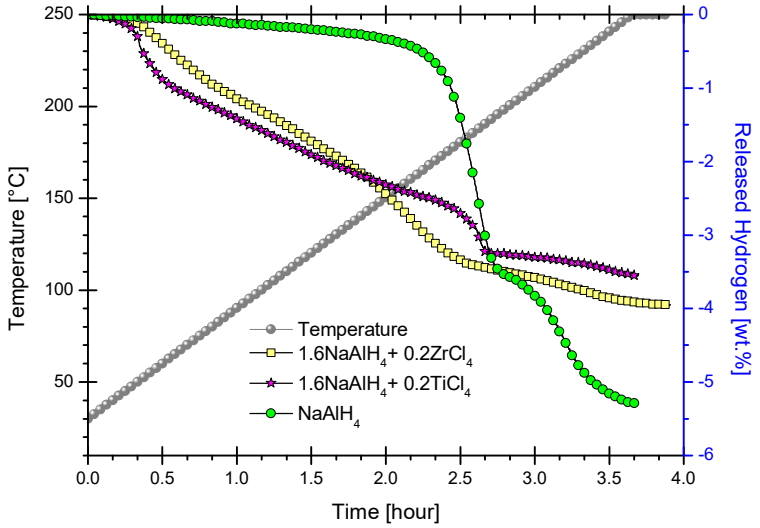

Fig. 2. Temperature programmed desorption curves of $NaAlH_4$, $NaAlH_4/TiCl_4$ and $NaAlH_4/ZrCl_4$ mixtures.

Figure 3 presents the X-ray diffraction and infrared spectroscopy characterization. The X-ray diffraction confirms the dehydrogenation of $NaAlH_4$ to Al and NaH. However, the infrared spectroscopy reveals that the second dehydrogenation step (eq. (2)) of $NaAlH_4$ was not completed and some residual Na_3AlH_6 is present. This confirms the 0.2 wt.% hydrogen missing in the dehydrogenation curves. The X-ray diffraction of the $NaAlH_4/ZrCl_4$ and $NaAlH_4/TiCl_4$ mixtures present the Al and NaCl as the main dehydrogenation products. This confirms the formation of reactive mixtures and the change in the dehydrogenation pathway from the equations (1) and (2). The proposed dehydrogenation reaction of the reactive mixtures are:

$1.6NaAlH_4 + 0.2ZrCl_4 \rightarrow xZr\text{-}Al + yAl + zNaCl + wH_2$ (3)

$1.6NaAlH_4 + 0.2TiCl_4 \rightarrow xTi\text{-}Al + yAl + zNaCl + wH_2$ (4)

No metallic nor other Ti and Zr compounds were found. Normally Al can form alloys with elements such as Ti or Zr with the same crystalline cell parameters. Additionally, the infrared spectroscopy reveals the presence of some residual Na_3AlH_4.

As mentioned in the introduction section, several works have produced mixtures of alanates ($LiAlH_4$ or $NaAlH_4$) and $TiCl_4$ and $ZrCl_4$. In these works, the normal result is the reduction of the released hydrogen due to the partial to total decomposition during ball milling. It is necessary to remember that during the ball milling process, local high local temperatures and pressures can be developed during the ball-ball and ball-vial collisions. The use of cryomilling reduced dramatically the decomposition of materials during ball milling due to the careful control of the temperature.

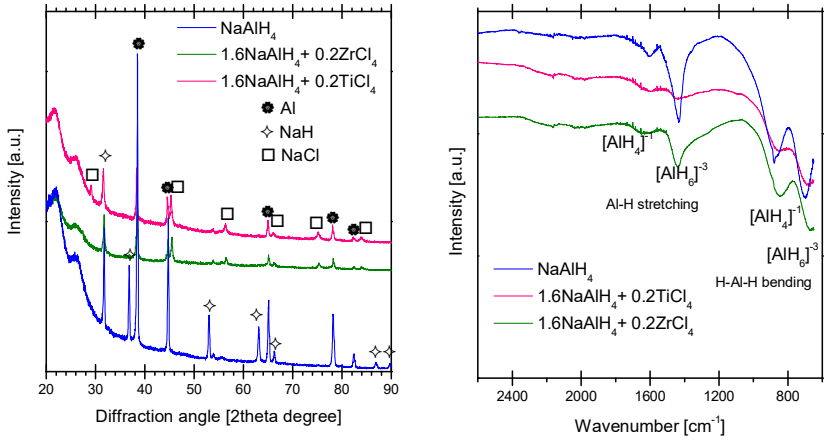

Fig. 3. (a) X-ray diffraction and (b) infrared spectroscopy characterization of the mixtures of $NaAlH_4$, $TiCl_4$ and $ZrCl_4$.

4. Conclusion

Mixtures of $NaAlH_4/ZrCl_4$ and $NaAlH_4/TiCl_4$ were produced and studied for hydrogen release. The studied mixtures can be classified as reactive mixtures. A detailed FT-IR and XRD characterization of the

milled and dehydrogenated samples confirms the formation of reactive mixtures and the on-set dehydrogenation temperature of 60°C. This temperature is particularly low and is the result of the formation of the mixtures in cryogenic conditions. The dehydrogenation reactions of the studied mixtures differ from the dehydrogenation reactions of pure $NaAlH_4$.

Acknowledgements

Research carried out thanks to the Basic Science project of CONACyT 251347: "Non-conventional alanates for hydrogen storage at low temperature".

References

[1] Suárez-Alcántara K, Tena-Garcia JR, Guerrero-Ortiz R. Alanates, a Comprehensive Review. Materials 2019;12:2724-64. doi:10.3390/ma12172724

[2] Bogdanović B, Brand RA, Marjanović A, Schwickardi M, Tölle J. Metal-doped sodium aluminium hydrides as potential new hydrogen storage materials. J. Alloys Compd. 2000;302:36–58. doi:10.1016/S0925-8388(99)00663-5

[3] Von Egon W, Usón R. Zur Kenntnis eines Titan-aluminium-wassestoffs $Ti(AlH_4)_4$. Z. Naturforsch. 1951;6b:392-393.

[4] Reid WE, Bish JM, Brenner A. Electrodeposition of metals from organic solutions. J. Electrochem Soc. 104;1957:21-29. doi: 10.1149/1.2428488.

[5] Epshteyn A, Miller JB, Pettigrew KA, Stroud RM, Purdy AP. Surface passivated air and moisture stable mixed zirconium aluminum metal-hydride nanoparticles. Mater. Res. Soc. Symp. Proc. 2008; 1056: 1056-HH03-16.

[6] Carrillo-Bucio JL, Tena-Garcia JG, Armenta-Garcia EP, Hernandez-Silva O, Cabañas-Moreno JG, Suarez-Alcantara K. Low-cost Sieverts-type apparatus for the study of hydriding/dehydriding reactions. HarwareX 2018;4:00036. doi: 10.1016/j.ohx.2018.e00036.

E101. TWO NEW CO-ADSORBENTS FOR DYE-SENSITIZED SOLAR CELLS: STRUCTURE-PROPERTIES RELATIONSHIP

Luciano da Silva[1,*], Harold Freeman[2]

[a] Departamento de Procesos de Transformación de Plásticos, Centro de Investigación en Quimica Aplicada, Saltillo, CP 25294, México.

[b] Polymer and Color Chemistry Program, North Carolina State University, Raleigh, NC, 27695, USA.

* Corresponding author: luciano.dasilva@ciqa.edu.mx 844 3908175

ABSTRACT

Two new compounds based on the phenyltetrazole system, 5-(4-decyloxyphenyl)tetrazole (LTz-4) and N,N-diethyl-4-{[(4'-nitro-2'-tetrazoyl)phenyl]diazenyl}aniline (SD-3), were synthesized and characterized as co-adsorbents in Dye-Sensitized Solar Cells (DSSCs). The effects of hydrophobic chain length and anchoring group on the properties of DSSCs containing the previously reported dye HD-14 and compared with the benchmark deoxycholic acid (DCA) are described. The charge-transfer resistance of dye/TiO_2 interface followed the order HD-14 – SD-3 > HD-14 – LTz-4 > HD-14 –DCA. However, the V_{OC} for the dye HD-14 with co-adsorbent DCA was 0.71 V, for the and the dye HD-14 with co-adsorbent LTz-3 was 0,70 V and for the dye HD-14 with co-adsorbent SD-3 was 0,67 V. Co-adsorbents LTz-3 and SD-3 achieved mean solar-to-power conversion efficiencies (%η), for three devices, of 9.22 and 7.50, respectively, compared to 9.14 for DCA under the same experimental device conditions. For LTz-3 co-adsorbent, the results can be attributed to the repellent effect of the long alkyl chain. For SD-3, it is possible that the volume of the co-adsorbent chain makes it difficult to form a more compact layer between the dye and the co-adsorbent. This allows the electrolyte to approaches, reducing the electron-injection efficiency into TiO_2.

Keywords: Dye-Sensitized Solar Cells; Co-adsorbent; Tetrazole

1. Introduction

Dye-sensitized solar cells (DSSCs) based on nanocrystalline oxide semiconductors are a type of solar cells that convert the sun's energy to electric energy using a sensitizing dye [1-3]. A typical DSSC consists of a nanoparticle TiO_2 photoelectrode sensitized by a ruthenium bipyridine complex and a platinum counter-electrode separated by an iodide-triiodide (I^{-1}/I_3^{-1}) liquid electrolyte [4]. In DSSCs, the photosensitizer is a key component to harvest light and inject electrons. Until now, hundreds of photosensitizers have been designed and synthesized for improving the photovoltaic performance and exploring the relationship of structure and performance of DSSCs. Among them, the ruthenium complex dyes, such as N719, N3, C101 and HD14, have dominated the highly efficient DSSCs for many years [5-8, 10]. For example, the efficiency of DSSC based on N719 has exceeded 12% [9]. However, the scarcity of ruthenium metal is a big problem for the future commercial development and applications. Compared with the metal complex dyes, the metal-free organic dyes have some advantages, such as the relative simplicity of synthesis and purification, convenient structural modification and high molar extinction coefficient. Thus, searching new metal-free organic dyes with excellent photovoltaic performance has attracted considerable attention. Many organic dyes, which exhibit comparably excellent photovoltaic performances to ruthenium complexes, have been designed and obtained [11-13]. However, designing the new organic dyes via simple and convenient synthetic routes is still a challenge in DSSCs. In last decade, various kinds of functional groups and their derivatives have been combined to generate D-π-A organic dyes. Among them, an arylamine group, thiophene derivatives and cyanoacrylic acid moiety are the most common subunits that act as an electron donor, p-linker, and an electron acceptor/anchoring group, respectively. Especially, the p-linker as a bridge that connects the donor and acceptor exerts a significant influence on the transmission and recombination of electron during the photoelectric conversion process in DSSCs. Generally, the crucial step for the construction of D-π-A organic dyes is to connect the donor group and p-linker. The introduction of 1,2,3-triazole group as an electron deficient unit in the linear D-π-A organic dyes can effectively enhance the open-circuit voltage of the DSSCs with good efficiency [14]. The introduction of tetrazole group as an anchoring group has been related. The photovoltaic results further obtained with the tetrazole derivative outperformed those of the carboxylic analogue showing a significant increase in photovoltage for a device using the tetrazole dye [15].

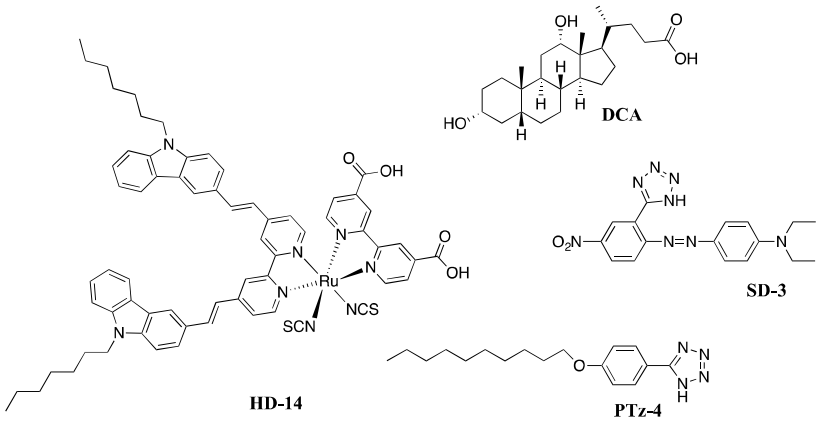

Fig. 1. Molecular structures of Dye (HD-14) and co-adsorbents: DCA, LTz-4 and SD-3.

Much effort has been paid to widen the light absorption by increasing the conjugation at both donor and π-linages. Unfortunately, their photovoltaic performance are still not significantly improved due to their aggregation during the photoelectrode fabrication process. Thus, co-sensitization using two or more sensitizers is an effective approach to achieve panchromatic harvest. Plenty work has been realized including ruthenium complex co-sensitized with an organic dye [16-25]. The co-sensitizations of organic dyes have been extensively investigated, which exhibit an effective and promising photovoltaic performance [26-31].

Here we report the photovoltaic performance of DSSCs derived from co-sensitization of HD14 and co-adsorbent SD3 and PTz-4 (Fig. 1).

2. Materials and Methods

2.1. General Information

The solvents and chemicals were purchased from Sigma-Aldrich, Fisher Scientific or TCI-America and used as received. The mass spectrometry analysis was carried out on a high-resolution mass spectrometer – Thermo Fisher Scientific Exactive Plus MS, a benchtop full-scan OrbitrapTM mass spectrometer using Heated Electrospray Ionization (HESI). Samples were dissolved in methanol and sonicated for 15 min. They were then diluted 1:1 with 20 mM ammonium acetate and analyzed via syringe injection into the mass spectrometer at a flow rate of 10 mL/min. The mass spectrometer was operated in negative ion mode. FT-IR (ATR) spectra were recorded on a Nicolet Nexus 470 FT-IR spectrometer (Thermo Scientific, USA) and UV-Visible spectra were measured by using Cary 300 spectrophotometer.

Fluorescence, recorded at room temperature on a Fluorolog-3 spectrofluorometer (HORIBA Jobin Yvon Inc.). ^{1}HNMR (Hydrogen Nuclear Magnetic Resonance) and ^{13}CNMR (Carbon Nuclear Magnetic Resonance) spectra were recorded in a Bruker 500 MHz spectrometer.

2.2. Synthesis

2.2.1. Synthesis of 2-(1H-tetrazol-5-yl)-4-Nitro-benzenamine (1):

The synthesis of the tetrazole system (1) was carried out as depicted in the literature [32,33]. Yield 65%; mp 264-266 °C; $mp_{Lit.}$ 268-270 °C [34]. FTIR-ATR ν_{max} = 3420, 2710–2630 (br), 1613, 1597, 1504, 1292, 842. ^{1}HNMR (500MHz, $CDCl_3$) δ = 7.45 (s, 1H, C_6H_3), 7.05 (d, J=8.4 Hz, 1H, C6H3), 6.62 (d, J=8.4 Hz, 1H, C_6H_3) 3.38 (br s, 1H, CN4H). ^{13}CNMR (100 MHz, DMSO-d_6): 155.8 (1C), 137.3 (1C), 134.5 (1C), 117.1 (1C), 114.3 (1C), 112.6 (2C), 111.1(1C).

2.2.2. Synthesis of azo dyes N,N-diethyl-4-{[(4′-nitro-2′-tetrazoyl) phenyl]diazenyl}aniline (SD-3):

2-(1H-tetrazol-5-yl)-4-Nitro-benzenamine (2) (2.06 g, 0.01 mol) was dissolved in hydrochloric acid (20 mL) with stirring. After, the solution was cooled to 0 °C in an ice-bath. A solution of sodium nitrite (0.69 g, 0.01 mol) in 5mL water, cooled to 0 °C was added. The mixture was stirred for 30 min at 0 °C to get the clear diazonium salt solution. The coupling component N,N-diethylaniline (1.60 g, 0.01 mol) was dissolved in NaOH (15 mL, 1N) and then solution cooled 0 °C. To this well stirred solution, the above diazonium salt solution was added slowly so that temperature did not rise above 4 °C while maintaining the pH 4-5 by the action of sodium acetate solution (10% w/v). The mixture was stirred for 3 h at 0 °C. After, the solid obtained was collected by filtration, washed three times with cold water and dried. The crude product was recrystallized from hexane:ethylacetate (1:1). Violet crystals, 3,04 g, yield 83% m.p. >300 °C. FTIR-ATR: 1381.4 cm^{-1} and 1518.9 cm^{-1} (N-O stretch), 1603.1 cm^{-1} (C=C stretch). ^{1}H-NMR (500 MHz, DMSO-d_6): 8.69 (s, 1H), 8.45 (d, J = 10 Hz, 1H), 7.96 (d, J = 10 Hz, 1H), 7.76 (d, J=10 Hz, 2H), 6.87 (d, J=10 Hz, 2H), 3.50 (q, J = 5 Hz, 4H), 1.15 (t, J=5 Hz, 6H). ^{13}CNMR (100 MHz, DMSO-d_6): 153.4 (1C), 152.0 (1C), 146.2 (1C), 143.1 (1C), 127.5 (1C), 126.7 (1C), 125.8 (1C), 123.0 (1C), 117.2 (2C), 111.5 (2C), 44.4 (2C), 12.5 (2C). HRMS (ESI Full) m/z: calcd for $C_{17}H_{19}N_8O_2$ [M+H]+, 367.1626; Found, 367.1636.

2.2.3. Synthesis of 5-(4-decyloxyphenyl)tetrazole (LTz-4):

To a round-bottomed flask were added 4-hydroxybenzonitrile (10.0 g, 0.084 mol), 1-bromodecano (18.6 g, 0.084 mol), KOH (46.4 g, 0.336 mol), and toluene/DMF (200 ml; 1:1) and the mixture was stirred under

reflux for 6 h. The suspension was filtered and the solid was washed with toluene. The filtrate was concentrated and the obtained solid dissolved in diethylether. The organic phase was washed with NaOH (5%; 50 ml), HCl (5%; 50 ml), and H_2O (50 ml) and dried over anhydrous Na_2SO_4. The product was obtained after removal of the solvent, as a white solid. To this solid (compound 2) were added NaN_3 (13.50 g; 0.208 mol), NH_4Cl (11.10 g, 0.208 mol) and DMF (100 ml) and the mixture was refluxed for 20 h. The suspension was cooled to room temperature and poured into 400 ml of ice/water and acidified to pH 3 using HCl, (10%). The mixture was filtered and the solid was washed several times with water. Recrystallization from ethanol gave a white solid; yield 65.0%, mp 164-166 °C, FT-IR ν_{max} = 3090, 2956, 2924, 2855, 3100–2600 (broad), 1627, 1522, 1345, 788. ^{1}H NMR (200 MHz, CDCl3) δ = 8.04 (d, J = 9.0 Hz, 2H, Ar-H), 7.14 (d, J = 9.0 Hz, 2H, Ar-H), 4.11 (t, J = 6.6 Hz, 2H, -CH_2O-), 1.81 (qui, J = 6.6 Hz, 2H, -$C\underline{H}_2CH_2$O-), 1.50 (m, 2H, -CH_2-), 1.24 – 1.40 (m, 12H, -CH_2-), 0.87 (t, J = 6.7 Hz, 3H, CH_3). ESI HRMS $[M+H]^+$ = Theo. M/z 247.15534; Found. M/z 247.15500, Error -1.366 ppm.

2.2.3 Synthesis of HD-14. HD-14 was synthesized according to the procedures reported by Cheema et al. [10].

2.3. Measurements of ground state oxidation potential (GSOP) by cyclic voltammetry

The experimental HOMO and E0-0 energy values for SD-3 and LTZ-4 were measured using a cyclic voltammetry (CV) whereas E0-0 was determined from the absorption onset of the relevant compound [10].

2.4. TiO_2 electrode preparation and device fabrication

The photo-anodes composed of nanocrystalline TiO_2 and counter electrodes were prepared using a known procedure [35].

2.5. Photo-electrochemical measurements

Photocurrent-voltage characteristics of DSSCSs were measured using a Keithley 2400 source meter under illumination of AM 1.5 G solar light from solar simulator (SOL3A, Oriel) equipped with a 450 W xenon lamp (91160, Oriel). The incident light intensity was calibrated using a reference Si solar cell (Newport Oriel, 91150V) to set 1 Sun (100 mW cm^{-2}). The measurement was fully controlled by Oriel IV Test Station software. IPCE (incident monochromatic photon to current conversion efficiency)

experiments were carried out using a system (QEX10, PV Measurements, USA) equipped with a 75 W short arc xenon lamp (UXL-75XE, USHIO, Japan) as a light source connected to a monochromator. Calibration of incident light was performed before measurements using a silicone photodiode (IF035, PV Measurements). All the measurements were carried out without the use of anti-reflecting film.

2.6. Electrochemical impedance spectroscopy (EIS)

The electrochemical impedance spectra were measured with an impedance analyzer potentiostat (Bio-Logic SP-150) under illumination using a solar simulator (SOL3A, Oriel) equipped with a 450 W xenon lamp (91160, Oriel).

3. Results and Discussion

3.1. Synthesis of co-adsorbents:

The synthesis of proposed co-adsorbent SD-3 and LTz-4 was carried out in the two-steps shown in Scheme 1 and Scheme 2. In order to determine the practical utility of the synthesized molecules (LTz-4 and SD-3) as co-adsorbent in DSSCs, deoxycholic acid (DCA) was used as the standard and HD-14 was used as the dye. Nanocrystalline TiO_2 electrodes were prepared according to the procedure reported previously [35]. Sandwich types DSCs were prepared from the stained photodiodes and Pt coated cathode. Photovoltaic measurements were carried out after introducing the electrolyte between the glass electrodes.

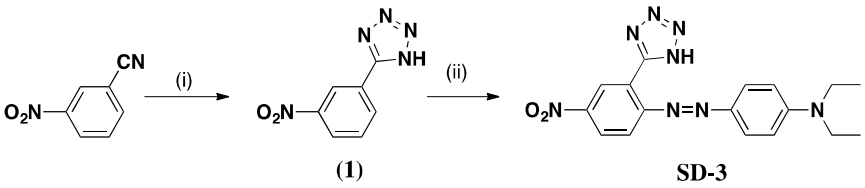

Scheme 1. Synthetic route of co-adsorbent SD-3. Reaction conditions: (i) = NaN3/NH4Cl/DMF, yield 65%; (ii) = $NaNO_2$, HCl, 5 °C, $C_6H_5N(C_2H_5)_2$.

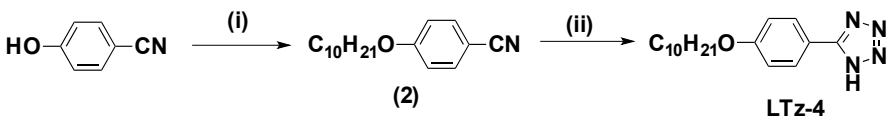

Scheme 2. Synthetic route of co-adsorbent LTz-4. Reaction conditions: (i) = $C_{10}H_{21}Br$, KOH, Toluene/DMF; (ii) = NaN3/NH4Cl/DMF, yield 65%.

3.2. Photophysical Measurements

The UV–Vis absorption and photoluminescence spectra of the co-adsorbent SD-3 and LTz-4 in DMF (concentration of 1,8 x 10^{-5} M) are depicted in Figure 2 and the corresponding photophysical data are summarized in Table 1.

Table 1. Excited state oxidation potential – ESOP (E*), ground state oxidation potential (GSOP) and the lowest electronic transitions (E_{0-0}) for SD-3 and LTz-4.

Sensitizer	Experimental (eV)		
	[a]E_{0-0} (eV)	[b,c]GSOP (E_{HOMO})	ESOP (E^*)
SD-3	1.98	-5.84	-3.83
LTz-4	4.28	-1.91	-6.19

[a] E0-0 = calculated from the onset of absorption spectra (DMF).
[b] GSOP = ground state oxidation potential = EHOMO.
[c] GSOP was measured in DMF with 0.1 M [TBA] [PF6] and with a scan rate of 50 mV s-1. It was calibrated with Fc/Fc+ as internal reference and converted to NHE by addition of 0.63 V; Excited-state oxidation potential ESOP (E*) was calculated from: E* = GSOP + aE0-0

These results suggest that LTz-4 dye possesses the strongest photoinduced intramolecular charge transfer ability over the π-conjugation backbone, leading to larger red shifts in absorption and emission spectra.

3.3. Photovoltaic parameters of DSCs

The Fig. 2 shows the IPCE response as function of wavelength. Incident photon to current conversion efficiency (IPCE) response of higher than 50% was exhibited by HD-14 – LTz-4 from 340 nm to 650 nm (reaching a maximum of 73% at 520-570 nm.) and by HD-14 – SD-3 from 390 nm to 560 nm (reaching a maximum of 55% at 410-420 nm). IPCE response high than 50% was achieved by HD-14 – DCA from 340 nm to 650 nm (reaching a maximum of 73% at 520-550 nm). These results indicate that, for this system, there is no direct relationship between amphiphilic characteristic and co-adsorbent effect

for DSSCs. This possibility is confirmed by the result presented by the HD-14 - LTz-4 dye which one presented results very close to that presented by the HD-14 - DCA dye. On the other hand, the IPCE presented by the dye HD-14 – SD-3 was inferior to the result presented by the dye HD-14 – DCA, this must be probably due to the difficulty of anchoring on TiO_2 surface.

The photovoltaic parameters including the short-circuit photocurrent density (Jsc), open-circuit voltage (Voc), fill factors (ff) and overall cell efficiencies (%η) are summarized in Table 2. HD-14 – DCA resulted in photocurrent densities (Jsc) of 19.50 mA cm^{-2}, HD-2 – LTz-4 resulted in Jsc of 19.71 mA cm^{-2} and HD-2 – SD-3 resulted in Jsc of 17.22 mA cm^{-2}, respectively. The fact that some compositions have higher values of photocurrent density can be attributed to the co-adsorbent favoring of photons capture and the more favorable injection of electrons into TiO_2. The dye HD-14 – DCA resulted in open-circuit photovoltage (V_{OC}) of 0.71 V, the dye HD-14 – LTz-4, resulted in V_{OC} of 0.70 V and the dye HD-14 – SD-3, resulted in V_{OC} of 0.67 V.

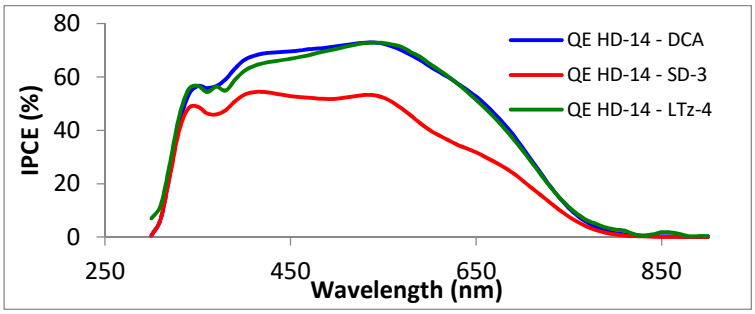

Fig. 2. Photocurrent action spectra (IPCE) obtained with the dyes HD-14 – DCA, HD-14 – LTz-4, and HD-14 – SD-3. The concentration of the co-adsorbent used was 20 mM for all dyes.

The use of LTz-4 as a co-adsorbent was shown to be more efficient. The dye HD-14 - LTz-4 resulted in a Jsc of 19.71 mA cm^{-2} and Voc of 0.70 V, translating into a total conversion efficiency (%η) of 9.21% and, the dye HD-14 – SD-3 resulted in a Jsc of 17.22 mA cm^{-2} and V_{OC} of 0.67 V, translating into a total conversion efficiency (%η) of 7.48%, while the benchmark HD-14 - DCA show a total conversion efficiency (%η) of 9.22%.

3.4. Electrochemical impedance spectroscopy

Electrochemical impedance spectroscopy (EIS) successfully models the charge transfer and chemical capacitance at the interface of TiO_2 dye/electrolyte and Pt/electrolyte in DSSC under operational conditions. Combination of charge transfer resistance (Rct) and chemical capacitance gives rise to a semi circle at the complex plan. Combination of charge transfer resistance and chemical capacitance give rise to a semi circle at the complex plan. In a typical EIS experiment, the first semicircle at high frequency corresponds to the cathode in a DSC, the middle semicircle corresponds to charge transfer resistance at the interface of dye/TiO_2 combined with chemical capacitance of electrons in TiO_2 ($eTiO_2$), and the third semicircle corresponds to finite Warburg impedance element [37-38]. The studies indicate that to the middle semicircle, the increase in its diameter is due to retardation of the charge recombination resistance (Rrec) at the interface of the TiO_2/dye/electrolyte.

Table 2. Photocurrent–voltage characteristics of DSSCs sensitized with HD-14 – DCA, HD14 – LTz-4 and HD-14 – SD-3.

DYE[a]	Voc [b] (V)	Jsc [b] (mA/cm^2)	Fill Factor[b]	Efficiency[b] (%)	Best Efficiency (%)
HD-14 – DCA	0,71	19.50 ± 0.04	0,67	9.14 ± 0.09	9.22
HD14 – LTz-4	0,70	19.71 ± 0.01	0,67	9.20 ± 0,01	9.21
HD-14 – SD-3	0,67	17.22 ± 0.02	0,65	7.48 ± 0,01	7.49

[a] Concentration of 0.3 mM in 1:1:1 acetonitrile/t-butyl alcohol/DMSO. The concentration of the co-adsorbent was 20 mM for all dyes.

[b] Averages taken over 3 to 4 devices.

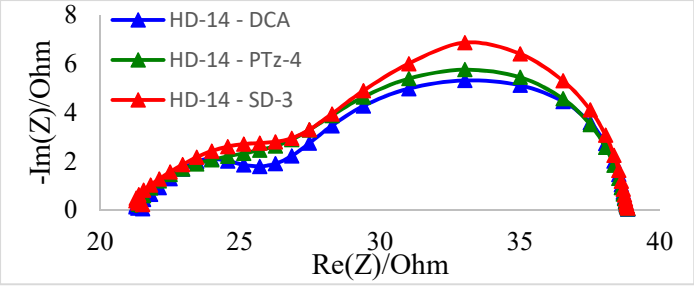

Fig. 4. EIS Nyquist plots for DSSCs sensitized with HD-14 – DCA, HD-14 – LTz-4 and HD-14 – SD-3.

In Nyquist plot (Fig. 4), the middle frequency semicircles were in the following order of increased charge recombination resistance HD-14 – SD-3 > HD-14 – LTz-4 > HD-14 – DCA, which was in the order of the actual photovoltage obtained from the corresponding solar devices. Thus, the higher the charge recombination resistance in Nyquist plot, the higher the photovoltage obtained from solar cells will be owing to slower charge recombination of electrons in TiO_2 ($eTiO_2$) and electron acceptors in electrolyte, resulting in higher $eTiO_2$ lifetime.

In Bode plots, the frequency response in the range of 1-100 Hz indicates the recombination of $eTiO_2$ with electrolyte as the function of $eTiO_2$ lifetime. The injected electron lifetime $eTiO_2$ can be determined by using the relation ($\tau CB = 1/(2\pi f)$, where τ is the lifetime of electrons in TiO_2 and f is the mid-frequency peak in Bode plots. $eTiO_2$ depends on the density of charge traps, which is ultimately related to V_{OC}. In other words, the Bode plot results complement the Nyquist plot. The frequency peak of the DSCs in the range of 1-100 Hz based on HD-14, with different co-adsorbents were at 53Hz, corresponding to $eTiO_2$ of 3.0ms, respectively, thus resulting in similar V_{OC} for different co-adsorbent, which correlates well with the actual V_{OC} reported for the solar cells (Table 2). A similar trend was also observed in the Nyquist plots (Figure 4).

The tetrazole system allows identification of two distinct effects that correlate with the magnification of the photovoltaic effect. The first one is related to the amphiphilic characteristic of the co-adsorbent and the second effect is related to the capacity of formation of the compact layer between co-adsorbent and dye.

4. Conclusion

The development of new materials for DSSCs and understanding the interaction between them remains a major challenge in creating innovative hybrid materials with valuable functionality. The photovoltaic performance of phenyltetrazoles in DSSCs, were explored and compared to DCA co-adsorbent. Overall, the results demonstrate the effectiveness of the tetrazole functional group as an alternative co-adsorbent moiety for organic photosensitizers. These results demonstrate a strong dependence of the electron injection process on TiO_2 to increase the efficiency of DSSCs.

Acknowledgments

The authors wish to thank Dr. Hammad Cheema for providing the sample of HD-14 used in this investigation.

References

[1] O'Regan B, Gra¨tzel M. Nature 1991;353:737-740.

[2] Kalyanasundaram K, Ed., Dye-sensitized solar cells, EPFL press, Lausanne, 2010.

[3] Hagfeldt A, Boschloo G, Sun L, Kloo L, Pettersson H. Chem Rev 2010;110:6595-6663.

[4] Magne C, Dufour F, Labat F, Lancel G, Durupthy O, Cassaignon S, Pauporte T. J Photochem Photobiol A 2012; 232:22-31.

[5] Nazeeruddin M K, Pechy P, Renouard T, Zakeeruddin SM, Humphry-Baker R, Comte P, et al. J Am Chem Soc 2001;123:1613-1624.

[6] Gao F, Wang Y, Shi D, Zhang J, Wang M, Jing X, et al.. J Am Chem Soc 2008;130:10720-10728.

[7] Chen C, Wang M, Li J, Pootrakulchote N, Alibabaei L, Ngoc-le CH, et al.. ACS Nano 2009;3:3103-3109.

[8] Chou C, Wu K, Chi Y, Hu W, Yu S, Lee G, et al. Angew Chem Int Ed 2011;50:2054-2058.

[9] I to S, Nazeeruddin MK, Liska P, Comte P, Charvet R, Pechy P, et al.. Prog Photovolt 2006;14:589-601.

[10] Cheema H, Islam A, Younts R, Gautam B, Bedja I, Gupta R K, El-Shafei A. Phys Chem Chem Phys 2014;16(48):27078–27087.

[11] Zhang G, Bala H, Cheng Y, Shi D, Lv X, Yu Q, et al. Chem Commun 2009; 2198-200.

[12] Im H B, Kim S K, Park C M, Jang S H, Kim C J et al.. Chem Commun 2010;46:1335-1337.

[13] Zeng W, Cao Y, Bai Y, Wang Y, Shi Y, Zhang M, et al.. Chem Mater 2010;22: 1915-1925.

[14] Heredia D, Natera J, Gervaldo M, Otero L, Fungo F, Lin CY, et al.. Org Lett 2010;12:12-15.

[15] Massin J, Ducasse L, Toupance T, Olivier C. J Phys Chem C 2014;118:10677−10685.

[16] Ogura R Y, Nakane S, Morooka M, Orihashi M, et al.. Appl Phys Lett 2009;94:073308,1-3.

[17] Holliman P J, Davies M L, Connell A, et al... Chem Commun 2010;46:7256-7258.

[18] Fan S Q, Kim C, Fang B, Liao K X, Yang G J, et al.. J Phys Chem C 2011;115:7747-7754.

[19] Han L, Islam A, Chen H, Malapaka C, et al.. Energy Environ Sci 2012; 5:6057-6060.

[20] Nguyen L H, Mulmudi H K, Sabba D, Kulkarni S A, Batabyal S K, Nonomura K, Grätzel M, Mhaisalkar S G. Phys Chem Chem Phys 2012;14:16182-16186.

[21] Ozawa H, Shimizu R, Arakawa H. RSC Adv 2012;2:3198-3200.

[22] Zhang S, Islam A, Yang X, Qin C, Zhang K, et al.. J Mater Chem A 2013;1:4812-4819.

[23] Singh S P, Chandrasekharam M, Gupta K S V, Islam A, Han L, Sharma G D. Org Electron 2013;14:1237-1241.

[24] Lee C L, Lee W H, Yang C H. J Mater Sci 2013;48: 3448-3453.

[25] Qin C, Numata Y, Zhang S, Islam A, Yang X, Sodeyama K, Tateyama Y, Han L. Adv Funct Mater 2013, 23, 3782-3789.

[26] Chen Y, Zeng Z, Li C, Wang W, Wang X, Zhang B. New J Chem 2005;29:773-776.

[27] Kuang D, Walter P, Nüesch F, Kim S, Ko J, Comte P, Zakeeruddin S M, Nazeeruddin M K, Grätzel M. Langmuir 2007;23:10906-10909.

[28] Yum J H, Jang S R, Walter P, Geiger T, Nüesch F, Kim S, Ko J, Grätzel M, Nazeeruddin M K. Chem Commun 2007;4680-4682.

[29] Magne C, Urien M, Pauporté T. RSC Adv 2013, 3, 6315-6318.

[30] Pang A, Xia L, Luo H, Li Y, Wei M. Electrochim Acta 2013, 94, 92-97.

[31] Zhang M, Wang Y L, Xu M F, Ma W T, Li R Z, Wang P. Energy Environ Sci 2013;6:2944-2949.

[32] Silva L, Gallardo H, Magnago R, Begnini I M. Mol Cryst Liq Cryst 2005;432:1-13.

[33] Santos D R, Oliveira A G S, Coelho R L, Begnini I M, Magnago R F, Da Silva L. ARKIVOC 2008;v.XVII:157-166.

[34] Akhlaghinia B, Rezazadeh S. J Braz Chem Soc 2012;23(12):2197-2203.

[35] Ito S, Murakami T N, Comte P, Liska P, Grätzel C , Nazeeruddin M K et al.. Thin Solid Films 2008;516:4613-4619.

[36] Nazeeruddin M K, Splivallo R, Liska P, Comte P, Grätzel M. Chem Commun 2003;1456-1457.

[37] Wang Q,. Moser J E, Gräatzel M. J Phys Chem B 2005;109:14945-14953.

[38] Bisquert J, J Electroanal Chem 2010;646:43-51.

E103. HYDROGEN PRODUCTION BY ETHANOL STEAM REFORMING OVER Pt-*x*TiO_2/SBA-15: EFFECT OF THE TITANIUM CONTENT

N. L. Torres-Garcia[a*]; R. Huirache-Acuña[a]; F. Fresno[b]; V.A. de la Peña O'Shea[b]

[a] Faculty of Chemical Engineering, Universidad Michoacana de San Nicolas de Hidalgo, Francisco J. Mugica s/n, 58060, Morelia, Michoacan, Mexico

[b] Photoactivated Process Unit, IMDEA Energy, Ramon de la Sagra Ave. 3, 28935, Mostoles, Madrid, España. * +524431697798, nidialibia.tg@gmail.com

ABSTRACT

Due to stricter environmental legislation and the reduction of fossil fuels reserves, energy requirements will have to be replaced by renewable, sustainable, economically efficient and safe systems. Ethanol, produced from the fermentation of biomass, as a source of hydrogen, represents great interest in the academic and industrial field.

The development of active, selective and stable catalysts for the ethanol steam photo-reforming is one of the key factors for the implementation of the process. It must maximize the production of hydrogen while at the same time reducing the formation of by-products. Various catalysts have been studied in the reaction of ethanol steam photo-reforming, including metal oxides, transition metal systems and noble metals supported in oxides, with a wide range of redox and acid-base properties.

In recent years, the development of nanostructured systems has been a breakthrough in catalytic reactions of energy and environmental interest. Recently, mesoporous materials have been widely used as support for active centers by such features: a high surface area and a uniform pore diameter and an improved dispersion of the active phase.

In this work, semiconductor catalysts were supported on mesoporous silica SBA-15 and were synthetized with different weight % (10, 20, 40, 60 and 80) of TiO_2 and 0.5wt% Pt nanoparticles as co-catalyst. The catalysts have been tested in the gas-phase ethanol steam photo-reforming By means of different characterization techniques, it was possible to determine the interaction between the active phase, the metallic nanoparticle and the catalytic support. These studies indicate that the use of mesoporous silica SBA-15 as a support increases the dispersion of the active phase, resulting in an increase in the evolution of H_2.

Keywords: Ethanol steam reforming; hydrogen production, SBA-15, titanium

1. Introduction

Hydrogen has been identified as an ideal energy carrier because it has been considered as the least polluting fuel that can be promisingly used in a fuel cell for electricity generation [1]. However, nearly 95% of hydrogen is currently produced from fossil-based feedstocks, being the steam reforming of methane the most used and nowadays the most economical option. In this process, carbon is released into the atmosphere as carbon dioxide, leading to global climate change [2].

In this mean, interest is focusing on search for effective alternatives to produce renewable hydrogen cleanly and safely. In particular, ethanol has shown good features for hydrogen production and it owns a series of advantages: a) high hydrogen content, b) good availability and low production costs, c) easy and save handling and transportation, d) non-toxicity and e) the possibility of distribution in a logistic net similar to the conventional fuel stations. In addition, ethanol could be bio-produced from a wide variety of biomass sources, including energy plants, waste materials from agroindustries or forestry residue materials, and therefore, it does not contribute to increase the greenhouse effect [3, 4].

Photo-reforming of natural gas to produce H_2 is the most energy-efficient technology currently available [5, 6]. Furthermore, the photo-reforming process could extract H_2 not only from the hydrocarbon fuels but also from water. The reaction is fast, although H_2 production is limited by thermodynamic balance [7]. In addition, catalytic photo-reforming of natural gas is, by far, the most cost-effective process.

Photo-reforming is a cost-effective and an efficient process. In addition to ethanol being a biorenewable resource, the ethanol steam photo-reforming is a promising choice in H_2-based energy systems. Stoichiometrically, the overall steam reforming reaction of C_2H_5OH could be represented as follows [8].

$$C_2H_5OH + 3H_2O \rightarrow 2CO_2 + 6H_2 \qquad (\Delta H°_{298} = +347.4 \text{ kJ/mol}) \qquad (1)$$

The intent of the reforming process is to make as much H_2 and CO_2 as possible by cracking C_2H_5OH in the presence of steam over a catalyst. However, from the reaction network, it is clear that the overall reaction is very complex and involves over a dozen of potential products. Therefore, it is important to reduce the production of undesirable intermediate compounds.

Mesostructured titania, combining high surface area, crystalline framework and high thermal stability is a promising material as photocatalyst for hydrogen production [9]. The main advantages provided by the mesoporous structure with nanocrystalline walls are: a) shorter distance of the photogenerated electron-hole pairs to reach the photocatalyst surface and b) higher surface to deposit metals or other compounds in order to modulate its activity [10]. Both aspects are beneficial for improving the photocatalytic efficiency of TiO_2 since the electron-hole pair recombination rate, which is one of its main limitations, may be drastically reduced.

Titanium oxide had been considered as a photocatalyst because of its easy availability, low-cost, non-toxicity and high stability [11]. However, bulk TiO_2 has low efficiency due to its rapid bulk recombination of photoexcited charge carriers and its low surface area [12]. Synthesized composites using materials with high surface area and mesoporous structures, such as silicas (e.g., SBA-15, HMS ad MCM-41), have provided efficient TiO_2/porous nanocomposites with enhanced photocatalytic performances [13-16]. That is, the role of support in photocatalysis is related to the TiO_2 dispersion, as well as to the supply of electrons to maintain the formation of the electron-hole pair. Consequently, mesoporous supports have become good alternatives due to their high specific areas [17].

2. Materials and Methods

2.1 Catalysts preparation

2.1.1 Synthesis of SBA-15

Mesoporous silica SBA-15 was synthesized according to the method reported by Zhao [18] and Jun et al. [19]. In this typical process, 4 g of Pluronic P123 block copolymer acting as a structural directing agent was dispersed in 150 ml of aqueous HCl 2 M while stirred. After complete dissolution of P123, 5 ml of tetraethylorthosilicate (TEOS), used as a silica source, was added dropwise to the solution. The mixture was stirred for 24 h at a well-controlled temperature of 35 °C until the TEOS was completely dissolved. After the gel solution was aged into a Teflon bottle and heated at 90 °C for 24 h without stirring. After it was cooled to room temperature, the white precipitate was collected by filtration and washed with plenty deionized water, dried at 110 °C overnight. The product was obtained by removing the template at 550 °C in air for 6 h at a heating rate of 1° C/min.

2.1.2 Synthesis of TiO_2/SBA-15

To obtain the supported TiO_2/SBA-15 materials were synthesized by internal hydrolysis method described by Van Grieken et al. [20], where a solution with the required amount of titanium tetraisopropoxide (TTiP) in isopropanol (TTiP:*i*-PrOH weight ratio 1:8) to get 10, 20, 40, 60 and 80 wt% TiO_2 loading was added to each silica support. After stirring the mixture for 45 min at room temperature, water was added until a molar ratio 160 H_2O:TTiP was reached. The stirring was then continued for other 45 min. The mixture was centrifuged and the recovered solid was dried at 110 °C overnight and calcined at 400 °C for crystallization. Throughout the subsequent discussion, the samples will be named by indicating in the first place the titania content and next the support code: # T/S, e.g. 60 T/S. As reference, a 100% TiO_2 material was prepared following the procedure described above without addition of any silica support.

2.1.3 Synthesis of Pt-TiO_2/SBA-15 by photodeposition

For this procedure, the photodeposition method described previously by Serrano et al. [10] was used. In a Pyrex reactor with an inner irradiation system consisting in a UV medium-pressure 150W mercury lamp, one liter of 10% (v/v) aqueous methanol solution containing 0.1g of catalyst and a certain amount of $H_2PtCl_6 \cdot H_2O$ corresponding to a load of 0.5wt% of Pt were placed at room temperature and kept under stirring. The system was continuously evacuated with a 50ml/min argon flow. The H_2 evolution was measured in an online gas chromatograph Micro GC Varian connected to a thermal conductivity detector (TCD). The reaction was stopped as soon as hydrogen production was detected. Subsequently, the solid was filtered and dried in an oven at 100°C overnight.

2.2 Photocatalytic reactions procedure

All the catalysts were tested in the ethanol photo-reforming reaction. For that purpose, approximately 6 mg of catalyst was coated on a glass fibre support and placed in a stainless steel reactor (16.2cm^3) with a borosilicate glass window and irradiated with two 6 W fluorescent lamps with a maximum emission at 365 nm. The reactor was kept at 40 ºC and fed by bubbling an Ar flow (20 ml/min) through a vessel contaning a 10 vol.% ethanol aqueous solution at 60 ºC. The outlet gas was analyzed

by a quadrupole mass spectrometer (Pfeiffer OMINISTAR). Each experiment was done for 3 h with cycles of turn on and off the UV light every 30 min.

3. Results and Discussion

Fig 1 shows N_2 adsorption isotherms (77 K) for calcined samples with varying titanium loadings. All materials give typical irreversible type IV adsorption isotherms with a H1 hysteresis loop as defined by IUPAC [26], main characteristic of mesoporous materials. The calculated BET or specific surface area of SBA-15 without TiO_2 phase is around 894.1 m^2/g. From the wide angle XRD analysis (Fig 2) it was confirmed that anatase was the predominant allotropic phase of TiO_2, with brookite as minor phase only in the materials with more amount of TiO_2.

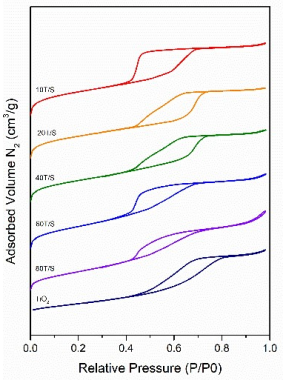

Fig 1. N_2 adsorption–desorption isotherms of TiO_2/SBA-15 calcined at 400°C.

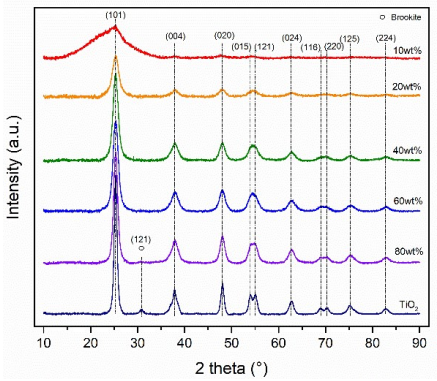

Fig 2. The wide range XRD patterns of the TiO_2/SBA-15 samples calcined at 400°C.

The Raman spectra in Fig 3 reveal that peaks corresponding to vibrations of the anatase lattice at ca. 143 (E_g; strong), 398 (B_{1g}; medium), 517 (A_{1g} + B_{1g}; medium) and 637 (E_g; medium) [27], are present in all cases except for the samples with the lowest titania charge, which looks amorphous to Raman spectroscopy probably due to an increased amount of mesoporous silica SBA-15. Band gap energy was estimated through DRS spectra from a plot of Kubelka-Munk [F(R)] versus photon energy (Table 1). The intercept of the tangent to the plot direct gives a good approximation of the band gap energy for indirect band gap materials such as TiO_2 [28, 29]. The larger band gap of these catalysts is with a load of 20wt% TiO_2, which can be attributed to the quantum size effect [30]. This is because the prepared TiO_2 nanoparticles have smaller crystal size limited by SBA-15 nanometer channels [31].

Table 1. Band gap estimated from a plot of Kubelka-Munk versus photon energy.

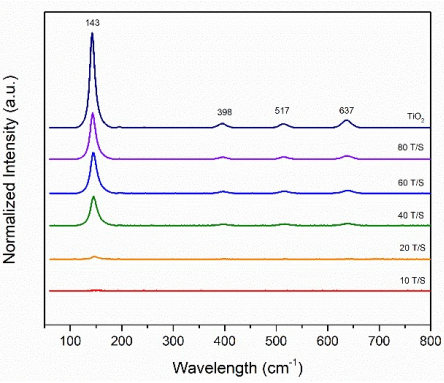

Fig 3. Raman spectra of TiO_2/SBA-15 catalysts calcined at 400°C.

Catalyst	eV
TiO_2	3.07
80 T/S	3.07
60 T/S	3.10
40 T/S	3.14
20 T/S	3.17
10 T/S	3.26

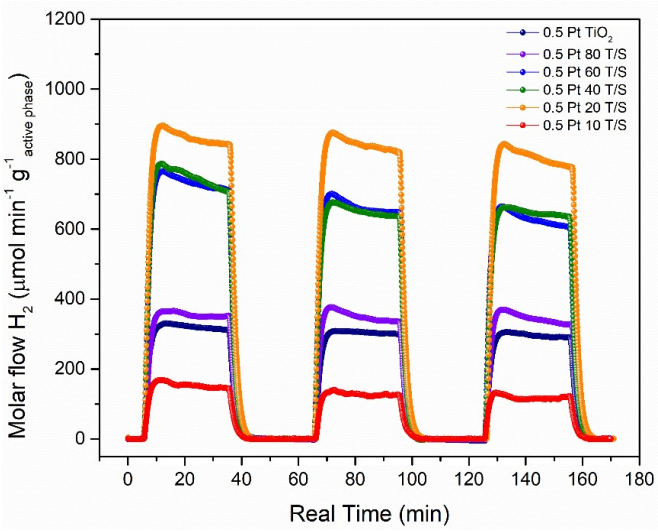

Fig 4. Catalytic activity for ethanol steam photo-reforming under UV light of 0.5wt%Pt-$x$$TiO_2$ supported on mesoporous silica SBA-15.

In the presence of UV light, as can be seen in fig 4, all the materials, with the exception of the lowest amount of active phase, show an increase in the production of hydrogen due to the use of the mesoporous support SBA-15 since it is more dispersed the active phase, you can see an increase in hydrogen production with respect to the material that has no support.

It could be said that the mesoporous support allows a better interaction between the metallic nanoparticle of Pt and the TiO_2 semiconductor, which allows a more appropriate e^-/h^+ recombination.

4. Conclusion

Photo-active Pt-loaded titania supported on SBA-15 samples have been obtained and evaluated in ethanol photo-reforming as an alternative for H_2 production. Pt species have proved to be effective co-catalyst for this reaction, with the preparation method being more determining in the attained productivity. Moreover, mesoporous silica SBA-15 helped to disperse the active phase and improve the hydrogen production. In fact, the 0.5wt%Pt-20wt%TiO_2/SBA-15 had the lower amount of active phase Pt-TiO_2 and, because it has a better dispersion of the active phase, had a better hydrogen production, so this type of supported cocatalysts could be promising for ethanol steam photo-reformating reactions.

Acknowledgements

The authors appreciate the support of CIC UMSNH 2019 Project, the CONACyT for the scholarship (465563) to NLTG, Spanish Ministry of Science, Innovation and Universities(ENE2016-79608-C2-1-R) and the European Research Council (contract number. 648319) are acknowledged. The authors wish to thank Comunidad de Madrid for its support to the FotoArt-CM Project (S2018/NMT-4367).

References

[1] Zhang L, Li W, Liu J, Guo C, Wang Y, Zhang J. Ethanol steam reforming reactions over Al_2O_3.SiO_2-supported Ni–La catalysts. Fuel 2009;88:511–8.

[2] Vizcaíno AJ, Carrero A, Calles JA. Hydrogen production by ethanol steam reforming over Cu–Ni supported catalysts. Int J Hydrogen Energy 2007;32:1450–61.

[3] Fierro V, Akdim O, Provendier H, Mirodatos C. Ethanol steam reforming over Ni-based catalysts. J Power Sources 2005;145: 659–66.

[4] Comas J, Mariño F, Laborde M, Amadeo N. Bio-ethanol steam reforming on Ni/Al_2O_3 catalysts. Chem Eng J 2004; 98:61–8.

[5] Armor JN. Review: The multiple roles for catalysis in the production of hydrogen. Appl Catal A 1999; 176:159-76.

[6] Spilsbury C. Hydrogen. Production, supply and distribution. Presented at the Hydrogen Production Workshop, University of Glamorgan, Pontypridd, Wales, UK. February 14, 2001.

[7] Chen Z, Yan Y, Elnashaie SSEH. Catalyst deactivation and engineering control for steam reforming of higher hydrocarbons in a novel membrane reformer. Chem Eng Sci 2004; 59:1965-78.

[8] Velu S, Satoh N, Gopinath CS, Suzuki K. Oxidative reforming of bio-ethanol over CuNiZnAl mixed oxide catalysts for hydrogen production. Catal Lett 2002; 82 (1):145-52.

[9] Jing D, Guo L. WS_2 sensitized mesoporous TiO_2 for efficient photocatalytic hydrogen production from water under visible light irradiation. Catal Commun 2007;8:795-9.

[10] Serrano DP, Calleja G, Pizarro P, Galvez P. Enhanced photocatalytic hydrogen production by improving the Pt dispersion over mesostructured TiO_2. Int J Hydrogen Energy 2014; 39: 4812-19.

[11] Bian Z, Zhu J, Li H. Solvothermal alcoholysis synthesis of hierarchical TiO_2 with enhanced activity in environmental and energy photocatalysis. J Photochem Photobiol C Photochem Rev 2016; 28:72-86.

[12] Müller V, Schmuki P. Efficient photocatalysis on hierarchically structured TiO_2 nanotubes with mesoporous TiO_2 filling. Electrochem Commun. 2014; 42: 21-25.

[13] Conceição DS, Graça CAL, Ferreira DP, Ferraria AM, Fonseca IM, Botelho do Rego AM, Teixeira ACSC, Vieira Ferreira LF. Photochemical insights of TiO_2 decorated mesoporous SBA-15 materials and their influence on the photodegradation of organic contaminants. Micro Meso Mater 2017; 253:203-14.

[14] Wang XJ, Lin FT, Hao YJ, Liu SJ, Yang ML. TiO_2/SBA-15 composites prepared using H_2TiO_3 by hydrothermal method and its photocatalytic activity. Mater Lett 2013; 99:38-41.

[15] Zhuang Y, Song HY, Li G, Xu YJ. Ti-HMS as a single-site photocatalyst for the gas-phase degradation of benzene. Mater Lett 2010; 64:2491-93.

[16] Chen H, Peng YP, Chen KF, Lai CH, Lin YC. Rapid synthesis of Ti-MCM-41 by microwave-assisted hydrothermal method towards photocatalytic degradation of oxytetracycline. J Environ Sci 2016; 44:76-87.

[17] Conceição DS, Graça CAL, Ferreira DP, Ferraria AM, Fonseca IM, Botelho do Rego AM, Teixeira ACSC, Vieira Ferreira LF. Photochemical insights of TiO_2 decorated mesoporous SBA-15 materials

and their influence on the photodegradation of organic contaminants. Micro Meso Mater 2017; 253: 203-14.

[18] Zhao D, Feng J, Huo Q, Melosh N, Freedrickson GH, Chemelka BF, Stucky GD. Triblock copolymer syntheses of mesorporous silica with periodic 50 to 300 angstrom pores, Science 1998; 279: 548-52.

[19] Jun S, Joo SH, Ryoo R, Kruk M, Jaroniec M, Liu Z, Ohsuna T, Terasaki O. Synthesis of new, nanoporous carbon with hexagonally ordered mesostructured, J Am Chem Soc 2000; 122: 10712-13.

[20] Van Grieken R, Aguado J, Lopez-Muñoz MJ, Marugán J. Synthesis of size-controlled silica-supported TiO_2 photocatalysts. J Photochem and PhotoBiol A: Chem 2002; 148: 315-22.

[21] Brunauer S, Emmet PH, Teller E. Adsorption of gases in multimolecular layers. J Am Chem Soc 1938; 60:309-19.

[22] Barrett EP, Joyner LG, Halenda PP. The determination of pore volume and area distribution in porous solids. I: computation from nitrogen isotherms. J Am Chem Soc 1951; 73: 373-80.

[23] Stanick AI, Brauns EB. A simple asymmetric lineshape for fitting infrared absorption spectra, Vib Spectrosc 2008; 47: 66-69.

[24] Klaas J, Schulz-Ekloff G, Jaeger NI. UV-visible diffuse reflectance spectroscopy of zeolite-hosted mononuclear titanium oxide species. J Phys Chem B 1997; 101: 1305-11.

[25] Wang Y, Suna A, Mahler W, Kasowski R. PbS in polymer from molecules to bulk solids. J Chem Phys 1987; 87(12):7315.

[26] Sing KSW, Everett DH, Haul RAW, Moscow L, Pierotti RA, Rouquerol J, Siemieniewska T. Pure Appl Chem 1985; 57:603.

[27] Zeng T, Qiu Y, Chen L, Song X. Microstructure and phase evolution of TiO_2 precursors prepared by peptization-hydrolisis method using polycarboxylic acid as peptizing agent. Mater Chem Phys 1998; 56: 163-70.

[28] Rahman NM, Krishna KM, Soga T, Jimbo T, Umeno M. Optical properties and X-ray photoelectron spectroscopic study of pure and Pd-doped TiO_2 thin films. J Phys Chem 1999; 60(2): 201-10.

[29] Kormann C, Bahnemann DW, Hoffmann MR. Preparation and characterization of quantum-size titanium dioxide. J Phys Chem 1998; 92: 5196-5201.

[30] Lachheb H, Ahmed O, Houas A, Nogier JP. Photocatalytic activity of TiO_2-SBA-15 under UV and visible light. J Photochem Photobio A: Chem. 20111; 226: 1-8.

[31] Gao F, Lu Q, Zhao D. In situ adsorption method for synthesis of binary semiconductor CdS nanocrystals inside mesoporous SBA-15. Chem Phys Lett 2002; 360(5): 585-91.

E104. ZEOLITES FROM GEOTHERMAL NANOSILICA AND ITS EVALUATION IN THE DEHYDRATION OF BIOETHANOL

J.A. Trejo García[1], A. Medina Ramirez[1*], B. Ruiz Camacho[1], J.I. Minchaca Mojica[1], C.M. López Badillo[2]

[1]Departamento de Ingeniería Química, División de Ciencias Naturales y Exactas, Universidad de Guanajuato, Campus Guanajuato. Noria Alta s/n, 36050, Guanajuato, Guanajuato, Mexico

[2]Facultad de Ciencias Químicas, Universidad Autónoma de Coahuila, Blvd. V. Carranza y José Cárdenas, 25280, Saltillo, Coahuila, Mexico

* Corresponding author: 473 7320006; adriana.medina@ugto.mx

ABSTRACT

Investigations related to the bioethanol production from different kind of biomass has atracted the attention due to the bioethanol increase the octane number of gasoline, minimice the emissions, and it can reemplace some additives. Additionally the biotehanol can be use in the fuel cells. Nevertheless the challenge in the production of biotehanol is that during fermentation process the bioethanol contains water, this generate inmiscible mixture of hydrocarbons affecting the performance of engine. Among different separations techniques the adsorption is a proper alternative and its effectivess depends of the adsorbent nature. For these reasons in the present work zeolitic materials were synthesized from geothermal nanosilica by hydrothermal method, the effect of time and temperature of crystallization were evaluated. The products were characterized by TEM, SEM and XRD techniques. Solutions of water-ethanol of composition similar to bioethanol were used during adsorption trials. The content of ethanol was determined by UV-Vis spectroscopy. The XRD analysis allowed to identify the crystalline phases: LTA type and X type zeolites. The low crystallization temperature favors the formation of the X zeolite. The ageing allow to reduce the time of crystallization of X zeolite. The zeolites exhibited a cubic and octahedral morphology, the X-zeolite was obtained in nanometric size. The water adsorption capacity was influenced by the framework type of the zeolites. According to the results the X-zeolite presented more afinnity for water molecules and a higher water adsorption capacity reaching an alcohol concentration of 98.95% (v/v), make it potentially useful to obtaining of fuel grade bioethanol..

Keywords: zeolites, bioethanol, adsorption, separation

1. Introduction

Ethanol is generally used for chemical products and beverages; however its applications have been diversified in the last years, being one of them its use as fuel. It can contribute to solve the energy crisis and decrease the CO_2 emissions. Ethanol can be obtained from biomass rich in carbohydrates by sugars fermentation process, receiving the name of bioethanol [1, 2].

Additionally the bioethanol increase the octane gasoline, it can acts as anti-blocking agent and can replace some additives [3]. Nevertheless one of the main challenges for bioethanol as fuel is that during its production it is generated as ethanol-water mixture, requiring additional purification processes [4].

Through conventional fermentation processes along with distillation multiple stages are reached concentrations of 96.8% (v/v), this implies the ethanol must be concentrated to obtain anhydrous concentration. The purity of bioethanol is required due to the presence of water leads to formation of immiscible hydrocarbons mixtures which cause damage to the engine affecting its performance and even generate irreversible mechanical failures.

Different methodologies have been implemented to reduce the water content such as extractive distillation, azeotropic distillation, pervaporation and adsorption [5]. The extractive distillation and azeotropic distillation require the use of separation agents whose recovering complicate the separation technology, besides these technologies consume a high energy.

Adsorption allows producing bioethanol of combustible grade and its energy consumption is low. This method can perform by two approaches, first the water is removed from a solution of high concentration of ethanol-water; and the second one consist in adsorb the ethanol from an ethanol-water diluted solution from effluent of fermentation [6]. The main challenge in the adsorption is the adsorbent; it should be exhibit selectivity and high adsorption capacity. Several materials have been evaluated as adsorbent in bioethanol purification such as activated carbon [7], starch-base materials [8], biosorbents [9], polymeric resins [10] and some molecular sieves, particularly natural zeolites [11, 12], silicalite [6, 13], ZSM-5 [14,15], LTA, FAU, MOR [16] y Alpo´s [17].

Zeolites have specific properties such as frameworks constituted by channels, cavities and cages that confer them shape and size selectivity, chemical and thermal stability and reversible dehydration. The above mentioned give to zeolites important advantages for dehydration of alcohols: a) high

dehydration grade, b) low energy consume, c) not chemicals are required and d) allow a high recovering of alcohol [18].

According to diverse studies [12] the temperature, the pressure and the particle size of adsorbent influence the ethanol-water separation. Although different zeolites have been used for ethanol dehydration some parameters affect their efficiency, such as framework, Si/Al ratio, selectivity and stability. These parameters are determined by the batch composition and synthesis conditions.

Taking in account the zeolites properties and particle size of the adsorbent play a important role in the ethanol purification, the obtaining of zeolitic materials at nanometric scale potentize their application, because of these materials have enhanced textural properties and they may have hierarchical structure favoring the selectivity. The control of particle size depends of the method, synthesis conditions and precursors [19].

For these reasons in the present work hydrophilic zeolites were synthesized from geothermal nanosilica, evaluating the time and temperature of crystallization. The zeolitic materials were evaluated as adsorbents for dehydration of ethanol-water solutions.

2. Materials and Methods

The geothermal nanosilica was obtained from Cerro Prieto power plant (Baja California, Norte, Mexico). Sodium aluminate was used as alumina source, sodium hydroxide was used as mineralizing agent and deionized water was the reaction medium. Previous to the nanozeolites synthesis, the nanosilica was washed with hot water to eliminate the soluble salts. This procedure was repeated three times. The solid was filtered and dried at 110°C for 4 h.

2.1 Nanozeolites Synthesis

The nanozeolites were synthesized as follows: a alkaline solution of molar composition $1.83H_2O$:$0.0025Na_2O$ was prepared. Then the solution was divided in two equal volumes. To the first volume 0.02 mol of alumina was added and kept under stirring until complete dissolution (S1). 0.055 mol of nanosilica were collocated in a mortar and 0.036 mol of Na_2O were added, they were triturated until homogenized slurry was obtained. The slurry was added to second volume of alkaline solution and

sonicated for 1 h (S2). Afterwards de solution S2 was added to solution S1, the mixture was kept under stirring at 40°C, for 24 h.

The crystallization treatment was carried out by hydrothermal method using a Parr reactor of 43 mL, the gel was transferred to reactor and submitted to crystallization. Two temperatures were evaluated: 60°C and 99°C for two periods of time: 2 and 4 h. The reaction product was recovered, washed and dried at 100°C for 12 h.

2.2 Water adsorption on nanozeolites

Two concentrations of mixtures ethanol/water were evaluated: 90/10 and 97/3 (%v/%v), five hundred milligrams of nanozeolite were added to 100 mL of the ethanol/water solution, the slurry was kept under stirring for 3 h. Aliquots of 10 mL were taken at different intervals of time. The water adsorbed on the nanozelite was determined by UV-spectroscopy using cobalt chloride as chromophore. The sample was analyzed at 450-750 nm range and the absorbance was measured at 656 nm.

2.3 Characterization Techniques

The nanozeolites were characterized by XRD using a PANalytical Model Empyrean difractometer with a CuK α (λ=1.5604Å) radiation source in the 7-60° 2θ range. The morphology was examined by TEM using a JEOL 1010 field emission microscope. The elemental chemical composition and morphology of the samples were determined by EDS and SEM using a JEOL scanning electron microscope (model JSV-6610LV).

3. Results and Discussion

3.1 Physicochemical characterization

In figure 1 are showed the XRD patterns of the nanozeolites synthesized from geothermal nanosilica. It can be observed that under crystallization conditions (temperature and time) evaluated was possible the formation of zeolitic phases: X zeolite and LTA zeolite. Additionally the temperature has an important effect on the type zeolite obtained. At low temperature (60°C) the X zeolite (JCPDS 00-39-0218) is the predominant phase, and the increase in the crystallization time (4h) enhance the intensity of the peaks

of this phase. The presence of LTA is due to high Na/Al ratio used in the batch composition, it was of 1.8. According to literature [20] in order to avoid the formation of LTA together to X zeolite the Na/Al ratio should be lower to 0.07.

On the other the crystallization at 99°C promote the coexistence of the LTA (JCPDS-04-016-9920) and X zeolites. This behavior can be associated to the both zeolites exhibit similar secondary building units: sodalite cage and four double member rings. Oleksiak et al., [21] reported that the stability of zeolitic structure tends to increase with higher framework density and high aluminum content. Nevertheless these effects competing in this synthesis, LTA is richer in aluminum and X zeolite is denser. This would explain the presence of both phases. Additionally the temperature (99°C) is closer to the crystallization of LTA than X zeolite (90°C).

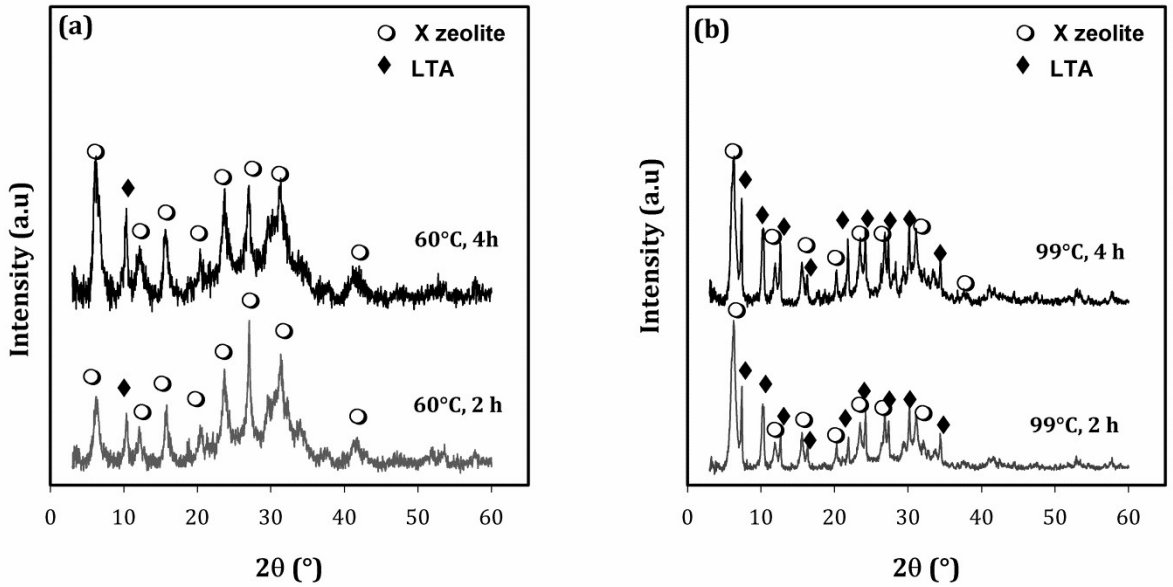

Fig. 1 XRD patterns of nanozeolites synthesized from geothermal nanosilica, crystallized at (a) 60°C and (b) 99°C.

According to TEM analysis (Fig. 2) the nanozeolites exhibited morphology of octahedral for X zeolite and cubic morphology for LTA zeolite. It can be observed that the particle size was smaller for X zeolite than LTA zeolite. These results are agree to that those observed by XRD where the patterns of zeolite synthesized at 60°C where the X zeolite was the majority phase, presented broader peaks.

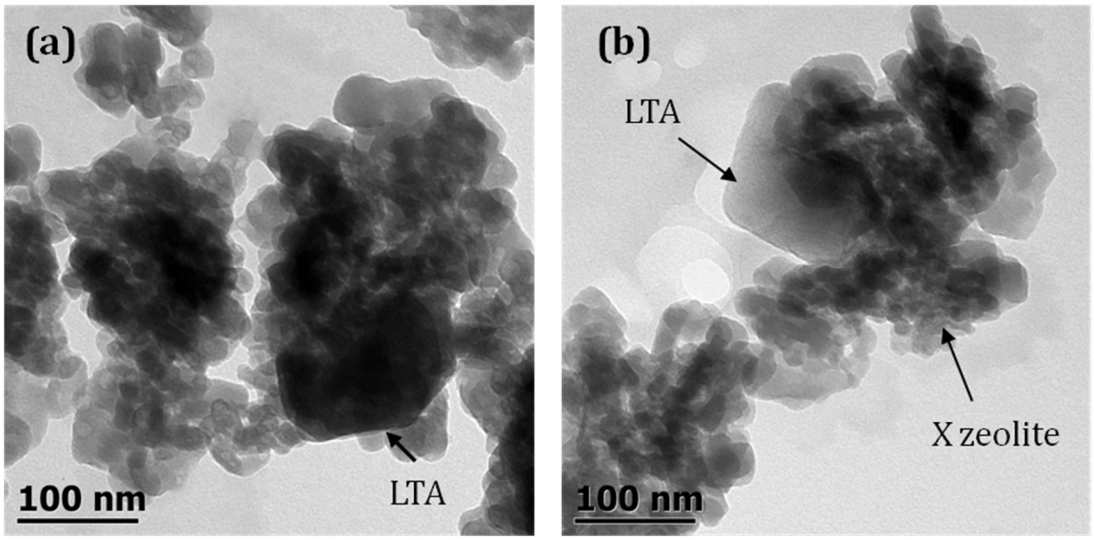

Fig. 2 TEM micrographs of nanozeolites synthesized from geothermal nanosilica at 99°C for (a) 2 h and (b) 4 h.

The nanozeolite synthesized at 60°C for 2 h presented a more homogeneous morphology corresponding to mainly octahedral (Fig. 3). According to EDS analysis the nanozeolite presented a Si/Al ratio of 1.15.

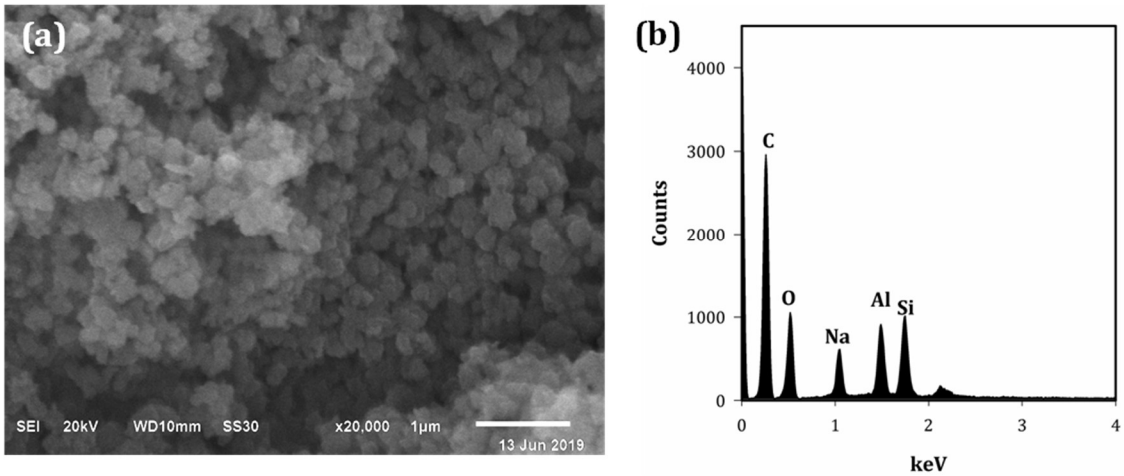

Fig. 3 (a) SEM micrograph and (b) EDS spectrum of nanozeolite synthesized from geothermal nanosilica at 60°C for 2 h

3.2 Water adsorption capacity of nanozeolites

The zeolite type obtained from geothermal nanosilica had an important effect on the water adsorption capacity from ethanol/water solutions. As can be observed in Fig. 4, the four nanozeolites showed affinity for water molecules. Nevertheless the water adsorption capacity was higher for the nanozeolites synthesized at 60°C, for both concentrations of ethanol/water evaluated. These findings are associated to these nanozeolites are mainly X zeolite, whose framework posses larger cavities (~ 6Å) than LTA framework (~4Å), it allows that a higher number of water molecules will be adsorbed on the X zeolite. Additionally, the specific surface area of X zeolite (~300 m^2/g) is higher than LTA zeolite enhancing a higher contact between the water molecules and zeolitic surface.

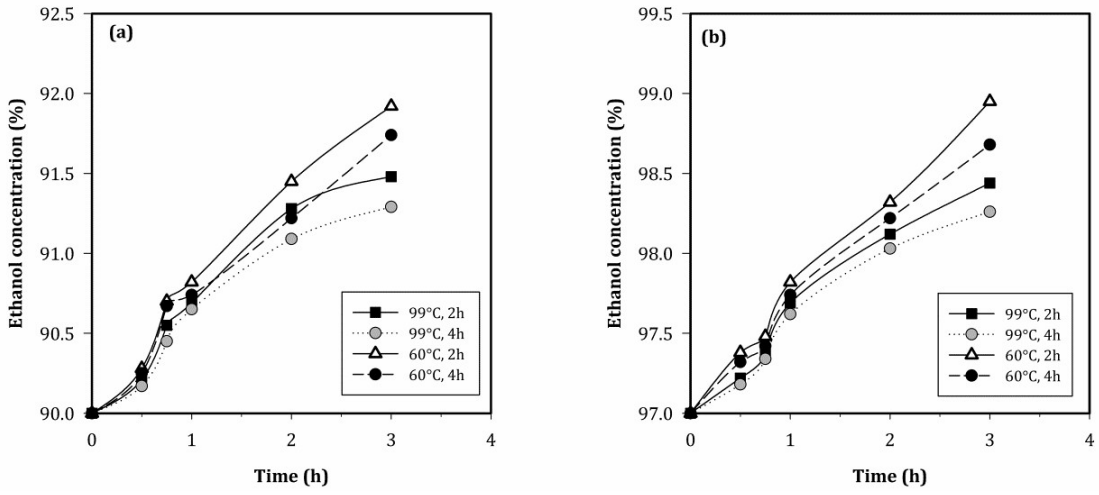

Fig. 4 Water adsorption capacity of nanozeolites synthesized from geothermal nanosilica at different conditions, using ethanol/water solutions of concentration (a) 90/10 (% v/v) and (b) 97/3 (%v/v).

4. Conclusion

Type X and LTA nanozeolites were synthesized from geothermal silica by hydrothermal method. The formation of X zeolite was favored at low temperature. The ageing allowed reducing the crystallization

time. The X nanozeolite synthesized from geothermal nanosilica showed more affinity and higher adsorption capacity for water molecules reaching to obtain ethanol of high purity (98.95%). These results are encouraging to use these materials for ethanol purification. Nevertheless additional studies are required to determine the selectivity of these nanozeolites, and evaluate them on real bioethanol samples.

Acknowledgements

The authors acknowledge to Universidad de Guanajuato through the DAIP office for the financial support of this work, project: 107/2019 "*Síntesis y caracterización de nanoadsorbentes para obtención de bioetanol grado combustible*". J.A. Trejo Garcia acknowledge to Universidad de Guanajuato for the fellowship received.

References

[1] Roback K, Balcerek M, Review of Second Generation Bioethanol Production from Residual Biomass, Food Technol. Biotechnol. 2018, 56, 174-187

[2] Khan Z, Dwived A.K, Fermentation of Biomass for Production of Ethanol: A Review, Universal Journal of Environmental Research and Technology, 2013, 3, 1-13

[3] Frolkova A. K, Raeva V. M. Bioethanol Dehydration: State of the Art, Theoretical Foundations of Chemical Engineering, 2010, 44, 545–556

[4] Megawati, Rengga, W.D.P, Fardhyanti D.S, Akhir A.E, Sendiawan, W.B. Modelling of Adsorptive-distillation of Ethanol-water Using Natural and Synthetic Zeolites as Adsorbent, Journal of Physical Science, 2018, 29, 243-256

[5] Gravelle S, Yoshida H, Joly L, Ybert C, Bocquet L. Carbon membranes for efficient water-ethanol separation, 2016, https://arxiv.org/pdf/1609.02084.pdf

[6] Hajilari M, Shariati A, Khosravi-Nikou M. Equilibrium adsorption of bioethanol from aqueous solution by synthesized silicalite adsorbents: experimental and modeling, Adsorption, 2019, 25, 13-31

[7] Romero-Anaya A.J, Lilo-Rodenas M.A, Linares-Solano A, Factors governing the adsorption of ethanol on spherical activated carbons, Carbon, 2015, 85; 240-249

[8] Okewale, A.O, Etuk, B.R, Igbokwe, P.K. Comparative Studies on Some Starchy Adsorbents for the Uptake of Water from Ethanol – Water Mixtures. International Journal of Engineering & Technology, 2011, 11, 18-27

[9] Ranjbar Z, Tajallipour M, Niu CH, Dalai AK. Water removal from ethanol vapor by adsorption on canola meal after protein extraction. Ind Eng Chem Research 2013, 52, 14429–14440.

[10] Delgado J.A., Águeda V.I., Uguina M.A, Sotelo J.L., García A., Brea P., García-Sanz A. Separation of ethanol–water liquid mixtures by adsorption on a polymeric resin Sepabeads Chemical Engineering Journal, 2013, 220, 89-97

[11] Herlina N, Harahap I.S.D, The Addition of Zeolite Adsorbents and Calcium Oxide on Purification of Bioethanol from Sugar Palm (Arenga pinnata Merr), IOP Conf. Series: Earth and Environmental Science, 2018, 130, 012035

[12] Karimi S, Ghobadian B, Omidkhah MR. Towfighi J, Yaraki MT, Experimental investigation of bioethanol liquid phase dehydration using natural clinoptilolite, Journal of Advanced Research, 2016, 7, 435–444

[13] Delgado JA, Uguina M.A, Sotelo JL, Águeda VI, García A, Roldán A, Separation of ethanol–water liquid mixtures by adsorption on silicalite, Chemical Engineering Journal, 2012, 180, 137– 144

[14] Zhang K, Lively RP, Noel JD, Dose ME, McCool BA, Chance RR, Koros WJ, Adsorption of Water and Ethanol in MFI-Type Zeolites, Langmuir, 2012, 28, 8664-8673

[15] Ueno K, Negishi H, Miyamoto M, Uemiya S, Oumid Y, Effect of Si/Al ratio and amount of deposited MFI-type seed crystals on the separation performance of silicalite-1 membranes for ethanol/water mixtures in the presence of succinic acid, Microporous and Mesoporous Materials 2018, 267 1–8

[16] Yamamoto T, Kim YH,, Kim B.Ch, Endo A, Thongprachan N, Ohmori T, Adsorption characteristics of zeolites for dehydration of ethanol: Evaluation of diffusivity of water in porous structure. Chemical Engineering Journal 2012, 181– 182, 443– 448

[17] Cekova B, Kocev D, Kolkakovska E, Stojanova D, Zeolites as alcohol adsorbents from aqueous solutions, APTEFF, 2006, 37, 83-87

[18] Chopade V.J, Khandetod Y. P, Mohod A.G, Dehydration of Ethanol-Water Mixture Using 3a Zeolite Adsorbent, International Journal of Emerging Technology and Advanced Engineering, 2015, 5, 152-155

[19] Mintova S, Gilson JP, Valtchev V, Advances in nanosized zeolites, Nanoscale, 2013, 5, 6693-6703

[20] Wang B, Li Y, Shao Ch, Cui M, Duta PK, Rapid and high yield synthesis method of colloidal nano faujasite, Microporoues Mesoporous Mater, 2016, 230, 89-9

[21] Oleksiak MD, Soltis JA, Conato MT, Penn RL, Rimer JD, Nucleation of FAU and LTA Zeolites from Heterogeneous Aluminosilicate Precursors, Chem Mater, 2016, 28, 4906-4916

E106. SYNTHESIS OF NI BASED ELECTROCATALYSTS BY USING INTERMITTENT MICROWAVE HEATING REDUCTION PROCESS FOR ETHANOL OXIDATION REACTION

L.R. Vidales-Gallardo[1], Eddie N. Armendáriz-Mireles[1], E. Rocha-Rangel[1], W.J. Pech-Rodríguez[1*]

[1] Universidad Politécnica de Victoria, Av. Nuevas Tecnologias 5902, Parque Cientifico y Tecnológico de Tamaulipas, Ciudad Victoria, Tamaulipas, C.P. 87138. México.

* Corresponding author: wpechr@upv.edu.mx

ABSTRACT

At today, Pt based catalysts has been extensively used as anode for fuel cell technology. Nevertheless, there is some drawbacks that need to be overcomed for widespread application of fuel cell in real world. The high cost of Pt electrocatalysts and the poisoning of these electrodes are the major obstacles for the development of fuel cell devices so great effors has been paid in the development of cost-effecttive electrocatalysts.

This work is focused on the design and development of Ni based electrocatalysts by using the well known intermittent microwave heating polyol reduction process. The electrocatalysts were synthesized under different sequences of irradiation time and Ni concentration in order to obtain NiO nanoparticles. The obtained electrocatalyst was chemical characterized by Fourier-Transform Infrared Spectroscopy. Meanwhile, their electrochemical activity for ethanol oxidation reaction (EOR) was studied by cyclic voltammetry, chronoamperometry and electrochemical impedance spectroscopy. From the experimental part its observed that factors sucha as time, tempearture and NaOH concentration play a crucial role to succesfully obtain NiO nanoparticles. Cyclic voltammetry measurements shows the peaks related to reduction and oxidation of Ni species. The electrochemical measurements shows that NiO nanoparticles are active for ethanol oxidation reaction and the rate of reaction increases as the concentration of ethanol is increased. The results indicated that the synthesized parameters play a key role into the electrochemical activity of the materials. Therefore, it is demonstrated that intermittent microwave irradiation is a promising method to synthetize in a short time and in large scale Ni based electrocatalyst to be used in direct alcohol fuel cells.

1. Introduction

Direct alcohol fuel cells (DAFC) are devices that can be used as renewable energy power source to meet the future electrical demand [1, 2]. DAFC are advantageous because they use liquid fuel that can be produced by biomass fermentation and also they can use the actual gasoline infrastructure with some modifications. At today, this technology needs to overcome some important barrier to be used in practical applications. One of them is the slow alcohol oxidation reaction at the anode that results in low electrical efficiencies. With the aim to enhance the electrochemical kinetic at the anode Pt based electrocatalyst has been used [3-5]. Nevertheless, the use of Pt-based electrocatalyst limited the widespread implementation of DAFC due to issues relate to the scarcity, high cost, deactivation and stability of Pt [6, 7]. In order to overcome the aforementioned issues extensive research has been devoted to develop electrocatalyst using non-noble transition metals [8, 9]. Danaee and coworkers modified a glassy carbon electrode by galvanostatic electrodeposition to study the methanol oxidation reaction in alkaline media. They found that Ni present activity for methanol oxidation and a chemical equation was prosed to elucidate the pathway for this electrochemical reaction [10]. On the other hand, it has been demonstrated that Ni-based electrocatalyst can be synthesized by chemical methods [11, 12]. For example, the research group of Prabhakarn synthesized Ni-CuO nanocomposites by using the coprecipitation method that involves a vacuum dried process and thermal treatment [13]. In this work, we proposed a rapid and efficient method to synthesize Ni nanoparticles by using microwave heating polyol process for DAFC applications.

2. Materials and Methods.

The reagent used for NiO synthesis were ethylene glycol (CH_2OHCH_2OH), sodium hydroxide(NaOH), anhydrous ethanol(CH_3CH_2OH), nickel chloride hexahydrate ($NiCl_2*6H_20$), , isopropyl alcohol (2-propanol) from Jalmek.

For the preparation method, 500 mg of $NiCl_2$ were dissolved in 60 mL of ethylene glycol using an ultrasonic bath. Then, 2 mL of 1 mol L^{-1} NaOH was added to the mixture and the round bottom flaks was put inside of modified microwave oven. The sample was filtered and washed with 20 ml of anhydrous ethanol and deionized water. The as synthesized electrocatalyst was dried at 100 °C for 20 min to remove moisture from the nickel particles.

The catalytic activity of the NiO nanoparticles we investigated in a three-electrode cell setup using a Gill AC potenciostat/galvanostat. The working electrode was obtained by transferring an aliquot of catalytic ink composed of 5 mg of NiO nanoparticles, 0.5 mL of 2-propanol and 15 µL of Nafion®. The counter electrode was a graphite bar while the reference electrode was Ag/AgCl.

3. *Results and Discussion*

The surface of the Ni powder was characterized by FTIR and the spectrum is displayed in ¡Error! No se encuentra el origen de la referencia.. The band located at 466 cm^{-1} is attributed to Ni-O stretching mode and also the perturbation bands at 653 cm^{-1} and 785 cm^{-1} are due to Ni-O vibrations [13, 14] . This result suggests that Ni^{2+} species has reduced to NiO after the microwave heating process. Besides, the peak at 1081 cm^{-1} may be due to the adsorbed species of ethylene glycol during the synthesis [15]. The vibration band at 1629 cm^{-1} is ascribed to bending vibration of water molecule [16]. The band at 3400 cm^{-1} is assigned to O-H stretching vibrations.

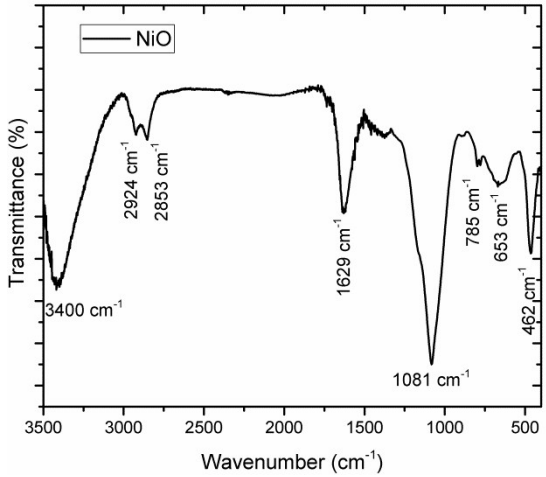

Figure 7. FTIR spectra for the synthesized NiO nanoparticles.

¡Error! No se encuentra el origen de la referencia. shows the obtained stabilized CV for GCE and modified NiO electrode in 0.5 mol L^{-1} NaOH, after a pre-activation of 40 cycles at scan rate of 50 mV s^{-1}. As can be observed these electrodes display different CV pattern. The GCE electrode shows an increase in current density in the forward scan close to 0.37 V that is ascribed to oxygen evolution reaction (OER)[17], no other process was observed. Meanwhile, Ni modified electrode presents a broad band, in the in the positive scan, between 0.18 V and 0.4 V. This anodic peak is ascribed to $Ni(OH)_2$ oxidation to

form the NiOOH species[18, 19] and the reduction process occurs in the reverse scan near to 0.14 V. The OER reaction process is overlapped with the Ni anodic peak. From ¡Error! No se encuentra el origen de la referencia. it also be concluded that GCE deliver more density currents due to the OER at more negative potentials compared with the modified Ni electrode. The latter might be due to the fact that NiO electrode consumes O^- species.

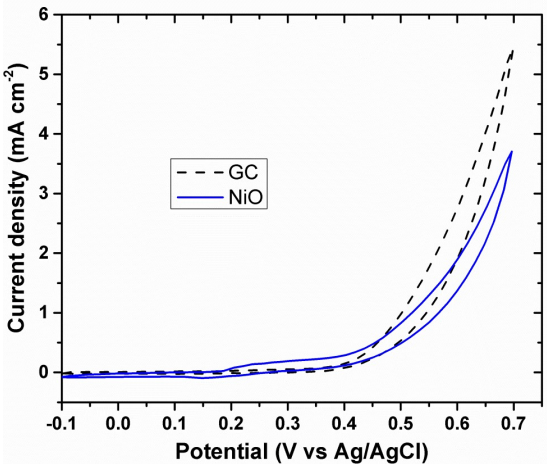

Figure 8. Cyclic voltammogram for glassy carbon and NiO electrode in 0.5 mol L^{-1} NaOH at scan rate of 20 mV s^{-1}.

¡Error! No se encuentra el origen de la referencia. display the CVs for GCE and NiO electrode in presence of 0.5 mol L^{-1} EtOH at scan rate of 50 mV s^{-1}. It can be seen that GCE electrode do not present any change in their curve shape suggesting not electrochemical activity for ethanol oxidation under this condition. Notably, Ni electrode shows a change in their patters in presence of ethanol where high current density is presented. From ¡Error! No se encuentra el origen de la referencia. it is observed that Ni electrode has an onset potential for ethanol oxidation reaction near to 0.2 V with a peak current density of 1.16 mA cm^{-1} at 0.33 V. In the forward direction is observed the oxidation of sub-products.

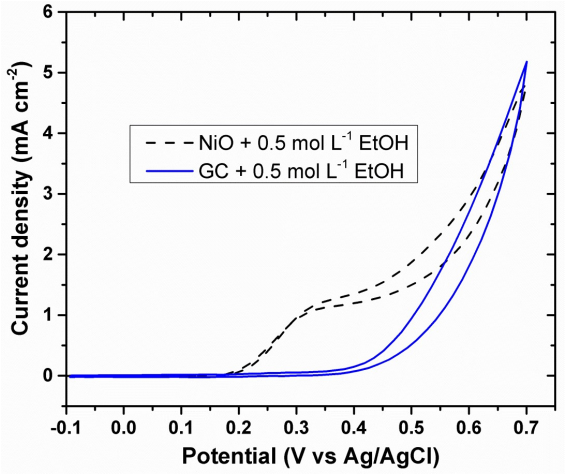

Figure 9. Cyclic voltammogram for glassy carbon and NiO electrode in absence of ethanol and 0.5 mol L^{-1} NaOH at scan rate of 20 mV s^{-1}.

¡Error! No se encuentra el origen de la referencia. presents the effect of ethanol concentration onto NiO electrode. As expected NiO electrode delivers more current densities at any increase of ethanol concentration. Moreover, it can be seen that a 2 mol L^{-1} of EtOH the current densities for OER are suppressed that indicated a competition between the EOR and the OER.

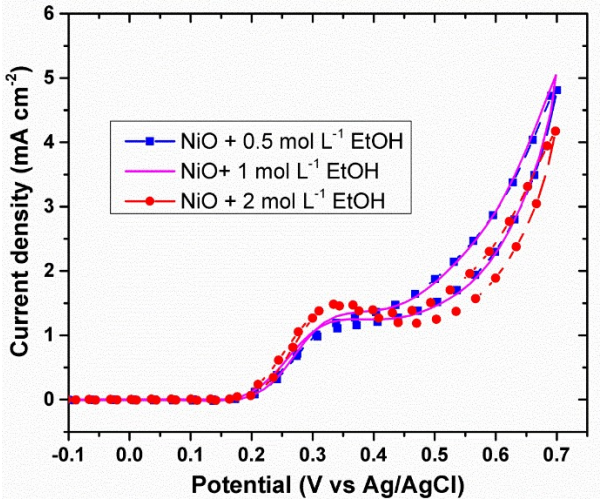

Figure 10. Cyclic voltammogram of modified NiO electrodes at different EtOH concentration.

4. Conclusion

Herein, is demonstrated that NiO nanoparticles can be successfully synthesized by microwave heating polyol process. It is noteworthy to mention that other research groups reported that not Ni nanoparticles is formed when NiCl2 is used as salt precursor in ethylene glycol. Therefore, this investigation could open up new route to the development of Ni nanostructures.

5. Acknowledgements

I thank CONACYT for the scholarship granted to LR. Vidales-Gallardo In addition, I am grateful for the help I received from the Doctors of the Polytechnic University of Victoria, especially because the road so far has not been easy, but thanks to their contributions, support and effort, this research has been carried out. I especially thank Dr. Wilian Pech Rodriguez for his good teaching and advice.

6. References

[1] Guo J, Li Y, Cheng Y, Dai L, Xiang Z. Highly Efficient Oxygen Reduction Reaction Electrocatalysts Synthesized under Nanospace Confinement of Metal–Organic Framework. ACS Nano. 2017;11:8379-86.
[2] Kumar JA, Kalyani P, Saravanan R. Studies on PEM Fuel Cells Using Various Alcohols for Low Power Applications Int J Electrochem Sci. 2008;3:961-9.
[3] Pramanik H, Wragg AA, Basu S. Studies of some operating parameters and cyclic voltammetry for a direct ethanol fuel cell. J Appl Electrochem. 2008;38:1321-8.
[4] Zhou WJ, Song SQ, Li WZ, Sun GQ, Xin Q, Kontou S, et al. Pt-based anode catalysts for direct ethanol fuel cells. Solid State Ionics. 2004;175:797-803.
[5] Chu Y-Y, Wang Z-B, Gu D-M, Yin G-P. Performance of Pt/C catalysts prepared by microwave-assisted polyol process for methanol electrooxidation. J Power Sources. 2010;195:1799-804.
[6] Zhang K, Feng C, He B, Dong H, Dai W, Lu H, et al. An advanced electrocatalyst of Pt decorated SnO2/C nanofibers for oxygen reduction reaction. J Electroanal Chem. 2016;781:198-203.
[7] Salgado JRC, Duarte RG, Ilharco LM, Botelho do Rego AM, Ferraria AM, Ferreira MGS. Effect of functionalized carbon as Pt electrocatalyst support on the methanol oxidation reaction. Applied Catalysis B: Environmental. 2011;102:496-504.
[8] Jafarian M, Moghaddam RB, Mahjani MG, Gobal F. Electro-Catalytic Oxidation of Methanol on a Ni–Cu Alloy in Alkaline Medium. J Appl Electrochem. 2006;36:913-8.
[9] Taraszewska J, Rosłonek G. Electrocatalytic oxidation of methanol on a glassy carbon electrode modified by nickel hydroxide formed by ex situ chemical precipitation. J Electroanal Chem. 1994;364:209-13.
[10] Danaee I, Jafarian M, Forouzandeh F, Gobal F, Mahjani MG. Electrocatalytic oxidation of methanol on Ni and NiCu alloy modified glassy carbon electrode. Int J Hydrogen Energy. 2008;33:4367-76.

[11] Hall DS, Lockwood DJ, Bock C, MacDougall BR. Nickel hydroxides and related materials: a review of their structures, synthesis and properties. Proceedings of the Royal Society A: Mathematical, Physical and Engineering Science. 2015;471.
[12] Gu Y, Luo J, Liu Y, Yang H, Ouyang R, Miao Y. Synthesis of Bimetallic Ni-Cr Nano-Oxides as Catalysts for Methanol Oxidation in NaOH Solution. J Nanosci Nanotechnol. 2015;15:3743-9.
[13] Prabhakarn A, Nagarani S, Saradh P, Mohamad SA, Abdullah MA-M, Meera Moydeen A, et al. Facile coprecipitation synthesis of nickel doped copper oxide nanocomposite as electrocatalyst for methanol electrooxidation in alkaline solution. Materials Research Express. 2018;5:015512.
[14] Chen D, Giroud F, Minteer SD. Nickel Cysteine Complexes as Anodic Electrocatalysts for Fuel Cells. J Electrochem Soc. 2014;161:F933-F9.
[15] Pech-Rodríguez WJ, Calles-Arriaga C, González-Quijano D, Vargas-Gutiérrez G, Morais C, Napporn TW, et al. Electrocatalysis of the Ethylene glycol oxidation reaction and in situ Fourier-transform infared study on PtMo/C electrocatalysts in alkaline and acid media. J Power Sources. 2018;375:335-44.
[16] González-Quijano D, Pech-Rodríguez WJ, González-Quijano JA, Escalante-García JI, Morais C, Napporn TW, et al. Performance and In-Situ FTIR Evaluation of Pt–Sn/C Electrocatalysts with Several Pt : Sn Atomic Ratios for the Ethanol Oxidation Reaction in Acidic Media. ChemElectroChem.0.
[17] Hameed RMA, El-Khatib KM. Ni–P and Ni–Cu–P modified carbon catalysts for methanol electro-oxidation in KOH solution. Int J Hydrogen Energy. 2010;35:2517-29.
[18] Dessources S, del Jesús González-Quijano DX, Pech-Rodríguez WJ. Non-Noble Metal as Catalysts for Alcohol Electro-oxidation Reaction. In: Rodríguez-Varela FJ, Napporn TW, editors. Advanced Electrocatalysts for Low-Temperature Fuel Cells. Cham: Springer International Publishing; 2018. p. 263-90.
[19] Cui X, Guo W, Zhou M, Yang Y, Li Y, Xiao P, et al. Promoting Effect of Co in NimCon (m + n = 4) Bimetallic Electrocatalysts for Methanol Oxidation Reaction. ACS Appl Mater Interfaces. 2015;7:493-503.

E108. BIOAUGMENTATION ON HYDROGEN PRODUCTION FROM FOOD WASTE

Edith Villanueva-Galindo[1], Yeinner Tarazona[1], Iván Moreno-Andrade[1*]

[1]Laboratory for Research on Advanced Processes for Water Treatment, Unidad Académica Juriquilla, Instituto de Ingeniería, Universidad Autónoma de México, Blvd. Juriquilla 3001, 76230 Querétaro, México.

* Corresponding author: imorenoa@iingen.unam.mx

ABSTRACT

Biohydrogen production using food waste as a substrate has been reported [1]. However, due to the substrate characteristics and different process variables, low H_2 production rates have been observed. Recently, the bioaugmentation (the process of adding selected strains/mixed cultures to improve the catabolism of specific compounds) into the reactor may accelerate the transformation of the substrate, increasing the H_2 production [2]. The objective of this work was to evaluate the effect of the microorganisms that enhance the production of H_2 (*Paenibacillus polymyxa*, *Bacillus subtilis* and *Clostridium saccharobutylicum*) in a batch test using food waste as substrate. The results indicated an increase in H_2 production due to the increment in the microorganisms added to the media (for all the species tested independently of the concentration evaluated). The maximum cumulative volume of H_2 increased up to 209% and 408% for the case of *P. polymyxa* and *B. Subtilis*, respectively, compared to no bioaugmented tests. On the contrary, *C. saccharobutylicum* obtained an increase of only 6%. *Bacillus subtillis* showed the best performance with the highest values of cumulative volume of H_2 and H_2 yield (429.5 mL H_2 and 42.95 mL H_2/g VS, respectively) when the strain was added 400 mL, followed by *P. polymyxa* (429.5 mL H_2 and 42.95 mL H_2/g VS), which was added 400 mL, and finally, *C. saccharobutylicum* (218.95 mL H_2 and 21.89 mL H_2/g VS), corresponding to 100 mL bioaugmentation. In summary, adding specific strains like facultative anaerobes can be an attractive strategy to improve hydrogen production using recalcitrant substrates such as food waste.

Keywords: food waste; bioaugmentation; hydrogen production; microbial community.

1. Introduction

One option for biohydrogen production that showed high potential to scale at industrial level is the use of food waste as substrate [1-2]. Due to its combustion produces only water vapor instead of greenhouse gases and its yield is 2.75 times higher (122 kJ/g) than fossil fuels, hydrogen is an interesting energy vector [3]. The use of mixed cultures in anaerobic digestion (AD) processes has obtained special attention among others H_2-producing biotechnologies because of different types of organic matter can be converted to hydrogen [4]. However, the nature recalcitrant of many solid organic wastes due to the presence of lignocellulose can significantly affect the AD conversion efficiencies because of the long degradation time it requires. As a result, capital costs for larger reactor volumes increase and the economic value of the process is reduced [5].

A method to enhance the performance of AD is the bioaugmentation, a practice of adding specific microorganisms to a system, it has reported the reduction of the start-up period [6], shortened hydraulic retention time [7], and the decreased the recovery time of anaerobic digesters stressed by oxygen [8]. The ability to produce H_2 in anaerobic mesophilic fermentative ecosystems was previously thought to be restricted to *Clostridium* species. However, with the emergence of molecular characterization techniques several works reported genomic evidence of the presence, diversity and activity of other bacteria in hydrogen-producing communities [9].

It has been reported the bioaugmentation with species as *Escherichia coli, Bacillus subtillis* and *Enterobacter aerogenes* on hydrogen production from organic fraction of municipal solid waste. The highest cumulative and volumetric H_2 production (564.4 ± 10.9 mL and 1.61 $L_{H2}/L_{substrate}$ respectively) was obtained with *Bacillus subtilis*, followed by *Enterobaacter aerogenes* (486.3 ± 10.6 mL and 1.38 $L_{H2}/L_{substrate}$) and *E. coli* (423.4 ± 10.6 mL and 1.20 $L_{H2}/L_{substrate}$) at bacteria/sludge ratio of 0.25, 0.20 and 0.20 [2].

Buttiauxella sp., *Rahnella* sp. and *Raoultella* sp. were tested in order to enhance the conversion of vegetable waste to hydrogen. All single strain promoted a significant increase of H_2 production yield, compared to no bioaugmentation. *Rahnella* sp. showed the lowest performance (47.54 mL H_2/g VS), followed by *Raoultella* sp. (69.70 mL H_2/g VS) and *Buttiauxella* sp. (71.27 mL H_2/g VS) [10].

Based on those experiments, it can be considered that bioaugmentation is a valid alternative for improving biohydrogen production, especially while using recalcitrant material as substrate.

2. Materials and Methods

2.1 Strains

The strains used in the present work were *Paenibacillus polymyxa* ATCC 842, *Bacillus subtilis* 6051a, and *Clostridium saccharobutylicum* BAA-117 from the Colección Nacional de Cepas Microbianas y Cultivos Celulares (CINVESTAV-IPN, México City). *Paenibacillus and Bacillus strains* were aerobically cultured in ATCC Medium 3 Nutrient Broth under static conditions at 30 °C. For the other hand, *Clostridium* strain was anaerobically culture in ATCC Medium 2107 Modified Reinforced Clostridial Broth with shaking at 37 °C. Anhydrous dextrose (15 g/L) was used as carbon source. Single cultures were prepared separately in 100 mL serum bottles with a working volume of 50 mL.

2.2 Inoculum for hydrogen production

The inoculum used was an anaerobic sludge that was provided from a brewery factory. This sludge was pretreated as follows: dried at 105 °C for 24 hours, grinded and sifted in order to obtain a particle size <65 mm according to [11]. The COD_{total}, total and volatile solids (TS and VS) were determined according to standard methods [12]. The total carbohydrates were measured by the phenol-sulphuric acid method [13].

2.3 Substrate

The food waste was obtained from a restaurant located in Querétaro, México. The residues samplings were performed using a dividing sampling method, where the total simple is divided into four portions and two of them are discarded [14]. The physical composition of the food waste was: flour derived waste (bread, tortilla, cookies, etc.) 30 ± 8%, citrus waste 22 ± 4%, fruits and vegetables waste 17 ± 4%, meat waste 10 ± 3% and other material (bones, inert material, etc.) 21 ± 7%. Bones and inert material as plastic or paper were discarded in order to keep the fermentable matter. Then, the samples were mashed with a blender to homogenize the particle size (<0.5 mm) and stored at -20 °C. The COD_{total}, TS, VS and total carbohydrates were determined according to the methods previously described.

2.4 Procedure and experimental design

Batch dark fermentation experiments were carried out in duplicate using an AMPTS II (Automatic Methane Potential Test System) equipment in order to evaluate the biochemical hydrogen for each bio-augmented strain. They were based on the Specific hydrogen production protocol of the Latin America BioHydrogen Network [15]. Schott bottles with a total volume of 600 mL and a working volume of 460 mL were used. 22 mL of mineral medium with nutrients and Mes, 10 g VS/L of food waste and 5 g VS/L of pretreated anaerobic sludge were added in each bottle with the corresponding bioaugmentation of the strain: no bioaugmented (NB), 100 mL (B100), 200 mL (B200), 300 mL (B300) and 400 mL (B400). Finally, the initial pH was adjusted to 7.5 with a 10N solution of NaOH. The head space of the bottles were purged with nitrogen to ensure anaerobic conditions. The temperature and shaking in the equipment were adjusted at 37 °C and 120 rpm (during one minute for every three minutes during the whole experiment), respectively.

2.5 Statistical and kinetic analysis

The effect of the bioaugmentation on hydrogen production were evaluated using a two-way analysis of variance (ANOVA) with 95% confidence interval to determine significant difference ($p<0.05$). The cumulative H_2 production (H) data were fitted to a modified Gompertz equation [16] [16]:

$$P(t) = P_{max}\, exp\left\{-exp\left[\frac{R_{max}}{P_{max}}\,(\lambda - t\right]\right\} \quad (1)$$

Where, P(t) (mL H_2 /L) is the total amount of hydrogen produced during the experiment (h); P_{max} (mL) is the maximal amount of hydrogen produced. R_{max} (mL H_2 /h) is the maximum hydrogen rate and λ (h) is the lag time before the exponential hydrogen production.

3. Results and Discussion

The bioaugmentation with the strain *P. polymyxa* (Pp), *B. subtilis* (Bs) and *C. saccharobutylicum* (Cs) had a significant effect on the production of H_2 ($p < 0.05$) compared to the trials without bioaugmentation.

In the case of Pp (figure 1A), the maximum cumulative volume of H_2 and H_2 yield was obtained with B400 (429.5 mL H_2 and 42.95 mL H_2/g VS, respectively), followed by B300 (397.8 mL H_2 and 39.78 mL H_2/g VS), B200 (326.6 mL H_2 and 32.66 mL H_2/g VS) and B100 (267.8 mL H_2 and 26.78 mL H_2/g VS) compared to non-bioaugmentation (205.15 mL H_2 and 20.51 mL H_2/g VS).

Bioaugmentation with Bs strain also significantly improved the cumulative volume of H_2 and H_2 yield, obtaining the best results with B400 (839.69 mL H_2 and 83.69 mL H_2/g VS), followed by B300 (723.53 mL H_2 and 72.35 mL H_2/g VS), B200 (560.65 mL H_2 and 56.06 mL H_2/g VS) and finally B100 (365.5 mL H_2 and 36.55 mL H_2/g VS).

Finally, the addition of Cs obtained the lowest results compared to the previous strains (figure 1B). The best performance was obtained with B100 (218.95 mL H_2 and 21.89 mL H_2/g VS), followed by B300 (203.8 mL H_2 and 20.38 mL H_2/g VS), B200 (166.4 mL H_2 and 16.64 mL H_2/g VS) and B400 (164.34 mL H_2 and 16.43 mL H_2/g VS).

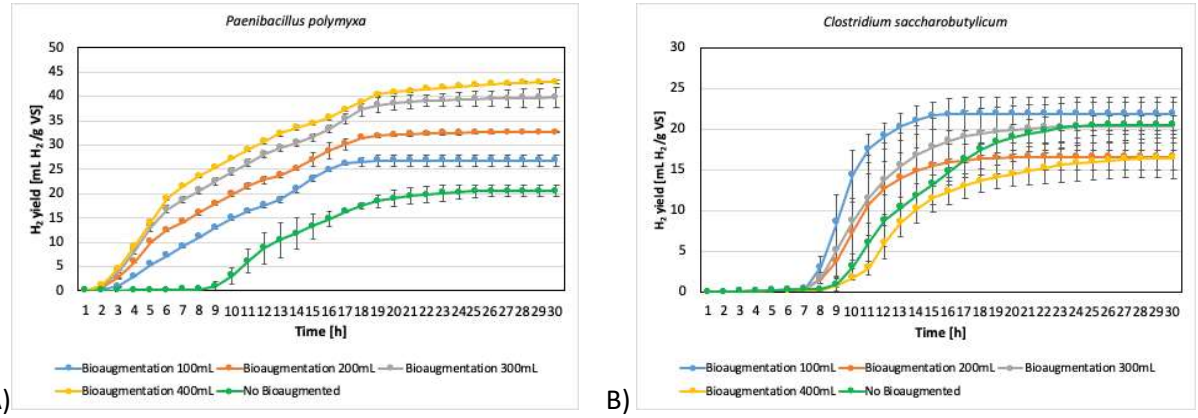

Fig. 1. H_2 yield obtained with bioaugmentation of A) *P. polymyxa and B) C. saccharobutylicum*

The three relevant parameters (P_{max}, R_{max} and λ) obtained by adjusting the data to the modified Gompertz equation are shown in the following table 1.

Table 10. Gompertz equation parameters and Mean squared error (MSE) for bioaugmentation of each strain.

	NB	B100	B200	B300	B400
P_{max} (mL H_2)					
Pp	206.23	277.15	334.42	401.05	429.57
Bs	205.58	366.43	564.19	721.08	862.76
Cs	205.96	218.55	166.18	202.42	163.02
R_{max} (mL H_2 /h)					
Pp	68.11	61.57	67.35	89.65	85.99
Bs	67.85	112.77	151.07	272.22	180.36
Cs	67.99	160.80	95.35	92.81	61.74
λ (h)					
Pp	10.97	6.66	5.63	5.46	5.85
Bs	10.96	5.06	7.035	5.17	8.92
Cs	10.97	7.92	8.70	8.91	11.08
MSE					
Bp	31.35	76.37	116.99	101.68	86.11
Bs	27.64	10.30	68.35	40.67	51.88
Cs	30.79	7.43	2.363	15.12	8.43

It can be seen that the highest P_{max} value is obtained with the strain Bs with B400 (862.76 mL H_2) followed by Pp with B300 (401.05 mL H_2) and Cs with B100 (218.55 mL H_2). For R_{max}, the maximum value was obtained with Bs in B300 (272.22 mL H_2 /h), followed by the strain Pp with B300 (89.65 mL H_2 /h) and Cs with B100 (160.80 mL H_2 /h). Finally, the strain that reported the lowest lag phase was Bs with B100 (5.06 h), followed by Pp with B300 (5.46 h) and Cs with B100 (7.92 h).

These results allow to point out that bioaugmentation with *Bacillus subtillis* significantly improves the production of H_2, which coincides with other studies using organic solid waste. Sharma & Melkania (2018) acquired the best performance with *B. subtillis* in the cumulative volume of H_2, volumetric hydrogen production and R_{max} (564.4 mL, 1.61 $L_{H2}/L_{substrate}$ and 47.03 mL/h, respectively), compared to

E. coli (423.4 mL, 1.20 $L_{H2}/L_{substrate}$ and 35.28 mL/h) and *Enterobaacter aerogenes* (486.3 mL, 1.38 $L_{H2}/L_{substrate}$ and 40.5 mL/h) [2].

The increased hydrogen production observed in bioaugmentation with Bs indicates that there might be a synergistic cooperation between this strain and indigenous bacterial consortia [17]. Also, it is know that *B. subtillis* produces extracellular enzymes (as hydrolases) that facilitate the solubilization of organic matter. *Paenibacillus Polymyxa* also shares this feature, however, it is not able to produce H_2 by its metabolic activity [18], which may explain the best performance of Bs, which is recognized by many authors as a microorganism capable of produce hydrogen [2] [19] [20]. By the other hand, *Clostridium saccharobutylicum* did not show the best performance in any recorded parameters, even though the ability to produce H_2 in anaerobic mesophilic fermentative ecosystems is conventionally attributed to *Clostridium* species [9].

Therefore, it is attractive to use facultative microorganisms for H_2, such as the strains used by Marone *et al* (2012), *Buttiauxella* sp. 4 and *Raoultella* sp. 47, which are characterized for their ability to produce H_2 on different sugars. Both strains showed a significant increase of H_2 yield compared to no bioaugmentation (71.27 mL H_2/g VS and 69.70 mL H_2/g VS, respectively) [10].

4. Conclusion

In general, all bioaugmentations carried out increased the production of H_2 (except for the case of *C. beijerinckii*). *Bacillus subtillis* showed the best performance, obtaining the highest values of cumulative volume of H_2 (839.69 mL), H_2 yield (83.69 mL H_2/g VS), R_{max} (272.22 (mL H_2 /h) and lower lag phase (5.06 h), compared to *Paenibacillus polymyxa* (429.5 mL, 42.95 mL H_2/g VS, 89.65 mL H_2 /h and 5.46 h, respectively) and *Clostridium saccharobutylicum* (218.95 mL, 21.89 mL H_2/g VS, 160.80 mL H_2 /h and 7.92). Therefore, facultative anaerobes as *Bacillus subtillis* and *Paenibacillus polymyxa,* turn out to be attractive in order to improve hydrogen production.

Acknowledgements

The support by "Fondo de Sustentabilidad Energética SENER-CONACYT (Mexico)" (project 247006 Gaseous Biofuels Cluster) is acknowledged. Gloria Moreno and Jaime Perez are acknowledged for their technical assistance. Edith Villanueva-Galindo is grateful to CONACYT for the scholarship.

References

[1] C. Ramos, G. Buitrón, I. Moreno-Andrade and R. Chamy, "Effect of the initial total solids concentration and initial pH on the bio-hydrogen production from cafeteria food waste," *International Journal of Hydrogen Energy 37*, pp. 13288-13295, 2012.

[2] P. Sharma and U. Melkania, "Effect of bioaugmentation on hydrogen production from organic fraction of municipal solid waste.," *International Journal of Hydrogen Energy 43*, pp. 7290-7298, 2018.

[3] J. X. W. Hay, T. Y. Wu and J. C. Juan, "Biohydrogen production through photo fermentation or dark fermentation using waste as a substrate: Overview, economics, and future prospects of hydrogen usage.," *Biofuels, Bioproducts and Biorefining 7*, p. 334–52, 2013.

[4] R. Kleerebezem and M. C. M. van Loosdrecht , "Mixed culture biotechnology for bioenergy production," *Current Opinion in Biotechnology 18*, p. 207–2012, 2007.

[5] J. Mumme, B. Linke and R. Tölle, "Novel upflow anaerobic solid-state (UASS) reactor.," *Bioresource Technology 101*, pp. 592-599, 2010.

[6] P. Lins, C. Reitschuler and P. Illmer, "Methanosarcina spp., the key to relieve the start-up of a thermophilic anaerobic digestion suffering from high acetic acid loads," *Bioresource Technology 152*, pp. 347-354, 2014.

[7] G. Baek, J. Kim, S. G. Shin and C. Lee, "Bioaugmentation of anaerobic sludge digestion with iron-reducing bacteria: process and microbial responses to variations in hydraulic retention time," *Applied Microbiology and Biotechnology 100*, pp. 927-937, 2016.

[8] U. Bhattad, K. Venkiteshwaran, J. S. Maki and D. H. Zitomer, "Biochemical methane potential assays and anaerobic digester bioaugmentation using freeze dried biomass.," *Environmental Science: Water Research & Technology 3*, pp. 1152-1161, 2017.

[9] L. Cabrol, A. Marone, E. Tapia-Venegas, J.-P. Steyer, G. Ruiz-Filippi and E. Trably, "Microbial ecology of fermentative hydrogen producing bioprocesses: Useful insights for Useful insights for driving the ecosystem function.," *FEMS Microbiology Reviews 41*, pp. 158-181, 2017.

[10] A. Marone, G. Massini, C. Patriarca, A. Signorini, C. Varrone and G. Izzo, "Hydrogen production from vegetable waste by bioaugmentation of indigenous fermentative communities," *International Joruanl of Hydrogen Energy 37*, pp. 5612-5622, 2012.

[11] G. Buitrón and C. Carvajal, "Biohydrogen production from Tequila vinasses in ana anaerobic sequencing bath reactor: effect of initial substrate concentration, temperature and hydraulic retention time.," *Bioresource Technology 23*, pp. 9071-9077, 2010.

[12] APHA, Standard Methods for the Examination of Water and Wastewater (21th edn), Washington, DC.: American Public Health Association, 2005.

[13] M. Dubois, K. A. Gilles, J. K. Hamilton, P. Rebers and F. Smith, "Colorimetric method for determination of sugars and related substances.," *Analytical Chemistry 28*, pp. 350-356, 1956.

[14] "NMX-AA-15-1985. Norma Mexicana. Protección al ambiente -contaminación del suelo- residuos sólidos municipales- muestreo- método de cuarteo.".

[15] J. Carrillo-Reyes , A. C. Tapia-Rodríguez , G. Buitrón , I. Moreno-Andrade , R. Palomo-Briones, E. Razo-Flores, O. C. Juárez , J. Arreola-Vargas , N. Bernet , A. F. M. Braga, E. Castelló, L. Chatellard, C. Etchebehere, I. Fuentes , E. León-Becerril, H. O. Méndez-Acosta, G. Ruiz-Filippi, E. T. Venegas, E. Trably, J. Wenzel and M. Zaiat, "A standardized biohydrogen potential protocol: an international round robin test approach.," *International Journal of Hydrogen Energy, In press.*, 2019.

[16] S. Van Ginkel, S. Sung and J. J. Lay, "Biohydrogen production as a function of pH and substrate concentration.," *Environmental Science and Technology 35*, pp. 4726-4730, 2001.

[17] V. N. Nkemka, B. Gilroyed, J. Yanke, R. Gruninger, D. Vedres , T. McAllister and X. Hao, "Bioaugmentation with an anaerobic fungus in a two-stage process for biohydrogen and biogas production using corn silage and cattail," *Bioresource Technology 185*, pp. 79-88, 2015.

[18] M. T. Madigan, J. M. Martinko, D. Stahl and D. P. Clark, Brock Biology of microorganisms, UK: Prentice Hall-Pearson Education, 2004.

[19] C. Li and H. H. P. Fang, "Fermentative Hydrogen Production From Wastewater and Solid Wastes by Mixed Cultures," *Critical Reviews in Environmental Science and Technology 37*, pp. 1-39, 2007.

[20] R. K. Goud, O. Sarkar, P. Chiranjeevi and S. Venkatan Mohan, "Bioaugmentation of potent acidogenic isolates: a strategy for enhancing biohydrogen production at elevated organic load.," *Bioresource Technology 165*, pp. 223-232, 2014.

[21] Y. Li, L. Li, Y. Sun and Z. Yuan, "Bioaugmentation strategy for enhancing anaerobic digestion of high C/N ratio feedstock with methanogenic enrichment culture.," *Bioresource Technology 261*, pp. 188-195, 2018.

E109. MODIFICATION OF CARBON NANOFIBERS WITH M-N (M=CO, NI AND FE) AS ELECTROCATALYSTS FOR THE OXYGEN REDUCTION REACTION WITH APPLICATIONS IN ENERGY STORAGE.

Deysi Gómez-Cholula[1*], Guadalupe Ramos-Sánchez[1,2], Ignacio.González[1]

[1] *Departamento de Química, Área de Electroquímica, Universidad Autónoma Metropolitana-Iztapalapa, Avenida San Rafael Atlixco 186, Vicentina, 09340, Iztapalapa, CDMX, México.*
deysigcholula@gmail.com
[2] *Conacyt Research Fellowship*

ABSTRACT

The ORR plays a vital role on the lifecycle and cost of several electrochemical systems, among them fuel cells[6]. This paper proposes new carbon-based electrocatalysts of the type M-N/CNFs (where M is Fe, Co, Ni and N/CNFs are N-doped carbon nanofibers) that allow improving the electrocatalytic activity of the ORR[1]. In this work, two modifications are investigated: metallic nanoparticles mechanically introduced in N-CNFs and the electrospinning[7] of M-N/CNFs with PAN (polyacrylonitrile)-DFM (dimethylformamide) and metallic phthalocyanines. Preliminary results have shown a slight improvement in the kinetics of ORR, however, further characterization is needed to determine the nature of the doping process taking place.

Keywords: electrocatalysts, carbon nanofibers, electrospinning.

1. Introduction

Converting energy from renewable sources is a promising solution for reducing the dependence on fossil fuels; however, the so called renewable and "green" electricity generated from natural sources, such as solar or wind, is inherently fluctuating and intermittent due to the variety of climatic conditions[1]. Large scale energy storage devices are thus required to counteract its variability.

In a medium- to long-term scenario in which hydrogen is expected to be the main energy carrier, fuel cells are presented in the following way as the most efficient and reasonable form of energy

consumption, with respect to traditional power generation systems. Fuel cells convert chemical energy directly into electrical energy with high efficiency and low pollutant emissions.

Oxygen Reduction Reaction (ORR) is an important and limiting process in fuel cells, therefore many efforts have been devoted to reducing or replacing catalysts based on non-precious metals or carbonaceous materials enriched with nitrogen. Carbon nanofibers have been proposed as potential metal-free catalysts for ORR because they not only exhibit excellent electrocatalytic activity, but also have the advantages of low costs, long durability, and respect for the environment.

This paper proposes the synthesis of a new carbon-based electrocatalyst to improve the electrocatalytic activity of ORR[1,3,4] to be used in fuel cells.

In addition, quantum mechanics calculations and experimental research reveal that the incorporation of nitrogen, especially pyridine or/and graphite nitrogen in carbon frames plays an important role. Additionally, DFT calculations are used to investigate the role of the inclusion of the metal into the carbonaceous structure.

2. Materials and Methods

For the synthesis of the nanofibres, the following precursors were used: polyacrylonitrile (PAN) with an average molecular mass of 150,000 uma, Tg = 85 °C, transition temperature of 317 °C and was used without further purification. The solvent N,N-dimethylformamide (DMF) anhydrous grade, with a purity of 99.8 % and density=0.944 g/mL, and three different phthalocyanines, cobalt phthalocyanine, nickel phthalocyanine and iron phthalocyanine. KOH in granular form was used for the electrochemical tests. All were acquired from Sigma Aldrich.

The electrothreading process requires a high voltage power supply to provide the electrical charge, a syringe with a metal needle for the polymer solution, a metal collector (aluminium) to deposit the nanofibres and an infusion pump to control the flow rate between the needle tip and the collector.

Synthesis of M-N/CNFs (where M is Fe, Co and Ni).

Two synthesis methods are proposed in this project:

The first consists in the formation of N-CNFs by means of the electrospinnning method, once formed, the N-CNFs are impregnated with the phthalocyanines of the corresponding metals and calcined to specific I-M-N/CNFs conditions (Figure 1).

The second method (E-M-N/CNFs) consists of electrolysing the components including the metallic precursor and the nitrogen source. This stage is intended to achieve an intimate interaction of metallic and carbonaceous precursors in order to include all the components within the nanofibers with the subsequent calcination process at controlled conditions. (Figure 2).

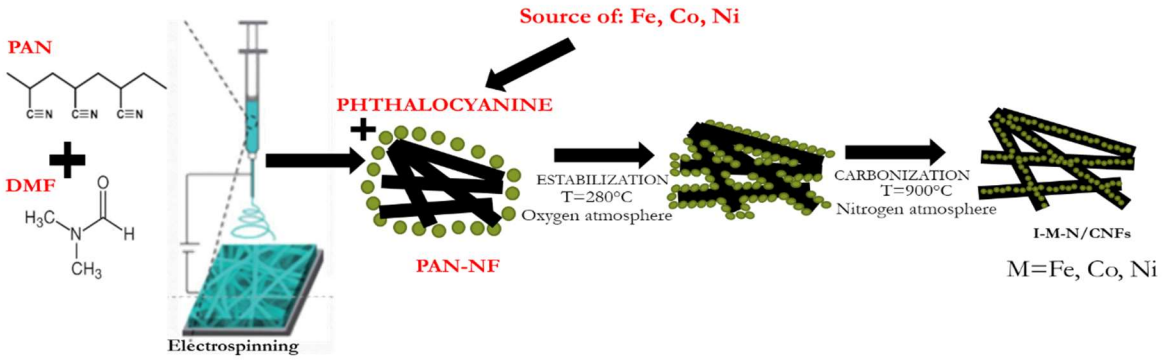

Figure 1. Synthesis process for obtaining I-M-N/CNFs via impregnation.

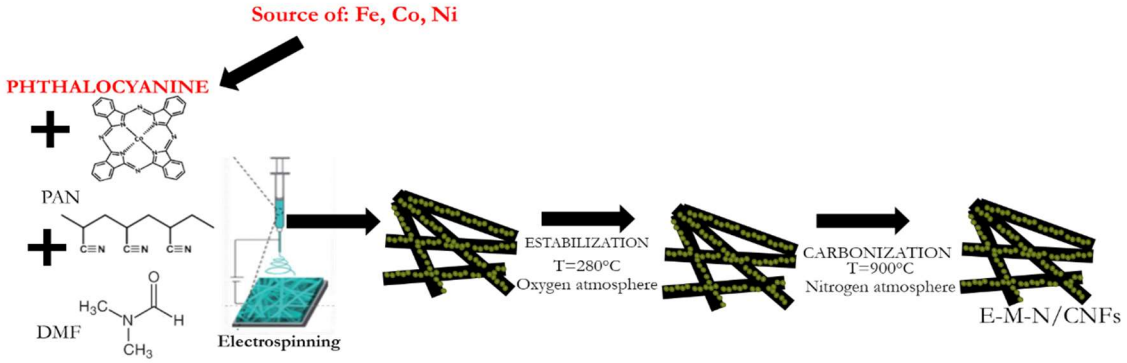

Figure 2. Synthesis process for obtaining E-M-N/CNFs via electrospinning.

The synthesis method used to obtain the E-M-N/CNFs via electrospinning (second method) consists in the preparation of a polymer solution based on 2 g of polyacrylonitrile (PAN) in 19 mL of dimethylformamide (DMF), this mixture is subjected to a heating of 70°C with vigorous agitation for a period of 2 hours. Subsequently, the corresponding phthalocyanine is added to the previous solution and agitated at room temperature for 20 hours.

The prepared solution is transferred to a plastic syringe to carry out the electrospinning applying a voltage of 17 kV, with a working distance between the collector and the end of the syringe of ~14 cm. The supply speed for the solution is 0.5 mL/h. The previously prepared fibrous film is dried at 90°C for 12h, then stabilized in a muffle at 280°C under oxygen atmosphere for 2h. The film is then placed in a porcelain chalupa and heat treated at 900°C for 2 h in a nitrogen atmosphere.

3. Results and Discussion

Results obtained by XRD and SEM for the impregnation method

The XRD pattern for each I-M-N/CNFs (where M is Fe, Co and Ni), figures 3-4, shows two wide peaks at values of 2θ ~23° and ~46°[5] that are present in all samples; and other fine peaks specific to each of the samples. According to doping studies of CNFs doped with nitrogen the peaks at ~23° and ~46° are characteristic of the planes (001) and (100) of the graphical structure of N-CNFs[5]. Therefore, the presence of each of these peaks in the samples indicates that the formation of a structure similar to N-CNFs was effectively achieved; in addition, the results by SEM (figures 3-5 b) indicate the presence of long structures corresponding to CNFs. In addition, a search was made in the X'Pert Highschore Plus package to determine the nature of the other peaks in the diffraction pattern, the result of the database that best agrees with the experimental results (figures 3 and 4) indicates that on the N-CNFs were formed metal clusters of Co and Ni, while in the sample modified with Fe metal oxides were formed (figure 5).

Therefore, this first synthesis route (similar to wet impregnation) resulted in the formation of carbon nanofiber composites coated with metal particles and metal oxides. The structure was not as expected; however, the electrochemical study of this new material was carried out.

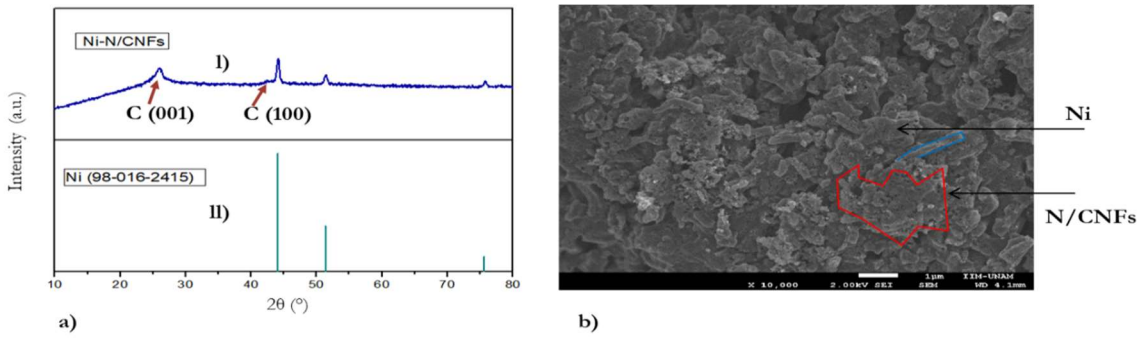

Figure 3. Structural characterization of NPCs synthesized by impregnation with Ni precursors. a) (I) Diffractogram of CNFs modified with Ni, (II) Crystallographic chart of metallic Ni (98-016-2415). b) Electronic micrography of I-Ni-N/CNFs, red: contour of a nanofiber, blue: agglomeration of metals.

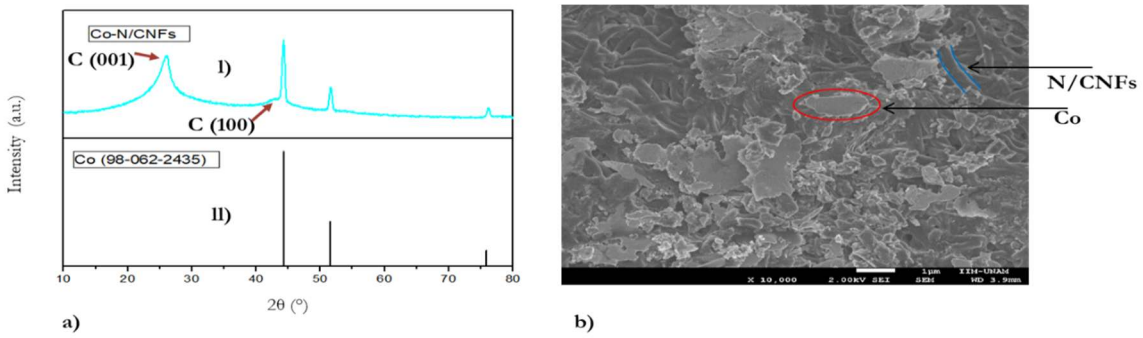

Figure 4. Structural characterization of CNFs synthesized by impregnation with precursors of Co. a) (I) Diffractogram of CNFs modified with Co, (II) Crystallographic chart of metallic Co (98-062-2435). b) Electronic micrography of I-Co-N/CNFs, red: contour of a nanofiber, blue: agglomeration of metals.

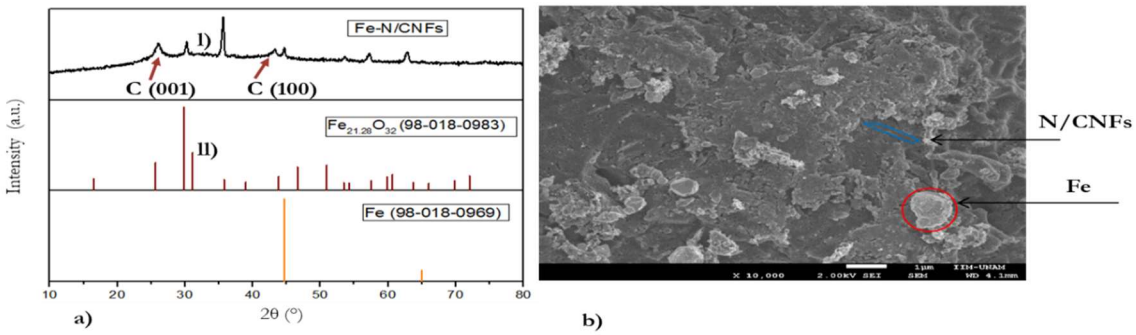

Figure 5. Structural characterization of CNFs synthesized by impregnation with Fe precursors. a) (I) Diffractogram of Fe-modified CNFs, (III) Crystallographic chart of $Fe_{21.28}\ O_{32}$ (98-018-0983) and (IV) Crystallographic chart of metallic Fe (98-018-0969). b) Electronic micrography of I-Fe-N/CNFs, red: contour of a nanofiber, blue: agglomeration of metals.

Electrocatalytic activity in I-M-N/CNFs obtained by the impregnation synthesis method.

To determine the catalytic activity of the I-M-N/CNFs electrocatalysts, measurements of linear scanning voltammetry (LSV) obtained by using a rotary disc electrode (RDE) at different rotation speeds (100, 200, 400, 900, 1600 and 2500 rpm), in an alkaline medium 0.1 M KOH saturated with oxygen. After each measurement the electrolyte was again saturated with oxygen and during the measurement an atmosphere of oxygen was maintained over the electrolyte.

The polarization curves of the three synthesized materials I-Fe-N/CNFs, I-Co-N/CNFs and I-Ni-N/CNFs (Figures 6-8) show significant differences between them. The polarization curves of the three materials present a well defined charge transfer control zone; however, only in the case of I-Co-N/CNFs the mass transfer control zone is well defined. The polarization curves for the I-Fe-N/CNFs and I-Ni-N/CNFs catalysts do not show a significant increase in current with respect to rotation speed, which may indicate an absence of catalytic activity, due to several factors; among them, the presence of obstructed active sites or the lack of them On the other hand, the polarization curves of the material I-Co-N/CNFs have well defined the charge transfer control zone where the current (i) is independent of the rotation speed, a second zone that is controlled by charge and mass transfer (mixed control), and finally a third zone where there is a variation of the current density with respect to the rotation speed.

In the case of I-Co-N/CNFs the onset potential for ORR (0.86 V) is higher than that reported for N-CNFs (0.8 V), which represents an improvement in catalytic activity by including Co to N-CNFs. At the moment

no detailed study of the kinetic parameters is presented and once the behaviour of all the samples is checked, a detailed analysis of these parameters will be calculated.

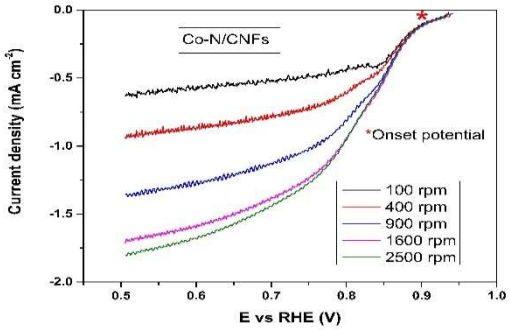

Figure 6. EDR polarization curves for material I-Co-N/CNFs. In KOH 0.1 M saturated with oxygen at v=0.5 mV/s, with a linear sweep from the OCP to cathode potentials.

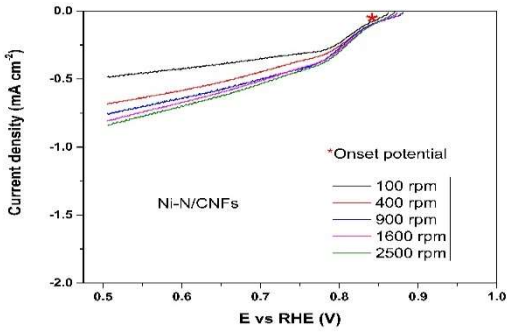

Figure 7. EDR polarization curves for I-Ni-N/CNFs material. In KOH 0.1 M saturated with oxygen at v=0.5 mV/s, with a linear sweep from the OCP to cathode potentials.

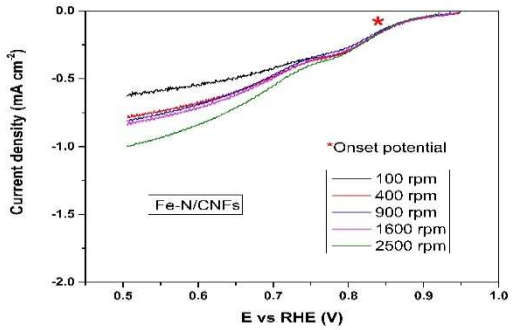

Figure 8. EDR polarization curves for I-Ni-N/CNFs material. In KOH 0.1 M saturated with oxygen at v=0.5 mV/s, with a linear sweep from the OCP to cathode potentials.

Results obtained by means of XRD and SEM for the method of synthesis via electrospinning.

The XRD pattern for each E-M-N/CNFs (where M is Fe, Co and Ni), figures 9-11 a), shows two wide peaks at values of 2θ ~23° and ~46°11 which are present in all samples. According to doping studies of CNFs doped with nitrogen the peaks at ~23° and ~46° are characteristic of the planes (001) and (100) of the graphical structure of the N-CNFs. Therefore, the presence of each of these peaks in the samples indicates that the formation of a structure similar to N-CNFs was effectively achieved; in addition, the results by SEM (figures 9-11 b) indicate the presence of long structures corresponding to N-CNFs. In the case of micrographs for E-Ni-N/CNFs and E-Co-N/CNFs materials, no agglomerations are observed on top of the nanofibres, so that possibly the metals in elemental state are inside the structure of the nanofibres. As far as micrography for E-Fe-N/CNFs material is concerned, there are agglomerations, not as significant as in the material obtained by impregnation, but they are still present.

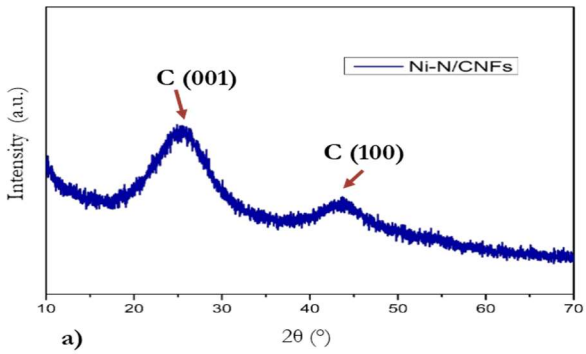

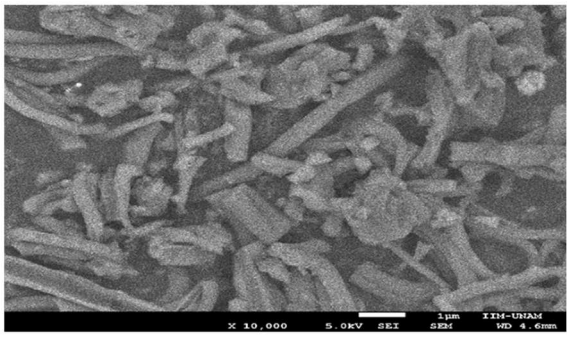

Figure 9. Structural characterization of NPCs synthesized via electrospinning with Ni precursors. a) Diffractogram of CNFs modified with Ni. b) Electronic micrograph of E-Ni-N/CNFs.

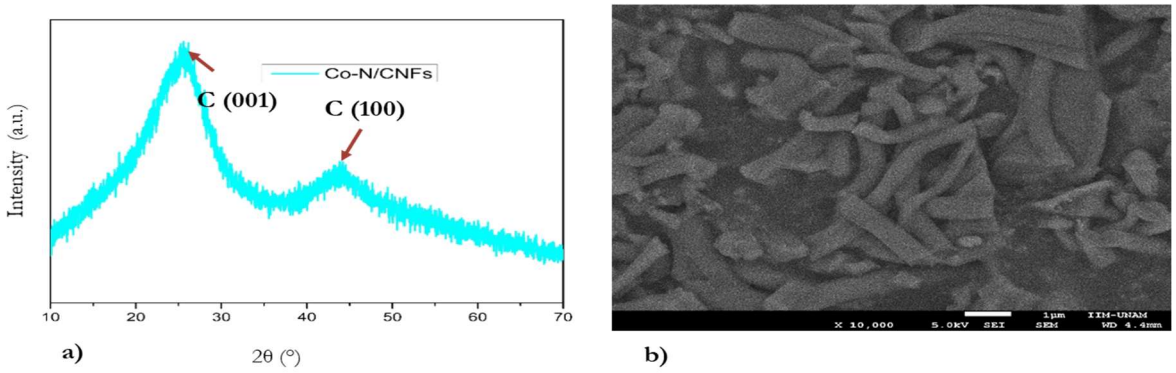

Figure 10. Structural characterization of NPCs synthesized via electrotyping with Co precursors. a) Diffractogram of CNFs modified with Co. b) Electronic micrograph of E-Co-N/CNFs.

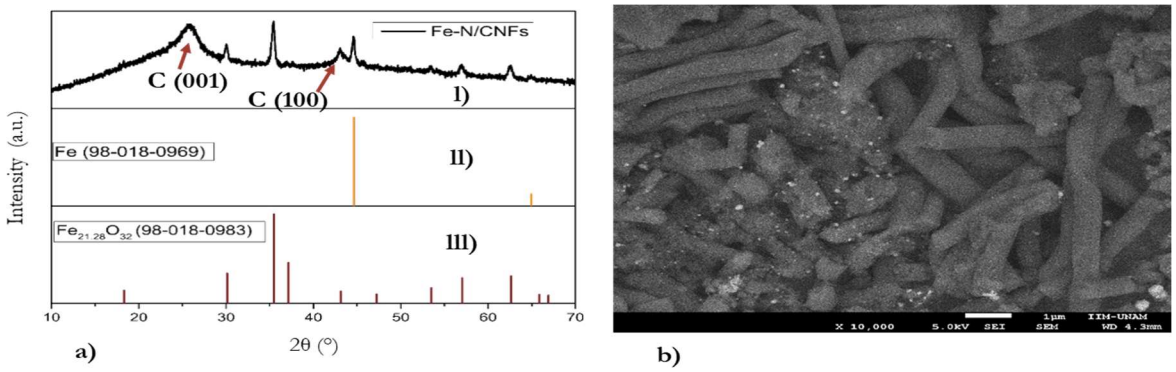

Figure 11. Structural characterization of CNFs synthesized via electrospinning with Fe precursors. a) (I) Diffractogram of NPCs modified with Co. (II) Crystallographic chart of metallic Fe and (III) Crystallographic chart of $Fe_{21.28}O_{32}$. b) Electronic micrograph of E-Fe-N/CNFs.

Therefore, the structural characterization of this method of synthesis indicated that the electrospinning process containing the metallic precursor favored the carbon structures and the integration of Cobalt and Nickel, while for doping with Iron agglomerations are still observed. Subsequently, other studies will be carried out to effectively determine the presence of the precursors in the bulk of the nanofiber and their concentration.

Electrocatalytic activity in the E-M-N/CNFs obtained by the electrolytic synthesis method.

Preliminary EDR tests of these materials have been carried out, however, the values obtained in OCP (~0.9 V) and onset potential (~0.8 V) are lower than those reported in the materials obtained by the first synthesis method. Due to experimental problems with reference electrodes, these values are unreliable and will be carefully repeated.

4. Conclusion

Nanofibres obtained by the first method of synthesis (impregnation) for I-Co-N/CNFs showed good catalytic behaviour, with a potential onset ~0.9 V, while I-Ni-N/CNFs and I-Fe-N/CNFs showed low electrocatalytic activity, which can possibly be attributed to the few catalytic sites formed and the presence of metal clusters on the fiber as observed in electron microscopy images. However, the samples obtained by method two allow the formation of longer and well-formed nanofibers, which probably contain the metals included in their structure. However, structural and electrochemical characterization is still needed to determine their properties.

Acknowledgements

This project has been performed with the financial support from SECITI SECITI/080/2017

References

[1] Wang, Z. L., Xu, D., Xu, J. J. & Zhang, X. B. Oxygen electrocatalysts in metal-air batteries: From aqueous to nonaqueous electrolytes. Chem. Soc. Rev. 43, 7746–7786 (2014).

[2] Cheng, F. & Chen, J. Metal-air batteries: From oxygen reduction electrochemistry to cathode catalysts. Chem. Soc. Rev. 41, 2172–2192 (2012).

[3] Xiao, Y., Dai, A., Hu, C., Lin, Y. & Connell, J. W. Carbon-Based , Metal-Free Catalysts for Metal – Air Batteries. (2018).

[4] Wu, Z. S. et al. High-performance electrocatalysts for oxygen reduction derived from cobalt porphyrin-based conjugated mesoporous polymers. Adv. Mater. 26, 1450–1455 (2014).

[5] Ojeda-López, R. Nanofibras de carbono preparadas vía electrohilado: caracterización de las propiedades estructurales y electrocatalíticas. (2018).
[6] Yoo, H.D., Markevich, E., Salitra, G., Sharon, D., Aurbach, D., 2014. Biochem. Pharmacol. 17, 110–121.
[7] Zhang, L., Aboagye, A., Kelkar, A., Lai, C., Fong, H., 2014. J. Mater. Sci. 49, 463–480.

E111. METAL-FREE ELECTROCALYST FOR ORR OBTAINED BY SOLAR PYROLYSIS OF AGAVE BIOMASS

D.C. Martínez-Casillas[a,b,*]; G. Longinos Salazar[c]; C.A. Campos Roldán[c]; A. Ayala-Cortés[d], R.G. González-Huerta[c]; H.I. Villafán-Vidales[d]; C.A. Arancibia-Bulnes[d]; A.K. Cuentas-Gallegos[d].

[a] CONACYT / TecNM-ITD, Blv. Felipe Pescador 1830 Ote., Col. Nueva Vizcaya, CP 34080 Durango, Dgo, México.

[b] Maestría en Sistemas Ambientales, División de Estudios de Posgrado e Investigación, TecNM-ITD. Felipe Pescador 1830, Nueva Vizcaya, CP 34080 Durango, Dgo, México.

[c] ESIQIE-IPN, Laboratorio de Electrocatálisis, UPALM Edificio 5, CP 07738, Ciudad de México, México.

[d] IER-UNAM, Priv. Xochicalco s/n, Col. Centro, CP 62580, Temixco, Morelos, México.

* Corresponding author: dmartinez@itdurando.edu.mx

ABSTRACT

In this work, the synthesis and characterization of a novel metal-free electrocatalyst obtained by solar pyrolysis from alcoholic beverage industry waste are reported. The electrocatalyst was prepared from Agave bagasse waste using a sustainable process where concentrated solar energy is used as heat source. The Agave biomass was processed in a glass spherical solar reactor at 500 °C with a heating ramp of 30°C min^{-1} in an inert atmosphere. From physical characterization we observed that our prepared metal-free electrocatalyst (C-AB-S) is an amorphous carbon, which has a macroporous structure with a surface area of 100 m^2 g^{-1}. The electrocatalyst was electrochemically evaluated by cyclic voltammetry and rotating disk electrode in 1M KOH using a three-electrode system, obtaining high performance as electrocatalyst for the Oxygen Reduction Reaction (ORR). The metal-free electrocatalysts are a promising eco-friendly alternative as cathode materials for alkaline fuel cells. Our study provides a novel sustainable approach to use agricultural waste biomass to produce useful electrode materials for electrochemical energy devices using concentrated solar energy.

Keywords: Solar carbon material; ORR electrocatalyst; Biomass waste; Concentrated solar energy

1. Introduction

Polymer electrolyte membrane fuel cells (PEMFCs) are efficient electrical power sources with the potential to be used for vehicles, small devices, and stationary applications [1]. PEMFCs represent an environmentally clean and friendly energy source, for generating electricity by electrochemical reduction of oxygen and oxidation of hydrogen producing water and heat as the by-products. The oxygen reduction reaction (ORR) is the key process in PEMFCs, due to its slow kinetic limits the overall performance of the cell [1,2]. The most suitable electrocatalysts for ORR are platinum and Pt-alloys based electrodes [3,4]. Nevertheless, the scarcity and the high cost of Pt are the primary barriers to large-scale commercialization of the Pt based electrocatalyst for PEMFCs. Therefore, research efforts have been devoted to seeking alternative non-noble metal electrocatalysts with low cost and high activity towards ORR [4,5].

In this sense, carbon-based materials, such as ordered mesoporous carbons, graphene, carbon nanotubes, as well as their heteroatoms-doped compounds have emerged as novel metal-free electrocatalysts showing good catalytic activity for ORR in fuel cell research [5-9]. However, all these carbon materials are still expensive, and their production is not environmentally friendly. Recently, some research groups have studied the use of biomass as raw materials for the synthesis of ORR electrocatalysts [10-13]. Thus, preparing metal-free electrocatalysts from biomass is a further improvement in PEMFCs, since it can make the process more sustainable and reduce the production costs. Moreover, if the precursor is an agroindustrial biomass waste (ABW), its use as raw material will give an added value to the ABW by decreasing its costs of waste disposal, and its negative impact to the environment.

On the other hand, Mescal is one of the principal and traditional products of alcoholic beverage industry in Mexico. This distilled beverage is produced from the agave plant, particularly the "head" or also called "piña" is the agave's part used for the Mescal production. In 2018 the national production of Mescal was around 5 million litters [14], generating 700 000 tons of agave bagasse as residue. Nonetheless, some research groups have investigated potential uses for this ABW [15-17], most of this waste is still burned generating large amounts of ash and particulated matter.

The present research is aimed to evaluate the electrochemical activity for the ORR in alkaline medium of an electrocatalyst, obtained from Agave bagasse waste by solar pyrolysis. This study provides an environmentally friendly approach to use ABW to produce metal-free electrocatalyst materials for electrochemical energy devices using concentrated solar energy.

2. Materials and Methods

2.1 Electrocatalyst preparation

The *Agave angustifolia* waste used to produce the electrocatalyst by solar pyrolysis was kindly supplied by the company Imago, a local mescal producer in Oaxaca, Mexico. The agave bagasse fibers were previously dried to remove moisture excess, and then ~10 g of fibers were pyrolyzed in a glass spherical solar reactor at 500 ºC under argon atmosphere. Solar pyrolysis was performed in a 25 kW solar furnace during one hour with an averaged heating rate of 30 ºC min^{-1}, this process was described in detail in a previous paper [18]. The obtained carbonaceous material was washed with 5M HCl during 16 hours at 60 °C, in order to remove the ashes. Then the biochar was filtered and rinsed with deionized water until neutral pH was reached. Finally, the agave waste-derived electrocatalyst (C-AB-S) was dried overnight at 100 °C.

2.2 Physical characterization

The C-AB-S electrocatalyst obtained from agave waste biomass was characterized by scanning electron microscopy (SEM) in a FE SEM Hitachi S-5500 microscope equipped with a Bruker EDAX detector. N_2 adsorption-desorption isotherms were measured at 77 K, with a Quantachrome NOVA instrument.; before these analyses the samples were degassed at 200 ºC for 16h. X-Ray Diffraction (XRD) was performed in a Rigaku DMAX 2200 diffractometer with a Cu-Kα= 1.54 Å. The sample was measured between a 2θ range of 5° and 80° at a scan of 5° min^{-1}. Raman measurements were performed in a Thermo Scientific DXR Raman Microscope.

2.3 Electrocatalytic evaluation

The electrochemical studies of the C-AB-S were performed at room temperature in a conventional three-electrode system by cyclic voltammetry (CV), and rotating disk electrode (RDE) in alkaline electrolyte (KOH 1 M), using an Autolab potentiostat. The three electrodes in the system were a Hg/HgO reference electrode (E = -0.92 V vs. ESH), a Pt mesh counter electrode, and a thin film of our agave waste-derived material as the working electrode. For the WE 1 ml of solution (200 μL of isoprophanol and 4 μL of Nafion® 796 μL of Mili-Q water and 5 mg of electrocatalyst) was prepared and mixed in an ultrasonic bath during 30 min at 30 °C. Then, an aliquot of 8 μL of the ink was carefully dropped onto the mirror-finished glassy carbon (GC) disk electrode, geometric surface of 0.196 cm^2. The ink was, thereafter, dried during 30 min, using a rotation rate of 900 rpm at room temperature, the rotation drying thin-film leads to a uniform layer covering the GC surface. Hydrodynamics experiments were recorded in the rotation rate range 400–2500 rpm at 5 mV s^{-1}. At least three electrodes were prepared.

Prior to the electrochemical measurements, the electrolyte was degassed with nitrogen for the working electrode activation. The electrode activation was carried out by scanning the potential between 1 V and 0.2 (RHE) at 50 mV s^{-1} for 20 times. Afterwards, the electrolyte was saturated with oxygen whose flux was maintained above the electrolyte during the measurements.

3. Results and Discussion

3.2 Physical characterization

The results of the structural characterization of the C-AB-S are shown in Figure 1. A three-dimensional structure with a variable size of macropores is observed (Fig. 1a). The formation of these cavities is due to the gas generation, and later liberation during the pyrolysis. The chemical composition determinate by EDAX indicates that the electrocatalyst is mainly composed by C (93 at%) and O (5 at%). However, other elements as Mg, Cl, K, and Ca were detected in agave waste-derived electrocatalyst at concentrations below 1 at% and are considered as impurities coming from the ashes present in the agave bagasse [18]. The presence of Cl is due to the final washing process with HCl.

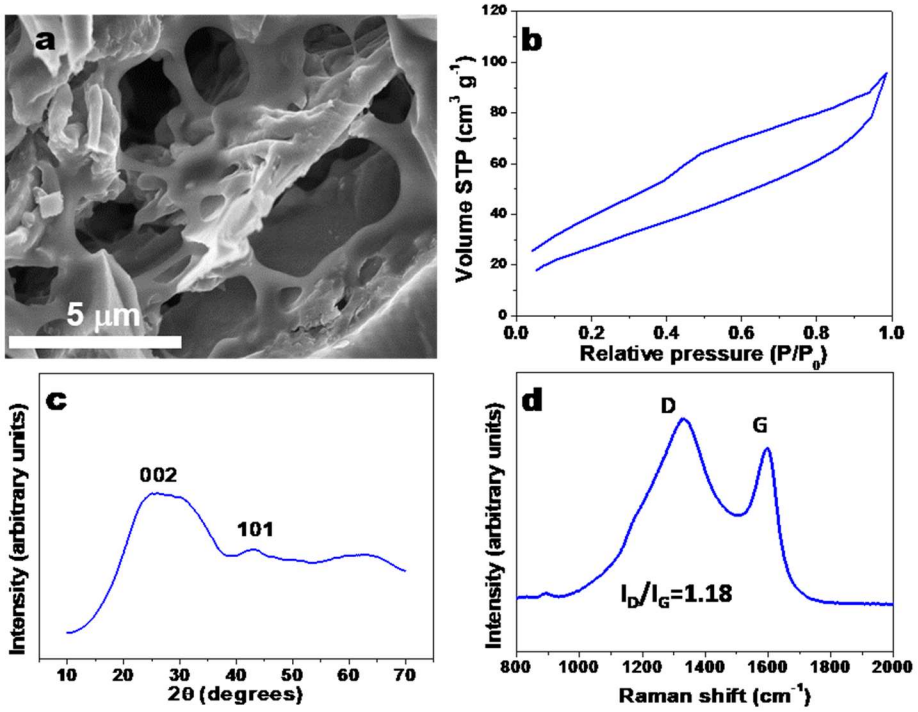

Fig. 1. (a)SEM image; (b) Nitrogen isotherm; (c) XRD diffraction pattern; (d) Raman spectra of agave-waste derived electrocatalyst.

The pore structure and BET surface area (S_{BET}) of C-AB-S were obtained using N_2 isotherm. As can be appreciated in Figure 1b, the C-AB-S electrocatalyst show isotherm type II associated with macroporous materials, according with the IUPAC classification [19]. The S_{BET} and the pore volume (V_P) values are 103.3 m^2g^{-1} and 0.127 cm^3g^{-1}, respectively. Figure 1c shows the X–ray diffraction pattern of the electrocatalyst, where two broad diffraction peaks are observed at 2θ ≈ 25° and 44°. These peaks are attributed to the (002) and (101) planes respectively, corresponding to graphite 2H (JCPDS 41-1487). The widest peak related to the 002 plane indicates a low crystallinity and confirms that solar pyrolysis of agave waste biomass produces amorphous carbon. The Raman spectra in Figure 1d shows the two characteristic bands of carbon materials at 1580-1620 cm^{-1} (I_G) and 1355-1380 cm^{-1} (I_D) [20]. The intensity ratio of these bands (I_D/I_G) provides information related with the structural properties. I_D/I_G of our material is above 1 (Fig. 1d), indicating that defects are present in mayor proportion in the structure of the electrocatalyst, in good agreement with the XRD patterns.

3.3 Electrocatalytic evaluation

Cyclic voltammograms of the C-AB-S electrocatalyst incorporated into a Nafion film were recorded in a small potential region, 0.67–0.77 V (RHE), Figure 2a, where a dependence of non-faradaic currents on the sweep rate was obtained. These voltammograms were recorded after scanning the electrode potential between 1 V and 0.2 (RHE) at 50 mV/s for 20 times in N_2 saturated, in order to eliminate impurities and oxides, until a defined capacitive current was reached. A good linear relationship was observed in the range 10–40 mV s^{-1}. From the slope of the linear region of the double layer charging current versus sweep rate measured at 0.74 V, the capacitance of the electrode/solution interface (C=dq/ dE=di/dv) was calculated, normalizing the capacitance to the geometrical surface area. An average value of 2.29 mF cm^{-2} was obtained (polished to mirror metal electrode: 10 a 40 μF cm^{-2}), Fig. 2b.

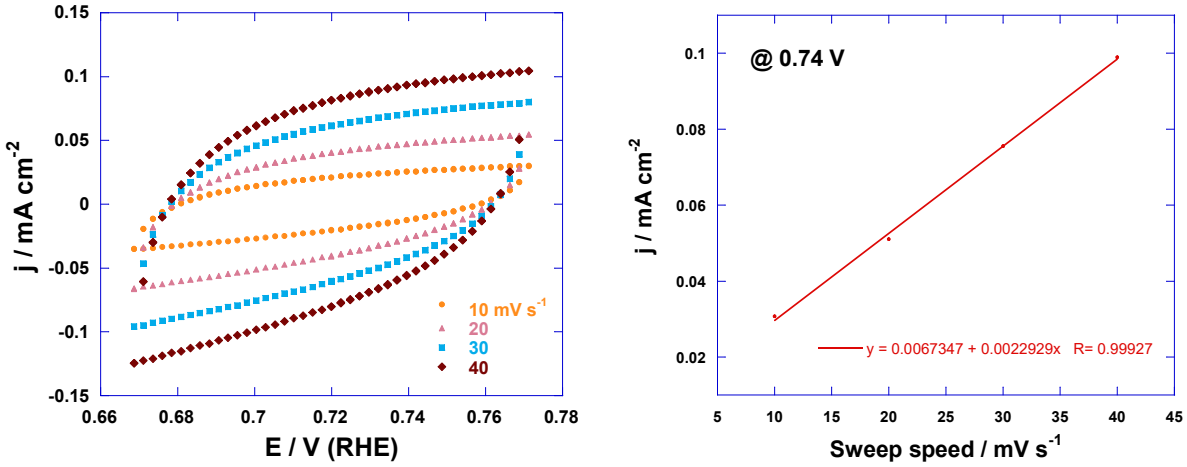

Fig. 2. (a) Cyclic voltammograms of non-faradaic currents and (b) capacitance of the electrode/solution interface for the agave-waste derived electrocatalyst in alkaline electrolyte

Figure 3a shows the current–potential curves for the C-AB-S electrocatalyst for oxygen reduction obtained at four rotation rates (400, 900, 1600 and 2500 rpm), scanning the potential from the open circuit potential to 0.1 V/RHE at 5mVs^{-1}. A charge-transfer kinetics control with rotation rate-independent current is observed in the range of 0.8–0.7 V/RHE. Mixed control in the range 0.7–0.60 V/RHE and, at higher cathodic potentials, a dependence of a defined limiting current on rotation rate is observed between of 0.6–0.1 V/RHE. With increasing rotation speed, limiting currents were increased due to the increase of oxygen diffusion through the film electrode surface. The Koutecky-Levich plots corresponding to the experimental values of Fig. 3a are shown in Fig. 3b, using the following first-order reaction kinetics:

$$\frac{1}{j} = \frac{1}{j_k} + \frac{1}{B\omega^{-1/2}} \quad (1)$$

where j is the measured current density, j_k the kinetic contribution to the current and ω is the electrode rotation rate. The theoretical value of the Levich slope, B, is evaluated from Eq. 2:

$$B = 0.2nFD_{O_2}^{2/3}v^{-1/6}C_{O_2} \quad (2)$$

where 0.2 is a constant used when ω is expressed in rpm, n is the number of electrons related to the oxygen reduction reaction, F the Faraday constant (96,500 C mol^{-1}), C_{O2} is the concentration of oxygen

in 1 M KOH ($1.22 \cdot 10^{-6}$ mol cm^{-3}), D_{O2} is the diffusion coefficient of oxygen in the solution ($1.9 \cdot 10^{-5}$ cm^2 s^{-1}) and ν is the kinematic viscosity of the KOH ($8.7 \cdot 10^{-3}$ cm^2 s^{-1})

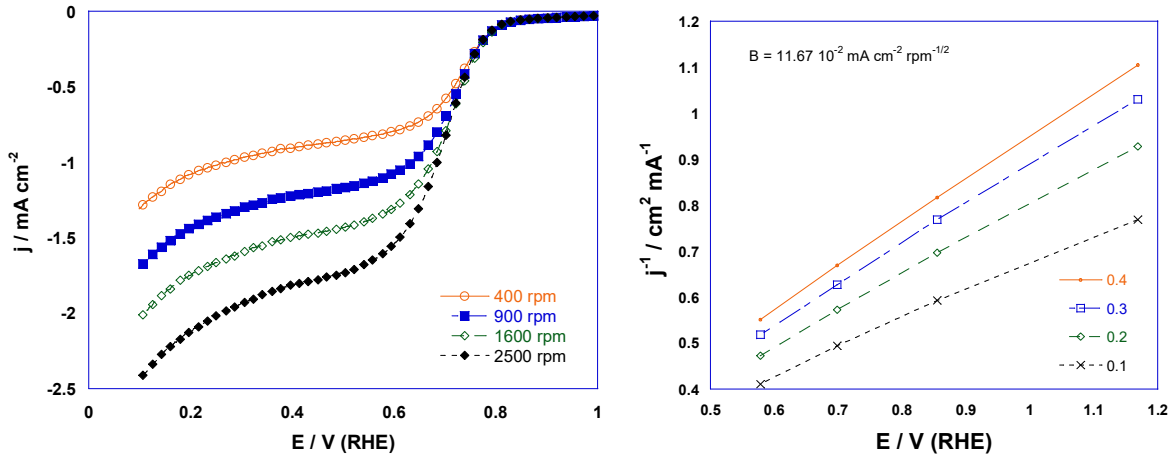

Fig. 3. (a) ORR in O_2-saturated electrolyte (Polarization curves at 5 mV s^{-1}); (b) Koutecky–Levitch plots for oxygen reduction on C-AB-S electrocatalyst.

From the data in Fig. 3a, the Koutecky–Levich plots (j^{-1} versus $\omega^{-1/2}$) were drawn Fig. 3b. At all the rotation speeds, a series of essentially parallel straight lines in a broad potential range is illustrated in this figure, which indicates that the reaction order for the O_2 reduction at a C-AB-S electrocatalyst electrode is unity. Parallelism of the straight lines in Fig. 3b also indicates that the number of electron transferred per O_2 molecule and active surface area for the reaction not change significantly within the potential range studied. The theoretical slope calculated with the parameters described above for the transfer of four electrons is 9.41×10^{-2} mA cm^{-2} $rpm^{-1/2}$. The behavior of the experimental and theoretical slopes is 20% higher (11.67×10^{-2} mA cm^{-2} $rpm^{-1/2}$, although it should be noted that due to the uncertainly of the real area of the ink-type electrode, the number of electrons transferred per O_2 molecule could not be calculated precisely.

Fig. 4 shows the mass transport corrected Tafel plots obtained for the C-AB-S electrocatalyst ink-type electrode on which oxygen reduction kinetics studies were conducted in 1 M KOH at 298K. The Tafel plot was obtained after that the measured currents were corrected for diffusion to give the kinetic currents in the mixed activation–diffusion region, calculated from Eq. (3):

$$j_k = \frac{j\, j_l}{j_l - j} \quad (3)$$

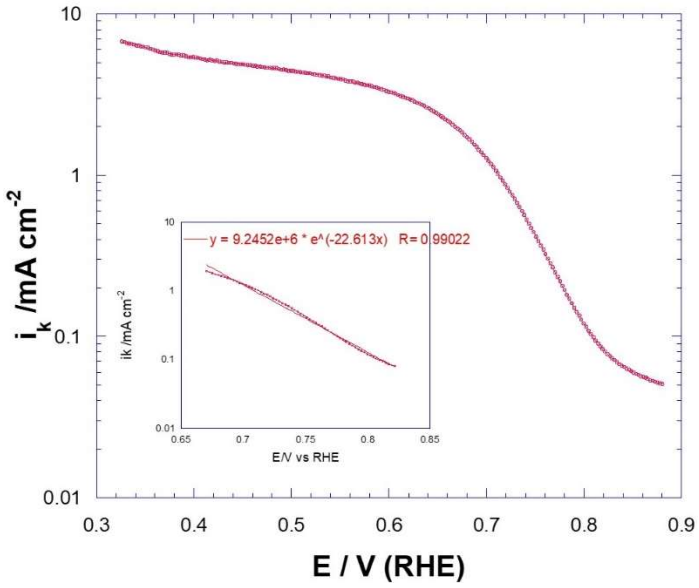

Fig. 4. Tafel plots of the agave-waste derived electrocatalyst.

The Tafel slope is used as one of the most frequently diagnostic criteria in the elucidation of the reaction mechanism. The Tafel slope of 0.102 V dec^{-1} with the C-AB-S electrocatalyst, Fig. 4, corresponds to the transfer of the first electron to the adsorbed oxygen as the rate-determining step:

$$S\text{-}O_{2ads} + H_2O + e^- \rightarrow S\text{-}O_2H + OH^-$$

Where "S" is an adsorption site for oxygen.

4. Conclusion

Results of the physicochemical characterization demonstrate that the solar pyrolysis of agave waste produces a macroporous amorphous biochar with high specific surface area. The electrocatalytic evaluation of the C-AB-S indicates that this material exhibits high activity for the ORR. The use of concentrated solar energy to produce an agave waste-derived electrocatalyst, shows the feasibility to obtain low-cost and environmentally friendly electrode materials for electrochemical energy devices. Moreover, our study promotes the use of agroindutrial biomass waste which is produced in large

volumes and burned to produce useful sustainable electrocatalyst. Our metal-free electrocatalyst (C-AB-S) is a promising eco-friendly alternative as cathode materials for alkaline fuel cells.

Acknowledgements

The authors acknowledge the financial support from DGAPA-PAPIIT-UNAM "Propiedades de Electrodos de Carbón producidos a partir de biomasa mediante concentración solar" and CEMIE-Sol "Combustibles solares y Procesos Industriales" (grants IG100217 and P-10, respectively). We acknowledge to Imago for supply us the *Agave angustifolia* solid residue. Technical support of C.E. Arreola-Ramos in the setup and operation of solar experiment, Rogelio Morán-Elvira for the operation of the SEM, María Luisa Ramón-García for XRD measurements, Diego R. Lobato-Peralta for Physisorption analyses, and José Martín Baas López for Raman measurements. IPN project Multi-Red 2024 and CONACYT project CEMIE-Ocean-249795: Transversal Line I-LT1.

References

[1] Barbir F, PEM Fuel Cells: Theory and Practice, Elsevier Academic Press; 2005.

[2] Yuan X, Wang H. PEM Fuel Cell Fundamentals. In: Zhang J, editor. PEM Fuel Cell Electrocatalysts and Catalyst Layers. Springer; 2008.

[3] Sui S, Wang X, Zhou X, Su Y, Riffat S, Liu C. A comprehensive review of Pt electrocatalysts for the oxygen reduction reaction: Nanostructure, activity, mechanism and carbon support in PEM fuel cells. J Mater Chem A 2017;5:1808-1825.

[4] Stacy J, Regmi YN, Leonard B, Fan M. The recent progress and future of oxygen reduction reaction catalysis: A review. Renew Sust Energ Rev 2017; 69:401–414.

[5] Yang L, Zhao Y, Chen S, Wu Q, Wang X, Hu Z. A mini review on carbon-based metal-free electrocatalysts for oxygen reduction reaction. Chinese Journal of Catalysis 2013;34:1986–1991.

[6] Wang DW, Su D. Heterogeneous nanocarbon materials for oxygen reduction reaction. Energy and Environmental Science 2014;7(2):576-591.

[7] Wang L, Jia W, Liu X, Li J, Titirici MM. Sulphur-doped ordered mesoporous carbon with enhanced electrocatalytic activity for the oxygen reduction reaction. J Energy Chem 2016; 25:566–570.

[8] Gong K, Du F, Xia Z H, Durstock M, Dai L. Nitrogen-doped carbon nanotube arrays with high electrocatalytic activity for oxygen reduction. M. Science 2009;323:760-4.

[9] Qu L, Liu Y, Baek J-B, Dai L. Nitrogen-doped graphene as efficient metal-free electrocatalyst for oxygen reduction in fuel cells. ACS Nano 2010;4:1321-6.

[10] Zhang J, Wu S, Chen X, Pan M, Mu S. Egg derived nitrogen self-doped carbon/carbon nanotube hybrids as noble-metal free catalysts for oxygen reduction. J Power Sources 2014;271:522-9.

[11] Liu F, Peng H, Qiao X, Fu Z, Huang P, Liao S. High performance doped carbon electrocatalyst derived from soybean biomass and promoted by zinc chloride. Int J Hydrogen Energy 2014;39:10128-34.

[12] Alonso Lemus IL, Rodríguez-Varela FJ, Figueroa-Torres MZ, Sanchez-Castro ME, Hernandez-Ramírez A, Lardizabal-Guitierrez D, Quintana-Owen P. Novel self-nitrogen-doped porous carbon from waste leather as highly active metal-free electrocatalyst for the ORR. Int J Hydrogen Energy 2016;41:23409-16.

[13] Preuss K, Kannuchamy VK, Marinovic A, Isaacs M, Wilson K, Abrahams I, Titirici M.M. Bio-inspired carbon electro-catalysts for the oxygen reduction reaction. J Energy Chem 2016; 25:228–235.

[14] Consejo Nacional de Productores de Maguey Mezcal. Informe estadístico 2018, http://www.crm.org.mx/PDF/INF_ACTIVIDADES/INFORME2018.pdf; 2018 [accessed 21.06.20].

[15] Idarraga G, Ramos J, Zuniga V, Sahin T, Young RA. Pulp and paper from blue agave waste from tequila production. J Agric Food Chem 1999;47:4450-5.

[16] Iniguez-Covarrubias G, Lange SE, Rowell RM. Utilization of by products from the tequila industry: part 1: agave bagasse as a raw material for animal feeding and fiberboard production. Bioresour Technol 2001;77:25-32.

[17] Nieto-Delgado C, Terrones M, Rangel-Mendez JR. Development of highly microporous activated carbon from the alcoholic beverage industry organic by-products. Biomass Bioenerg 2011;35:103-112.

[18] Ayala-Cortés A, Lobato-Peralta DR, Arreola-Ramosa CE, Martínez-Casillas DC, Pacheco-Catalán DE, Cuentas-Gallegos AK, Arancibia-Bulnes CA, Villafán-Vidales HI. Exploring the influence of solar

pyrolysis operation parameters on characteristics of carbon materials. J Anal Appl Pyrol 2019;140, 290-299.

[19] Sing KSW, Everett DH, Haul RAW, Moscou L, Pierotti RA, Rouquerol J, Siemieniewska T. Reporting physisorption data for gas/solid systems with special reference to the determination of surface area and porosity. Pure Appl Chem 1985;57:603-19.

[20] Ferrari AC, Robertson J. Resonant raman spectroscopy of disordered, amorphous, and diamondlike carbon. Phys Rev B 2001;64:075414-13.

E115. TEMPERATURE DEPENDENCE FOR HYDROGEN STORAGE IN METAL HYDRIDES $Mg_{1-x}M_x$ (M=Al, Zn, Ni, x=0.10, 0.12,..., 0.20)

O. Ramírez-Rodríguez [a*]; G. Ramírez-Dámaso[a]

[a] Escuela Superior de Ingeniería y Arquitectura "Unidad Ticomán" del Instituto Politécnico Nacional (SEPI), Av. Ticomán No. 600, Col. San José Ticomán, C. P. 07340, Del. Gustavo A. Madero, CDMX, México.

* Corresponding author: phone number 55-65-04-97-85; e-mail omarod672@gmail.com

ABSTRACT

Hydrogen is a promising alternative to fossil fuels; however for tangible applications, it is necessary to develop hydrogen storage material. The purpose of this research was to determine theoretically what happens to hydrogen molecule, when it interacts on the surface of metals, magnesium base, at different temperatures. Calculations were performed with the help of computational molecular modeling software, Materials Studio 6.0, particularly with CASTEP and Dmol3 modules, based on the theory of electron density functional (DFT). The main objective is to find what alloys and that temperatures it these metal hydrides are more efficient to store hydrogen, whose potential use could be in transport. Molecular simulations of Magnesium-Aluminum, Magnesium-Nickel and Magnesium-Zinc alloys, in order to know the temperature dependence where greater adsorption of H2 molecules on the surface (110) of the metal alloy occurs.
The advantage of the use of metal hydrides, in the storage of hydrogen, would radically change the size of the containers and in the same way the level of safety would represent a real alternative.

Keywords: hydrogen storage; metal alloy; temperature dependence; adsorption

1. Introduction

The search for alternative forms of energy that are not derivable from oil sources has led to greater advances in the study of energy sources such as solar, wind, sea waves or hydrogen sources,. Hydrogen is the lightest of all gases, which makes its storage complicated in the gaseous state because it requires huge containers; also is important to consider its high explosiveness, when it reacts with oxygen. There are different studies of metal hydrides, particularly magnesium alloys, such as magnesium-aluminum

(MgAl) [1-3], magnesium-nickel (Mg2Ni) [4, 5] and magnesium-zinc (MgZn) [3]. Magnesium can store about 7.6 wt % [6], however has a low rate of adsorption and a high temperature of adsorption (about 600 K), which makes difficult their use. Magnesium is used in nanostructured form, which significantly decreases the value of the adsorption and desorption temperatures and increases the rates of adsorption and desorption [7-9].

Andreasen A., Bouaricha et al. and Milanese et al. [1-3], have reported that the temperatures of adsorption and desorption decreases when aluminum is added, while the rate of adsorption decreases at the same time. Schlapbach et al. [4] found that the addition of nickel dissociates the hydrogen molecules when nickel is added to magnesium, a phenomenon that improves the adsorption of hydrogen. Saluzki et al. [5] determined that the adsorption temperature occurs at 500 K and a desorption temperature of 600 K.

Different theoretical results have been obtained for magnesium, such as the work of Norskov et al. [7] who computed the energy of activation for the adsorption hydrogen molecule of about 0.5 eV. Liang et al. [8] found that increasing the thickness of films, the enthalpy of formation moves toward the enthalpy of formation of the bulk MgH_2.

2. Materials and Methods

The module DMoL^3 was used to construct a bulk alloy $Mg_{1-x}M_x$, with x=0.10, 0.12, ..., 0.20 and M = Al, Ni or Zn. This module let us build every bulk element of the periodic table, in a unit cell of its structure (Wigner-Seitz cell). The crystal structure of these alloys is hexagonal close packed (hcp), because the concentration of magnesium is greater than the concentration of M. We cleave in the direction of the plane (110), to create a surface of interaction with the hydrogen molecule; this module can cleave the surface, having its Miller indices.

We optimized these crystal structures with a *molecular dynamics* menu at the temperatures indicated previously; we used the thermodynamic ensemble NVT that considers a volume and temperature constant, with a total simulation time step of 0.15 ps. Then we built a supercell that we optimized again at the proposed temperatures, when tha hydrogen molecule was interacting on its surface. Figure 1 shows the supercell of $Mg_{0.88}Ni_{0.12}$ after it was optimized at 400 K.

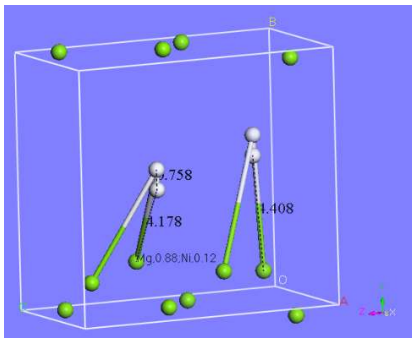

Figure 1. Optimized supercell $Mg_{0.88}Ni_{0.12}$ alloy with hydrogen.

The optimizations carried out for the concentration intervals of 90, 88, ..., 80% weight magnesium yielded the results of the enthalpy of formation on: a) surfaces of $Mg_{1-x}M_x$ (110) without hydrogen, b) supercell (2x1) without hydrogen, and c) supercell (2x1) with hydrogen. These values were used to obtain the chemisorption energy ($\mathbf{\Delta E_{chem}}$) and the repulsion energy ($\mathbf{\Delta E_{rep}}$) of the hydrogen molecule on the surface of the alloy [9, 10].

3. Results and Discussion

The results obtained for enthalpies of these alloys are presented in Fig. 2 showing the chemisorption and repulsion energies of the hydrogen molecule on the surface of the alloy for a concentration of 90 and 88 % Mg as a function of temperature,

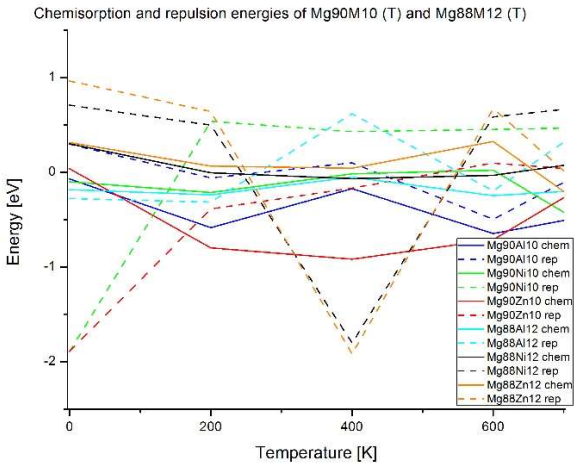

Figure 2. Chemisorption and repulsion of $Mg_{0.90}M_{0.10}$ and $Mg_{0.88}M_{0.88}$ as a function of temperature.

In this figure, $Mg_{0.90}Al_{0.10}$ and $Mg_{0.90}Zn_{0.10}$ are the alloy with the major energies of chemisorption and with small values of repulsion from temperatures between 200 and 700 K. The two alloys are the best for hydrogen storage, when repulsion energy tends to zero.

Fig. 3 show results of energy of $Mg_{0.86}M_{0.14}$ and $Mg_{0.84}M_{0.16}$ for temperatures from 0 to 700 K. In this figure, chemisorption is favored for $Mg_{0.86}Al_{0.14}$, when values of repulsion energies are close to zero.

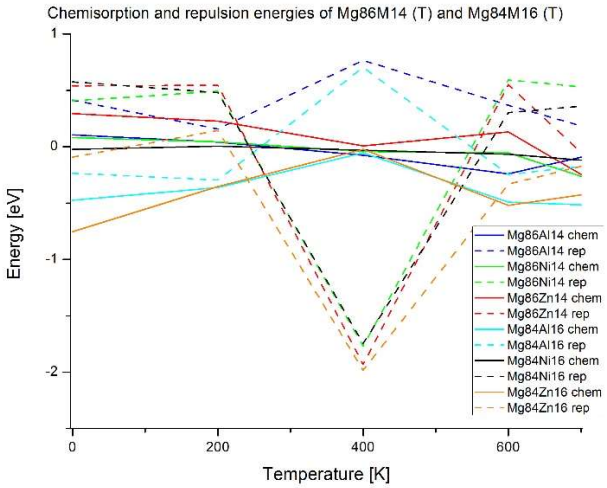

Figure 3. Chemisorption and repulsion of $Mg_{0.86}M_{0.14}$ and $Mg_{0.84}M_{0.16}$ as a function of temperature.

Finally, Figure 4 show the results for chemisorption and repulsion energies of $Mg_{0.82}M_{0.18}$ and $Mg_{0.80}M_{0.20}$ as a function of temperature.

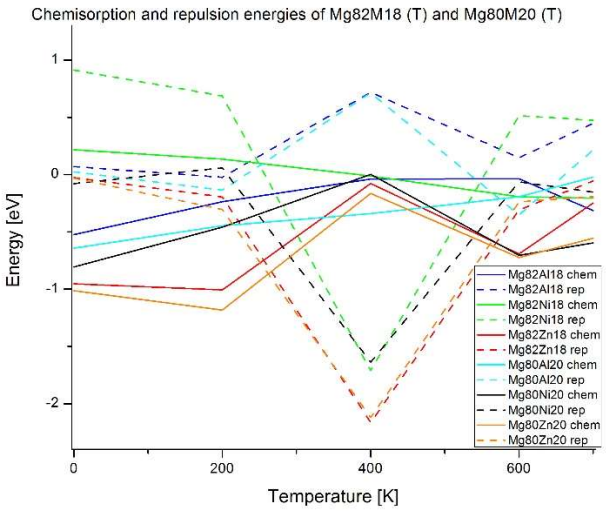

Figure 4. Chemisorption and repulsion of $Mg_{0.82}M_{0.18}$ and $Mg_{0.80}M_{0.20}$ as a function of temperature.

All the alloys, except $Mg_{0.82}Ni_{0.18}$, have good properties for hydrogen storage, but for temperatures before 200 K.

4. Conclusion

The considered alloys improved their capacity of hydrogen storage when the repulsion energy is close to zero. The best alloys for hydrogen storage are $Mg_{0.90}Al_{0.10}$, $Mg_{0.90}Zn_{0.10}$, $Mg_{0.84}Al_{0.16}$, $Mg_{0.82}Al_{0.18}$, and $Mg_{0.80}Al_{0.20}$.

Acknowledgements

G. Ramírez-Dámaso acknowledges the partial support provided by the projects SIP 20181898 and SIP 20190256 by Instituto Politécnico Nacional, MEXICO.

References

[1] Andreasen A., Hydrogenation of Mg-Al alloys. International Journal of Hydrogen Energy 33 (2008) 7489-7497.

[2] Bouaricha S., Dodelet J. P., Guay D., Huot J., Boily S., Schulz R., Simple Metal and Intermetallic Hydrides, J. Alloys Compd. (2000) 297: 282–293.

[3] Milanese C., Girella A., Bruni G., Berbenni V., Cofrancesco P., Marini A., Villa M., Matteazzi P., Hydrogen storage in magnesium–metal mixtures: Reversibility, kinetic aspects and phase analysis, Journal of Alloys and Compounds 465 (2008) 396–405.

[4] Schlapbach L., Seiler A., Stucki F. and Siegmann H. C., Surface effects and the formation of metal hydrides, Journal of the Less-Common Metals, 73 (1980) 145-160

[5] Zaluski L., Zaluska A., Strom-Olsen J. O., Nanocrystalline metal hydrides, Journal of Alloys and Compounds 253–254 (1997) 70–79

[6] Zaluska A., Zaluski L., Strom-Olsen J. O., Nanocrystalline magnesium for hydrogen storage, J. Alloys Comp. (1999) 288: 217–225

[7] Norskov J. K., Houmoller A., Johansson P. K., and Lundqvist B. I., Adsorption and Dissociation of H2 on Mg Surfaces, Phys. Rev. Lett. Vol. 46, No. 4, 257-260, (1981).

[8] Liang J, J. Theoretical insight on tailoring energetics of Mg hydrogen absorption/desorption through nano-engineering, Appl. Phys. A (2005) 80(1): 173–178.

[9] G. Ramírez-Dámaso, I.E. Ramírez-Platón, E. López-Chávez, F.L. Castillo-Alvarado, A. Cruz-Torres, F. Caballero, R. Mondragón-Guzmán, E. Rojas-Hernández, A DFT study of hydrogen storage on surface (110) of Mg1-xAlx ($0 \leq x \leq 0.1$), Int. J. Hydrogen Energy 41 (2016) 23388-23393.

[10] O. Ramírez-Rodríguez, "DEPENDENCIA DE LA TEMPERATURA PARA EL ALMACENAMIENTO DE HIDROGENO EN HIDRUROS METALICOS $Mg_{1-x}M_x$ (M=Al, Ni, Zn, x= 0.00, 0.02,..., 0.20)", Master Degree Thesis, SEPI-ESIA TICOMAN, Instituto Politécnico Nacional, México (2019), in Spanish.